Les glissements sous-marins dans l'estuaire du Saint-Laurent, Québec, Canada

Méril Mérindol

▶ **To cite this version:**

Méril Mérindol. Les glissements sous-marins dans l'estuaire du Saint-Laurent, Québec, Canada. Géophysique [physics.geo-ph]. Université de Bretagne occidentale - Brest; Université du Québec à Rimouski, 2022. Français. NNT : 2022BRES0075 . tel-04099291

HAL Id: tel-04099291
https://theses.hal.science/tel-04099291

Submitted on 16 May 2023

HAL is a multi-disciplinary open access archive for the deposit and dissemination of scientific research documents, whether they are published or not. The documents may come from teaching and research institutions in France or abroad, or from public or private research centers.

L'archive ouverte pluridisciplinaire **HAL**, est destinée au dépôt et à la diffusion de documents scientifiques de niveau recherche, publiés ou non, émanant des établissements d'enseignement et de recherche français ou étrangers, des laboratoires publics ou privés.

THESE DE DOCTORAT EN COTUTELLE INTERNATIONALE DE

L'UNIVERSITE
DE BRETAGNE OCCIDENTALE
ECOLE DOCTORALE N° 598
Sciences de la Mer et du littoral
Spécialité : Géosciences marines

L'UNIVERSITE DE QUEBEC A RIMOUSKI
INSTITUT DES SCIENCES DE LA MER DE RIMOUSKI
Spécialité : Géosciences marines

Par

Méril MÉRINDOL

Les glissements sous-marins dans l'estuaire du Saint-Laurent, Québec, Canada

Thèse présentée et soutenue à Plouzané, le 14 décembre 2022

Unités de recherche : Geo-Ocean UMR6538, Ifremer, CNRS, UBO, UBS, F-29280 Plouzané, France
Laboratoire de géologie marine, ISMER, UQAR, G5L 2Z9 Rimouski, Canada

Rapporteurs avant soutenance :
Nathalie FEUILLET – Professeure, Institut Physique du Globe à Paris, France
Thierry MULDER – Professeur, Université de Bordeaux, France

Composition du Jury :

Président
Jacques DEVERCHÈRE – Professeur, Université de Bretagne Occidentale, France

Examinateurs
Nathalie BABONNEAU – Maître de conférence, Université de Bretagne Occidentale, France
Stéphanie GIRARDCLOS – Chercheure, Université de Genève, Suisse
Nathalie FEUILLET – Professeure, Institut Physique du Globe à Paris, France
Elda MIRAMONTES – Assistante professeure, Bremen, Allemagne
Thierry MULDER – Professeur, Université de Bordeaux, France

Directeurs de thèse
Guillaume ST-ONGE – Professeur, Université du Québec à Rimouski - ISMER, Canada
Nabil SULTAN – Chercheur, Ifremer, France

Invités :

Sébastien GARZIGLIA – Ingénieur de recherche, Ifremer, France
Patrick LAJEUNESSE – Professeur, Université de Laval, Canada

REMERCIEMENTS

ACKNOWLEDGEMENTS

Je tiens à exprimer toute ma gratitude à Nabil Sultan et Guillaume St-Onge pour leur accompagnement tout au long de la réalisation de ma thèse. Vos conseils, votre expertise et votre soutien ont été d'une importance cruciale pour l'aboutissement de ce travail de recherche. Je suis reconnaissant d'avoir eu la chance de travailler sous votre supervision et d'avoir pu bénéficier de votre expérience et de votre savoir.

Je tiens également à remercier Sébastien Garziglia et Patrick Lajeunesse pour leur engagement, leur disponibilité et leur expertise. Vos suggestions et vos encouragements ont été indispensables pour mener à bien cette thèse.

Je souhaite également exprimer ma reconnaissance envers les membres du jury de thèse et les rapporteurs pour leur précieux temps, leur lecture attentive et leurs commentaires constructifs. Vos remarques et suggestions m'ont permis de me projeter dans mes recherches et d'améliorer la qualité de mon travail.

De plus, je remercie Nathalie Babonneau, Pascal Bernatchez et Gueorgui Ratzov pour leur participation aux comités de suivis individuel de thèse. Votre écoute et vos précieux conseils tout au long de la réalisation de ma thèse ont été un soutien précieux dans la progression de mes travaux de recherche.

Enfin, je remercie tous ceux qui m’ont entouré à Rimouski ou/et à Brest, au travail et à l’extérieur, de près ou de loin. Ces trois années ont été marquées par de belles réalisations et vous en avez été des acteurs majeurs.

SOMMAIRE

CONTENTS

Résumé 10
Abstract 11
Liste des figures 13
Liste des tableaux 21

CHAPITRE I - INTRODUCTION
1. Contexte général 25
2. L'estuaire du Saint-Laurent 26
2.1. Géographie et géologie 26
2.2. Dynamiques sédimentaires 27
2.2.1. Sédimentation du Quaternaire 27
2.2.2. Sédimentation actuelle 27
2.3. Sismicité 29
2.3.1. Sismicité historique 29
2.3.2. Origines de la sismicité 29
2.3.3. Impacts des séismes 31
3. Les glissements sous-marins 32
3.1. Le préconditionnement 33
3.2. Le déclenchement 33
3.3. Le développement 35
4. Objectifs et Problématiques 35
5. Déroulement de la thèse 38
6. Communications scientifiques 38
6.1. Publications 38
6.2. Présentations 39
6.3. Contributions des auteurs 39

CHAPITRE I - INTRODUCTION (ENGLISH)
1. General context 40
2. The St. Lawrence Estuary 41
2.1. Geography and Geology 41
2.2. Sedimentary dynamics 42
2.2.1. Quaternary sedimentation 42
2.2.2. Actual sedimentation 42
2.3. Seismicity 44
2.3.1. Historical seismicity 44
2.3.2. Origins of seismicity 45
2.3.3. Impacts of earthquakes 46
3. Submarine landslides 46

3.1. Preconditioning 47
3.2. Triggering 48
3.3. Evolution 49
4. Objectives and issues 49
5. The thesis 52
6. Scientific communications 52
6.1. Publications 52
6.2. Oral presentations 53
6.3. Author contributions 53

CHAPITRE II - MATERIELS ET METHODES

1. Géophysique 57
1.1. Données bathymétriques 57
1.2. Données sismiques 57
2. Carottes sédimentaires 58
2.1. Carottier à boîte – Box Core (BC) 58
2.2. Carottier à gravité – Gravity Core (GC) 59
2.3. Sites d'échantillonnage 59
3. Analyses sédimentaires 60
3.1. CAT-Scan 60
3.2. Multi-Sensor Core Logger (MSCL) 61
3.2.1. Photographie 61
3.2.2. Susceptibilité magnétique 61
3.2.3. Gamma-densité 61
3.2.4. Vitesse des ondes P 61
3.2.5. Réflectance spectrale 61
3.2.6. Fluorescence X (XRF) 62
3.3. Description lithostratigraphique 62
3.4. Granulométrie 62
4. Géochronologie 63
4.1. Datation radiocarbone – 14C AMS 63
4.2. Vitesse de sédimentation – 210Pb 64
5. Mesures géotechniques 65
5.1. Teneur en eau et porosité 65
5.2. Hand shear-vane – ASTM D8121 65
5.3. Essais œdométriques – ASTM D2435 66
5.3.1. Consolidation 66
5.3.2. Compression 67
5.3.3. Perméabilité – ASTM D5084-16a 67
5.4. Essais triaxiaux 68
5.4.1. Essais triaxiaux statiques – ASTM D4767-11 68
5.4.2. Essais triaxiaux cycliques – ASTM D5311/D5311M-13 70

6. Modélisation numérique 71
6.1. Accélérogramme 71
6.2. Atténuation du PGA 71
6.3. Détermination du Factor of Safety (FoS) 72
6.4. OpenSees 73
6.4.1. Modèles de comportement 73
6.4.2. Sensibilité du modèle 74
6.4.3. Détermination des paramètres d'entrée 76

CHAPITRE III - PALEO-SISMICITE (ENGLISH)
1. Introduction 81
2. Regional setting 82
2.1. The St. Lawrence Estuary (Eastern Canada) 82
2.2. Quaternary sedimentation 85
2.3. Regional seismicity and sediment liquefaction 85
3. Data and methods 86
3.1. Geophysics 86
3.2. Core sampling 87
3.3. Sedimentological analysed 88
3.4. Dating 91
4. Results 91
4.1. Facies identification 91
4.2. Age of the RDLs 95
4.2.1. Baie-Comeau 95
4.2.2. Betsiamites-Rimouski 95
4.2.3. Forestville 95
4.2.4. Saguenay 96
4.2.5. La Malbaie 97
4.3. Correlation with seismic data 97
5. Discussion 99
5.1. Relationship between submarine landslides and rapidly deposited layers (RDL) 99
5.2. Chronology of the RDLs and triggering factors 100
5.3. Relative importance of the 1663 CE event 102
6. Conclusion 103

CHAPITRE IV - EPICENTRE DU SEISME DE 1663 CE (ENGLISH)
1. Introduction 109
2. Background 110
2.1. Regional seismicity 110
2.2. Liquefaction process 111
2.3. Evidence of liquefaction 112
3. Methods 112
3.1. Sedimentary and geotechnical analyses 112

3.1.1. Sediment cores ... 112
3.1.2. Cyclic triaxial testing ... 113
3.2. Methods used for liquefaction calculation ... 114
3.2.1. Accelerogram ... 114
3.2.2. Attenuation of PGA ... 114
3.2.3. Factor of Safety calculation using equivalent number of uniform stress cycles (ENUSC) ... 115
3.2.4. Opensees with the PDMY02 constitutive soil model ... 116
4. Results ... 117
4.1. Seismostratigraphic analysis ... 117
4.2. Cyclic triaxial tests and liquefaction potential ... 120
4.3. Working hypothesis: slope failure development ... 122
4.4. Determination of the source-to-site distance through the ENUSC method ... 123
4.5. Source-to-site distance using OpenSees ... 125
4.5.1. Determination of model parameters ... 125
4.5.2. Calibration of model parameters ... 126
4.5.3. Liquefaction prediction using OpenSees ... 127
5. Discussion ... 128
5.1. Predicted liquefaction compared to observed earthquake-triggered submarine landslides ... 128
5.2. Comparison between ENUSC and OpenSees methods ... 129
5.3. The 1663 epicenter location ... 131
5.4. Limitations of the approach ... 132
6. Conclusion ... 133

CHAPITRE V - STABILITE DES PENTES (ENGLISH)
1. Introduction ... 139
2. Data and methods ... 140
2.1. Geophysics ... 140
2.2. Sedimentary and geotechnical analyses ... 141
2.2.1. Sediment cores ... 141
2.2.2. Cyclic triaxial testing ... 141
2.3. Numerical modeling ... 141
2.3.1. Accelerogram and PGA attenuation ... 142
2.3.2. Constitutive soil model ... 143
2.3.3. Slope modeling ... 144
3. Results ... 146
3.1. Seismostratigraphic analysis ... 146
3.2. Slope stability 2D ... 147
3.3. Slope stability 1D ... 148
3.3.1. Scenarios of destabilization ... 148
3.3.2. Thickness of sediment destabilized ... 150
4. Discussion ... 151
4.1. Predicted geomorphology after submarine landslide ... 151

4.2. Weak layers and retrogressive failure 152
4.3. Geohazard approach 152
5. Conclusion 155

CHAPITRE VI - CONCLUSION
1. Paléo-sismologie 161
2. Liquéfaction et instabilités gravitaires 162
3. Evaluation de la stabilité des pentes actuelles 163
4. Perspectives des travaux 164
4.1. Matériel sédimentaire disponible 164
4.2. Paléoclimat – « red bed » 164
4.3. Glissements sous-marins non datés 165
4.4. Activité de la faille de Tadoussac 165
4.5. Calculs de stabilité de pente 166
4.6. Glissement sous-marin tsunamigénique ? 167

CHAPITRE VI - CONCLUSION (ENGLISH)
1. Paleoseismology 168
2. Liquefaction and gravity instabilities 169
3. Evaluation of current slope stability 170
4. Perspectives of the work 171
4.1. Available sedimentary material 171
4.2. Paleoclimate – “red bed” 171
4.3. Undated submarine landslides 172
4.4. Activity of the Tadoussac fault 172
4.5. Slope stability calculations 172
4.6. Tsunamogenic submarine landslide? 173

Bibliographie 175
Annexes 187

RESUME : LES GLISSEMENTS SOUS-MARINS DANS L'ESTUAIRE DU SAINT-LAURENT, QUEBEC, CANADA

L'estuaire du Saint-Laurent, situé dans la province du Québec au sud-est du Canada, abrite près d'une centaine de glissements sous-marins. Leur présence dans cette région avec un haut niveau d'aléa sismique a conduit à supposer qu'ils ont été déclenchés par la sismicité régionale. Le présent projet de doctorat a donc pour objectif de comprendre l'origine de ces glissements sous-marins. Le projet utilise une grande quantité de données géophysiques (bathymétrie, profils sismiques), sédimentologiques (carottages, images X-Ray, descriptions, rapports XRF, propriétés physiques MSCL, granulométrie), d'âges (^{14}C, ^{210}Pb) et géotechniques (essais triaxiaux) qui sont intégrées dans des modèles numériques.

Les glissements sous-marins de l'estuaire du Saint-Laurent ont des âges synchrones sur près de 220 km et sont corrélés aux séismes historiques majeurs : 1663 CE ($M \geq 7$), 1860/1870 CE (M = 6,1/6,6), 1925 CE (M = 6,1) et 1988 (M = 5,9). Ainsi, seule la sismicité peut les avoir déclenchés. L'établissement de cette relation permet d'identifier deux évènements sismiques antérieurs à la colonisation européenne en ~645 CE et ~1145 CE. De plus, le séisme de 1663 CE ressort comme l'évènement majeur des derniers 2000 ans car il a déclenché le plus de glissements sous-marins. Son épicentre positionné dans la région de Charlevoix n'avait pas été révisé depuis près d'un siècle. A partir des glissements sous-marins déclenchés par la liquéfaction du sédiment, l'épicentre du séisme de 1663 CE a pu être repositionné à plus de 120 km au nord-est de sa position initiale. Ainsi, il serait associé à une faille active au large de la ville de Tadoussac, proche de l'embouchure du fjord du Saguenay. Enfin, les plans de rupture des glissements sous-marins se développent aux interfaces d'unités sédimentaires qui correspondent à des transitions d'environnement de dépôt. L'intégration de ces niveaux de décollement dans des modèles numériques permettent de prédire les zones qui en cas de séisme majeur glisseront.

En conclusion, la sismicité est le facteur déclencheur de glissements sous-marins dans l'estuaire du Saint-Laurent et cela s'explique par la liquéfaction de niveaux grossiers (silt à sable) générée par les secousses sismiques. De futurs glissements sous-marins sont susceptibles de se produire soulignant la nécessité d'étudier cet aléa naturel au Québec.

ABSTRACT: SUBMARINE LANDSLIDES IN THE ST. LAWRENCE ESTUARY, QUÉBEC, CANADA

The St. Lawrence Estuary, located in the province of Québec in southeastern Canada, is home to almost one hundred submarine landslides. Their presence in this region of high seismic hazard has led to the assumption that they were triggered by regional seismicity. The aim of this PhD project is to understand the origin of these submarine landslides. The project comprises a huge amount of geophysical (bathymetry, seismic profiles), sedimentological (coring, X-Ray images, descriptions, XRF ratios, MSCL physical properties, grain size), age (^{14}C, ^{210}Pb) and geotechnical (triaxial tests) datas which are integrated into numerical simulations.

Submarine landslides in the St. Lawrence Estuary have synchronous ages over 220 km and are correlated with major historical earthquakes: 1663 CE ($M \geq 7$), 1860/1870 CE ($M = 6.1/6.6$), 1925 CE ($M = 6.1$) and 1988 ($M = 5.9$). Thus, only seismicity can have triggered them. Establishing this relationship allows us to identify two seismic events prior to European colonization around 645 CE and 1145 CE. Moreover, the 1663 CE earthquake appears to be the major event of the least 2000 years because it triggered the greatest number of submarine landslides. Its epicenter located in the Charlevoix region had not been revised for almost century. Using submarine landslides triggered by sediment liquefaction, the epicenter of the 1663 CE earthquake could be repositioned more than 120 km northeast of its originally presumed position. Thus, it could be associated with an active fault off the city of Tadoussac, near the mouth of the Saguenay Fjord. Finally, submarine landslide failure planes develop at interfaces of sedimentary units that correspond to depositional environment transitions. The integration of these levels of detachment in numerical models allows the prediction of areas that will slip in the future, in the case of a major earthquake.

In summary, seismicity is the triggering factor for submarine landslides in the St. Lawrence Estuary and this is due to the liquefaction of coarse levels (silt to sand) generated by seismic shaking. Submarine landslides are likely to occur in the future, hence the need to study this natural hazard in Québec.

LISTE DES FIGURES

LIST OF FIGURES

CHAPITRE I - INTRODUCTION

Figure 1-1. Carte d'accélération maximale du sol dans un terrain ferme pour une probabilité de 2%/50 ans. La zone de CKBSL qui représente un haut niveau d'aléa est délimitée en noir (modifiée d'après Locat, 2011). 25

Figure 1-2. Carte géologique simplifiée de la région du Saint-Laurent (modifié d'après Mazzotti *et al.*, 2005). Les ellipses en pointillés correspondent à des zones sismiques actives (CSZ : zone de Charlevoix-Kamouraska, LSZ : zone du Bas Saint-Laurent). 26

Figure 1-3. Carte bathymétrique de l'estuaire du Saint-Laurent. En bleu sont reportés les mass-transport-complexes et en rouge les séismes historiques majeurs (< 400 ans). CKSZ : Charlevoix-Kamouraska Seismic Zone. 30

Figure 1-4. Schéma d'un glissement sous-marin (modifié d'après Hampton *et al.*, 1996). 32

Figure 1-5. Schéma du développement d'un glissement sous-marin de la rupture à son produit final qui correspond à un dépôt turbiditique (modifiée d'après Bryn *et al.*, 2005). 36

CHAPITRE I - INTRODUCTION (ENGLISH)

Figure 1-1. Map of peak ground acceleration in firm ground for a 2%/50-years probability. The area of CKBSL that represents a high level of hazard corresponds to the black square (modified from Locat, 2011). 40

Figure 1-2. Simplified geological map of the St. Lawrence region (modified from Mazzotti *et al*., 2005). Dotted ellipses correspond to seismically active zones (CSZ: Charlevoix-Kamouraska zone, LSZ: Lower St. Lawrence zone). 41

Figure 1-3. Bathymetric map of the St. Lawrence Estuary. Dark blue areas indicate the mass-transport complexes and red circles indicate major historical earthquakes (< 400 years). CKSZ: Charlevoix-Kamouraska Seismic Zone. 44

Figure 1-4. Schematic of a submarine landslide (modified from Hampton *et al.*, 1996). 47

Figure 1-5. Schematic of the development of a submarine landslide from rupture to its final product: a turbidite deposit (modified from Bryn *et al.*, 2005). 50

CHAPITRE II - MATERIELS ET METHODES

Figure 2-1. Glissements dans la région de Baie-Comeau. Haut : bathymétrie bruitée ; Bas : après traitement. 57

Figure 2-2. Profil sismique acquis dans la région de Baie-Comeau. Transversal a un glissement sous-marin, il permet d'identifier le sédiment intact (non-glissé) où la séquence sédimentaire quaternaire est identifiable au-dessus du socle, la cicatrice et les dépôts en contrebas (en rouge). Les flèches rouges indiquent le sens du transport sédimentaire. 58

Figure 2-3. Déploiement du carottier à boîte sur le pont du N/R Coriolis II lors de la mission SLIDE-2020. 58

Figure 2-4. Déploiement du carottier à gravité sur le pont du N/R Coriolis II lors de la mission SLIDE-2020. 59

Figure 2-5. Carte de l'estuaire du Saint-Laurent avec les sites de carottage. En gris les carottes à boîtes et en rouge les carottes à gravité. 59

Figure 2-6. GEOTEK MSCL-XCT du laboratoire de géologie marine de l'ISMER 60

Figure 2-7. MSCL GEOTECK du laboratoire de géologie marine de l'ISMER. Sont montés en lignes de droite à gauche : l'appareil photo, la source gamma, les transducteurs des ondes P, le senseur MS2E1 de Bartington, le XRF et le spectrocolorimètre. 61

Figure 2-8. Planche de résultats des analyses sédimentologiques menées sur la carotte COR20-02-04GC. De gauche à droite : imagerie rayons-X, photo, granulométrie, description, densité gamma, susceptibilité magnétique, L*, Zr/Rb (proxy granulométrie) et Ca/Fe (proxy détritisme). Ces données ont permis d'identifier une turbidite d'une épaisseur de 11,5 cm à 66,5 cm de profondeur. 63

Figure 2-9. Compteur gamma GMX50-S d'Ortec dans le laboratoire sous-terrain de la station aquicole (ISMER). 64

Figure 2-10. Méthode pour calculer une vitesse de sédimentation à partir de la décroissance radioactive du ^{210}Pb. Les premiers centimètres bioturbés sont exclus. 64

Figure 2-11. Hand shear-vane utilisé pour mesurer de la résistance au cisaillement non-drainé des argiles. 65

Figure 2-12. Sections de carottes entières destinées aux mesures géotechniques. 65

Figure 2-13. Photo du dispositif des essais œdométriques et de perméabilité au laboratoire de l'Ifremer. 66

Figure 2-14. Courbe de consolidation de l'essai œdométrique COR20-02-25GC à 3.97-3.99 m de profondeur pour le palier de charge 4 kg soit ~ 220 kPa. 67

Figure 2-15. Résultat de l'essai œdométrique COR20-02-25GC à 3.97 – 3.99 m de profondeur. 67

Figure 2-16. Perméabilité mesurée pour les différents chargements lors de l'essai œdométrique COR20-02-25GC à 3.97 – 3.99 m de profondeur. 68

Figure 2-17. Cellule triaxiale du laboratoire géotechnique d'Ifremer. 68

Figure 2-18. Mise en place de l'échantillon dans sa membrane, sur son socle et dans la cellule triaxiale. 69

Figure 2-19. Détermination de l'angle de frottement interne effectif, φ', et de la cohésion effective, c', à partir de la méthode des Cercles de Mohr. Ici, les cercles sont tracés à partir des essais triaxiaux statiques menés sur les échantillons 02GC, 06 GC et 10 GC. 69

Figure 2-20. Photo après la liquéfaction de l'échantillon COR20-02-02GC (3.75-3.85 m). La base, plus silteuse comme le montre la granulométrie, est la zone de liquéfaction. 71

Figure 2-21. Accélérogramme du séisme de 1988 enregistré à la station de St-Ferreol (Québec). Le pic de l'accélération (PGA) radiale mesuré est de 0,12 g à 14 secondes. 71

Figure 2-22. Diagramme du nombre de cycles pour atteindre la liquéfaction en fonction de la distance à l'épicentre et de la magnitude du séisme (Liu *et al.*, 2001). 71

Figure 2-23. Distribution des PGA de séismes ayant eu dans l'est du Canada. En rouge la loi de Pezeshk *et al.* (2018) pour des magnitudes de 4.6 et 5.9 et une erreur de ± 1 σ. 72
Figure 2-24. Schéma du modèle PDMY02 montrant (a) la réponse de la contrainte octaédrique τ avec la contrainte effective p' et (b) la réponse de la contrainte octaédrique τ avec la déformation octaédrique γ Yang *et al.*, 2003). 73
Figure 2-25. Analyse paramétrique du modèle PDMY02 dans OpenSees. La sensibilité du modèle a été testée pour les paramètres *G* et *B*. Les flèches noires et leur longueur indiquent l'influence des variations des paramètres. 74
Figure 2-26. Analyse paramétrique du modèle PDMY02 dans OpenSees. La sensibilité du modèle a été testée pour les paramètres c_1, c_3, d_1, d_3, Φ_{PT} et Φ'. Les flèches noires et leur longueur indiquent l'influence des variations des paramètres. 74

CHAPITRE III - PALEO-SISMICITE (ENGLISH)

Figure 3-1. Bathymetric map of the St-Lawrence Estuary and location of significant East Canadian Earthquakes of the period 1663-2005 (red circles) from Lamontagne *et al.* (2018). Dark blue areas indicate the mass-transport complexes mapped by Pinet *et al.* (2015). CKSZ corresponds of the Charlevoix-Kamouraska Seismic Zone. 82
Figure 3-2. Bathymetric maps of the Betsiamites – Baie Comeau – Rimouski a), of the Forestville – Saguenay b) and of the Charlevoix sectors c). The gravity and box cores are respectively represented by red and white circles. The black lines correspond to track lines of the acoustic sub-bottom profiler survey. 83
Figure 3-3. a) Seismic profile RIM_1T (see **Figure 3-1** for the locations) on which reflectors R5 and R6 corresponds respectively to turbidites T2 and T1 in core COR20-02-03GC. b) Seismic profile RIM_1A, transversal to the Betsiamites lobe in the Laurentian Channel. Labels U3 to U5 refer to seismic units and R1 to R5 to seismic horizons described by Cauchon-Voyer *et al.*, (2008). The black square is a close-up view of R5. Reflector R5 correlates with turbidite T1 in the core 20-02-04GC. c) Seismic profile BET_B_2T with R5 and R6 reflectors (cf. detailed view in the black square) which correspond to turbidites T3 and T2 in COR20-02-18GC. d) Southern part of seismic profile BET_D_2T. Core COR20-02-19GC reaches reflectors R6 and R5 at ~ 0.5 mbsf and ~ 1.2 mbsf, which are respectively interpreted as turbidites T1 and T2. See supplementary data for uninterpreted seismic profiles. 87
Figure 3-4. a) Seismic profile BET_D_3T in the Betsiamites area (see **Figure 3-1** for the locations). The reflector R6 reached by core COR07-03-11PC, corresponds to turbidite T1 or T2 dated around 1845-1865 CE. b) Seismic profile FOR_A_1T. Turbidite T1 in COR20-02-20GC corresponds to R5. c) Seismic profile ESC_BCD_1T. Reflector R5 (cf. detailed view in the black square) correlates with turbidite T1 sampled in core COR20-02-21GC. See supplementary data for the uninterpreted seismic profiles. d) The seismic profile SAG_H_1T with reflector R5 at the toe of a mass transport deposit. It corresponds to turbidites T2 or T3 observed in core COR20-02-26GC. See supplementary data for the uninterpreted seismic profiles. 88

Figure 3-5. Results of the sedimentological analyses carried out on cores a) COR20-02-04GC and b) COR20-02-26GC. From left to right: X-ray image, digital photography, sedimentological description, γ-density, magnetic susceptibility *k*, lightness *L**, Zr/Rb and Ca/Fe. 89

Figure 3-6. Results of the sedimentological analyses carried out on cores a) COR20-02-29GC and b) COR20-02-50GC. From left to right: X-ray image, digital photography, sedimentological description, γ-density, magnetic susceptibility *k*, lightness *L**, Zr/Rb and Ca/Fe. 90

Figure 3-7. Age models for cores COR20-02-03GC a), COR20-02-04GC b), COR20-02-20GC c) and COR20-02-21GC d). The hemipelagic depth, i.e., depth excluding RDLs, is plotted as a function of calibrated ages (BP and CE/BCE). The black circles correspond to the dated samples and the red crosses to the turbidites. The age probability of 2 σ and that of 1 σ, are respectively shown in light and medium gray tone. 93

Figure 3-8. Sedimentation rates (SR) calculated with the ^{210}Pb activity in cores COR20-02-18BC-A (SR = 0.32 cm.yr^{-1}, a), COR20-02-20BC-B (SR = 0.15 cm.yr^{-1}, b), COR20-02-26BC-A (SR = 0.42 cm.yr^{-1}, c) and COR20-02-28BC-B (SR = 0.37 cm.yr^{-1}, d). SR are calculated from the slope of Ln (^{210}Pb$_{excess}$) in the radioactive zone by excluding the biological mixing. 96

Figure 3-9. Chronology of the RDLs (turbidites and debrites) dated by ^{14}C (colored diamonds) and ^{210}Pb (colored circles). The black triangles correspond to evidences provided by previous studies of aerial or submarine landslides in Québec (Doig, 1990, Filion *et al.*, 1990, St-Onge *et al.*, 2004, Cauchon-Voyer *et al.*, 2008, Locat *et al.*, 2016). The gray intervals highlight periods of synchronous RDLs. The black arrows show the distance of synchronous submarine landslides for each period. The yellow stars indicate the timing of major historical earthquakes with their magnitude. To the right, the range of reflectors R5 (blue) and R6 (gray) considering a statistical error of ± 1 σ and ± 2 σ. 100

CHAPITRE IV - EPICENTRE DU SEISME DE 1663 CE (ENGLISH)

Figure 4-1. Bathymetric map of the St. Lawrence Estuary. The studied mass-transport complexes (MTC) are indicated in blue. Red lines indicate seismic profiles crossing the MTCs and used in this study. The black squares and triangle indicate the locations of the epicenter of the 1663 CE earthquake proposed by Pinet *et al.* (2021) and Locat (2011) respectively. The area of the 1663 CE epicenter proposed by Tuttle and Atkinson (2010) coincides with the Charlevoix-Kamouraska Seismic Zone (CKSZ) and is indicated with a gray dashed line. 109

Figure 4-2. Evolution of the peak ground acceleration for the instrumented earthquakes of New-Hampshire (M 4.7), Val-des-Bois (M 5.0), Miramichi (M 5.4) and Saguenay (M 5.9) versus the distance predicted by the Ground-Motion Prediction Equations for central and eastern North America (Pezeshk *et al.*, 2018). The colored line corresponds to the mean PGA. The dark tone and the light gray, correspond to the standard deviation of the GMPE for CENA to within ± 0.5 σ and ± 1 σ, respectively. The instrumented earthquakes follow the proposed PGA-distance relationship by Pezeshk *et al.* (2018). 116

Figure 4-3. Seismic profiles acquired in the Baie-Comeau (A), Betsiamites (B and C), Rimouski (D), Tadoussac (E) and Charlevoix (F) areas (see **Figure 4-1** for the locations). Labels U1 to U5 refer to seismic units and R1 to R2 to seismic horizons described by Cauchon-Voyer *et al.* (2008) and the black line to the bedrock. The red squares correspond to the reference sedimentary columns considered in the liquefaction calculation and shown as lithostratigraphic logs to the right. 119

Figure 4-4. Grain size profile (D_{50}) and photograph of the cyclically sheared sample (core COR20-02-12GC at a depth of 4.47-4.57 m). The highest observed strain corresponds to a localized liquefaction of the silty layer. 121

Figure 4-5. Results from cyclic triaxial test carried on core COR20-02-12GC at depth of 4.47 – 4.57 m. A) shows the effective stress path followed during the test in terms of CRR and normalized mean effective stress. B) shows the CRR versus the shear strain with stress path. The strain path corresponds to loops that gradually move towards the zero CRR. C) depicts a trend with a number of cycles of cyclically induced pore pressure, normalized to σ'_3. $r_u > 0.95$ after 15 cycles. D) shear strain response to cyclic loading. It reaches 6% double amplitude after 31 cycles. 121

Figure 4-6. CRR versus number of cycles to liquefaction obtained from undrained triaxial cyclic tests on 15 samples from the St. Lawrence Estuary. The black line shows the global trend with CRR min and max values of ± 0.04 σ. The green line shows the trend of the two tests carried out on core COR20-02-45GC which sample the base of seismic Unit 4. 122

Figure 4-7. Slope failure and liquefaction hypotheses established from the interpretation of seismic profiles and the dating of submarine landslides. The "superficial slip surface" hypothesis (green) considers liquefaction of the superficial layer at the interface between seismic Units 4 and 5. This hypothesis explains the presence of debris flow deposits and turbidite that overlie old mass-transport deposits. The "deep-slip surface" hypothesis (red) considers that liquefaction at the interface between seismic Units 3 and 4 would be at the origin of major landslides. 123

Figure 4-8. Evolution of the bulk density measured and interpolated as a function of depth (black curve) for the areas of Baie-Comeau (A), Betsiamites (B and C), Rimouski (D), Tadoussac (E) and Charlevoix (F). The interpolation is based on the lithostratigraphic logs presented in **Figure 4-3**. The depths of the layers where liquefaction potentially occurred are shown by gray dashed lines. The evolution of calculated FoS for different peak ground acceleration (PGA) is shown by the red, green and blue curves. 124

Figure 4-9. Calibration of model parameters for core COR20-02-12GC at 4.47 – 4.57 m (A) and COR20-02-45GC at 2.13 – 2.23 m (B). Experimental data in black and modeling results in red. 126

Figure 4-10. Results of OpenSees calculations carried out on the reference sedimentary column at the Baie-Comeau area (seismic and log lithostratigraphique) for a PGA of 0.270 g (blue curves, FoS ≤ 1) and for PGA < 0.270 g (gray curves, FoS ≥ 1). The profiles of normalized excess pore pressure, r_u, and effective stress, σ'_i, show maximum values at depths of 1.5 m and 19 m. The displacement induced by the earthquake is around 7 m for the layers above 19 m suggesting a slope failure at 19 m depth. 127

Figure 4-11. Determination of the possible epicentral region of the 1663 CE earthquake from the ENUSC method considering + 0.5 σ and + 1.0 σ statistical errors of GMPE for CENA and both working hypotheses (**Figure 4-7**). The yellow areas or the yellow stars show the convergence zone(s). The stars indicate the center of the ellipsoids. 130

Figure 4-12. Determination of the possible epicentral region of the 1663 CE earthquake from the OpenSees method considering + 0.5 σ and + 1.0 σ statistical errors of GMPE for CENA and both testing hypotheses (**Figure 4-7**). The areas or the yellow stars show the convergence zone(s). 130

Figure 4-13. The two regions of the possible epicenter of the 1663 CE earthquake based on the study of sediment liquefaction in the St. Lawrence Estuary. The yellow star indicates the location of the point of convergence calculated with the OpenSees method. This site is located ~ 30 km from the Tadoussac fault mapped by Normandeau *et al.* (2015) and Pinet *et al.* (2021) (cf. detailed view in the black square). This scenario seems to be the most probable because is included in the "southwest zone", near the Charlevoix-Kamouraska Seismic Zone (CKSZ) and close to this Holocene active fault. 132

CHAPITRE V - STABILITE DES PENTES (ENGLISH)

Figure 5-1. Bathymetric map of the St. Lawrence Estuary. The studied mass-transport complexes (MTCs) are indicated green: (A) Rimouski, (B) Baie-Comeau, (C) Betsiamites II, (D) Betsiamites I, (E) Tadoussac and (F) Charlevoix. The yellow star indicates the epicenter of the 1663 CE earthquake, relocated on an active fault near Tadoussac (Mérindol *et al.*, 2022b). 139

Figure 5-2. Upper panel: seismic profiles acquired in the Baie-Comeau and Betsiamites (II) areas. Middle panel: schematic geometry. The red rectangles correspond to the sedimentary columns considered in the numerical simulations and are shown as lithostratigraphic logs in the lower panel. 142

Figure 5-3. Upper panel: seismic profiles acquired in the Betsiamites (I) and Rimouski areas. Middle panel: schematic geometry. The red rectangles correspond to the sedimentary columns considered in the numerical simulations and are shown as lithostratigraphic logs in the lower panel. 143

Figure 5-4. Upper panel: seismic profiles acquired in the Tadoussac and Charlevoix areas. Middle panel: schematic geometry. The red rectangles correspond to the sedimentary columns considered in the numerical simulations and are shown as lithostratigraphic logs in the lower panel. 144

Figure 5-5. Peak ground acceleration versus distance predicted by the Ground-Motion Prediction Equations for central and eastern North America (Pezeshk *et al.*, 2018). The three earthquakes (M 7.0, M 7.7 and M 8.4) were used in numerical simulations and correspond to the 1663 CE earthquake (M 7.7 ± 0.7). The distances between the 1663 CE epicenter (Mérindol *et al.*, 2022b) and each area are reported in blue. Below, is the accelerograms of the 1988 CE earthquake (Saguenay, Québec). 146

Figure 5-6. Modelling steps: (A) simplification (in black) of bathymetric profile (in red); (B) definition of layer geometry and materials properties (four sedimentary layers and the bedrock in gray); (C) creation of free-field columns, definition of the lysmer dashpot (red circle) and generation of the mesh; the red points

correspond to the nodes; (D) definition of the boundaries conditions including impeded for vertical displacements at the base of the model (Δz) and the absence of excess pore pressure (R_u) along the top. 147
Figure 5-7. Results of the numerical simulation for Baie-Comeau (A), Betsiamites II and I (respectively B and C), Rimouski (D), Tadoussac (E) and Charlevoix (F) areas. From top to bottom: columns A, B and C. The evolution of excess pore pressure (R_u), first effective stress invariant (σ'_i) and displacement is shown in three separate graphs. The value of the slope gradient is expressed by α in percent. 150
Figure 5-8. Interpretation of the post-earthquake morphology of submarine slopes for each area: Baie-Comeau (A), Betsiamites II and I (respectively B and C), Rimouski (D), Tadoussac (E) and Charlevoix (F). The dashed lines indicate the present day slope. For the different scenarios, liquefaction is predicted to occur where the yellow stars are plotted. The thickness of sediments above potential failure surfaces is shown in blue. 154
Figure 5-9. Synthesis of mass transport complexes which can be generated in the St Lauwrence Estuary by an earthquake similar to the 1663 CE event (in green). The surrounding graphs indicate the liquefaction potential in terms of distance and earthquake magnitude for each site. The red line is the limit of the liquefaction of silty-sandy layers. The black line shows the liquefaction of the interface between Units 3 and 4. 155

CHAPITRE VI - CONCLUSION
Figure 6-1. Identification et datation de RDLs dans une carotte prélevée dans le lac Témiscouata (Québec, Canada) par Lajeunesse *et al.*, 2017. La coulée de débris à ~1,30 m datée à 1280 cal BP, i.e., ~ 670 CE serait associée à une séisme régional majeur. 161
Figure 6-2. Propriétés physico-chimiques de la carotte COR20-02-24GC. De gauche à droite : photo, densité, a* et rapport Zr/Rb. Le « red bed » correspond à la zone en rouge entre 85 cm et 185 cm. 165
Figure 6-3. Image bathymétrique des glissements sous-marins qui s'organisent le long de la faille de Tadoussac. 166
Figure 6-4. A) Modélisation de la pente de Baie-Comeau. B) Implémentation des différentes couches sédimentaires (unités 3 à 5 et le socle) avec leurs caractéristiques géomécaniques. 167

CHAPITRE VI - CONCLUSION (ENGLISH)
Figure 6-5. Identification and dating of RDLs in a core sampled from Lake Temiscouata (Quebec, Canada) by Lajeunesse *et al.*, 2017. The debris flow at ~1.30 m dated to 1280 cal BP, i.e., ~ 670 CE could be associated with a major regional earthquake. 168
Figure 6-6. Physico-chemical properties of core COR20-02-24GC. From left to right: photo, density, a* and Zr/Rb ratio. The "red bed" corresponds to the red layer between 85 cm and 185 cm. 171
Figure 6-7. Bathymetric image of the submarine slides along the Tadoussac fault. 172
Figure 6-8. A) Modeling of the Baie-Comeau slope. B) Integration of the different sedimentary layers (seismic units 3 to 5 and the basement) with their geomechanical characteristics. 173

LISTE DES TABLEAUX

LIST OF TABLES

CHAPITRE I - INTRODUCTION

Tableau 1-1. Caractéristiques et âges des unités sismiques composant la séquence quaternaire. R renvoie aux réflecteurs internes, G à la géométrie des réflecteurs, A à l'amplitude et U aux caractéristiques de la transition supérieure des unités (complété d'après Cauchon-Voyer *et al.*, 2008 et Duchesne *et al.*, 2010). 28

Tableau 1-2. Synthèse des causes d'initiation des glissements gravitaires (modifié d'après Hampton *et al.*, 1996). 34

CHAPITRE I - INTRODUCTION (ENGLISH)

Table 1-1. Characteristics and ages of the seismic units composing the Quaternary sequence. R refers to internal reflectors, G to reflector geometry, A to amplitude, and U to characteristics of the upper transition of units (completed according to Cauchon-Voyer *et al.*, 2008 and Duchesne *et al.*, 2010). 43

Table 1-2. Summary of causes of landslide triggering (modified from Hampton *et al.*, 1996). 48

CHAPITRE II - MATERIELS ET METHODES

Tableau 2-1. Liste des essais œdométriques réalisés. 66

Tableau 2-2. Liste des essais triaxiaux statiques menés. 68

Tableau 2-3. Synthèse des essais cycliques triaxiaux menés. 70

Tableau 2-4. Paramètres du modèle PDMY02. 73

Tableau 2-5. Paramètres du modèle PIMY. 74

CHAPITRE III - PALEO-SISMICITE (ENGLISH)

Table 3-1. Location and length of the studied cores. 84

Table 3-2. Radiocarbon analyses from cores recovered in the St. Lawrence Estuary (Québec). 92

Table 3-3. Sedimentation rates calculated and used in this study. 97

Table 3-4. Age ^{14}C (CE/BCE) of turbidites, hyperpycnites and debrites identified in the 15 cores used in this study (see supplementary data for all age models and sedimentological analyses of all cores). 98

Table 3-5. List of major historical earthquakes in the St. Lawrence Estuary (from Lamontagne *et al.*, 2018). 102

CHAPITRE IV - EPICENTRE DU SEISME DE 1663 CE (ENGLISH)

Table 4-1. Location, length and water depth of studied cores. 113

Table 4-2. Coefficients for the Empirical-Scaling Approach (M > 6) and for the Stochastic-Scaling Approach determined by Pezeshk *et al.* (2018). 115

Table 4-3. PDMY02 parameters for silt and sand layers. 117

Table 4-4. PIMY parameters for clay layers. 117

Table 4-5. Results from the cyclic triaxial tests carried out on samples from SLIDE-2020 cores. 120

Table 4-6. Summary of the distances required to liquefy sediment in the six distinct study areas from the ENUSC method compared to the historical reference location of the EQ1663. 125

Table 4-7. Summary of the distances required to liquefy sediment in the six distinct study areas from the numerical simulation method compared to the initial location of the 1663 CE epicenter. 128

CHAPITRE V - STABILITE DES PENTES (ENGLISH)

Table 5-1. Location, length and water depth of studied cores. 145

Table 5-2. Heights destabilized for each scenario in the six MTC areas. 151

CHAPITRE I – INTRODUCTION

CHAPTER I – INTRODUCTION

L’estuaire du Saint-Laurent, NASA Worldview, 17 avril 2022
The St. Lawrence Estuary, NASA Worldview, april 17, 2022

CHAPITRE 1. RÉSUMÉ

CHAPTER 1. ABSTRACT

Ce projet de doctorat est une coopération scientifique internationale entre deux pôles d'excellence de la recherche en océanographie. En cotutelle, il a été encadré par Guillaume St-Onge, directeur de l'Institut des sciences de la mer de Rimouski (ISMER) et détenteur de la Chaire de recherche du Canada en géologie marine (niveau I), et par Nabil Sultan, chercheur à l'Ifremer au Laboratoire des ALéas MArins (ALMA) de l'UMR Geo-Ocean. De plus, il a été co-encadré par : Sébastien Garziglia, ingénieur géotechnique à l'Ifremer (Geo-Ocean-ALMA) et Patrick Lajeunesse, géomorphologue à l'Université de Laval. Ce doctorat d'une durée de 3 ans s'est réalisé à moitié entre la France et le Québec.

Ce premier chapitre a pour vocation de situer les travaux de recherche du doctorat dans un contexte scientifique global. Il sera discuté de ce contexte général puis de la zone d'étude de l'estuaire du Saint-Laurent : localisation, géologie, dynamique sédimentaire et sismicité régionale. De plus, les glissements sous-marins seront abordés dans leur globalité afin de mieux comprendre l'aléa naturel qu'ils représentent. Enfin, seront présentés les objectifs et problématiques autour desquels la thèse s'organise.

This PhD project is an international scientific cooperation between two centres of excellence in oceanography research. It was supervised by Guillaume St-Onge, director of *Institut des sciences de la mer de Rimouski* (ISMER) and holder of the Tier I Canada Research Chair in Marine Geology, and by Nabil Sultan, researcher at Ifremer in the ALéas MArins (ALMA) Laboratory of the UMR Geo-Ocean. Moreover, two co-directors supervised it: Sébastien Garziglia, geotechnical engineer at Ifremer (Geo-Ocean-ALMA) and Patrick Lajeunesse, geomorphologist at the *Université Laval*. This 3-year PhD was carried out half in France and half in Québec.

The purpose of this first chapter is to situate the PhD in a global scientific context. This general context will be discussed, followed by the study area of the St. Lawrence Estuary: location, geology, sedimentary dynamics and regional seismicity. In addition, the submarine landslides will be discussed in their entirety in order to better understand the natural hazard they represent. Finally, the objectives and questions around which the thesis is organized will be presented.

1. CONTEXTE GENERAL

À l'est du Canada, la zone sismique de Charlevoix-Kamouraska/Bas-Saint-Laurent (CKBSL) a un aléa sismique pratiquement aussi élevé que les zones actives du Pacifique (**Figure 1-1**). L'évènement majeur du 5 février 1663, d'une magnitude estimée à 7 ou plus, et les cinq séismes aux magnitudes supérieures à 6 recensés depuis 1663 illustrent ce haut niveau d'aléa (Smith, 1962 ; Lamontagne *et al.*, 2003 ; Locat, 2011 ; Lamontagne *et al.*, 2018). Afin de pallier aux risques associés à ces séismes de forte magnitude (victimes, stabilité des infrastructures, glissements sous-marins et tsunamis), il est nécessaire d'améliorer la connaissance de l'aléa sismique de la région, car elle est actuellement trop imprécise en raison de la courte période d'enregistrement des séismes (moins de 400 ans), alors que le code du bâtiment du Canada exige de considérer une période de retour de 2500 ans.

Dans ce contexte, le premier objectif de cette thèse de doctorat est de déterminer la fréquence des couches sédimentaires déposées rapidement telles que les débrites et les turbidites aussi appelées *Rapidly Deposited Layers* (RDLs, St-Onge *et al.*, 2012). Ces couches sont associées aux glissements sous-marins recensés dans l'estuaire du Saint-Laurent (e.g., Pinet *et al.*, 2015). Dans le cas où les glissements sous-marins seraient directement reliés à l'activité sismique, leur datation permettra de reconstruire la paléo-sismicité de l'Est du Canada.

La localisation précise des épicentres des séismes ayant eu lieu avant le déploiement des sismographes au 19ème siècle représente un enjeu majeur. Ainsi, le second objectif s'organise autour de cet axe de recherche et consiste à déterminer la localisation des séismes historiques majeurs à partir de l'analyse de l'accélération nécessaire à la déstabilisation des pentes sous-marines.

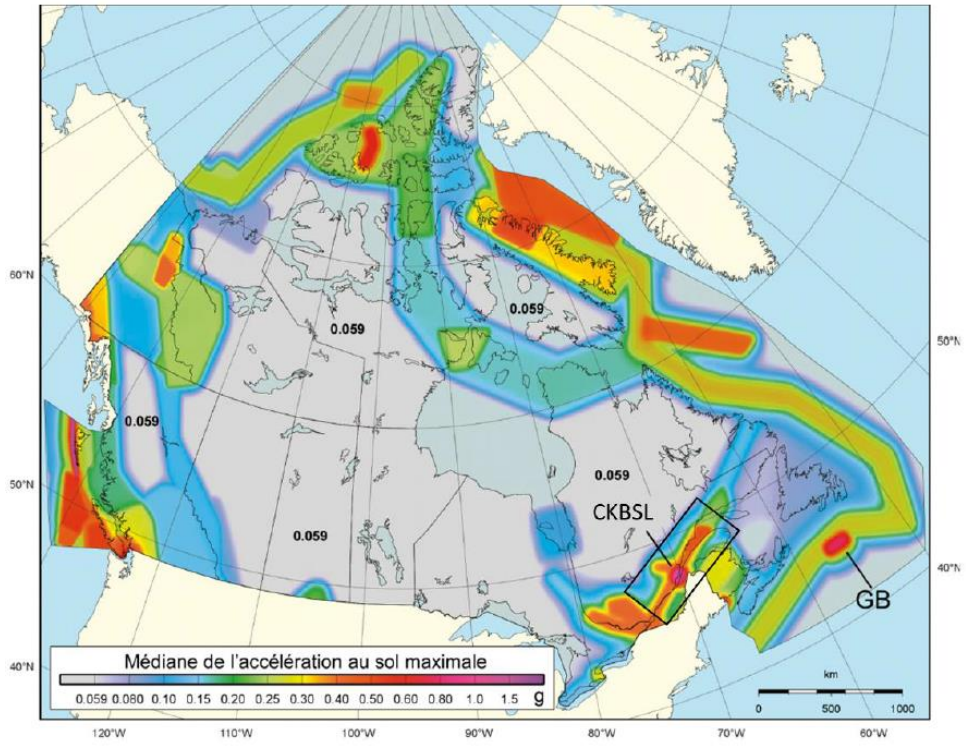

Figure 1-1. Carte d'accélération maximale du sol dans un terrain ferme pour une probabilité de 2%/50 ans. La zone de CKBSL qui représente un haut niveau d'aléa est délimitée en noir (modifiée d'après Locat, 2011).

Enfin, le troisième objectif consiste à quantifier l'aléa naturel que représentent les glissements sous-marins dans la région à partir de la combinaison des données sédimentologiques, géophysiques et géotechniques. L'intégration de ces données dans des modèles numériques permettra l'évaluation de la stabilité des pentes sous-marines sous l'effet de séismes majeurs pour prédire les déstabilisations futures. À terme, ces travaux de recherche participeront à améliorer la connaissance de l'aléa sismique au Québec ce qui permettra de mieux appréhender les risques associés en rendant possible l'adaptation des infrastructures par les institutions gouvernementales, paragouvernementales et privées et ainsi de diminuer leur vulnérabilité.

2. L'ESTUAIRE DU SAINT-LAURENT

2.1. Géographie et géologie

Le fleuve Saint-Laurent, l'un des plus grands fleuves au monde, se situe au sud-est du Canada dans la province du Québec. Il prend naissance à l'embouchure du lac Ontario (Grands Lacs ; **Figure 1-2**) proche de la ville de Kingston. Le fleuve prend la forme d'un estuaire à partir du lac Saint-Pierre, au niveau de la ville de Trois-Rivières, jusqu'à Pointe-des-Monts. Au-delà, s'étend le golfe du Saint-Laurent compris entre le détroit de Cabot et de Belle Isle (Saucier *et al.*, 2000). L'estuaire et le golfe du Saint-Laurent forment une grande mer épicontinentale constituant un environnement marin de transition entre le fleuve Saint-Laurent et l'Océan Atlantique Nord (de Vernal *et al.*, 1993).

L'estuaire du fleuve Saint-Laurent est généralement subdivisé en deux segments avec d'une part l'estuaire moyen qui s'étend jusqu'à l'embouchure de la rivière Saguenay et d'autre part l'estuaire maritime qui s'étend jusqu'à la ville de Sainte-Anne-des-Monts (Pinet *et al.*, 2011). La profondeur maximale dans l'estuaire est de 355 m pour atteindre 500 m dans le golfe du Saint-Laurent

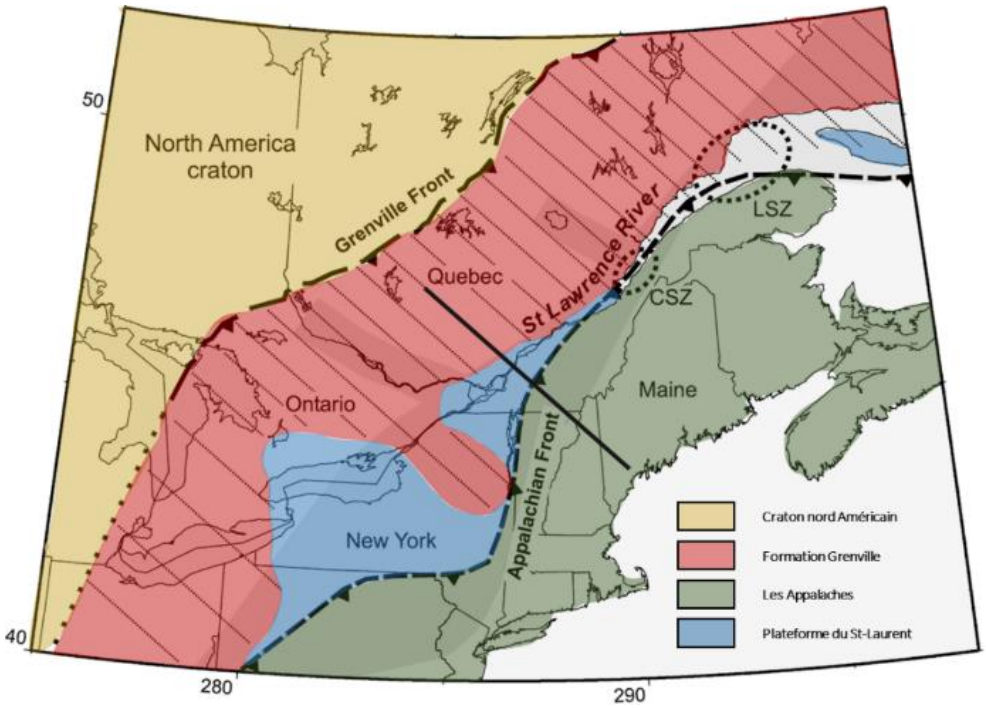

Figure 1-2. Carte géologique simplifiée de la région du Saint-Laurent (modifiée d'après Mazzotti *et al.*, 2005). Les ellipses en pointillés correspondent à des zones sismiques actives (CSZ : zone de Charlevoix-Kamouraska, LSZ : zone du Bas Saint-Laurent).

(Syvitski et Praeg, 1989). Les apports sédimentaires proviennent de ces cinq principales rivières en plus du fleuve Saint-Laurent : Saguenay, Rimouski, Betsiamites, Aux-Outardes et Manicouagan.

L'estuaire du Saint-Laurent repose sur un socle composé principalement de roches carbonatées et silicatées qui constituent la plateforme du Saint-Laurent (Duchesne *et al.*, 2007 ; **Figure 1-2**), totalement recouverte par la sédimentation quaternaire, exceptée à Anticosti et Mingan (Haworth, 1978). La plateforme du Saint-Laurent est bordée au nord par la formation de Greenville composée de roches métamorphiques et au sud, par la chaîne des Appalaches, composée de roches sédimentaires paléozoïques (e.g., Duchesne *et al.*, 2007 ; **Figure 1-2**). Le chenal Laurentien, au centre de l'estuaire, présente une morphologie en auge directement associée à l'érosion glaciaire quaternaire (Josenhans et Lehman, 1999 ; Shaw *et al.*, 2002).

2.2. Dynamiques sédimentaires

Par rapport aux bassins ouverts, un estuaire est considéré comme favorable pour la conservation des dépôts sédimentaires (Duchesne *et al.*, 2010), mais l'interaction des processus sédimentaires terrestres et marins rend la compréhension de l'environnement plus complexe (St-Onge *et al.*, 2003 ; Dalrymple et Choi, 2007). De nombreuses études ont été menées sur le remplissage sédimentaire quaternaire de l'estuaire du Saint-Laurent (e.g., Syvitski et Praeg, 1989 ; Josenhans et Lehman, 1999 ; Duchesne *et al.*, 2007), sur la chronostratigrahie au cours de l'Holocène (e.g., St-Onge *et al.*, 2008 ; Duchesne *et al.*, 2010) et sur la relation entre la fonte de la calotte Laurentidienne, le niveau marin relatif et la sédimentation (e.g., Casse *et al.*, 2017).

2.2.1. Sédimentation du Quaternaire

La corrélation entre l'épaisseur des dépôts quaternaires et la topographie montre que l'architecture des dépôts est contrôlée par l'architecture du socle (Duchesne *et al.*, 2010) à l'image des failles normales sur la Côte-Nord de l'estuaire (Lamontagne *et al.*, 2003) et des structures s'apparentant aux cuesta (Pinet *et al.*, 2008). L'importante épaisseur de la séquence sédimentaire du Quaternaire (~400 m), sa bonne préservation et sa présence sur l'ensemble de l'estuaire du Saint-Laurent font qu'elle ressort clairement sur les profils sismiques (Syvitski et Praeg, 1989 ; Duchesne *et al.*, 2007). Cependant, cela rend compliqué l'échantillonnage des unités les plus profondes. Ainsi, les informations lithologiques et géochronologiques sont incomplètes (Syvitski et Praeg, 1989 ; St-Onge *et al.*, 2003, 2008). En revanche, les sédiments de la fin du Wisconsinien jusqu'à aujourd'hui ont pu être carottés et datés, ce qui a permis de corréler les unités sismiques avec les données chronostratigraphiques (e.g., St-Onge *et al.*, 2008). L'interprétation et la description des cinq principales unités sismiques sont synthétisées dans le **Tableau 1-1**.

2.2.2. Sédimentation actuelle

À la fin de l'Holocène, la vitesse de sédimentation était de 0,15 $cm.an^{-1}$. Au cours du 20ème siècle, son augmentation progressive permet d'atteindre une vitesse de 0,28 $cm.an^{-1}$ pour finalement atteindre les valeurs actuelles de 0,74 $cm.an^{-1}$ au niveau de l'embouchure de l'estuaire maritime (St-Onge *et al.*, 2003).

Tableau 1-1. Caractéristiques et âges des unités sismiques composant la séquence quaternaire. R renvoie aux réflecteurs internes, G à la géométrie des réflecteurs, A à l'amplitude et U aux caractéristiques de la transition supérieure des unités (complété d'après Cauchon-Voyer *et al.*, 2008 et Duchesne *et al.*, 2010).

Séquence sismo-stratigraphique	Interprétations géologiques	Caractéristiques sismiques	Ages (ka)
Unité 5	Sédiments postglaciaires	R : réflexion faible à moyenne G : conforme à l'unité 4 avec peu d'horizons internes réfléchissants A : amplitude moyenne à forte U : contact franc entre les sédiments et l'eau	< 6 ka
Unité 4	Sédiments paraglaciaires	R : réflexion forte à haute fréquence G : horizons réfléchissants très rapprochés, conforme à l'unité 3 A : alternance de faible à forte amplitude U : transition brusque ou graduelle de l'Unité 4 à l'Unité 5	8.7-6 ka
Unité 3	Sédiments glaciaires distaux	R : réflexion faible G : quand ils sont apparents, les réflecteurs sont conformes à l'unité 2 A : faible amplitude U : transition nette de l'Unité 3 à l'Unité 4	9.6-8.7 ka
Unité 2	Sédiments glaciaires proximaux	R : réflexions fortes et à haute fréquence G : réflecteurs très rapprochés conformes à l'Unité 1 A : alternance d'amplitude faible à moyenne U : transition nette de l'Unité 2 à l'Unité 3	10,6-9,6 ka
Unité 1	Sédiments en contact avec la glace	R : absence de réflexions et absorption de l'énergie acoustique G : pas d'horizons A : amplitude moyenne U : transition nette de l'Unité 1 à l'Unité 2	> 10.6 ka

Cependant, ces vitesses de sédimentation ne sont pas homogènes sur l'ensemble de l'estuaire du Saint-Laurent. Elles décroissent exponentiellement pour atteindre 0,04 $cm.an^{-1}$ dans le golfe du Saint-Laurent et 0,01 $cm.an^{-1}$ à la limite avec l'Océan Atlantique Nord (Zhang *et al.*, 2000 ; St-Onge *et al.*, 2003).

Les vitesses de sédimentation modernes sont en partie influencées par l'activité anthropique au cours de la deuxième moitié du 20ème siècle avec l'industrialisation et l'utilisation intense des terres le long du Saint-Laurent, le développement de l'agriculture, l'implantation et le développement de villes (Zhang, 2000 ; St-Onge *et al.*, 2003). Depuis plusieurs dizaines d'années, sur le plateau continental et en particulier sur le long de Côte-Nord du Saint-Laurent, est observé une hausse de la sédimentation. Elle s'explique par l'augmentation significative de l'érosion côtière qui, dans un contexte de changement climatique global, devrait se poursuivre et prendre de l'ampleur en raison des prévisions de la hausse du niveau marin global (Mörner, 2004). Les données géophysiques révèlent l'important rôle des canyons sous-marins, dans le transfert des sédiments issus de l'érosion côtière vers le fond du chenal Laurentien, contribuant ainsi

au budget sédimentaire négatif observé le long de la côte (Gagné *et al.*, 2009). Cependant, il a été démontré que dans l'estuaire maritime, ce ne sont pas les apports sédimentaires qui contrôlent principalement l'activité des canyons, mais plutôt l'inclinaison de la pente (Nomandeau *et al.*, 2015).

2.3. Sismicité

2.3.1. Sismicité historique

Le haut niveau d'aléa sismique dans l'Est du Canada est en grande partie dû au séisme majeur qui s'est produit le 5 février 1663 dans la région de Charlevoix/Kamouraska avec une magnitude estimée à 7 ou plus (Smith, 1962 ; Gouin, 2001 ; Locat, 2011 ; Lamontagne *et al.*, 2018 ; **Figure 1-3**). Ses effets ont été ressentis sur tout le Nord-Est du continent nord-américain. Il causa de grands glissements de terrains tant terrestres (St-Jean Vianney, Shawinigan, Betsiamites, Mont Éboulé) que subaquatiques (Fjord du Saguenay, estuaire du Saint-Laurent). La distribution des grands glissements au nord et le long de la rive nord du Saint-Laurent sont en faveur d'une localisation de son épicentre non loin du graben du Saguenay avec un degré d'incertitude de ± 50 km (Locat, 2011). Le Québec était moins peuplé en 1663 CE qu'aujourd'hui en raison du développement urbain et démographique. Ainsi, un tel séisme causerait aujourd'hui des dommages bien plus considérables et ce tant sur le plan de la stabilité des infrastructures (e.g., viaducs, routes, ponts) que sur la sécurité des populations.

Outre le séisme majeur de 1663 CE, d'autres séismes majeurs expliquent le haut niveau d'aléa sismique de la région de CKBSL. En effet, ce ne sont pas moins de 5 séismes de magnitude 6 et plus qui sont survenus dans cette région en 1791, 1860, 1870, 1925 et 1988 (Smith, 1962 ; Lamontagne *et al.*, 2018 ; **Figure 1-3**).

La zone sismique de Charlevoix-Kamouraska (CK) correspond à la zone la plus active de l'Est du Canada avec en moyenne 200 séismes par an (Locat, 2011). Seule une petite proportion de ces tremblements de terre dépasse une magnitude 3 alors que la plupart sont indétectables sans instruments (Lamontagne *et al.*, 2018). Les cinq principaux séismes de l'Est du Canada (Smith, 1962 Lamontagne *et al.*, 2018) se concentrent dans cette zone entre Charlevoix (rive Nord) et Kamouraska (rive Sud). La plupart des séismes sont confinés dans une zone de 70 km de long et large de 35 km sous le Saint-Laurent (Anglin, 1984) à des profondeurs entre 5 et 25 km dans le socle précambrien.

Contrairement à la zone sismique de Charlevoix, aucun séisme majeur n'a été rapporté ou enregistré dans la zone sismique du Bas-Saint-Laurent (BSL). Cependant deux évènements de magnitudes supérieures à 5 s'y sont produits (1944 et 1999). La plupart des tremblements de terre instrumentés ont une magnitude de 4 ou moins avec en moyenne 60 tremblements de terre par an.

2.3.2. Origines de la sismicité

Les séismes intra-plaques de l'Est du Canada ont deux origines probables : une origine tectonique et une origine postglaciaire (incluant le chargement et le déchargement glaciaire) (Wu, 1998). Plusieurs évidences géologiques et géophysiques supportent une dominance du rebond postglaciaire dans la génération des séismes intra plaques (Goodacre et Hasegawa, 1980), mais il existe également d'autre

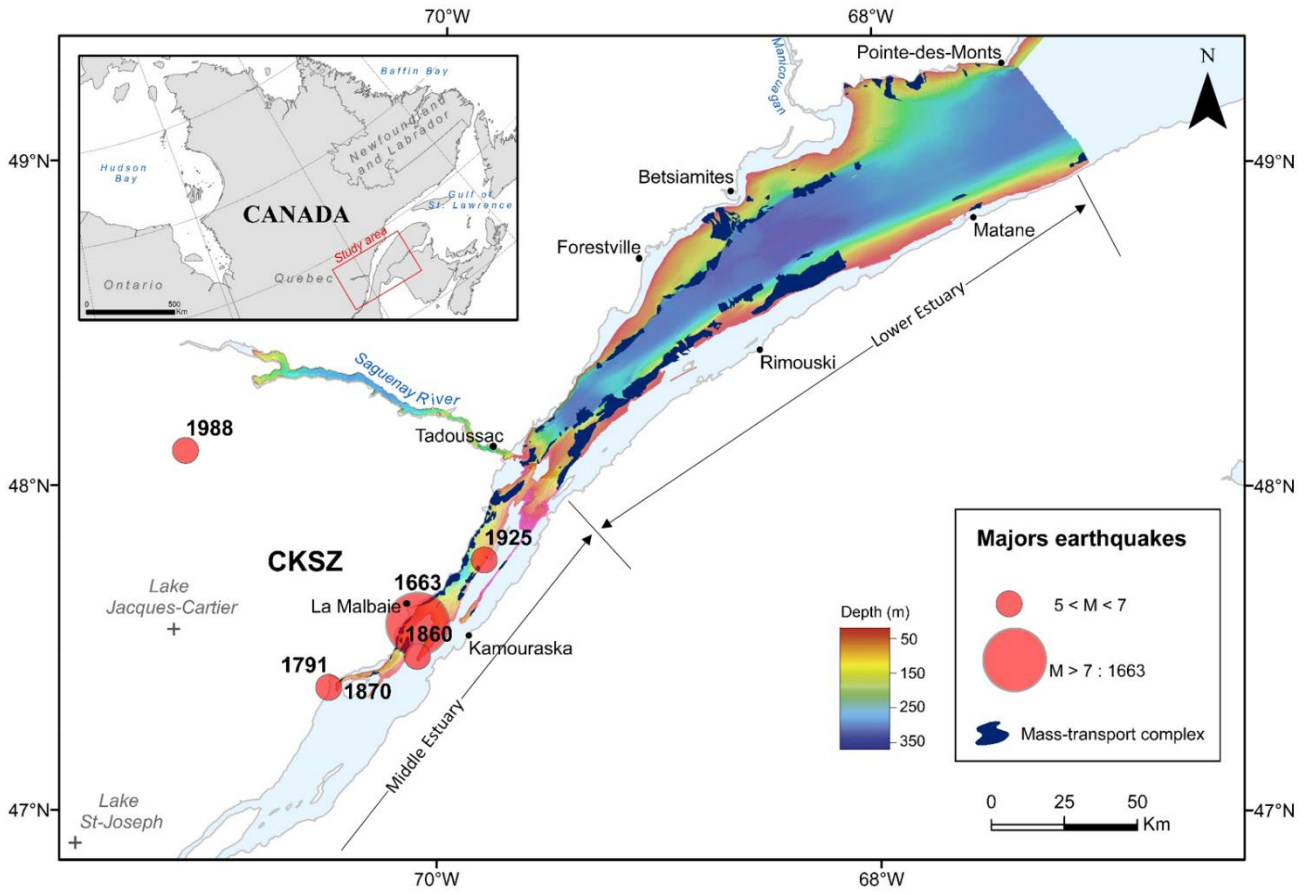

Figure 1-3. Carte bathymétrique de l'estuaire du Saint-Laurent. En bleu sont reportés les mass-transport-complexes et en rouge les séismes historiques majeurs (< 400 ans). CKSZ : Charlevoix-Kamouraska Seismic Zone.

évidences favorisant la dominance des contraintes tectoniques (Adams et Basham, 1989).

Tectonique

Dans l'Est du Canada, l'activité sismique se situe principalement le long de trois zones de faiblesse (Grands bancs de Terre-Neuve, vallée du Saint-Laurent et graben d'Ottawa-Bonnechere) qui sont réactivées par des processus tectoniques (Adams et Basham, 1989 ; Wu et Hasegawa, 1996). La plupart des séismes de Charlevoix sont concentrés le long ou entre des failles héritées de l'océan Iapetus (ouverture entre 700 et 600 Ma) constituant le paléo-rift du Saint-Laurent (Anglin, 1984 ; Adams et Basham, 1989). Leur profondeur dans le bouclier canadien varie entre la surface et 30 km, soit sous la faille de Logan (faille de chevauchement) et les Appalaches (Assameur et Mareschal, 1995 ; Locat, 2011). De plus, la composante de contrainte horizontale maximale déterminée à l'aide des mesures de forage est plus élevée que la contrainte lithosphérique (Sbar et Sykes, 1973). Le déviateur des contraintes peut atteindre plusieurs dizaines de MPa (Sbar et Sykes, 1973). Ce haut niveau de contrainte régionale serait principalement lié à l'ouverture de la dorsale médio-atlantique qui causerait une compression orientée NO-SE (Richardson et Reding, 1991). Ces observations vont dans le sens d'une origine tectonique de la sismicité régionale.

Post-glaciaire

Des failles inverses impactent les structures géologiques formées lors de la présence des glaciers

or ce mécanisme de faille est cohérent avec le rebond postglaciaire. Cela indique une activité postglaciaires associée au rebond isostatique pouvant donc générer des séismes (Wu, 1998). De plus, l'orientation de ces failles inverses est principalement NW-SE, soit conforme à la direction du retrait de la glace (Adams et Basham, 1989). Actuellement la contrainte induite par le déchargement glaciaire, n'est pas suffisamment importante pour générer de nouvelles failles mais peut réactiver les failles préexistantes (Du Berger *et al.*, 1991).

Dans la région du Saint-Laurent, la déglaciation se termine il y a environ 9 ka ce qui prédit la plus grande instabilité des failles postglaciaires dans la période 7 – 4 ka (Wu, 1998). Or, plusieurs études révèlent que la fréquence de turbidites (St-Onge *et al.*, 2004) et de glissements sous-marins (Cauchon-Voyer *et al.*, 2011) est supérieure à cette période. Dans ce sens, la datation d'évènement de liquéfaction dans la vallée de la Wabash (frontière Etats-Unis/Canada) donne également une période postglaciaire active sismiquement entre 8 et 1 ka BP (Obermeier *et al.*, 1991).

Météoritique

Une étude menée par Roy et du Du Berger (1983) révèle la présence d'un astroblème dans la région de Charlevoix indiquant un impact de météorite il y a 350 Ma qui aurait alors fracturé et affaibli la croûte terrestre jusqu'à 14 km de profondeur. La faiblesse de la croûte fracturée couplée à l'ajustement isostatique pourrait expliquer la sismicité de cette région étant donné que les séismes se produisent dans les fractures d'impact (Roy et Du Berger, 1983 ; Onwuemeka *et al.*, 2018). Cependant, les séismes ne sont pas confinés à l'astroblème suggérant que ce n'est pas la seule cause de la sismicité régionale.

2.3.3. Impacts des séismes

L'aléa sismique est un aléa naturel qui nécessite d'être décrit par sa nature, sa localisation, sa fréquence (probabilité et/ou occurrence) et son intensité. Si les effets d'un séisme peuvent être directs avec la chute d'objets et l'effondrement de bâtiments, bien souvent ils sont indirects avec les mouvements de terrain et la génération de tsunamis liée à un mouvement de faille brutal dans le fond océanique ou une masse qui glisse dans le milieu marin (e.g., 1883 : Krakatoa ; 1979 : Nice) (Hampton *et al.*, 1996). L'évaluation du niveau d'aléa sismique d'une région passe par l'élaboration d'un catalogue de la paléo-sismicité (e.g., Lamontagne *et al.*, 2018 pour l'Est Canadien). Il permet de constituer des cartes d'accélération sismique telle que celle présentée en **Figure 1-1**. Elles permettent aux autorités publiques de mettre en œuvre des actions visant à atténuer et prévenir les risques liés aux tremblements de terre (Basham *et al.*, 1979 ; Adams et Atkinson, 2003). Le risque évoque l'éventualité d'occurrence d'un évènement dommageable liée à l'exposition d'enjeux vulnérables à un aléa. Etant relié à la vie humaine et à la notion de propriété, le risque est nul si les humains, leurs possessions et leurs activités ne sont pas impliquées (McCaal, 2012). Plusieurs facteurs peuvent accroître l'incidence, l'échelle et les effets de l'aléa dont la concentration des populations, la mauvaise gestion dans la construction, l'eau et les déchets ou encore la mauvaise considération des effets possibles à long terme des désastres (McCaal, 2012).

3. LES GLISSEMENTS SOUS-MARINS

Dans le domaine sous-marin, trois grands groupes de phénomènes sédimentaires interviennent. Le premier groupe rassemble les processus dit de « resédimentation » qui correspondent au transfert de sédiments d'un domaine peu profond vers un domaine plus profond sous l'action de la force de gravité, on parle alors de processus gravitaires (Pickering *et al.*, 1986). Ce type de processus géologique est d'importance majeure dans le transfert de matière vers les grands fonds (Stow et Mayall, 2000). Les courants de fond et les courants superficiels avec la décantation pélagique constituent les deux autres groupes.

Ce n'est qu'après le séisme majeur des Grands bancs de Terre-Neuve (1929) que les scientifiques se sont penchés sur cet aléa géologique en domaine marin, motivés par les importants impacts qu'ils peuvent générer (e.g., rupture de câbles téléphoniques, tsunami ; Piper et Aksu, 1987 ; Higman *et al.*, 2018 ; Normandeau *et al.*, 2019). Le processus de glissement désigne la mise en mouvement de la colonne sédimentaire selon une surface de rupture qui définit un plan de cisaillement basal (**Figure 1-4** ; Hampton *et al.*, 1996 ; Locat et Lee, 2002). La masse sédimentaire déplacée peut conserver sa morphologie initiale ou être déformée (Hampton *et al.*, 1996). Les récents progrès technologiques dans le domaine de l'imagerie acoustique et sismique ont permis leur meilleure compréhension. Ainsi, en imagerie sismique, il est possible de discerner un glissement de masse par son faciès acoustique transparent et/ou ses réflecteurs très déformés traduisant des dépôts chaotiques. En fonction de la nature et de l'intensité de la déformation qui affectent le matériel mobilisé, trois catégories de glissements de masse sont distinguées : slides, slumps et creeping (e.g., Mulder et Cochonat, 1996).

Les glissements sous-marins se produisent sur l'ensemble des océans et dans une grande variété d'environnements géologiques et tectoniques

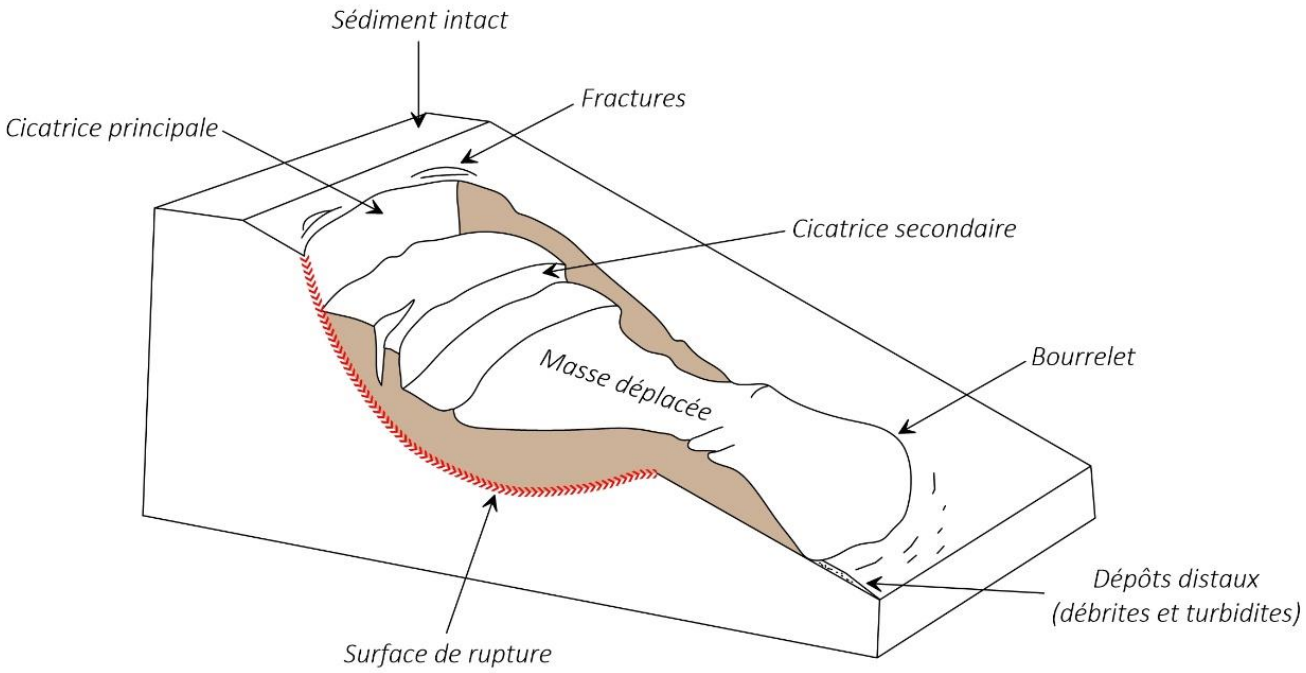

Figure 1-4. Schéma d'un glissement sous-marin (modifiée d'après Hampton *et al.*, 1996).

(Vanneste *et al.*, 2014). L'eau de mer prenant la place de l'air comme fluide ambiant, ces phénomènes sont relativement plus fréquents en mer qu'à terre, peuvent affecter des zones à faible gradient de pente et mobiliser des volumes considérables (e.g., Storrega, Stow et Piper, 1984 ; Bugge *et al.*, 1988). Leur mobilité et leur écoulement peuvent être très élevés (Mulder *et al.*, 1998), engendrant parfois de véritables catastrophes (e.g., Storegga à ~8.1 ka ; Talling *et al.*, 2014).

La quasi-totalité des glissements sous-marins se développent suivant le schéma commun de pré-rupture, rupture et post-rupture, indépendamment de leur nature (Leroueil, 2001, 2004). Ces différentes phases de déformation et chaque processus de glissements dépendent d'un certain nombre de facteurs prédisposants, déclenchants ou aggravants (Vaunat et Leroueil, 2002). Ces facteurs sont souvent mal compris, car ils sont souvent spécifiques à un site et que les données disponibles (e.g., sismicité, pluviométrie, pression interstitielle) sont très limitées ; c'est pour cela que la surveillance en continue de la stabilité des pentes continentale particulièrement exposées à la sismicité et aux surpressions de fluides est un enjeu majeur afin de mieux appréhender les risques liés aux aléas gravitaires sous-marins (e.g., Garziglia *et al.*, 2021).

3.1. Le préconditionnement

Le préconditionnement correspond à la phase de pré-rupture durant laquelle une combinaison de facteurs environnementaux locaux et régionaux amène à la rupture de la pente (Locat et Lee, 2002). Une stratification sédimentaire défavorable, l'érosion qui exacerbe les pentes et la circulation de fluides (e.g., déstabilisation des hydrates de gaz, chargement en gaz) sont considérés comme étant des facteurs prédisposants (Locat et Lee, 2002 ; Leroueil, 2004). De plus, la géomorphologie du fond marin peut agir comme un facteur prédisposant. Par exemple, dans l'estuaire maritime du Saint-Laurent, il n'est pas observé d'accumulation sédimentaire sur les pentes fortes (Duchesne *et al.*, 2010 ; Pinet *et al.*, 2015), car l'un des paramètres contrôlant le déclenchement de la rupture est l'angle critique de rupture du matériau qui est atteint plus rapidement sur des pentes à forte déclivité (Bromhead et Dixon, 1986). Enfin, une sédimentation rapide est un facteur préconditionnant à la rupture car il génère une surpression interstitielle qui a pour effet de réduire la contrainte effective et donc la résistance à la rupture (e.g., Dan *et al.*, 2007 ; Das, 2013 ; Pinet *et al.*, 2015). Dans l'estuaire du Saint-Laurent, à l'embouchure de la rivière Manicouagan qui compose le plus grand système en éventail sous-marins de l'estuaire, les taux de sédimentation y sont les plus élevés mais aucun glissement sous-marin n'y a été recensé (Pinet *et al.*, 2011). Cela suggère qu'un apport sédimentaire relativement élevé n'est actuellement pas un facteur de préconditionnement prédominant dans l'estuaire (Pinet *et al.*, 2015). Cependant, le taux de sédimentation très élevé associé au retrait de la calotte Laurentienne de 23 à 6 ka a joué un rôle prépondérant dans l'instabilité des fonds marins (Clark *et al.*, 1978 ; Normandeau *et al.*, 2017).

3.2. Le déclenchement

La rupture apparaît au moment où la contrainte de cisaillement, notée τ, est supérieure à la résistance au cisaillement du sédiment, notée τ_f (Lee *et al.*, 1991 ; Hampton *et al.*, 1996). Ce critère de

rupture de Mohr-Coulomb est le plus simple et le plus utilisé afin d'évaluer la stabilité d'une pente infinie. Le facteur déclenchant est le processus qui va générer le glissement. Le déclenchement est facilité par des affaiblissements locaux et régionaux qui se produisent durant la phase de pré-rupture (Leroueil, 2001). Le déclenchement dépend de l'état d'avancement du préconditionnement, mais aussi du comportement du sédiment. Deux manières sont possibles pour déclencher un glissement sous-marin : en réduisant la résistance au cisaillement ou en augmentant la contrainte de cisaillement (Kopula, 1984 ; Lee *et al.*, 1991) par le biais des facteurs synthétisés dans le **Tableau 1-2**. Ces facteurs peuvent mener à la rupture avant que la résistance au cisaillement n'ait été réduite à zéro (Hampton *et al.*, 1996).

Tableau 1-2. Synthèse des causes d'initiation des glissements gravitaires (modifié d'après Hampton *et al.*, 1996).

Réduit la résistance au cisaillement	Augmente la contrainte
Séismes	Séismes
Vagues	Vagues
Eustatisme	Eustatisme
Climat	Diapirisme
Sédimentation	Sédimentation
Gaz et dissociation des hydrates de gaz	Érosion
Variation pression artésienne	
Exacerbation des pentes	

La sismicité est considérée comme le déclencheur majeur des glissements sous-marins en agissant de trois manières différentes. Premièrement, les accélérations horizontales et verticales du sol générées par les ondes sismiques s'ajoutent aux forces de déstabilisation de la colonne sédimentaire (Hack *et al.*, 2007). Deuxièmement, dans un sol où la cohésion permet la résistance à la traction, les déplacements dus aux ondes sismiques peuvent être suffisamment importants pour rompre les liaisons entre les particules du sol et ainsi entraîner la perte de résistance à la traction (Ishihara, 1985). Troisièmement, l'effet des ondes sismiques sur le sol s'apparente à des charges cycliques. Ce phénomène conduit dans les sols grossiers non cohésifs (e.g., sable) à la réduction de la porosité et donc à la compaction. Le chargement étant très rapide, l'eau interstitielle ne peut pas s'écouler assez rapidement. Les contraintes déviatoriques cycliques, générées par le séisme, se reportent sur l'eau provoquant l'augmentation de la pression interstitielle (u) d'un petit incrément à la suite de chaque cycle. Or, la contrainte effective (σ') correspond à la contrainte totale (σ) moins la pression interstitielle (Terzaghi *et al.*, 1996). Lorsque la pression interstitielle tend progressivement à être égale à la pression de confinement, la contrainte effective tend vers zéro. En conséquence, les contacts entre les particules diminuent jusqu'à ce que le sable perde sa résistance. Il se liquifie, i.e., il se déforme indéfiniment dans la direction de la contrainte principale (Norem *et al.*, 1990).

Les premières études pour expliquer et comprendre la liquéfaction des sols (Yoshimi et Tokimatsu, 1977 ; Seed, 1979 ; Finn, 1981 ; Robertson et Fear, 1995) ont été réalisées à la suite

des séismes de Niigata (1964) et de Kobe (1995) au Japon où la majeure partie des dommages n'a pas été provoquée par les secousses sismiques mais par la liquéfaction du sol qui a suivi. Ce phénomène est une préoccupation majeure pour l'évaluation des risques sismiques (Robertson et Wride, 1998). Au Québec, à la suite des séismes de 1870 CE et de 1925 CE, des coulées de sable sortant de fissures dans le sol ont été répertoriées dans la région de Charlevoix (Gouin, 2001). À la suite du séisme de 1663 CE, une centaine de volcans de sable se sont formés et ont été interprétés par Chagnon et Locat (1988) comme des « sand boils » correspondant à la liquéfaction du sable en profondeur et à sa remontée vers la surface.

Dans l'estuaire du Saint-Laurent de nombreux niveaux sableux superficiels ont été identifiés (e.g., Cauchon-Voyer *et al.*, 2011 ; Normandeau *et al.*, 2015 ; Pinet *et al.*, 2015). Leur présence permet d'émettre l'hypothèse qu'en cas de tremblement de terre, les accélérations générées peuvent liquéfier ces niveaux sableux et donc déclencher des glissements sous-marins.

Finalement, la charge cyclique lors d'un séisme ne mène pas nécessairement à la liquéfaction, elle peut induire une dégradation de la rigidité et de la résistance au cisaillement des niveaux sableux et argileux (Pestana *et al.*, 2000).

3.3. Le développement

Une fois la rupture initiée, la masse sédimentaire (de quelques mètres à dizaines de mètres d'épaisseur) commence à glisser le long du plan de rupture et évolue rapidement. Son pouvoir abrasif sur le fond marin peut entrainer l'incorporation de débris et d'eau faisant perdre progressivement sa structure et sa composition initiale. Le glissement se transforme progressivement en une coulée de débris qui peut transporter de très gros blocs en suspension (Lastras *et al.*, 2005 ; Vanneste *et al.*, 2006 ; **Figure 1-5**). Sur une pente forte, la coulée de débris accélère permettant l'incorporation accrue d'eau et de sédiments lors de son déplacement (Mulder et Cochonat, 1996 ; Piper *et al.*, 1999). Des turbulences apparaissent à sa surface jusqu'à ce que la coulée de débris se soit entièrement transformée en courant de turbidité (**Figure 1-5**). Lors de la phase de post-rupture, les sédiments remobilisés peuvent atteindre des vitesses élevées (plusieurs dizaines de km/h) et parcourir de très longues distances même sur un fond plat (Kvalstad *et al.*, 2005). Cependant, en fin de parcours, l'énergie cinétique tend à diminuer. Le matériel jusqu'alors en suspension grâce à la turbulence commence à se déposer pour former une turbidite (Ravenne et Béghin, 1983 ; **Figure 1-5**). Le volume de matériel transféré peut être considérable. Par exemple, le dépôt lié à l'avalanche sous-marine déclenchée par le séisme de 1929 dans les Grands Bancs de Terre-Neuve, a recouvert 260 000 km² de la surface abyssale avec une épaisseur moyenne d'environ 1 m (Kvalstad *et al.*, 2005).

4. OBJECTIFS ET PROBLEMATIQUES

Le haut niveau d'aléa sismique de la région de CKBSL est lié aux séismes majeurs qui ont ébranlé le Sud-Est du Canada depuis près de 400 ans. L'évènement majeur du 5 février 1663, d'une magnitude estimée à 7 ou plus, et les 5 séismes aux magnitudes supérieures à 6 recensés depuis 1663 illustrent ce haut niveau d'aléa. Cependant, l'évaluation précise de l'aléa sismique d'une région requiert une compréhension détaillée de la sismicité passée. L'un des éléments primordiaux de cette

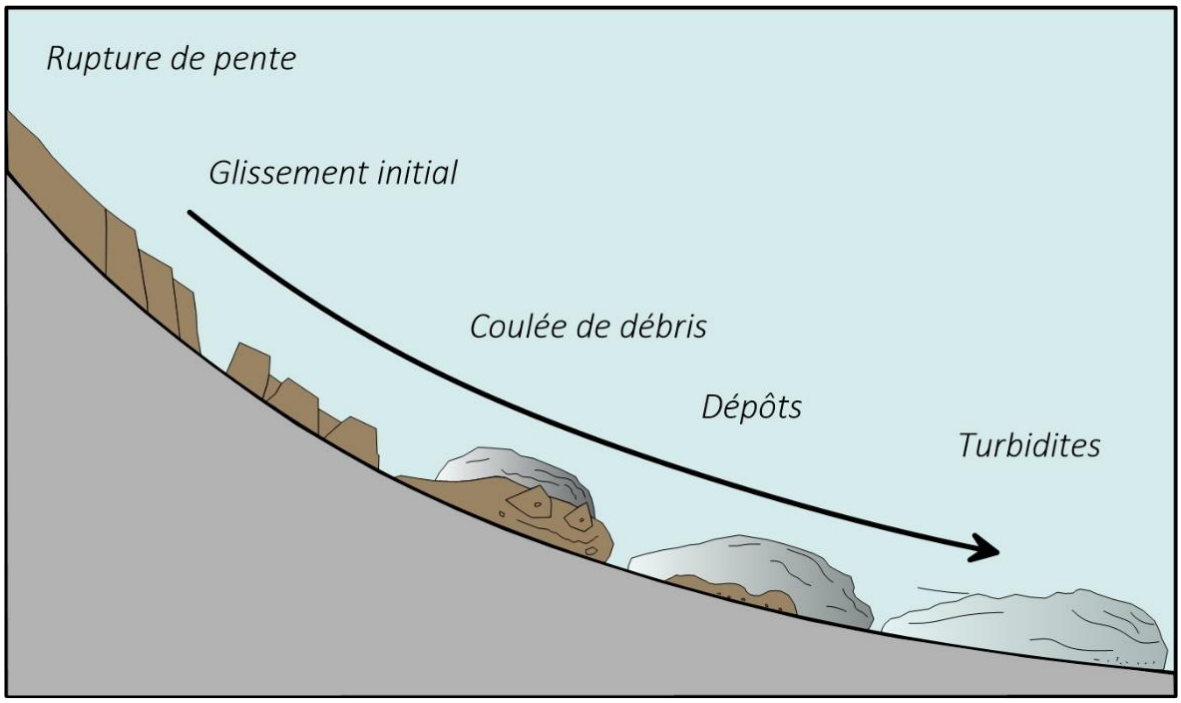

Figure 1-5. Schéma du développement d'un glissement sous-marin de la rupture à son produit final qui correspond à un dépôt turbiditique (modifiée d'après Bryn *et al.*, 2005).

évaluation est la détermination du tremblement de terre maximal qui peut se produire dans une région donnée (e.g., Ebel, 2011). Or, au Canada, l'estimation du plus grand séisme est difficile, car il n'y a pas de certitude que le plus grand séisme ait été observé au cours des quatre derniers siècles, i.e., le début de la colonisation européenne et des informations historiques sur l'activité sismique.

En revanche, le milieu subaquatique peut préserver les traces des grands séismes régionaux ayant eu lieu dans le passé. Ces traces peuvent remonter au de-delà de l'implantation des civilisations européennes dans l'Est du Canada. Ce type de registre des séismes au-delà des archives historiques a déjà été réalisé en milieu subaquatique tel que sur la côte Ouest des Etats-Unis où la description et la datation des dépôts sédimentaires déposés rapidement (turbidites) ont permis de déterminer la récurrence de séismes de magnitude élevée le long de la faille San Andreas au cours des derniers 3000 ans (Goldfinger *et al.*, 2012). A l'instar de cet exemple, depuis les vingt dernières années, les turbidites ont été utilisées comme proxys de la paléo-sismicité dans de nombreux contexte géologiques à travers le monde (Lebreiro *et al.*, 1997 ; Gracia *et al.*, 2010 ; St-Onge *et al.*, 2012 ; Ratzov *et al.*, 2015 ; Babonneau *et al.*, 2019 ; Seibert *et al.*, 2019 ; Piper *et al.*, 2019 ; Howarth *et al.*, 2021) et au Québec dans le fjord du Saguenay (St-Onge *et al.*, 2004), ainsi qu'en domaine lacustre (Philibert, 2012 ; Locat *et al.*, 2016 ; Lajeunesse *et al.*, 2017 ; Trottier *et al.*, 2019). Cependant, dans l'estuaire du Saint-Laurent, seul un glissement a été supposé déclenché par un ou plusieurs séismes historiques par Cauchon-Voyer *et al.* (2008). Ainsi, il n'y a actuellement pas d'étude à l'échelle de l'estuaire permettant de relier les glissements sous-marins à la sismicité régionale du Québec et ainsi de connaître la récurrence des séismes majeurs régionaux. Le premier objectif de ces travaux de recherche répondra à la nécessité de retracer la paléo-sismicité régionale.

OBJECTIF I – LA PALEO-SISMICITE DE L'EST DU CANADA

(1) Peut-on identifier et caractériser les couches déposées rapidement (RDLs), sous-produits des glissements sous-marins ?
(2) Quelles est la fréquence des RDLs ? Retrouve-t-on une synchronicité des glissements à l'échelle de l'estuaire ?
(3) Dans le cas où les glissements sous-marins sont associés aux séismes historiques majeurs, peut-on remonter au-delà de 400 ans ?
(4) Quel est le séisme majeur des derniers millénaires ?

L'objectif principal de cette thèse de doctorat est de déterminer la fréquence des RDLs, sous-produits des glissements sous-marins, recensées dans l'estuaire du Saint-Laurent. L'analyse des propriétés sédimentologiques et la datation des RDLs permettra de dater ces évènements et de déterminer le mécanisme responsable de leur dépôt. Dans le cas où les glissements sous-marins seront directement reliés à l'activité sismique, la combinaison de ces données permettra d'identifier les paléo-séismes majeurs dans la zone sismique de CKBSL.

Le deuxième objectif de ce projet de recherche est d'étudier le comportement des couches sableuses sous l'effet des séismes et plus particulièrement le phénomène de liquéfaction.

OBJECTIF II – LA LIQUEFACTION DU SEDIMENT ET EPICENTRES DES SEISMES HISTORIQUES MAJEURS

(1) Quelle est le comportement géomécanique des sédiments sous l'effet d'un séisme ?
(2) Quelles sont les couches les plus liquéfiables et responsables des déstabilisations ?
(3) Peut-on actualiser la localisation des séismes régionaux à partir de l'accélération nécessaire à la déstabilisation ?

Cet objectif nécessite la caractérisation du comportement mécanique du sédiment intact par son analyse géotechnique. Les essais expérimentaux en laboratoire permettront d'évaluer le potentiel de liquéfaction du sédiment. Le carottage des différentes unités sédimentaires supérieures de la séquence quaternaire permettra l'évaluation de ce potentiel pour chacune d'entre elles et ainsi d'identifier les interfaces les plus critiques, i.e., les plus susceptibles de localiser le plan de rupture. Enfin, la position des épicentres joue un rôle crucial dans la gestion du risque sismique. Or, pour les séismes antérieurs à l'instrumentation sismique, il est difficile de les localiser avec précision et certains n'ont pas été révisés depuis plusieurs décennies. En utilisant la datation de glissements sous-marins déclenchés par la sismicité régionale (objectif I), les épicentres des séismes historiques majeurs pourront être localisés avec précision et possiblement repositionnés.

OBJECTIF III – LA STABILITE DES PENTES SOUS-MARINES

(1) Quelle est la stabilité des pentes dans les zones de glissement en cas de séisme ?
(2) Quel est le séisme critique qui sera capable de déstabiliser la pente actuelle ?

Une approche utilisant des simulations numériques sera mise en place pour définir la stabilité des pentes les plus critiques sous l'effet des accélérations générées par des séismes de forte magnitude. La modélisation permettra de valider les causes et les conditions à l'origine des déstabilisations passées et futures. En couplant les calculs de stabilité avec la fréquence des principaux séismes, il sera rendu possible d'anticiper les déstabilisations futures et de mieux appréhender les aléas associés tels que les tsunamis (Hampton *et al.*, 1996 ; Poncet *et al.*, 2010).

Si ce projet de recherche n'a pas vocation de constituer des mesures d'atténuation, il participera toutefois à l'amélioration des connaissances sur l'activité sismique de l'Est du Canada. En effet, les mesures d'atténuation, essentielles pour réduire les impacts des glissements sur les infrastructures, reposent sur l'intégration de données de terrain avec des tests approfondis en laboratoire et des simulations numériques (Zakeri *et al.*, 2008). L'approche multidisciplinaire qui est mise en œuvre dans ce projet de doctorat correspond aux recommandations de Vanneste *et al.* (2014) qui préconise d'utiliser conjointement la géophysique, la géotechnique, la géochimie, la sédimentologie et la modélisation pour l'étude des instabilités gravitaires.

5. DEROULEMENT DE LA THESE

Ce projet de doctorat s'est déroulée entre le Québec (18 mois) et la France (18 mois). La première année de la thèse a été consacrée à la complétion des cours obligatoires pour valider le doctorat. Le premier cours intitulé « examen doctoral » consistait à répondre à deux questions scientifiques générales en océanographie. Ces réponses prenaient la forme de deux rapports écrits et de deux présentations orales dans un temps imparti de deux mois plus un mois de préparation. Les réponses devaient prendre en considération les quatre disciplines phare de l'océanographie qui sont la géologie, la biologie, la chimie et la physique. Le deuxième cours (5 – 6 mois) avait pour vocation de préparer un rapport écrit devant présenter la problématique, les objectifs, les hypothèses, la méthodologie et l'échéancier du projet de doctorat. Ce document a fait l'objet d'une présentation orale en mai 2020 afin de valider le cours « Séminaire I ».

La préparation de la campagne en mer dans l'estuaire du Saint-Laurent a été partie intégrante du projet (~2 mois). Ce travail a consisté à la préparation du plan de mission (zones d'études, levés géophysiques, sites de carottage). La mission SLIDE-2020 du 18 au 29 juillet 2020, a fait l'objet d'un rapport de mission que j'ai écrit à la suite du débarquement.

Jusqu'à mai 2021, les données de la mission ont été analysées à l'ISMER afin de compléter l'objectif I. En mai 2021, le cours « Séminaire II » a été présenté et le projet de recherche a continué à l'Ifremer, en France. Les analyses géotechniques en laboratoire ont duré 6 à 7 mois et s'en est suivie la modélisation pendant une durée équivalente. Les objectifs II et III ont ainsi pu être complétés. Enfin, les derniers mois ont été consacrés à la rédaction du manuscrit de thèse.

6. COMMUNICATIONS SCIENTIFIQUES

6.1. Publications

Mérindol, M., Sultan, N., St-Onge, G., Garziglia, S., Lajeunesse, P., 2022. *Location of the 1663 AD earthquake (M ~ 7) in the St. Lawrence Estuary*

(Canada) using sediment liquefaction analysis. Engineering Geology. En revision.

Mérindol, M., St-Onge, G., Sultan, N., Lajeunesse, P., Garziglia, S., 2022. *Earthquake-triggered submarine landslides in the St. Lawrence Estuary (Québec, Canada) during the last two millennia and the record of the major 1663 CE M ≥ 7 event*. Quaternary Science Reviews, 291, 107640.

6.2. Présentations

Mérindol, M., St-Onge, G., Sultan, N., Lajeunesse, P., Garziglia, S., 2022. *Paleoseismicity of eastern Canada based on earthquake-triggered submarine landslides in the St. Lawrence Estuary, Québec*. 18ème congrès français de sédimentologie.

Mérindol, M., St-Onge, G., Sultan, N., Lajeunesse, P., Garziglia, S., 2022. *Earthquake-triggered submarine landslides in the St. Lawrence Estuary (Québec, Canada) during the last two millennia and the record of the major 1663 CE M ≥ 7 event* (No. EGU2022-4835). Copernicus Meetings.

Mérindol, M., St-Onge, G., Sultan, N., Lajeunesse, P., Garziglia, S., 2022. *Earthquake-triggered submarine landslides in the St. Lawrence Estuary (Québec, Canada) during the last two millennias: importance of the 1663 ad (M>7) earthquake*. Congrès annuel du Géotop, 29 – 31 mars 2022.

Mérindol, M., Sultan, N., St-Onge, G., Garziglia, S., Lajeunesse, P., 2022. *Submarine landslides triggered by the 1663 earthquake (M>7) in the St. Lawrence Estuary, Quebec, Canada: implication on the location of its epicenter*. Rassemblement scientifique de Québec-Océan, 31 janvier 2022.

Mérindol, M., St-Onge, G., Sultan, N., Lajeunesse, P., Garziglia, S., 2021. *Submarine landslides in the St. Lawrence Estuary, Québec, Canada*. Congrès annuel du Géotop, 16 – 19 mars 2021.

6.3. Contributions des auteurs

Méril Mérindol

- → Ecriture des articles et du mémoire de thèse ;
- → Préparation de la mission en mer ;
- → Participation mission en mer ;
- → Conception et réalisation des analyses ;
- → Acquisition des données ;
- → Contribution aux données et outils d'analyses ;
- → Réalisation des analyses.

Guillaume St-Onge

- → Correction des articles et du mémoire de thèse ;
- → Préparation de la mission en mer ;
- → Participation mission en mer ;
- → Conception et réalisation des analyses ;
- → Contribution aux données et outils d'analyses.

Nabil Sultan

- → Correction des articles et du mémoire de thèse ;
- → Préparation de la mission en mer ;
- → Conception et réalisation des analyses ;
- → Contribution aux données et outils d'analyses.

Patrick Lajeunesse

- → Correction des articles et du mémoire de thèse ;
- → Contribution aux données et outils d'analyses.

Sébastien Garziglia

- → Correction des articles et du mémoire de thèse ;
- → Contribution aux données et outils d'analyses.

1. GENERAL CONTEXT

In eastern Canada, the Charlevoix-Kamouraska/Bas-Saint-Laurent (CKBSL) seismic zone presents a seismic hazard level almost as high as the active Pacific zone (**Figure 1-1**). The major event of February 5, 1663, with a magnitude estimated at > 7, and the five earthquakes with magnitudes greater than 6 recorded since 1663, all point to this high level of seismic hazard (Smith, 1962; Lamontagne *et al.*, 2003; Locat, 2011; Lamontagne *et al.*, 2018). To mitigate the risks associated with these high-magnitude earthquakes (casualties, infrastructure stability, submarine landslides and tsunamis), there is a need to improve regional seismic hazard knowledge currently too approximate due to the short historical record used (less than 400 years), while the new requirements of the Canadian building code imposes a return period of 2500 years for the evaluation of seismic hazard.

In this context, the first objective of this doctoral thesis is to determine the frequency of rapidly deposited layers (RDLss, St-Onge *et al.*, 2012) such as debrites and turbidites. These layers are associated with submarine landslides recorded in the St. Lawrence Estuary (e.g., Pinet *et al.*, 2015). In the event that the submarine slides are directly related to seismic activity, their dating will enable the reconstruction of paleoseismicity of eastern Canada.

The precise location of the epicenters of earthquakes that occurred before the deployment of seismographs in the 19th century represents a major challenge. The second objective is organized along this line of research, the essence of which is to determine the location of major historical earthquakes from the analysis of the rates of acceleration involved in the destabilization of submarine slopes.

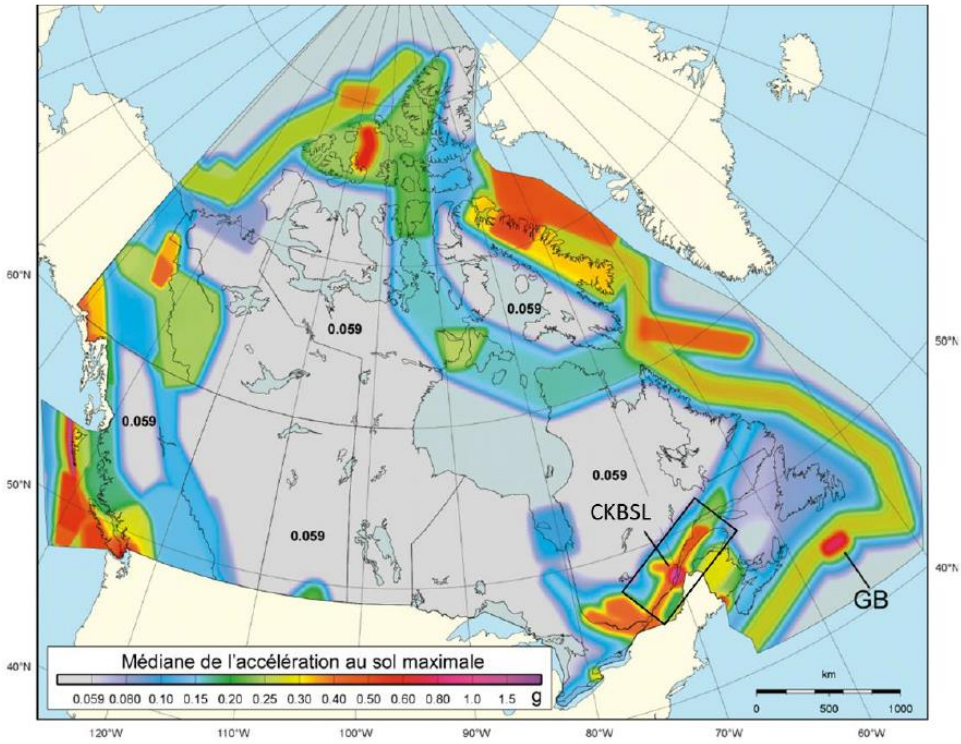

Figure 1-1. Map of peak ground acceleration in firm ground for a 2%/50-years probability. The area of CKBSL that represents a high level of hazard corresponds to the black square (modified from Locat, 2011).

The third objective of this work is to quantify the natural hazard of submarine landslides in the region by combining sedimentological, geophysical and geotechnical data. The integration of these data in numerical models will make it possible to evaluate the stability of submarine slopes under the effect of major earthquakes in order to predict future destabilization. Ultimately, this research will help improve knowledge of the seismic hazard in Québec, leading to a better understanding of the associated risks, making it possible for governmental, paragovernmental and private institutions to consequently adapt their infrastructures and reduce their vulnerability.

2. THE ST. LAWRENCE ESTUARY

2.1. Geography and Geology

The St. Lawrence River, one of the largest rivers in the world, is located in southeastern Canada in the Province of Québec. It rises at the mouth of Lake Ontario (Great Lakes; **Figure 1-2**) near the city of Kingston. The river turns into an estuary from Lake Saint-Pierre, near the city of Trois-Rivières, to Pointe-des-Monts. Beyond, the Gulf of St. Lawrence extends between the Cabot Strait and the Straut of Belle Ilse (Saucier *et al.*, 2000). The Estuary and Gulf of St. Lawrence constitute a large epicontinental sea that forms a transitional marine environment between the St. Lawrence River and the North Atlantic Ocean (de Vernal *et al.*, 1993).

The St. Lawrence Estuary is traditionally subdivided into two segments with the Upper Estuary extending to the mouth of the Saguenay River and the Lower Estuary extending to the city of Saint-Anne des Monts (Pinet *et al.*, 2011). The maximum estuary depth is 355 m to 500 m in the Gulf of St. Lawrence (Syvitski and Praeg, 1989). Sedimentary inputs come from the following five main rivers in addition to the St. Lawrence River: Saguenay, Rimouski, Betsiamites, Aux-Outardes and Manicouagan.

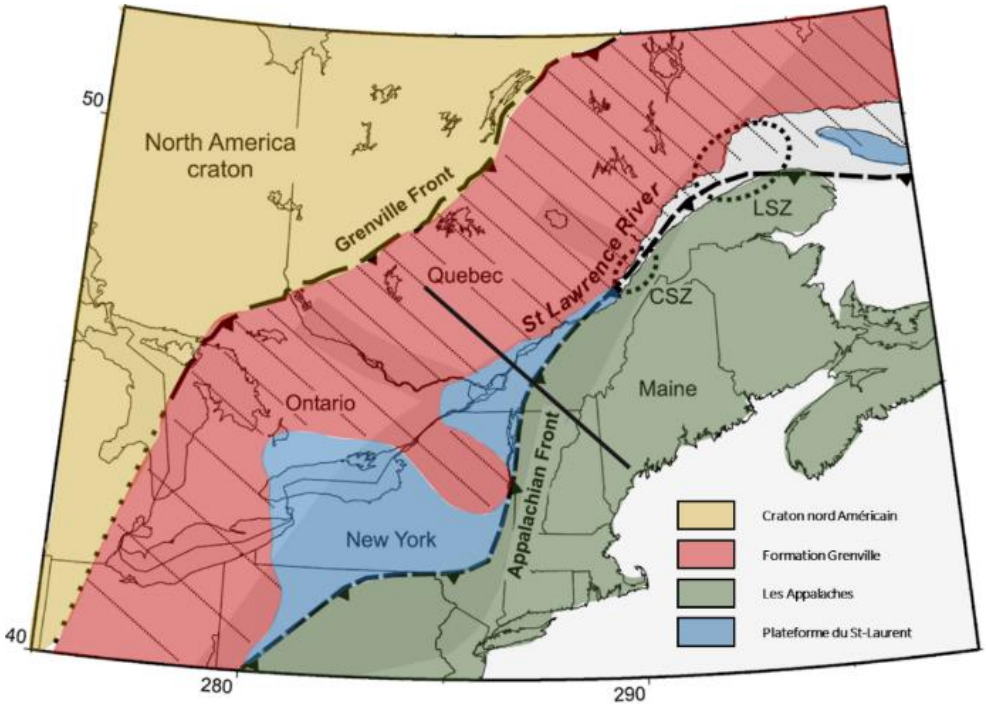

Figure 1-2. Simplified geological map of the St. Lawrence region (modified from Mazzotti *et al.*, 2005). Dotted ellipses correspond to seismically active zones (CSZ: Charlevoix-Kamouraska zone, LSZ: Lower St. Lawrence zone).

The St. Lawrence Estuary is underlain by a basement composed mainly of carbonate and silicate rocks that constitute the St. Lawrence Platform (Duchesne *et al.*, 2007; **Figure 1-2**). It is totally covered by Quaternary sedimentation, except at Anticosti and Mingan (Haworth, 1978). The St. Lawrence platform is bordered to the north by the Greenville Formation composed of metamorphic rocks and to the south by the Appalachian chain, composed of Paleozoic sedimentary rocks (e.g., Duchesne *et al.*, 2007; **Figure 1-2**). The Laurentian Channel in the center of the estuary is a U-shaped incised-valley inherited from Quaternary glacial erosion (Josenhans and Lehman, 1999; Shaw *et al.*, 2002).

2.2. Sedimentary dynamics

Compared to open basins, an estuary is considered as favorable for the preservation of sedimentary deposits (Duchesne *et al.*, 2010), but the interaction of terrestrial and marine sedimentary processes makes understanding the environment more complex (St-Onge *et al.*, 2003; Dalrymple and Choi, 2007). Numerous studies have been conducted on the Quaternary sedimentation of the St. Lawrence Estuary (e.g., Syvitski and Praeg, 1989; Josenhans and Lehman, 1999; Duchesne *et al.*, 2007), on chronostratigraphy during the Holocene (e.g., St-Onge *et al.*, 2008; Duchesne *et al.*, 2010), and on the relationship between Laurentide ice-sheet melt, relative sea level and sedimentation (e.g., Casse et al., 2017).

2.2.1. Quaternary sedimentation

Correlation between the thickness of the Quaternary deposits and the topography shows that the architecture of the deposits is controlled by the architecture of the basement (Duchesne *et al.*, 2010), just like the normal faults on the North Shore of the estuary (Lamontagne *et al.*, 2003) and the cuesta-like structures (Pinet *et al.*, 2008). The substantial thickness of the Quaternary sedimentary sequence (~400 m), its good state of preservation and its presence throughout the St. Lawrence Estuary make it clearly visible on seismic profiles (Syvitski and Praeg, 1989; Duchesne *et al.*, 2007). However, this does complicate the sampling of the deepest units. Thus, lithological and geochronological data sets are incomplete (Syvitski and Praeg, 1989; St-Onge *et al.*, 2003, 2008). In contrast, sediments from the late Wisconsinan to the present day could be cored and dated, allowing seismic units to be correlated with chronostratigraphic data (e.g., St-Onge *et al.*, 2008). The interpretation and description of the five main seismic units are summarized in **Table 1-1**.

2.2.2. Actual sedimentation

At the end of the Holocene, the sedimentation rate was 0.15 cm.year^{-1}. During the 20th century, it gradually increased to 0.28 cm.yr^{-1} and finally reached the current value of 0.74 cm.yr^{-1} at the mouth of the Lower Estuary (St-Onge *et al.*, 2003). However, these sedimentation rates are not homogeneous throughout the St. Lawrence Estuary. They decrease exponentially to 0.04 cm.yr^{-1} in the Gulf of St. Lawrence and 0.01 cm.yr^{-1} at the boundary with the North Atlantic Ocean (Zhang *et al.*, 2000; St-Onge *et al.*, 2003).

Modern sedimentation rates are partially influenced by anthropogenic activity during the second half of the 20th century with industrialization and intense land use along the St. Lawrence, the development of agriculture, and the establishment and development of cities (Zhang, 2000; St-Onge *et*

al., 2003). For several decades, an increase in sedimentation has been observed on the continental shelf, particularly along the north shore of the St. Lawrence. This is explained by the significant increase in coastal erosion which, in a context of global climate change, is expected to continue and increase in magnitude due to predictions of global sea-level rise (Mörner, 2004). Geophysical data reveal the important role of submarine canyons in transferring sediment from coastal erosion to the bottom of the Laurentian Channel, contributing to the negative sediment budget observed along the coast (Gagné *et al.*, 2009). However, it has been shown that in the Lower Estuary, it is not sediment supply that primarily controls canyon activity, but rather slope steepness (Nomandeau *et al.*, 2015).

Table 1-1. Characteristics and ages of the seismic units composing the Quaternary sequence. R refers to internal reflectors, G to reflector geometry, A to amplitude, and U to characteristics of the upper transition of units (completed according to Cauchon-Voyer *et al.*, 2008 and Duchesne *et al.*, 2010).

Seismostratigraphic sequence	Geological interpretation	Seismic attributes	Ages (ka)
Unit 5	Postglacial sediments	R: Medium to strong reflections G: Few internal reflecting horizons conformable with Unit 4 A: Medium to strong amplitude U: Sharp sediment-water contact	< 6 ka
Unit 4	Paraglacial sediments	R: Strong high frequency reflections G: Closely packed reflecting horizons, conformable with Unit 3 A: Alternating low to strong amplitude U: Sharp or gradational transition from Unit 4 to Unit 5	8.7-6 ka
Unit 3	Ice distal sediments	R: Weak reflections G: When apparent, reflecting horizons conformable with Unit 2 A: Low amplitude U: Sharp transition from Unit 3 to Unit 4	9.6-8.7 ka
Unit 2	Ice proximal sediments	R: Strong and high frequency reflections G: Closely packed reflecting horizons conformable with Unit 1 A: Alternating low to medium amplitude U: Sharp transition from Unit 2 to Unit 3	10.6-9.6 ka
Unit 1	Ice contact sediments	R: Absent reflections and absorption of acoustic energy G: No reflecting horizon A: Medium amplitude U: Sharp transition from Unit 1 to Unit 2	> 10.6 ka

2.3. Seismicity

2.3.1. Historical seismicity

The high level of seismic hazard in eastern Canada is largely due to the major earthquake that occurred on February 5, 1663 in the region of Charlevoix/Kamouraska with an estimated magnitude of 7 or greater (Smith, 1962; Gouin, 2001; Locat, 2011; Lamontagne *et al.*, 2018; **Figure 1-3**). Its effects were felt throughout the northeastern North American continent. It caused large landslides both on land (St-Jean Vianney, Shawinigan, Betsiamites, Mont Éboulé) and underwater (Saguenay Fjord, St. Lawrence Estuary). The distribution of large landslides to the north and along the north shore of the St. Lawrence supports the location of its epicenter not far from the Saguenay graben with an uncertainty of ± 50 km (Locat, 2011). Quebec was less populated in 1663 CE than today because of urban and demographic development. Obviously, such an earthquake today would cause much greater damage to the stability of infrastructure (e.g., viaducts, roads, bridges) as well as to the safety of populations.

In addition to the major earthquake of 1663, five other major earthquakes explain the high level of seismic hazard in the CKBSL region. Indeed, no less than five earthquakes of magnitude 6 and more occurred in this region in 1791, 1860, 1870, 1925 and 1988 (Smith, 1962; Lamontagne *et al.*, 2018; **Figure 1-3**).

The Charlevoix-Kamouraska (CK) seismic zone corresponds to the most active area in eastern Canada with an average of 200 earthquakes per year (Locat, 2011). Only a small proportion of these

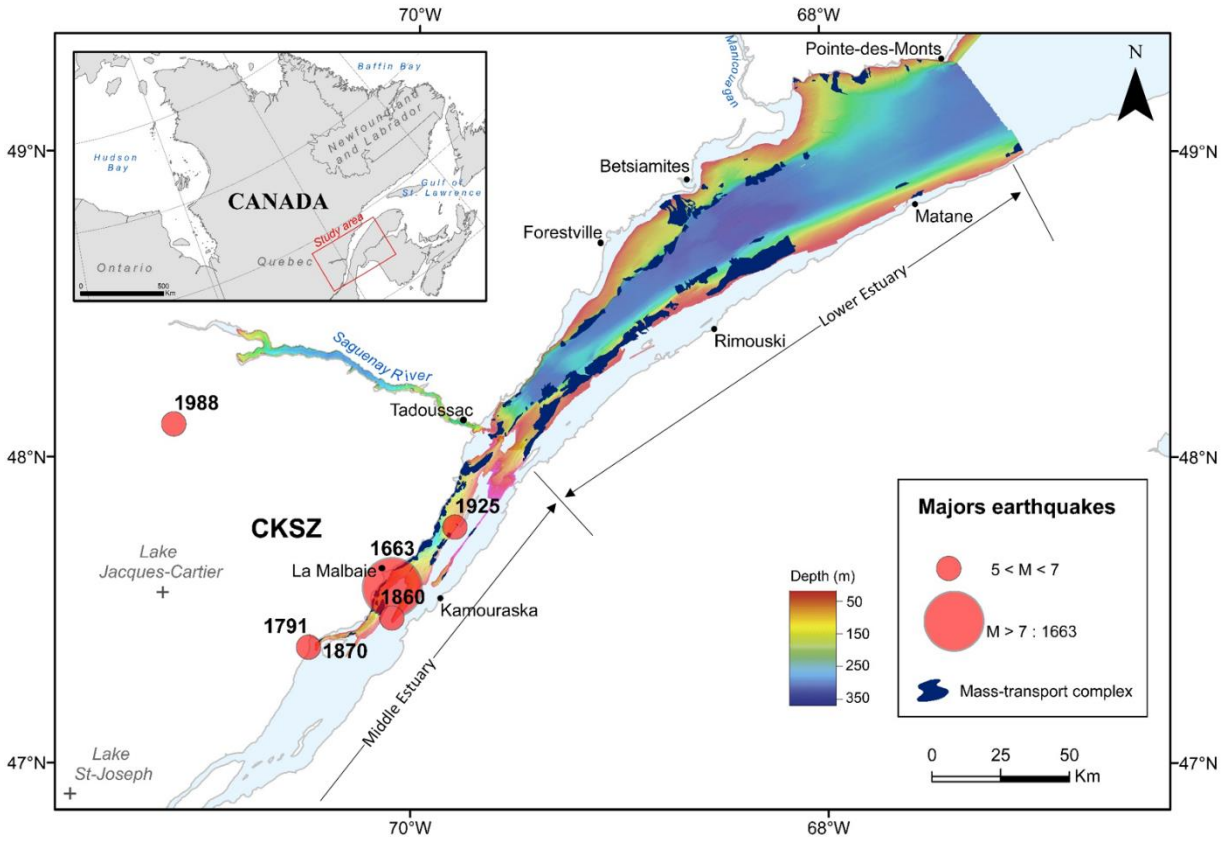

Figure 1-3. Bathymetric map of the St. Lawrence Estuary. Dark blue areas indicate the mass-transport complexes and red circles indicate major historical earthquakes (< 400 years). CKSZ: Charlevoix-Kamouraska Seismic Zone.

earthquakes exceed magnitude 3 while most are undetectable without instruments (Lamontagne *et al.*, 2003). The five major earthquakes to have occurred in eastern Canada (Smith, 1962; Lamontagne *et al.*, 2018) were concentrated in this area, between Charlevoix (north shore) and Kamouraska (south shore). Most earthquakes are confined to a 70 km long and 35 km wide zone beneath the St. Lawrence (Anglin, 1984) at depths between 5 and 25 km in the Precambrian basement.

Unlike the Charlevoix seismic zone, no major earthquake has been reported or recorded in the Lower St. Lawrence (BSL) seismic zone. However, two events with magnitudes greater than 5 have occurred (1944 and 1999). Most of the instrumented earthquakes have a magnitude of 4 or less with an average of 60 earthquakes per year.

2.3.2. Origins of seismicity

Intraplate earthquakes in eastern Canada have two probable origins: a tectonic origin and a postglacial origin (including glacial loading and unloading) (Wu, 1998). Several geological and geophysical evidences support a dominance of postglacial rebound in the generation of intraplate earthquakes (Goodacre and Hasegawa, 1980), but there is also other evidence supporting the dominance of tectonic stresses (Adams and Basham, 1989).

Tectonic

In eastern Canada, seismic activity occurs mainly along three zones of weakness (Grand Banks of Newfoundland, St. Lawrence Valley, and Ottawa-Bonnechere graben), which are reactivated by tectonic processes (Adams and Basham, 1989; Wu and Hasegawa, 1996). Most of the Charlevoix earthquakes are concentrated along or between faults inherited from the Iapetus Ocean (opening between 700 and 600 Ma) constituting the paleo-rift of the St. Lawrence (Anglin, 1984; Adams and Basham, 1989). Their depth in the Canadian Shield ranges from the surface to 30 km below the Logan Fault (thrust fault) and the Appalachians (Assameur and Mareschal, 1995; Locat, 2011). Furthermore, the maximum horizontal stress component determined from borehole measurements is higher than the lithospheric stress level (Sbar and Sykes, 1973). Deviatoric stress can reach several tens of MPa (Sbar and Sykes, 1973). This high level of regional stress is possibly mainly related to the opening of the Mid-Atlantic Ridge, which could cause a NW-SE oriented compression (Richardson and Reding, 1991). These observations are consistent with a tectonic origin of regional seismicity.

Glacio-isostatic

Trust faults impact geological structures formed during the presence of glaciers and this faulting mechanism is consistent with postglacial rebound. This indicates postglacial activity associated with isostatic rebound that can generate earthquakes (Wu, 1998). In addition, the orientation of these trust faults is predominantly NW-SE, consistent with the direction of ice retreat (Adams and Basham, 1989). Currently, the stress induced by glacial unloading, is not strong enough to generate new faults but may reactivate pre-existing faults (Du Berger *et al.*, 1991).

In the St. Lawrence region, deglaciation ended around 9 ka which predicts the greatest instability of postglacial faults in the 7-4 ka period (Wu, 1998). Several studies reveal that the frequency of turbidites (St-Onge *et al.*, 2004) and submarine

slides (Cauchon-Voyer *et al.*, 2011) is greater during this period. In this regard, dating of liquefaction events in the Wabash Valley (US/Canada border) also gives a seismically active postglacial period between 8 and 1 ka BP (Obermeier *et al.*, 1991).

Asteroid impact

A study by Roy and Du Berger (1983) revealed the presence of an astrobleme in the Charlevoix region indicating a meteorite impact 350 Ma ago that fractured and weakened the earth's crust to a depth of 14 km. The weakness of the fractured crust coupled with isostatic adjustment could explain the seismicity of this region given that earthquakes occur in impact fractures (Roy and Du Berger, 1983; Onwuemeka *et al.*, 2018). However, earthquakes are not confined to the astroblast suggesting that this is not the only cause of regional seismicity.

2.3.3. Impacts of earthquakes

The seismic hazard is a natural hazard that needs to be described by its nature, its location, its frequency (probability and/or occurrence) and its intensity. If the effects of an earthquake can be direct with the fall of objects and the collapse of buildings, they are often indirect with land movements and the generation of tsunamis related to a brutal fault movement in the ocean floor or a mass that slides in the marine environment (e.g., 1883: Krakatoa; 1979: Nice) (Hampton *et al.*, 1996). The assessment of seismic hazard requires the development of a paleoseismicity catalog (e.g., Lamontagne *et al.*, 2018 for Eastern Canada). This in turn allows to build seismic acceleration maps such as the one presented in **Figure 1-1**. These maps allow public authorities to implement actions to mitigate and prevent earthquake-related risks (Basham *et al.*, 1979; Adams and Atkinson, 2003). Risk refers to any possible damaging event related to the exposure of vulnerable issues to a hazard. Risk is related to human life and the concept of property, the risk is therefore zero if humans, their possessions, and activities are not involved (McCaal, 2012). Several factors can increase the incidence, scale, and effects of the hazard including increased population concentration, poor management in construction, water and waste provision and treatment, and poor consideration of possible long-term effects of disasters (McCaal, 2012).

3. SUBMARINE LANDSLIDES

In the submarine domain, three main groups of sedimentary processes occur. The first group includes the processes know as “resedimentation” which correspond to the transfer of sediment from shallow to deep water under the action of gravity, known as gravity processes (Pickering *et al.*, 1986). This type of geological process is of major importance in the transfer of material to the deep sea (Stow and Mayall, 2000). Bottom currents and surface currents with pelagic sedimentation constitute the two other groups.

After the major Grand Banks earthquake (1929), scientists began to investigate this geological hazard in the marine domain, motivated by the significant impacts that they can cause (e.g., telephone cable rupture, tsunami; Piper et Aksu, 1987; Higman *et al.*, 2018; Normandeau *et al.*, 2019). The sliding process refers to the movement of a sediment column along a failure surface, which defines a basal shear plane (**Figure 1-4**; Hampton *et al.*, 1996; Locat and Lee, 2002). The displaced

sedimentary mass may conserve its initial morphology or be deformed (Hampton *et al.*, 1996). Recent technological advances in acoustic and seismic imaging have led to a better understanding of submarine landslides. Thus, in seismic imaging, it is possible to recognize a sliding mass by its transparent acoustic facies and/or its highly deformed reflectors that reflect chaotic deposits. Depending on the nature and intensity of the deformation that affect the mobilized material, three categories of mass slides are distinguished: slides, slumps and creeping (e.g., Mulder and Cochonat, 1996).

Submarine landslides occur across the oceans and in a wide variety of geologic and tectonic settings (Vanneste *et al.*, 2014). Because seawater takes the place of air as the ambient fluid, these phenomena are relatively more frequent at sea than on land, can affect areas of low gradient, and mobilize considerable volumes (e.g., Storrega; Stow and Piper, 1984; Bugge *et al.*, 1988). Their mobility and flow can be very high (Mulder et al., 1998), sometimes generating large catastrophes (e.g., Storegga at ~8.1 ka; Talling *et al.*, 2014).

Almost all submarine landslides develop according to the common pattern of pre-failure, failure and post-failure, independently of their nature (Leroueil, 2001, 2004). These different deformation phases and each landslide process depend on a number of predisposing, triggering or aggravating factors (Vaunat and Leroueil, 2002). These factors are often poorly understood, because they are often site-specific and the available data (e.g., seismicity, rainfall, pore pressure) are limited; this is why continuous monitoring of the stability of continental slopes particularly exposed to seismicity and fluid overpressure is a major issue to better understand the risks associated with submarine landslides (e.g., Garziglia et al., 2021).

3.1. Preconditioning

Preconditioning is the pre-failure phase during which a combination of local and regional environmental factors lead to slope failure (Locat and Lee, 2002). Unfavorable sediment

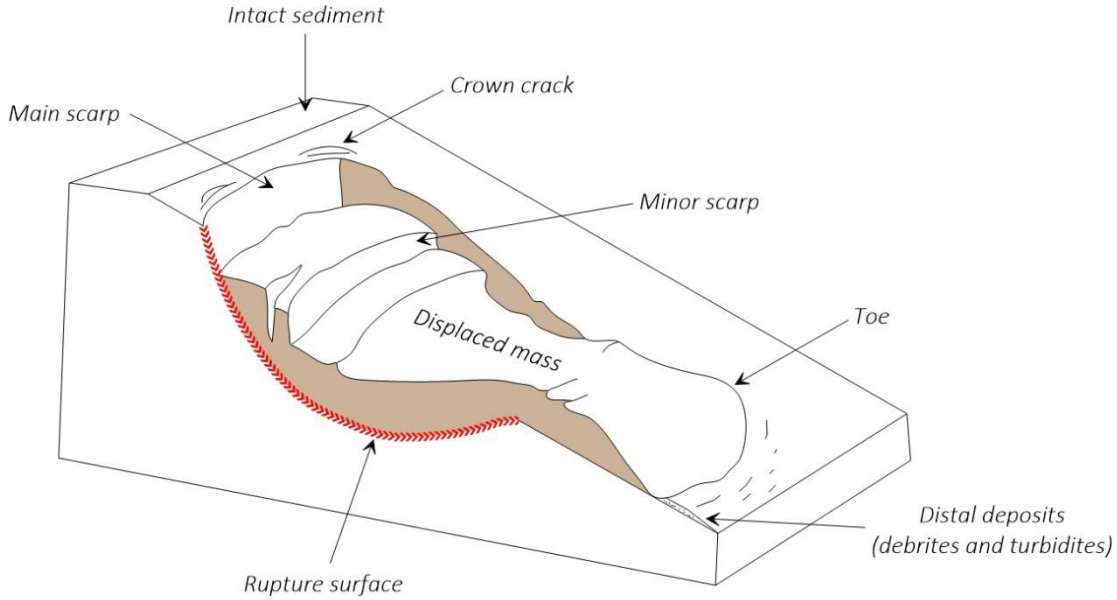

Figure 1-4. Schematic of a submarine landslide (modified from Hampton *et al.*, 1996).

stratification, slope-exacerbating erosion, and fluid flow (e.g., gas hydrate destabilization; gas loading) are considered as predisposing factors (Locat and Lee, 2002; Leroueil, 2004). In addition, the geomorphology of the seafloor may act as a predisposing factor. For example, in the St. Lawrence Estuary, sediment accumulation is not observed on steep slopes (Duchesne et *al.*, 2010; Pinet *et al.*, 2015), because one of the parameters that controls the initiation of rupture is the critical angle of failure of the material, which is reached more quickly on steep slopes (Bromhead and Dixon, 1986). Finally, rapid sedimentation is a preconditioning factor for failure because it generates interstitial overpressure, which results in lower effective stress and thus strength on failure (e.g., Dan *et al.*, 2007; Das, 2013; Pinet *et al.*, 2015). In the St. Lawrence Estuary, at the mouth of the Manicouagan River, which composes the largest submarine fan system in the estuary, sedimentation rates are highest but no submarine slides have been recorded (Pinet *et al.*, 2011). This suggests that relatively high sediment supply is not currently a predominant preconditioning factor in the estuary (Pinet et al., 2015). However, the very high sedimentation rate associated with the retreat of the Laurentian ice sheet from 23 to 6 ka has played a dominant role in seafloor instability (Clark *et al.*, 1978; Normandeau *et al.*, 2017).

3.2. Triggering

Failure occurs when the shear stress, noted τ, is greater than the shear strength of the sediment, noted τ_f (Lee *et al.*, 1991; Hampton *et al.*, 1996). This Mohr-Coulomb failure criterion is the simplest and most widely used to assess the stability of an infinite slope. The triggering factor is the process that will generate the sliding. Triggering is facilitated by local and regional weakening that occurs during the pre-failure phase (Leroueil, 2001). Triggering depends on the state of preconditioning progress, but also on the behavior of the sediment. There are two possible ways to trigger submarine landslides: by reducing shear strength or by increasing shear stress (Kopula, 1984; Lee *et al.*, 1991) through the factors summarized in **Table 1-2**. These factors can lead to failure before the shear strength has been reduced to zero (Hampton *et al.*, 1996).

Table 1-2. Summary of causes of landslide triggering (modified from Hampton *et al.*, 1996).

Reducing the strength	Increasing the stress
Earthquakes	Earthquakes
Wave loading	Wave loading
Eustatic changes	Eustatic changes
Climate	Diapirism
Sedimentation	Sedimentation
Gas and hydrates dissociation	Erosion
Artesian level change	
Erosion	

Seismicity is considered as the primary triggering factor of submarine landslides (Seed and Idriss, 1967; Hampton *et al.*, 1996) acting in three different ways. First, ground acceleration generated by seismic waves adds to destabilizing forces on the sedimentary column (Hack *et al.*, 2007). Second, tensile strength between soil particles can be broken by soil displacement during an earthquake, resulting in a loss of tensile strength and cohesion (Ishihara, 1985). Third, the effect of seismic waves on the

ground is equivalent to cyclic loading (Ishihara, 1985; Norem *et al.*, 1990) resulting in degradation of sediment stiffness and shear strength, and an increase in the pore pressure (u) of coarse sediment layers (e.g., silt to sand; Idriss *et al.*, 1976). Thus, the effective confining stress tends to zero (Terzaghi *et al.*, 1996) and the soil may lose all its shear strength. It deforms indefinitely in the direction of maximum stress, liquefying (Norem *et al.*, 1990). The first studies to explain and understand soil liquefaction (Yoshimi and Tokimatsu, 1977; Seed, 1979; Finn, 1981; Robertson and Fear, 1995) were conducted following the Niigata (1964) and Kobe (1995) earthquakes in Japan where most of the damage was not caused by the seismic shaking but by the subsequent soil liquefaction. This phenomenon is a major concern for seismic hazard assessment (Robertson and Wride, 1998). In Québec, following the 1870 CE and 1925 CE earthquakes, sand flows emerging from cracks in the ground were recorded in the Charlevoix region (Gouin, 2001). After the 1663 CE earthquake, about 100 sand volcanoes were formed and were interpreted by Chagnon and Locat (1988) as “sand boils” corresponding to the liquefaction of sand at depth and its ascent to the surface.

In the St. Lawrence Estuary, numerous superficial sandy layers have been identified (e.g., Cauchon-Voyer *et al.*, 2011; Normandeau *et al.*, 2015; Pinet *et al.*, 2015). Their presence allows us to hypothesize that in the case of an earthquake, the accelerations generated can liquefy these sandy levels and thus trigger submarine landslides.

Finally, cyclic loading during an earthquake does not necessarily lead to liquefaction, it can induce degradation of stiffness and shear strength of sandy and clayey layers (e.g., Pestana *et al.*, 2000).

3.3. Evolution

Once the failure is initiated, the sedimentary mass (a few meters to tens of meters thick) begins to slide along the failure plane and evolves rapidly. Its abrasion on the seabed can lead to the incorporation of debris and water, causing the progressive loss of its initial structure and composition. The landslide gradually transforms into a debris flow that can transport large suspended blocks (Lastras *et al.*, 2005; Vanneste *et al.*, 2006; **Figure 1-5**). On a steep slope, the debris flow accelerates allowing increased incorporation of water and sediment during its movement. Turbulence appears on its surface until the debris flow has completely transformed into a turbidity current (**Figure 1-5**). During the post-failure phase, remobilized sediments can reach high velocities (several tens of km/h) and travel very long distances even over a low slope seafloor (Kvalstad *et al.*, 2005). However, at the end of the course, the kinetic energy tends to decrease. The material that was in suspension through turbulence begins to deposit to form a turbidite (Ravenne and Béghin, 1983; **Figure 1-5**). The volume of displaced material can be significant. For example, the deposit associated with the submarine landslide triggered by the 1929 earthquake on the Grand Banks of Newfoundland covered 260 000 km² of the abyssal surface with an average thickness of about 1 m (Kvalstad *et al.*, 2005).

4. OBJECTIVES AND ISSUES

The high level of seismic hazard in the CKBSL region is related to the major earthquakes that have

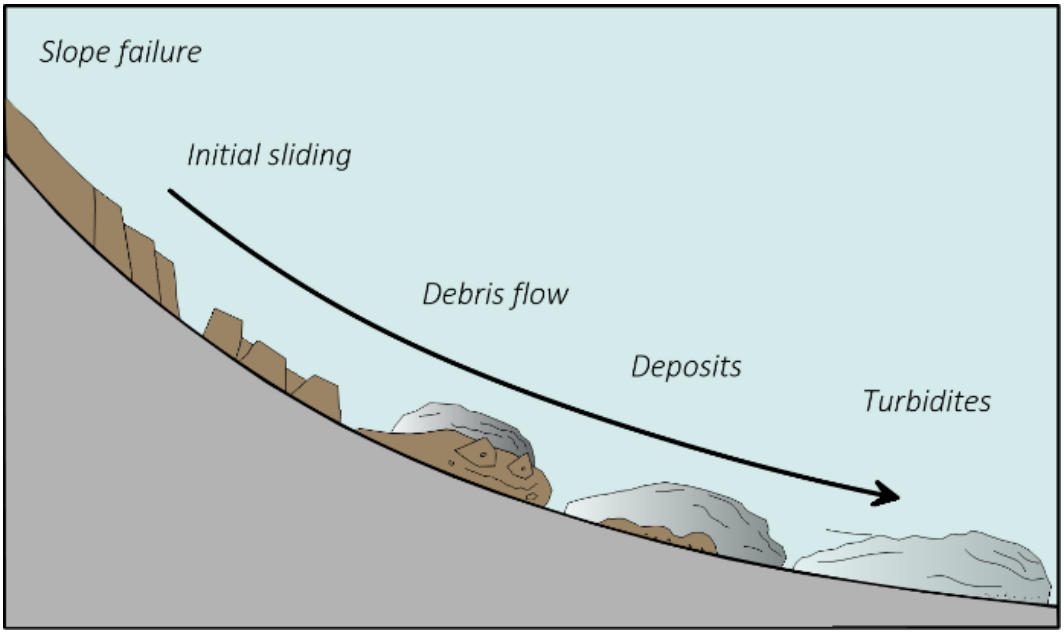

Figure 1-5. Schematic of the development of a submarine landslide from rupture to its final product: a turbidite deposit (modified from Bryn *et al.*, 2005).

occurred in southeastern Canada over the past 400 years. The major event of February 5, 1663, with an estimated magnitude of 7 or more, and the 5 earthquakes with magnitude greater than 6 recorded since 1663 reflect this high level of hazard. However, accurate assessment of seismic hazard requires a detailed understanding of past seismicity. One of the most crucial elements of this assessment is the determination of the maximum earthquake in a given area (e.g., Ebel, 2001). In Canada, estimating the largest earthquakes is difficult because there is no guarantee that the largest earthquake occurred in the last four centuries, i.e., the beginning of European settlement and of historical information on seismic activity.

However, the underwater environment can preserve evidence of major regional earthquakes. These records may go back beyond the settlement of European civilizations in eastern Canada. This type of earthquake recording beyond the historical record has been achieved in the submarine environment, such as on the west coast of the United States, where the description and dating of rapidly deposited layers (turbidites) have allowed the recurrence of high-magnitude earthquakes along the San Andreas Fault to be determined for the past 3000 years (Goldfinger *et al.*, 2012). Similarly, for the last twenty years, turbidites have been used as proxies for paleoseismicity in numerous geological contexts around the world (Lebreiro *et al.*, 1997; Gracia *et al.*, 2010; St-Onge *et al.*, 2012; Ratzov *et al.*, 2015; Babonneau *et al.*, 2019; Seibert *et al.*, 2019; Piper *et al.*, 2019; Howarth *et al.*, 2021), in Québec in the Saguenay Fjord (St-Onge *et al.*, 2004), and in the lacustrine domain (Philibert, 2012; Locat *et al.*, 2016; Lajeunesse *et al.*, 2017; Trottier *et al.*, 2019). However, in the St. Lawrence Estuary, only one landslide was assumed to be triggered by one or more historical earthquakes by Cauchon-Voyer *et al.* (2008). Thus, there is currently no

study at the scale of the estuary to link submarine landslides to the regional seismicity of Québec and thus to know the recurrence of major regional earthquakes. The first objective of this research work will respond to the need to reconstruct regional paleoseismicity.

OBJECTIVE I – PALEOSEISMICITY OF EASTERN CANADA

(5) Can we identify and characterize rapidly deposited layers (RDLs), final products of submarine landslides?

(6) What is the frequency of the RDLs? Do we find a synchronicity of landslides at the estuary scale?

(7) In the case where submarine landslides are associated with major earthquakes, can we go back more than 400 years?

(8) What is the major earthquake of the last millennia?

The main objective of this thesis is to determine the frequency of RDLs, final products of submarine landslides identified in the St. Lawrence Estuary. The analysis of sedimentological properties and dating of RDLs will allow to date these events and determine the trigger mechanism. In the case where submarine landslides are directly related to seismic activity, the combination of these data will allow the identification of major paleo-earthquakes in the CKSBL seismic zone.

The second objective of this research project is to study the behavior of sandy layers under the effect of earthquakes and more particularly the liquefaction phenomenon.

OBJECTIVE II – SEDIMENT LIQUEFACTION AND EPICENTERS OF MAJOR HISTORICAL EARTHQUAKES

(4) What is the geomechanical behavior of sediments under the effect of an earthquake?

(5) Which layers are the most liquefiable and cause destabilization?

(6) Can we update the location of regional earthquakes from the acceleration required to destabilize?

This objective requires the characterization of the mechanical behavior of intact sediment through its geotechnical analysis. Experimental laboratory tests will evaluate the liquefaction potential of the sediment. Coring of the upper sedimentary units of the Quaternary sequence will allow the evaluation of this potential for each of them and thus to identify the most critical interfaces, i.e., those most likely to locate the failure plan. Finally, the position of epicenters plays a crucial role in seismic risk assessment. However, for earthquakes prior to seismic instrumentation, it is difficult to locate them accurately and some have not been revised for several decades; By using the dating of submarine landslides triggered by regional seismicity (objective I), the epicenters of major earthquakes can be precisely located and possibly repositioned.

OBJECTIVE III – STABILITY OF UNDERWATER SLOPES

(3) What is the state of stability of slopes in submarine landslide zones under earthquakes loading?

(4) What is the size of critical earthquake that will destabilize the current slope?

An approach using numerical simulations will be developed to calculate the stability of the most critical slopes under the effect of accelerations generated by high magnitude earthquakes. The modeling will validate the causes and conditions at the origin of past and future destabilizations. By coupling stability calculations with the frequency of major earthquakes, it will be possible to anticipate future destabilizations and better understand the associated hazards such as tsunamis (Hampton *et al.*, 1996; Poncet *et al.*, 2010).

Although this research project is not intended to propose mitigation measures, it will contribute to the knowledge of seismic activity in eastern Canada. Indeed, mitigation measures, which are essential to reduce the impacts of landslides on infrastructures, rely on the integration of field data with laboratory tests and numerical simulations (Zakeri et al., 2008). The multidisciplinary approach that is implemented in this PhD project is consistent with the recommendation of Vanneste et al. (2014), which supports the combined use of geophysics, geotechnical engineering, geochemistry, sedimentology and modeling to study gravity instabilities.

5. THE THESIS

This PhD project took place between Québec (18 months) and France (18 months). The first year of the thesis was dedicated to the completion of the required classes to validate the PhD. The first class entitled "doctoral exam" consisted in answering two general scientific questions in oceanography. These responses took the form of two written reports and two oral presentations within a time limit of two months plus one month of preparation. The responses had to consider the four main oceanographic fields: geology, biology, chemistry and physics. The second class (5-6 months) was designed to prepare a written report that would present the subject, objectives, hypotheses, methodology and timeline of the PhD project. This document was the subject of an oral presentation in May 2020 to validate the "Seminar I" course.

Preparation of the expedition to the St. Lawrence Estuary was an important part of the project (~2 months). This work consisted in the preparation of the mission plan (study areas, geophysical surveys, coring sites). The SLIDE-2020 mission from July 18 to 29, 2020, was the subject of a mission report that I wrote after the mission.

Until May 2021, the mission data were analyzed at ISMER to complete Objective I. In May 2021, the "Seminar II" course was presented and the research project continued at Ifremer, France. The geotechnical laboratory analyses lasted 6 to 7 months and modeling followed for an equivalent duration. Objectives II and III were thus completed. Finally, the last months were dedicated to writing the thesis manuscript.

6. SCIENTIFIC COMMUNICATIONS

6.1. Publications

Mérindol, M., Sultan, N., St-Onge, G., Garziglia, S., Lajeunesse, P., 2022. *Location of the 1663 AD earthquake (M ~ 7) in the St. Lawrence Estuary (Canada) using sediment liquefaction analysis.* Engineering Geology. In revision.

Mérindol, M., St-Onge, G., Sultan, N., Lajeunesse, P., Garziglia, S., 2022. *Earthquake-triggered submarine landslides in the St. Lawrence Estuary (Québec, Canada) during the last two millennia and the record of the major 1663 CE M ≥ 7 event.*

Quaternary Science Reviews, 291, 107640. https://doi.org/10.1016/j.quascirev.2022.107640

6.2. Oral presentations

Mérindol, M., St-Onge, G., Sultan, N., Lajeunesse, P., Garziglia, S., 2022. *Paleoseismicity of eastern Canada based on earthquake-triggered submarine landslides in the St. Lawrence Estuary, Québec.* 18ème congrès français de sédimentologie.

Mérindol, M., St-Onge, G., Sultan, N., Lajeunesse, P., Garziglia, S., 2022. *Earthquake-triggered submarine landslides in the St. Lawrence Estuary (Québec, Canada) during the last two millennia and the record of the major 1663 CE M ≥ 7 event* (No. EGU2022-4835). Copernicus Meetings.

Mérindol, M., St-Onge, G., Sultan, N., Lajeunesse, P., Garziglia, S., 2022. *Earthquake-triggered submarine landslides in the St. Lawrence Estuary (Québec, Canada) during the last two millennias: importance of the 1663 ad (M>7) earthquake*. Congrès annuel du Géotop, 29 – 31 mars 2022.

Mérindol, M., Sultan, N., St-Onge, G., Garziglia, S., Lajeunesse, P., 2022. *Submarine landslides triggered by the 1663 earthquake (M>7) in the St. Lawrence Estuary, Quebec, Canada: implication on the location of its epicenter.* Rassemblement scientifique annuel de Québec-Océan, 31 janvier 2022.

Mérindol, M., St-Onge, G., Sultan, N., Lajeunesse, P., Garziglia, S., 2021. *Submarine landslides in the St. Lawrence Estuary, Québec, Canada.* Congrès annuel du Géotop, 16 – 19 mars 2021.

6.3. Author contributions

Méril Mérindol

- → Writing of articles and thesis;
- → Preparation of the expedition at sea;
- → Participation in the expedition at sea;
- → Conceived and designed the analysis;
- → Collected data;
- → Contributed data and analysis tools;
- → Conducted analyses.

Guillaume St-Onge

- → Correction of articles and thesis;
- → Preparation of the expedition at sea;
- → Participation in the expedition at sea;
- → Conceived and designed the analysis;
- → Contributed data and analysis tools.

Nabil Sultan

- → Correction of articles and thesis;
- → Preparation of the expedition at sea;
- → Conceived and designed the analysis;
- → Contributed data and analysis tools.

Patrick Lajeunesse

- → Correction of articles and thesis;
- → Contributed data and analysis tools.

Sébastien Garziglia

- → Correction of articles and thesis;
  Contributed data and analysis tools.

CHAPITRE II – MATERIELS ET METHODES

CHAPTER II. MATERIALS AND METHODS

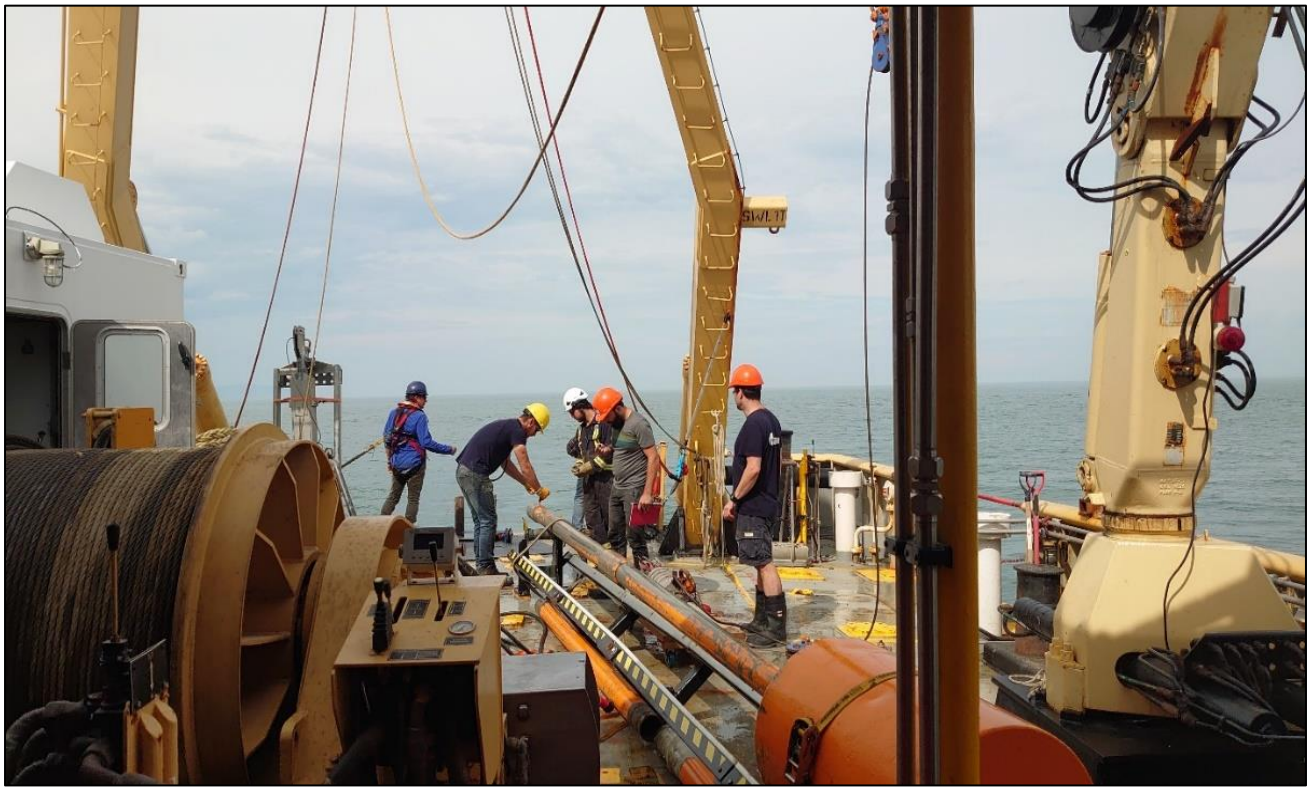

Déploiement du carottier à gravité lors de la mission SLIDE-2020 sur le N/R Coriolis II.
Deployment of the gravity corer during the SLIDE-2020 expedition on board the R/V Coriolis II.

CHAPITRE 2. RÉSUMÉ

Pour répondre aux problématiques liées aux glissements sous-marins, il est essentiel d'utiliser et de croiser plusieurs disciplines des géosciences marines. En effet, il est à la fois nécessaire de pouvoir travailler sur des cartographies en surface et en profondeur tout en ayant des informations sur la stratigraphie, le type de sédiment, le taux d'accumulation, l'âge de la rupture, le mécanisme de dépôt etc. Ainsi, la mission SLIDE-2020 à bord du N/R Coriolis II avait pour objectif de réaliser des levés géophysiques et des opérations de carottage autour des zones de glissements sous-marins réparties sur 250 km le long de l'estuaire du Saint-Laurent dans l'Est du Canada. Ce chapitre détaille les données acquises et utilisées ainsi que les méthodes d'analyses menées durant le doctorat. Sa structure est la suivante : **(1)** la géophysique acquise par le sondeur multifaisceaux et le profileur de sous-surface ; **(2)** l'échantillonnage par les carottiers à gravité et à boîte ; **(3)** les analyses sédimentologiques dont l'imagerie à Rayons-X, les mesures MSCL, la description lithostratigraphique ; **(4)** la datation avec les méthodes de datation (^{14}C) et (^{210}Pb) ; **(5)** les analyses géotechniques dont les essais œdométriques, l'utilisation de la cellule triaxiale et **(6)** la modélisation numérique avec un modèle de comportement qui considère la liquéfaction du sédiment et l'étude de sa sensibilité. L'ensemble des résultats est présenté en annexes.

CHAPTER 2. ABSTRACT

To answer the issues related to submarine landslides, it is essential to use and cross several disciplines of marine geosciences. Indeed, it is necessary to work on surface and depth maps with information on the stratigraphy, the sediment type, the accumulation rate, the age of rupture, the mechanism of deposition etc. Thus, the objective of the SLIDE-2020 mission aboard the R/V Coriolis II was to carry out geophysical surveys and coring operations around the submarine landslide zones distributed along the St. Lawrence Estuary in eastern Canada, over 250 km. This chapter details the data acquired and useds as well as the methods of analysis carried out during the PhD. Its structure is as follows: **(1)** geophysics acquired by multibeam echosounder and subsurface profiler; **(2)** sampling by gravity and box corers; **(3)** sedimentological analyses including X-ray imaging, MSCL measurements, lithostratigraphic description ; **(4)** ^{14}C and ^{210}Pb dating methods; **(5)** geotechnical analyses including œdometer tests, the use of the triaxial cell; **(6)** numerical modeling with a behavioral model that considers sediment liquefaction and the study of its sensitivity. All the results are presented in the appendices.

1. GEOPHYSIQUE

L'utilisation de la géophysique marine permet une meilleure compréhension des phénomènes gravitaires sous-marins et de l'aléa géologique qu'ils représentent (Vanneste *et al.*, 2014). En effet, le couplage de l'imagerie sismique et bathymétrique permet à la fois de cartographier les preuves d'instabilités récentes présentes sur le fond marin mais aussi passées, enfouies dans la colonne sédimentaire.

1.1. Données bathymétriques

Les données bathymétriques sont la principale source d'identification des déformations et instabilités récentes qui ont une empreinte géomorphologique sur le fond marin. Le sondeur multifaisceaux est devenu la norme pour la cartographie des fonds marins. Les informations bathymétriques dépendent du temps de propagation des ondes acoustiques. La résolution spatiale des données bathymétriques diminue avec l'augmentation de la profondeur de l'eau et des fréquences de la source.

La bathymétrie de l'estuaire du Saint-Laurent a été acquise entre 1997 et 2005 par le Service hydrographique du Canada à l'aide de sondeurs multifaisceaux montés sur le navire de la Garde côtière Frederick G. Creed (avant 2005 : Kongsberg EM-1000 ; en 2005 : EM-1002) et Guillemot (avant 2005 : EM-3000 ; en 2005 : EM-3002). Ces levées permettent d'avoir une couverture totale du fond de l'estuaire à partir de 30 m de profondeur avec une résolution de 5 m.

La mission SLIDE-2020 à bord du N/R Coriolis II (18 – 29 juillet 2020) a permis de cartographier près de 30 zones de glissements sous-marins en améliorant la résolution à 1 m (**Figure 2-1**). L'équipement utilisé consiste en un sondeur multifaisceaux Kongsberg EM-2040 couplé à la station inertielle Applanix POS/MV. Le logiciel Caris Hips & Sips a été utilisé pour le traitement et la correction des données brutes (navigation, marée, géométrie, nettoyage ; **Figure 2-1**). Enfin, ces données ont pu être corrigées à l'aide des mesures au célérimètre Minos de AML oceanographic qui mesure la variabilité de la vélocité du son dans la colonne d'eau.

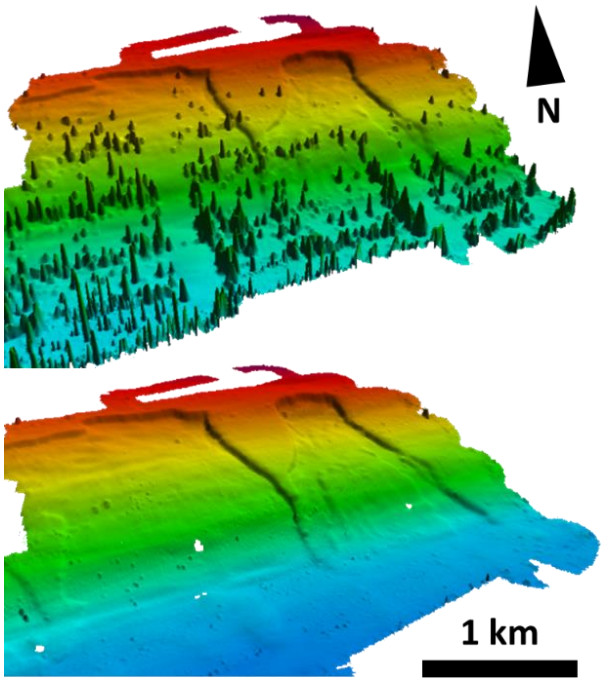

Figure 2-1. Glissements dans la région de Baie-Comeau. Haut : bathymétrie bruitée ; Bas : après traitement.

Les levés bathymétriques transversaux aux cicatrices des glissements, i.e., perpendiculaires à la pente, ont permis de réaliser des profils bathymétriques d'une grande précision et ont été utilisés dans les calculs numériques de stabilité des pentes.

1.2. Données sismiques

La sismique réflexion des ondes acoustiques permet d'approcher l'histoire géologique par l'établissement de la stratigraphie et ainsi de retrouver les glissements sous-marins du passé.

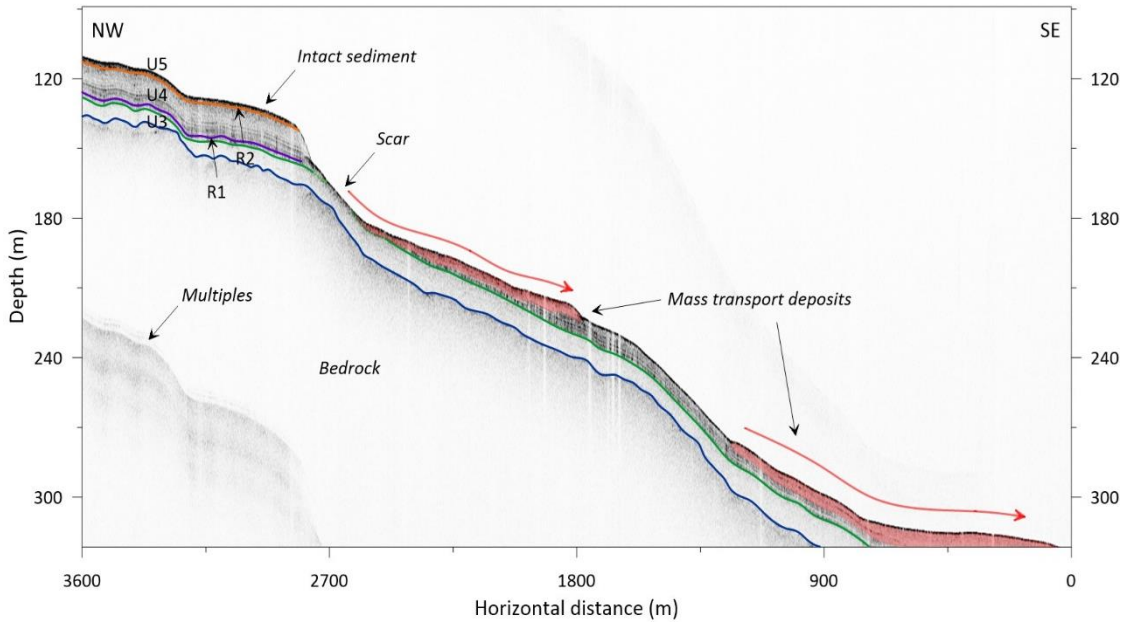

Figure 2-2. Profil sismique acquis dans la région de Baie-Comeau. Transversal a un glissement sous-marin, il permet d'identifier le sédiment intact (non-glissé) où la séquence sédimentaire quaternaire est identifiable au-dessus du socle, la cicatrice et les dépôts en contrebas (en rouge). Les flèches rouges indiquent le sens du transport sédimentaire.

La mission SLIDE-2020 a permis d'acquérir ~1500 km de profil sismique à l'aide du profileur de sous-surface Edgetech X-Star 2.1 monté sur la coque (**Figure 2-2**). La source Chirp utilisée avait une fréquence de 2 à 12 kHz et des pulses de 3 à 20 ms. Afin de convertir les profondeurs-temps, une vitesse de 1500 $m.s^{-1}$ a été utilisée, i.e., la vitesse moyenne du son dans l'eau et mesurée dans les sédiments.

L'interprétation de la séquence sismostratigraphique est basée sur les attributs sismiques tels que la réflexion, la géométrie et l'amplitude des réflecteurs détaillés par Cauchon-Voyer *et al.* (2008) et Duchesne *et al.* (2010).

2. CAROTTES SEDIMENTAIRES

2.1. Carottier à boîte – Box Core (BC)

Le carottier à boîte (**Figure 2-3**) permet d'échantillonner la partie superficielle de la colonne sédimentaire. Son intérêt réside dans la rapidité de son déploiement (~30 min) et dans la préservation de l'interface eau/sédiment. La boîte de sédiment est sous-échantillonnée à l'aide de *push-core*s qui sont raccordées à une pompe permettant de limiter la compaction du sédiment lors de l'enfoncement des tubes.

Figure 2-3. Déploiement du carottier à boîte sur le pont du N/R Coriolis II lors de la mission SLIDE-2020.

Le carottier à boîte (**Figure 2-3**) a été systématiquement déployé sur chacun des sites de prélèvement sédimentaire afin de (1) déterminer les vitesses de sédimentation récentes et (2) donner un aperçu de la nature du fond lorsque l'interprétation des profils sismiques ne le permet pas. Quand le

fond était constitué de trop nombreuses roches, le carottage à l'aide du carottier à gravité ne pouvait être envisagé. Ainsi, dans ce type de situation, ce dernier n'était pas déployé pour le préserver et gagner du temps.

2.2. Carottier à gravité – Gravity Core (GC)

Le carottier à gravité (**Figure 2-4**), d'un poids de 900 kg, permet de prélever des séquences sédimentaires de ≤ 9 m de longueur (3 tubes de PVC de 3 m). Il est muni d'un *core catcher* qui maintient le sédiment dans le tube de PVC lors de la remontée du carottier. La chute libre du carottier permet son enfoncement dans les sédiments. Il est relié à un treuil afin de le remonter à bord du navire. Lors de la campagne, il était majoritairement utilisé dans sa configuration de 6 m. Lorsque le sédiment permettait sa bonne pénétration, il était mis dans la configuration 9 m. Dans le cas échéant, il était raccourci à 3 m.

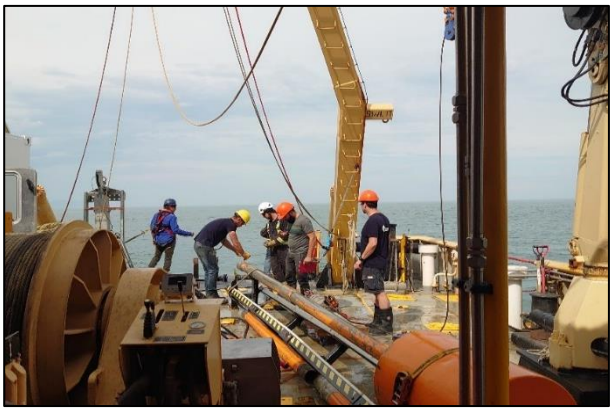

Figure 2-4. Déploiement du carottier à gravité sur le pont du N/R Coriolis II lors de la mission SLIDE-2020.

2.3. Sites d'échantillonnage

Durant la campagne SLIDE-2020, les carottes ont été récupérées sur une distance de plus 250 km le long de l'estuaire du Saint-Laurent a des profondeurs d'eau comprises entre 34 et 354 m (**Figure 2-5**). Les sites de carottage devaient

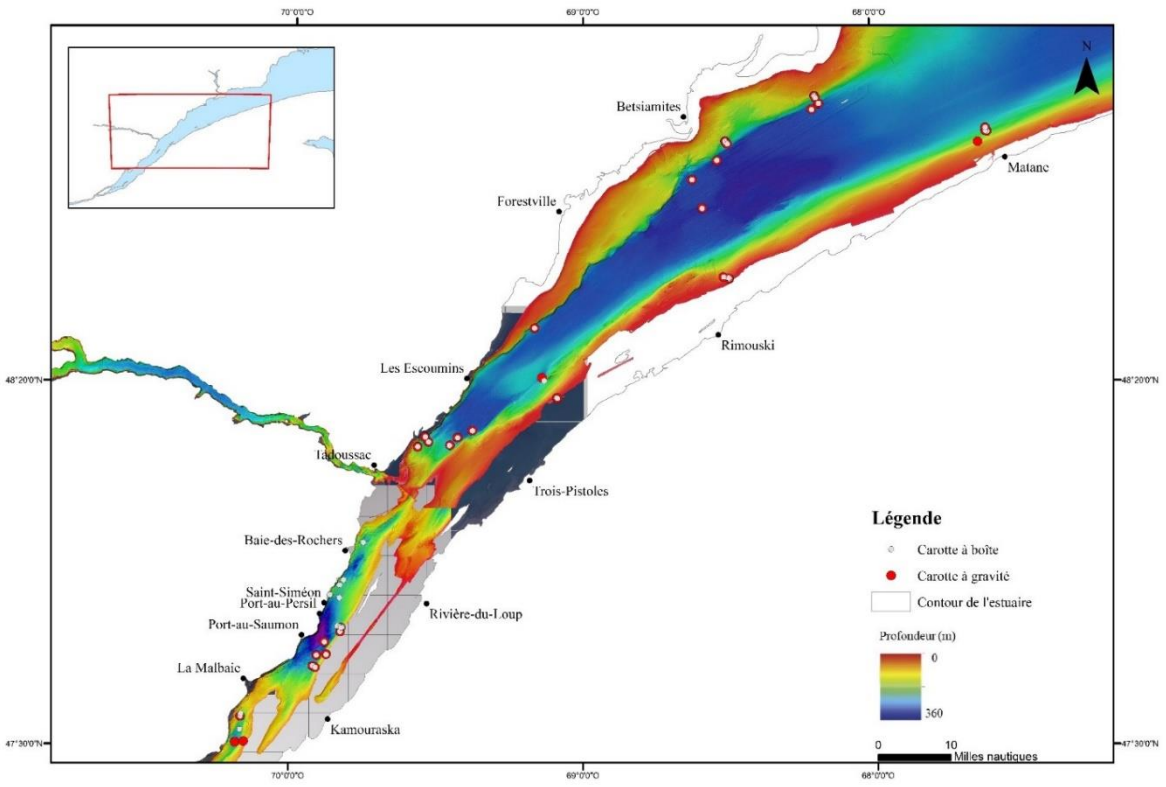

Figure 2-5. Carte de l'estuaire du Saint-Laurent avec les sites de carottage. En gris les carottes à boîtes et en rouge les carottes à gravité.

répondre à plusieurs problématiques. Pour la datation des dépôts associés aux glissements sous-marins, les cibles correspondaient aux réflecteurs sismiques subhorizontaux dans la partie distale des dépôts chaotiques en contrebas des cicatrices d'arrachement (**Figure 2-2**). Cela avait pour but de n'échantillonner que la partie la plus fine des glissements (e.g., turbidite, débrite) pour dater le sédiment au-dessus et en-dessous des RDLs. Les sites d'échantillonnage sont éloignés des embouchures des rivières et ne sont ni en pied de chenaux turbiditiques actifs, ni dans des zones avec des pockmarks cartographiés par Pinet *et al.* (2015). Ainsi, les RDLs visées ne sont en théorie pas affectées par des processus sédimentaires locaux. En revanche, le contexte estuarien peut mener à l'enregistrement de processus sédimentaires régionaux tels que les courants hyperpycnaux.

Pour la caractérisation géotechnique et sédimentologique des différentes unités sédimentaires, des carottes ont été prélevées dans le sédiment intact (**Figure 2-2**), i.e., non affecté par un glissement sous-marin, et dans les cicatrices d'arrachement pour accéder aux couches les plus profondes.

3. ANALYSES SEDIMENTAIRES

Les analyses sédimentaires suivaient un ordre précis qui débutait par (1) les mesures XCT (radiographies digitales), puis par (2) les mesures MSCL (densité, susceptibilité magnétique et vitesse des ondes P) sur carotte entière. À l'issue de ces premières analyses et après isolation des échantillons géotechniques, les carottes ont été ouvertes à l'aide du banc de découpe. Les demi-sections ont été analysées une deuxième fois au MSCL (3) (photographie, susceptibilité magnétique avec senseur ponctuel, densité, spectrophotomètre et fluorescence X). Le pas de mesure variait de 0,5 cm pour les carottes en boîte à 1 cm pour les carottes à piston et à gravité. Au total, j'ai analysé plus de 100 carottes durant la thèse ce qui représente près de 160 m de sédiment. Toutes n'ont pas été utilisées, mais les planches de résultats sont présentées en annexe pour l'entièreté des carottes à gravité.

3.1. CAT-Scan

La tomographie axiale informatisée (CAT-scan) permet une visualisation rapide des sections longitudinales (topogramme) et transversales (tomogramme) des carottes de sédiments. L'acquisition de ces images a été réalisée par le XCT (GEOTEK) de l'ISMER (**Figure 2-6**) avec une résolution allant de 40 à 300 µm. Les images résultantes sont affichées en nuances de gris et peuvent être corrélées avec les profils de densité. En effet, les nuances claires traduisent une densité élevée alors que les nuances foncées, une densité faible. Cette mesure non destructive permet d'identifier les structures sédimentaires, de déterminer le mode de déposition, d'établir une stratigraphie haute-résolution et d'évaluer les propriétés physiques du sédiment (St-Onge *et al.*, 2007). A l'aide des données du CAT-Scan, j'ai pu

Figure 2-6. GEOTEK MSCL-XCT du laboratoire de géologie marine de l'ISMER

identifier les niveaux les plus grossiers (silt à sable) qui nous intéressaient pour la géotechnique. Ainsi, des sections de carotte destinées à la géotechnique et devant rester entières, ont pu être sélectionnées.

3.2. Multi-Sensor Core Logger (MSCL)

3.2.1. Photographie

Les photographies prises à l'aide du *Geoscan IV* (**Figure 2-7**) sont une mémoire visuelle du sédiment après l'ouverture de la carotte, avant que toute forme d'oxydation et/ou de modification chimique ne s'opèrent. Elles permettent de distinguer des structures sédimentaires et la présence de couches déposées rapidement à une résolution de 200 pixel.cm^{-1} (**Figure 2-8**).

3.2.2. Susceptibilité magnétique

La susceptibilité magnétique volumétrique, notée k_{LF} est un indicateur de la concentration en minéraux ferrimagnétiques. Sa mesure se réalise à l'aide du senseur MS2E1 Bartington (**Figure 2-7**). Sa valeur est également sensible à la variation de la taille des grains magnétiques (St-Onge *et al.*, 2007). Cette mesure est utilisée pour corréler les carottes sédimentaires par rapport à la lithologie, mais aussi pour identifier les bases grossières des RDLs (*e.g.*, Bieber *et al.*, 2021 ; **Figure 2-8**).

3.2.3. Gamma-densité

La source radioactive de ^{137}Cs (**Figure 2-7**) émet des rayons gamma qui en traversant le sédiment subissent une atténuation. Sachant que cette dernière est fonction de la densité et après calibration des données à l'aide de l'aluminium d'une densité et d'un diamètre connus, la mesure de l'atténuation permet d'obtenir des profils de densité. Ces profils sont utilisés pour identifier les différentes unités lithologiques et les RDLs (**Figure 2-8**), mais aussi pour les incréments dans les modèles de comportement.

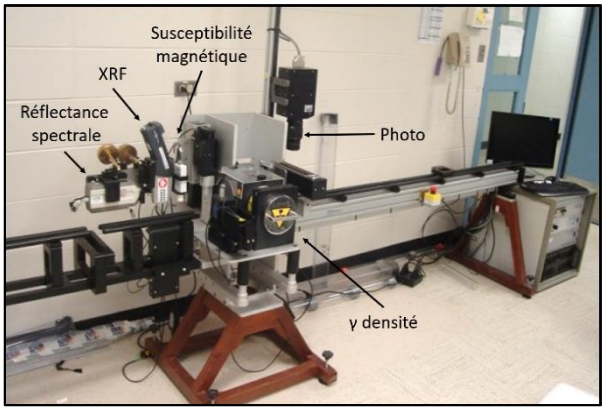

Figure 2-7. MSCL GEOTECK du laboratoire de géologie marine de l'ISMER. Sont montés en lignes de droite à gauche : l'appareil photo, la source gamma, les transducteurs des ondes P, le senseur MS2E1 de Bartington, le XRF et le spectrocolorimètre.

3.2.4. Vitesse des ondes P

Le système de mesure de vitesse de propagation des ondes P (ondes de compression) est composé d'une paire de transducteurs (fréquence autour de 230 kHz) de part et d'autre de la carotte sédimentaire servant d'émetteur et de récepteur (**Figure 2-7**). Leur vitesse de propagation dans les sédiments marins est influencée par les variations de lithologie, de densité, de porosité, de pression lithostatique, de la fracturation, de la consolidation et de la présence de gaz libre ou sous la forme d'hydrates (St-Onge *et al.*, 2007). Ces vitesses sont aussi utiles afin d'estimer des profondeurs de réflecteurs acoustiques dans les profils sismiques de la colonne sédimentaire et ainsi de les corréler avec les carottes sédimentaires.

3.2.5. Réflectance spectrale

La variation de réflectance spectrale traduit une variation de la couleur du sédiment. Plusieurs facteurs peuvent l'expliquer dont la minéralogie, la teneur en carbonate et la matière organique (St-

Onge *et al.*, 2007). La réflectance spectrale s'exprime par les paramètres *L**, *a** et *b** définis par la Commission internationale de l'éclairage (*International Commission on Illumination*). Elle se mesure à l'aide du capteur *Minolta CM-2600d* (**Figure 2-7**). *L** traduit la variation de la couleur entre le blanc (100) et le noir (0) qui peut être induite par la teneur en carbonate (e.g., St-Onge *et al.*, 2004 ; **Figure 2-8**). *a** exprime la variation entre le vert (-60) et le rouge (+60) (e.g., teneur en hématite), et *b** entre le bleu (-60) et le jaune (+60).

3.2.6. Fluorescence X (XRF)

La composition géochimique (**Figure 2-7**) était mesurée sur les demi-sections des carottes en utilisant le scanner non-destructif Olympus Innov-X Delta en ligne avec le MSCL. Le pas de mesure était de 1 cm pour les GC contre 0,5 cm pour les BC. J'ai principalement utilisé les ratios de Ca/Fe, un proxy de la proportion détritique et biogénique, et de Rb/Zr, un proxy de la granulométrie (**Figure 2-8**). Ainsi, ces rapports permettent l'identification des RDLs (Croudace *et al.*, 2006) et d'aider à distinguer précisément le sommet des RDLs de la sédimentation hémipélagique.

3.3. Description lithostratigraphique

La description lithostratigraphique se réalise sur une demi-carotte juste après son ouverture. Lors de cette description, les différents faciès sont différenciés en fonction de la granulométrie, de la couleur et des structures sédimentaires (**Figure 2-8**). Ces dernières peuvent par exemple inclure des contacts francs, des surfaces érosives, des laminations parallèles ou entrecroisées et la présence de galets indurés ou de bioturbations. Cette fiche descriptive est un outil de travail, car elle est utilisée comme base pour les mesures suivantes : granulométrie, géotechnique, datations ; et pour une première interprétation en termes de processus de dépôt.

3.4. Granulométrie

Un total de 1320 analyses granulométriques a été réalisé à l'ISMER par Sandrine Ouellet et moi-même. Elles se répartissent sur 42 carottes de la mission SLIDE-2020 et 2 carottes de la mission COR0703. Le pas d'échantillonnage variait entre 50 cm, pour les niveaux homogènes, et 1 cm lorsqu'il y avait des variations sédimentologiques (e.g., transition de faciès, turbidite).

La mesure granulométrique est basée sur la diffraction d'un rayon laser par les grains (Loizeau *et al.*, 1994) à l'aide du granulomètre *MasterSizer 3000* de l'entreprise *Malvern*. Dans un milieu homogène, le rayon lumineux se propage en ligne droite et ne dévie que s'il rencontre des particules. L'angle avec lequel ce rayon est dévié est dépendant de la taille du grain sédimentaire. La distribution granulométrique des grains est mesurée de 0,1 à 2000 µm. Avant d'effectuer la mesure, les échantillons sont dilués dans une solution composée d'eau distillée et d'hexametaphosphate de sodium puis agités pendant 24 h pour défloculer les particules d'argile. Les grains excédant 2000 µm sont triés à l'aide d'un tamisage.

Les données brutes une fois traitées permettent d'établir la répartition des grains en pourcentage de chaque classe granulométrique : argile (< 2 µm), silt (2 – 63 µm) et sable (63 µm – 2 mm) (**Figure 2-8**).

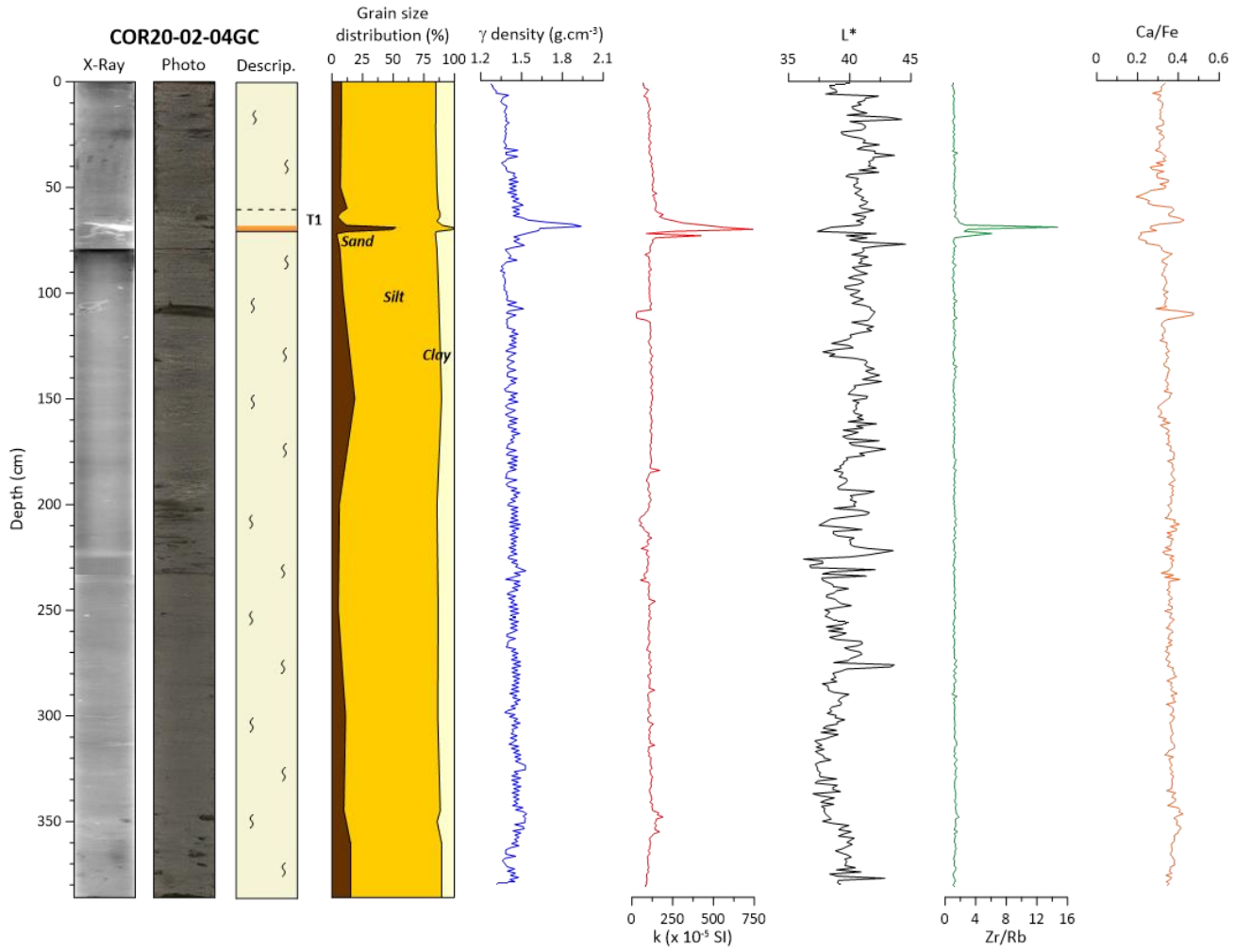

Figure 2-8. Planche de résultats des analyses sédimentologiques menées sur la carotte COR20-02-04GC. De gauche à droite : imagerie rayons-X, photo, granulométrie, description, densité gamma, susceptibilité magnétique, L*, Zr/Rb (proxy granulométrie) et Ca/Fe (proxy détritisme). Ces données ont permis d'identifier une turbidite d'une épaisseur de 11,5 cm à 66,5 cm de profondeur.

4. GEOCHRONOLOGIE

4.1. Datation radiocarbone – 14C AMS

La datation au radiocarbone a été effectuée sur 45 échantillons de coquilles ou de matière organique que j'ai prélevé proche des bases des RDLs, mais dans les sédiments hémipélagiques. Après un prétraitement et une graphitisation au Centre d'études nordiques de l'Université Laval (Québec), ils ont été mesurés au Keck-Carbon Cycle AMS de l'Université de Californie à Irvine (USA). Pour obtenir une chronologie précise des RDLs, les âges radiocarbones des échantillons hémipélagiques ont été calibrés à l'aide du logiciel Calib 8.2 (Stuiver et Reimer, 1993) et de la courbe Marine20 (Heaton *et al.*, 2020). Afin de considérer le décalage local par rapport au réservoir océanique global (ΔR), trois âges de réservoir de McNeely *et al.* (2006) ont été utilisés et moyennés pour les échantillons de coquilles. Dans l'estuaire maritime, le ΔR est de 39 ± 63 ans tandis que dans l'estuaire moyen le ΔR est 80 ± 94 ans. Enfin, les âges radiocarbones ont été convertis en âges calendaires (CE) pour être comparés aux séismes historiques.

Pour construire les modèles d'âge les mieux ajustés, le logiciel R Bacon 2.3 (Blaauw et Christen, 2011) a été utilisé. Il prend en compte les

statistiques bayésiennes avec une distribution normale. Les deux écarts types de 2 σ (probabilité de 0,95) et de 1 σ (probabilité de 0,68) ont été utilisés dans les calculs. Dans ces calculs, l'érosion des turbidites est supposée négligeable, car il n'a pas été possible de quantifier l'érosion basale (e.g., Gracia *et al.*, 2010 ; Pouderoux *et al.*, 2014 ; Moernaut *et al.*, 2017) et la méthode proposée par Goldfinger *et al.* (2012) ne pouvait s'appliquer aux carottes prélevées.

4.2. Vitesse de sédimentation – 210Pb

Le plomb 210 (^{210}Pb ; $T_{1/2}$ = 22,3 ans) est largement utilisé pour les études portant sur les processus sédimentaires récents au cours des 150 dernières années (e.g., Hubert *et al.*, 2020). Le taux de sédimentation peut être dérivé des profils de ^{210}Pb (e.g., Appleby et Oldfield, 1978 ; St-Onge *et al.*, 2004 ; Levesque *et al.*, 2006). Il permet de déterminer l'âge de la couche sous la sédimentation récente hémipélagique.

Les taux de sédimentation ont été dérivés des mesures de ^{210}Pb sur les sédiments de 6 carottes boîtes. J'ai échantillonné les carottes à boite à des intervalles allant de 1 à 5 cm. Les échantillons ont été lyophilisées, puis broyés en une poudre fine et homogène. L'activité du ^{210}Pb a été mesurée à l'aide d'un compteur gamma GMX50-S d'Ortec (**Figure 2-9**) et d'un compteur GX7020 de Canberra au laboratoire souterrain de la station aquicole de l'ISMER. Ces mesures ont été réalisées par Pascal Rioux au laboratoire souterrain de la station aquicole de l'ISMER. En considérant le modèle de flux constant et de taux constant (Appleby et Oldfield, 1978), les taux de sédimentation (cm.an^{-1}) ont été dérivés de la pente de Ln (^{210}Pb$_{excess}$) (**Figure 2-10**). Les âges des turbidites ont ensuite été

Figure 2-9. Compteur gamma GMX50-S d'Ortec dans le laboratoire sous-terrain de la station aquicole (ISMER).

calculés en extrapolant un taux de sédimentation constant jusqu'à la profondeur hémipélagique des turbidites. La compaction des sédiments est négligée car la courbe de densité de la sédimentation hémipélagique, dans les carottes étudiées, est constante avec la profondeur (**Figure 2-10**).

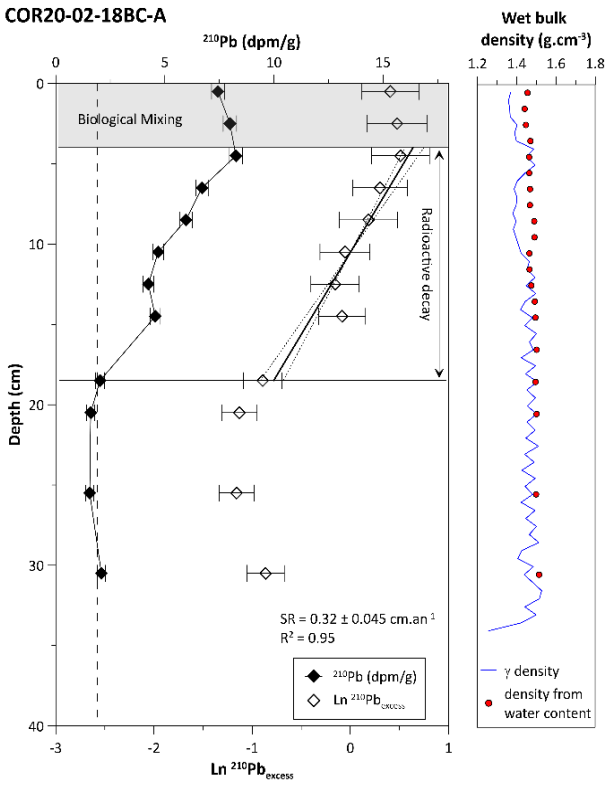

Figure 2-10. Méthode pour calculer une vitesse de sédimentation à partir de la décroissance radioactive du ^{210}Pb. Les premiers centimètres bioturbés sont exclus.

5. MESURES GEOTECHNIQUES

Les analyses géotechniques ont été menées sur du sédiment prélevé autour et dans les cicatrices des glissements sous-marins afin de caractériser mécaniquement le sédiment intact et la couche d'interface du glissement dans la cicatrice. À partir des profils MSCL et XCT sur carottes entières, des échantillons destinés à la géotechnique ont été sélectionnés et découpés (**Figure 2-11**). J'ai porté une attention particulière aux sédiments grossiers qui sont les plus susceptibles de se liquéfier. Afin de pouvoir réaliser trois essais par couche d'environ 10 cm de longueur, j'ai sélectionné des sections de 45 cm. Ces sections ont été isolées pour conserver leur humidité et ont été convoyés de l'ISMER jusqu'au laboratoire de géotechnique de l'Ifremer à une température avoisinant 4° C.

Figure 2-11. Sections de carottes entières destinées aux mesures géotechniques.

5.1. Teneur en eau et porosité

J'ai réalisé des mesures de teneur en eau tout au long de la carotte en prélevant du sédiment sur demi-sections une fois la carotte ouverte, ainsi que sur les échantillons géotechniques. La mesure consiste à réaliser deux pesées, une avant et l'autre après le passage à l'étuve (24 h à ~105°C), ce qui donne respectivement (*Ws* + *Ww*) et *Ws*.

$$w = \frac{(Ws + Ww) - Ws}{Ws} * 100 \qquad (1)$$

où *Ww* est la masse de l'eau et *Ws* la masse du sédiment.

La mesure de teneur en eau a été utilisée pour déterminer l'indice des vides (*e*) des sédiments, c'est à dire le rapport entre le volume de vide (*Vv*) et le volume de particules solides (*Vs*) grâce à l'équation :

$$e = w \frac{\rho s}{\rho e} \qquad (2)$$

avec *w* la teneur en eau, ρ_s la densité des particules solides (2,65) et ρ_e la densité de l'eau de mer (1,024).

5.2. Hand shear-vane – ASTM D8121

La résistance au cisaillement non-drainé du sédiment a été mesurée sur l'ensemble des carottes en demi-sections après avoir isolé les sections géotechniques. Le pas d'échantillonnage était de 10 à 50 cm. Je réalisais les mesures seulement dans les faciès argileux, i.e., cohésifs. Ces mesures ont été réalisées après ouverture des carottes à l'ISMER à l'aide du « hand shear-vane » (**Figure 2-12**). Cet instrument est composé d'une tige sur laquelle sont montées des pales qui sont insérées puis tournées dans le sédiment. Une jauge située au sommet de la tige mesure le couple nécessaire pour atteindre la

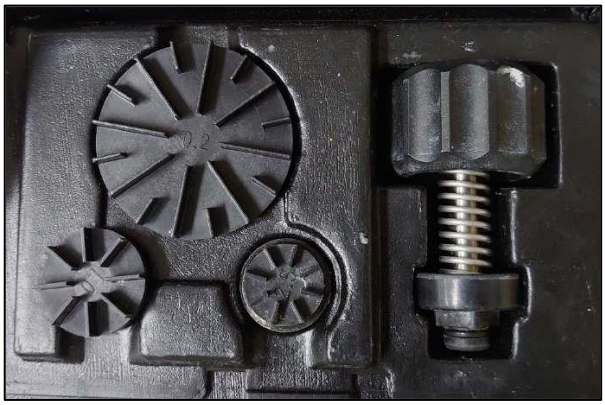

Figure 2-12. Hand shear-vane utilisé pour mesurer de la résistance au cisaillement non-drainé des argiles.

rupture et fournit une conversion en terme de résistance au cisaillement non-drainé, notée Su et exprimée en kPa.

5.3. Essais œdométriques – ASTM D2435

L'œdomètre est un instrument qui permet de réaliser sur un échantillon de sédiment un essai de consolidation unidimensionnelle (**Figure 2-13**). Il consiste à appliquer sur l'échantillon une contrainte verticale uniforme et à mesurer le tassement correspondant au cours du temps. La déformation latérale de l'échantillon est empêchée par un anneau métallique. L'échantillon est maintenu complétement saturé en eau et comprimé entre deux pierres poreuses permettant le drainage par le haut et le bas. Le tassement est mesuré sous la charge puis le gonflement lors de la décharge. La charge se fait par pallier de 24 h : à chaque fois, la charge appliquée est doublée.

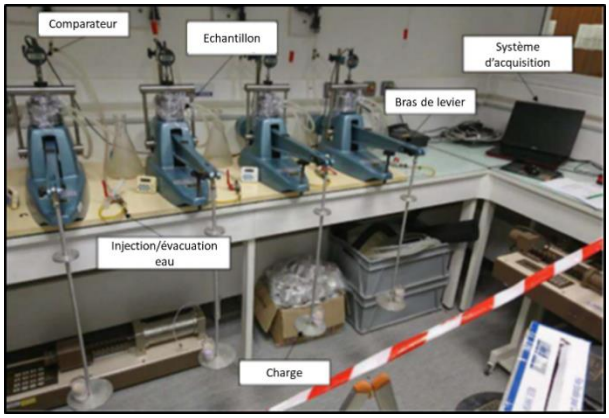

Figure 2-13. Photo du dispositif des essais œdométriques et de perméabilité au laboratoire de l'Ifremer.

Un total de 16 essais a été réalisés au laboratoire de l'Ifremer sur 12 carottes de la mission SLIDE-2020. Les essais sont listés dans le **Tableau 2-1**.

Tableau 2-1. Liste des essais œdométriques réalisés.

Nom de carotte	Profondeurs (m)
COR20-02-01GC	0,77 – 0,79 2,41 – 2,43 4,12 – 4,14
COR20-02-02GC	3,87 – 3,89 4,47 – 4,49
COR20-02-05GC	2,77 – 2,79
COR20-02-06GC	1,73 – 1,75
COR20-02-10GC	2,52 – 2,54 3,97 – 3,99
COR20-02-11GC	3,71 – 3,73
COR20-02-12GC	4,31 – 4,33
COR20-02-15GC	0,92 – 0,94
COR20-02-16GC	3,71 – 3,73
COR20-02-25GC	2,17 – 2,19 3,97 – 3,99
COR20-02-45GC	2,37 – 2,39

5.3.1. Consolidation

La consolidation est le phénomène caractérisé par la réduction de volume d'une couche de sol saturé sous l'action d'une contrainte normale. Cette propriété est généralement caractérisée par le coefficient de consolidation *Cv*. Celui-ci est classiquement déterminé pour chaque palier de charge (au-delà de la pression de préconsolidation) à l'œdomètre en représentant le tassement (déplacement vertical) en fonction du logarithme du temps (**Figure 2-14**). Une construction graphique permet de déterminer le temps pour atteindre 50% de déformation, noté t_{50}, à partir de laquelle on peut déduire *Cv* par la formule suivante (Das, 2013) :

$$C_v = \frac{0{,}197 * h^2}{t_{50\%}} \qquad (3)$$

avec *h* la hauteur de l'échantillon qui correspond à la hauteur initiale moins la valeur du comparateur.

Le fluage correspond à la consolidation secondaire, c'est-à-dire une déformation viscoplastique, fonction du temps et du niveau de

chargement, qui intervient après la déformation instantanée lorsque la pression d'eau s'est dissipée dans l'échantillon (**Figure 2-14**). La propriété de fluage *Cα* est déterminée grâce à la pente de l'asymptote après avoir dépassé la consolidation primaire :

$$C_\alpha = \frac{\Delta e}{\Delta \log t} \qquad (4)$$

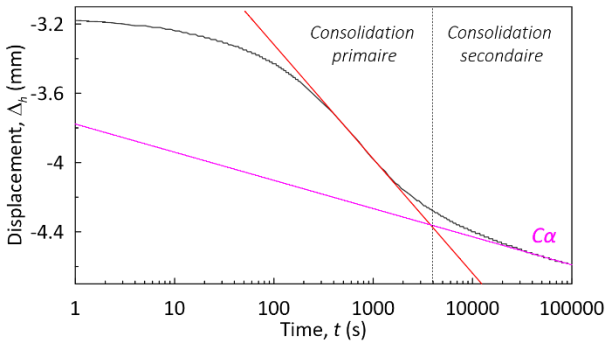

Figure 2-14. Courbe de consolidation de l'essai œdométrique COR20-02-25GC à 3.97-3.99 m de profondeur pour le palier de charge 4 kg soit ~ 220 kPa.

5.3.2. *Compression*

Différents indices de compressibilité peuvent être obtenus à partir du tracé de l'évolution de l'indice des vides (*e*) d'un échantillon en fonction du logarithme de la contrainte qui lui est appliquée (**Figure 2-15**), tels que le *Cc* (indice de compression en déformation plastique) et le *Cs* (indice de gonflement lors de la décharge) :

$$C_C \; ou \; C_s = \frac{\Delta e}{\Delta \log \sigma'} \qquad (5)$$

Graphiquement, une limite de comportement élastique et plastique du sédiment est déterminée. La **Figure 2-15** illustre cette construction graphique pour l'essai œdométrique COR20-02-25GC à une profondeur entre 3.97 et 3.99 m.

Cette limite *σ'vy* correspond à la contrainte verticale effective maximale que le sédiment peut supporter avant de se déformer de manière permanente. Les trois méthodes graphiques

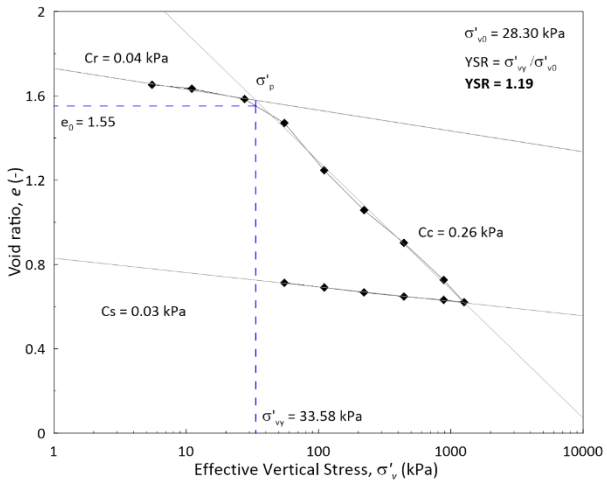

Figure 2-15. Résultat de l'essai œdométrique COR20-02-25GC à 3.97 – 3.99 m de profondeur.

différentes de Silva (Silva, 1970), Casagrande (Casagrande, 1936) et Onitsuka (Onitsuka *et al.*, 1995) ont été utilisées pour déterminer *σ'vy*. L'interprétation des valeurs de *σ'vy* est facilitée en la rapportant à la valeur de la contrainte verticale effective in situ *σ'v0* :

$$YSR = \frac{\sigma'_{vy}\,(Oedo)}{\sigma'_{v0}\,(MSCL)} \qquad (6)$$

Ce rapport, défini comme le ratio de limite élastique (*Yield Stress Ratio*, YSR), permet notamment de détecter si un sédiment se caractérise par une structure particulièrement résistante aux contraintes :

- YSR = 1 ⇔ σ'vy = σ'v0 : sédiment normalement consolidé, sans structure ;
- YSR > 1 ⇔ σ'vy > σ'v0 : sédiment sur-consolidé, forte structure ;
- YSR < 1 ⇔ σ'vy < σ'v0 : sédiment sous-consolidé, structure fragile.

5.3.3. *Perméabilité – ASTM D5084-16a*

Lors des essais œdométriques j'ai mesuré la perméabilité à l'aide d'un perméamètre à charge variable pour chacune des contraintes verticales imposées. Le dispositif est constitué d'une jauge

remplie d'eau en parallèle d'une règle graduée et d'un chronomètre. La perméabilité d'un sédiment est sa capacité à laisser circuler de l'eau par unité de temps ($m.s^{-1}$). Au t_0, le niveau de l'eau est approximativement à 45 cm. À un pas de temps de 15 min, et ce pendant une heure, le niveau d'eau de la jauge est mesuré. L'évolution du niveau d'eau en fonction du temps est ainsi obtenue pour une contrainte donnée. Les mesures permettent d'avoir une valeur de perméabilité mesurée ($k_{mesurée}$) en fonction de la contrainte et de remonter à la perméabilité *in situ* (**Figure 2-16**).

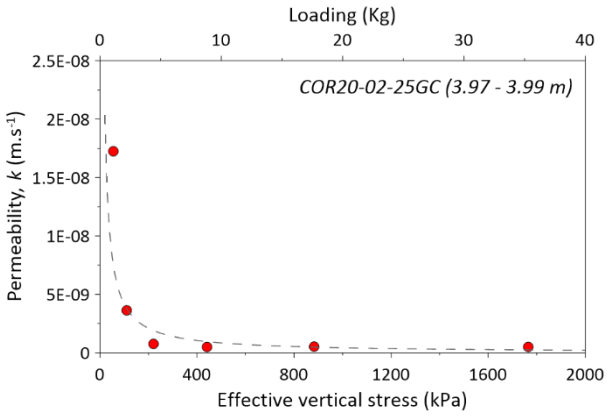

Figure 2-16. Perméabilité mesurée pour les différents chargements lors de l'essai œdométrique COR20-02-25GC à 3.97 – 3.99 m de profondeur.

5.4. Essais triaxiaux

5.4.1. Essais triaxiaux statiques – ASTM D4767-11

Ces essais couramment utilisés en géotechnique permettent de caractériser les propriétés de résistance au cisaillement des sols. Ces propriétés incluent l'angle de frottement interne effectif φ' et la cohésion effective c'. J'ai mené 14 essais répartis sur 8 carottes au laboratoire de géotechnique d'Ifremer (**Tableau 2-2** ; **Figure 2-17**). Ces essais ont été exclusivement des essais consolidés non-drainés (*Consolidated Undrained, CU)* lors desquels les échantillons sont cisaillés sans permettre le drainage de leur eau interstitielle.

Tableau 2-2. Liste des essais triaxiaux statiques menés.

Nom de carotte	Profondeurs (m)	σ'_3 (kPa)
COR20-02-01GC	2,45 – 2,55	75
	2,57 – 2,67	50
COR20-02-02GC	3,51 – 3,61	50
	3,63 – 3,73	75
COR20-02-05GC	2,65 – 2,75	50
COR20-02-06GC	1,77 – 1,87	75
	1,89 – 1,99	50
COR20-02-10GC	3,61 – 3,71	50
	3,73 – 3,83	100
	3,85 – 3,95	75
COR20-02-11GC	3,75 – 3,85	75
	3,87 – 3,97	50
COR20-02-25GC	2,07 – 2,17	50
COR20-02-45GC	2,01 – 2,11	50

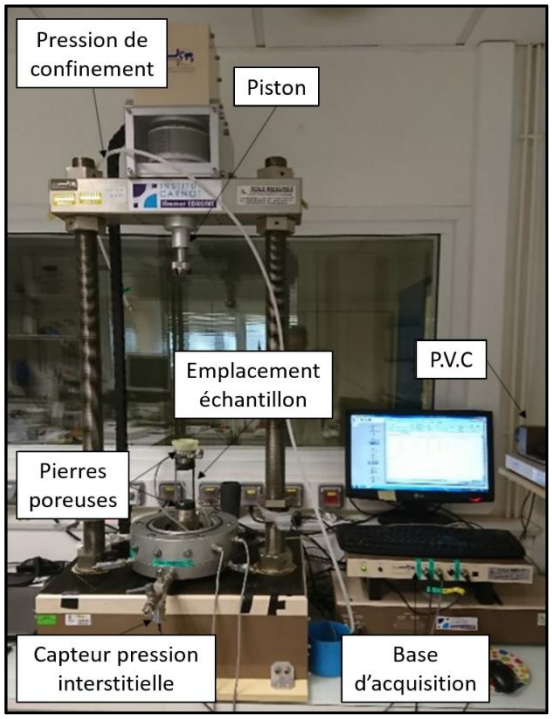

Figure 2-17. Cellule triaxiale du laboratoire géotechnique d'Ifremer.

Pour réaliser un essai, j'ai sous-échantillonné dans la section entière de la carotte un cylindre de sédiment mesurant 5 cm de diamètre sur environ 10 cm de haut (ratio diamètre/hauteur = ½). Il est placé dans une membrane imperméable ne contraignant pas les déformations (**Figure 2-18**). L'échantillon est placé entre deux capuchons munis de benders

(**Figure 2-18** ; Pennington *et al.*, 2001) qui mesurent la vélocité des ondes cisaillantes (Vs) et compressives (Vp) tout au long de l'essai. Il est ensuite mis dans une cellule remplie d'eau. Le dispositif est saturé en eau et la mesure du Skempton-B permet de s'en assurer (B > 0.95).

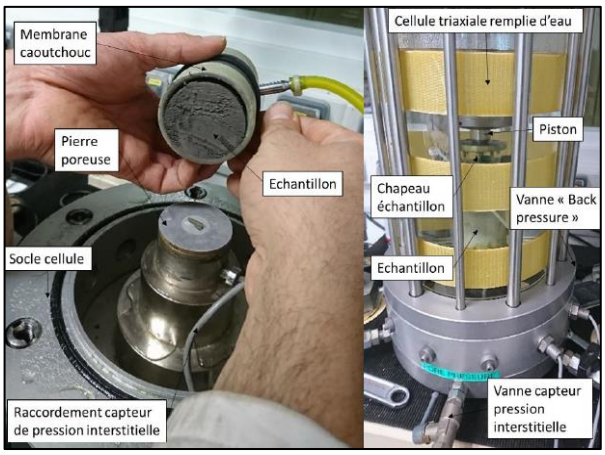

Figure 2-18. Mise en place de l'échantillon dans sa membrane, sur son socle et dans la cellule triaxiale.

Les phases de consolidation se font à plusieurs états de contraintes. Lors de ces phases, le volume de fluide diminue au cours du temps. Le contrôleur de pression par volume (*Pressure Volume Controller*, PVC) permet de suivre la variation de cette quantité de fluide dans l'échantillon (ΔV). Pour remonter à la déformation volumique (%), la formule suivante est utilisée :

$$\varepsilon_v = \frac{\Delta V}{V_0} * 100 \qquad (7)$$

avec V_0 le volume initial de l'échantillon, avant essai.

Une fois la consolidation terminée, c'est-à-dire quand la pression interstitielle en excès s'est entièrement dissipée, une phase de cisaillement en condition non-drainée est réalisée. La phase de cisaillement se fait à contrainte de confinement σ_3 constante avec le piston qui se déplace à vitesse constance. Pour assurer l'homogénéité des pressions dans l'échantillon lors du cisaillement, cette vitesse a été fixée à 0,01% de la hauteur initiale de l'échantillon par minute (ASTM D4767-11). La réponse de l'échantillon pendant le cisaillement se représente en traçant le déviateur des contraintes $q = \sigma_1 - \sigma_3$ (en kPa) en fonction de la déformation axiale ε_a (en %) mesurée par un capteur de déplacement vertical. Dans ce repère des propriétés d'élasticité du sédiment peuvent être déterminées graphiquement. Il s'agit du module d'Young initial E_0 et du module d'Young sécant E_{50}. Le premier reflète le comportement purement linéaire élastique du sédiment. Le second intègre son comportement élasto-plastique puisqu'il est déterminé à un niveau de déformation correspondant à la moitié de celui atteint au moment où le déviateur est maximum ou, en d'autres termes que la rupture est atteinte.

Lorsque le cisaillement est non-drainé et que la pression de fluide dans l'échantillon est mesurée, il est possible d'obtenir les propriétés de résistance effective du sédiment à l'aide de la méthode des cercles de Mohr (**Figure 2-19**) : la cohésion effective notée *c'*, en kPa, et l'angle de frottement interne effectif noté *φ'*, en degrés. La multiplication

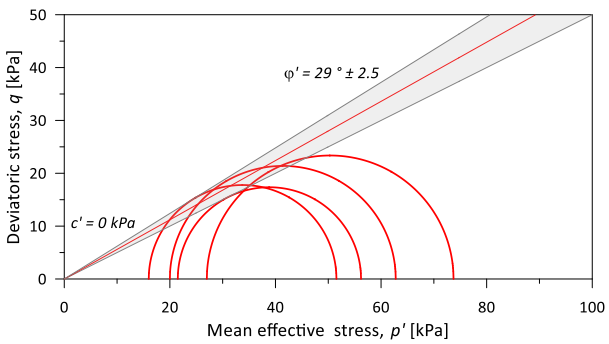

Figure 2-19. Détermination de l'angle de frottement interne effectif, φ', et de la cohésion effective, c', à partir de la méthode des Cercles de Mohr. Ici, les cercles sont tracés à partir des essais triaxiaux statiques menés sur les échantillons 02GC, 06 GC et 10 GC.

des essais triaxiaux CU à différents états de contrainte effective m'a permis de tracer dans un même graphique les cercles de Mohr correspondants et d'en ressortir une cohésion effective et un angle de frottement interne effectif.

5.4.2. Essais triaxiaux cycliques – ASTM D5311/D5311M-13

J'ai réalisé un total de 16 essais triaxiaux cycliques (**Tableau 2-3**) à l'aide du GDS Dynamic Cyclic combiné avec le Dynamic Triaxial Testing System, aussi appelé GDS Enterprise Level Dynamic Triaxial Testing System (ELDYN). Sachant que la liquéfaction est un phénomène qui ne touche qu'aux niveaux les plus grossiers (e.g., sable et silt ; Idriss *et al.*, 1976), les essais se sont concentrés sur ces niveaux. Seul un essai a été réalisé sur un échantillon argileux (**Tableau 2-3**). La **Figure 2-20** montre un échantillon testé cycliquement. La zone la plus silteuse à la base, concentre la liquéfaction.

Les essais triaxiaux cycliques sont identiques aux essais statiques jusqu'à la fin de la phase de consolidation. La consolidation de l'échantillon se réalise à une contrainte effective de σ'_3 = 50 kPa. Une fois le sédiment consolidé il est soumis à une phase de chargement cyclique. Lors de cette phase, une contrainte déviatorique notée Δq est appliquée lors de cycles sinusoïdaux uniformes d'une fréquence de 0,5 Hz. Cela permet de calculer le Cyclic Stress Ratio (CRR) exprimé par :

$$CRR = \frac{\Delta q}{2\sigma'_3} \qquad (8)$$

Deux critères de liquéfaction ont été considérés. Le premier critère est le critère de pression interstitielle qui définit la liquéfaction lorsque le rapport de la pression interstitielle en excès (R_u) tend à ~0.95 (Ishihara, 1993). R_u est normalisée par la pression de confinement initiale lors de l'essai. Le ratio de la pression interstitielle en excès normalisée est exprimé par :

$$r_u = \frac{\Delta u}{\sigma'_3} \qquad (9)$$

où Δu est la pression interstitielle en excès.

Tableau 2-3. Synthèse des essais cycliques triaxiaux menés.

Core name	Depths (m)	Lith	σ'_3 (kPa)	$\Delta q/\sigma'_3$
COR20-02-01GC	2.69–2.79	Silt	50	0.40
COR20-02-02GC	3.75–3.85	Silt	50	0.42
COR20-02-05GC	2.41–2.51	Silt	50	0.46
COR20-02-05GC	2.53–2.63	Silt	50	0.41
COR20-02-06GC	1.61–1.71	Silt	50	0.45
COR20-02-11GC	3.99–4.09	Clay	50	*no liq.*
COR20-02-12GC	4.35–4.45	Silt	50	0.37
COR20-02-12GC	4.47–4.57	Silt	50	0.39
COR20-02-12GC	4.59–4.69	Silt	50	0.48
COR20-02-16GC	3.75–3.85	Silt	50	0.36
COR20-02-16GC	3.87–3.97	Silt	50	0.43
COR20-02-16GC	3.99–4.09	Silt	50	0.39
COR20-02-25GC	1.81–1.91	Silt	50	0.46
COR20-02-25GC	1.95–2.05	Silt	50	0.42
COR20-02-45GC	2.13–2.23	Sand	50	0.48
COR20-02-45GC	2.25–2.35	Sand	50	0.40

Le deuxième critère considère la liquéfaction de l'échantillon à partir de la déformation cisaillante.

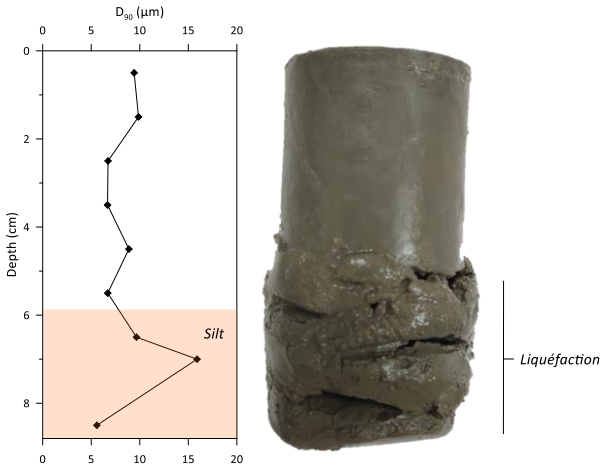

Figure 2-20. Photo après la liquéfaction de l'échantillon COR20-02-02GC (3.75-3.85 m). La base, plus silteuse comme le montre la granulométrie, est la zone de liquéfaction.

Dans ce cas, la liquéfaction est atteinte lorsque la contrainte cisaillante cumulée de l'échantillon dépasse 6% (Wu *et al.*, 2004). Ce critère de liquéfaction a été privilégié pour définir le potentiel de liquéfaction car la pression interstitielle n'a pas toujours été bien enregistrée lors des essais contrairement à la déformation cisaillante.

Le potentiel de liquéfaction du sédiment du Saint-Laurent est déterminé à partir de la représentation du nombre de cycles nécessaire pour liquéfier en fonction du CRR imposé durant les tests (Ishihara *et al.*, 1985). Ce nombre de cycle peut être traduit en distance et magnitude d'un séisme à partir du diagramme de Liu *et al.* (2001) présenté **Figure 2-21**.

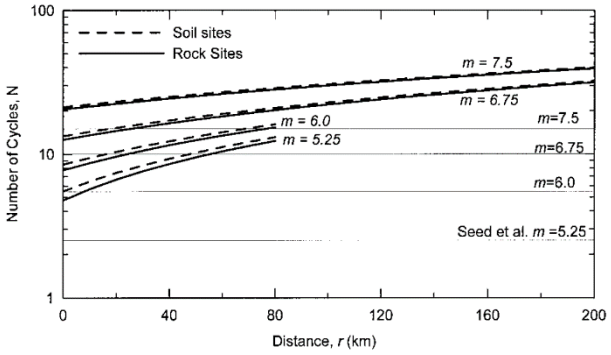

Figure 2-21. Diagramme du nombre de cycles pour atteindre la liquéfaction en fonction de la distance à l'épicentre et de la magnitude du séisme (Liu *et al.*, 2001).

6. MODELISATION NUMERIQUE

6.1. Accélérogramme

Les simulations de la stabilité des pentes sous l'action d'un séisme nécessitent l'implémentation d'un accélérogramme qui exprime l'accélération au sol au cours d'un séisme. Ces données ne sont disponibles que pour les évènements postérieurs à l'avènement des accélérographes (~1950). Ainsi, seul le séisme majeur du Saguenay (Québec) de 1988 et d'une magnitude de 5,9 a pu être enregistré. L'accélérogramme utilisé lors des simulations numériques correspond à l'enregistrement de la station de St-Ferreol, à 120 km de l'épicentre où le pic de l'accélération maximale, notée PGA pour « *Peak Ground Acceleration* » (Douglas, 2002), est de 0,12 g (**Figure 2-22**).

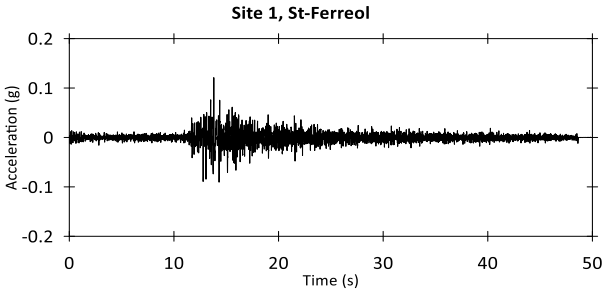

Figure 2-22. Accélérogramme du séisme de 1988 enregistré à la station de St-Ferreol (Québec). Le pic de l'accélération (PGA) radiale mesuré est de 0,12 g à 14 secondes.

Cet accélérogramme a été utilisé comme référence afin de simuler des séismes historiques plus vieux et non-instrumentés tel que celui de 1663 CE. Pour l'adapter à un séisme d'une certaine magnitude son accélération a été multiplié par un facteur multiplicateur.

6.2. Atténuation du PGA

Le PGA est fonction de plusieurs paramètres régionaux tels que la magnitude du séisme, la distance source-site, les conditions géologiques et le type mécanisme focal. Ainsi, pour déterminer le

PGA a une certaine distance de l'épicentre d'un séisme, il est nécessaire d'utiliser des équations d'atténuation du PGA. Le réseau sismologique de l'Amérique du Nord-Ouest a permis d'établir des équations de prédiction du PGA par régression statistique de l'accélération des séismes mesurés (e.g., Douglas, 2003, 2011 ; Abrahamson *et al.*, 2014). Pezeshk *et al.* (2018) ont établi ces relations pour l'Amérique du Nord Est à partir de paramètres régionaux. La relation empirique reliant l'accélération à la distance à l'épicentre est exprimée par :

$$\begin{aligned}&\log(\bar{Y})\\&= c_1 + c_2 M + c_3 M^2\\&+ (c_4 + c_5 M) \times min[\log(R), \log(60)]\\&+ (c_6 + c_7 M)\\&\times \max\left[min\left\{\log\left(\frac{R}{60}\right), \log\left(\frac{120}{60}\right)\right\}, 0\right]\\&+ (c_8 + c_9 M) \times max\left[\log\left(\frac{R}{120}\right), 0\right]\\&+ c_{10} R \qquad (10)\end{aligned}$$

où

$$R = \sqrt{R_{rup}^2 + c_{11}^2} \qquad (11)$$

Dans les équations (10) et (11), Y est la valeur médiane de PGA, *M* est la magnitude du moment, et R_{rup} est la distance la plus proche de la surface de la faille-rupture (km). Les coefficients dans ces équations sont fournis par Pezeshk *et al.* (2018).

Cette loi se vérifie par les séismes régionaux tel que présenté **Figure 2-23** où les PGA des différents séismes suivent les prédictions de la loi de Pezeshk *et al.* (2018) avec une erreur de ± 1 σ.

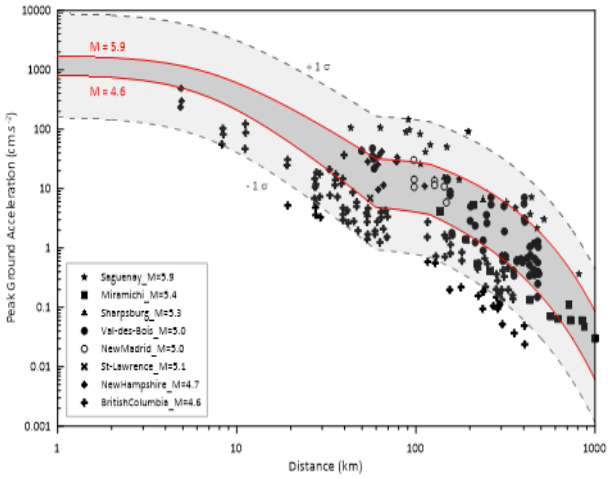

Figure 2-23. Distribution des PGA de séismes ayant eu dans l'est du Canada. En rouge la loi de Pezeshk *et al.* (2018) pour des magnitudes de 4.6 et 5.9 et une erreur de ± 1 σ.

6.3. Détermination du Factor of Safety (FoS)

Le Cyclic Stress Ratio, noté CSR, correspond à la contrainte cyclique induite par un séisme sur un niveau sédimentaire. Il est calculé à partir de l'équation empirique formulée par Seed et Idriss (1971) :

$$CSR = \frac{\tau_{av}}{\sigma'_v} \approx 0.65 \left(\frac{a_{max}}{g}\right)\left(\frac{\sigma_v}{\sigma'_v}\right) r_d \qquad (12)$$

où τ_{av} est la contrainte cisaillante cyclique moyenne, supposée égale à 0,65 de la contrainte maximale induite, a_{max} est l'accélération horizontale maximale à la surface du sol déterminé par l'équation d'atténuation du PGA formulée par Pzeshk *et al.* (2018), g l'accélération de la gravité, σ_v la contrainte verticale totale, σ'_v la contrainte verticale effective interpolée et déterminée à partir du MSCL. r_d est le facteur non-linéaire de participation de la masse au cisaillement calculé à partir des équations de Liao *et al.* (1988) :

$$r_d = 1.0 - 0.00765\, z \qquad (13)$$

pour z ≤ 9,15 m;

$$r_d = 1.174 - 0.0267\, z \qquad (14)$$

pour 9,15 m < z ≤ 23 m.

où *z* est la profondeur sous la surface du fond marin.

Le FoS correspond au rapport du CRR et CSR :

$$FoS = \frac{CRR}{CSR} \qquad (15)$$

La liquéfaction se produit lorsque FoS ≤ 1. Le FoS a été calculé pour six zones de glissements sous-marins pour différentes accélérations. Ces accélérations sont choisies pour diminuer ou augmenter la distance qui sépare une zone d'étude de l'épicentre d'un séisme à partir de l'équations d'atténuation du PGA.

6.4. OpenSees

OpenSees (Open System for Earthquake Engineering Simulation) est un logiciel en libre accès permettant le développement d'application en éléments finis pour la géo-ingénierie sismique (McKenna *et al.*, 2009). Il est développé par le Pacific Earthquake Engineering Simulation Research Center (PEER) pour modéliser et simuler des systèmes géotechniques exposés à des chargements cycliques.

Son utilisation a été couplée au logiciel GID qui permet le prétraitement (définition d'une géométrie, maillage) et le post-traitement (graphiques, surfaces) d'une simulation numérique.

6.4.1. Modèles de comportement

Plusieurs modèles de comportement implémentés dans OpenSees ont été utilisés. Le modèle Pressure Dependant Multi-Yield 02 (PDMY02) permet de simuler le comportement contrainte-déformation du sédiment grossier sous l'effet d'un séisme, i.e., chargement cyclique en conditions non-drainées (Elgamal *et al.*, 2002 ; Yang *et al.*, 2003 ; **Figure 2-24**).

La surface de charge consiste en une surface de charge conique dans le plan de la contrainte principale et déviatorique (Yang *et al.*, 2003). Le modèle considère une loi de durcissement cinématique déviatorique pour générer la réponse hystérétique associée au chargements cycliques. La

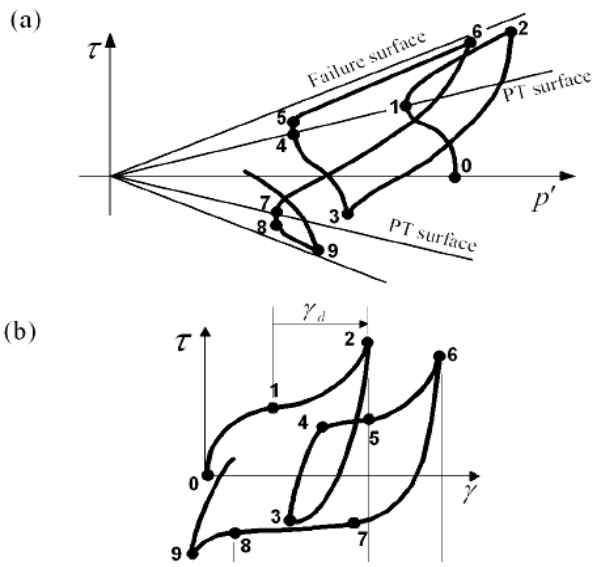

Figure 2-24. Schéma du modèle PDMY02 montrant (a) la réponse de la contrainte octaédrique τ avec la contrainte effective p' et (b) la réponse de la contrainte octaédrique τ avec la déformation octaédrique γ Yang *et al.*, 2003).

règle d'écoulement utilisée dans le modèle PDMY02 contrôle la déformation volumétrique et reflète trois comportements différents : contraction, dilatation et état critique, i.e., liquéfaction. Ce modèle dépend de quinze paramètres listés dans le **Tableau 2-4**.

Tableau 2-4. Paramètres du modèle PDMY02.

Parameter	Unit	Description
ρ	g.cm^{-3}	Density
p_{ref}	kPa	Reference mean effective confining pressure
G_{ref}	MPa	Reference shear modulus
B_{ref}	MPa	Reference bulk modulus
k	m.s^{-2}	Permeability
γ_{max}	%	Maximum shear strain
d	-	Pressure dependency coefficient
Φ'	(°)	Triaxial friction angle
Φ'_{pt}	(°)	Phase transformation angle
c_1, c_3	-	Contraction coefficients
d_1, d_3	-	Dilation coefficients
NYS	-	Number of yields surface
e_0	-	Initial void ratio

Pour les couches d'argile non liquéfiables, le modèle constitutif Pressure Independent Multi-

Yield (PIMY) considérant un comportement linéaire-élastique classique a été utilisé (Yang *et al.*, 2003). Ce modèle est contrôlé par les six paramètres listés dans le **Tableau 2-5**.

Tableau 2-5. Paramètres du modèle PIMY.

Parameter	Unit	Description
ρ	g.cm^{-3}	Density
G_{ref}	MPa	Reference shear modulus
B_{ref}	MPa	Reference bulk modulus
k	m.s^{-2}	Permeability
c	kPa	Cohesion
e_0	-	Initial void ratio

6.4.2. *Sensibilité du modèle*

Une étude paramétrique a été réalisée afin de comprendre l'influence de chaque paramètre des modèles indépendamment (**Figure 2-25** et **Figure**

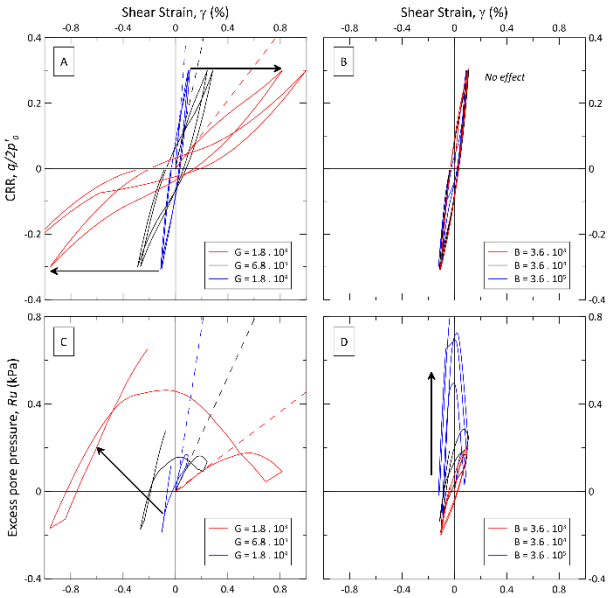

Figure 2-25. Analyse paramétrique du modèle PDMY02 dans OpenSees. La sensibilité du modèle a été testée pour les paramètres *G* et *B*. Les flèches noires et leur longueur indiquent l'influence des variations des paramètres.

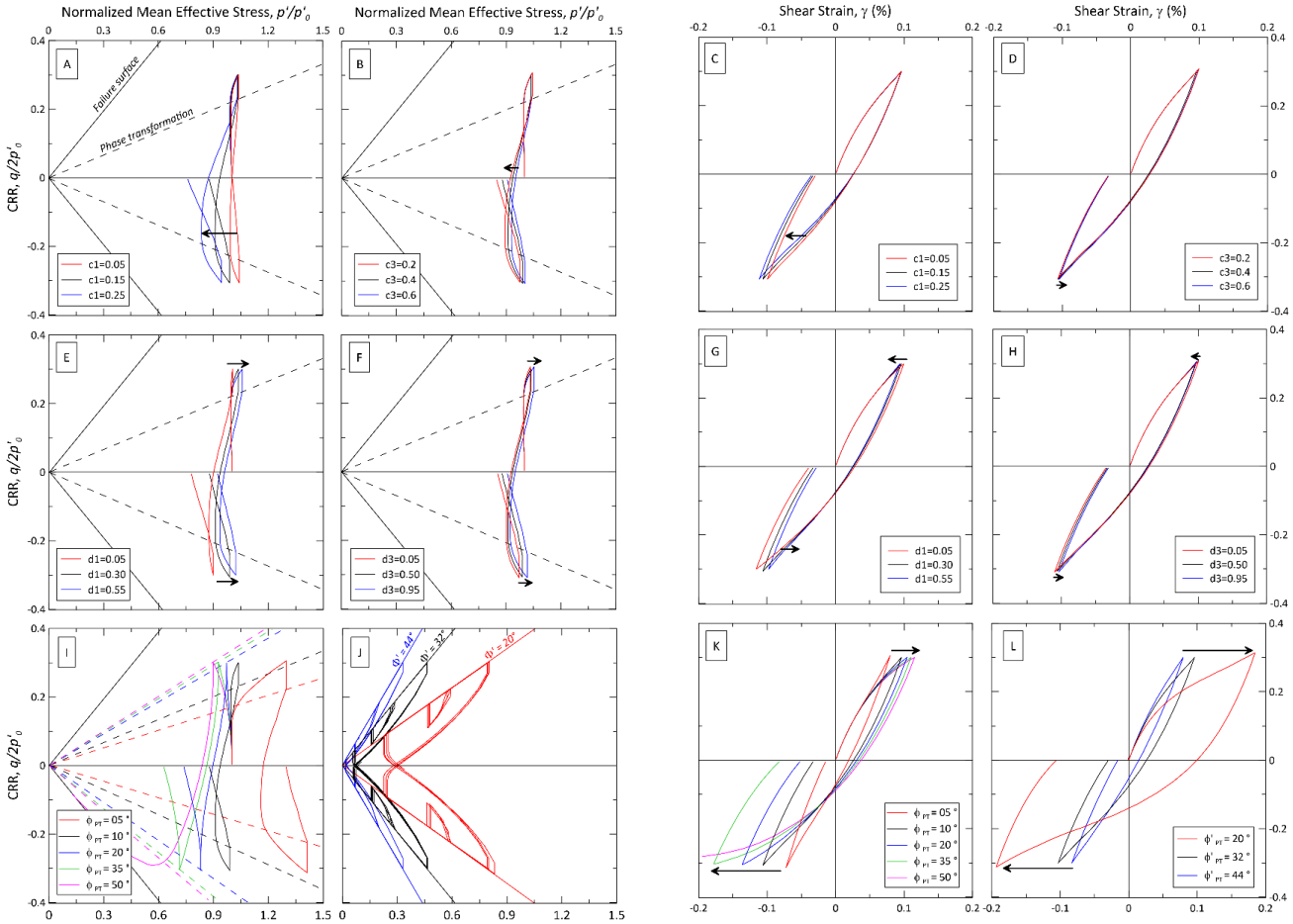

Figure 2-26. Analyse paramétrique du modèle PDMY02 dans OpenSees. La sensibilité du modèle a été testée pour les paramètres c_1, c_3, d_1, d_3, Φ_{PT} et Φ'. Les flèches noires et leur longueur indiquent l'influence des variations des paramètres.

2-26). Les paramètres c_1, c_3, d_1, d_3, Φ_{PT} and Φ', G, B ont été testés tout en gardant ρ, e_0, p_{ref} et CSR constants. La sensibilité du modèle est discutée en termes de CRR en fonction de la déformation cisaillante et de la contrainte effective moyenne normalisée tel que présenté **Figure 2-25** et **Figure 2-26**.

Il en ressort que les paramètres c_1 et c_3 contrôlent le comportement pendant les phases de contraction au-dessous de la surface de transformation de phase (PT), tandis que d_1 et d_3 contrôlent le comportement pendant les phases de dilatation au-dessus de la surface de PT.

Lorsque c_1 augmente, la valeur de la contrainte effective normalisée moyenne diminue (**Figure 2-26 A)** impliquant une déformation volumétrique plus importante (**Figure 2-26 C**) et une liquéfaction plus rapide. Inversement, des valeurs élevées de c_3 conduisent à une diminution du temps pour atteindre la liquéfaction (**Figure 2-26 B**). c_3 a moins d'impact que c_1 et n'a aucune influence sur la déformation volumétrique (**Figure 2-26 D**). Une valeur élevée de d_1 engendre la dilatation et donc la diminution de la pression interstitielle, réduisant à la fois la contrainte effective moyenne normalisée (**Figure 2-26 E**) et la déformation cisaillante (**Figure 2-26 G**). Le paramètre d_3 affecte, comme dans le cas de d_1, le comportement des sédiments au-dessus de la surface de PT. La quantité de dilatation est cependant moins affectée par d_3 que par d_1 (**Figure 2-26 F – H**).

L'influence de l'angle de PT (Φ'_{PT}) dépend du fait qu'il soit supérieur ou inférieur à l'angle de frottement interne (Φ'). Dans le cas où $\Phi'_{PT} < \Phi'$ et la valeur de Φ'_{PT} est faible, la dilatation prend effet plus rapidement par rapport à la contraction (courbe rouge de la **Figure 2-26 I**). Lorsque Φ'_{PT} est élevé, la dilatation est plus courte et la déformation cisaillante associée est augmentée (courbe noire de la **Figure 2-26 I – K**). Dans l'autre cas où $\Phi'_{PT} < \Phi'$, seule la contraction est simulée et non la dilatation (courbes verte et violette **Figure 2-26 I – K**). Ainsi, dans cette configuration, seuls les paramètres c_1 et c_3 contrôlent le comportement tandis que d_1 et d_3 n'ont plus d'influence. Un Φ'_{PT} plus grand augmente le potentiel de liquéfaction et conduit donc plus rapidement à la rupture. L'impact de la valeur de Φ' est observé sur la **Figure 2-26 J – L**. Une valeur élevée de Φ' augmente la pente de la ligne de rupture (courbe bleue) et génère moins de déformation, ce qui augmente le nombre de cycles nécessaires à la liquéfaction. Au contraire, lorsque la valeur de Φ' est faible, l'angle de rupture de pente est moins fort et la déformation induite diminue. Par conséquent, le nombre de cycles nécessaires à la liquéfaction est plus élevé.

Enfin, le module d'élasticité volumique (B) et le module de cisaillement (G) sont tous deux considérés afin de comprendre leur effet sur la simulation du comportement sédiment (**Figure 2-25**). Les sensibilités de B et G sont analysée sur la base des diagrammes de CRR, d'excès de pression interstitielle et de déformation en cisaillement. La **Figure 2-25 A** et la **Figure 2-25 C** montrent les résultats de simulation obtenus pour trois valeurs différentes de G. Comme attendu, G contrôle la pente des courbes CRR-γ. En termes d'excès de pression d'interstitielle, elle augmente avec la diminution de G. Cependant, B n'affecte pas la déformation de cisaillement. En effet, pour la valeur de B la plus élevée (courbe bleue **Figure 2-25**), l'excès de pression interstitielle montre une

augmentation plus rapide et moins rapide lorsque *B* est faible (courbe rouge, **Figure 2-25**). En conclusion, le module d'élasticité volumique ne contrôle que l'accumulation de la pression de pore alors que le module de cisaillement contrôle à la fois la déformation de cisaillement et la pression interstitielle.

6.4.3. Détermination des paramètres d'entrée

La détermination des paramètres d'entrées des modèles PDMY02 et PIMY sont basées à la fois sur des résultats d'analyses en laboratoire et sur une calibration par essai-erreur.

La perméabilité (k) est mesurée par lors des essais œdométriques. La densité (ρ) est la valeur moyenne mesurée par le MSCL. La vitesse des ondes de cisaillement, *Vs*, est mesurée pendant l'essai triaxial cyclique et est directement liée au module de cisaillement G_{ref} par :

$$G_{ref} = \rho V_s^2 \qquad (16)$$

Le module d'élasticité volumique B_{ref} est dérivé de la vitesse de l'onde de compression *Vp* mesurée pendant l'essai triaxial :

$$V_p = \sqrt{\frac{B_{ref} + \frac{4}{3}G}{\rho}} \qquad (17)$$

La pression effective de confinement moyenne, notée p_{ref}, correspond à la pression de confinement pendant l'essai triaxial cyclique. La transition de phase (φ_{PT}) exprimée en degrés, sépare les phases de contraction et de dilatation. Elle est déterminée graphiquement à partir des résultats de l'essai triaxial cyclique. L'angle de frottement interne (φ) est dérivé à partir de la pente d'état critique déterminé par les essais triaxiaux cycliques. Pour chaque spécimen géotechnique, des mesures de la teneur en eau ont été effectuées pour calculer le taux de vide initial (e_0). Enfin, les valeurs par défaut ont été attribuées pour la déformation de cisaillement maximale (γ_{max}), le coefficient de dépendance à la pression (d) et le nombre de surface de charge (*NYS*) (Yang *et al.*, 2003).

EN BREF

(1) Géophysique

- *Imagerie du fond marin en haute résolution ;*
- *Imagerie en 2D des glissements sous-marins;*
- *Identification des zones de carottage ;*
- *Identification de la séquence sédimentaire quaternaire.*

(2) Échantillonnage

- *Pour datation : partie distale ;*
- *Pour stabilité des pentes : sédiment intact et cicatrice ; sélection et envoi d'échantillons*

(3) Analyses sédimentologiques

- *Identification des différents faciès ;*
- *Description des RDLs.*

(4) Datation

- *Prélèvement de coquilles entières pour datation au ^{14}C permettant l'élaboration des modèles d'âge ;*
- *Echantillonnage pour mesurer le ^{210}Pb permettant d'établir des vitesses de sédimentation.*

(5) Analyses géotechniques

- *Caractérisation des paramètres mécaniques intrinsèques du sédiment ;*
- *Détermination du potentiel de liquéfaction.*

(6) Modélisation numérique

- *Simulation de paléoséismes à partir d'un accélérogramme et de la loi d'atténuation du PGA ;*
- *Utilisation du modèle PDMY02 qui tient compte de la liquéfaction du sédiment ;*
- *Compréhension de la sensibilité du modèle de comportement.*

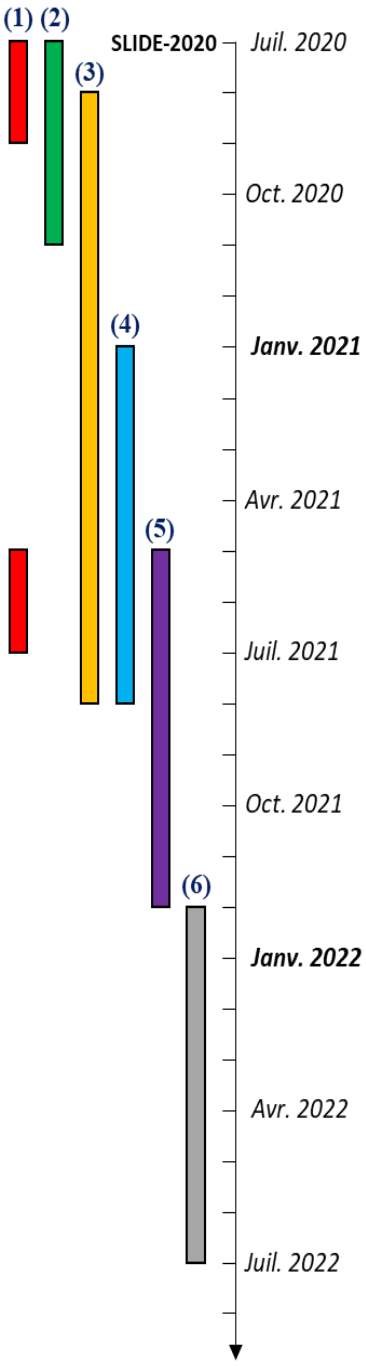

IN SHORT

(1) Geophysics

- *High-resolution seafloor imaging;*
- *2D submarine landslide imaging;*
- *Identification of the coring areas;*
- *Identification of the Quaternary sedimentary sequence.*

(2) Sampling

- *For dating: distal part;*
- *For slope stability: intact sediment and scar; selection and sample shipment.*

(3) Sedimentological analyses

- *Identification of the different facies;*
- *Description of the RDLs.*

(4) Dating

- *Sampling of intact shells for ^{14}C dating to develop age models;*
- *Sampling to measure ^{210}Pb to establish sedimentation rates.*

(5) Geotechnical analyses

- *Characterization of the intrinsic mechanical parameters of the sediment;*
- *Determination of the liquefaction potential.*

(6) Numerical model

- *Simulation of paleoearthquakes from an accelerogram and the PGA attenuation law;*
- *Use of the PDMY02 model considering sediment liquefaction;*
- *Understanding the sensitivity of the behavioral model.*

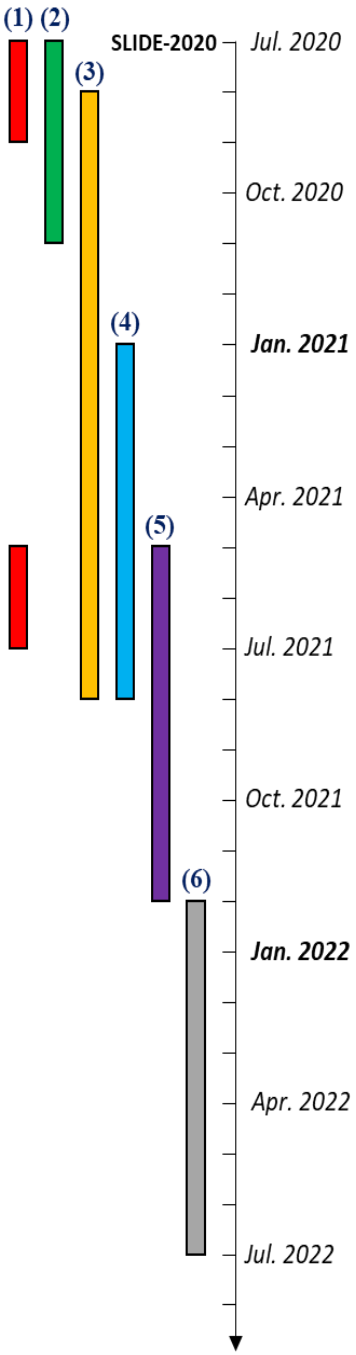

CHAPITRE III. GLISSEMENTS SOUS-MARINS DECLENCHES PAR LES SEISMES DANS L'ESTUAIRE DU SAINT-LAURENT (QUEBEC, CANADA) AU COURS DES DEUX DERNIERS MILLENAIRES ET ENREGISTREMENT DE L'EVENEMENT MAJEUR DE 1663 CE M ≥ 7

CHAPTER III. EARTHQUAKE-TRIGGERED SUBMARINE LANDSLIDES IN THE ST. LAWRENCE ESTUARY (QUÉBEC, CANADA) DURING THE LAST TWO MILLENNIA AND THE RECORD OF THE MAJOR 1663 CE M ≥ 7 EVENT

From Merindol et al., 2022. Quaternary Science Reviews. doi: 10.1016/j.quascirev.2022.107640

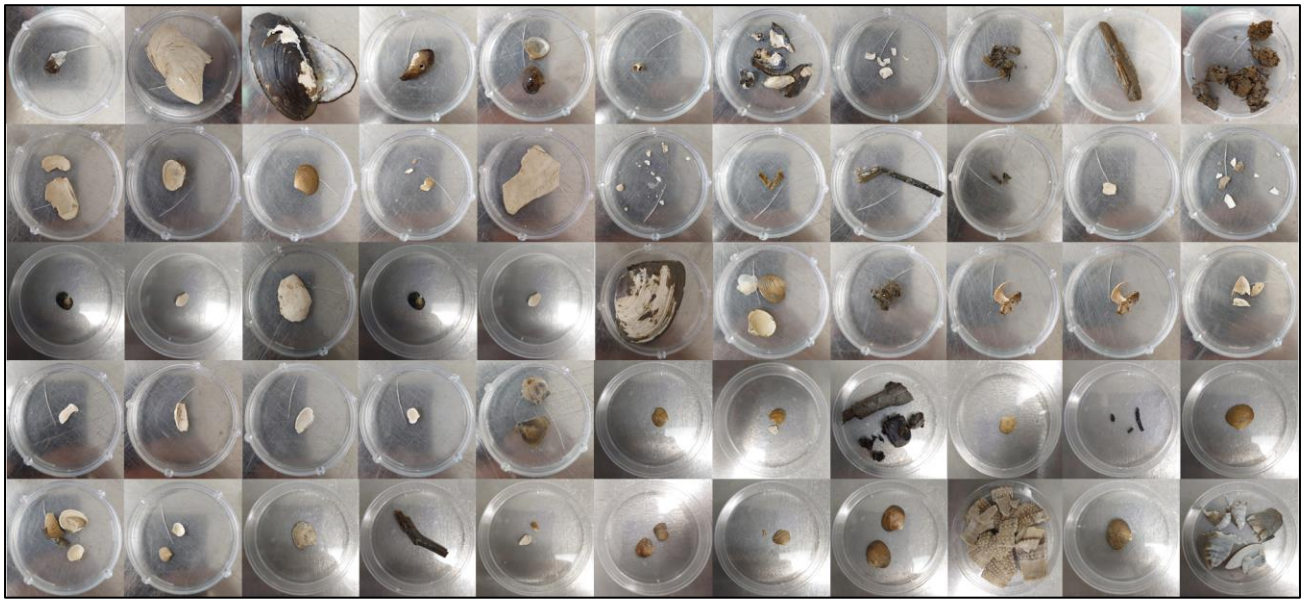

Matière organique et fragments de coquilles prélevés dans les carottes de la mission SLIDE-2020
Organic matter and shell fragments collected from the SLIDE-2020 core

CHAPITRE 3. RÉSUMÉ

Dans l'est du Canada, la zone sismique de Charlevoix-Kamouraska/Bas-Saint-Laurent (CK-BSL) présente un aléa sismique comparable à celui de la zone active du Pacifique. L'évènement majeur du 5 février 1663 CE, d'une magnitude estimée à ≥ 7, souligne l'importance de cet aléa sismique. Les nombreux glissements sous-marins cartographiés dans l'estuaire du Saint-Laurent dans la zone sismique de CKBSL suggèrent que les séismes ont déclenché des séries de ruptures sous-marines. Dans ce contexte, l'expédition SLIDE-2020 à bord du Coriolis II dans l'estuaire du Saint-Laurent visait à cartographier, imager et échantillonner plus de 12 zones d'instabilités sous-marines et leurs dépôts associés. L'analyse des carottes de sédiment prélevées dans les dépôts sédimentaires distaux de ces glissements révèle la présence de couches rapidement déposées (turbidites, hyperpycnites et débrites) directement reliées aux glissements sous-marins. La datation de ces glissements à l'aide des techniques ^{210}Pb et ^{14}C a permis d'identifier quatre périodes de glissements sous-marins synchrones correspondant aux séismes historiques majeurs : 1663 CE, 1860/1870 CE, 1925 CE et 1988 CE (M ≥ 7, M = 6.1/6.6, M = 6.2, M = 5.9). Ce synchronisme des glissements sous-marins sur une distance atteignant 220 km soutient une relation entre leur déclenchement dans l'estuaire du Saint-Laurent et la sismicité régionale. Le fait que pas moins de neuf glissements sous-marins semblent avoir été déclenchés par le séisme de 1663 CE suggère que cet évènement est le plus fort enregistré au cours des deux derniers millénaires dans la région.

CHAPTER 3. ABSTRACT

In eastern Canada, the Charlevoix-Kamouraska/Bas-Saint-Laurent (CKBSL) seismic zone presents a seismic hazard almost as high as that of the active Pacific zone. The major event of February 5, 1663 CE, with an estimated magnitude of ≥ 7, highlights the importance of this seismic hazard. The numerous submarine landslides mapped in the St. Lawrence Estuary in the CKBSL seismic zone suggest that earthquakes triggered series of submarine slope failures. In this context, the SLIDE-2020 expedition on board the RV Coriolis II in the St. Lawrence Estuary aimed to map, image and sample more than 12 zones of submarine instabilities and their associated deposits. The analysis of sediment cores sampled in the distal sedimentary deposits from these landslides reveals the presence of rapidly deposited layers (turbidites, hyperpycnites and debrites) directly linked to the submarine landslides. Dating these landslides with ^{210}Pb and ^{14}C techniques led to the identification of four periods of synchronous submarine landslides corresponding to the strongest historical earthquakes: 1663 CE, 1860/1870 CE, 1925 CE and 1988 CE (M ≥ 7, M = 6.1/6.6, M = 6.2, M = 5.9). This synchronicity over a distance reaching 220 km of several landslides supports a relationship between their triggering in the St. Lawrence Estuary and regional seismicity. The fact that as many as nine submarine landslides appear to have been triggered by the 1663 CE earthquake suggests that this event is the strongest recorded in the last two millennia in the region.

1. INTRODUCTION

One of the strongest historical earthquakes felt in eastern North America occurred on February 5, 1663, along the St. Lawrence River, in southern Québec, Canada, when the region was sparsely inhabited and the European settling was at its beginning. Therefore, the precise epicenter and magnitude of this event are estimated only from written and personal accounts of the event (Gouin, 2001). Previous studies converge to indicate that its epicenter was located in the Charlevoix-Kamouraska seismic zone (CKSZ), in the western part of the St. Lawrence Estuary (**Figure 3-1**), although its exact localisation is still debated (Hodgson, 1928; Locat *et al.*, 2003; Locat, 2011; Locat *et al.*, 2016; Pinet *et al.*, 2021). Gouin (2001) has compiled testimonies of damage to barns, chimneys and houses in eastern America in an area reaching 600 km around the suspected epicenter. From this historical data, Ebel (2011) estimated the magnitude (M) of the 1663 earthquake at 7.5 while the Canadian catalog of historical earthquakes, used to map the seismic hazard in Canada, considers a magnitude slightly lower, of M = 7 (Smith, 1962; Lamontagne *et al.*, 2018).

Jesuits writings contemporary to the 1663 CE earthquake (e.g., Ebel, 1996) report "the formation of new lakes", "the disappearance of mountains" and "the displacement of forest down to the St. Lawrence River" as consequences of subaerial landslides most likely triggered by the 1663 earthquake. The historical observations are consistent with studies carried out on regional landslides which established a link between the 1663 CE earthquake and the landslides observed at Saint-Jean-Vianney (Lasalle and Chagnon, 1968), the Gouffre River (Filion *et al.*, 1991), the Mont-Eboulé (Dubé, 1998) and Colombier (Cauchon-Voyer *et al.*, 2008). The recent study conducted in the CKSZ (**Figure 3-1**) by Pinet *et al.* (2015), indicates that more than one hundred submarine mass-movements occurred in the St. Lawrence Estuary. The high density of submarine landslides in the CKSZ suggests a possible link between submarine slope destabilization and seismicity (e.g., Cauchon-Voyer *et al.*, 2008; Campbell *et al.*, 2008). Some submarine landslides have been related to regional seismicity such as in the Betsiamites River area, where Cauchon-Voyer *et al.* (2008, 2011) combined terrestrial and marine data to relate submarine landslides to major earthquakes occurring before 9280 cal yr BP, in 7250 cal yr BP and in 1663 CE. Other authors have observed this relationship in Québec using geomorphological, sedimentological and dating methods but outside the St. Lawrence Estuary such as in the Saguenay Fjord (Syvitski and Schafer, 1996; Locat *et al.*, 2003; St-Onge *et al.*, 2004) and in lacustrine environments (Doig, 1990; Ouellet, 1997; Locat *et al.*, 2016; Trottier *et al.*, 2018).

Submarine landslides, through erosion of the seafloor and incorporation of sediments and water, can evolve into a debris flow and a turbidity current (Bryn, 2005; Strachan, 2008). Over the last two decades, the marine turbidite record has been increasingly used as a proxy for earthquake recurrence (Lebreiro *et al.*, 1997; Gracia *et al.*, 2010; Goldfinger *et al.*, 2012; St-Onge *et al.*, 2012; Ratsov *et al.*, 2015; Piper *et al.*, 2019; Howarth *et al.*, 2021). The recurrence of strong regional earthquakes and the risks they pose when associated with submarine slope failures can have major

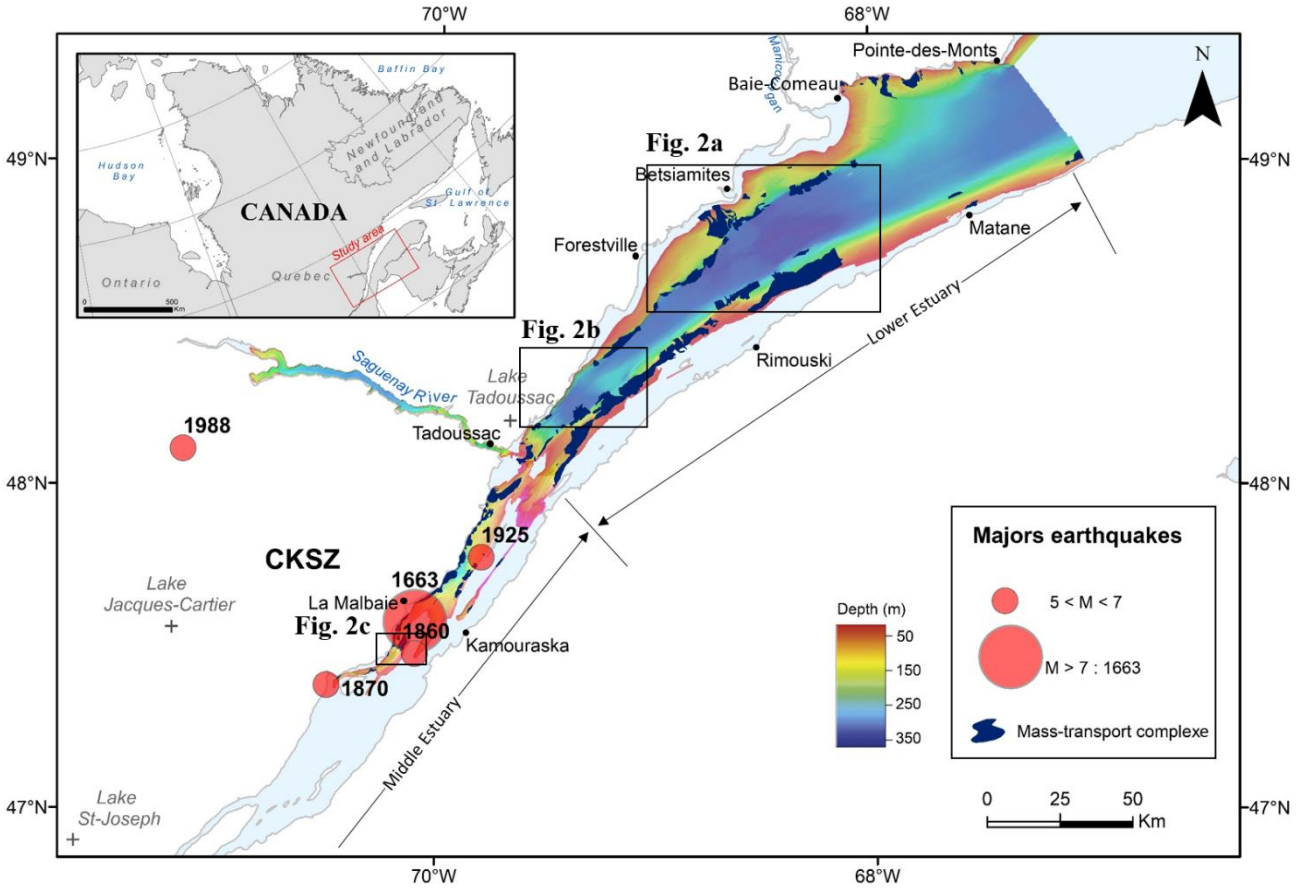

Figure 3-1. Bathymetric map of the St-Lawrence Estuary and location of significant East Canadian Earthquakes of the period 1663-2005 (red circles) from Lamontagne *et al.* (2018). Dark blue areas indicate the mass-transport complexes mapped by Pinet *et al.* (2015). CKSZ corresponds of the Charlevoix-Kamouraska Seismic Zone.

impacts on coastal environments (e.g., damage to coastal infrastructures and threats to coastal communities, risk of tsunamis, cable rupture, coastal erosion), particularly with increasing human populations along the coast. It is therefore essential to improve our knowledge of natural hazards by establishing a chronology of submarine landslides triggered by earthquakes.

Mapping and dating of submarine landslides at a regional scale provide the opportunity to assess their synchronicity and thus their possible triggering by an earthquake (Goldfinger *et al.*, 2012, 2018; Patton *et al.*, 2015). This paper involves 19 sediment cores recovered near 12 submarine landslides located over a distance of ~220 km in the St. Lawrence Estuary with the aim of: (1) identifying and characterizing rapidly deposited layers (RDLs) resulting from landslides (e.g., debrite, turbidite) dated by radiocarbon and ^{210}Pb; and (2) relate them to historical earthquakes (**Figure 3-1**).

2. REGIONAL SETTING

2.1. The St. Lawrence Estuary (Eastern Canada)

The St. Lawrence Estuary, located in Québec (eastern Canada), is one of the world's largest estuarine basins (~8 000 km²). It is generally considered to be divided into two parts: the Lower

Estuary, from the mouth of the Saguenay River to Pointe-des-Monts, and the Middle Estuary, upstream and southwest of the Saguenay River (**Figure 3-1**) (e.g., Pinet *et al.*, 2011). The maximum water depth of 355 m is reached in the central part of the estuary, in the Laurentian Channel, where the seafloor presents a sub-horizontal depression ~900 km long. This major feature is a U-shaped incised-valley bounded by steep escarpments inherited from Quaternary glacial successive erosions (Josenhans and Lehman, 1999; Shaw *et al.*, 2002) and phases of preglacial subaerial erosion (King and MacLean, 1970). In the Lower Estuary, its topography is mostly shaped by mass-transport deposits and pockmarks (Locat *et al.*, 2004; Pinet *et al.*, 2008). In this study, six regions with submarine landslides were considered representing the estuary over its entire length (**Figure 3-2** and **Table 3-1**). The Rimouski, Baie-Comeau and Betsiamites sectors are located in the eastern part of the Lower Estuary and the Forestville and Saguenay sectors are located in its western part. Only the La Malbaie area is located in the Middle Estuary.

The basement of the St. Lawrence Estuary is mostly composed of carbonate and siliciclastic rocks from the St. Lawrence Platform (Duchesne *et al.*, 2007). It is predominantly covered by Quaternary sediments, except in narrow strips at Anticosti and Mingan (Haworth, 1978). The St.

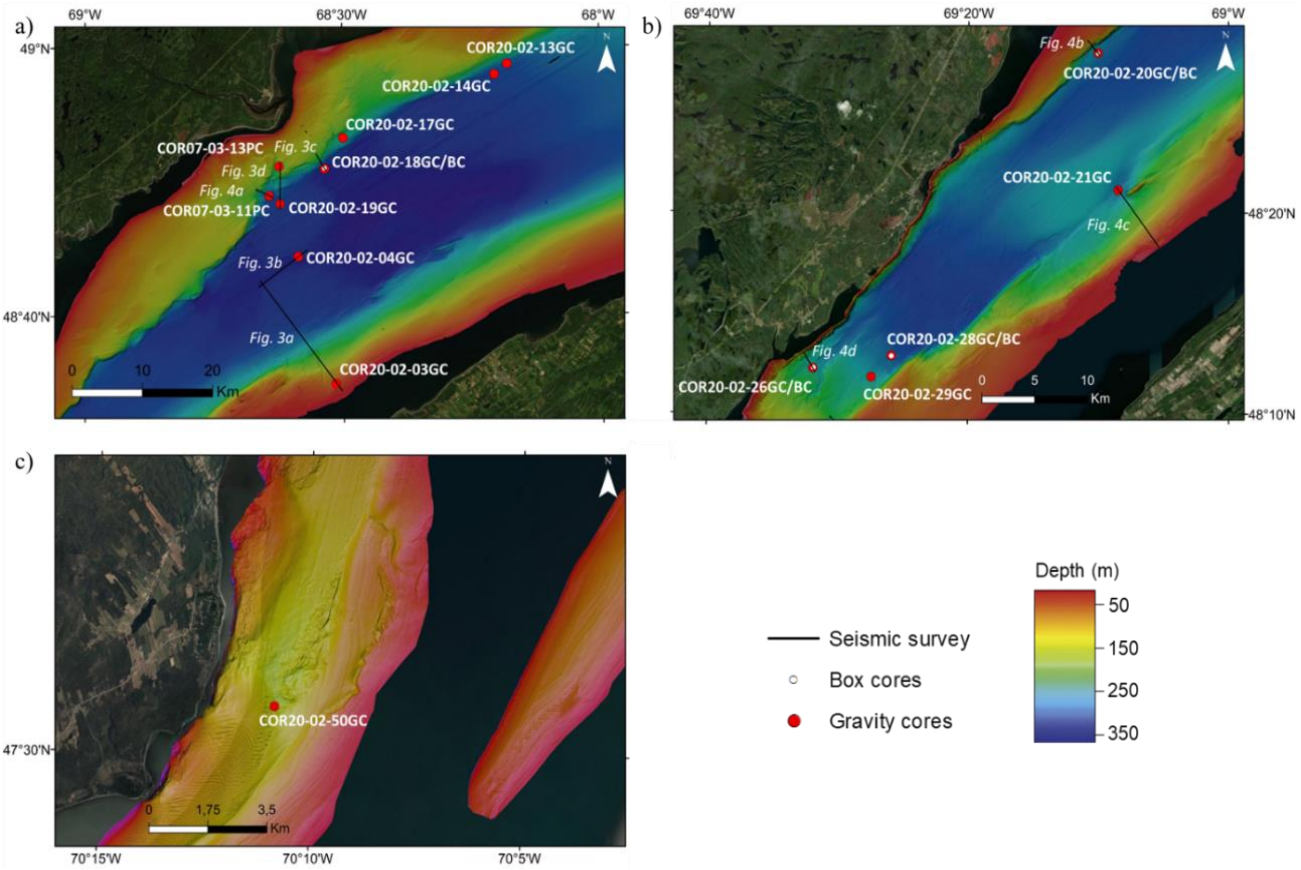

Figure 3-2. Bathymetric maps of the Betsiamites – Baie Comeau – Rimouski a), of the Forestville – Saguenay b) and of the Charlevoix sectors c). The gravity and box cores are respectively represented by red and white circles. The black lines correspond to track lines of the acoustic sub-bottom profiler survey.

Table 3-1. Location and length of the studied cores.

Area and core name	Zone	Lat. (°N)	Long. (°W)	Length (m)
Rimouski				
COR20-02-03GC	Slope	48°34.71	68°29.66	3.87
Baie-Comeau				
COR20-02-13GC	Slope - Deposit	48°58.71	68°10.74	4.20
COR20-02-14GC	Deposit	48°57.94	68°12.25	3.87
Betsiamites				
COR20-02-17GC	Deposit	48°53.27	68°29.93	3.45
COR20-02-18GC/BC	Deposit	48°50.97	68°32.10	3.97
COR20-02-04GC	Lobe	48°34.77	68°29.76	3.86
COR07-03-11PC	Deposit	48°48.58	68°38.34	2.45
COR07-03-13PC	Scar	48°51.10	68°37.24	4.09
COR20-02-19GC	Deposit	48°48.37	68°37.30	2.32
Forestville				
COR20-02-20GC/BC	Deposit	48°27.96	69°10.04	5.05
COR20-02-21GC	Deposit	48°21.14	69°08.47	2.49
Saguenay				
COR20-02-26GC/BC	Deposit	48°12.25	69°31.87	2.83
COR20-02-28GC/BC	Deposit	48°12.88	69°25.87	1.01
COR20-02-29GC	Deposit	48°11.82	69°27.40	1.60
La Malbaie				
COR20-02-50GC	Deposit	47°30.72	70°10.84	2.28

Lawrence Platform is bordered to the north by the Grenville Formation, composed of metamorphic rocks, and to the south by the Appalachian Mountains, composed of Paleozoic sedimentary rocks (e.g., Duchesne *et al.*, 2007). Less resistant to erosion, the Laurentian Channel is parallel to these two formations (Pinet *et al.*, 2008). The estuary is divided into three physiographic regions: the shelf, the slope and the Laurentian Channel. In the Middle Estuary, the shelf is reduced and even absent (**Figure 3-2**).

Inputs of sediments to the estuary originate from five main rivers in addition to the St. Lawrence River: the Saguenay, Rimouski, Betsiamites, Aux-Outardes and Manicouagan Rivers. The associated discharge areas correspond to gently sloping submarine fans (Pinet *et al.*, 2015) with active turbiditic channels (Normandeau *et al.*, 2017). One of the largest mass-transport complexes is located near a former mouth of the Betsiamites River (Cauchon-Voyer *et al.*, 2008). Holocene mass-transport deposits are not consistently present near the mouth of major rivers, suggesting that the actual sedimentary inputs are not the predominant preconditioning factor for seafloor instability (Normandeau *et al.*, 2015). However, most of them are located on steep slopes (> 5°) bordering the Laurentian Channel, indicating that the seafloor

gradient is an important preconditioning factor for slope instability (Normandeau *et al.*, 2015; Pinet

et al., 2015). If gas charging is considered a preconditioning factor for submarine slope instability (e.g., Riboulot *et al.*, 2013), no link was clearly established between the presence of free gas and the mass-transport complexes in the St. Lawrence Estuary (Pinet *et al.*, 2015).

2.2. Quaternary sedimentation

The carbonate platform of the St. Lawrence Estuary is covered by Quaternary sediments with a maximum thickness of ~ 400 m controlled by the underlying topography of the bedrock (Duchesne *et al.*, 2010). The seismo-stratigraphic sequence of Quaternary sedimentation in the St. Lawrence Estuary, first established by Syvitski and Praeg (1989), and completed with samples and dating (St-Onge *et al.*, 2008; Duchesne *et al.*, 2010), is composed of five units. Seismic Unit 1 overlies the bedrock. It is interpreted as ice-contact sediments (Syvitski and Praeg, 1989) when the ice extension was maximum during the Last Glacial Maximum (LGM: 21000 cal yr BP). Unit 2 corresponds to ice-proximal, coarse-grained sediments in a glaciomarine environment. Fine-grained, ice-distal sediments characterize Unit 3. Units 2-3 were deposited when the Goldthwait Sea was present in the St. Lawrence Estuary and Gulf from 13000 to 9000 cal yr BP (Dionne, 2001). Unit 4 marks the transition between glaciomarine and postglacial sedimentation. It comprises hemipelagic sediments (Duchesne *et al.*, 2010) following the rerouting of meltwaters of the Laurentide Ice Sheet (LIS) from the St. Lawrence to Hudson Bay after the collapse of the proglacial Lake Agassiz-Ojibway around 8500 cal yr BP (St-Onge *et al.*, 2003). Cauchon-Voyer *et al.* (2011) described stratified silty clays with thin layers of sand in Unit 4. Finally, Unit 5 differs from Unit 4 by the presence of coarser sediments that were deposited under modern oceanographic conditions. Modern sedimentation rates range between 0.74 $cm.yr^{-1}$ at the mouth of the Lower Estuary to 0.04 $cm.yr^{-1}$ in the Gulf, with an exponential decrease (Zhang *et al.*, 2000).

2.3. Regional seismicity and sediment liquefaction

In addition to the 1663 CE earthquake, four earthquakes with M 5.9 to 6.6 occurred in the CKSZ in 1860, 1870, 1925 and 1988 CE (Smith, 1962; Lamontagne *et al.*, 2003; Lamontagne *et al.*, 2018) (**Figure 3-1**). An average of 200 earthquakes are recorded annually in CKSZ and 50 to 100 in the Lower St. Lawrence zone (Lamontagne *et al.*, 2003). They are localized at depths between 5 to 25 km in the Precambrian bedrocks (Anglin, 1984). Only a small proportion exceeds M 3.

The origin of intraplate earthquakes in Eastern Canada is not clearly identified, but two principal causes are conceivable: tectonic and glacio-isostatic (Wu, 1998). Most earthquakes are concentrated in the St. Lawrence Valley and related to a fault inherited from Paleozoic rifting (Adams and Basham, 1989). The depth of the hypocenters corresponds to the Appalachian thrust fault over the St. Lawrence Platform, named Logan fault (Anglin, 1984). These evidences support a tectonic origin but only a portion of the recorded earthquakes can be related to tectonics.

Thus, regional studies highlighted a higher frequency of mass movements in the early Holocene (St-Onge *et al.*, 2004; Cauchon-Voyer *et al.*, 2011) and liquefaction events interpreted as markers of enhanced seismic activity between 8000 and 1000 cal yr BP (Obermeier *et al.*, 1992). These

observations are consistent with deglaciation in the St. Lawrence region, which resulted in significant glacio-isotactic adjustment during the early Holocene (Wu, 1998).

In addition to tectonic and glacio-isostatic processes, earthquakes can be influenced by fracturing caused by an asteroid impact in the Charlevoix region about 350 Ma ago (Roy and Du Berger, 1983). The weakness of the fractured crust coupled with glacio-isostatic rebound could partially explain regional seismicity and the high earthquake concentration observed by Roy and Du Berger (1983) in the CKSZ.

Seismicity is the main cause of sediment liquefaction (Seed and Idriss, 1967) which can destabilize submarine slopes and generate submarine landslides (Tuttle and Atkinson, 2010). Indeed, Cauchon-Voyer *et al.*, (2008, 2011) suggest that the alternation of silty clays and sand layers in Unit 4 of the St. Lawrence Quaternary sedimentation could influence the permeability of materials and favor an increase in pore pressure in the case of an earthquake. Consequently, a weak layer in Unit 4 could be generated during an earthquake, thus promoting the development of slip surface. Based on geotechnical analyses and numerical simulations, Martin *et al.* (2001) showed that this alternation of silty clays and sand in Saguenay Fjord sediments implies high liquefaction susceptibility during an earthquake.

3. DATA AND METHODS

3.1. Geophysics

High-resolution swath bathymetry data was collected from 1997 to 2005 between Île-aux-Coudres and Pointe-des-Monts by the Canadian Hydrographic Service using multibeam echosounder systems mounted on the Coast Guard Ship *Frederick G. Creed* (before 2005: Kongsberg EM-1000; in 2005: EM-1002) and launch *Guillemot* (before 2005: EM-3000; in 2005: EM-3002). These surveys provided a full-bottom coverage below 30 m depths at a resolution of 5 m.

In summer 2020, the bathymetric coverage was completed during the SLIDE-2020 cruise on board the RV *Coriolis II* using a Kongsberg EM-2040 multibeam echosounder system coupled with the Applanix POS/MV inertial platform. Surveys were conducted in areas where Pinet *et al.* (2015) had previously mapped mass-transport complexes with the aim to significantly increase the resolution. A new bathymetric grid with a cell size of 1 m was generated using the Caris Hips & Sips software. Data acquired during the SLIDE-2020 cruise with the celerimeter *Minos* from *AML oceanographic* were used to account for the variability of sound velocity in the water column.

In addition, high-resolution seismic data were collected (**Figure 3-3** and **Figure 3-4**) using the hull-mounted Edgetech X-Star 2.1 subsurface profiler. Hence, about 1500 km of seismic profiles were acquired during the SLIDE-2020 expedition. The source frequency was between 2 and 12 kHz with chirp pulses between 3 and 20 ms. Time-to-depth conversion of the seismic profiles was done using an average sound wave velocity value of 1500 $m.s^{-1}$ corresponding to the velocity in water and the mean value measured on sediment cores using the Multi Sensor Core Logger. Interpretation of the seismostratigraphic sequence was based on seismic attributes such as reflections, geometry and amplitude of reflecting horizons detailed by Cauchon-Voyer *et al.* (2008).

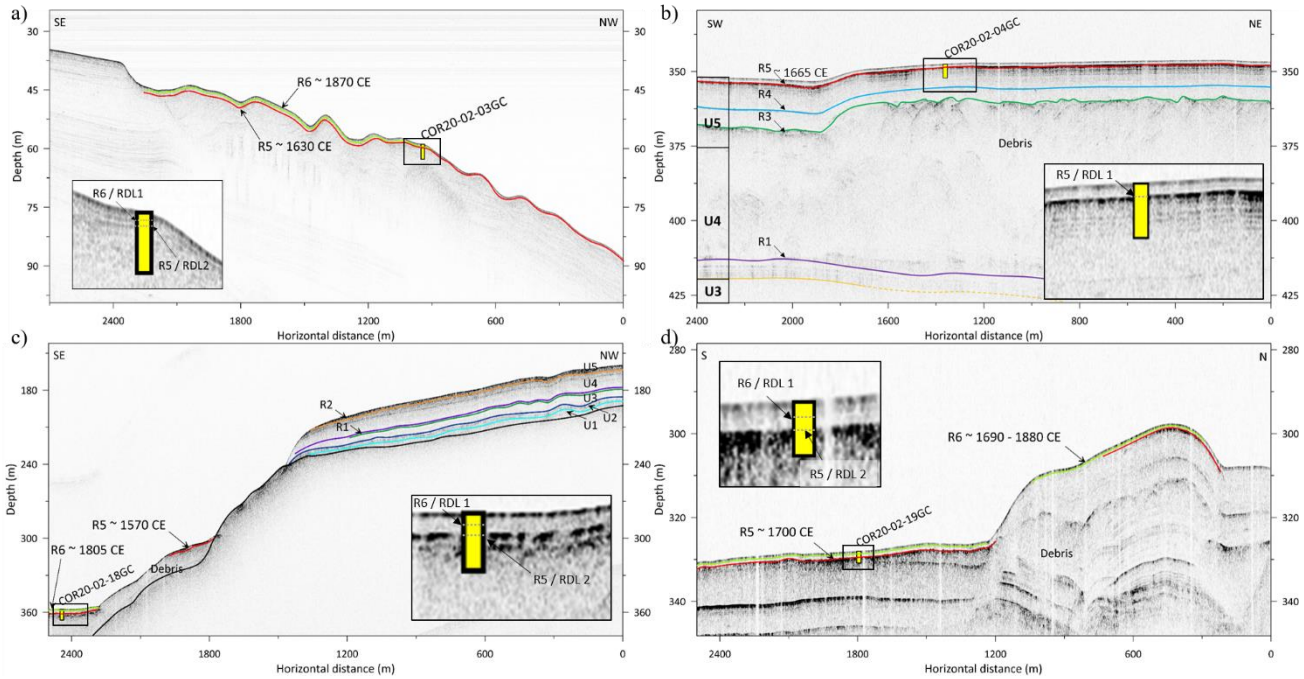

Figure 3-3. a) Seismic profile RIM_1T (see **Figure 3-1** for the locations) on which reflectors R5 and R6 corresponds respectively to turbidites T2 and T1 in core COR20-02-03GC. b) Seismic profile RIM_1A, transversal to the Betsiamites lobe in the Laurentian Channel. Labels U3 to U5 refer to seismic units and R1 to R5 to seismic horizons described by Cauchon-Voyer *et al.*, (2008). The black square is a close-up view of R5. Reflector R5 correlates with turbidite T1 in the core 20-02-04GC. c) Seismic profile BET_B_2T with R5 and R6 reflectors (cf. detailed view in the black square) which correspond to turbidites T3 and T2 in COR20-02-18GC. d) Southern part of seismic profile BET_D_2T. Core COR20-02-19GC reaches reflectors R6 and R5 at ~ 0.5 mbsf and ~ 1.2 mbsf, which are respectively interpreted as turbidites T1 and T2. See supplementary data for uninterpreted seismic profiles.

3.2. Core sampling

During the SLIDE-2020 expedition, cores were recovered over a distance of more than 200 km along the St. Lawrence Estuary, at water depths between 34 and 354 m **Figure 3-2**). The cores were collected in the CKBSL seismic zone. All thirteen gravity cores and four box cores recovered during SLIDE-2020 are used in this study (**Table 3-1** and **Figure 3-2**). Box cores were subsampled with push cores connected to a pump to avoid compaction of sediment. Unlike gravity cores, they do not disturb the sediment/water interface, which allows for correlation of the gravity and box cores, as well as the use of ^{210}Pb dating on the box cores. The gravity corer used had a maximum length of 6 m. This study also used two piston cores of 2.5 m and 4.1 m long that were recovered during the COR07-03 expedition (RV *Coriolis II*, Cauchon-Voyer *et al.*, 2007).

The core sites are located in the distal part of the mass-transport deposit in order to sample the finest part of the submarine landslide allowing to date the hemipelagic sediment above and below the RDLs. The targeted RDLs are theoretically not affected by local sedimentary processes because they were selected neither at the mouth of active rivers, nor at the end of active turbidity current channels (e.g., Normandeau *et al.*, 2017), or in pockmark-rich areas described by Pinet *et al.* (2015). However, due to the estuarine context, regional sedimentary processes such as hyperpycnal flows could occur in the St. Lawrence Estuary.

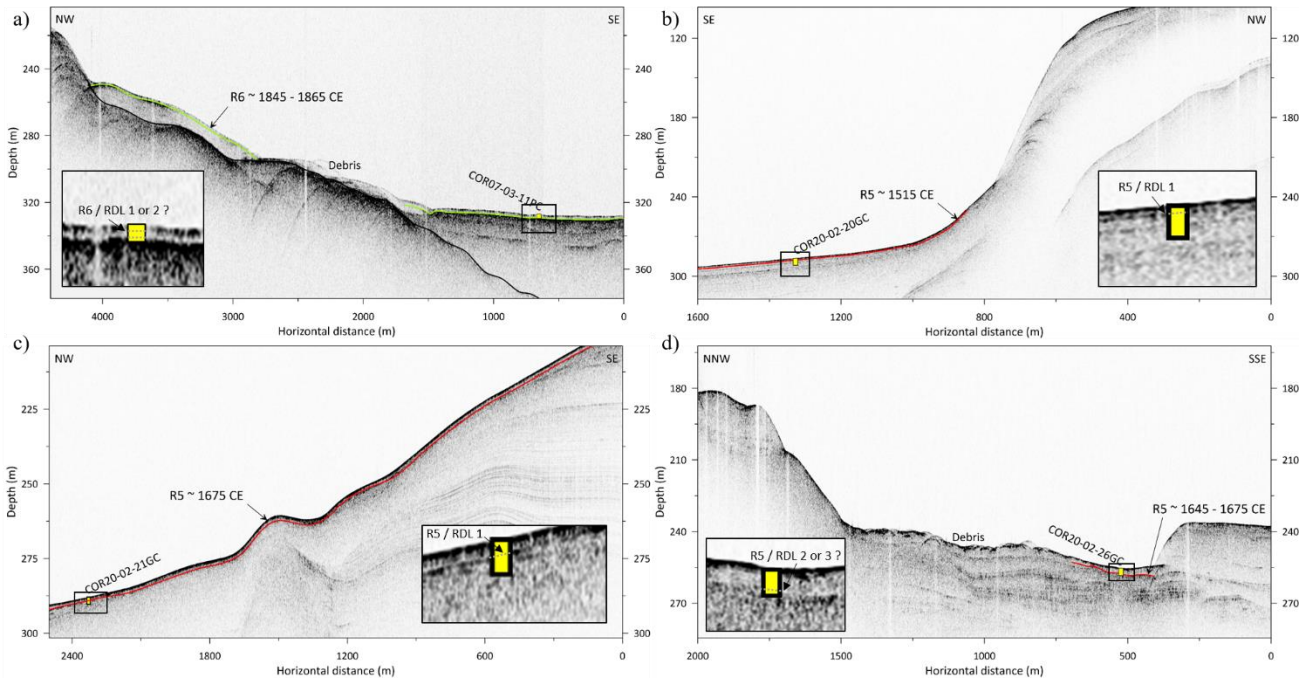

Figure 3-4. a) Seismic profile BET_D_3T in the Betsiamites area (see **Figure 3-1** for the locations). The reflector R6 reached by core COR07-03-11PC, corresponds to turbidite T1 or T2 dated around 1845-1865 CE. b) Seismic profile FOR_A_1T. Turbidite T1 in COR20-02-20GC corresponds to R5. c) Seismic profile ESC_BCD_1T. Reflector R5 (cf. detailed view in the black square) correlates with turbidite T1 sampled in core COR20-02-21GC. See supplementary data for the uninterpreted seismic profiles. d) The seismic profile SAG_H_1T with reflector R5 at the toe of a mass transport deposit. It corresponds to turbidites T2 or T3 observed in core COR20-02-26GC. See supplementary data for the uninterpreted seismic profiles.

3.3. Sedimentological analysed

Wet bulk density, low-field volumetric magnetic susceptibility (*k*) and P-Wave velocity were measured using the GEOTECK MSCL (Multi Sensor Core Logger) at ISMER (St-Onge *et al.*, 2007; **Figure 3-5** and **Figure 3-6**). Measurements were performed at intervals of 1 cm on whole sections of gravity cores and 0.5 cm on whole sections subsampled from the box cores.

After splitting the cores, archived halves were photographed and described (texture, color, lithology, structures and bioturbation). Subsequent digital X-ray images were then acquired with the GEOTECK XCT scanner. This non-destructive measurement allows to visualize the sedimentary structures. The denser materials that compose the RDLs appear as light gray on the X-ray images. On split cores, bulk magnetic susceptibility (*k*) was measured with a point source sensor, while *L**, *a** and *b** color parameters were determined using the Minolta CM-2600d spectrophotometer at 1 cm intervals (**Figure 3-5** and **Figure 3-6**). Because *k* increases slightly with increasing grain size, this parameter is used to identify RDLs following the method presented by St-Onge *et al.* (2007). Grain-size analysis (1 to 2 000 µm) was performed using the Master Sizer 3000 (Malvern) laser grain size analyzer with sampling intervals of 1 to 2 cm in each RDL and 5 to 20 cm for the background sedimentation. Prior to their analysis, the samples were diluted in a solution composed of distilled water and hexametaphosphate and stirred for 24 h to deflocculate clay particles.

The geochemical composition was measured on archive halves using the non-destructive Olympus Innov-X Delta X-Ray Fluorescence (XRF) scanner in line with the MSCL. The spacing of XRF measurements was similar to that of the other measurements previously mentioned. In this study,

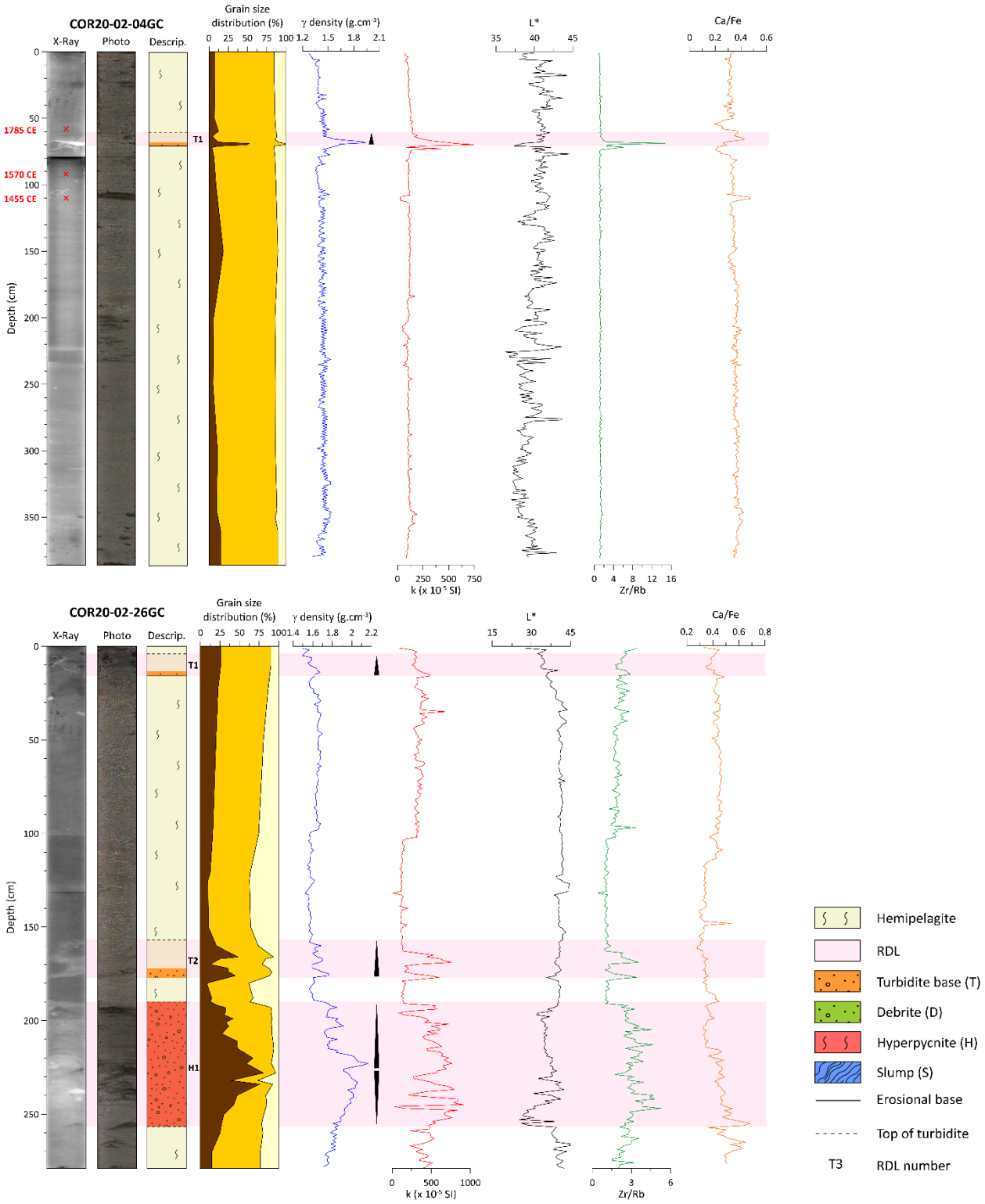

Figure 3-5. Results of the sedimentological analyses carried out on cores a) COR20-02-04GC and b) COR20-02-26GC. From left to right: X-ray image, digital photography, sedimentological description, γ-density, magnetic susceptibility *k*, lightness *L**, Zr/Rb and Ca/Fe.

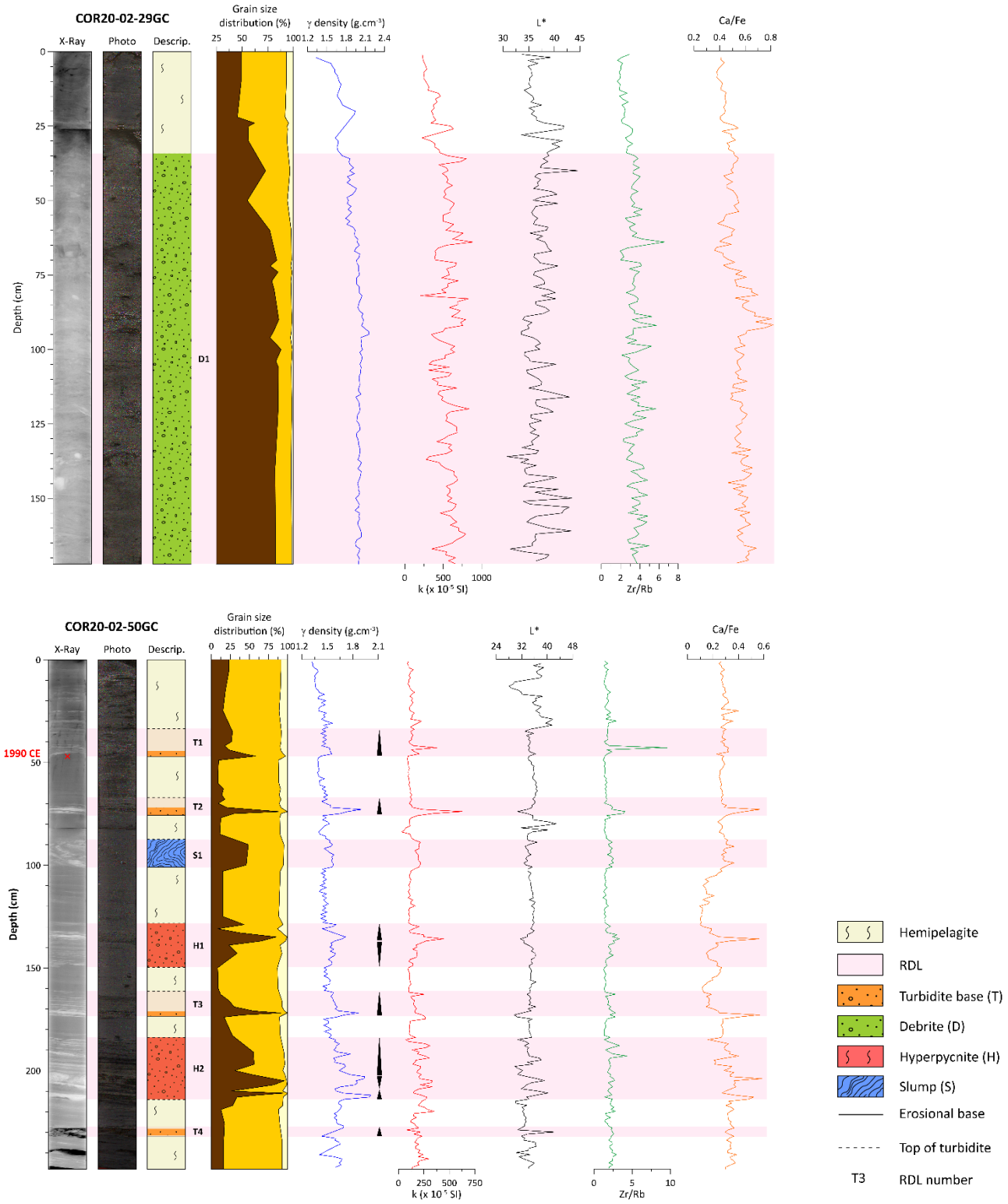

Figure 3-6. Results of the sedimentological analyses carried out on cores a) COR20-02-29GC and b) COR20-02-50GC. From left to right: X-ray image, digital photography, sedimentological description, γ-density, magnetic susceptibility *k*, lightness *L**, Zr/Rb and Ca/Fe.

the Ca/Fe ratio (biogenic/detrital proxy) and the Rb/Zr ratio (grain size proxy) were used as criteria to identify RDL (Croudace *et al.*, 2006) and to help distinguish the top of RDLs from hemipelagic sedimentation (**Figure 3-5** and **Figure 3-6**). RDLs are numbered between 1 for the youngest and 7 for

the oldest and are site-specific. As such, the RDL numbers do not refer to the synchronicity of the deposits.

3.4. Dating

Radiocarbon dating was performed on 45 samples of shells or organic matter that were sampled close to the bases of RDL in the hemipelagic sediments (**Table 3-2**). After pre-treatment and graphitization at the *Centre d'études nordiques* at Université Laval (Québec City), they were measured at the Keck-Carbon Cycle AMS facility at the University of California Irvine (USA). To obtain accurate RDL chronology, the ^{14}C ages of hemipelagic samples were calibrated using the Calib 8.2 software (Stuiver and Reimer, 1993) and the Marine20 curve (Heaton *et al.*, 2020). To consider the local offset from the global ocean reservoir (ΔR), two reservoir ages from McNeely *et al.* (2006) were used. These reservoir ages are closest to the study area with one at Matane of $\Delta R = 77 \pm 60$ ^{14}C yr and one at Pointe John of $\Delta R = -13 \pm 70$ ^{14}C yr. They were averaged to have a final reservoir age of $\Delta R = 39 \pm 63$ ^{14}C yr for shell samples. Finally, the radiocarbon ages were converted to calendar ages (CE) for comparison with historical earthquakes (**Table 3-2**).

To construct the best-fit age models, the R software package Bacon 2.3 (Blaauw and Christen, 2011) was used. It considers Bayesian statistics with a normal distribution. Both standard deviations of 1 σ (probability of 0.95) and 2 σ (probability of 0.68) were used in calculations (**Figure 3-7**). In these calculations, turbidite erosion was assumed negligible because it was not possible to quantify basal erosion.

Sedimentation rates were derived from ^{210}Pb measurements on sediments from 4 box cores (**Table 3-3** and **Figure 3-8**). The cores were sampled at intervals ranging from 1 to 5 cm and freeze-dried, then ground to a fine, homogenous powder. The ^{210}Pb activity was measured using a GMX50-S gamma counter from Ortec and GX7020 counter from Canberra. Considering the constant flux and constant rate model (Appleby and Oldfield, 1978), the sedimentation rates ($cm.yr^{-1}$) were derived from the slope of Ln ($^{210}Pb_{excess}$) in the region of radioactive decay (**Figure 3-8**). The ages of turbidites were then calculated by extrapolating a constant sedimentation rate down to the hemipelagic depth of turbidites. Sediment compaction is neglected because the density curve of hemipelagic sedimentation appears constant with depth (**Figure 3-8**).

4. RESULTS

4.1. Facies identification

The four cores presented in **Figure 3-5** and **Figure 3-6** show the sedimentary facies observed on analyzed cores. They were selected to best illustrate the characteristics of the different types of RDLs. An exhaustive list of all the sediment cores is presented in the supplementary data. The results of core analysis identified two mains facies: hemipelagites and RDLs (**Figure 3-5** and **Figure 3-6**). Hemipelagites are consistent with normal "background", hemipelagic sedimentation while RDLs are a result of almost instantaneous deposition. Hemipelagites consist of homogenous gray-colored silts (Munsell value 5YR 5/1). The gray tone varies with the intensity of bioturbation from dark gray (5YR 4/1) to very dark gray (5YR

Table 3-2. Radiocarbon analyses from cores recovered in the St. Lawrence Estuary (Québec).

Core	Lab. num.	Depth (cm)	Sample type	^{14}C age (BP)	ΔR	Calibrated age (yr BP) ± 1σ	Calibrated age (CE) ± 1σ
COR07-03-13PC	ULA-9628	10.00	Organic matter	255 ± 15	-	300 ± 5	1650 ± 5
COR20-02-03GC	ULA-9787	8.00	Shell	Modern	39 ± 63	-55 ± 5	2005 ± 5
	ULA-9788	89.50	Shell	765 ± 15	39 ± 63	180 ± 95	1770 ± 95
	ULA-9789	99.50	Shell	780 ± 20	39 ± 63	195 ± 100	1755 ± 100
	ULA-9790	135.50	Shell	920 ± 15	39 ± 63	345 ± 85	1605 ± 85
	ULA-9791	356.75	Shell	2020 ± 20	39 ± 63	1380 ± 90	570 ± 90
COR20-02-04GC	ULA-9645	47.00	Shell	745 ± 15	39 ± 63	165 ± 95	1785 ± 95
	ULA-9642	92.50	Shell	965 ± 15	39 ± 63	380 ± 80	1570 ± 80
	ULA-9644	109.50	Shell	1095 ± 15	39 ± 63	495 ± 80	1455 ± 80
COR20-02-13GC	ULA-9652	17.50	Shell	1190 ± 15	39 ± 63	570 ± 50	1380 ± 50
	ULA-9653	19.50	Shell	1210 ± 15	39 ± 63	585 ± 70	1365 ± 70
	ULA-9647	84.75	Shell	2915 ± 15	39 ± 63	2465 ± 115	-515 ± 115
	ULA-9648	161.50	Shell	4875 ± 15	39 ± 63	4920 ± 110	-2970 ± 110
COR20-02-14GC	ULA-9792	9.25	Shell	675 ± 20	39 ± 63	110 ± 80	1840 ± 80
	ULA-9793	46.0.	Shell	1640 ± 15	39 ± 63	995 ± 95	955 ± 95
	ULA-9794	65.00	Shell	2020 ± 15	39 ± 63	1380 ± 175	570 ± 175
	ULA-9816	71.50	Shell	2125 ± 15	39 ± 63	1490 ± 195	465 ± 195
	ULA-9817	97.50	Shell	2780 ± 15	39 ± 63	2280 ± 220	-330 ± 220
COR20-02-17GC	ULA-9818	73.50	Shell	1655 ± 20	39 ± 63	1010 ± 95	940 ± 95
	ULA-9819	198.75	Shell	3285 ± 20	39 ± 63	2895 ± 105	-945 ± 105
	ULA-9820	259.50	Shell	4590 ± 15	39 ± 63	4565 ± 120	-2615 ± 120
COR20-02-18GC	ULA-9654	80.25	Shell	1180 ± 15	39 ± 63	565 ± 70	1385 ± 70
	ULA-9682	204.50	Shell	3690 ± 20	39 ± 63	3395 ± 105	-1445 ± 105
	ULA-9620	213.25	Wood	3395 ± 15	-	3030 ± 80	-1135 ± 80
	ULA-9655	331.50	Shell	8485 ± 20	39 ± 63	8835 ± 125	-6885 ± 125
COR20-02-19GC	ULA-925	14.00	Alga	Modern	-	-45 ± 5	1995 ± 5
	ULA-9646	201.50	Shell	2460 ± 15	39 ± 63	1885 ± 210	65 ± 210
COR20-02-20GC	ULA-9650	40.00	Shell	790 ± 20	39 ± 63	205 ± 100	1745 ± 100
	ULA-9669	204.50	Shell	2255 ± 20	39 ± 63	1635 ± 100	315 ± 100
	ULA-9670	423.50	Shell	3915 ± 15	39 ± 63	3670 ± 110	-1720 ± 110
COR20-02-21GC	ULA-9671	96.00	Shell	920 ± 15	39 ± 63	345 ± 85	1605 ± 85
	ULA-9672	178.50	Shell	2175 ± 15	39 ± 63	1545 ± 105	405 ± 105
COR20-02-50GC	ULA-9784	46.50	Wood	Modern	-	-40 ± 5	1990 ± 5

3/1). The hemipelagites are composed of 10 – 20 % clay (< 2 µm), 65-75 % silt (2-63 µm) and 10 – 20 % sand (63µm - 2 mm). Their gamma density values are constant with depth and oscillate between 1.4 and 1.6 g.cm^{-3}. On X-ray images, hemipelagites appear in homogenous black gray and their values of magnetic susceptibility are relatively low (~125.10^{-5} SI) compared to RDLs (~500.10^{-5} to 750.10^{-5} SI). Overall, hemipelagites have the same properties across the St. Lawrence Estuary, though they are generally coarser in the Middle Estuary with 10% clay, 80% silt and 10% sand (e.g., COR20-02-50GC). Likewise, the thickness of hemipelagites is between 10 – 20 cm in the Lower

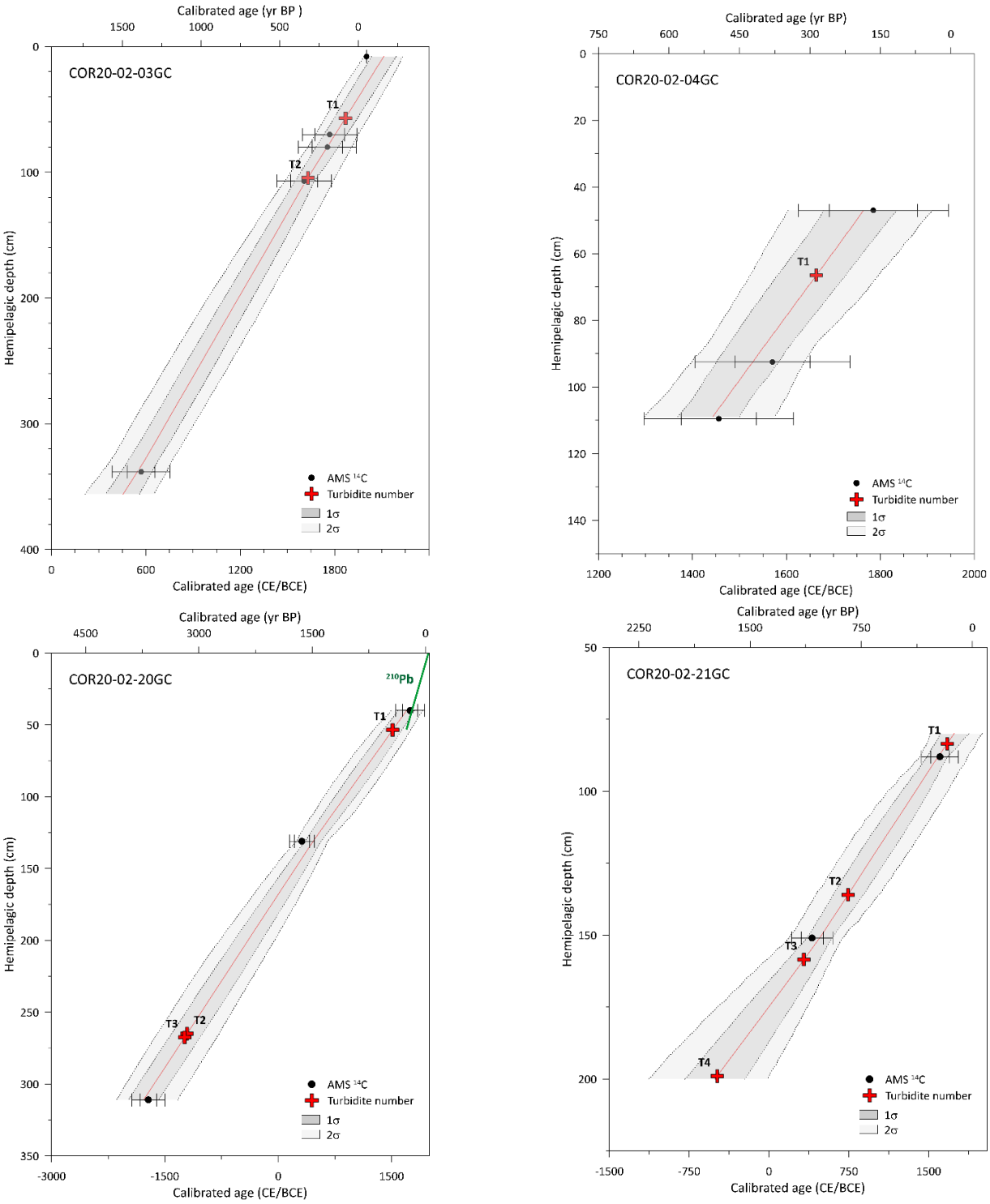

Figure 3-7. Age models for cores COR20-02-03GC a), COR20-02-04GC b), COR20-02-20GC c) and COR20-02-21GC d). The hemipelagic depth, i.e., depth excluding RDLs, is plotted as a function of calibrated ages (BP and CE/BCE). The black circles correspond to the dated samples and the red crosses to the turbidites. The age probability of 2 σ and that of 1 σ, are respectively shown in light and medium gray tone.

Estuary (e.g., COR20-02-50GC) and higher than 50 cm in the Middle Estuary (e.g., COR20-02-04GC).

On X-Ray images, light gray layers intersect the hemipelagic sedimentation. These layers correspond to RDL facies. Their physical properties, detailed below, contrast clearly with background sedimentation and their bases are mainly sharp, while their upper contacts are

gradational. The internal structure and grain size distribution vary between RDLs, such that four groups can be distinguished: turbidites (T), debrites (D), hyperpycnites (H) and slump (S).

In the 15 cores, 43 turbidites (T) were identified (see supplementary data). Their thickness varies between ~3 and 73.5 cm with a mean value of 18.5 cm (**Table 3-4**). The bases are sharp and the grain size analyses reveal a normal grading typical of the Bouma-type turbidite (Bouma, 1962). Indeed, turbidites are characterized by a sandy base (fine to coarse sand) with sometimes gravels or rock fragments (< 2 mm) as in turbidite T1 in core COR20-02-21GC. The coarser material at the base of the turbidite layers is associated with high values of density and magnetic susceptibility, contrasting sharply with the overlying and underlying hemipelagic sediments. In core COR20-02-04GC (**Figure 3-5**), turbidite T1 presents a maximum density of 1.93 g.cm^3 and a magnetic susceptibility of 744.10^{-5} SI, which both contrast with values of 1.45 g.cm^3, and 144.10^{-5} SI in hemipelagic sediments. The coarse base of this turbidite layer likely comprises heavy minerals such as magnetite (e.g., Goldfinger *et al.*, 2007; Jaegle, 2015) and is darker (L* = 37.5) compared to the under- and overlying background sediments (L* = 40.5), suggesting that this parameter could be used to discriminate the base of turbidites. Furthermore, the two chosen geochemical ratios in core COR20-02-04GC are relatively constant in the hemipelagites (Zr/Rb = 1.22 and Ca/Fe = 0.34), but follow the grain size evolution of the turbidites with the highest values at the base (Zr/Rb = 14.75 and Ca/Fe = 0.43) gradually decreasing toward the top. These geochemical signatures, sensitive to grain size, can be used in addition to the previous parameters to accurately identify the base and top of turbidites.

Debrites (D) produced by debris flows constitute the second type of RDL identified in sediment cores. Only four debrites are identified in four cores. These deposits are more proximal to the source of submarine landslides than turbidites. The debrites include rock fragments up to ~10 cm in length, observable on XCT images **Figure 3-6**). As shown in D1 of core COR20-02-29GC, these rock fragments vary in nature, size, angularity and orientation in a sandy-silty matrix composed of 75% sand, 20% silt and 5% clay (D_{50} ~150 µm). Thus, cores containing debrite layers are relatively short because the corer could not fully penetrate these deposits, unlike turbidites. Density and magnetic susceptibility are high with average values of respectively 1.95 g/cm^3 and 560.10^{-5} SI in core COR20-02-29GC. In addition, contrary to turbidites, the debrites are massive and chaotic with no observable grading. The debrite in core COR07-03-11PC (D1) (see supplementary data) is composed of a block of terrestrial organic material. Larger rock fragments are observed at the base of the debrite layer.

The RDLs characterized by reverse grading at the base followed by normal grading are interpreted as hyperpycnites (H) resulting from a hyperpycnal flow (Mulder *et al.*, 2003; St-Onge *et al.*, 2004). Hyperpycnites were observed in core COR20-02-26GC (**Figure 3-5**) recovered near the mouth of the Saguenay Fjord (~5 km). The reverse grading at its base (256.5 – 226 cm) corresponds to the rising limb of the flood. Above 226 cm, the normal grading (226 – 190 cm) reflects the falling limb. Two hyperpycnites are also found in core COR20-

02-50GC (**Figure 3-6**) sampled in the La Malbaie area.

A fourth type of RDL is characterized by the presence of a slump deposit (S) (**Figure 3-6**). This deposit was found only at 100 cm in core COR20-02-50GC. This is a 13.5-cm thick layer of silty-sand inducing peaks in density, magnetic susceptibility and Zr/Rb. The grains are not sorted and strong internal deformation is recognizable on the X-ray images. In summary, 43 of the RDLs are turbidites, four are debrites, three are hyperpycnites and one is a slump, highlighting the higher proportion of turbidites.

4.2. Age of the RDLs

The radiocarbon and ^{210}Pb results provided dating of 51 RDLs from 15 different cores (**Table 3-4**). The ages are between around 5035 cal yr BP and ~1991 CE. Only four age models are presented here (**Figure 3-7**), the others are available in the supplementary data. In the next sections, the age of the RDLs are described for each area.

4.2.1. Baie-Comeau

In the Baie-Comeau sector, turbidites T1, T2, T3, T4 and T5 in core COR20-02-13GC were deposited respectively ~1145 CE, 520 CE, 4525 cal yr BP, 4905 cal yr BP and 4940 cal yr BP. In COR20-02-14GC, four turbidites were deposited more recently around 1580 CE for the uppermost turbidite T1 and 1085 CE, 635 CE and 3270 cal yr BP for turbidites T2, T3 and T4.

4.2.2. Betsiamites-Rimouski

Further west, in the Betsiamites area, the most recent turbidites (T1) in cores COR20-02-17GC and COR20-02-18GC are both dated ~ 1640 – 1680 CE while turbidite T2 in core COR20-02-17GC is dated around 1560 CE. The age of the oldest turbidites is estimated at 5035 cal yr BP (T7) and 4830 cal yr BP (T6). Sedimentation rates calculated from the box core COR20-02-18BC-A provide respective ages of 1905 CE and 1805 CE for turbidites T1 and T2. In core COR07-03-13PC recovered in the submarine landslide scar of the Betsiamites area, debrite D1 is estimated to be ~ 1650 CE based on dating of an intact block of terrestrial material. Turbidites T1 in cores COR20-02-04GC and COR20-02-19GC are dated to 1665 CE and 1690 CE respectively. Turbidite T2 in core COR20-02-19GC is older with an age of 1115 CE. The ^{210}Pb-derived sedimentation rate of 0.32 cm.yr^{-1} in box core COR20-02-18BC-A yields more recent ages of 1880 CE and 1700 CE for T1 and T2 respectively. When considered for the nearby core COR07-03-11PC, this sedimentation rate gives an age of 1865 CE for turbidite T1 and 1845 CE for T2. On the other side of the St. Lawrence Estuary, near of the city of Rimouski, turbidite T1 is dated at 1870 CE and T2 at 1630 CE.

4.2.3. Forestville

In core COR20-02-20GC, collected in the Forestville area, turbidite T1 at a depth of 53.5 cm is dated at 1515 CE. Based on a ^{210}Pb-derived sedimentation rate of 0.15 cm.yr^{-1} calculated from the associated box core COR20-02-20BC-B, turbidite T1 dates back to 1665 CE. The older turbidites T2 and T3 are dated respectively to 3155 cal yr BP and 3190 cal yr BP. In core COR20-02-21GC, recovered near a submarine landslide, turbidite T1 is observed at 83.5 cm depth and dated at 1675 CE. Turbidites T2, T3 and T4 in core COR20-02-21GC have older ages of 745 CE, 325 CE and 2435 cal yr BP.

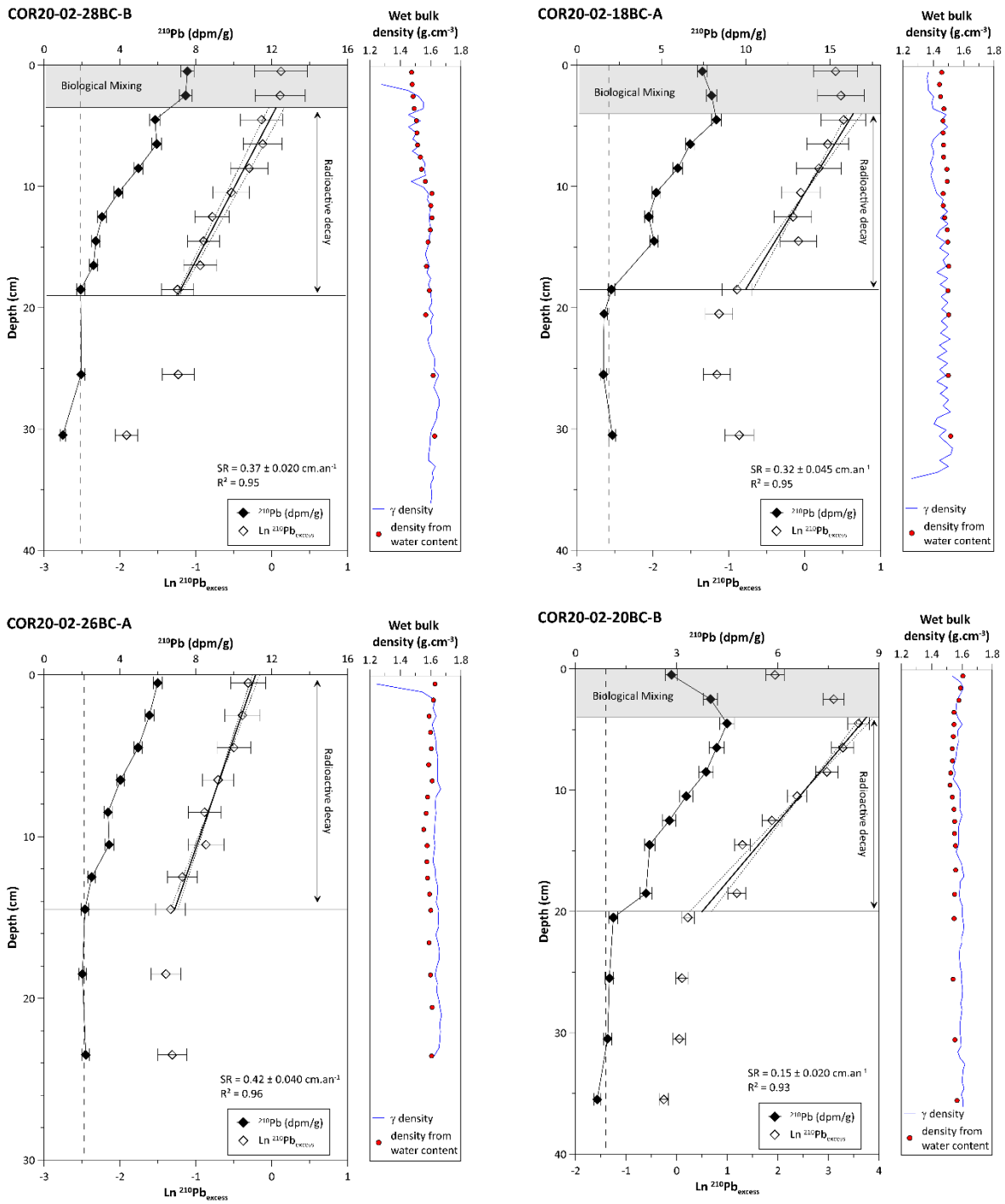

Figure 3-8. Sedimentation rates (SR) calculated with the ^{210}Pb activity in cores COR20-02-18BC-A (SR = 0.32 cm.yr^{-1}, a), COR20-02-20BC-B (SR = 0.15 cm.yr^{-1}, b), COR20-02-26BC-A (SR = 0.42 cm.yr^{-1}, c) and COR20-02-28BC-B (SR = 0.37 cm.yr^{-1}, d). SR are calculated from the slope of Ln (^{210}Pb$_{excess}$) in the radioactive zone by excluding the biological mixing.

4.2.4. Saguenay

In the Saguenay area, the RDLs could not be dated by ^{14}C due to the absence of datable material. However, two sedimentation rates of 0.42 cm.yr^{-1} and 0.37 cm.yr^{-1} were calculated from the ^{210}Pb measurements in box cores COR20-02-26BC-A and COR20-02-28BC-B, respectively. The turbidite T1 found at 4 cm depth in core COR20-02-26GC can thus be dated to 2010 CE, whereas turbidite T2 at 145 cm is dated at 1675 CE and the hyperpycnite

Table 3-3. Sedimentation rates calculated and used in this study.

Box cores #	Date of sample (mm-dd-yyyy)	Sedimentation rate (cm.yr^{-1})	Error ± 1 σ (cm.yr^{-1})
COR20-02-18BC-A	07-22-2020	0.32	0.045
COR20-02-20BC-B	07-23-2020	0.15	0.020
COR20-02-26BC-A	07-24-2020	0.42	0.040
COR20-02-28BC-B	07-24-2020	0.37	0.020

H1 (158 cm) at 1645 CE. The debrite D1 identified in COR20-02-28GC-3 was dated at 1885 CE using the ^{210}Pb derived sedimentation rate of 0.37 cm.yr^{-1} in box core COR20-02-28BC. Close to this coring site (~2.5 km), at the same water depth, core COR20-02-29GC sampled the deposit linked to another submarine landslide. By using the sedimentation rate of box core COR20-02-28GC-3, the debrite D1 at 34 cm depth was dated at 1930 CE.

4.2.5. La Malbaie

In core COR20-02-50G from the Malbaie area, only one wood fragment could be sampled and dated at 1990 CE. As the hemipelagic sediments are close to the base of turbidite T1 from that core (~ 0.5 cm), we can consider an age of 1990 CE for T1. With seven RDLs preserved in a relatively short core (~2.28 m), core COR20-02-50GC presents the highest frequency of RDLs of all the studied cores.

4.3. Correlation with seismic data

A sub-horizontal reflector with strong amplitude was identified at shallow depths (< 2.0 m) on seismic profiles acquired across the different submarine landslide areas (**Figure 3-2**). This reflector drapes the underlying sediments and is covered (**Figure 3-2** and **Figure 3-3**). According to the description and interpretation made by Cauchon-Voyer *et al.* (2008), the sedimentary deposits of the submarine landslide triggered by the 1663 CE earthquake were also characterized by the presence of a high amplitude reflector called R5 by these authors, underlying a transparent facies.

Near Rimouski, at the southern side of the Laurentian Channel, a reflector similar to R5 was identified in seismic profile RIM_1T (**Figure 3-3**) at ~ 1.3 m depth below the deformed seafloor and shows an angular discordance with deeper, reflector was identified in seismic profile RIM_1A that crosses the lobe deposit of Betsiamites (Bernatchez, 2003) at a depth of ~ 0.75 m below the seafloor (**Figure 3-3**). The deeper reflectors R1 to R4 and the seismic units U3 to U5 described by Cauchon-Voyer *et al.* (2008) are also visible and delimited. In seismic profiles BET_B_2T, R5 type reflector is found at a depth of ~ 1.8 mbsf (**Figure 3-3**) while further to the south, it is identified at a depth of ~ 1.2 mbsf in the BET_D_2T profile (**Figure 3-3**). In the Forestville area, the R5 type reflector is visible on both sides of the Laurentian Channel at a depth between ~ 1.0 mbsf and ~ 1.3 mbsf, in the seismic profiles FOR_A_1T and ESC_BCD_1T (**Figure 3-4**). The R5 type reflector is again identified in the Saguenay area in seismic profile SAG_H_1T at about 2.0 mbsf depth (**Figure 3-4**).

A correlation between sedimentological data and seismic profiles reveals that the R5 type

Table 3-4. Age ^{14}C (CE/BCE) of turbidites, hyperpycnites and debrites identified in the 15 cores used in this study (see supplementary data for all age models and sedimentological analyses of all cores).

Layer	Total depth (cm)	Hemipelagic depth (cm)	Thickness (cm)	Type of deposit	Estimated ^{14}C age (yr BP), or (CE) when reported	Error ± 1 σ	Estimated age ^{210}Pb (CE)	Error ± 1 σ
Baie-Comeau								
COR20-02-13GC								
RDL1	23	23	13	Turbidite	1145 CE	110		
RDL2	50.5	37.5	18.5	Turbidite	520 CE	260		
RDL3	181	149.5	11	Turbidite	4525	645		
RDL4	210.5	168	55.5	Turbidite	4905	640		
RDL5	268	170	33	Turbidite	4940	660		
COR20-02-14GC								
RDL1	15	15	15	Turbidite	1580 CE	135		
RDL2	43	28	3	Turbidite	1085 CE	95		
RDL3	64	46	3	Turbidite	635 CE	315		
RDL4	153.5	132.5	8.5	Turbidite	3270	320		
Betsiamites								
COR20-02-17GC								
RDL1	14	14	4.5	Turbidite	1680 CE	180		
RDL2	25.5	21	12.5	Turbidite	1560 CE	180		
RDL3	104	87	7	Turbidite	195 CE	220		
RDL4	124	100	11	Turbidite	2075	235		
RDL5	173	138	21.5	Turbidite	3020	175		
RDL6	241.5	185	15	Turbidite	4540	395		
RDL7	279	207.5	18	Turbidite	5035	430		
COR20-02-18GC								
RDL1	37.5	37.5	13.5	Turbidite	1640 CE	100	1905	15
RDL2	82	68.5	10	Turbidite	1245 CE	135	1805	30
RDL3	167	143.5	22	Turbidite	3200	240		
RDL4	193	147.5	8	Turbidite	3335	225		
RDL5	236.5	183	38	Turbidite	4630	540		
RDL6	279	187.5	8.5	Turbidite	4830	590		
COR07-03-11PC								
RDL1	50	50	62.5	Turbidite			1865	25
RDL2	118.5	56	126.5	Debrite			1845	25
COR07-03-13PC								
RDL1	3	3	101.5	Debrite	1650 CE	5		
RDL2	357	354	25	Turbidite				
RDL3	386	358	11.5	Turbidite				
COR20-02-04GC								
RDL1	66.5	66.5	11.5	Turbidite	1665 CE	70		
COR20-02-19GC								
RDL1	44.5	44.5	4	Turbidite	1690 CE	90	1880	20
RDL2	107	103	10.5	Turbidite	1115 CE	140	1700	50
Rimouski								
COR20-02-03GC								
RDL1	57	57	19.5	Turbidite	1870 CE	75		
RDL2	124	104.5	9	Turbidite	1630 CE	60		
Forestville								
COR20-02-20GC								
RDL1	53.5	53.5	73.5	Turbidite	1515 CE	125	1665	35
RDL2	338.5	265	10.5	Turbidite	3155	140		
RDL3	351.5	267.5	28.5	Turbidite	3190	150		
COR20-02-21GC								
RDL1	83.5	83.5	18	Turbidite	1675 CE	115		
RDL2	154	136	19.5	Turbidite	745 CE	140		
RDL3	196	158.5	10.5	Turbidite	325 CE	150		
RDL4	247	199	11	Turbidite	2435	275		
Saguenay								
COR20-02-26GC								
RDL1	4	4	12	Turbidite			2010	5
RDL2	157	145	20	Turbidite			1675	30
RDL3	190	158	66.5	Hyperpycnite			1645	35
COR20-02-28GC-3								
RDL1	50	50	not fully cored	Debrite			1885	10
COR20-02-29GC								
RDL1	34	34	not fully cored	Debrite			1930	5
La Malbaie								
COR20-02-50GC								
RDL1	33.5	33.5	13	Turbidite	1990 CE	5		
RDL2	67	54	9	Turbidite				
RDL3	87.5	65.5	13.5	Slump				
RDL4	128.5	93	21.5	Hyperpycnite				
RDL5	161	104	12.5	Turbidite				
RDL6	184	114.5	30	Hyperpycnite				
RDL7	227	127.5	5	Turbidite				

reflector systematically corresponds to the base of RDLs. Thus, the RDLs correspond to strong sub-horizontal and parallel reflectors above and at the end of mass-transport deposits characterized by a chaotic and transparent seismic facies (**Figure 3-3** and **Figure 3-4**). In the Betsiamites area, reflector R5 corresponds to the presence of turbidite T1 dated to 1665 CE in core COR20-02-04GC. In COR20-02-19GC, R5 corresponds to turbidite T2 estimated at 1700 CE based on the ^{210}Pb derived

sedimentation rate. Turbidite T3 in core COR20-02-18GC is also related to reflector R5 and is dated to 1570 CE based on the ^{210}Pb derived sedimentation rate. In the Rimouski area, turbidite T2 dated to 1630 CE is at the same depth as the R5 reflector. In Forestville, the turbidites T1 in core COR20-02-20GC and T2 in core COR20-02-21GC, are respectively dated around 1515-1665 CE and 1675 CE and located at a depth corresponding to that of reflector R5. Finally, this reflector is at the same depth as turbidites T2 or T3 in core COR20-02-26GC collected at the mouth of the Saguenay River and dated between 1645 and 1675 CE. The similarity of these ages with the age interpreted by Cauchon-Voyer *et al.* (2008) confirms that the sub-horizontal reflectors described in the present study correspond to the seismic reflector R5.

A second reflector R6, shallower than R5 (< 1 m) and characterized by a weaker amplitude is observed in the Betsiamites and Rimouski areas (**Figure 3-3**). R6 correlates with the depth of turbidite T2 (~ 0.80 m) in COR20-02-18GC, turbidite T1 (~ 0.50 m) in core COR20-02-19GC, turbidite T1 or T2 (~ 0.50 – 1.20 m) in core COR07-03-11PC and turbidite T1 (~ 0.60 m) in core COR20-02-03GC. These three turbidites dated 1805 CE, 1690 - 1880 CE and 1870 CE, respectively.

5. DISCUSSION

5.1. Relationship between submarine landslides and rapidly deposited layers (RDL)

The irregularity of deposits and the presence of coarse material and debris in submarine landslides makes coring difficult. During the SLIDE-2020 expedition, the coring sites were determined in order to overcome this limitation by targeting sub-horizontal reflectors in the distal part of submarine landslides where they are thin enough for their underlying and overlying sediments to be dated (e.g., Piper *et al.*, 2019). The relationship between these reflectors and the mass-transport deposits is observed in the Betsiamites area (seismic profile BET_D_2T) and the Saguenay area (seismic profile SAG_H_1T) where the R5 reflector corresponding to RDLs is in the continuity with the sliding mass and above (Strachan, 2008). However, the fact that this geometry is not systematically identified, does not imply that this genetic link does not exist. Indeed, the coring revealed that the R5 reflector extending over the Lower Estuary corresponds to RDLs that may have been triggered by a submarine landslide or debris flow. The large number of turbidites observed in the cores recovered during the SLIDE2020 expedition validates their correspondence with sub-horizontal seismic reflectors distal to submarine landslides. Furthermore, it implies that the submarine landslides have progressively transformed into turbidity currents. The proximal turbidites have a higher proportion of coarse sediment (e.g., T2 in COR20-02-19GC, d_{50} ~ 103 µm) than distal turbidites (e.g., T1 in COR20-02-04GC, d_{50} ~ 28 µm) and the cores recovered from a site very close to mass transport deposits revealed debrites (e.g., COR20-02-29GC) confirming that the RDLs are deposited by submarine landslides. The fragment of terrestrial soil in debrite D1 of core COR07-03-13PC which may have been transported by the 1663 CE Colombier event along coast of the Betsiamites area (see Bernatchez, 2003) tends to support this relationship.

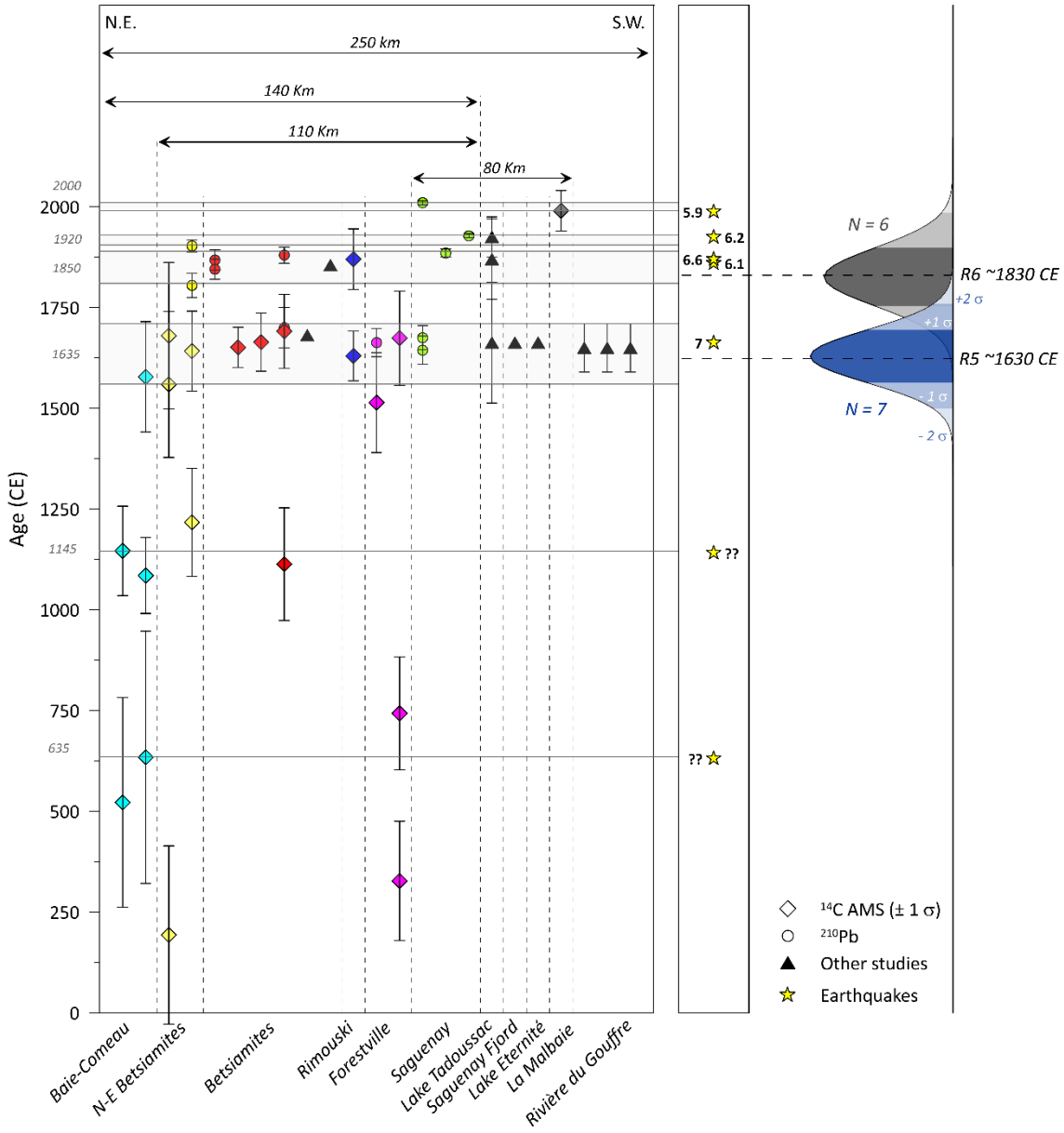

Figure 3-9. Chronology of the RDLs (turbidites and debrites) dated by ^{14}C (colored diamonds) and ^{210}Pb (colored circles). The black triangles correspond to evidences provided by previous studies of aerial or submarine landslides in Québec (Doig, 1990, Filion *et al.*, 1990, St-Onge *et al.*, 2004, Cauchon-Voyer *et al.*, 2008, Locat *et al.*, 2016). The gray intervals highlight periods of synchronous RDLs. The black arrows show the distance of synchronous submarine landslides for each period. The yellow stars indicate the timing of major historical earthquakes with their magnitude. To the right, the range of reflectors R5 (blue) and R6 (gray) considering a statistical error of ± 1 σ and ± 2 σ.

5.2. Chronology of the RDLs and triggering factors

The dated RDLs are assembled in **Figure 3-9**. This figure reveals four distinct periods with at least twelve concomitant submarine landslides at the regional scale. The first period is between 1560 CE and 1710 CE with nine submarine landslides with a mean age of 1635 ± 75 CE spread over 140 km. RDLs deposited at this period correspond to reflector R5, observed regionally and dated to 1630 ± 65 CE (**Figure 3-9**). The second period begins at 1800 CE and ends at 1900 CE. It includes

six submarine landslides over a distance of 110 km and RDLs deposited in this period correlate with the seismic reflector R6 dated to 1830 ± 70 CE. The third period spans from 1910 CE to 1930 CE with two submarine landslide in the Betsiamites area and another 110 km away in the Saguenay. Finally, the fourth period extends from 1990 CE to 2010 CE with two submarine landslides 80 km apart.

The dating of RDLs presented in **Table 3-4** includes ages beyond 2000 years, but they are not included in the synthesis in **Figure 3-9**. Indeed, from ages older than 2000 years, the uncertainties become more important and it is difficult to establish with certainty that RDLs are synchronous. Moreover, it is not possible to establish a link between these deposits and historical seismicity.

During the four periods identified, four to five major historical earthquakes occurred in the St. Lawrence Estuary region (Lamontagne *et al.*, 2018): 1663 ($M \leq 7$), 1860 ($M = 6.1$) or 1870 ($M = 6.6$), 1925 ($M = 6.2$) and 1988 ($M = 5.9$) (**Table 3-5**). The difference between the ^{14}C ages and ages calculated from sedimentation rates for the different RDLs may be related to the accuracy of the dating method and RDL thickness measurements. The most accurate cases correspond to turbidites T1 in cores COR20-02-04GC and COR20-02-20GC. Indeed, in core COR20-02-04GC, turbidite T1 is already considered to be associated with the 1663 CE earthquake by Cauchon-Voyer *et al.* (2008) and has been dated at 1665 CE based on ^{14}C dating of the immediately underlying hemipelagic deposits. The ^{210}Pb dating of turbidite T1 in core COR20-02-20GC yields an age of 1665 ± 35 CE, in agreement with the ^{14}C age considering the dating uncertainties (1515 CE ± 125 at 1σ and 1515 CE ± 245 at 2σ). The density profiles obtained with the MSCL and from water content measurements do not show a linear evolution with depth, but a rather stable density over the upper 2 m, suggesting that compaction can be neglected for the age calculations of the RDL with ^{210}Pb-derived sedimentation rates. The reliability of these dates supports the correlation between submarine landslides and historical seismicity but the close age of the 1860 and 1870 CE earthquakes does not lend to differentiate these events from our chronology owing to the age uncertainty of the dated RDLs.

Submarine landslides triggered by earthquakes have already been described in other regions of the world (e.g., Bryn *et al.*, 2005; Dan *et al.*, 2009). Ground shaking during an earthquake constitutes a major factor for slope destabilisation (Hampton *et al.*, 1996) and its influence can exceed several hundreds of kilometers to trigger several independent failures (Goldfinger *et al.*, 2012, 2017). The synchronicity between RDLs in a seismic region is increasingly used for the study of paleoseismicity during the Holocene (Goldfinger *et al.*, 2007, Gracia *et al.*, 2010, Ratsov *et al.*, 2015, Howarth *et al.*, 2021). Storms, river floods and rapid relative sea level rise can also trigger submarine landslides and turbidites at the regional scale (~ 100 km) (Talling, 2014). However, the RDLs in this study were not connected to river mouths. At the scale of the last 500 years, relative sea level variations are insignificant (Dionne, 2001; Shaw *et al.*, 2002; Remillard *et al.*, 2017). Storms

Table 3-5. List of major historical earthquakes in the St. Lawrence Estuary (from Lamontagne *et al.*, 2018). CK = Charlevoix-Kamouraska.

Year	Lat (°N)	Long (°W)	Area	Magnitude	MMI	Magnitude information	Source
1663	47.60	-70.10	CK	7.0	IX	Estimated	Gouin, 2001
1860	47.50	-70.10	CK	6.1	VIII	Estimated	Gouin, 2001
1870	47.40	-70.50	CK	6.6	IX-X	Estimated	Gouin, 2001
1925	47.80	-69.80	CK	6.2	VIII	Instrumented	Bruneau & Lamontagne, 1994
1988	48.12	-71.18	Saguenay	5.9	VIII	Instrumented	North *et al.*, 1989

in eastern Canada are much weaker than tropical storms (e.g., Taiwan, New-Zealand) and the physiography of the estuary allows it to be relatively sheltered from oceanic swells (Bernatchez *et al.*, 2012). Therefore, the synchronicity of submarine landslides that are reported here over a large area of a known seismic zone is a strong argument for relating their triggering to the regional seismicity of the CKBSL seismic zone.

The RDL 3 observed in core COR20-02-26GC and dated around 1645 CE in the Saguenay area is interpreted as a hyperpycnite. In the Saguenay Fjord, St-Onge *et al.* (2004) and Syvitski and Schafer (1996) describe a similar deposit related to the 1663 CE earthquake. It was interpreted as a flood-induced hyperpycnal flow after the breach of a natural dam generated by an earthquake-triggered turbidite. Historical observations reported by the Jesuit mission and synthesized by Gouin (2001) support the generation of a hyperpycnal flow by the 1663 CE earthquake in the Saguenay area (e.g., Tadoussac) and throughout the estuary : *"Rivers were thoroughly polluted, the waters of some becoming yellow and of others red; and our great river St. Lawrence appeared all whitish as far as the region of Tadoussacq"*; *"displaced lands […] caused their gradual detrition by the water of the Rivers, which are still so thick and turbid as to change the colour of the whole great St. Lawrence river."*

In the Middle Estuary, the tidal range and currents are stronger (Saucier and Chassé, 2000) as evidenced by the coarser sediments composing the hemipelagites observed in core COR20-02-50GC. These forcings, particularly effective at low water depths could play a major role in preconditioning submarine landslides in the CKSZ, as currents can erode submarine slopes causing oversteepening (Hampton *et al.*, 1996). These preconditioning factors combined with the high seismicity of the CKSZ (Lamontagne *et al.*, 2018) could increase the submarine landslide hazard in the Middle Estuary, which in turn could explain the high frequency of RDL observed in core COR20-02-50GC (four turbidites, two hyperpycnites and one slump). Moreover, the 1663 CE earthquake may have occurred in this region (Lamontagne *et al.*, 2018).

5.3. Relative importance of the 1663 CE event

The 1663 CE earthquake was the strongest historical earthquake in Eastern Canada (Locat *et al.*, 2003; Ebel, 2011; Lamontagne *et al.*, 2018). This statement is confirmed by our study that

allowed identifying at least 12 RDLs dated at ~1663 CE in 10 sediment cores distributed over a distance of 140 km, whereas only five RDLs dated at ~1860/1870 CE and two at ~1925 CE and ~1988 CE were observed over a less extensive area. The seismic survey revealed a strong shallow reflector present in almost all the studied area in the slopes and in the submarine landslide deposits. Intersecting cores analyzed and dated this reflector R5 (**Figure 3-3** and **Figure 3-4**). Its approximate age is near to that of the 1663 CE earthquake. A second reflector has been identified (R6) and dated at about 1830 – 1860 CE, which is very close to the two other major historical earthquakes of 1860 and 1870 CE (**Figure 3-3**). Shallower than R5, this seismic reflector is identified at fewer locations, confirming the relative importance of the 1663 CE earthquake compared to more recent events such as the 1860 and 1870 CE earthquakes.

In this study, it thus appears that the 1663 CE earthquake has triggered more submarine landslides over a larger area than more recent earthquakes (**Figure 3-9**), attesting to the importance of this event at the scale of the last two millennia and corroborating historical observations reported by the first European settlers (Gouin, 2001, Ebel, 2011). Other studies in Québec (Doig, 1990, Filion *et al.*, 1991, St-Onge *et al.*, 2004; Cauchon-Voyer *et al.*, 2008, Poncet *et al.*, 2010; Locat *et al.*, 2016) highlight the highest intensity of this major event. In comparison, more recent earthquakes (**Figure 3-5**) appear to have had less impact than the 1663 CE earthquake. However, the relation between earthquake magnitude and the number of submarine landslides is not linear (e.g., Papadopoulos and Plessa, 2000). Some factors can interfere such as the sedimentary budget and predisposing factors (Hampton *et al.*, 1996).

The compilation of submarine landslide ages leads to identify two older periods with synchronous ages of RDLs. The first at 1145 ± 145 CE with four synchronous deposits distributed over a distance of 40 km and the second at 645 ± 400 CE with three synchronous RDLs over a distance of 100 km. The first period has already been identified by Philibert *et al.* (2012) by the dating of RDL at ~ 1200 CE in Lake Jacques-Cartier (**Figure 3-1**) and correlated with the seismicity of CKSZ. Moreover, Normandeau *et al.* (2013) found an earthquake-triggered submarine landslide deposit in Lake St-Joseph (**Figure 3-1**) dated at ~1250 CE. Trottier *et al.* (2019) in Lake Maskinongé (CKSZ) also identified mass transport deposits about the same period at ~1180 CE through geomorphic and core analyses. Additionally, the major event identified and dated around 650 CE by Lajeunesse *et al.*, (2017) in Lake Témiscouata near the Charlevoix area is likely synchronous with the RDLs dated at 645 ± 400 CE period in this study. The link between regional seismicity and the submarine landslides established in addition to these studies tends to suggest that two earthquakes could have triggered these older RDLs in the St. Lawrence Estuary.

6. CONCLUSION

The dating of 12 submarine landslides distributed over a distance of 220 km along the axis of the St. Lawrence Estuary allowed correlating them to the major historical earthquakes of 1663 CE, 1860 and/or 1870 CE and 1925 CE. The observation of older submarine landslide deposits suggests that two large earthquakes may have occurred around 645 CE and 1145 CE, in a period

when historical data are not available. The criteria used to infer these relationships are:

1) The careful location of the coring sites outside areas influenced by storms, sediment input (e.g., rivers) and active turbiditic channels;
2) The ^{14}C and ^{210}Pb dating of turbidites and debrites revealing concomitant ages with the historical earthquakes;
3) The synchronicity of submarine landslides and their associated turbidites described over a distance of ~ 220 km in a seismically active zone;

The results reported in this paper provide evidence that allow estimating the paleoseismicity of the last 2000 years in the St. Lawrence Estuary, which in turn improves the seismic hazard assessment in Eastern Canada. These results also allow demonstrating that the 1663 CE earthquake was the most important event of the last two millennia, although several submarine landslides observed in this study still remain to be dated. Investigating in detail these landslides would allow going even further back into the paleoseismological archives, refining the location of the epicenter of the 1663 CE earthquake and assess landslide-related hazards. Additionally, characterizing of the mechanical behavior of sediments recovered in the St. Lawrence Estuary could help in evaluating the stability of slopes during an earthquake with specific attention on the stratified seismic unit 4, which seems susceptible to failure. Additional investigations are needed to characterize and understand the behavior and role of this unit during an earthquake, in particular its liquefaction potential.

EN BREF

- Des glissements sous-marins répartis sur 220 km dans l'estuaire du Saint-Laurent ont été datés.
- Les dépôts des glissements sous-marins sont synchronisés avec les principaux séismes historiques.
- Deux dépôts de glissements sous-marins plus anciens ont été datés autour de 645 et 1145 CE.
- L'évènement de 1663 CE semble être le plus fort tremblement de terre des 2000 dernières années.

IN SHORT

- Submarine landslides distributed over 220 km in the St. Lawrence Estuary were dated.
- Submarine landslide deposits are synchronized to major historical earthquakes.
- Two older coeval submarine landslide deposits were dated around 645 and 1145 CE.
- The 1663 CE event appears to be the strongest earthquake of the last 2000 years.

CHAPITRE IV. LOCALISATION DU SEISME DE 1663 CE (M ≥ 7) DANS L'ESTUAIRE DU SAINT-LAURENT (CANADA) PAR L'ANALYSE DE LA LIQUEFACTION DES SEDIMENTS

CHAPTER IV. LOCATION OF THE 1663 CE EARTHQUAKE (M ≥ 7) IN THE ST. LAWRENCE ESTUARY (CANADA) USING SEDIMENT LIQUEFACTION ANALYSIS

From Merindol et al., 2022. Engineering Geology. Submitted.

Figures de liquéfaction dans une carotte sédimentaire prélevée dans la région de Charlevoix
Liquefaction features in a sediment core from the region of Charlevoix

Le séisme de 1663 CE, d'une magnitude estimée à ≥ 7, est l'un des plus forts séismes historiques jamais ressentis dans l'est du Canada. Cependant, l'épicentre de séisme n'a pas encore été déterminé avec précision. Dans cette perspective, l'expédition SLIDE-2020 à bord du NO Coriolis II dans l'estuaire du Saint-Laurent visait à imager et échantillonner six zones où des glissements de sous-marins ont été déclenchés par le séisme de 1663 CE. Des analyses sédimentologiques et géotechniques ont été utilisées pour déterminer le potentiel de liquéfaction des sédiments quaternaires du Saint-Laurent. Deux interfaces entre les unités sismiques ont été caractérisées comme des couches sédimentaires hautement liquéfiables et donc considérées comme des facteurs contribuant aux ruptures de pente en réponse au séisme de 1663 CE. Une nouvelle localisation de l'épicentre du séisme de 1663 a été calculée avec précision en utilisant (1) la loi d'amortissement de l'accélération maximale du sol liée à la distance à l'épicentre et (2) la simulation numérique du comportement mécanique des sédiments pendant la charge du séisme. Ce nouvel emplacement est situé à environ 120 km au nord-est du dernier emplacement suggéré et à seulement 30 km d'une faille active proche de Tadoussac. La nouvelle localisation de l'épicentre pourrait avoir un impact majeur sur l'évaluation des risques sismiques dans la Province du Québec. De plus, cette étude propose deux nouvelles approches pour déterminer l'épicentre d'un séisme survenu avant l'avènement de l'instrumentation sismographique.

The 1663 CE earthquake, with an estimated magnitude of ≥ 7, is one of the strongest historical earthquakes ever felt in eastern Canada. However, the epicenter of this earthquake has not been yet precisely determined. In this perspective, the SLIDE-2020 expedition on board the RV Coriolis II in the St. Lawrence Estuary aimed to image and sample six zones where submarine landslides were triggered by the 1663 CE earthquake. Sedimentological and geotechnical analysis have been used to determine the liquefaction potential of the St. Lawrence Quaternary sediments. Two interfaces between seismic units were characterized as highly liquefiable sedimentary layers and thus considered as contributing factors to slope failures in response to the 1663 CE earthquake. A new location of the 1663 CE earthquake epicenter has been accurately calculated by using (1) the peak ground acceleration damping law related to the distance to the epicenter and (2) the numerical simulation of the mechanical behaviour of sediments during earthquake loading. This new location is about 120 km northeast of the last suggested location, only 30 km from an active fault near Tadoussac. The new epicenter location could have a major impact on seismic hazard assessment in the Province of Québec. Furthermore, this study proposes two new approaches to determine the epicenter of an earthquake that occurred prior to the advent of seismographic instrumentation

1. INTRODUCTION

Locating the epicenter of an earthquake is crucial in assessing seismic hazard and associated risks. However, the location of earthquake epicenters prior to the advent of seismological instrumentation could only be approximated from felt information, historical archives and accounts archaeology, or field surveys. The catalog of significant Canadian earthquakes for the period 1600-2017 (Lamontagne *et al.*, 2018) is largely based on such indirect information for pre-19th century earthquakes before the development of seismographs. Eastern Canada and the Charlevoix-Kamouraska/Lower St. Lawrence seismic zones (CKSZ/LSLSZ) have a strong seismicity, as demonstrated by the February 5, 1663 CE earthquake (EQ1663), estimated to be at least seven in magnitude (Smith, 1962; Gouin, 2001; Locat, 2011). Because the seismic zoning of eastern Canada is sensitive to EQ1663, revision of the epicenter position may have repercussions on the assessment of the seismic hazard (Locat, 2011). However, the compilation of earthquakes in the Province of Québec by Lamontagne *et al.* (2018) indicates that the epicenter position of the EQ1663 is accurate by ± 50 km in the Charlevoix region (**Figure 4-1**). This location is based on the historical writings of Mercier in 1665 (Ebel, 2011). Without additional information, Hodgson (1928) considers that the EQ1663 epicenter has the same position as the 1925 earthquake (M~6.2; Bruneau and

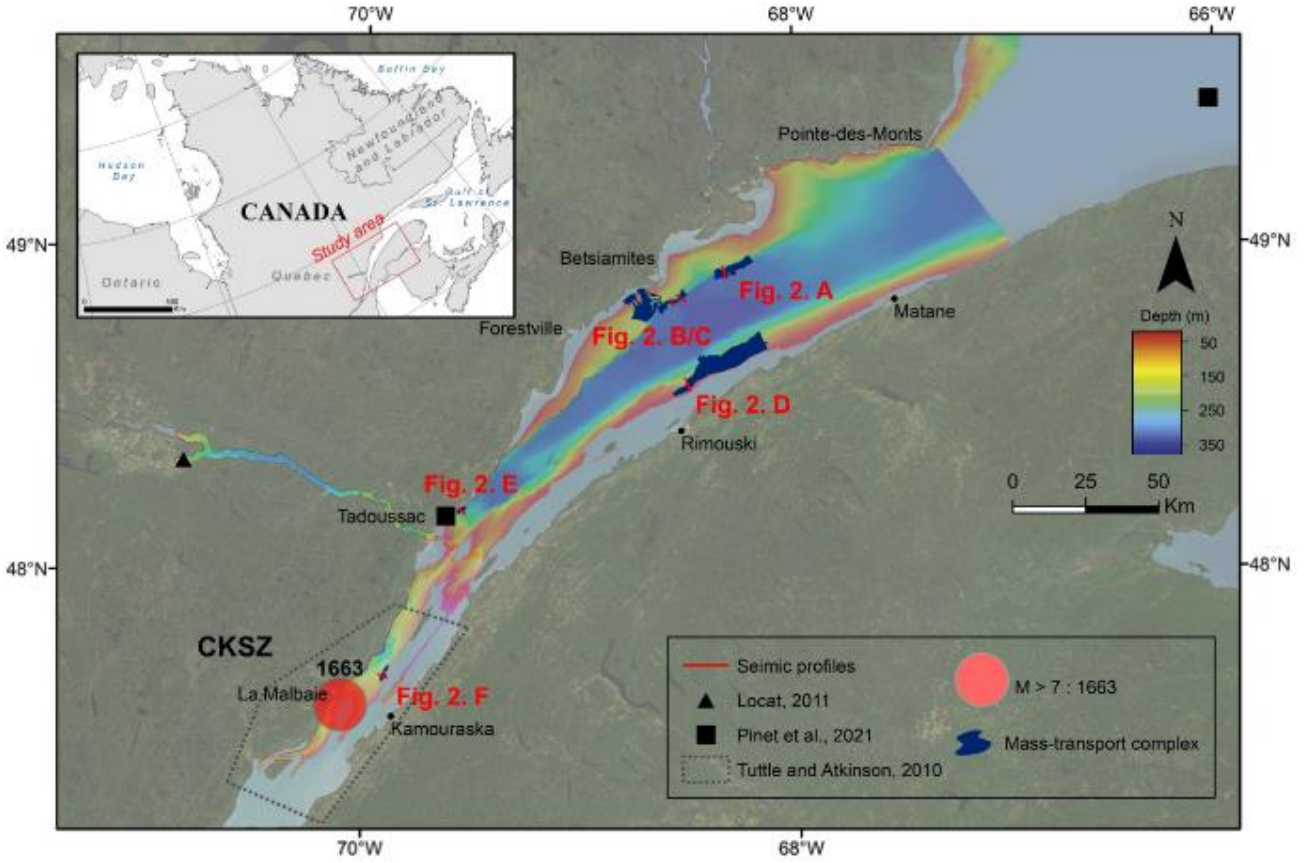

Figure 4-1. Bathymetric map of the St. Lawrence Estuary. The studied mass-transport complexes (MTC) are indicated in blue. Red lines indicate seismic profiles crossing the MTCs and used in this study. The black squares and triangle indicate the locations of the epicenter of the 1663 CE earthquake proposed by Pinet *et al.* (2021) and Locat (2011) respectively. The area of the 1663 CE epicenter proposed by Tuttle and Atkinson (2010) coincides with the Charlevoix-Kamouraska Seismic Zone (CKSZ) and is indicated with a gray dashed line.

Lamontagne, 1994). Hereafter, the proposed Hodgson (1928) location of EQ1663 will be referred to as the "historical reference location".

Studies over the last decade have enabled scientists to better constrain the EQ1663 epicenter. By analyzing the distribution of large sub-aerial landslides on the shores of the St. Lawrence, Locat (2011) located the epicenter not far from the Saguenay graben with an uncertainty of ±50 km (**Figure 4-1**). Additionally, by analysing the distribution and geomorphology of submarine landslides in Lake Eternity, Locat *et al.* (2016) placed the EQ1663 epicenter to the NW or NE of the lake (i.e., closer to the Saguenay Fjord). However, in both studies, the fault at the origin of this major earthquake is not clearly identified. More recently, two postglacial active faults identified on the seafloor of the St. Lawrence are likely to have generated a sufficiently large and recent earthquake comparable to the EQ1663. One fault is located in the northeastern part of the St. Lawrence Estuary in the LSLSZ (Pinet *et al.*, 2021), while the second is located at the mouth of the Saguenay Fjord (Normandeau *et al.*, 2015; Pinet *et al.*, 2021) (**Figure 4-1**). Although these studies have failed to converge concerning the position of the EQ1663 epicenter, they show that the initial position defined by Hodgson (1928) was most likely inaccurate.

Based on ^{14}C and ^{210}Pb dating methods, Mérindol *et al.* (2022) have established a temporal relationship between 12 submarine landslides in the St. Lawrence Estuary and regional seismicity, confirming what was previously suggested by several authors (Bernatchez, 2003; St-Onge *et al.*, 2004; Cauchon-Voyer *et al.*, 2008; Pinet *et al.*, 2015). Evidence of slope failure found in the Charlevoix-Kamouraska seismic zone by Tuttle and Atkinson (2010) and reported by historical observations following the 1663 CE earthquake (Gouin, 2001), supports the occurrence in our study zone of failure phenomenon during earthquakes and mainly the EQ1663. The phenomenon of liquefaction of silty or sandy layers that occurs during an earthquake could explain the generation of such submarine slope failures within stratified layers (Cauchon-Voyer *et al.*, 2008, 2011).

In the present work, our aim is to define the accurate location of the 1663 CE historical earthquake. This will be achieved by (1) relying on geotechnical laboratory tests to characterize the sediment mechanical behavior during earthquake loading, (2) using a Peak Ground Acceleration (PGA) damping law related to the distance to the epicenter and (3) simulating, using an elasto-plastic finite elements analysis, the liquefaction potential of the sediments under earthquake loading. Sediment liquefaction depends on the intensity of seismic shaking, which is closely related, for a given earthquake magnitude, to the distance from the epicenter (e.g., Tuttle and Atkinson, 2010). By considering the submarine landslides triggered by the EQ1663, it is possible to determine by back-analysis the critical distance from an earthquake equivalent to the EQ1663. We argue that the intersection of the epicenter distances obtained from the different landslides should refine the EQ1663 epicenter location.

2. BACKGROUND

2.1. Regional seismicity

The CKSZ/LSLSZ present a seismic hazard almost as high as that of the active Pacific zone. The major event of February 5, 1663 CE, with an estimated magnitude of ≥ 7, highlights the

importance of this seismic hazard. In addition to the 1663 CE earthquake, four earthquakes with M 5.9 to 6.6 occurred in the CKSZ/LSLSZ in 1860, 1870, 1925 and 1988 CE (Smith, 1962; Lamontagne *et al.*, 2018). The 1663 CE earthquake was felt throughout the northeastern part of the North American continent (Locat, 2011) and it caused large landslides both on land and underwater in the St. Lawrence Estuary and Saguenay Fjord areas (e.g., Doig, 1990; Filion *et al.*, 1991; Ouellet, 1997; St-Onge *et al.*, 2004; Cauchon-Voyer *et al.*, 2008; Locat *et al.*, 2016; Lajeunesse *et al.*, 2017). Such landslides may generate tsunami waves, exposing coastal communities in the Province of Québec, Canada (Poncet *et al.*, 2010; Turmel *et al.*, 2019). In addition to the major earthquake of 1663, no less than five earthquakes of M 6 and more occurred in CKSZ in 1791, 1860, 1870, 1925 and 1988 (Smith, 1962; Lamontagne *et al.*, 2018). The local seismograph network in Québec records significant background seismicity with more than 200 events ($M \geq 2$) each year (Pinet *et al.*, 2021). In comparison, the background seismicity of the LSLSZ corresponds to 50 annual events ($M \geq 2$) while the largest known earthquake had a magnitude of M4.5 (Lamontagne *et al.*, 2003). In both seismic zones, the predominant focal mechanism corresponds to reverse faulting interpreted as the reactivation of normal faults inherited from late Proterozoic to Paleozoic tectonic activity (Tremblay *et al.*, 2003; Pinet *et al.*, 2014). Hypocenters are located within the Precambrian shield at depths between 5 and 25 km (Anglin, 1984). However, the faults that caused these earthquakes, including the 1663 CE event, are still poorly identified because of sediment rapidly draping evidence of Holocene activities (Normandeau *et al.*, 2015; Pinet *et al.*, 2021). In terms of PGA, the Canadian building code of seismic zoning indicates for the CKSZ and LSLSZ a mean PGA between 0.4 g and 1.5 g (CNRC, 2005) with a 2% probability of exceedance in a 50-years period. These high values, largely influenced by the EQ1663, place the St. Lawrence region at the same level of seismic hazard as the Juan de Fuca subduction zone in western Canada (Locat, 2011).

2.2. Liquefaction process

Seismicity is considered as the primary trigger factor of submarine landslides (Seed and Idriss, 1967; Hampton *et al.*, 1996) acting in three different ways. First, ground acceleration generated by seismic waves adds to destabilizing forces on the sedimentary column (Hack *et al.*, 2007). Second, tensile strength between soil particles can be broken by soil displacement during an earthquake, resulting in a loss of tensile strength and cohesion (Ishihara, 1985). Third, the effect of seismic waves on the ground is equivalent to cyclic loading (Ishihara, 1985; Norem *et al.*, 1990) resulting in degradation of sediment stiffness and shear strength, and an increase in the pore pressure of coarse sediment layers (e.g., silt to sand; Idriss *et al.*, 1976). Thus, the effective confining stress tends to zero (Terzaghi *et al.*, 1996) and the soil may lose all its shear strength. It deforms indefinitely in the direction of maximum stress, liquefying (Norem *et al.*, 1990). Liquefaction can occur even where the seafloor is inclined as gently as 0.1-5% (Youd and Hoose, 1978) resulting in lateral spreading. In the case where the slope exceeds around 5%, the liquefied sediment can trigger landslides that can flow and gradually evolve into a turbidity current (Norem *et al.*, 1990).

Liquefaction depends on the relationship between the cyclic shear stress generated during an earthquake and the stress required to initiate liquefaction in the sediment (Obermeier, 1996). Consequently the potential of liquefaction is controlled by the nature of the deposit (i.e., grain-size distribution, clay proportion, water saturation) (Youd and Hoose, 1978, Obermeier, 1996) and by the peak ground acceleration (PGA) that may reach the sediment layer. This PGA is closely related to the distance of the study site from the earthquake epicenter (Campbell, 1997).

2.3. Evidence of liquefaction

Several evidence of liquefaction were observed after major earthquakes in the St. Lawrence region. After the earthquakes of 1870 AD and 1925 AD (M 5.9 and 6.6) in the Charlevoix area, it is reported that liquefied sand flowed from ground cracks (Gouin, 2001). Following the 1663 CE earthquake, the advent of a hundred sand volcanoes around Charlevoix is reported, which are interpreted by Chagnon and Locat (1988) as the expression of the liquefaction of sand due to seismic shacking (sand boiling). In addition, Tuttle and Atkinson (2010) identified earthquake-induced liquefaction features in Holocene sediments in the Charlevoix region (e.g., sand dike, deformed sand) and used them as proxies of the localization of the major paleo-earthquakes.

Cauchon-Voyer *et al.* (2011) described stratified silty clays with thin layers of sand within the St. Lawrence Quaternary sedimentation marking the transition between glaciomarine and postglacial sedimentation (Duchesne *et al.*, 2010). The alternation of silty clays and sand could influence the permeability of the sediment column and favor an increase in pore pressure in the case of an earthquake (Cauchon-Voyer *et al.*, 2008). Consequently, this stratified sedimentary layer could be weakened during an earthquake, thus promoting the development of a slip surface. Based on geotechnical analyses and numerical simulations, Martin *et al.* (2001) showed that a similar alternation of silty clays and sand in the Saguenay Fjord implies a high susceptibility to liquefaction during an earthquake.

3. METHODS

In the summer of 2020, during the SLIDE-2020 cruise on board the RV *Coriolis II*, six areas of submarine mass-transport complexes (MTCs) were surveyed based on the mapping carried out by Pinet *et al.* (2015). The high-resolution seismic data were collected using the hull-mounted Edgetech X-Star 2.1 subsurface profiler. These data allowed the sampling of different sedimentary units in a total of eleven cores. Their lengths vary between 2.51 m and 5.22 m at water depths ranging between 39 m and 236 m. Their sedimentological analyses, presented below, were carried out after the expedition at ISMER, while geotechnical measurements were carried out at Ifremer. Interpretation of the seismostratigraphic sequence is based on seismic attributes such as reflections, geometry and amplitude of reflecting horizons detailed by Cauchon-Voyer *et al.* (2008) and on the recovered cores.

3.1. Sedimentary and geotechnical analyses

3.1.1. Sediment cores

Wet bulk density, low-field volumetric magnetic susceptibility (k) and P-Wave velocity were measured using the GEOTECK MSCL (Multi

Sensor Core Logger) on whole sections. Measurements were performed at 1 cm intervals. Subsequent digital X-ray images were then acquired with the GEOTECK XCT scanner to visualize the internal structures. Based on these results and by tying cores to seismic profiles, sections for geotechnical analysis were selected and preserved, while the remaining core sections were split lengthwise in two halves. The selected sections for geotechnical investigation correspond to the coarsest layers considered to have a high liquefaction potential. They must be homogenous excluding the rapidly deposited layer (RDL) associated with turbidity currents or debris flow (St-Onge *et al.*, 2004; Mérindol *et al.*, 2022). Fifteen geotechnical samples of coarse materials (silt and sand) were selected to determine their susceptibility to liquefaction during an earthquake, while one sample of clay was selected. Triaxial samples were 50 mm in diameter and 100 mm in high. Grain-size analysis (1 to 2000 µm) was performed on these geotechnical samples using the Master Sizer 3000 (Malvern) laser grain size analyzer with sampling intervals of 1 to 2 cm.

Bulk density profiles were used to calculate profiles of vertical effective stress, σ'_{v0}, using the following equation:

$$\sigma'_{v0} = \sum_{i=1}^{n} (\rho_m - \rho_e) g \Delta x_i \quad (1)$$

where ρ_m is the bulk density measured by the MSCL, ρ_e the density of seawater (1.027 g.cm^{-3}) and Δx the measuring step length.

Sediment permeability was measured with the falling head method according to the ASTM-D5856-15 standard. These measurements were performed on samples from each core listed in **Table 4-1**.

The undrained shear strength was measured on split core sections using a hand-shear-vane (ASTM D8121) with a spacing of 10 to 50 cm. These measurements were carried out only in clay facies.

3.1.2. Cyclic triaxial testing

To characterize sediment response during earthquake loading we used the Enterprise Level Dynamic Triaxial Testing System (ELDYN) from Geotechnical Digital System (GDS). The test followed the ASTM-D5311M-13 standard

Table 4-1. Location, length and water depth of studied cores.

Area and core name	Zone	Lat. (°N)	Long. (°W)	Length (m)	Water depth (m)
Rimouski					
COR20-02-01GC	Intact	48°34.71	68°29.66	4.42	39
COR20-02-02GC	Scar	48°34.77	68°29.76	4.10	47
Matane					
COR20-02-05GC	Scar	48°54.65	67°35.68	3.53	197
COR20-02-06GC	Intact	48°54.61	67°35.66	3.93	152
Baie-Comeau					
COR20-02-10GC	Intact	48°59.80	68°11.66	4.63	133
COR20-02-11GC	Scar	48°59.71	68°11.59	4.40	153
COR20-02-12GC	Scar	48°59.49	68°11.42	5.22	193
Betsiamites					
COR20-02-15GC	Intact	48°53.66	68°30.35	4.49	177
COR20-02-16GC	Scar	48°53.47	68°30.21	4.30	236
Saguenay					
COR20-02-25GC	Scar	48°11.56	69°34.07	4.36	186
Charlevoix					
COR20-02-45GC	Scar	47°41.11	69°54.71	2.51	153

procedure. Bender elements mounted in the base and top cap of the triaxial cell were used to measure the velocities of shear wave (V_s) and compression wave (V_p) before and during the tests.

The cyclic loading phase was performed after a consolidation phase, where the sample was loaded isotropically to an effective confining stress of 50 kPa (σ'_3). During the cyclic loading phase, the deviatoric stress amplitude, noted Δq, was applied through uniform sinusoidal cycles at 0.5 Hz. This allows the calculation of the Cyclic Resistance Ratio (*CRR*) given by:

$$CRR = \frac{\Delta q}{2\sigma'_3} \quad (2)$$

The purpose of this test is to determine the liquefaction potential expressed by the CRR in terms of the number of cycles required to reach liquefaction. Both pore water pressure and strain criteria are considered. The first defines the liquefaction as the state at which the excess pore pressure ratio (r_u) reaches~ 0.95 (Ishihara, 1993). The excess pore pressure is usually normalized by the initial confining stress. The normalized excess pore pressure ratio is expressed by:

$$r_u = \frac{\Delta u}{\sigma'_3} \quad (3)$$

where Δu is the excess pore pressure.

The second criterion defines liquefaction as a threshold shear strain is reached. According to Wu *et al.* (2004), liquefaction occurs when the shear strain of the specimen exceeds 6%. This criterion is relatively insensitive to material properties such as the relative density and to testing conditions such as the consolidation stresses (Wu *et al.*, 2004). Hence, in the present study, the shear strain criteria was used to define liquefaction potential.

3.2. Methods used for liquefaction calculation

3.2.1. Accelerogram

The most recent major and instrumented earthquake that occurred in the province of Québec is the 1988 AD earthquake of Saguenay (M 5.9). It induced a maximal acceleration of 0.12 g measured at 120 km away at the St-Ferréol station (Québec). The accelerogram recorded at this station is used as a reference to simulate the load induced by older and non-instrumented earthquakes in the region, such as the EQ1663. The accelerogram is multiplied by a scale factor to simulate different distances between the study areas and the EQ1663 epicenter.

3.2.2. Attenuation of PGA

The load induced by an earthquake is expressed through the PGA. It is the amplitude of the largest peak acceleration recorded on an accelerogram at a site during an earthquake (Douglas, 2002). The PGA is related to seismological parameters in a specified region, such as earthquake magnitude, source-to-site distance, local sites conditions, and style of faulting. As for the EQ1663, the PGA for a particular site can only be estimated using ground-motion prediction equations (GMPEs). The dense instrumental recording in western North America associated with regional seismicity led to establish GMPEs empirically obtained from statistical regression of the ground-motion recordings (e.g., Douglas, 2003, 2011; Abrahamson *et al.*, 2014). Pezeshk *et al.* (2018) have established new GMPEs for Central and Eastern North America (CENA) excluding the Gulf Coast region from regional sets of seismological parameters. The GMPEs functional form is given by the expression:

$$\log(\bar{Y}) = c_1 + c_2 M + c_3 M^2 + (c_4 + c_5 M) \times min[\log(R), \log(60)] + (c_6 + c_7 M) \times \max\left[min\left\{\log\left(\frac{R}{60}\right), \log\left(\frac{120}{60}\right)\right\}, 0\right] + (c_8 + c_9 M) \times max\left[\log\left(\frac{R}{120}\right), 0\right] + c_{10} R \quad (4)$$

in which

$$R = \sqrt{R_{rup}^2 + c_{11}^2} \quad (5)$$

In equation (4) and (5), $\bar{Y}$ is the median value of PGA, M is moment magnitude, and R_{rup} is the closest distance to the fault-rupture surface (km). The coefficients in these equations are provided by Pezeshk *et al.* (2018) and are listed in **Table 4-2**. The GMPE for CENA function is plotted in **Figure 4-2** for four instrumented earthquakes that occurred in eastern Canada over the past 50 years. All of them follow the PGA-distance relationship proposed by Pezeshk *et al.* (2018) considering a total random standard deviation of ± 1 σ.

3.2.3. *Factor of Safety calculation using equivalent number of uniform stress cycles (ENUSC)*

The deterministic approach used to evaluate the liquefaction potential relies on the comparison between the seismic load expressed by the cyclic stress ratio (*CSR*) and the resistance to liquefaction expressed by the *CRR*. The ratio of these two variables provides the Factor of Safety (*FoS*) against liquefaction:

$$FoS = \frac{CRR}{CSR} \quad (6)$$

When FoS ≤ 1, liquefaction is predicted to occur. In this study, this approach is referred to as the ENUSC method.

The *CRR* was determined from cyclic triaxial tests. The equivalent number of uniform shear stress cycles corresponding to a given earthquake magnitude at a given distance was obtained from the diagram of Liu *et al.* (2001). The level of cyclic stress induced by the earthquake on a sediment layer (*CSR*) was calculated using the empirical equation formulated by Seed and Idriss (1971):

$$CSR = \frac{\tau_{av}}{\sigma'_v} \approx 0.65 \left(\frac{a_{max}}{g}\right)\left(\frac{\sigma_v}{\sigma'_v}\right) r_d \quad (7)$$

where τ_{av} is the average equivalent uniform cyclic shear stress caused by the earthquake and is assumed to be 0.65 of the maximum induced stress, a_{max} is the peak horizontal ground surface acceleration determined by the GMPE for CENA (Pezeshk *et al.*, 2018), g the acceleration of gravity, σ_v the total vertical stress and σ'_v the effective vertical stress derived from MSCL density data. r_d is the non-linear shear mass participation factor calculated using the Liao *et al.* (1988) equations:

$$r_d = 1.0 - 0.00765\, z \quad (8)$$

for z ≤ 9.15 m;

$$r_d = 1.174 - 0.0267\, z \quad (9)$$

for 9.15 m < z ≤ 23 m.

where z is the depth below the seafloor.

Table 4-2. Coefficients for the Empirical-Scaling Approach (M > 6) and for the Stochastic-Scaling Approach determined by Pezeshk *et al.* (2018).

	c_1	c_2	c_3	c_4	c_5	c_6	c_7	c_8	c_9	c_{10}	c_{11}
M > 6	$-7.655.10^{-1}$	$8.994.10^{-1}$	$-7.874.10^{-2}$	-3.534	$2.948.10^{-1}$	$-4.799.10^{-1}$	$-1.178.10^{-1}$	-2.182	$-3.029.10^{-1}$	$-2.327.10^{-3}$	-6.461

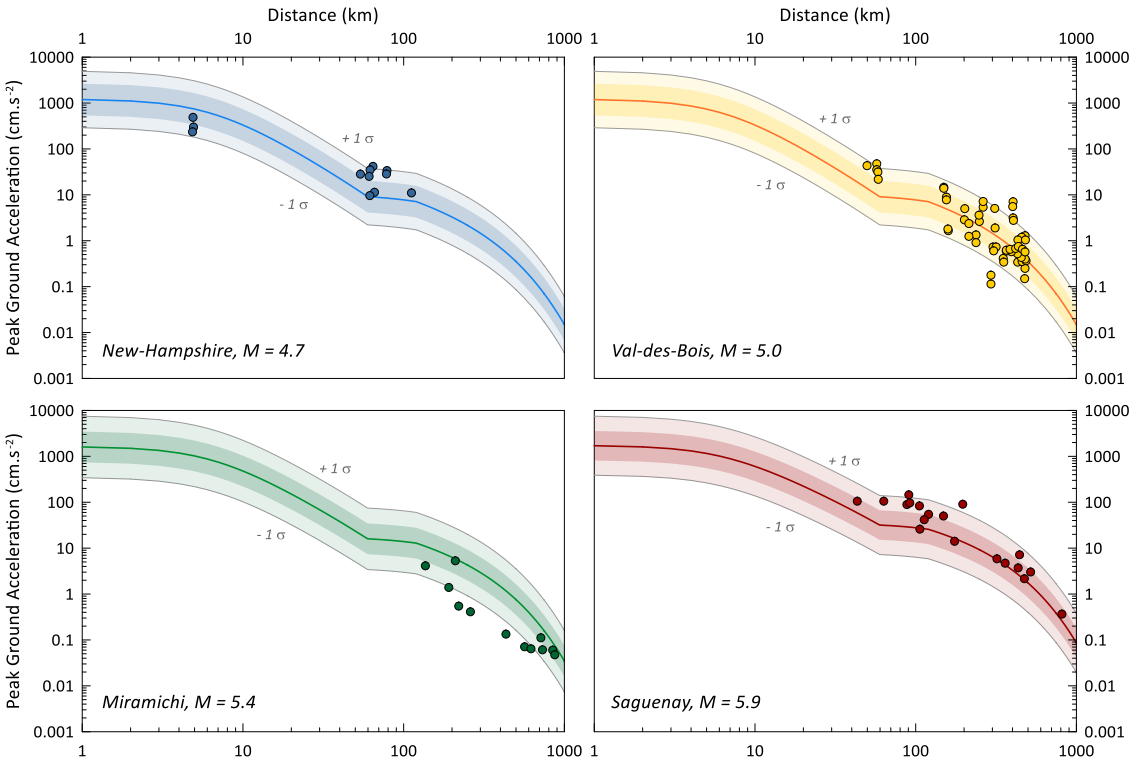

Figure 4-2. Evolution of the peak ground acceleration for the instrumented earthquakes of New-Hampshire (M 4.7), Val-des-Bois (M 5.0), Miramichi (M 5.4) and Saguenay (M 5.9) versus the distance predicted by the Ground-Motion Prediction Equations for central and eastern North America (Pezeshk *et al.*, 2018). The colored line corresponds to the mean PGA. The dark tone and the light gray, correspond to the standard deviation of the GMPE for CENA to within ± 0.5 σ and ± 1 σ, respectively. The instrumented earthquakes follow the proposed PGA-distance relationship by Pezeshk *et al.* (2018).

FoS are calculated for the six MTC zones at depths were the slope failure seems to have initiated. The approach is to determine the minimum acceleration bringing the FoS to 1. Because this threshold acceleration, expressed in *g*, is directly related to the source-to-site distance by the GMPE for CENA (Pezeshk *et al.*, 2018), it could thus be converted into the minimum distance to the epicenter needed to destabilize a study area. The liquefaction potential is evaluated for a magnitude M7 earthquake as estimated by Smith (1962) and Lamontagne *et al.* (2018) for the 1663 CE event.

3.2.4. Opensees with the PDMY02 constitutive soil model

To numerically simulate the mechanical behavior of the studied sediments (including the liquefaction process), the Open System for Earthquake Engineering Simulation (OpenSees; McKenna *et al.*, 2009) software was used. OpenSees is an open source software framework for developing finite element application in earthquake engineering. Developed by the Pacific Earthquake Engineering Simulation Research Center (PEER) it permits to model and simulate geotechnical systems exposed to cyclic loading. The model Pressure Dependant Multi-Yield 02 (PDMY02) (Elgamal *et al.*, 2002; Yang *et al.*, 2003) implemented in OpenSees, is used to simulate the stress-strain behavior of sand layers with a slope, under dynamic loading in undrained conditions. The PDMY02 plasticity model is formulated based on a multi-yield surface in 3D stress space (Yang *et al.*, 2003). The yield function corresponds to a conical yield surface in principal stress space and deviatoric

plane (Yang, 2000). The model considers a deviatoric kinematic hardening rule to generate the hysteretic response associated with cyclic shear loadings. The flow rule used in the PDMY02 model controls the volumetric strain and mainly reflects three different behaviors: contraction, dilation and critical state. The PDMY02 model relies on fifteen parameters listed in **Table 4-3**. For non-liquefiable clay layers, the constitutive model Pressure Independent Multi-Yield (PIMY) was used (Yang *et al.*, 2003). It is a linear elastic model relying on the five parameters listed in **Table 4-4**.

4. RESULTS

4.1. Seismostratigraphic analysis

The seismic profiles perpendicular to the six MTCs allow to distinguish intact sediments, landslide scars, mass-transport deposits (MTDs) and the underlying Quaternary sedimentary sequence above the bedrock (**Figure 4-3**). Slope gradients calculated from the seismic profiles are maximal at Baie-Comeau (6%) and decrease at the Betsiamites area with values between 4 and 5%. In the Rimouski area, the slope is gentler than 1% while in Tadoussac it is 3% and 5% in the Charlevoix area. These slope gradients are used with the OpenSees method. The Quaternary sedimentary sequence is either completely imaged, as in the Betsiamites and Charlevoix areas, or partially imaged as in the Rimouski and Tadoussac areas (**Figure 4-3**).

Seismostratigraphic analysis allows us to identify the critical depths where submarine landslides have been triggered. Indeed, for the Betsiamites, Baie-Comeau, and Charlevoix areas, the failures seem to have initiated above the seismic Unit 3, recognizable by its transparent acoustic signature. Indeed, it is not impacted by the submarine landslides as attested by its regular thickness (**Figure 4-3 a, b and c**). The failure events are located at the base of the stratified Unit 4, until Unit 5 (**Figure 4-3**). Unit 3 has been sampled in core COR20-02-11GC and is characterized by massive homogenous light clay

Table 4-3. PDMY02 parameters for silt and sand layers.

Parameter	Unit	Description	Values for silt layers	Values for sand layers
ρ	g.cm^{-3}	Density	1.6 – 1.8	1.9 – 2.1
p_{ref}	kPa	Reference mean effective confining pressure	50	
G_{ref}	MPa	Reference shear modulus	$1.8 \cdot 10^4$	$2.9 \cdot 10^4$
B_{ref}	MPa	Reference bulk modulus	$3.6 \cdot 10^4$	$6.6 \cdot 10^4$
k	m.s^{-2}	Permeability	$1.0 \cdot 10^{-8}$	
γ_{max}	%	Maximum shear strain	0.1	
d	-	Pressure dependency coefficient	0.5	
Φ'	(°)	Triaxial friction angle	34	60
Φ'_{pt}	(°)	Phase transformation angle	10	35
c_1, c_3	-	Contraction coefficients	0.08, 0.55	0.08, 0.55
d_1, d_3	-	Dilation coefficients	0.05, 0.05	0.05, 0.05
NYS	-	Number of yields surface	20	20
e_0	-	Initial void ratio	1.18 – 2.00	~ 0.80

Table 4-4. PIMY parameters for clay layers.

Parameter	Unit	Description	Values for clay layers
ρ	g.cm^{-3}	Density	1.67
G_{ref}	MPa	Reference shear modulus	$1.5 \cdot 10^5$
B_{ref}	MPa	Reference bulk modulus	$2.5 \cdot 10^5$
k	m.s^{-2}	Permeability	$1.0 \cdot 10^{-9}$
c	kPa	Cohesion	30
e_0	-	Initial void ratio	1.66

corresponding to glaciomarine sediments (Syvitski and Praeg, 1989; Praeg *et al.*, 1992; St-Onge *et al.*, 2008; Duchesne *et al.*, 2010). Its thickness varies regionally between 4 and 10 m. Unit 4 has been sampled in cores COR20-02-12GC, COR20-02-25GC and COR20-02-45GC. Their sedimentological analysis allows characterizing Unit 4 as an alternation of silt and coarser layers composed of fine sand to coarse sand. Its thickness varies between 5 and 20 m. The cores COR20-02-01GC/10GC/15GC sample the transition to Unit 5, corresponding to the change from a silty layer to a 1 m to 2 m thick layer composed of coarse sand.

In the Rimouski area (**Figure 4-3 d**), a rotating block structure is apparent, as evidenced by the angular discordance of the reflectors. The slip

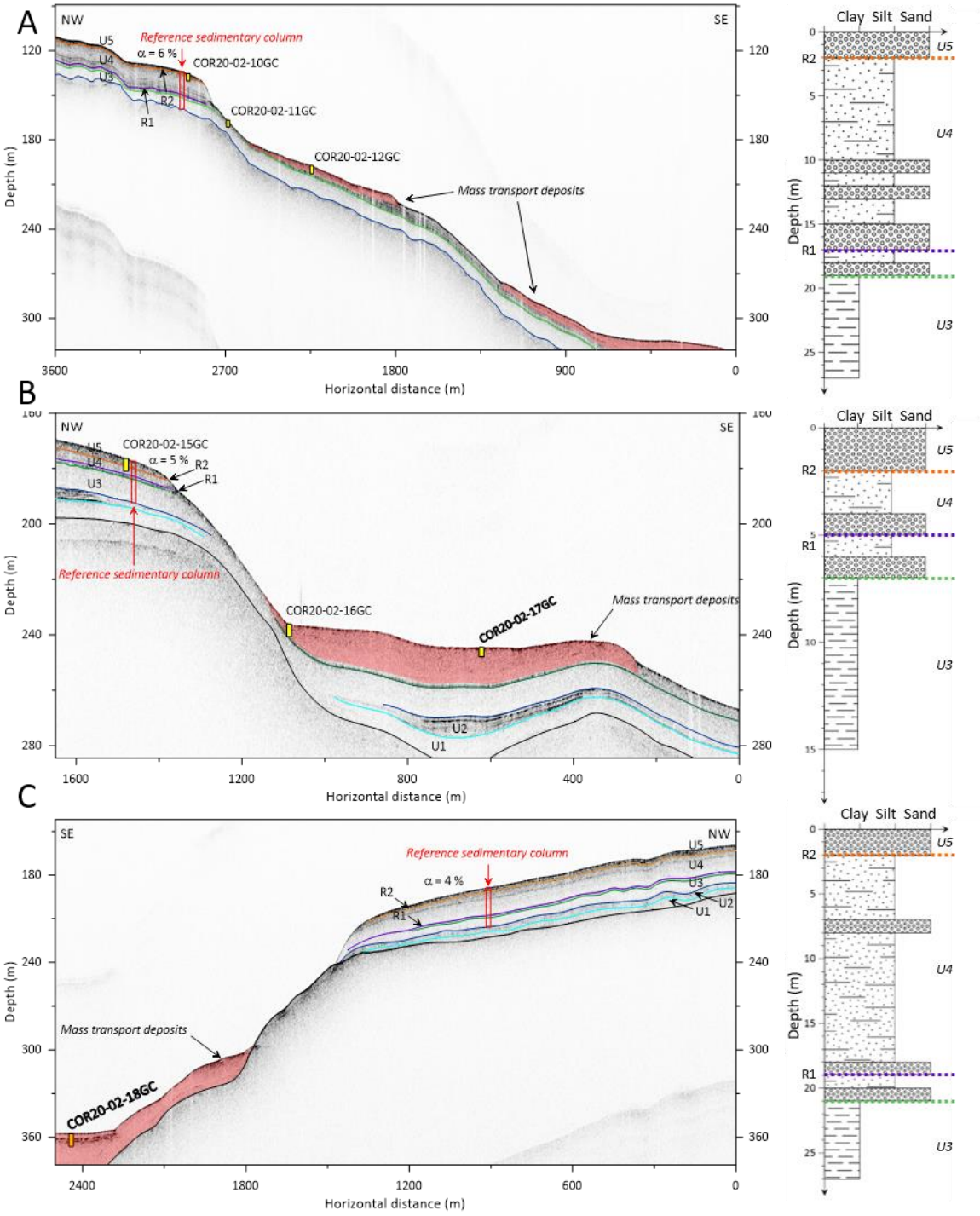

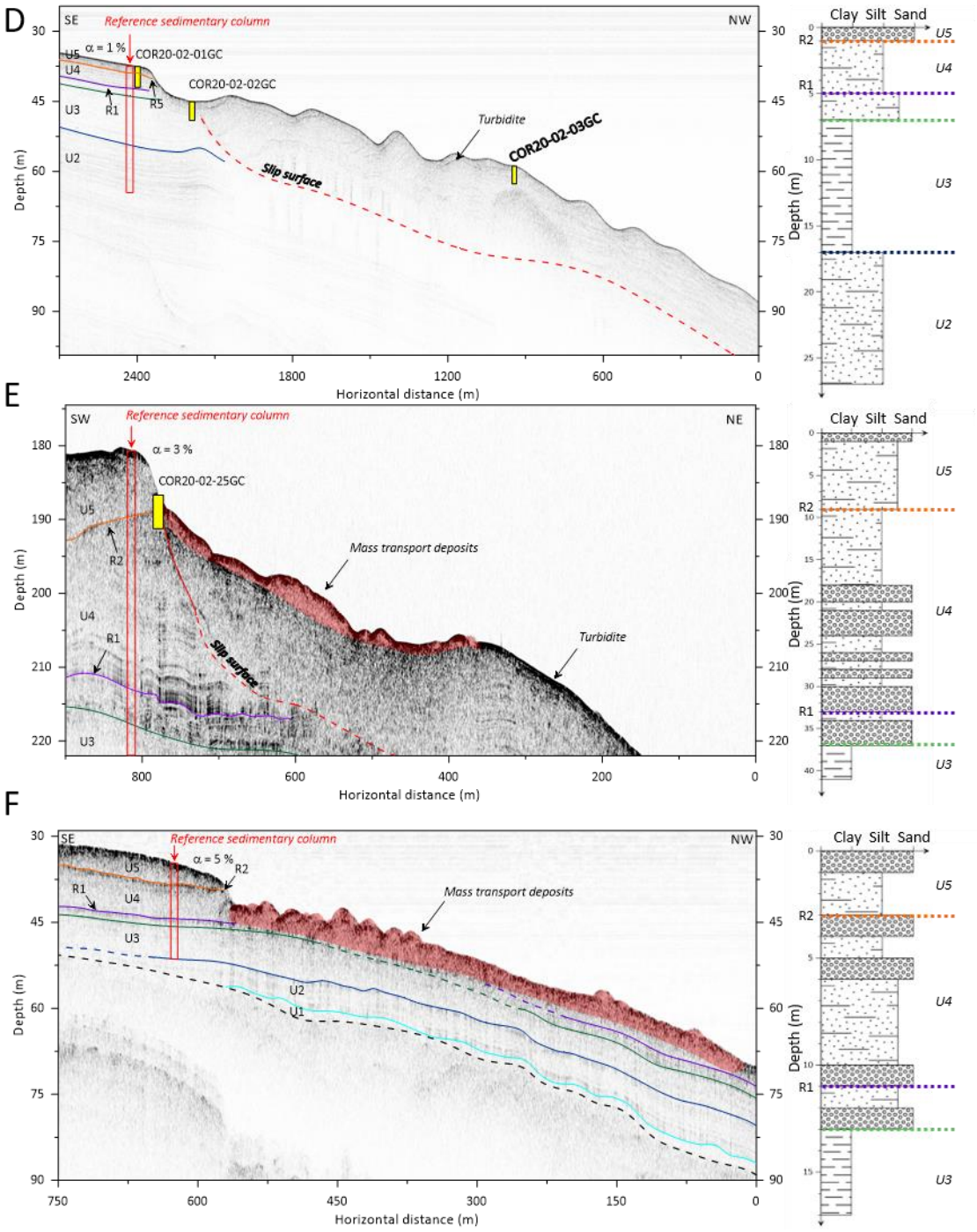

Figure 4-3. Seismic profiles acquired in the Baie-Comeau (A), Betsiamites (B and C), Rimouski (D), Tadoussac (E) and Charlevoix (F) areas (see **Figure 4-1** for the locations). Labels U1 to U5 refer to seismic units and R1 to R2 to seismic horizons described by Cauchon-Voyer *et al.* (2008) and the black line to the bedrock. The red squares correspond to the reference sedimentary columns considered in the liquefaction calculation and shown as lithostratigraphic logs to the right.

surface appears to be located about 20 m below the seafloor (mbsf) at the interface between the Units 2 and 3. A more recent event is identifiable within seismic Unit 4 at 2 mbsf and dated to 1663 CE (Mérindol *et al.*, 2022). Unit 2, which corresponds to the transition of ice-proximal and ice-distal context (Duchesne *et al.*, 2010), could not be sampled during SLIDE2020. However, the silt core 33PC, analyzed by St-Onge *et al.* (2008) provides

the sedimentological parameters necessary for the numerical simulation of the Rimouski area.

In the Tadoussac area, a recent MTD is identified at the seafloor with a rupture surface that appears to be located at the interface between U4 and U5 at about 7 mbsf (**Figure 4-3 e**). Deeper, a larger slip surface is identified at the base of Unit 4, characterized by an alternation of strong and weak reflectors (**Figure 4-3 e**).

The location of most landslide basal surfaces in Unit 4 suggests that sediment stratification has influenced the initiation of earthquake-triggered submarine landslides. Furthermore, the superposition of events as shown in **Figure 4-3 e**, suggests that slope failures might have developed over different layers. These hypotheses are presented, tested and discussed below.

4.2. Cyclic triaxial tests and liquefaction potential

Sixteen undrained triaxial tests were carried out on sediment samples from SLIDE-2020 (**Table 4-5**). For each cyclic test, the results are plotted in terms of: (a) the evolution of the normalized mean effective stress (p'/p'_0) with the CRR; (b) the shear strain (γ) with the CRR; (c) the normalized excess pore pressure (r_u) as a function of the number of cycles N; and (d) the evolution of shear strain as a function of the cycles N (**Figure 4-5**). Exhaustive results are presented in supplementary data. For triaxial conditions, the mean effective stress is expressed as:

$$p' = \sigma'_3 + \frac{q}{3} \qquad (10)$$

and is normalized by the initial mean effective stress ($p'_0 = \sigma'_3$), i.e., after the consolidation phase.

Figure 4-5 shows the results of the cyclic triaxial test carried out on a silty sample taken at 4.47-4.57 m depth on core COR20-02-12GC (**Figure 4-4**). Cyclic loading generates a rapid increase in pore pressure until r_u reaches 0.95 after 15 cycles (**Figure 4-5 c**). The associated shear strain increases to 3% after 8 cycles and reaches 6%, the considered liquefaction criterion, after 31 cycles (**Figure 4-5 d**). The effective stress path in terms of *CRR* shows loops with maximum and minimum *CRR* values of 0.35 and 0.43 (**Figure 4-5**). After the first cycle, the normalized mean effective stress is equal to 0.95; it decreases to 0.67 after the 5th cycle and to 0.50 after the 10th cycle (**Figure 4-5 a**). The

Table 4-5. Results from the cyclic triaxial tests carried out on samples from SLIDE-2020 cores.

Core name	Depths (m)	Lithology	σ'_3 (kPa)	$\Delta q/\sigma'_3$
COR20-02-01GC	2.69 – 2.79	Silt	50	0.40
COR20-02-02GC	3.75 – 3.85	Silt	50	0.42
COR20-02-05GC	2.41 – 2.51	Silt	50	0.46
COR20-02-05GC	2.53 – 2.63	Silt	50	0.41
COR20-02-06GC	1.61 – 1.71	Silt	50	0.45
COR20-02-11GC	3.99 – 4.09	Clay	50	*no liquefaction*
COR20-02-12GC	4.35 – 4.45	Silt	50	0.37
COR20-02-12GC	4.47 – 4.57	Silt	50	0.39
COR20-02-12GC	4.59 – 4.69	Silt	50	0.48
COR20-02-16GC	3.75 – 3.85	Silt	50	0.36
COR20-02-16GC	3.87 – 3.97	Silt	50	0.43
COR20-02-16GC	3.99 – 4.09	Silt	50	0.39
COR20-02-25GC	1.81 – 1.91	Silt	50	0.46
COR20-02-25GC	1.95 – 2.05	Silt	50	0.42
COR20-02-45GC	2.13 – 2.23	Sand	50	0.48
COR20-02-45GC	2.25 – 2.35	Sand	50	0.40

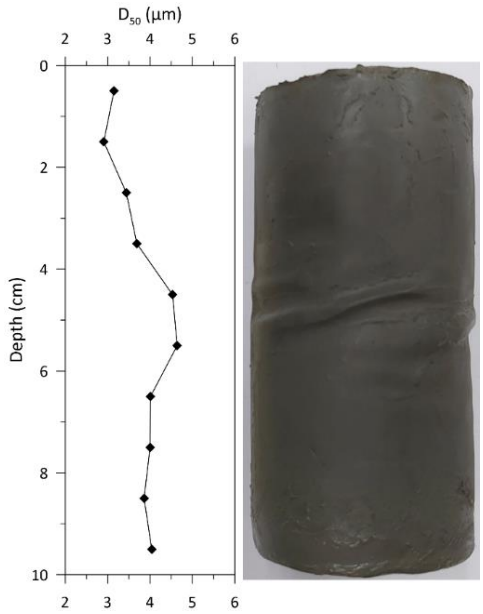

Figure 4-4. Grain size profile (D_{50}) and photograph of the cyclically sheared sample (core COR20-02-12GC at a depth of 4.47-4.57 m). The highest observed strain corresponds to a localized liquefaction of the silty layer.

loops tighten until they reach the critical state line around p'/p'_0 = 0.39. The angle of the critical state line corresponds to an internal friction angle φ' = 34°. A phase transformation angle, φ_{PT}, of about 10° is obtained from the slope of the dividing line between the contraction and dilation behavior. The *CRR* versus γ plot (**Figure 4-5 b**) exhibits a progressive asymmetric trend with higher values in extension than in compression. In addition, the shear strain path shows loops which gradually move towards a *CRR* of zero. Indeed, the first loop shows a mean CRR of 0.39 and 0.20 after 50 cycles.

The analysis of cyclic triaxial test results allowed us to characterize the liquefaction potential for different sediment layers of the St. Lawrence

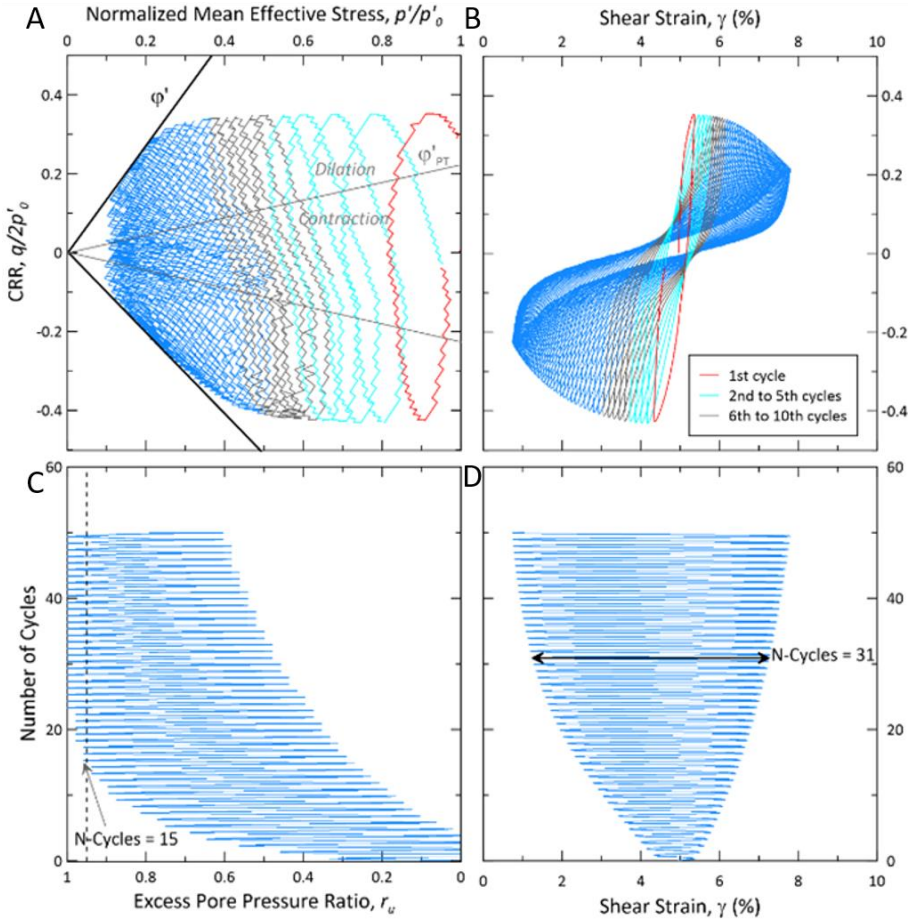

Figure 4-5. Results from cyclic triaxial test carried on core COR20-02-12GC at depth of 4.47 – 4.57 m. A) shows the effective stress path followed during the test in terms of CRR and normalized mean effective stress. B) shows the CRR versus the shear strain with stress path. The strain path corresponds to loops that gradually move towards the zero CRR. C) depicts a trend with a number of cycles of cyclically induced pore pressure, normalized to σ'_3. r_u > 0.95 after 15 cycles. D) shear strain response to cyclic loading. It reaches 6% double amplitude after 31 cycles.

Estuary. Only one test does not reach the liquefaction criteria (γ = 6 %), that is the test carried out on the clay sample (D_{50} ~ 1.8 µm) from the glaciomarine sediment of seismic Unit 3. However, for the 15 tests performed on the more recent and coarser-grained sediments corresponding to seismic Units 4 and 5, liquefaction is systematically reached by considering the cumulative strain criteria, i.e., γ = 6%. The potential of liquefaction determined through the number of cycles required to liquefy as a function of the CRR imposed during the tests shows one single trend (**Figure 4-6**) with ± 0.04 standard deviation. It can nevertheless be noted that the two tests carried out on core COR20-02-45GC (D_{50} ~ 55.4 µm) sampling the stratified sand layers at the base of seismic Unit 4, show a higher CRR-N slope (green curve in **Figure 4-6**) than the more superficial tests (D_{50} ~ 4 - 8 µm, e.g. **Figure 4-4**). For the test program, the CRR ranged from 0.35 to 0.48 and the numbers of cycles required to reach liquefaction were between 4 and 54 cycles.

4.3. Working hypothesis: slope failure development

Based on the interpretation of seismic profiles, two hypotheses are proposed to explain the development of slope failure in the St. Lawrence Estuary (**Figure 4-7**). These hypotheses will be used to test different scenarios for epicenter refinement. The first called “deep-slip surface” (below 7.5 m depth), is focussed at the interface between seismic Units 3 and 4 for each study area, except for the Rimouski area. This corresponds to the transition between a glaciomarine environment and a postglacial environment associated with a sedimentological contrast between clay and sand facies. At Rimouski, this hypothesis is applied to the interface between Units 2 and 3.

The second hypothesis called “superficial slip surface” (above 7.5 m depth), may explain thin submarine landslide flows that drape MTDs. In this hypothesis, we consider liquefaction to occur at the top of Unit 4 until the modern sediment of Unit 5 (**Figure 4-7**). At this shallow depth, no major scars

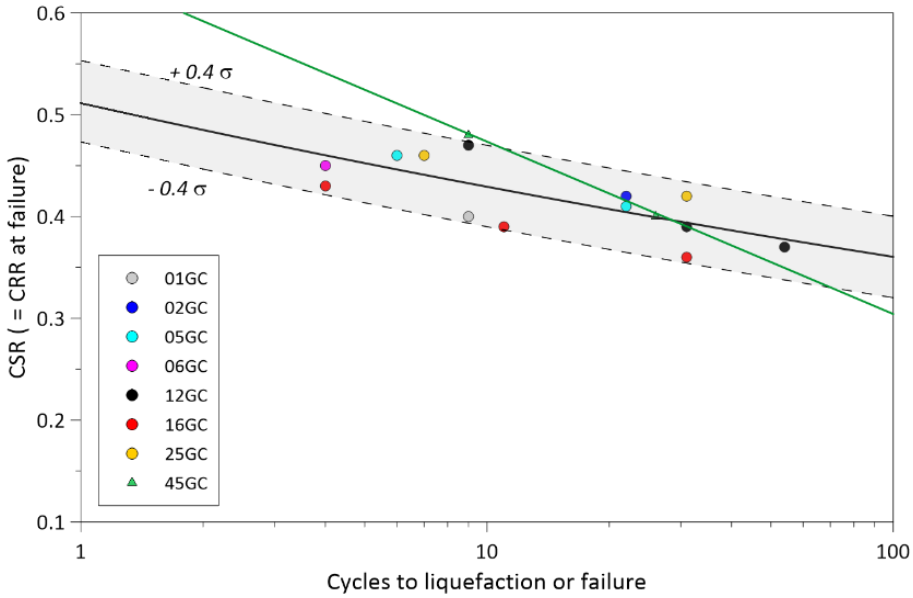

Figure 4-6. CRR versus number of cycles to liquefaction obtained from undrained triaxial cyclic tests on 15 samples from the St. Lawrence Estuary. The black line shows the global trend with CRR min and max values of ± 0.04 σ. The green line shows the trend of the two tests carried out on core COR20-02-45GC which sample the base of seismic Unit 4.

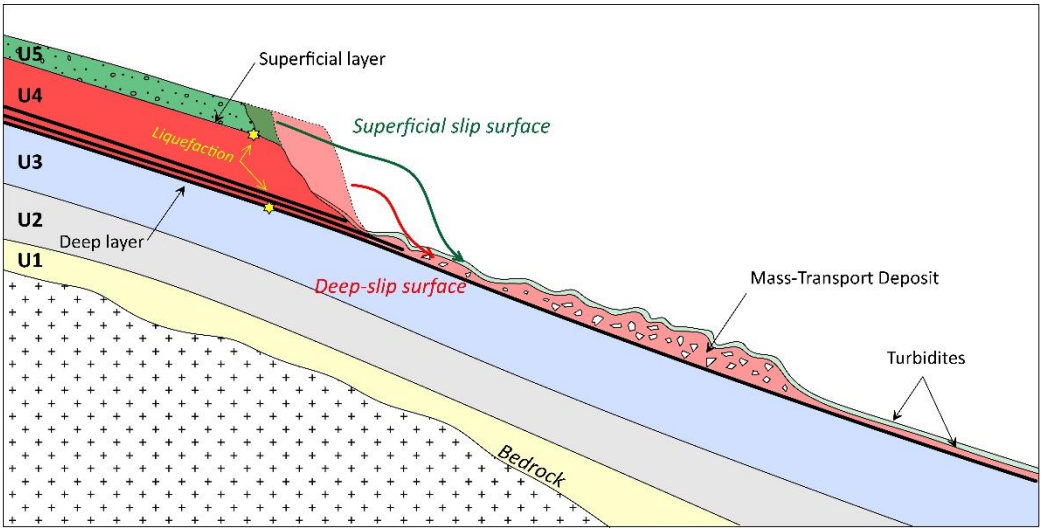

Figure 4-7. Slope failure and liquefaction hypotheses established from the interpretation of seismic profiles and the dating of submarine landslides. The "superficial slip surface" hypothesis (green) considers liquefaction of the superficial layer at the interface between seismic Units 4 and 5. This hypothesis explains the presence of debris flow deposits and turbidite that overlie old mass-transport deposits. The "deep-slip surface" hypothesis (red) considers that liquefaction at the interface between seismic Units 3 and 4 would be at the origin of major landslides.

of submarine landslide are identified. However, this does not exclude the possibility of generating a flow of liquefied sand that could explain the thin turbidite surface layers described and dated by Mérindol *et al.* (2022).

4.4. Determination of the source-to-site distance through the ENUSC method

The source-to-site distance, i.e., the distance between epicenter and the MTC, is evaluated in this section through the previously described ENUSC method (Seed *et al.*, 2001). It was conducted for each study area at the level of the layers where the failure surface of submarine landslides appears to have been be triggered according to our working hypothesis (**Figure 4-8**). In this method, the effective vertical stress is derived from the bulk density profiles (equation 1). In **Figure 4-8**, the bulk density measured by the MSCL and interpolated is plotted against depth. The interpolation is based on the lithostratigraphic logs interpreted from seismic profiles (**Figure 4-3**). The PGA required to destabilize the layers identified in the working hypotheses, is determined when the FoS is equal to 1, as shown in **Figure 4-8**. The source-to-site distances required to reach the PGA sufficient to liquefy for the two working hypotheses are synthetized in **Figure 4-6**. In this calculation, we considered the mean PGA calculated using equation (4) and two other additional cases that consider standard deviations of + 0.5 σ and 1.0 σ.

The PGA required to liquefy the superficial layers in Baie-Comeau and Betsiamites is between 0.220 g and 0.225 g. The calculated PGA for Rimouski is slightly lower than 0.185 g while for Tadoussac and Charlevoix they are the highest with a value of 0.250 g. Liquefaction of deeper layers is reached for higher PGA. Indeed, the PGA ranges between 0.230 g and 0.260 g for the Baie-Comeau, Betsiamites and Rimouski areas, between 0.260 g and 0.322 g for the Tadoussac zone and 0.275 g for the Charlevoix site (**Table 4-6**).

The equivalent distances required to destabilize the studied sites are between 26 and 38 km

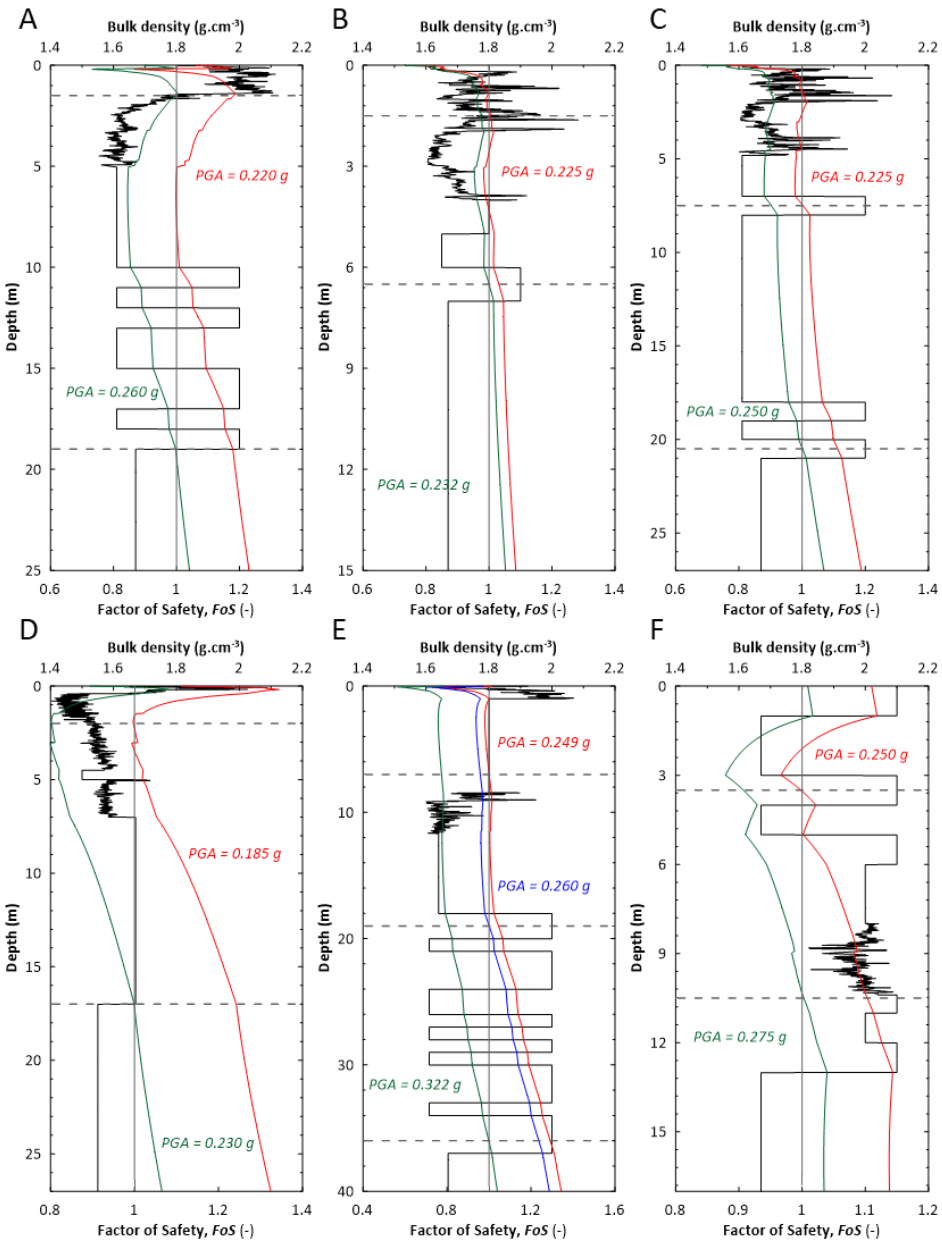

Figure 4-8. Evolution of the bulk density measured and interpolated as a function of depth (black curve) for the areas of Baie-Comeau (A), Betsiamites (B and C), Rimouski (D), Tadoussac (E) and Charlevoix (F). The interpolation is based on the lithostratigraphic logs presented in **Figure 4-3**. The depths of the layers where liquefaction potentially occurred are shown by gray dashed lines. The evolution of calculated FoS for different peak ground acceleration (PGA) is shown by the red, green and blue curves.

considering the mean PGA and between 41 and 57 km when considering the + 0.5 σ error in PGA. In both cases, the source-to-site distances calculated are largely lower than those to the historical reference location of the EQ1663 epicenter, except for the Charlevoix site. By considering the mean PGA and an error of + 0.5 σ the calculations converge to two distinct areas. One is located northeast of the CKSZ and one between Rimouski and Betsiamites areas. However, with a larger error of + 1.0 σ, all calculations predict one single region located around the mouth of the Saguenay Fjord and centred on Tadoussac. The FoS calculation on deep and superficial layers gives the same results.

Table 4-6. Summary of the distances required to liquefy sediment in the six distinct study areas from the ENUSC method compared to the historical reference location of the EQ1663.

Area	Depths (m)	PGA to liquefy (g)	Distance to historical epicenter	Distance PGA_{mean} (km)	Distance $PGA_{+0.5\sigma}$ (km)	Distance $PGA_{+1\sigma}$ (km)
Baie-Comeau	1.5	0.220	210	34	51	184
	19.0	0.260		31	46	155
Betsiamites (1)	1.5	0.225	185	34	51	180
	6.5	0.232		33	50	175
Betsiamites (2)	7.5	0.225	175	34	51	180
	20.5	0.250		31	48	162
Rimouski	2.0	0.185	160	38	57	215
	17.0	0.230		32	50	174
Tadoussac	7.5	0.249	75	31	48	162
	19.0	0.260		31	46	155
	36.0	0.322		26	41	112
Charlevoix	3.5	0.250	17	31	48	162
	10.5	0.275		29	45	145

4.5. Source-to-site distance using OpenSees

Complementary to source-to-site distance determination through the ENUSC method, numerical simulations were conducted with OpenSees. Because this analysis considers the sediment behavior through the PDMY02 and PIMY constitutive soil models, the results should be more realistic than the ENUSC method. The models require a set of input parameters determined from laboratory testing and calibration in OpenSees.

4.5.1. Determination of model parameters

This part of the study describes how the parameters of PDMY02 and PIMY models listed in **Table 4-3** and **Table 4-4** were determined. Their determination is based on both laboratory results and trial-and-error calibration.

The coefficient of permeability (k) is measured by falling head tests. Density (ρ) is the average value measured by the MSCL. The shear velocity V_s is measured during the cyclic triaxial test and is directly related to the shear modulus G_{ref} by:

$$G_{ref} = \rho V_s^2 \qquad (11)$$

The bulk modulus B_{ref} is derived from the compressional wave velocity Vp measured during the triaxial test, after the consolation phase:

$$V_p = \sqrt{\frac{B_{ref} + \frac{4}{3}G}{\rho}} \qquad (12)$$

The mean effective confining pressure reference, noted p_{ref}, corresponds to the confining pressure during the cyclic triaxial test. The Phase Transformation angle (φ_{PT}) expressed in degrees was determined graphically from cyclic triaxial test results (**Figure 4-5**). The friction angle (φ') was derived from the critical state line determined from consolidated undrained triaxial tests carried out on cores listed in **Table 4-5**. For each geotechnical specimen, water content measurements were made to calculate the initial void ratio (e_0). Finally, default values were assigned for maximum shear strain (γ_{max}), pressure dependency coefficient (d) and yield surface number (NYS) (Yang *et al.*, 2003). To understand how each parameter controls the simulated mechanical behavior, a sensitivity analysis of the PDMY02 model was performed and is presented in supplementary data.

The PIMY model requires five parameters which are ρ, G_{ref}, B_{ref}, k and the cohesion (c) listed in **Table 4-4**. These parameters were determined by the same methods as for the PDMY02 model, with the exception of the cohesion, which was determined by the hand shear vane test performed on split core sections.

4.5.2. Calibration of model parameters

The numerical analyses presented in this section aimed to calibrate and validate the response of the theoretical models based on test results. The calibration procedure was carried out with emphasis on reproducing the observed cycle-by-cycle accumulation of shear strain and pore pressure. Thus, two sets of test results were considered. The first one concerned silty layers while the second one concerned sand layers. The calibration of model parameters for the silt layers was carried out against the results of 13 cyclic triaxial tests. It is illustrated in **Figure 4-9 a** with the results obtained for a sampled taken in between 4.47 m and 4.57 m on core COR20-02-12GC. The calibration for the sand layers was performed using the sample taken in between 2.13 and 2.23 m on core COR20-02-45GC (**Figure 4-9 b**).

The set of parameters for the PDMY02 model was adjusted by a trial-and-error method until the theoretical results correctly reproduced tests results. The results presented in **Figure 4-9 a'** and **b'**

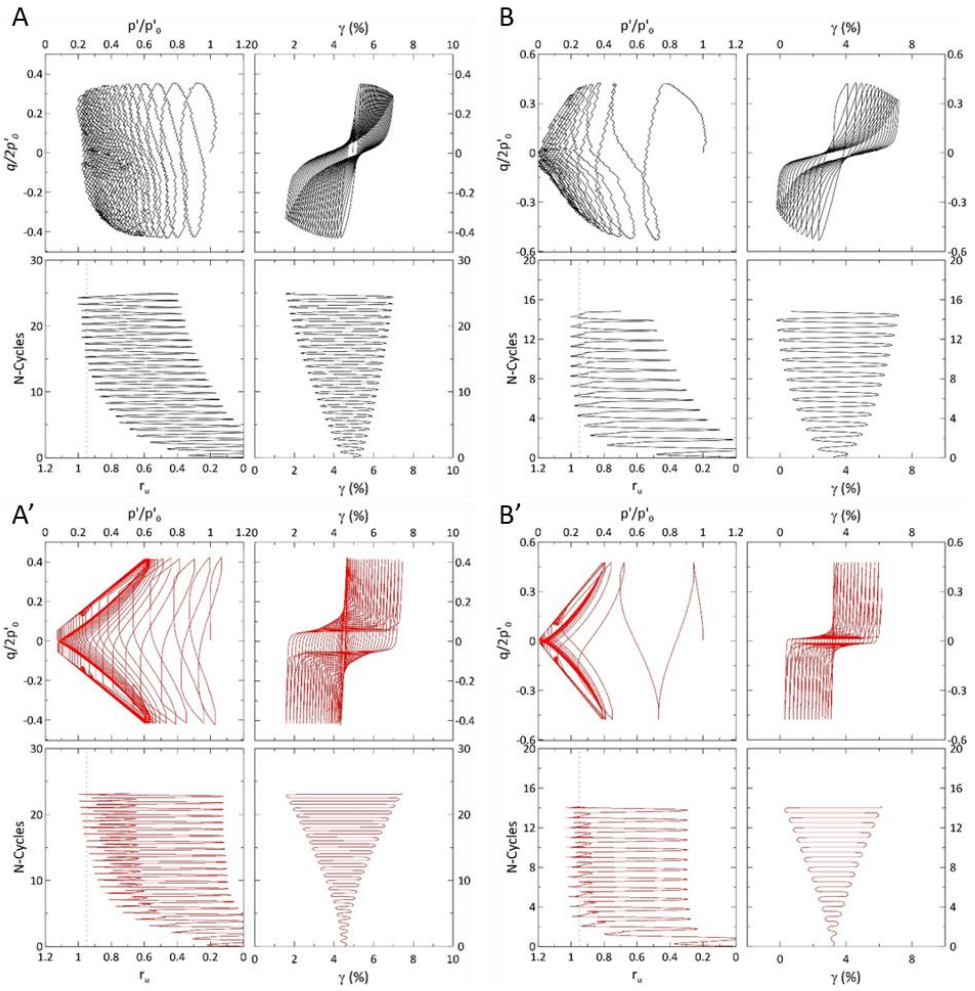

Figure 4-9. Calibration of model parameters for core COR20-02-12GC at 4.47 – 4.57 m (A) and COR20-02-45GC at 2.13 – 2.23 m (B). Experimental data in black and modeling results in red.

correspond to a calibrated set of parameters, which most closely reproduces the behavior observed during cyclic triaxial tests. For both specimens, the PDMY02 model adequately reproduced the measured pore pressure fluctuations. The shear strain curves are also reliably calculated, although the increase in shear strain is linear compared to the laboratory tests. The numerical simulation shows symmetric hysteresis loops while the experimental results show asymmetric hysteresis loops (e.g., COR20-02-12GC **Figure 4-9 a** and **a'**). This is due to the model, which considers plane deformation in compression and extension (e.g., Banarjee *et al.*, 2021). Lastly, for the COR20-02-12 specimen, the effective stress path is not correctly reproduced by the PDMY02 model. However, the spacing between the loops is correctly simulated as the angle of the critical state line. In contrast, the effective stress path for the COR20-02-45GC specimen is better reproduced (**Figure 4-9 b** and **b'**). After this calibration, the parameters c_1 and c_3 which control the contraction phases, and the parameters d_1 and d_3 which control the dilation phases, were determined as listed in **Table 4-3**.

4.5.3. Liquefaction prediction using OpenSees

In contrast to the ENUSC method, the numerical simulations with OpenSees does not provide FoS values. The occurrence of liquefaction is determined using the evolution with time of the normalized excess pore pressure (r_u), the first stress component (σ'_i) and the displacement along the slope (Δz). The liquefaction is reached for σ'_i equal to 0 kPa (**Figure 4-10**). The two other parameters corroborate this criterion: the increase in r_u reaching 1 with a displacement exceeding several meters (**Figure 4-10**). The numerical simulation for the Baie-Comeau area presented in **Figure 4-10** shows that liquefaction occurs at ~1.5 m depth and at the base of Unit 4 at 19 m depth when the PGA is equal

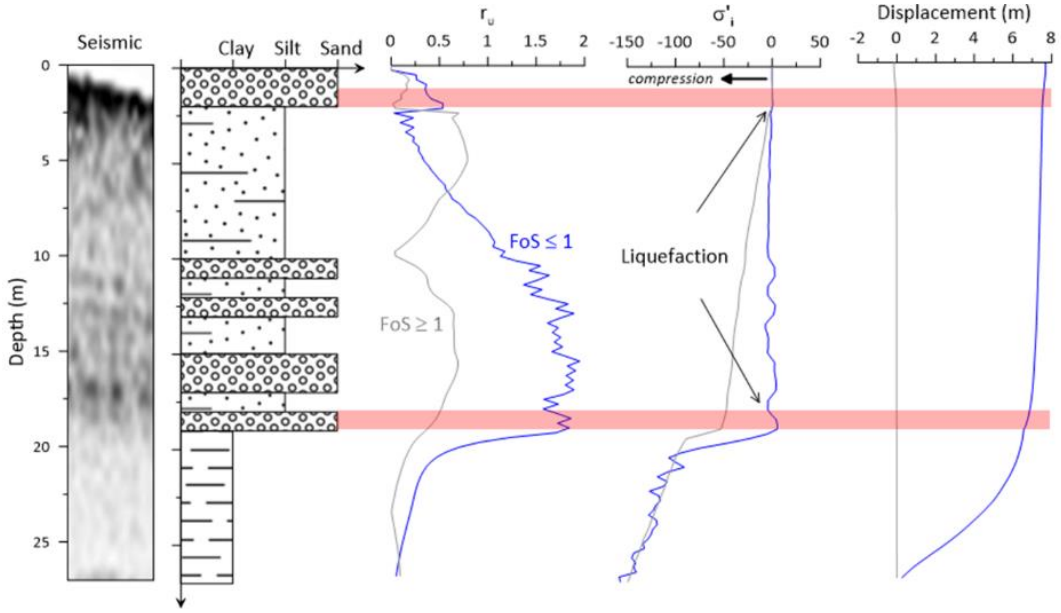

Figure 4-10. Results of OpenSees calculations carried out on the reference sedimentary column at the Baie-Comeau area (seismic and log lithostratigraphique) for a PGA of 0.270 g (blue curves, FoS ≤ 1) and for PGA < 0.270 g (gray curves, FoS ≥ 1). The profiles of normalized excess pore pressure, r_u, and effective stress, σ'_i, show maximum values at depths of 1.5 m and 19 m. The displacement induced by the earthquake is around 7 m for the layers above 19 m suggesting a slope failure at 19 m depth.

to 0.270 g (M 7 at epicenter distance between 30 and 150 km). Based on the slope of the displacement curve, failure can be expected to occur at about 19 m depth. Below 0.270 g, the displacement is close to zero and the pore pressure in the sand layers does not increase (gray curves in **Figure 4-10**). Only the layer at 1.5 m depth is susceptible to liquefy with σ'_i values around 0 kPa. The clay layer at the base of the reference sedimentary column shows low pore pressure and in consequence a low σ'_i signifying that the clay layer does not liquefy (**Figure 4-10**).

The PGA calculated with this method are relatively close to those obtained with the ENUSC method for the Baie-Comeau, Betsiamites and Charlevoix areas. The source-to-site distances calculated for each area and for the two working hypotheses with the OpenSees method are synthesized in **Table 4-7**. These calculated distances are mostly lower than the distance to the historical reference location of the EQ1663 epicenter and the distances calculated with the ENUSC method. The largest PGA of 0.762 g calculated for the Tadoussac area with the different working hypotheses suggests a source-to-site distance ranging from 14 km to 37 km. The fact that a low PGA is required to liquefy the superficial layers in Baie-Comeau, Betsiamites (1) and Charlevoix areas suggest a high liquefaction potential in these areas.

5. DISCUSSION

5.1. Predicted liquefaction compared to observed earthquake-triggered submarine landslides

Based on the dating of submarine landslides triggered by the 1663 CE earthquake, the liquefaction potential of six zones was calculated both by ENUSC and OpenSees methods. Two working hypotheses were tested, corresponding to the destabilization caused by the liquefaction of a deep layer ("deep-slip surface") and of a superficial layer ("superficial slip surface") as presented in **Figure 4-7**. The EQ1663 was chosen to test these hypotheses because it is the strongest historical seismic event in Eastern Canada with an estimated magnitude of M7 (Locat *et al.*, 2003; Ebel, 2011;

Table 4-7. Summary of the distances required to liquefy sediment in the six distinct study areas from the numerical simulation method compared to the initial location of the 1663 CE epicenter.

Area	Depths (m)	PGA to liquefy (g)	Distance to actual epicenter	Distance PGA_{mean} (km)	Distance $PGA_{+0.5\sigma}$ (km)	Distance $PGA_{+1\sigma}$ (km)
Baie-Comeau	1.5	0.072	210	134	258	384
	19.0	0.270		30	46	149
Betsiamites (1)	1.5	0.084	185	85	231	356
	6.5	0.252		31	48	161
Betsiamites (2)	7.5	0.360	175	25	38	58
	20.5	0.600		17	28	43
Rimouski	2.0	0.420	160	22	35	47
	17.0	0.720		15	25	39
Tadoussac	7.5	0.762	75	14	24	37
	19.0	0.762		14	24	37
	36.0	0.762		14	24	37
Charlevoix	3.5	0.084	17	80	230	356
	10.5	0.216		34	52	187

Lamontagne *et al.*, 2018) and because it triggered several submarine landslides in the St. Lawrence Estuary (Mérindol *et al.*, 2022).

Numerical simulations reveal that liquefaction and the resulting slip surface occurred at the base of Unit 4 and at its boundary with Unit 3. These results agree with the observed localized submarine slope failures within the stratified Unit 4 (Cauchon-Voyer *et al.*, 2008).

Furthermore, the numerical results reveal that modern sediments at the top of the sedimentary sequence, corresponding to coarse sands to silts, are highly susceptible to liquefaction and destabilization. This could explain the presence of earthquake-triggered submarine landslides subsequent to EQ1663 (Cauchon-Voyer *et al.*, 2008; Pinet *et al.*, 2015; Mérindol *et al.*, 2022) and would support the hypotheses presented in **Figure 4-7**.

Seismic Unit 3 presents a regular thickness and the submarine landslides appear to have moved over it (e.g., **Figure 4-3 a – b**). Thus, it was assumed that it was non-sensitive to earthquakes. Laboratory tests confirmed that Unit 3 is composed of non-liquefiable clay. The sedimentological contrast with Unit 4, composed at its base of highly liquefiable coarse sand, could thus act as a preconditioning factor for submarine landslides in the St. Lawrence Estuary.

5.2. Comparison between ENUSC and OpenSees methods

Estimates of source-to-site distances were obtained by two iterative approaches for the six studied MTCs. The ENUSC method is based on the liquefaction curve obtained from cyclic triaxial tests (**Figure 4-6**) and the FoS calculation formulated by Seed *et al.* (2001) (**Figure 4-8**). The OpenSees method relies on numerical simulations of the behavior of the sedimentary column in response to an earthquake. The former method is considered more realistic because it uses constitutive soil models calibrated against experimental data (**Figure 4-10**). However, the same GMPE for CENA is used in both methods to determine critical PGA values. **Figure 4-11** and **Figure 4-12** show the calculated areas of the EQ1663 epicenter as respectively determined by the ENUSC and OpenSees methods.

Considering mean PGA values, the ENUSC method predicts an epicenter 50 km northeast of the historical reference epicenter in an area between Rimouski and Betsiamites zones for both working hypotheses. With a statistical error of + 0.5 σ in PGA, the same two epicenter regions are predicted but with a larger radius. Lastly, considering a larger PGA error of + 1 σ, all circles are confounded and reveal a single area. For the "superficial slip surface" hypothesis, this area is an ellipsoid of ~150 km x 300 km located 50 km from the historical reference epicenter. Its center is 30 km northeast of the Tadoussac site. In the case of the "deep-slip surface" hypothesis, the possible area of the EQ1663 epicenter is also an ellipsoid, of ~170 km x 250 km whose center is located on the Tadoussac site (**Figure 4-11**).

Considering mean PGAs and the "superficial slip surface" hypothesis, the OpenSees method predicts two areas similar to those determined with the previous method (**Figure 4-12**). One area is located around the Tadoussac site, 70 km from the historical reference epicenter. However, considering the "deep-slip surface" hypotheses, the

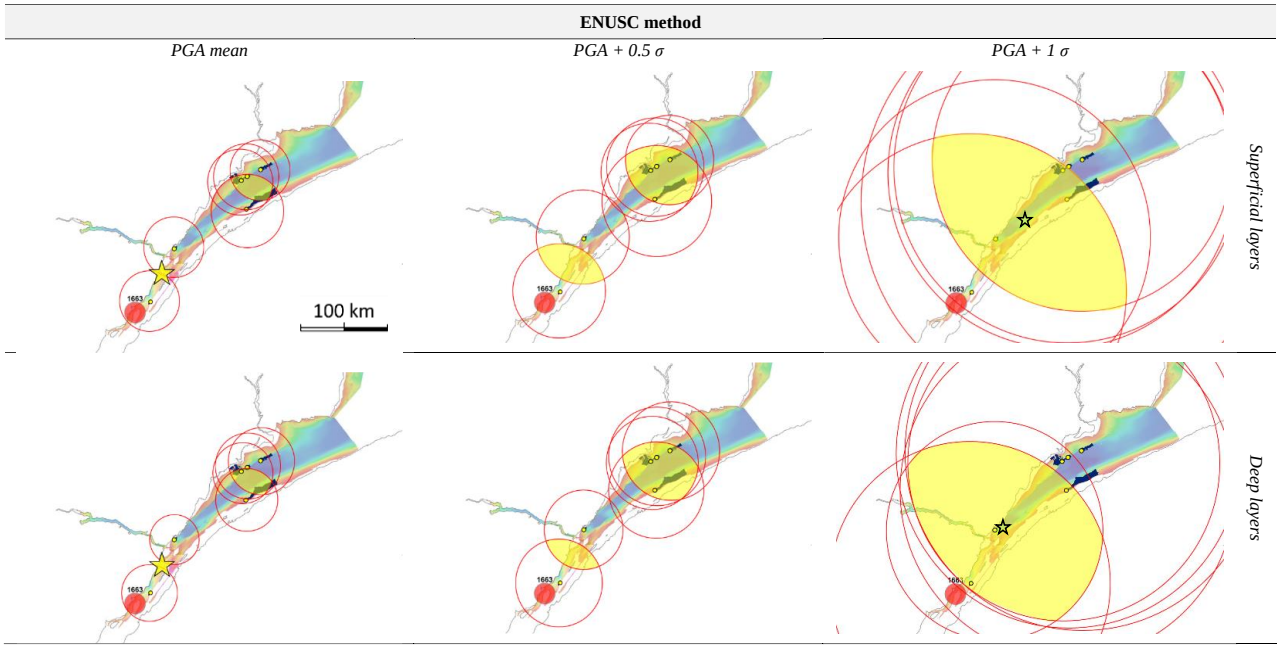

Figure 4-11. Determination of the possible epicentral region of the 1663 CE earthquake from the ENUSC method considering + 0.5 σ and + 1.0 σ statistical errors of GMPE for CENA and both working hypotheses (**Figure 4-7**). The yellow areas or the yellow stars show the convergence zone(s). The stars indicate the center of the ellipsoids.

circles intersect at a single point near the Rimouski zone, ~195 km to the northeast. Numerical simulation using a PGA with an error of + 0.5 σ shows two distinct large areas for both working hypotheses. Finally, for both hypotheses, the circles intersect at a single point considering a PGA with an error of + 1 σ. This point is located ~130 km northeast of the historical reference epicenter and ~ 30 km from the Tadoussac site (**Figure 4-12**).

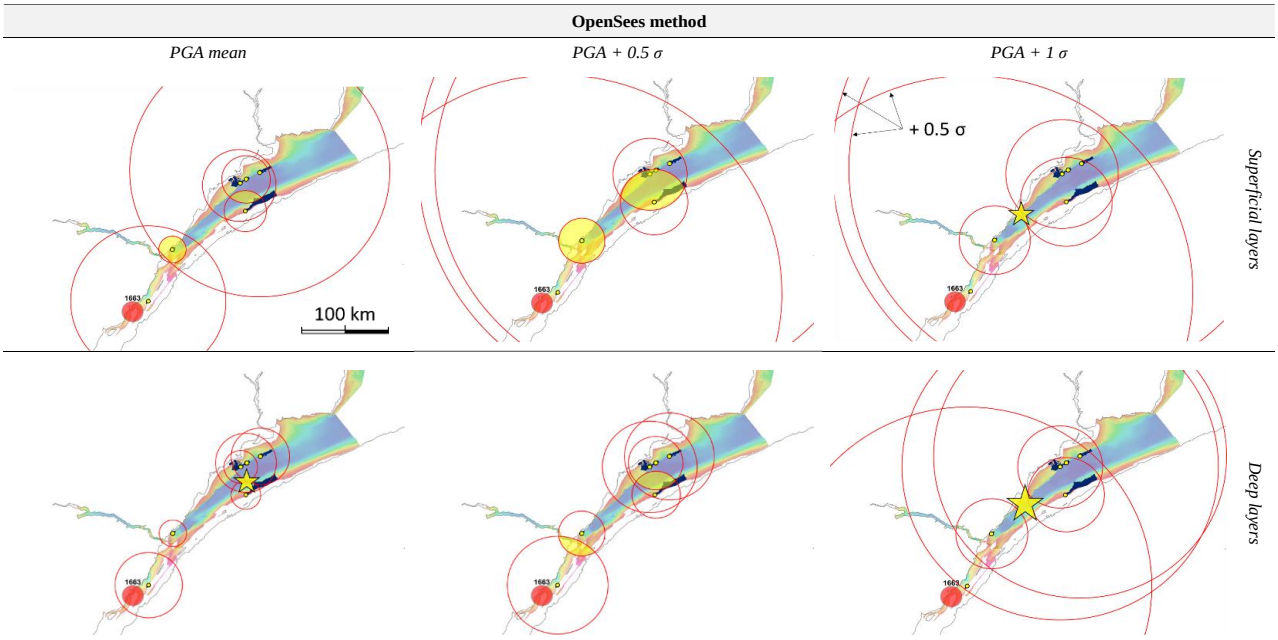

Figure 4-12. Determination of the possible epicentral region of the 1663 CE earthquake from the OpenSees method considering + 0.5 σ and + 1.0 σ statistical errors of GMPE for CENA and both testing hypotheses (**Figure 4-7**). The areas or the yellow stars show the convergence zone(s).

Considering of mean PGA and a + 0.5 σ statistical error does not allow to identify a single point or area of intersection of the circles. However, with a statistical error of + 1 σ, the ENUSC method indicates one large area for the possible epicenter location and the OpenSees method predicts one single point included in this area. Thus, the OpenSees method seems to be more accurate than the ENUSC method, but their very similar predictions reinforce the accuracy of the estimated epicenter location. The use of a statistical error of + 1 σ is still realistic, as shown in **Figure 4-2**, where the PGA measurements of historical earthquakes are distributed between ± 1 σ curves. Furthermore, based on the analysis of crustal deformation in eastern Canada, Mazzoti *et al.* (2005) suggest that the magnitude of the EQ1663 may have reached M7.8 ± 0.6, supporting the use of an error of + 1 σ in PGA.

5.3. The 1663 epicenter location

The investigation of the PGA required to induce liquefaction of coarse-grained sediments in the six studied areas shows that the historical reference epicenter of EQ1663 is not compatible with the synchronous triggering of six submarine landslides (**Figure 4-11** and **Figure 4-12**). The determination of the source-to-site distances allows to propose two new areas for this epicenter (**Figure 4-13**). The first one located between Rimouski and Betsiamites, is called “northeast - NE” zone. The second called “southwest - SW” zone, is located around the mouth of Saguenay Fjord and the Tadoussac site. Their extents are established from the compilation of the areas presented in **Figure 4-11** and **Figure 4-12**, i.e., where the prediction densities are the highest. The SW and NE zones here proposed are respectively ~ 50 km and ~ 250 km northeast of the historical reference epicenter of EQ1663 in Charlevoix.

The SW zone is the only one to satisfy the conditions to trigger slope failures in the six studied zones. Indeed, both the OpenSees and ENUSC methods predict the location of the epicenter in this zone. Recent seismic and multibeam bathymetry investigations reported by Normandeau *et al.* (2015) and Pinet *et al.* (2021) reveal a major, possibly recently active, faults in the SW zone (**Figure 4-13**), close to the site of Tadoussac. The predicted epicenter is only about 30 km from this active fault (**Figure 4-13**). This could explain why the calculated source-to-site distance for the Tadoussac site is shorter, i.e., the PGA required to destabilize are the strongest. The proximity of this fault could have produced steady ground movements and liquefaction in the sedimentary column. By inducing pore water drainage and thus causing sediment densification (e.g., Obermeier, 1996), non-failure earthquakes could have increased the resistance of sediments explaining the calculated high PGA. In addition, the SW zone is close to the CKSZ, the region where the major historical earthquakes of the last few hundreds of years are concentrated (Lamontagne *et al.*, 2018). Lastly, the SW zone is consistent with the lacustrine study of Locat *et al.* (2016), which proposes a large zone for the EQ1663 epicenter, northeast or north of Charlevoix.

The NE zone is included in the LSLZ, but compared to the CKSZ, the seismicity is generally considered as low (e.g., Pinet *et al.*, 2021). Indeed, the highest documented magnitude for 400 years in the LSLZ is M4.5 while in CKSZ, several events around M6 have been reported (Lamontagne *et al.*,

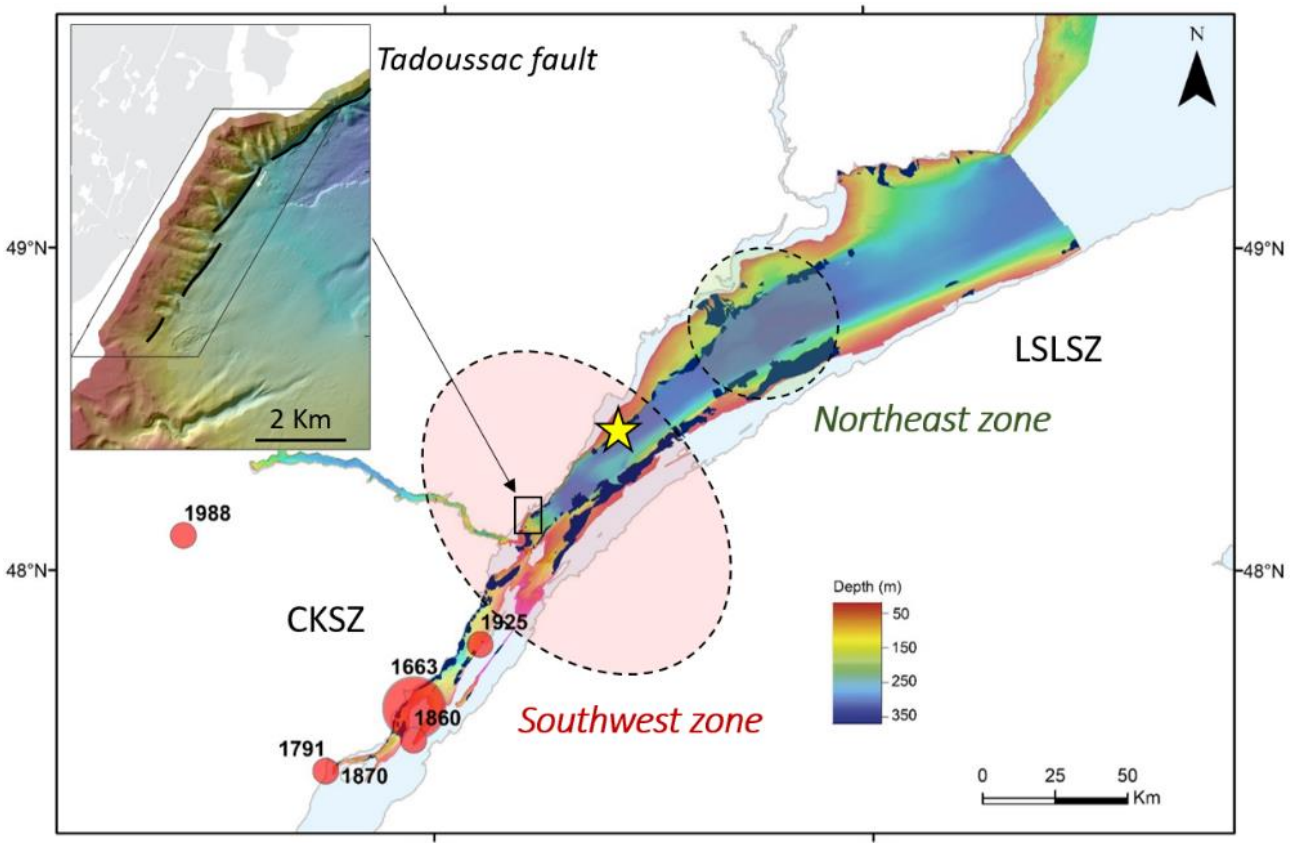

Figure 4-13. The two regions of the possible epicenter of the 1663 CE earthquake based on the study of sediment liquefaction in the St. Lawrence Estuary. The yellow star indicates the location of the point of convergence calculated with the OpenSees method. This site is located ~ 30 km from the Tadoussac fault mapped by Normandeau *et al.* (2015) and Pinet *et al.* (2021) (cf. detailed view in the black square). This scenario seems to be the most probable because is included in the "southwest zone", near the Charlevoix-Kamouraska Seismic Zone (CKSZ) and close to this Holocene active fault.

2003). However, the study of earthquake epicenters, focal mechanisms and the state of tectonic stress in the LSZ shows the probable existence of a fault that could have generated an earthquake with a magnitude greater than M6 (Plourde and Nedimović, 2021). Pinet *et al.* (2021) have identified an active fault in the western Gulf of St. Lawrence but it is 320 km further away (**Figure 4-1**). In addition, the NE zone is also far from the Tadoussac fault, at about 170 km. Finally, the seismic surveys conducted during the SLIDE-2020 expedition do not reveal any new active faults in the NE zone between Rimouski and Betsiamites. A location of the EQ1663 epicenter in the NE zone therefore seems less likely.

All these observations lead us to consider that the epicenter of EQ1663 is most likely located in the SW zone, i.e., near the Tadoussac site and the mouth of the Saguenay Fjord. The numerical simulations largely support this hypothesis with slight uncertainty on the location (**Figure 4-13**). Because the most likely location defined in this study is more than 120 km northeast of the historical reference epicenter it implies a major revision of the seismic hazard assessment in Eastern Canada.

5.4. Limitations of the approach

Despite cross-checking two different methods, revising the position of the epicenter of EQ1663 involves some uncertainties. Indeed, the PGA-distance law was used to determine the source-to-

site distances for both methods. This law, formulated by Pezeshk *et al.* (2018), was adjusted using a point-source stochastic model to take into account the source, path and site response for CENA. However, uncertainties may remain because this law was established from earthquakes near the St. Lawrence Estuary but also included earthquakes much further away. It therefore does not consider small-scale geological variations and focal mechanisms, which could affect the propagation of seismic waves.

The numerical simulations used the accelerogram of the Saguenay earthquake in 1988 because it is the only major instrumented earthquake near the study area. Although it was well recorded on a variety of instruments by the regional seismographic stations, it is an enigma in several respects (Boore and Atkinson, 1992). Indeed, its mainshock was particularly energetic at high frequencies, the high-frequency spectral level of radiation at the source was large and it was deeper than most previous events (28 km) (Gariel and Jacob, 1989; Somerville *et al.*, 1990; Boore and Atkinson 1992). These particularities could influence our results.

The liquefaction potential used in the FoS calculations was established by considering the cumulative shear strain criterion while the numerical simulations were based on excess pore pressure criteria. Knowing that these two criteria of liquefaction are correlated (Wu *et al.*, 2004), the influence of this difference can be considered low.

The cores used in this study do not exceed 5 m in length. While coring in submarine landslide scars allowed access deeper seismic units (e.g., Unit 3 with COR20-02-11GC), it was necessary to extrapolate sedimentological and geotechnical properties over several meters. This approximation does not take into account the small sedimentary variations that may exist within the sediment layers. In addition, the bases of the reference sedimentary column in the numerical simulations are considered as the bedrock. However, the seismic profiles show that this is not always the case but we made this approximation because no cores reach this depth. This should not greatly influence the behavior of the sedimentary column because the sediments at the base (Unit 3) are systematically composed of homogenous non-liquefiable clay (**Figure 4-10**). Furthermore, interpretation of the seismic profiles does not reveal that slip surfaces are generated at the base of the reference sedimentary column.

6. CONCLUSION

The approach developed in this paper consisted in cross-checking two methods to determine the source-to-site distances for six submarine landslides triggered by the EQ1663. The first method was used to determine these distances based on Factor of Safety calculations and the integration of the liquefaction potential obtained from 15 triaxial tests carried out on sediments from seismic Units 3 to 5. The second method was used to determine the source-to-site distances from numerical simulations considering the liquefaction behavior of sediment through constitutive models. The last method was shown to be more accurate even if both methods converged to the same location for the EQ1663 epicenter.

Determining the source-to-site distances for six earthquake-triggered submarine landslides along the St. Lawrence Estuary allowed to determine a new epicenter position for the EQ1663 ($M \geq 7$). The location of this epicenter has not been revised for

nearly 100 years and the present study indicates it might have been more than 120 km away from the historical reference location, to the northwest. The new calculated EQ1663 epicenter is only 30 km from an active fault of at least 8 km long, supporting our results.

Considering this new location of the epicenter of the most important earthquake in northedast America for 400 years, additional investigations are needed to image the fault at the Tadoussac area. Finally, slope stability around the new epicenter must be analysed to assess the possible triggering of future submarine landslides.

EN BREF

- Deux couches faibles régionales contrôlent les ruptures de pente dans l'estuaire du Saint-Laurent.
- Des essais en laboratoire et des calculs ont permis de déterminer l'épicentre du séisme de 1663 CE.
- La nouvelle position du séisme se situe à environ 120 km au nord-est de l'épicentre historique.
- L'épicentre pourrait correspondre à une faille active près de Tadoussac, Québec.

IN SHORT

- Two regional weak layers control slope failures in the St. Lawrence Estuary.
- Lab testing and calculations allowed to determine the 1663 CE earthquake epicenter.
- The new earthquake position is about 120 km northeast of the historical epicenter.
- The epicenter could correspond to an active fault near Tadoussac, Québec.

CHAPITRE V. IMPACT DES TREMBLEMENTS DE TERRE MAJEURS SUR LA STABILITE ACTUELLE DES PENTES SOUS-MARINE DANS L'ESTUAIRE DU SAINT-LAURENT (QUEBEC, CANADA)

CHAPTER V. IMPACT OF MAJOR EARTHQUAKES ON THE PRESENT SUBMARINE SLOPE STABILITY IN THE ST. LAWRENCE ESTUARY (QUÉBEC, CANADA)

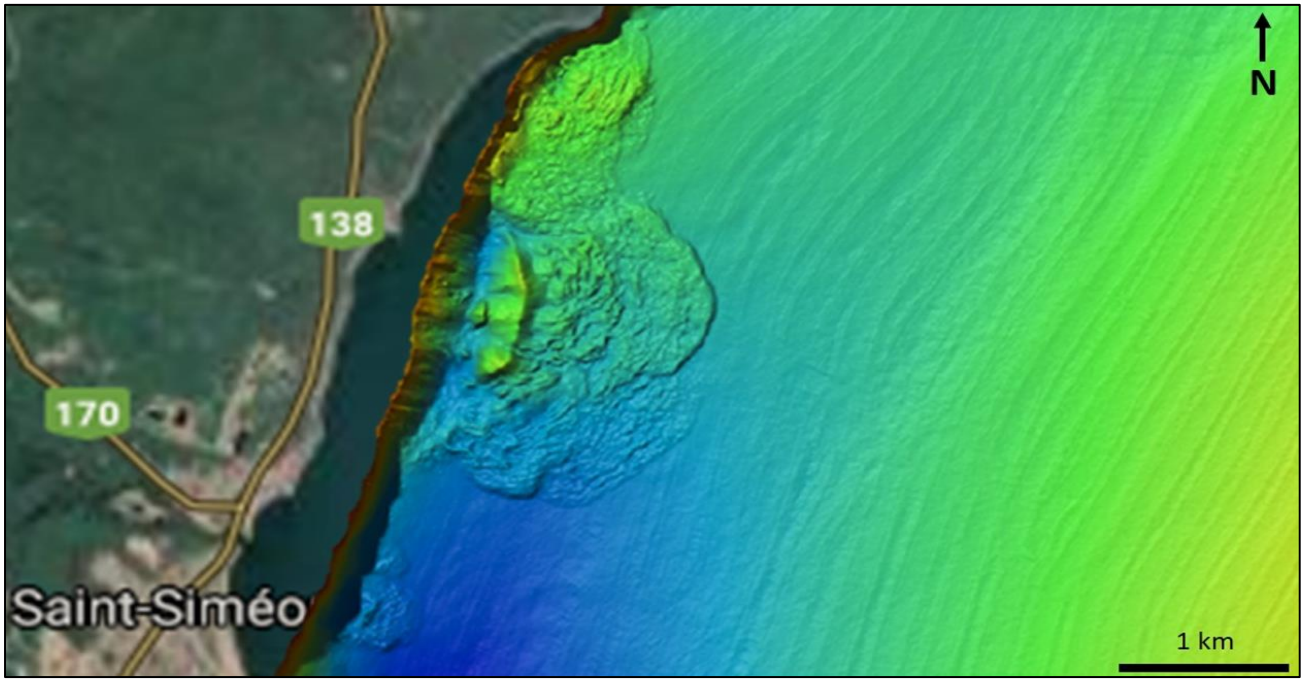

Carte bathymétrique du glissement sous-marin de Saint-Siméon
Bathymetric map of the Saint-Siméon submarine landslide

CHAPITRE 5. RÉSUMÉ

L'est du Canada est particulièrement exposé aux géorisques. En effet, le niveau élevé de sismicité peut causer des dommages directs et indirects. Parmi eux, les glissements sous-marins déclenchés par les séismes peuvent endommager les infrastructures côtières et sous-marines et générer des vagues de tsunami pouvant affecter les zones côtières. Les nombreux glissements sous-marins observés dans l'estuaire du Saint-Laurent confirment l'importance de ce géorisque et laissent présager de possibles déstabilisations futures. À cet égard, l'objectif de ce chapitre est d'évaluer la stabilité des pentes de six zones de glissements sous-marins entre Charlevoix et Baie-Comeau en évaluant le potentiel de liquéfaction des couches sédimentaires grossières (silt à sable) sous l'effet d'un séisme équivalent au séisme de 1663 CE (M 7,7 ± 0,7). Des analyses sédimentologiques et géotechniques couplées à des simulations numériques ont permis d'évaluer si des glissements sous-marins déclenchés par des séismes peuvent affecter les pentes actuelles dans l'estuaire du Saint-Laurent. Il a été démontré que les six zones de glissement sous-marin sont fortement affectées par le chargement sismique. Les épaisseurs maximales des glissements sous-marins déclenchés par des séismes ont été calculées entre 2 et 37 m. Cependant, en raison de l'impossibilité d'effectuer des simulations numériques en deux dimensions, il n'a pas été possible de calculer le volume potentiel des glissements sous-marins, paramètre essentiel pour l'estimation de la hauteur du tsunami. Enfin, une relation entre la distance et la magnitude d'un séisme a été établie pour les six zones étudiées afin de prédire le potentiel de liquéfaction qui pourra s'avérer être un outil pour la prévention des risques au Québec.

CHAPTER 5. ABSTRACT

Eastern Canada is particularly exposed to geohazards. Indeed, the high level of seismicity can cause direct and indirect damages. Among these, submarine landslides triggered by earthquakes can damage costal and underwater infrastructures and generate tsunami waves capable of affecting coastal areas. The numerous submarine landslides observed in the St. Lawrence Estuary confirm the importance of this geohazard and point to possible future destabilization. In this respect, the objective of this chapter is to estimate the slope stability of six submarine landslide areas from Charlevoix to Baie-Comeau by evaluating the liquefaction potential of coarse sedimentary layers (silt to sand) under the effect of an earthquake equivalent to the 1663 CE earthquake (M 7.7 ± 0.7). Sedimentological and geotechnical analyses with detailed numerical simulations made it possible to evaluate whether earthquake-triggered landslides can affect the present slopes in the St. Lawrence Estuary. The six submarine landslide zones were shown to be highly affected by seismic loading. The maximum calculated landslide thicknesses triggered by earthquakes range from 2 to 37 m. However, beacause two-dimensional numerical simulations could not be performed, it was impossible to calculate the potential volume of submarine landslides, as an essential parameter for tsunami run-up estimations. Finally, a relationship between the distance and magnitude of an earthquake was established for the six studied areas to predict the liquefaction potential. This can be a useful tool for risk prevention in Québec.

1. INTRODUCTION

Eastern Canada has been affected by submarine landslides triggered by seismicity in the past, as evidenced by the 1929 Grand Banks earthquake (Piper et Aksu, 1987). The turbidity current associated with the resulting submarine landslide caused a series of cable breaks (Doxsee, 1948) and the interruption of transatlantic communications for six months. The tsunami generated by the submarine landslide killed 29 people and caused major damage to public and private infrastructures, making it the most catastrophic tsunami in Canadian history (Clague *et al.*, 2003; Fine *et al.*, 2005). This event confirms that submarine landslides are a major natural hazard in eastern Canada that is still underestimated (Normandeau *et al.*, 2019) and that it is necessary to anticipate them in order to mitigate their impact on society, especially in Québec where human development and activities are mainly along the coast of the St. Lawrence Estuary.

In the St. Lawrence Estuary, the numerous submarine landslide deposits (~100) mapped by and Pinet *et al.* (2015) (**Figure 5-1**) reveal that the area is highly prone to slope failure at varying scales and periods. Recent studies revealed a relationship between submarine landslides and regional seismicity (St-Onge *et al.*, 2004; Cauchon-Voyer *et al.*, 2008; Mérindol *et al.*, 2022a), suggesting possible future slope failures. However, no cases of

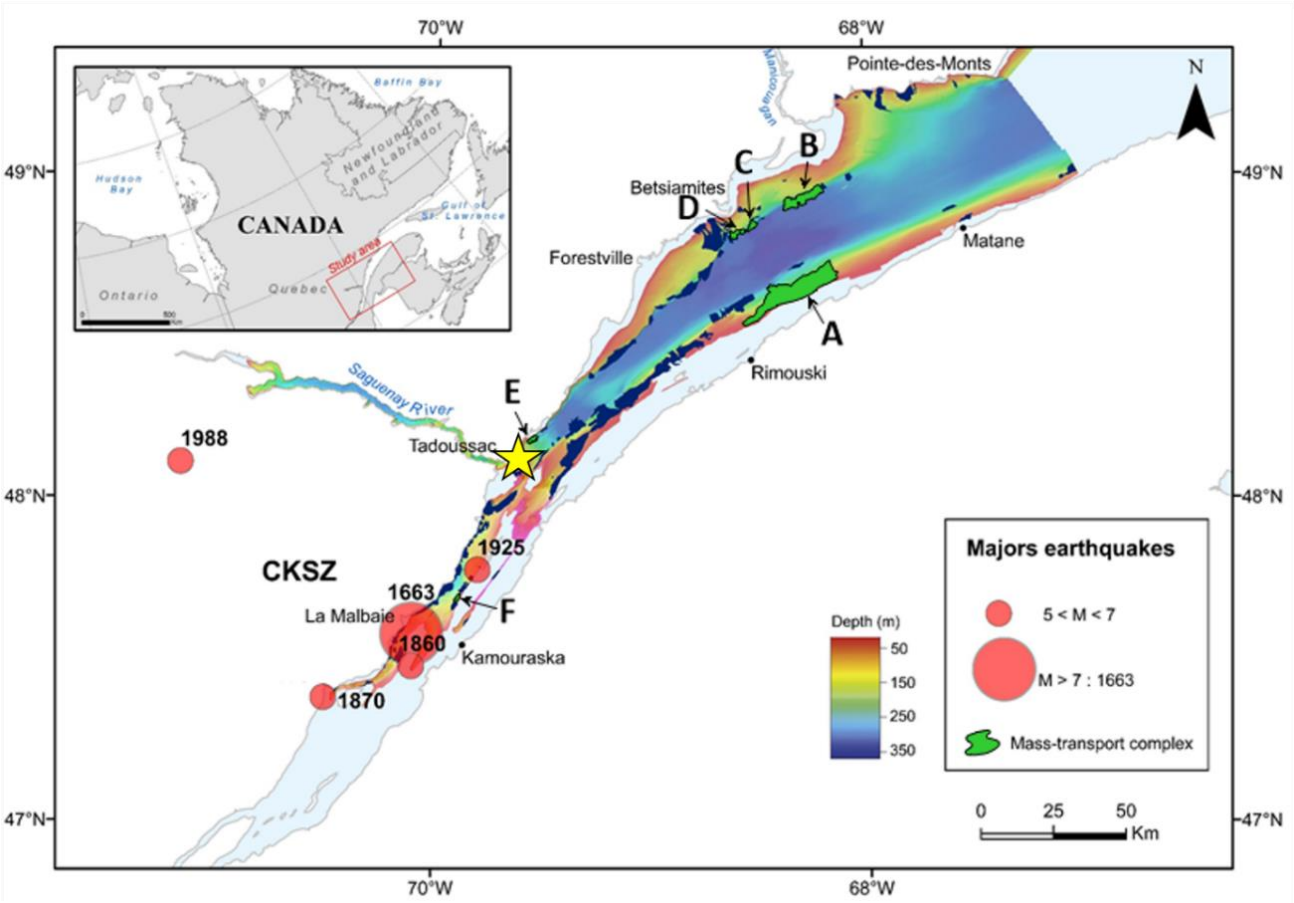

Figure 5-1. Bathymetric map of the St. Lawrence Estuary. The studied mass-transport complexes (MTCs) are indicated green: (A) Rimouski, (B) Baie-Comeau, (C) Betsiamites II, (D) Betsiamites I, (E) Tadoussac and (F) Charlevoix. The yellow star indicates the epicenter of the 1663 CE earthquake, relocated on an active fault near Tadoussac (Mérindol *et al.*, 2022b).

tsunamis triggered by submarine landslides have been reported in Québec, whereas tsunami waves generated by landslides are the second most important cause of tsunamis after earthquakes (Harbitz *et al.*, 2014). Poncet *et al.* (2010) studied two historic submarine landslides in Matane and St-Siméon for their tsunami-generation potential and Turmel *et al.* (2019) analyzed the Betsiamites landslide complex, the largest landslide in the Estuary (e.g., Cauchon-Voyer *et al.*, 2008). The authors calculated that the wave heights generated by these submarine destabilizations could have reached 2.5 m to 5 m, revealing the existence of a tsunami threat in the St. Lawrence Estuary.

The 1663 CE earthquake, with a magnitude estimated between M 7.0 (Locat, 2011; Lamontagne *et al.*, 2018) and M 8.4 (Mazzotti *et al.*, 2005, Locat, 2011), triggered at least twelve submarine landslides in the St. Lawrence Estuary, highlighting it as the major seismic event of the last 2000 years (Mérindol *et al.*, 2022a). Its epicenter, long considered in Charlevoix, was re-located at the mouth of the Saguenay Fjord and most likely corresponds to an active fault trace in the vicinity of Tadoussac (Mérindol *et al.*, 2022b; **Figure 5-1**. Today, such an earthquake could generate numerous direct and indirect damages (e.g., submarine landslides, tsunami) to infrastructures and the population.

In this context, the present work aims at evaluating the likely impact of major earthquakes on the triggering of future submarine landslides in six areas (**Figure 5-1**) where slope failures have been caused by the 1663 CE earthquake (M 7.7 ± 0.7; e.g., Locat, 2011). In addition, the thickness of sediments possibly involved in future failure events will be estimated in each of the six areas to assess the hazard they pose.

2. DATA AND METHODS

The SLIDE-2020 cruise on board the RV *Coriolis II* surveyed six areas of submarine mass-transport complexes (MTCs) in the St. Lawrence Estuary: Rimouski, Baie-Comeau, Betsiamites I, Betsiamites II, Saguenay, and La Malbaie (**Figure 5-1**). During the expedition, geophysical and sampling methods were deployed as detailed below. Sedimentological and geotechnical analyses were performed after the expedition at ISMER and Ifremer respectively.

2.1. Geophysics

High-resolution swath bathymetric coverage was obtained during the SLIDE-2020 cruise, using a Kongsberg EM-2040 multibeam echosounder system coupled with the Applanix POS/MV inertial platform. A bathymetric grid with a cell size of 1 m was generated using the Caris Hips & Sips software (Caris, 2013). Data acquired during the survey with the *Minos* celerimeter from *AML oceanographic* were used to account for the variability of sound velocity in the water column. These data were used to build accurate bathymetric profiles perpendicular to the six MTCs. In addition, high-resolution seismic data were collected using the hull-mounted Edgetech X-Star 2.1 subsurface profiler to image the sedimentary sequence. The source frequency was between 2 and 12 kHz with chirp pulses between 3 and 20 ms. Time-to-depth conversion of the seismic profiles was done using an average sound wave velocity value of 1500 $m.s^{-1}$ corresponding to the velocity in water and the mean value measured on sediment cores using the Multi

Sensor Core Logger (data presented in Mérindol *et al.*, 2022a). Interpretation of the seismostratigraphic sequence, composed of five Units overlying the bedrock (Syvistki and Praeg, 1989; St-Onge *et al.*, 2008; Duchesne *et al.*, 2010), relies on attributes such as reflectivity, geometry, and amplitude of the seismic reflectors detailed by Cauchon-Voyer *et al.* (2008) and on the newly recovered cores (**Figure 5-2** to **4**).

2.2. Sedimentary and geotechnical analyses

2.2.1. Sediment cores

Sedimentary sequences were sampled by eleven cores with lengths varying between 2.51 and 5.22 m, at water depths ranging from 39 m to 236 m. On whole sections, the GEOTEK Multi Sensor Core Logger (MSCL) measured wet bulk density and P-wave velocity at 1 cm intervals. The sections for geotechnical investigation were selected and preserved based on digital X-ray images acquired through the GEOTECK XCT scanner. They correspond to the coarsest layers that have a high liquefaction potential and are not the results of a rapidly deposited layer (RDL) associated with turbidity currents or debris flows (Mérindol *et al.*, 2022a). The remaining core sections were split lengthwise into two halves. Fifteen geotechnical samples of coarse materials (silt and sand) were selected to determine their potential of liquefaction under an earthquake loading, while one sample of clay was selected for the advanced geotechnical testing (Mérindol *et al.*, 2022b).

Sediment permeability was measured with the falling head method according to the ASTM-D5856-15 standard. These measurements were performed on samples from each core listed in **Table 5-1**. The undrained shear strength was measured on split core sections using a hand-shear-vane (ASTM D8121) with a spacing of 10 to 50 cm. These measurements were carried out only in clayey facies.

2.2.2. Cyclic triaxial testing

To characterize the sediment response to earthquake loading we used the Enterprise Level Dynamic Triaxial Testing System (ELDYN) from Geotechnical Digital System (GDS). Mérindol *et al.* (2022b) performed fifteen undrained cyclic triaxial tests. The test followed the ASTM-D5311M-13 standard procedure. Bender elements mounted in the base and top cap of the triaxial cell were used to measure the velocities of shear wave (V_s) and compressional wave (V_p) before and during the tests.

The cyclic loading phase was performed after a consolidation phase, where the sample was loaded isotropically to an effective confining stress of 50 kPa (σ'_3). During the cyclic loading phase, the deviatoric stress amplitude, noted Δq, was applied through uniform sinusoidal cycles at 0.5 Hz. This allows the calculation of the Cyclic Resistance Ratio (*CRR*) given by:

$$CRR = \frac{\Delta q}{2\sigma'_3} \quad (1)$$

The purpose of this test is to determine the liquefaction potential expressed by the CRR in terms of the number of cycles required to reach liquefaction. Both pore water pressure (Ishihara, 1993) and strain criteria are considered (Wu *et al.*, 2004).

2.3. Numerical modeling

The objective of the numerical modeling is to calculate the stability of submarine slope in the case

of an earthquake of magnitude 7.7 ± 0.7, i.e., equivalent to the 1663 CE earthquake. To realize these simulations, an input seismic signal, a sedimentary geometry, and a mechanical characterization of the sediment layers by constitutive soil models are necessary. This section describes each of these steps.

2.3.1. Accelerogram and PGA attenuation

The 1663 CE earthquake occurred before the 19th century and the advent of seismographs. Thus, in the absence of an accelerogram, to simulate this earthquake, it was necessary to use the 1988 CE Saguenay earthquake (M 5.9), the most recent and strongest instrumented earthquake in eastern Québec. This accelerogram (**Figure 5-5**) was multiplied by a scaling factor to simulate different earthquake magnitudes. The location of the epicenter of 1663 CE was considered to be at the location of the Tadoussac fault (Mérindol *et al.*, 2022b). The load induced by an earthquake is expressed determined by Peak Ground Acceleration (PGA) expressed in *g*, the gravitational constant. With the distance, the PGA decreases following a mathematical law of attenuation (**Figure 5-5**). PGA

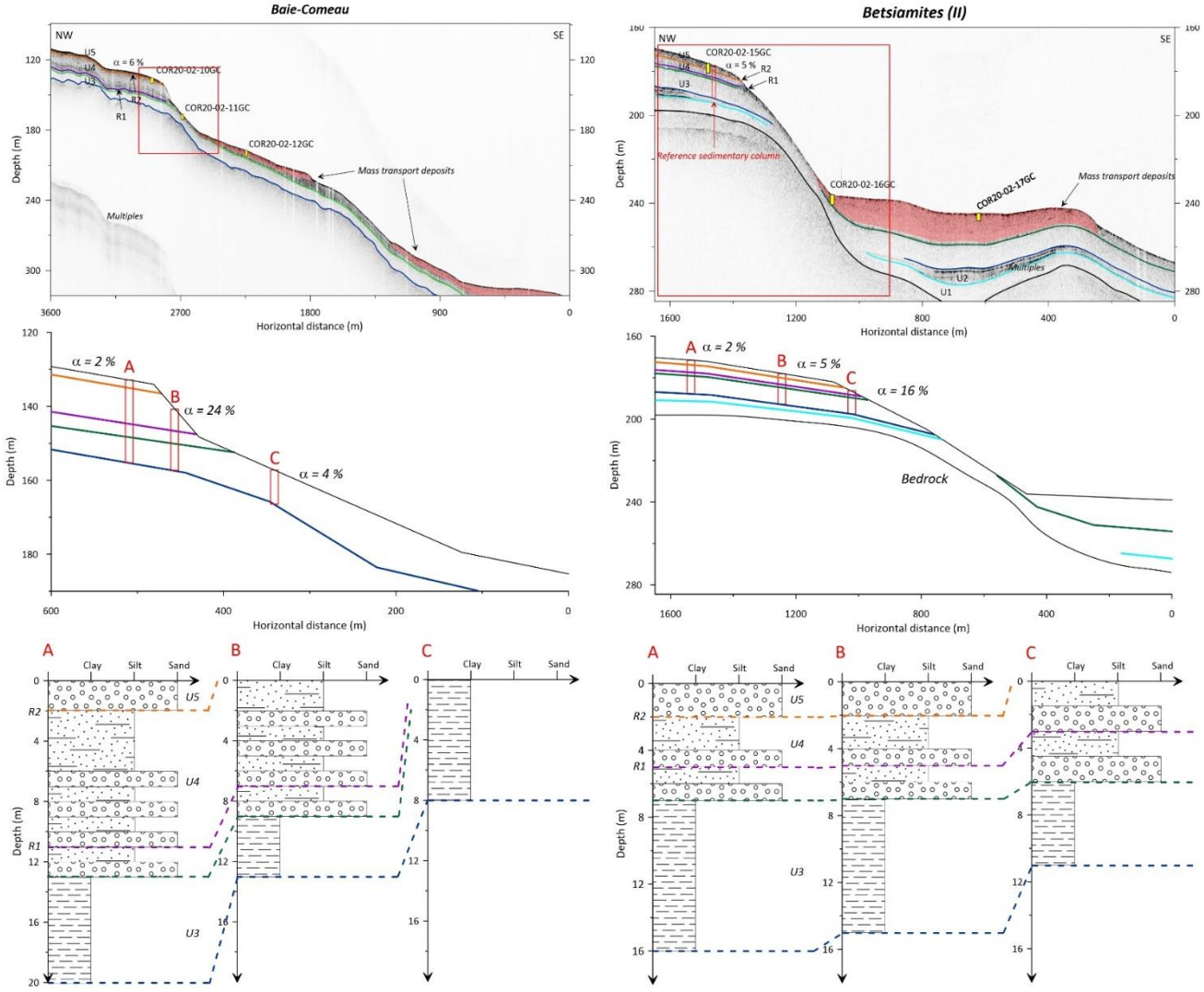

Figure 5-2. Upper panel: seismic profiles acquired in the Baie-Comeau and Betsiamites (II) areas. Middle panel: schematic geometry. The red rectangles correspond to the sedimentary columns considered in the numerical simulations and are shown as lithostratigraphic logs in the lower panel.

values were calculated for each MTC area using the ground-motion prediction equations (GMPEs) for Central and Eastern North America (CENA) established by Pezeshk *et al.* (2018) (**Figure 5-5**). The numerical simulations were performed with three earthquake magnitudes: M 7, M 7.7 and M 8.4., i.e., M 7.7 ± 0.7. They correspond respectively to the minimum, mean and maximum magnitude of the 1663 CE earthquake (Mazzotti *et al.*, 2005; Locat, 2011; Lamontagne *et al.*, 2018; **Figure 5-5**).

2.3.2. Constitutive soil model

The mechanical behavior of the sediments, including the liquefaction process, was numerically simulated using the Open System for Earthquake Engineering Simulation software (OpenSees; McKenna *et al.*, 2009). The constitutive model Pressure Dependant Multi-Yield 02 (PDMY02) (Elgamal *et al.*, 2002; Yang *et al.*, 2003) implemented in OpenSees has been used to simulate the stress-strain behavior of a column of sand layers with a slope gradient under dynamic loading and in undrained conditions. The PDMY02 model relies on fifteen parameters determined from cyclic

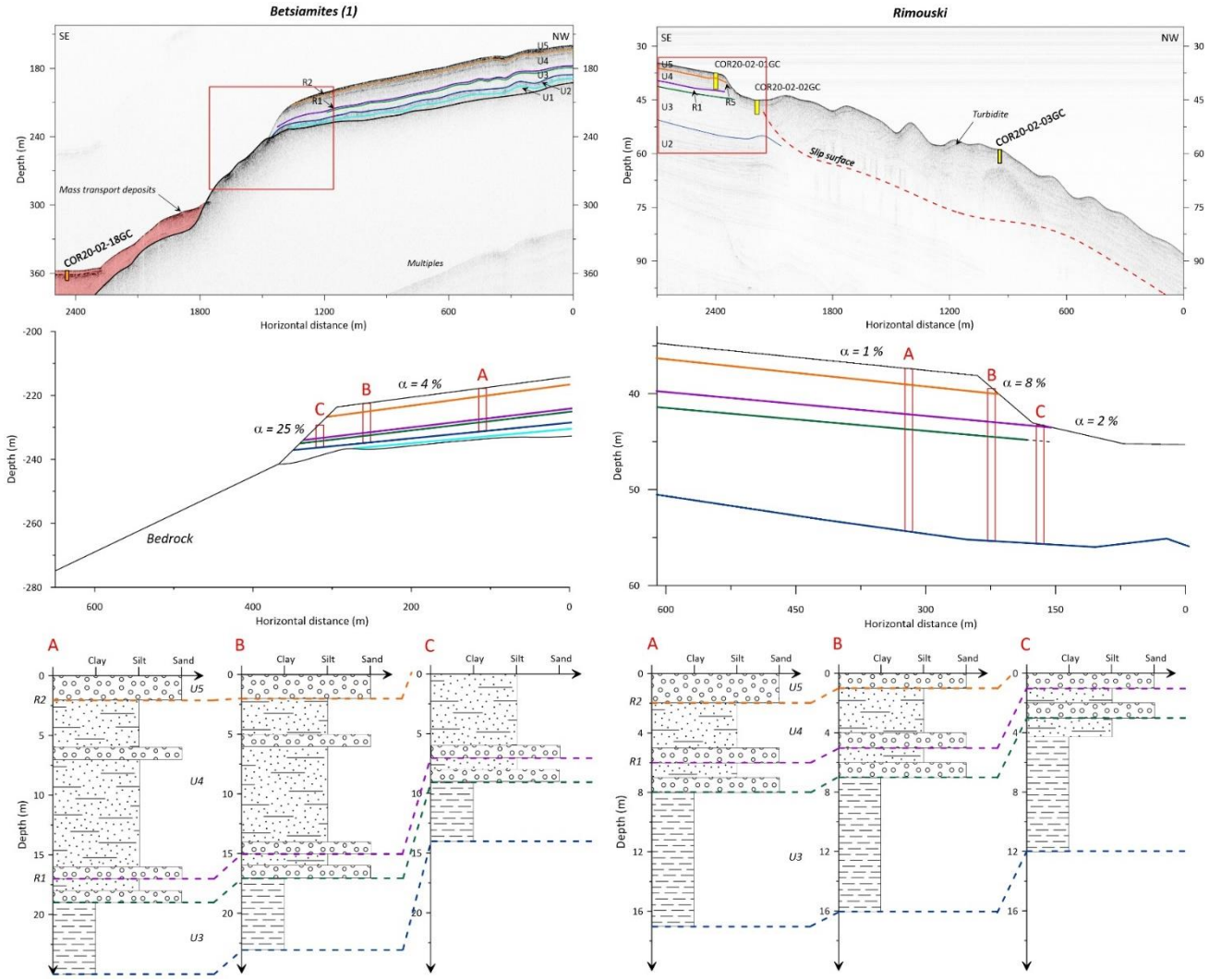

Figure 5-3. Upper panel: seismic profiles acquired in the Betsiamites (I) and Rimouski areas. Middle panel: schematic geometry. The red rectangles correspond to the sedimentary columns considered in the numerical simulations and are shown as lithostratigraphic logs in the lower panel.

triaxial tests, falling head tests, MSCL or derived from shear and compressional wave velocity measurements and trial-and-error calibration. For non-liquefiable clay layers, the constitutive model Pressure Independent Multi-Yield (PIMY) was used (Yang *et al.*, 2003). It is a linear elastic model relying on the five parameters determined by the same methods as for the PDMY02 model, except for the hand shear vane test. The model calibration and the determination of the parameters are detailed in Mérindol *et al.* (2022b).

2.3.3. Slope modeling

GiD is a software program used in numerical engineering simulations from pre to post-processing of Finite Element Analysis (Ribó *et al.*, 1998). It was used to format and syntax TCL file commands for OpenSees (McKenna *et al.*, 2009) including mesh geometry, initial and boundary conditions (e.g., nodal degrees of freedom, fixities), material behavior and applied loading. Six TCL files were prepared for the six studied MTCs. The two dimensions geometry was derived from the bathymetric profiles (**Figure 5-6A**). The geometries of sedimentary layers and their interpretations were

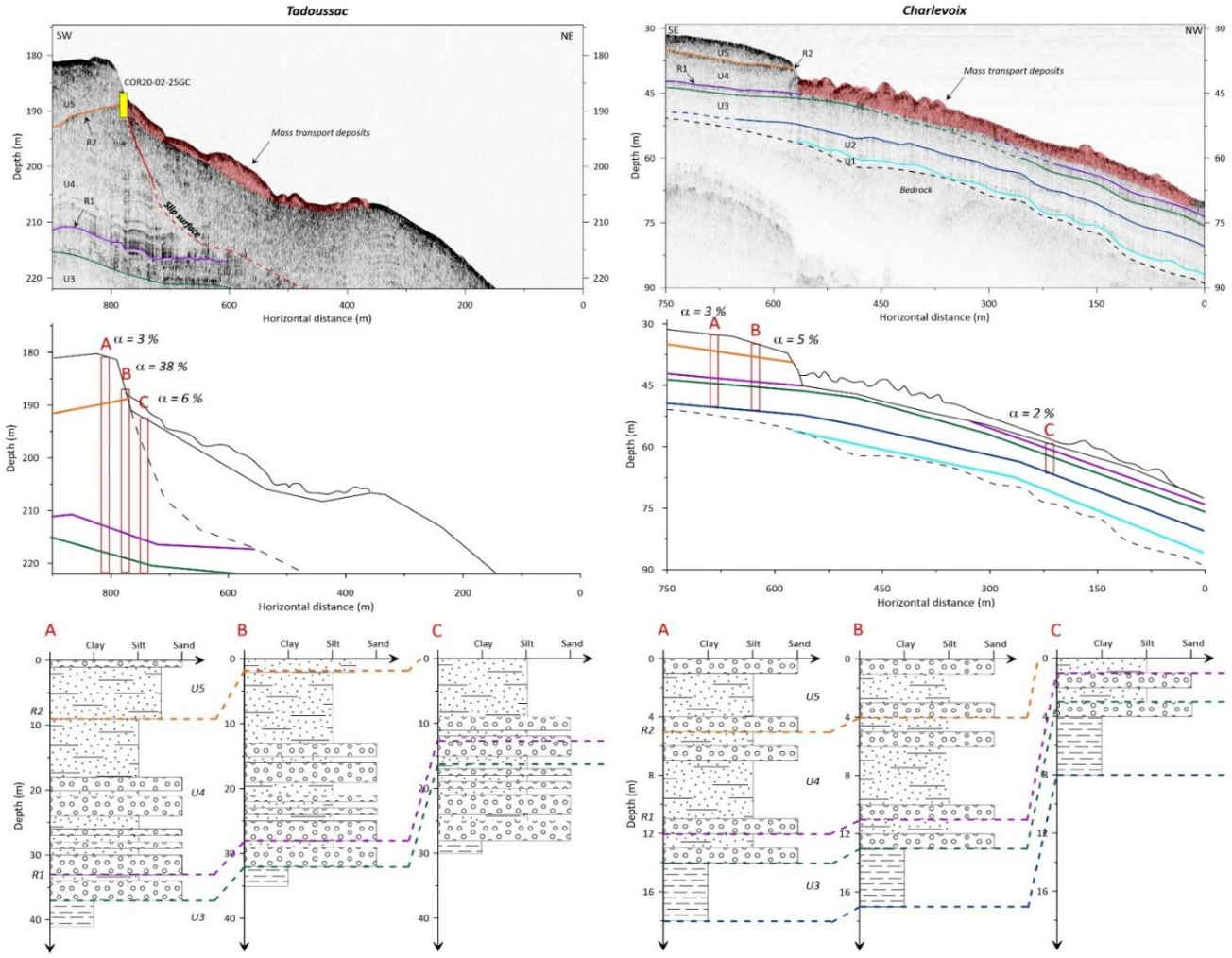

Figure 5-4. Upper panel: seismic profiles acquired in the Tadoussac and Charlevoix areas. Middle panel: schematic geometry. The red rectangles correspond to the sedimentary columns considered in the numerical simulations and are shown as lithostratigraphic logs in the lower panel.

Table 5-1. Location, length and water depth of studied cores.

Area and core name	Zone	Lat. (°N)	Long. (°W)	Length (m)	Water depth (m)
Rimouski					
COR20-02-01GC	Intact	48°34.71	68°29.66	4.42	39
COR20-02-02GC	Scar	48°34.77	68°29.76	4.10	47
Matane					
COR20-02-05GC	Scar	48°54.65	67°35.68	3.53	197
COR20-02-06GC	Intact	48°54.61	67°35.66	3.93	152
Baie-Comeau					
COR20-02-10GC	Intact	48°59.80	68°11.66	4.63	133
COR20-02-11GC	Scar	48°59.71	68°11.59	4.40	153
COR20-02-12GC	Scar	48°59.49	68°11.42	5.22	193
Betsiamites					
COR20-02-15GC	Intact	48°53.66	68°30.35	4.49	177
COR20-02-16GC	Scar	48°53.47	68°30.21	4.30	236
Saguenay					
COR20-02-25GC	Scar	48°11.56	69°34.07	4.36	186
Charlevoix					
COR20-02-45GC	Scar	47°41.11	69°54.71	2.51	153

defined based on seismic profiles (**Figure 5-6B**). The silt and sand layers behavior are modeled using the PMDY02 constitutive model while the clay layers behavior is modeled using PIMY. The morphologies of the six MTCs are simplified to be implemented in numerical models but the slope gradients remain faithfully reproduced.

The mesh geometry was generated using GiD as a pre-processor, which simplifies mesh generation for 2D problems (**Figure 5-6C**). The elements of the mesh correspond to quadrilaterals with four nodes (**Figure 5-6C).** The soil node in the lower left-hand corner of the model is defined as the Lysmer dashpot (Lysmer-Kuhlemeyer, 1969; **Figure 5-6C**). The seismic load was applied to this node, which is assumed to have bedrock properties. The free-field column conditions were applied to the horizontal boundaries of the model (**Figure 5-6C)**. The thickness of the elements in the free profile columns is increased in order to make them more massive than the elements inside the mesh, allowing the simulation of an infinite model. Each element node has three degrees of freedom: in the horizontal directions (displacements along the x-axis and z-axis) and for the fluid pressure. In terms of boundary conditions, vertical displacement was impeded at the base of the mesh (**Figure 5-6D**). On the upper boundary, the pore pressure is set to zero (**Figure 5-6D**).

Studies coupling GiD and OpenSees are rare (e.g., Masoudi *et al.*, 2019; Carlton *et al.*, 2020). These programs are not easy to use in comparison to other commercial software such as Plaxis (Brinkgreve *et al.*, 2016) or FLAC (Itasca Consulting Group Inc.). However, their interest lies in considering accurately the problems of liquefaction during earthquakes and their capacity to perform fast calculations. Moreover, the calibration in chapter 4 (Mérindol *et al.*, 2022b) of the constitutive models PMDY02 and PIMY has led us to use in this chapter the GID and OpenSees softwares. The calibrated constitutive models are not available in other commercial software.

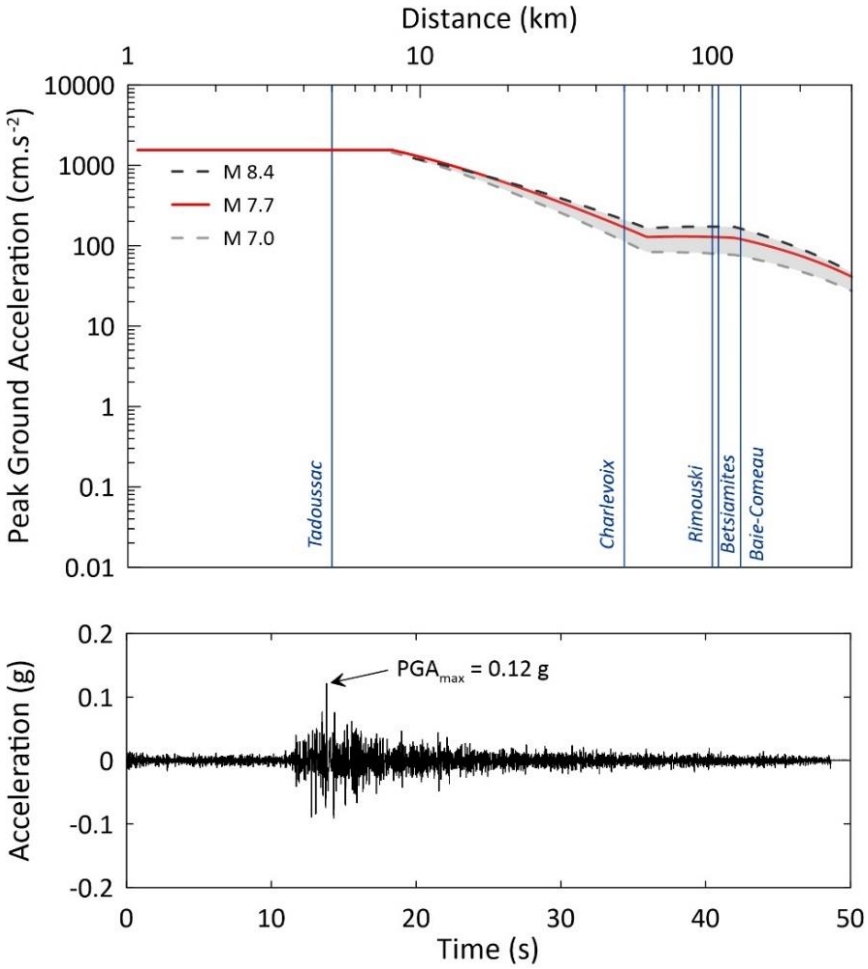

Figure 5-5. Peak ground acceleration versus distance predicted by the Ground-Motion Prediction Equations for central and eastern North America (Pezeshk *et al.*, 2018). The three earthquakes (M 7.0, M 7.7 and M 8.4) were used in numerical simulations and correspond to the 1663 CE earthquake (M 7.7 ± 0.7). The distances between the 1663 CE epicenter (Mérindol *et al.*, 2022b) and each area are reported in blue. Below, is the accelerograms of the 1988 CE earthquake (Saguenay, Québec).

3. RESULTS

3.1. Seismostratigraphic analysis

The seismic profiles of the six MTCs image Quaternary sedimentary sequences above the bedrock (**Figure 5-2** to **4**). Facies identification from sediment cores (**Table 5-1**) and acoustic facies signatures (e.g., Cauchon-Voyer *et al.*, 2008; Mérindol *et al.*, 2022b) allow the establishment of lithostratigraphic logs for each zone (**Figure 5-2** to **4**).

Above the bedrock, seismic Units 1 and 2 are not easily identifiable. In contrast, the seismic Unit 3 is recognizable at each site by its transparent acoustic signature (**Figure 5-2** to **4**). The failures surfaces in the Betsiamites, Baie-Comeau, and Charlevoix areas, seem to have been initiated above seismic Unit 3 (**Figure 5-2** to **4**). Unit 3 is characterized by massive homogenous light clay (cores COR20-02-11GC) corresponding to glaciomarine sediments (Syvitski and Praeg, 1989). Above, Unit 4 is characterized by alternating silt and coarser layers consisiting of fine to coarse sand (cores COR20-02-12GC, 25GC and 45GC) in a transitional context between glaciomarine and postglacial sedimentation (Duchesne *et al.*, 2010). Unit 5, the

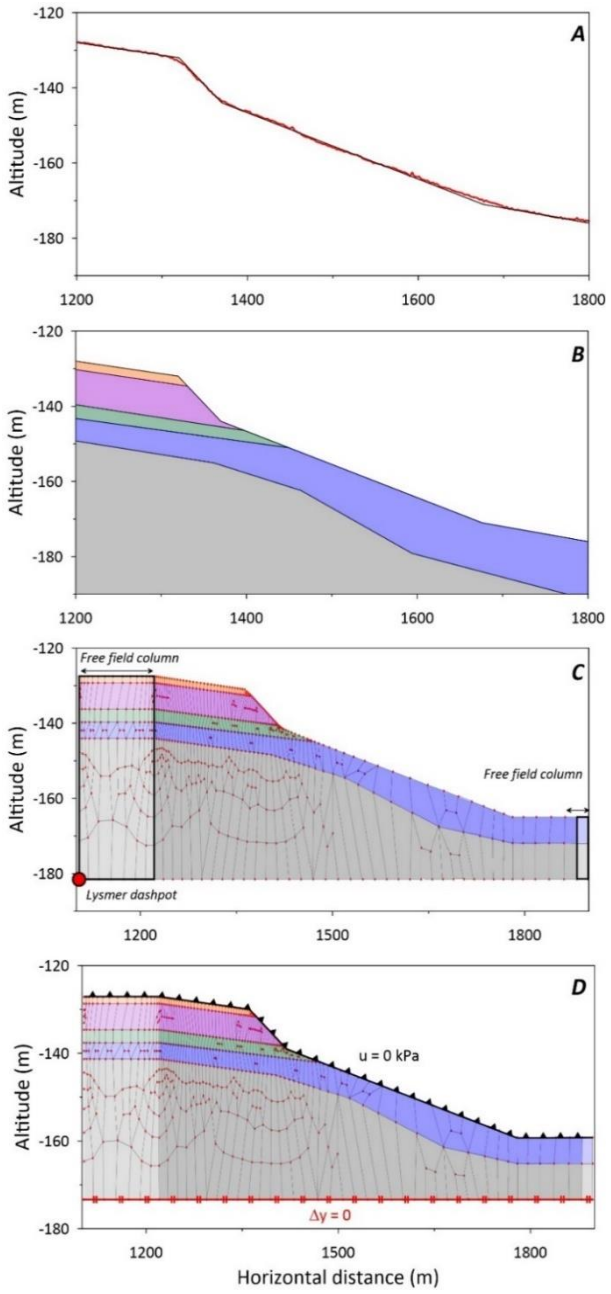

Figure 5-6. Modelling steps: (A) simplification (in black) of bathymetric profile (in red); (B) definition of layer geometry and materials properties (four sedimentary layers and the bedrock in gray); (C) creation of free-field columns, definition of the lysmer dashpot (red circle) and generation of the mesh; the red points correspond to the nodes; (D) definition of the boundaries conditions including impeded for vertical displacements at the base of the model (Δz) and the absence of excess pore pressure (R_u) along the top.

upper layer is characterized by a medium to strong amplitude and is composed of coarse sand. Chapter 4 (Mérindol *et al.*, 2022b) details the seismic interpretation of the six MTCs.

3.2. Slope stability 2D

The numerical simulations in two dimensions were expected to allow a precise determination of the failure plane and scar geometry. However, the use of 2D modeling in Opensees was much more complicated than I anticipated. I spent more than 1 month on this task, which unfortunately was not enough to prepare a 2D TCL command file. Four to six months would have certainly been necessary. The mesh consisting of about 2500 nodes has to be checked into the TCL file. This step can cause multiple errors. If some were corrected, the final error message after 1 month of work was still related to the mesh geometry. Boundary conditions are introduced manually which causes several numerical problems. OpenSees and GiD are not widely used and few resources are available to solve the errors encountered. However, several ways of solving the problems have been identified (new meshing method, simplification of free-field columns), but they require additional and longer time analysis.

Due to the difficulties in performing numerical simulations in two dimensions and the errors encountered, an alternative method was used. In this method, we split the complete 2D slope into several sedimentary columns to treat the slope stability problem in one dimension (Fig. 3). On each of the 1D columns, numerical simulation is performed with the corresponding slope angle and accurate results are obtained.

3.3. Slope stability 1D

The 1D calculation was carried out by following the numerical procedure presented in chapter 4 (Mérindol *et al.*, 2022b). The visualization of the results was performed using the GiD tool. Profiles of normalized excess pore pressure (*Ru*), first effective stress invariant (σ'_i), and displacement along the slope (Δz) can be read with GiD as post-process results. These profiles are calculated and plotted as a function of depth for columns A, B and C for the six areas (**Figure 5-7**). The occurrence of liquefaction is determined when σ'_i is equal to 0 kPa (**Figure 5-7**). The two other parameters corroborate this criterion: the increase in R_u exceeding 1 with an abnormally high positive displacement. From these liquefaction criteria, between one and three failure scenarios can be determined in each MTC area (**Figure 5-7**). A minimum, mean and maximum for each parameter evolution were calculated from an earthquake of magnitude 7.0, 7.7 and 8.4 respectively.

3.3.1. Scenarios of destabilization

In the Baie-Comeau area (**Figure 5-7A**), our 1D calculations indicate the possible occurrence of one of the following failure scenarios. The first one corresponds to the liquefaction of the uppermost sand layer composing Unit 5 upstream from the failure scar (**Figure 5-2**). This layer is liquefied for a magnitude of M 7.0. The second scenario involves deeper liquefaction of two thin sand layers at 3 m deep in the scar and 9 m below the seafloor upstream from the failure scar. Finally, the third scenario corresponds to the liquefaction of sand layers at the interface between Units 3 and 4. In each column, as expected, the simulations do not predict the liquefaction of Unit 3 composed of glaciomarine clay.

Only one liquefaction and failure scenario can be identified for the Betsiamites II area (**Figure 5-7B**). It corresponds to the liquefaction of the two layers at the interface between Units 3 and 4 lying between 4 and 8 m depth. This destabilization is expected to occur with a magnitude M ≥ 7.0. The displacement predicted is maximum (~5 m ± 0.5) in column C where the slope angle is the strongest (α = 24 %). The slope angle of column B is greater than that of column A. Thus, the calculated displacement for column B is slightly higher.

Three scenarios are recognized for the Betsiamites I area (**Figure 5-7C**). The first scenario involves the liquefaction of Unit 5 in columns A and B while the second scenario involves the liquefaction of the sand layer at 6 – 7 m depth. As for the previous zone, the third scenario predicts liquefaction at the interface between Units 3 and 4 around 15 – 20 m depth upstream from the failure scar. While the third scenario implies liquefaction triggering by an earthquake of magnitude M 8.4, the other two are expected to be triggered by earthquakes of magnitudes between M 7.0 and M 7.7.

The numerical simulations show two liquefaction scenarios in the Rimouski area (**Figure 5-7D**). The first scenario corresponds to the destabilization of Unit 5 while the second scenario implies a failure at the base of Unit 4. These predictions correspond to an earthquake of magnitude 7.0.

The case of Tadoussac is unique. Indeed, the site is very close to the fault at the hypothesized origin of the 1663 earthquake (Mérindol et al., 2022b). As

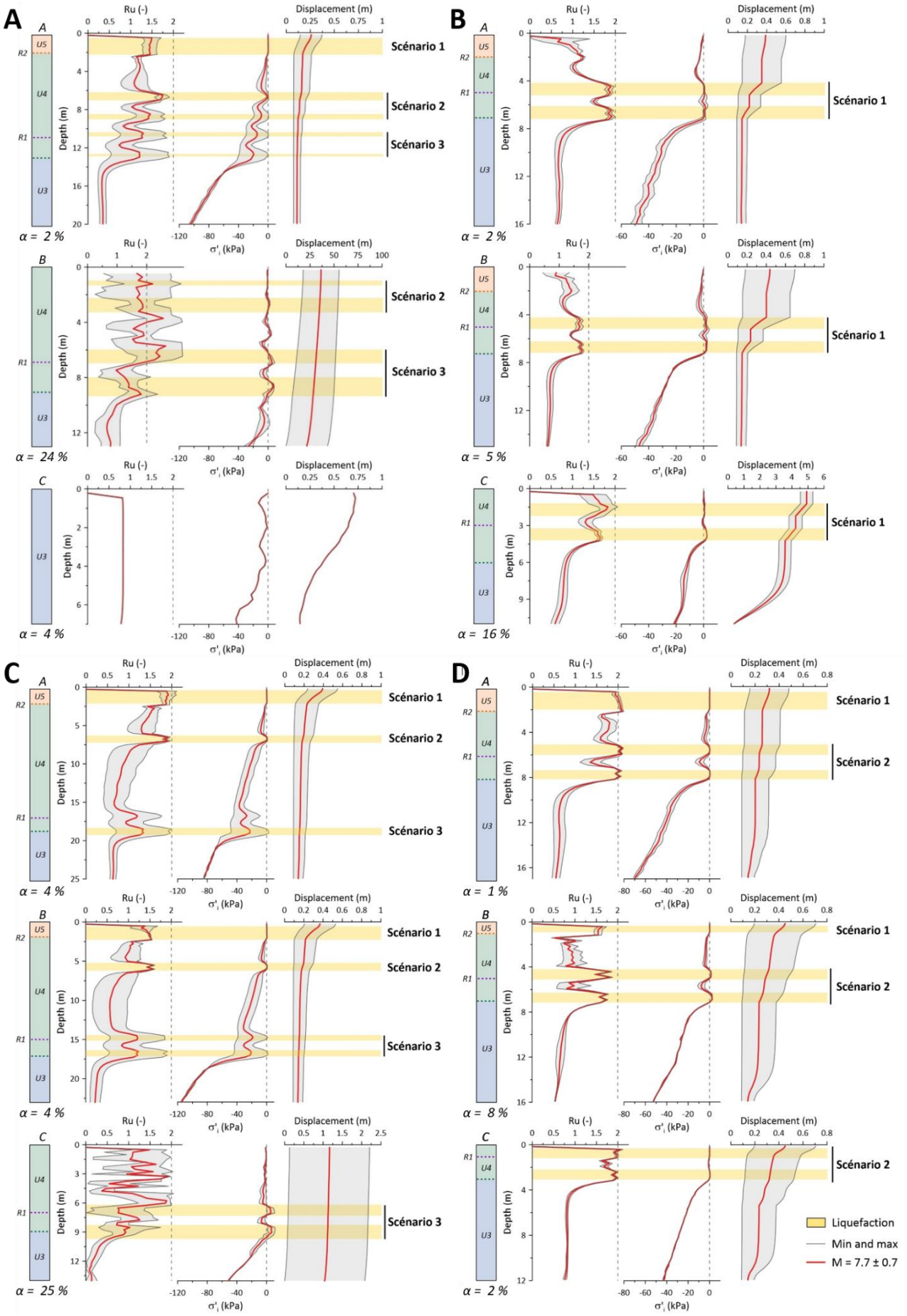
A
B
C
D
Ru (-)
Displacement (m)
Depth (m)
σ'v (kPa)
U5
U4
U3
R2
R1
Scénario 1
Scénario 2
Scénario 3
α = 2 %
α = 24 %
α = 4 %
α = 5 %
α = 16 %
α = 4 %
α = 25 %
α = 1 %
α = 8 %
α = 2 %
Liquefaction
Min and max
M = 7.7 ± 0.7

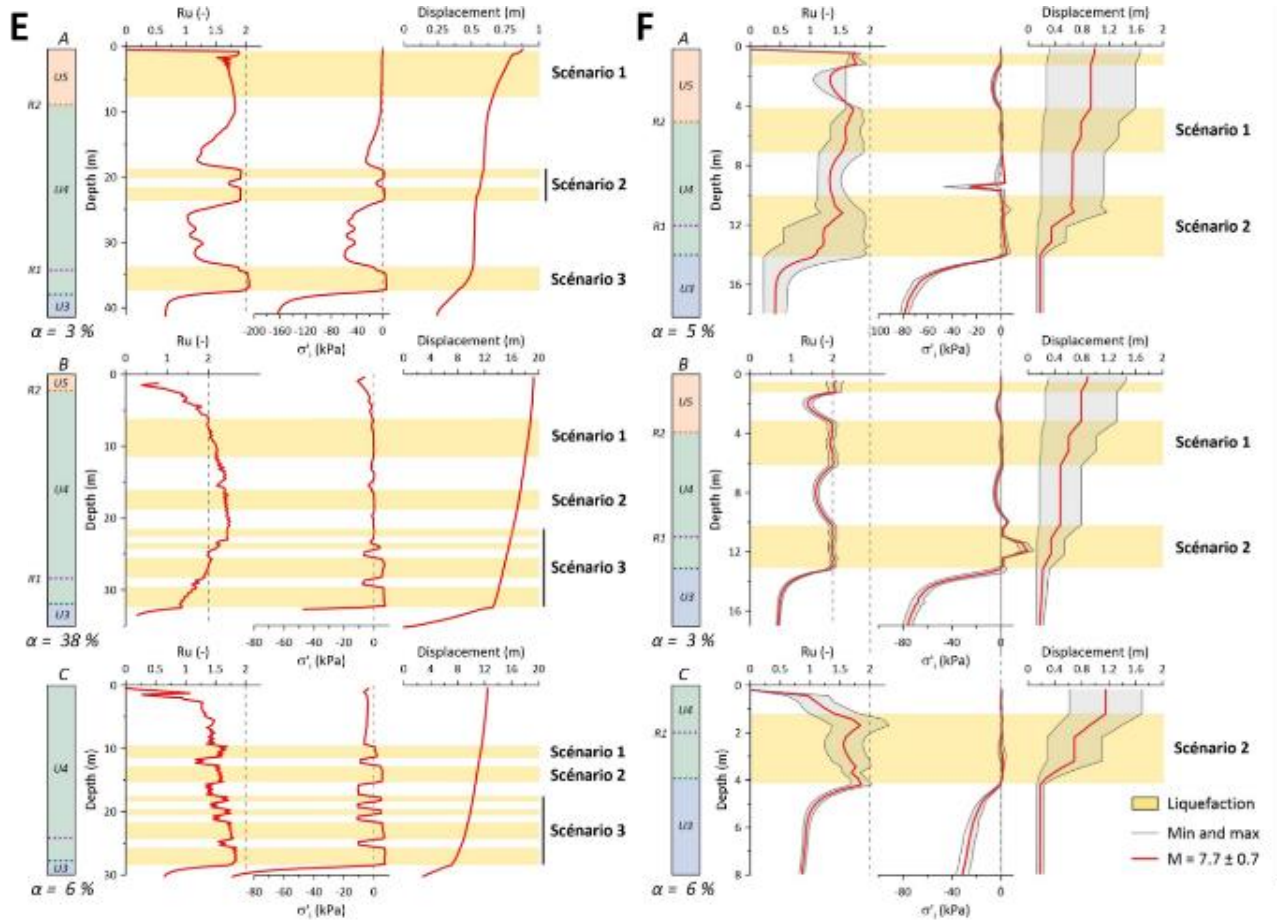

Figure 5-7. Results of the numerical simulation for Baie-Comeau (A), Betsiamites II and I (respectively B and C), Rimouski (D), Tadoussac (E) and Charlevoix (F) areas. From top to bottom: columns A, B and C. The evolution of excess pore pressure (R_u), first effective stress invariant (σ'_i) and displacement is shown in three separate graphs. The value of the slope gradient is expressed by α in percent.

can be seen in **Figure 5-1**, the distance is less than 10 km. Thus, the calculation predicts a PGA that is too large (~16 g) to be considered as realistic. At this distance, there is no difference between the simulations considering an earthquake of M 7.0 or M 8.4 (**Figure 5-7E)**. However, once again three scenarios can be considered. They correspond to the destabilization of the upper (Unit 5), intermediate (Unit 4), and deeper layers (Units 3 – 4 interface).

Lastly, the simulations at the Charlevoix area reveal two liquefaction scenarios in the case of an earthquake of magnitude M 7.7 ± 0.7 (**Figure 5-7F)**. The first scenario corresponds to the liquefaction of the sand layer at the interface between Units 4 and 5 and the second scenario to liquefaction at the interface between Units 3 and 4.

3.3.2. Thickness of sediment destabilized

The thickness of destabilized sediments is measured upstream of the failure scar. It corresponds to the thickness between the deepest liquefiable layers and the seafloor. The calculated thicknesses are summarized in **Table 5-2**. They are less than 10 m for Betsiamites II and Rimouski areas with respective values of 7 m, and 2 to 8 m. The thicknesses are similar at the Baie-Comeau, Betsiamites I and Charlevoix zones for the first scenarios, but reach 13 m, 18 m and 14 m,

Table 5-2. Heights destabilized for each scenario in the six MTC areas.

Area	Scenario #	Height destabilized (m)
Baie-Comeau	1	2
	2	9
	3	13
Betsiamites I	1	2
	2	6
	3	18
Betsiamites II	1	7
Rimouski	1	2
	2	8
Tadoussac	1	12
	2	23
	3	37
Charlevoix	1	7
	2	14

respectively, for the deeper failure scenarios. At Tadoussac, the scenarios foresee the larger thicknesses between 12 and 37 m.

In summary, in the case of the destabilization of Unit 5, the destabilized sedimentary columns are less than 7 m thick, while the liquefaction of the deeper sand layers at the interface between Units 3 and 4 generates larger submarine landslides with a maximum depth reaching 37 m at Tadoussac. Estimating the maximum thicknesses of submarine landslides is essential for geohazards assessment, but the determination of the volume is additionally essential to estimate the landslide induced tsunami potential. Unfortunately, the 1D calculation carried out in this study prevents the accurate determination of landslide volumes.

4. DISCUSSION

4.1. Predicted geomorphology after submarine landslide

Numerical simulations show that all six sites will be destabilized in the event of an earthquake similar to that of 1663 CE. Although the numerical simulations of the 1663 CE earthquake were only performed on three columns and not on the whole slope, the location of the failure plane can be determined by extrapolating between the different liquefaction sites. **Figure 5-8** presents the interpretation of the numerical simulations. Thus, the morphologies of the submarine slopes are schematically drawn for the six sites in the case of a future earthquake equivalent in magnitude and location to 1663 CE. All scenarios of liquefaction presented previously are considered (**Figure 5-8**). The location of the scars generated by future submarine landslides cannot be accurately determined. Sedimentary deposits triggered by submarine landslides may progressively evolve into mass transports, debris flows and finally turbidity currents in the distal part (**Figure 5-8**). The evolution of a submarine landslide in turbidite depends however on several factors (e.g., rheology, slope gradient, abrasion; Mulder and Cochonat, 1996). The evolution of submarine landslides is therefore speculative and can only be confirmed by flow models (e.g., Miramontes *et al.*, 2020; Ge *et al.*, 2022).

Post-earthquake morphologies at Betsiamites I, II and Baie-Comeau will be equivalent to the previous case, with sediments sliding on Unit 3 for the worst case scenarios, while for the other scenarios, only the upper part will slide. As the slope in Rimouski is low (~1%), it is expected that the deposits will be transported less far in case of massive slope failure. In contrast, at Tadoussac, the high slope gradient (38%) and the large predicted rupture (37 m) depth should result in a more massive and widespread MTD. In Charlevoix, the older submarine MTD is above the sand layers at the base of Unit 4. Thus, in the case of liquefaction

of this layer, the intact sediment and MTD may slide over Unit 3. This remobilization of older deposits could increase the hazard in this area.

4.2. Weak layers and retrogressive failure

For scenarios where the deeper layers liquefy, the failure plane seems to follow the sedimentary interface between the stratified Unit 4 and Unit 3 composed of glaciomarine clay. For the "upper-layer only" liquefaction scenarios, which required lower PGA (**Figure 5-8** - **Figure 5-9**), liquefaction occurs at the interface between Units 4 and 5. These sedimentary interfaces are associated to the ice sheet dynamics in eastern Canada during the last glaciation (Syvitski and Praeg, 1989). The transition between Units 3 and 4 marks the transition from glaciomarine to postglacial conditions. Layers of stratified silt and coarser sand characterize Unit 4. Liquefaction appears to be concentrated in these sandy levels and especially on the R1 reflector as assumed by Cauchon-Voyer *et al.* (2011). Unit 5 marks the transition from paraglacial to modern sedimentation characterized by coarser layers (Syvitski and Praeg, 1989). These sedimentary transitions have been characterized as highly liquefiable based on geotechnical testing (Mérindol *et al.*, 2022b).

Quaternary sedimentation in the St. Lawrence Estuary is conformable, i.e., the seismic reflectors are parallel (e.g., Cauchon-Voyer *et al.*, 2008). Thus, if the failure planes are consistently localized at the interface between Units 3 and 4 and between Units 4 and 5, the present day slope gradient should not significantly change following future earthquake-triggered slope failures (**Figure 5-8**). Retrogressive landslides are generally observed when slopes gradients are exacerbated after an initial slide event (Prior and Suhayda, 1979; Mulder and Cochonnat, 1996).

Thus, following an earthquake, it is not expected that a submarine landslide will generate a series of others in the short term. However, in the present study, we refer to retrogressive failure development because earthquakes may generate successive destabilizations that can, in the longer term, cause the upstream migration of head scars. This process can be verified by simulating successive slides and the progressive removal of destabilized areas (e.g., Lin *et al.*, 2016).

4.3. Geohazard approach

The geohazard posed by submarine mass-movements can only be accurately assessed through numerical simulations (e.g., Poncet *et al.*, 2010; Miramontes *et al.*, 2018; Turmel *et al.*, 2019). However, in this section, we attempt to compare the six areas and assess the relative slope failure hazard.

The most critical scenarios correspond to the liquefaction of the deepest sand layers at the interface between Unit 3 and Unit 4 because they would remobilize the thickest of sediment accumulation. In these scenarios, the volumes of sediment transported are expected to be larger if we consider the sediment column as laterally homogeneous (**Figure 5-8**). The resulting hazards are in these cases the most severe. Indeed, the thickness and the volume of submarine landslides in addition to the initial acceleration are the major parameters controlling the surface elevation of tsunamis (Harbitz *et al.*, 2006). In the area of Tadoussac, a future submarine landslide is estimated to reach ~ 40 m thick as it is the closest to

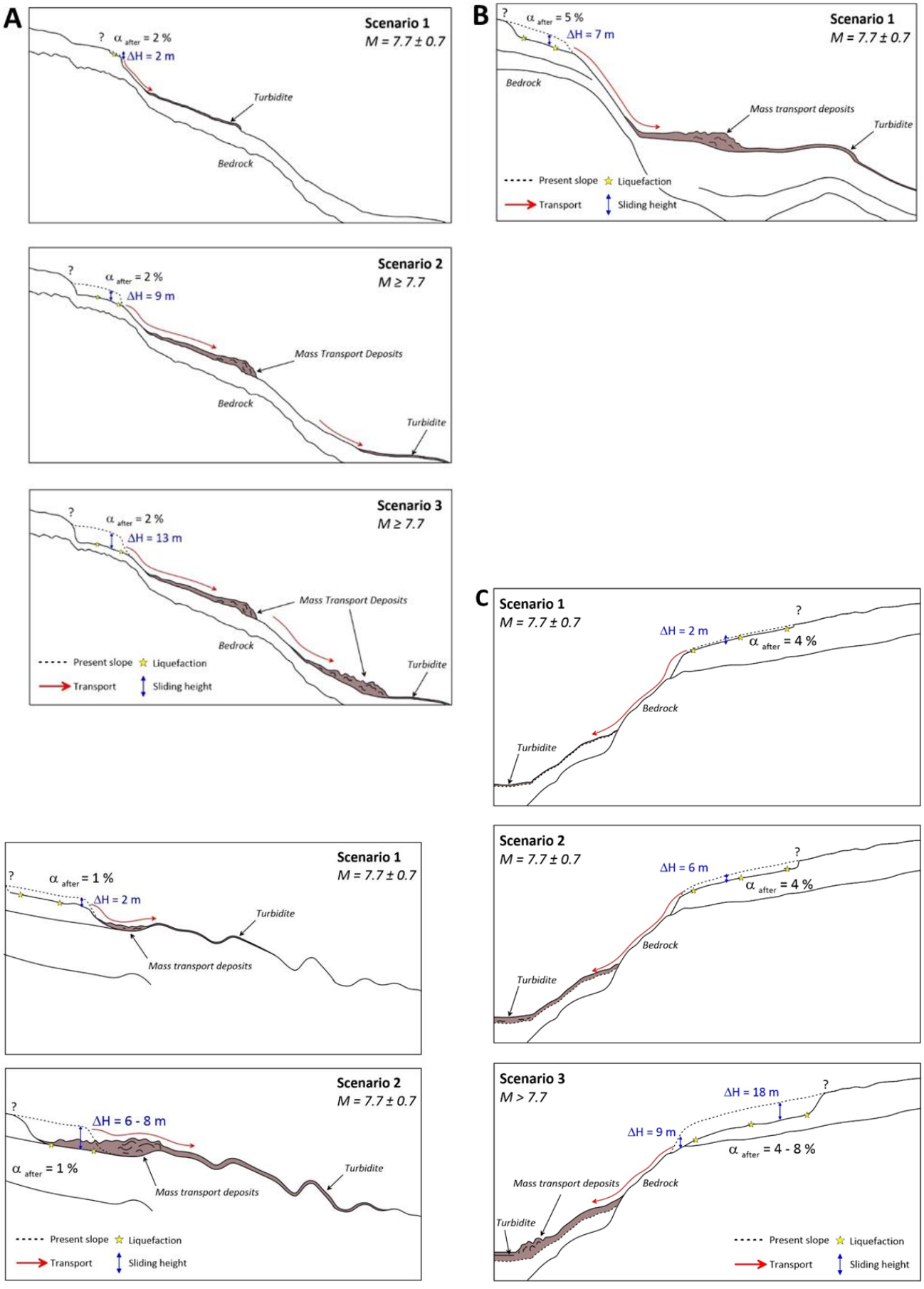
A
Scenario 1
M = 7.7 ± 0.7
? α after = 2 %
ΔH = 2 m
Turbidite
Bedrock
Scenario 2
M ≥ 7.7
? α after = 2 %
ΔH = 9 m
Mass Transport Deposits
Bedrock
Turbidite
Scenario 3
M ≥ 7.7
? α after = 2 %
ΔH = 13 m
Mass Transport Deposits
Bedrock
Turbidite
Present slope
Liquefaction
Transport
Sliding height
B
Scenario 1
M = 7.7 ± 0.7
? α after = 5 %
ΔH = 7 m
Bedrock
Mass transport deposits
Turbidite
Present slope
Liquefaction
Transport
Sliding height
C
Scenario 1
M = 7.7 ± 0.7
ΔH = 2 m
? α after = 4 %
Bedrock
Turbidite
Scenario 2
M = 7.7 ± 0.7
ΔH = 6 m
? α after = 4 %
Bedrock
Turbidite
Scenario 3
M > 7.7
ΔH = 18 m
ΔH = 9 m
? α after = 4 - 8 %
Mass transport deposits
Bedrock
Turbidite
Present slope
Liquefaction
Transport
Sliding height
D
Scenario 1
M = 7.7 ± 0.7
? α after = 1 %
ΔH = 2 m
Turbidite
Mass transport deposits
Scenario 2
M = 7.7 ± 0.7
? ΔH = 6 - 8 m
α after = 1 %
Turbidite
Mass transport deposits
Present slope
Liquefaction
Transport
Sliding height

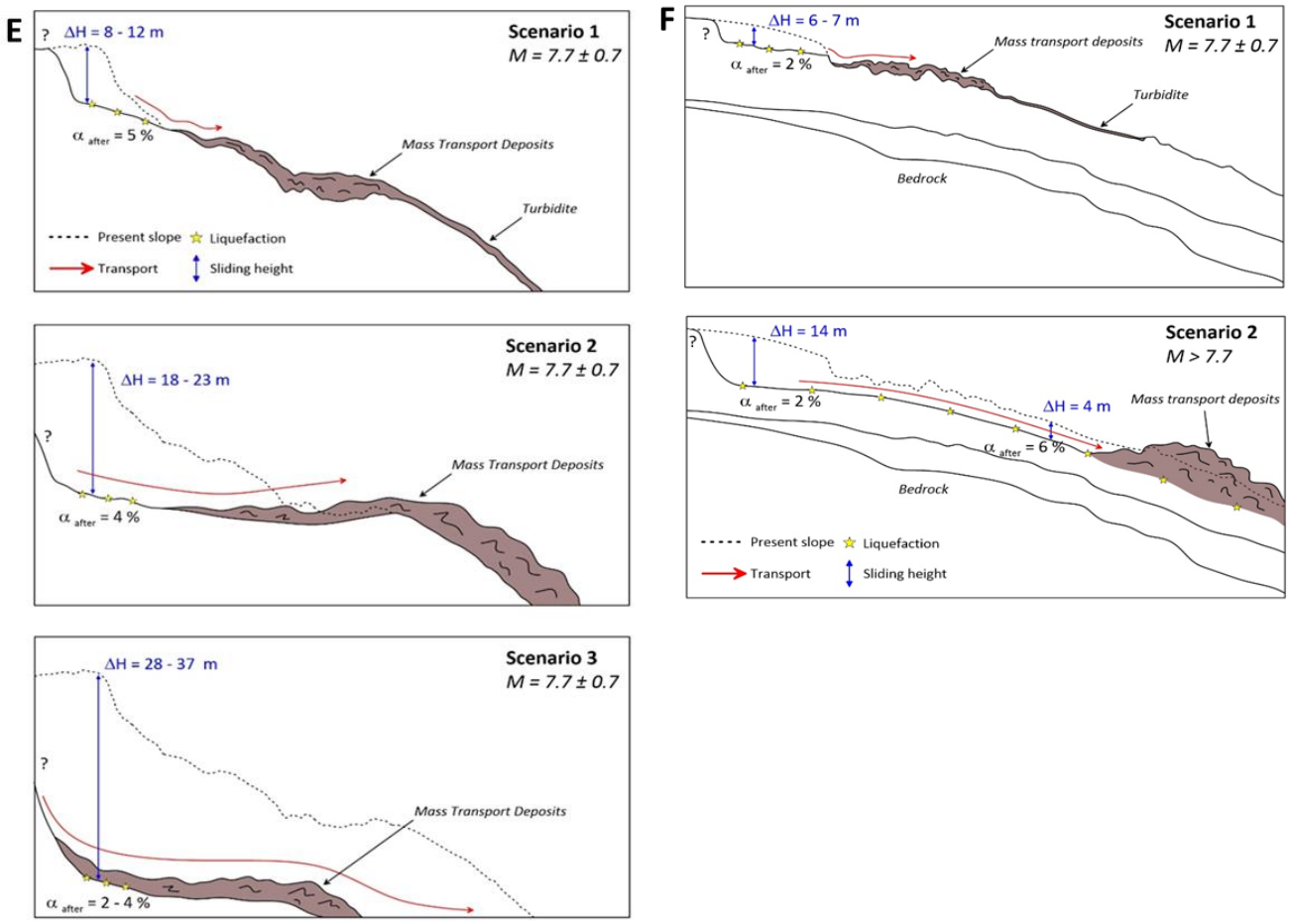

Figure 5-8. Interpretation of the post-earthquake morphology of submarine slopes for each area: Baie-Comeau (A), Betsiamites II and I (respectively B and C), Rimouski (D), Tadoussac (E) and Charlevoix (F). The dashed lines indicate the present day slope. For the different scenarios, liquefaction is predicted to occur where the yellow stars are plotted. The thickness of sediments above potential failure surfaces is shown in blue.

an active fault. The hazard in this area is therefore very high.

However, the tsunamis generated by submarine landslides are most dangerous when generated in shallow waters (Ward, 2001; Harbitz *et al.*, 2006). The shallowest sites are Rimouski and Charlevoix with water depths of ~ 35 m. Considering that the estuary is the narrowest in Charlevoix (~15 km), the generation of a tsunami in this area could probably have the greatest impact on the coast. In addition, the coastal town of Rivière-du-Loup, with a population of 20 000, is located nearby the Charlevoix site which significantly increases the risk level. However, the tsunami-generation potential depends on several other parameters such as the initial acceleration, the maximum speed, or the behavior of the sediments (Løvholt *et al.*, 2005; Harbitz *et al.*, 2006). Therefore, this hazard cannot be precisely assessed in the present work. All the observations presented here could be considered as a first step to developing future numerical analyses aiming at forecasting landslide-tsunami generation and associated hazards.

The PGA required to destabilize the six areas have been calculated, i.e., PGA to trigger liquefaction in the sedimentary column. From these PGA and using the GMPEs for CENA (Pezeshk *et al.*, 2018), the equivalent magnitudes-distances

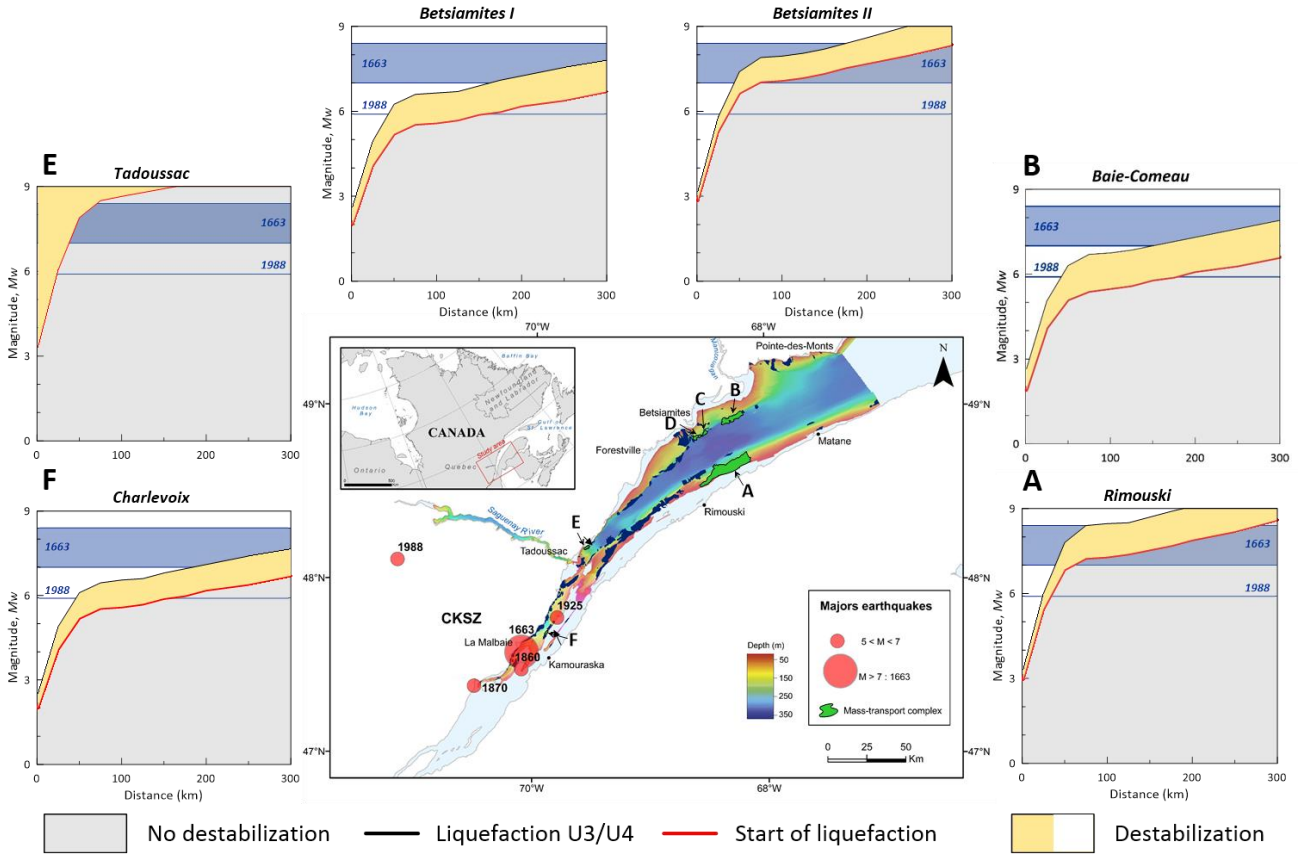

Figure 5-9. Synthesis of mass transport complexes which can be generated in the St Lauwrence Estuary by an earthquake similar to the 1663 CE event (in green). The surrounding graphs indicate the liquefaction potential in terms of distance and earthquake magnitude for each site. The red line is the limit of the liquefaction of silty-sandy layers. The black line shows the liquefaction of the interface between Units 3 and 4.

were calculated. **Figure 5-9** presents the relationship between the distance and magnitude required to liquefy sediments at the different sites. Thus, based on these diagrams, it is possible to determine for an earthquake of a given magnitude and epicenter location whether the six sites are susceptible to liquefaction. As the earthquake magnitude increases, the deep layers liquefy (**Figure 5-9**) and the hazards associated with submarine landslides are further increased. Two earthquakes are reported in **Figure 5-9**, 1663 CE (M 7.7 ± 0.7) and 1988 (M 5.9), to compare the distance from the source needed to destabilize sediments in the six MTCs areas. Rimouski, Betsiamites II and Tadoussac areas seem to be less susceptible to liquefaction compared to the three other zones (**Figure 5-9**).

5. CONCLUSION

As a critical part of the geohazards assessment of submarine landslide in Québec, slope stability analyses were carried out by considering an earthquake similar to that of 1663 CE, the strongest seismic event recorded in the last two millennia in the region (Mérindol *et al.*, 2022a). Even though 2D calculations were not successful, we were able to show that in case of an earthquake of magnitude M 7.7 ± 0.7 whit an epicenter located in Tadoussac, six MTC areas would destabilize again. The thickness of resulting submarine landslides was calculated to

provide input parameters to future risk studies considering landslide-tsunamis generation and propagation. We have also shown that the Tadoussac and Charlevoix sites seem to present the highest hazard in terms of earthquake-triggered landslides. In addition, a relationship was established to evaluate the potential of liquefaction for an earthquake with a given magnitude and distance, which could be an key ingredient in risk assessment.

Finally, it appears essential in future studies to carry out accurate two-dimensional or even three-dimensional slope stability analyses to better assess the risk associated with submarine landslides in the St. Lawrence Estuary. The risk can be significant, especially for landslides in shallow water areas (i.e., Rimouski and Charlevoix), where the danger is today largely unknown by the local population and institutions.

EN BREF

- Un séisme équivalent à l'évènement de 1663 CE déstabilisera les pentes sous-marines dans l'estuaire du Saint-Laurent de Charlevoix à Baie-Comeau (~200 km).
- Les épaisseurs maximales calculées des glissements sous-marins vont de 2 à 37 m.
- Les sites de Tadoussac et de Charlevoix présentent les aléas les plus élevés en termes de glissements sous-marins déclenchés par des séismes.
- Une relation a été établie pour évaluer le potentiel de liquéfaction en fonction de la magnitude et de la distance de l'épicentre du séisme.

IN SHORT

- An earthquake equivalent to 1663 CE event will destabilize submarine slopes in the St. Lawrence Estuary from Charlevoix to Baie-Comeau (~200 km).
- The maximum calculated landslide thicknesses range from 2 to 37 m.
- The Tadoussac and Charlevoix sites present the highest hazards in terms of earthquake-triggering landslides.
- A relationship was established for evaluating the liquefaction potential based on the magnitude and the distance from the earthquake epicenter.

CHAPITRE VI. CONCLUSIONS ET PERSPECTIVES

CHAPTER VI. CONCLUSIONS AND PERSPECTIVES

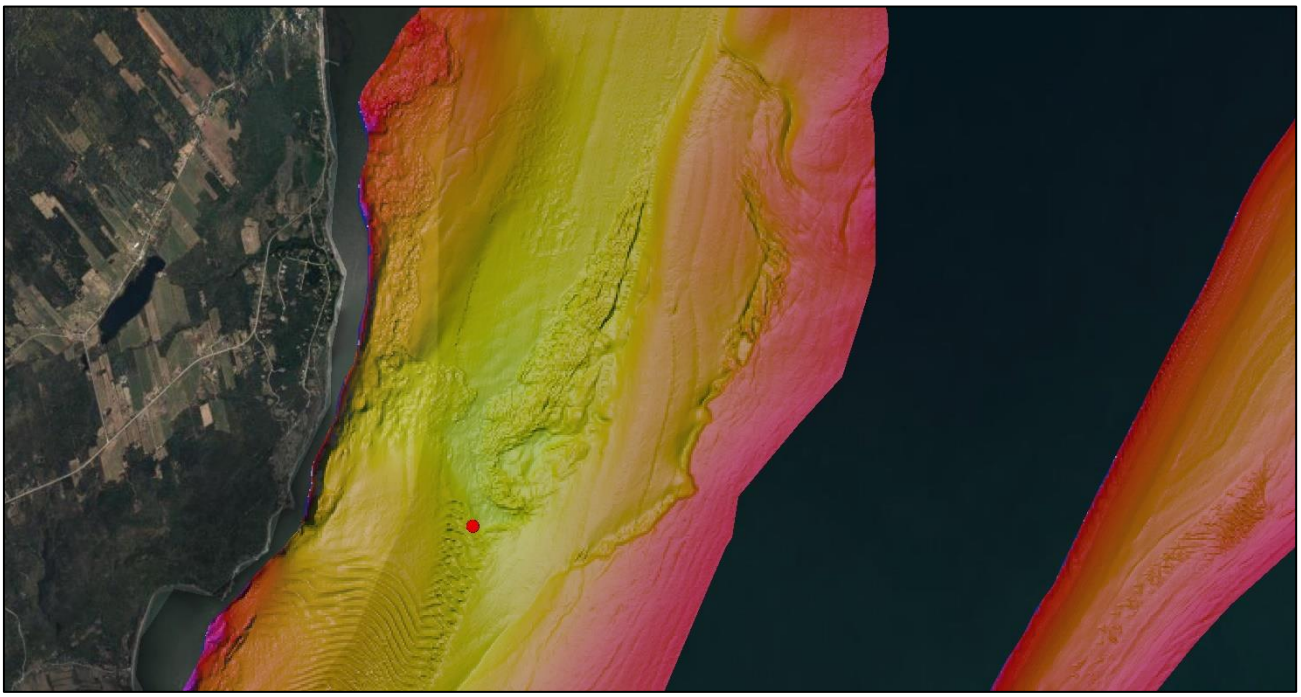

Glissement sous-marin cartographié dans la région de Charlevoix. Longueur cicatrice ~5 km
Submarine landslide mapped in the region of Charelvoix. Scar length ~5 km

CHAPITRE 6. RÉSUMÉ

CHAPTER 6. ABSTRACT

Les travaux de recherche de ce doctorat se sont structurés selon trois grands axes. Ils ont permis de répondre aux problématiques présentées en introduction et s'inscrivent dans un contexte scientifique visant à mieux appréhender les aléas naturels tels que la sismicité de l'Est du Canada et les glissements sous-marins dans l'estuaire du Saint-Laurent. En effet, ce travail a permis d'établir un lien entre les glissements sous-marins et la sismicité régionale et ainsi de retrouver des séismes préhistoriques. De plus, il a permis l'identification et la description des processus géomécaniques qui contrôlent la liquéfaction à l'origine des glissements sous-marins déclenchés par les séismes majeurs dont celui de 1663 CE. Ces résultats ont permis de proposer une corrélation entre une faille et l'épicentre du séisme de 1663 CE, le séisme majeur des derniers 2000 ans. Enfin, la thèse a abouti par l'étude des stabilités des pentes sous-marines dans l'estuaire et a permis de développer des scénarios de rupture en cas d'un futur séisme majeur.

Ce chapitre a pour but de synthétiser ces principaux résultats de ces travaux et de proposer des perspectives à ces travaux de recherche. Il se décompose en trois sous-parties correspondant aux trois thématiques abordées durant la thèse.

The PhD thesis is structured along three main axes. They allowed answering the questions presented in the introduction and are part of a scientific context aimed at better understanding natural hazards such as seismicity in Eastern Canada and submarine landslides in the St. Lawrence estuary. Indeed, this work has established a relationship between submarine landslides and regional seismicity and also allowed the identification and dating of prehistoric earthquakes. In addition, it has allowed the identification and description of the geomechanical processes that control liquefaction at the origin of submarine landslides triggered by major earthquakes including that of 1663 CE. These results proposed a correlation between a fault and the epicenter of the 1663 CE earthquake, the major earthquake of the last 2000 years. Finally, the thesis concluded with the study of the stability of the submarine slopes in the estuary and allowed the development of rupture scenarios in case of a future major earthquake.

The purpose of this chapter is to synthesize the main results of this work and to propose perspectives for this research work. It is divided into three sub-sections corresponding to the three themes addressed during the thesis.

1. PALEO-SISMOLOGIE

Les glissements sous-marins dans l'estuaire du Saint-Laurent, et plus largement dans la région du Québec, sont étudiés depuis plusieurs décennies. L'un des intérêts principaux de leur étude réside dans l'identification de leur mécanisme de déclenchement qui est souvent lié à la sismicité régionale. Ainsi, la datation de l'occurrence des glissements sous-marins peut permettre de dater des séismes au-delà de l'enregistrement historique et en conséquence d'être utilisée comme proxys de la sismicité du passé.

La mission SLIDE-2020 a permis l'identification par la géophysique et l'échantillonnage des sous-produits sédimentaires des glissements sous-marins qui correspondent aux Rapidly Deposited Layers (RDLs). En effet, les profils sismiques ont révélé la présence de réflecteurs sub-horizontaux de forte amplitude au prolongement des Mass-Transport Deposits (MTDs). Parce qu'à ces mêmes profondeurs, l'analyse sédimentologique montrait la présence de RDLs, ces réflecteurs ont pu être caractérisés. La datation des RDLs par les méthodes au ^{14}C et ^{210}Pb a permis de calculer l'âge des glissements sous-marins. Douze glissements sous-marins répartis sur l'ensemble de l'estuaire du Saint-Laurent ont ainsi pu être datés. Quatre périodes avec des glissements sous-marins synchrones sur une distance de ~220 km ont pu être identifiées. Ces périodes sont corrélées aux séismes historiques majeurs des 400 dernières années : 1663 CE ($M \geq 7$), 1860/1870 CE (M = 6,1/6,6), 1925 CE (M = 6,1) et 1988 CE (M = 5,9). Le synchronisme des glissements s'étendant sur une zone d'étude de près de 220 km de long et les sites de carottages se situant en dehors de zones influencées par les tempêtes, les crues de rivières ou les chenaux turbiditiques actifs supportent la relation entre les glissements sous-marins et la sismicité régionale. De plus, le séisme de 1663 CE ayant déclenché le plus de glissements sous-marins, apparait comme l'évènement majeur de ces deux derniers millénaires dans l'Est du Canada. L'établissement du lien entre les déstabilisations sous-marines et la sismicité a conduit à suggérer deux évènements sismiques autour de 645 CE et 1145 CE, c'est-à-dire antérieurs à la colonisation européenne. Ces évènements ont par ailleurs déjà été décrits dans des études passées (Normandeau *et al.*, 2013 ; Lajeunesse *et al.*, 2017 ; Trottier *et al.*, 2019 ; **Figure 6-1**).

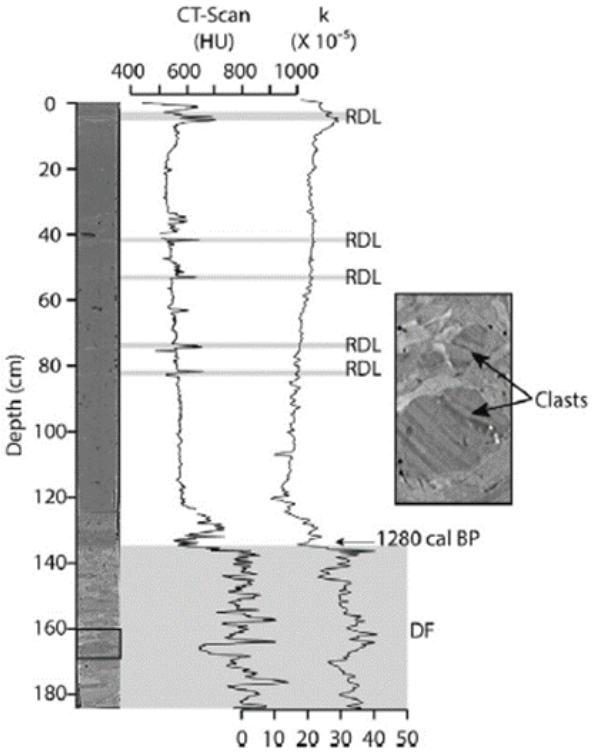

Figure 6-1. Identification et datation de RDLs dans une carotte prélevée dans le lac Témiscouata (Québec, Canada) par Lajeunesse *et al.*, 2017. La coulée de débris à ~1,30 m datée à 1280 cal BP, i.e., ~ 670 CE serait associée à une séisme régional majeur.

La méthode utilisée pour corréler les glissements sous-marins, i.e., synchronicité des dépôts sur une

large zone, n'est pas nouvelle et s'appuie sur les travaux menés par C. Goldfinger (e.g., Goldfinger *et al.*, 2012). Cependant, c'est la première fois que cette méthode a été appliquée à des turbidites déposées par des glissements sous-marins et non pas directement par des chenaux turbiditiques (e.g., Gracia *et al.*, 2010 ; Ratzov *et al.*, 2015). L'estuaire du Saint-Laurent s'est révélé être un site avantageux pour l'étude de la paléo-sismicité par le biais des turbidites déposées par les glissements sous-marins en n'étant pas influencé par des grandes tempêtes, des tsunamis distants et d'autre mécanisme déclencheurs, simplifiant le problème de distinguer les séismes des autres sources de déclenchement des glissements sous-marins. En effet, cette distinction est souvent difficile (e.g., Taïwan, Lallemand *et al.*, 2016) et c'est pour cette raison que l'utilisation des turbidites comme proxys de la paléo-sismicité est encore débattue (e.g., Talling *et al.*, 2021).

Enfin, la datation de 51 RDLs a permis l'élaboration d'une importante base de données qui participera à une meilleure compréhension de l'aléa sismique au Québec. Cette base de données pourra être mise en relation avec de futures études paléo-sismologiques en domaine lacustre, marin ou/et terrestre.

2. LIQUEFACTION ET INSTABILITES GRAVITAIRES

Le séisme de 1663 CE est l'évènement qui a déclenché le plus de glissements sous-marins dans l'estuaire du Saint-Laurent. Partant de cette première conclusion et sachant que son épicentre restait mal contraint, l'objectif était de proposer une nouvelle localisation de son épicentre à partir des datations établies dans le chapitre 1 couplées à l'analyse géotechnique et en combinant des approches expérimentales et numérique.

Contrairement aux carottes utilisées dans le chapitre 1, des carottes ont été prélevées dans le sédiment intact, i.e., non glissé, et dans les cicatrices de six zones de glissement sous-marin déclenchés par le séisme de 1663 CE afin de caractériser l'ensemble des faciès de la colonne sédimentaire. La caractérisation mécanique du sédiment et en particulier de son potentiel de liquéfaction, utilisé dans les calculs des facteurs de sécurité (FoS), impliquait la réalisation de 16 essais triaxiaux cycliques en laboratoire. Cette première approche théorique a conduit à déterminer à partir de quelles accélérations chacune des zones et couches sédimentaires se déstabilisait.

Les essais géotechniques ont également permis de déterminer les paramètres d'entrée du modèle de comportement mécanique PDMY02 (Yang *et al.*, 2003) qui tient compte du phénomène de liquéfaction. Une calibration de ce modèle à partir des essais triaxiaux cycliques a été réalisée afin de s'assurer qu'il reproduisait correctement le comportement du sédiment sous l'effet de charges cycliques. L'interprétation des profils sismiques et des données sédimentologiques a permis de reconstruire les logs lithostratigraphiques de la séquence sédimentaire quaternaire. Ils ont été intégrés dans les simulations numériques (OpenSees ; McKenna *et al.*, 2009) en tenant compte des paramètres qui régissent leur comportement mécanique. Le signal sismique considéré dans OpenSees correspondait à l'accélérogramme du séisme de 1988 au Saguenay (Québec). Des simulations successives ont été menées avec des intensités du signal variable afin

de déterminer l'accélération à partir de laquelle les couches se liquéfient.

Les deux méthodes ont ainsi permis de déterminer les accélérations nécessaires pour déstabiliser les six zones de glissement. L'utilisation d'une loi d'atténuation de l'accélération sismique en fonction de la distance, applicable à l'Est du Canada (Pezeshk *et al.*, 2018) a permis de convertir ces accélérations en distances. Deux scénarios de déstabilisations ont été identifiés avec un premier qui correspond à la liquéfaction de l'interface entre les unités sismiques 4 et 5 à moins de 7,5 m de profondeur, et un second où la liquéfaction se produit a plus de 7,5m, à l'interface entre les unités sismiques 3 et 4. Les distances minimales de l'épicentre du séisme de 1663 CE ont été calculées pour les six zones tout en considérant les deux scénarios de rupture.

Si la méthode utilisant les simulations numériques s'est révélée être plus précise, car elle prend en compte un vrai signal sismique et le comportement réel des sédiments, les deux méthodes ont convergé vers une localisation de l'épicentre du séisme de 1663 CE commune. Cette localisation se situe à 120 km au nord de l'épicentre jusqu'alors considéré dans le code du bâtiment du Canada, soit à 30 km d'une faille active au large de la ville de Tadoussac.

Ainsi, ces résultats permettront une meilleure évaluation des risques sismiques dans l'Est du Canada et suggèrent de réviser les cartes d'accélération au sol, outil crucial dans le code du bâtiment du Canada. En effet, ces cartes sont très sensibles à la localisation du séisme de 1663 CE. Son déplacement d'une centaine de kilomètres aura donc des répercussions majeures. De plus, ces résultats révèlent la nécessité de croiser de nouvelles méthodes de localisation des épicentres afin d'avoir des localisations plus précises, surtout dans le cas des séismes historiques antérieurs à l'avènement du déploiement massif des stations sismiques. Certaines études cherchant à déterminer l'épicentre de séismes à partir des phénomènes de liquéfaction (Obermeier, 1998) ou de glissement subaériens (Miles and Keefer, 2000 ; Locat, 2011) existent mais le couplage entre une approche théorique et une simulation numérique appliquée aux glissements sous-marins est inédit.

Au-delà de la détermination de l'épicentre du séisme de 1663 CE, les essais triaxiaux cycliques ont révélé un fort potentiel de liquéfaction des niveaux silteux à sableux. Ainsi, deux couches critiques, c'est-à-dire susceptible de se liquéfier lors d'un séisme, ont pu être identifiées. Elles correspondent à l'interface entre les unités sismiques 3 et 4 (profondeur ≤ 7,5 m), et 4 et 5 (profondeur > 7,5 m). La présence de ces niveaux hautement liquéfiables à ces interfaces sédimentaires supporte l'hypothèse que les glissements sous-marins sont déclenchés par les séismes régionaux. La caractérisation de ces interfaces identifiables par l'imagerie géophysique permet d'étendre considérablement les connaissances en termes d'instabilités gravitaires dans l'estuaire du Saint-Laurent.

3. EVALUATION DE LA STABILITE DES PENTES ACTUELLES

Les glissements sous-marins représentent un aléa géologique majeur dans l'Est du Canada (e.g., Grand Bancs, 1929). Même s'il est très difficile de prédire leur occurrence avec précision, il est possible d'évaluer des scénarios d'instabilité des

pentes sous-marines par des simulations numériques. Le but était ainsi d'évaluer la stabilité de zones de glissements actuelles réparties entre la région de Charlevoix et Baie-Comeau (~200 km). Ces zones déjà marquées par des glissements sous-marins présentent des cicatrices de glissements et des gradients de pentes pouvant dépasser 20%. Or, il est reconnu que les pentes fortes jouent un rôle prépondérant pour le préconditionnement des glissements sous-marins dans l'estuaire du Saint-Laurent (Pinet *et al.*, 2015). La stabilité de ces pentes a donc été évaluée dans le cas où un séisme similaire à celui de 1663 se reproduisait. Une magnitude de 7.7 ± 0.7 et un épicentre sur la faille de Tadoussac ont été considérés dans la modélisation en une dimension (OpenSees et GiD). Dans ces conditions, les six zones étudiées glisseraient en cas de séisme majeur avec des épaisseurs sédimentaires mobilisées variant de 2 à 37 m. Le site le plus proche de la faille de Tadoussac présenterait le plus fort aléa en termes d'épaisseur de glissement ainsi que la zone située dans Charlevoix en raison de la faible hauteur d'eau (< 40 m) et du rétrécissement de l'estuaire à cet emplacement.

Enfin, à partir des résultats des modélisations et de la loi d'atténuation de l'accélération sismique, une relation entre la distance et la magnitude d'un séisme pour atteindre la rupture a été établie. Ainsi, elle permet d'évaluer pour un séisme donné, si les zones se liquéfieront. Cela en fait un outil particulièrement utile dans l'évaluation des aléas futurs associés aux glissements sous-marins.

4. PERSPECTIVES DES TRAVAUX

4.1. Matériel sédimentaire disponible

Ces travaux de recherche reposent essentiellement sur les données collectées lors de la mission SLIDE-2020. Cela représente près de 30 glissements cartographiés soit 300 lignes géophysiques ou 1500 km de données. Les données sédimentaires consistent à 160 m cumulés de carotte sédimentaire répartis entre 50 sites de carottages. Pour répondre aux problématiques de la thèse, une centaine de carotte sédimentaires ont été ouvertes et analysées. Seulement une partie d'entre elles ont été utilisées pour dater 12 glissements sous-marins et caractériser la séquence sédimentaire. Ainsi, une grande partie des données (géotechniques et sédimentologiques) reste disponible. Les données géophysiques ont été utilisées seulement pour les glissements étudiés. Or, durant la mission, d'autres glissements ont été cartographiés, mais non carottés. L'ensemble de ces données pourrait donc être utilisées par la communauté scientifique pour compléter les travaux de la présente thèse ou explorer de nouvelles problématiques.

4.2. Paléoclimat – « red bed »

La séquence sédimentaire du Saint-Laurent est exceptionnelle car le contexte estuarien permet une bonne préservation des dépôts. Ainsi, il est possible de retrouver l'enregistrement des variations climatiques (de Vernal *et al.*, 1993), eustatiques (e.g., Dionne, 1988), paléo-magnétiques (St-Onge *et al.*, 2003) et anthropiques (e.g., St-Onge *et al.*, 2001). Plus au Nord, c'est dans la baie d'Hudson qu'a été décrit l'évènement climatique appelé « 8.2 ka event » où le drainage abrupt des lacs Agassiz et Ojibway a provoqué le refroidissement

global du climat (Broecker, 1997). Dans l'enregistrement sédimentaire, cet évènement a laissé un niveau rouge correspondant à des sédiments glacio-lacustres permettant des corrélations stratigraphiques régionales (Veillette, 1994 ; Barber *et al.*, 1999 ; Lajeunesse et St-Onge, 2008). Dans la carotte COR20-02-24GC, prélevées à proximité de l'embouchure du Fjord du Saguenay, l'analyse des propriétés physico-chimiques révèle la présence d'un niveau d'argile rouge d'environ 1 m d'épaisseur à 85 cm de profondeur (**Figure 6-2**). En effet, le paramètre a* est en moyenne de 3 pour cette couche contre -1 pour le reste de la carotte (**Figure 6-2**). La présence de ce niveau reste inexpliquée. S'il est peu probable que cette couche rouge provienne de la baie d'Hudson en raison de sa distance, une crue ou une débâcle glaciaire pourrait être à l'origine de ce dépôt. De nouvelles analyses minéralogiques et datations pourraient permettre d'interpréter l'origine de ce « red bed » et d'en faire un repère chrono-stratigraphique dans l'estuaire du Saint-Laurent.

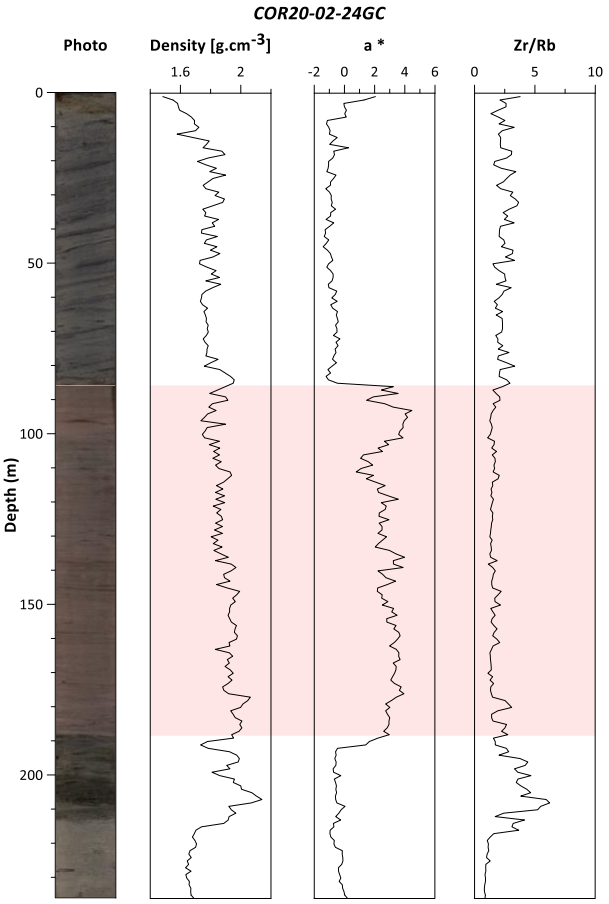

Figure 6-2. Propriétés physico-chimiques de la carotte COR20-02-24GC. De gauche à droite : photo, densité, a* et rapport Zr/Rb. Le « red bed » correspond à la zone en rouge entre 85 cm et 185 cm.

4.3. Glissements sous-marins non datés

Sur près de 100 glissements sous-marins recensés dans l'estuaire du Saint-Laurent (Pinet *et al.*, 2015), seul 12 d'entre eux ont été datés. Toutefois, ce nombre a permis d'établir une corrélation entre la sismicité historique et les glissements sous-marins. Dans l'optique de renforcer/valider cette relation, il pourrait être possible d'en dater un nombre encore supérieur. En outre, la datation de certains glissements pourrait expliquer l'origine de tsunamis encore inconnue, e.g., le tsunami de 1925 dans la région de Charlevoix (G. St-Onge, communication personnelle). Une datation exhaustive des glissements, permettrait également d'étudier la relation entre les caractéristiques des glissements, de leurs dépôts associés et la distance des épicentres des séismes (Uri *et al.*, 2008 ; Salamon *et al.*, 2019).

4.4. Activité de la faille de Tadoussac

La faille active de Tadoussac identifiée par Normandeau *et al.* (2015) et Pinet *et al.* (2021) est suspectée d'être à l'origine du séisme de 1663 CE. Des travaux supplémentaires pourraient être menés afin de valider cette conclusion. Il serait par exemple possible de dater le mouvement de la faille à l'aide de méthodes cosmogéniques (e.g., Brown *et al.*, 2002 ; Tesson *et al.*, 2016) ou par de nouveaux carottages sur la faille pour calculer des vitesses de sédimentation. De plus, des données

bathymétriques (**Figure 6-3**) et de sondeur de sédiment ont été acquises dans la zone de la faille lors de la mission SLIDE-2020 et par une mission AUV menée par P. Lajeunesse en 2020. Les résolutions des données bathymétriques sont nettement meilleures que celles utilisées par Normandeau *et al.* (2015) Pinet *et al.* (2021) pour identifier la faille. Le traitement et l'exploitation de ces données pourrait considérablement améliorer la connaissance de l'activité sismique de la faille.

4.5. Calculs de stabilité de pente

L'évaluation de la stabilité des pentes s'est focalisée sur des zones choisies pour être isolées de facteurs de déstabilisation autre que les séismes. Les zones investiguées ne permettent donc pas d'étudier par exemple le rôle de l'eau douce, du gaz ou de la charge sédimentaire sur la stabilité des pentes. Ainsi, afin de mieux caractériser l'aléa gravitaire régional il serait pertinent d'étendre les calculs de stabilité à de nouvelles zones non étudiées lors de la mission SLIDE-2020. Les simulations numériques pourraient également prendre en considération le rôle du gaz à partir de mesures *in situ* (e.g., piézomètres, Cauchon-Voyer *et al.*, 2011).

De plus, la modélisation de la stabilité des pentes à l'aide de GiD et OpenSees n'a pu se faire qu'en une dimension. Or, le logiciel peut permettre de faire des calculs de stabilité de pente en deux dimensions ce qui améliorerait considérablement la qualité et la fiabilité des résultats. En 1D, seules les épaisseurs des glissements ont pu être déterminés alors qu'en 2D, voire en 3D, les volumes pourraient être déterminés. Or, ce paramètre est crucial dans la modélisation des tsunamis. Ce travail en 2D a été mené durant plus d'un mois de la thèse (**Figure 6-4**), mais ce temps n'a pas été suffisant. En effet, plusieurs problèmes ont été rencontrés et n'ont pu être résolus. Ils ont entre autres attrait à la qualité du maillage et aux conditions aux limites (**Figure 6-4**). Également, le fichier d'entrée a été intégralement écrit à la main ce qui peut générer des erreurs de syntaxe. Cependant, plusieurs pistes pour les résoudre pourront être explorées dans le futur (i.e., maillage différent, codes pour vérifier le maillage, redéfinition de la géométrie etc.).

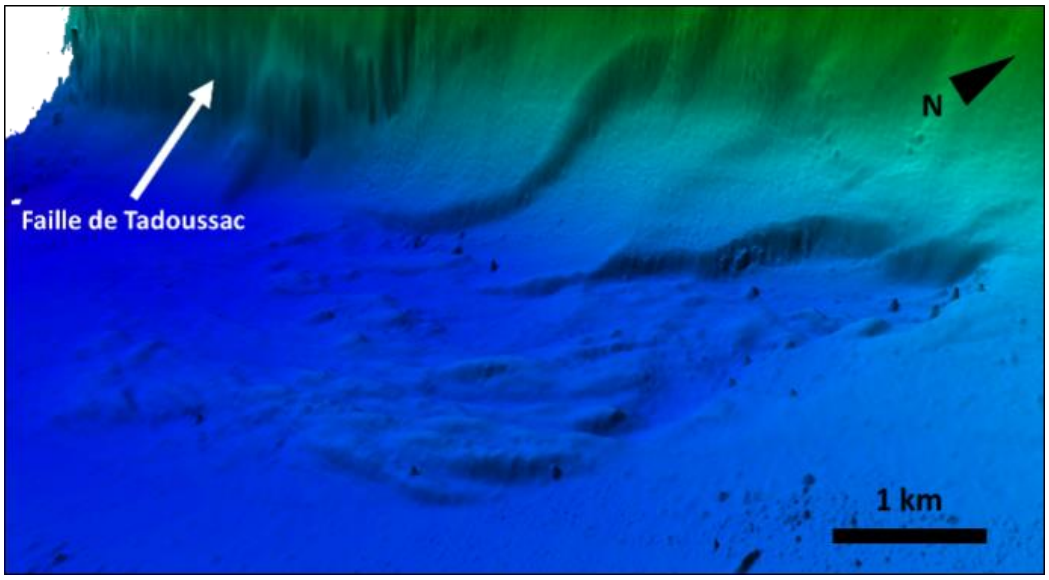

Figure 6-3. Image bathymétrique des glissements sous-marins qui s'organisent le long de la faille de Tadoussac.

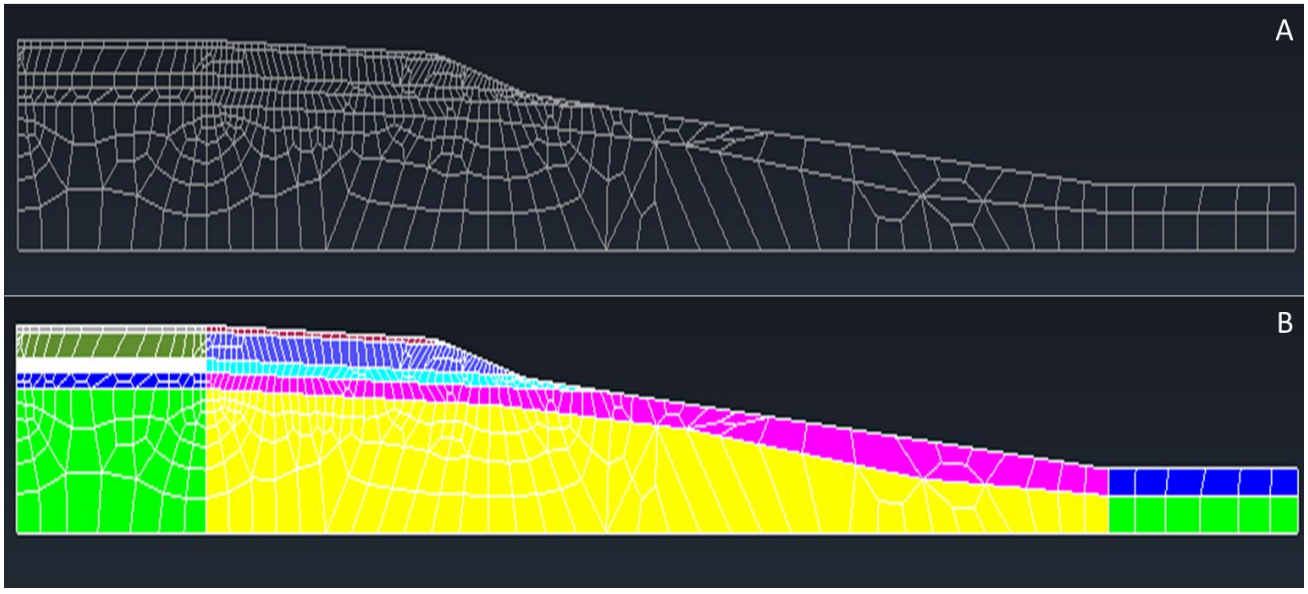

Figure 6-4. A) Modélisation de la pente de Baie-Comeau. B) Implémentation des différentes couches sédimentaires (unités 3 à 5 et le socle) avec leurs caractéristiques géomécaniques.

4.6. Glissement sous-marin tsunamigénique ?

Les instabilités des fonds marins et les processus de déformation ne présentent pas nécessairement un risque puisqu'ils peuvent se produire sans affecter la société par des dommages ou des risques non-contrôlés (Vanneste *et al.*, 2014). Cependant, un glissement sous-marin implique une variation brutale de la hauteur de la colonne d'eau pouvant ainsi générer un tsunami qui peut affecter les activités humaines implantées sur les zones côtières d'où la nécessité de cartographier les zones côtières inondables. L'élaboration de ces cartes repose sur une approche probabiliste (Probabilistic Tsunami Hazard Analysis, PTHA) qui considère la probabilité d'occurrence de tsunamis sur des périodes allant de plusieurs centaines à plusieurs milliers d'années (Grezio *et al.*, 2017). Si les tsunamis générés par les glissements de terrain se propagent moins efficacement que leurs homologues déclenchés par les tremblements de terre, leur élévation maximale et/ou leur mobilité peut être supérieure (Harbitz *et al.*, 2006). L'importance du tsunami dépend de l'accélération et du volume du glissement (Harbitz *et al.*, 2006). Au Québec (Canada), la majorité de la population vit à proximité de l'estuaire du Saint-Laurent et la perception du risque de tsunamis par les habitants reste encore faible comparée à l'érosion côtière (Friesinger et Bernatchez, 2010). À l'image des études de Poncet *et al.* (2010) à Saint-Siméon ou de Turmel *et al.* (2019) à Betsiamites, il devient primordial de mieux caractériser la génération de tsunamis par les glissements sous-marins. Cela pourrait être possible à l'aide des données acquises lors de la mission SLIDE-2020 (carottage et géophysique), des analyses géotechniques menées sur le sédiment et les volumes de glissement calculés par la modélisation (2D/3D). En effet, des modèles de propagation des tsunamis tenant compte des volumes glissés, des géométries, de la nature du sédiment, de la bathymétrie et des vitesses initiales de glissement (e.g., GeoClaw ; Turmel *et al.*, 2019) pourront être utilisés et appliqués pour les zones investiguées par la mission SLIDE-2020.

1. PALEOSEISMOLOGY

Submarine landslides in the St. Lawrence Estuary, and more widely in the Quebec region, have been studied for several decades. One of the main interests of their study lies in the identification of their triggering mechanism, which is often linked to regional seismicity. Thus, the dating of the occurrence of submarine landslides can allow to date earthquakes beyond the historical record and consequently to be used as proxies of paleoseismicity. Through geophysics and sampling of sedimentary by-products, the SLIDE-2020 expedition led to identifying submarine landslides that correspond to Rapidly Deposited Layers (RDLs). Indeed, seismic profiles revealed the presence of sub-horizontal reflectors of high amplitude at the prolongation of Mass-Transport Deposits (MTDs). At these same depths, a sedimentological analysis showed the presence of RDLs, and so we were able to characterize these reflectors. Dating of the RDLs by ^{14}C and ^{210}Pb methods allowed us to calculate the age of the submarine landslides. Four periods with synchronous submarine landslides were identified over a distance of ~220 km. These periods correlate with the major historical earthquakes of the last 400 years: 1663 CE ($M \geq 7$), 1860/1870 CE (M = 6.1/6.6), 1925 CE (M = 6.1), and 1988 (M = 5.9). The synchronicity of the slides extending over a study area of nearly 220 km and the coring sites being located outside areas influenced by storms, river flooding, or active turbiditic canyons, support the relationship between submarine landslides and regional seismicity. Moreover, the 1663 CE earthquake, which triggered the most submarine landslides, appears to be the major event of the last two millennia in eastern Canada. Establishing the link between submarine destabilization and seismicity has led to the suggestion of two other seismic events around 645 CE and 1145 CE, i.e., prior to European colonization. These events have, moreover, already been described in past studies (Normandeau *et al.*, 2013; Lajeunesse *et al.*, 2017; Trottier *et al.*, 2019; **Figure 6-1**).

The method used to correlate submarine slides, i.e., synchronicity of deposition over a large area, is not new and builds on work conducted by C. Goldfinger (e.g., Goldfinger *et al.*, 2012). However, this is the first time this method has been applied to turbidites deposited by submarine landslides and not directly by turbidic channels (e.g., Gracia *et al.*, 2010; Ratzov *et al.*, 2015). The St. Lawrence Estuary has proven to be an advantageous site for

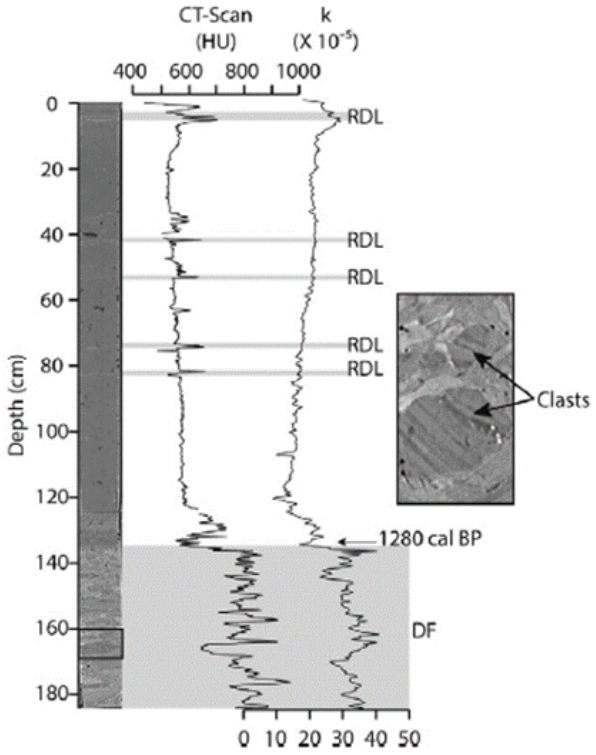

Figure 6-1. Identification and dating of RDLs in a core sampled from Lake Temiscouata (Quebec, Canada) by Lajeunesse *et al.*, 2017. The debris flow at ~1.30 m dated to 1280 cal BP, i.e., ~ 670 CE could be associated with a major regional earthquake.

studying paleoseismicity through turbidites deposited by submarine landslides because it is not influenced large storms, distant tsunamis and other triggering mechanisms, simplifying the problem of distinguishing earthquakes from other sources of landslide triggering. Indeed, this distinction is often difficult (e.g., Taiwan, Lallemand *et al.*, 2016) and for this reason the use of turbidites as proxies for paleoseismicity is still debated (e.g., Talling *et al.*, 2021).

Finally, the dating of 51 RDLs has allowed the elaboration of an important database that will contribute to a better understanding of the seismic hazard in Québec. This database could be linked to future paleoseismological studies in the lacustrine, marine and/or terrestrial domain.

2. LIQUEFACTION AND GRAVITY INSTABILITIES

The 1663 CE earthquake is the event that triggered the most submarine landslides in the St. Lawrence Estuary. Based on this first conclusion and knowing that its epicenter remained poorly constrained, the objective was to propose a new location of its epicenter based on the dates established in Chapter 1 coupled with geotechnical analysis and by combining experimental and numerical approaches.

Unlike the cores used in Chapter 1, cores were taken from the intact, i.e., non-slip, and from the scars of six submarine slip zones triggered by the 1663 CE earthquake in order to characterize the full range of facies in the sedimentary column. The mechanical characterization of the sediment and in particular its liquefaction potential, used in the calculation of the factors of safety (FoS), implied the realization of 16 cyclic triaxial tests in laboratory. This first theoretical approach led to the determination of the accelerations at which each of the sedimentary zones and layers would destabilize.

The geotechnical tests were also used to determine the input parameters for the PDMY02 mechanical behavior model (Yang *et al.*, 2003) that accounts for the liquefaction phenomenon. A calibration of this model from the cyclic triaxial tests was performed to ensure that it correctly reproduced the behavior of the sediment under cyclic loading. Interpretation of the seismic profiles and sedimentological data allowed the reconstruction of lithostratigraphic logs of the Quaternary sedimentary sequence. These were incorporated into numerical simulations (OpenSees; McKenna et al., 2009) taking into account the parameters that control their mechanical behavior. The seismic signal considered in OpenSees corresponded to the accelerogram of the 1988 Saguenay, Quebec earthquake. Successive simulations were conducted with varying signal intensities to determine the acceleration at which the layers liquefy.

Both methods thus determined the accelerations required to destabilize the six landslide zones. Using a distance-dependent seismic acceleration attenuation law applicable to eastern Canada (Pezeshk et al., 2018), these accelerations were converted to distances. Two destabilization scenarios were identified with the first corresponding to liquefaction at the interface between seismic units 4 and 5 at a depth of less than 7.5 m, and the second where liquefaction occurs at more than 7.5 m, at the interface between seismic units 3 and 4. Minimum distances from the epicenter of the 1663 CE earthquake were calculated for the six zones considering both rupture

scenarios. Although the method using numerical simulations proved to be more accurate, because it takes into account a real seismic signal and the real behavior of the sediments, both methods converged towards a common location of the epicenter of the 1663 CE earthquake. This location is 120 km north of the epicenter previously considered in the Canadian building code, or 30 km from an active fault off the town of Tadoussac.

Thus, these results will allow for a better assessment of the seismic risks in Eastern Canada and suggest a revision of the ground acceleration maps, a crucial tool in the Canadian building code. Indeed, these maps are very sensitive to the location of the 1663 EC earthquake. Its displacement of about 100 km will have major repercussions. Furthermore, these results reveal the need to combine new epicenter location methods to obtain more accurate locations, especially for historical earthquakes prior to the advent of large-scale seismic station deployment. Some studies seeking to determine the epicenter of earthquakes from liquefaction (Obermeier, 1998) or subaerial landslide (Milles and Keefer, 2000; Locat, 2011) exist, but the coupling between a theoretical approach and a numerical simulation applied to submarine landslides is novel.

Beyond the determination of the epicenter of the 1663 CE earthquake, the cyclic triaxial tests revealed a strong potential for liquefaction of the silty to sandy levels. Thus, two critical layers, i.e., likely to liquefy during an earthquake, have been identified. They correspond to the interface between seismic units 3 and 4 (depth ≤ 7.5 m), and 4 and 5 (depth > 7.5 m). The presence of these highly liquefiable levels at these sedimentary interfaces supports the hypothesis that regional earthquakes trigger submarine landslides. The characterization of these interfaces identifiable by geophysical imagery allows us to considerably extend our knowledge of gravity instabilities in the St. Lawrence Estuary.

3. EVALUATION OF CURRENT SLOPE STABILITY

Submarine landslides represent a major geological hazard in eastern Canada (e.g., Grand Banks, 1929). Although it is very difficult to predict their occurrence with precision, it is possible to evaluate instability scenarios of submarine slopes by numerical simulations. The aim was to evaluate the stability of current landslide zones distributed between the Charlevoix region and Baie-Comeau (~200 km). These areas, already affected by submarine landslides, present landslide scars and slope gradients that can exceed 20%. It is recognized that steep slopes play a dominant role in the preconditioning of submarine landslides in the St. Lawrence Estuary (Pinet *et al.*, 2015). Therefore, the stability of these slopes was assessed in the event of an earthquake similar to the 1663 earthquake. A magnitude of 7.7 ± 0.7 and an epicenter on the Tadoussac fault were considered in the one-dimensional modeling (OpenSees and GiD). In these conditions, the six zones studied would slip in the event of a major earthquake with mobilized sediment thicknesses ranging from 2 to 37 m. The site closest to the Tadoussac fault would present the greatest danger in terms of landslide thickness as well as the area located in Charlevoix due to the low water level (< 40 m) and the narrowing of the estuary at this location.

Finally, from the results of the modeling and the law of peak ground attenuation, a relationship

between the distance and magnitude of an earthquake to reach rupture was established. Thus, it allows to evaluate for a given earthquake, if the zones will liquefy. This makes it a particularly useful tool for assessing future risks related to submarine landslides.

4. PERSPECTIVES OF THE WORK

4.1. Available sedimentary material

This research work is mainly based on data collected during the SLIDE-2020 expedition. This represents nearly 30 landslides mapped, 300 geophysical lines and 1500 km of data. The sedimentary data consist of 160 m of cumulative sedimentary core distributed on 50 coring sites. To meet the challenges of the thesis, a hundred sedimentary cores were opened and analyzed. Only part of them were used to date 12 submarine slides and characterize the sedimentary sequence. Thus, a large part of the data (geotechnical and sedimentological) remains available. Geophysical data were used only for the slides studied. However, during the mission, other slides were mapped but not cored. All these data could be used by the scientific community to complete the work of this thesis or to explore new issues.

4.2. Paleoclimate – "red bed"

The sedimentary sequence of the St. Lawrence is exceptional because the estuarine context provides for good preservation of deposits. Thus, it is possible to find records of the variations in climate (Vernal *et al.*, 1993), eustatic (e.g., Dionne, 1988), paleo-magnetic (St-Onge *et al.*, 2003) and anthropogenic (e.g., St-Onge *et al.*, 2001). Further north, the so-called "8.2 ka event" is described in Hudson Bay, where abrupt drainage of lakes Agassiz and Ojibway caused global cooling of the climate (Broecker, 1997). In the sediment record, this event resulted in a red layer corresponding to glaciolacustrine sediments allowing regional stratigraphic correlations (Veillette, 1994; Barber *et al.*, 1999; Lajeunesse and St-Onge, 2008). In core COR20-02-24GC, collected near the mouth of the Saguenay Fjord, the analysis of physico-chemical properties reveals the presence of a red clay layer about 1 m thick at a depth of 85 cm (**Figure 6-2**). Indeed, the parameter a* is on average 3 for this layer against -1 for the rest of the core (**Figure 6-2**). The presence of this layer remains unexplained. Although it is unlikely that this red layer originated from the Hudson Bay because of the distance, a

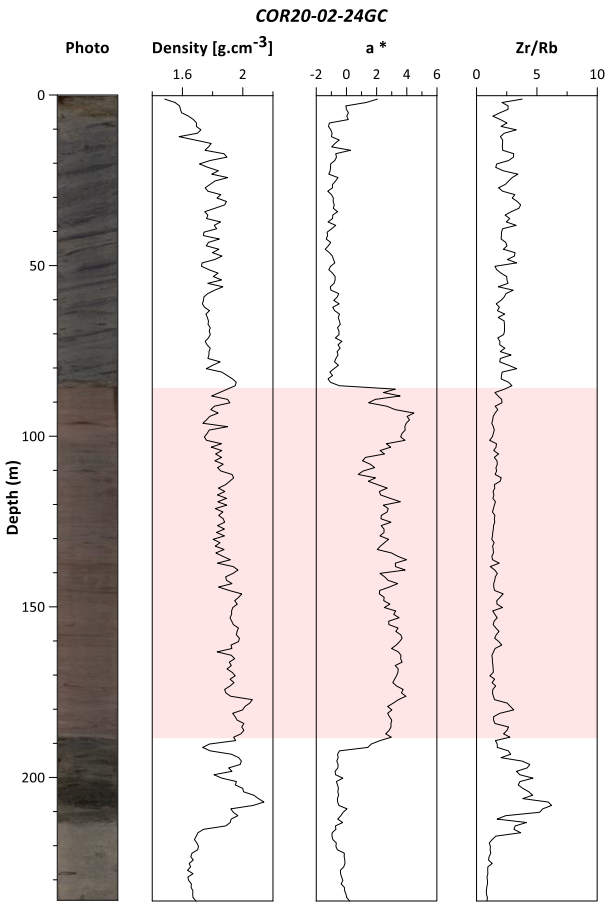

Figure 6-2. Physico-chemical properties of core COR20-02-24GC. From left to right: photo, density, a* and Zr/Rb ratio. The "red bed" corresponds to the red layer between 85 cm and 185 cm.

glacial flood or breakup could have caused this deposit. Additional mineralogical analyses and dating could help interpret the origin of this "red bed" and make it a chrono-stratigraphic marker in the St. Lawrence Estuary.

4.3. Undated submarine landslides

Of nearly 100 submarine landslides identified in the St. Lawrence Estuary (Pinet et al., 2015), only 12 have been dated. However, this number has allowed for a correlation between historical seismicity and submarine landslides. In order to strengthen/validate this relationship, it may be possible to date even more of them. In addition, the dating of some landslides could explain the origin of tsunamis with an undetermined origin, e.g., the 1925 tsunami in the Charlevoix region (G. St-Onge, personal communication). Comprehensive dating of landslides, would also allow investigation of the relationship between the characteristics of landslides, their associated deposits, and the distance from earthquake epicenters (Uri *et al.*, 2008; Salamon *et al.*, 2019).

4.4. Activity of the Tadoussac fault

The active Tadoussac fault identified by Normandeau *et al.* (2015) and Pinet *et al.* (2021) is suspected to be the origin of the 1663 CE earthquake. Further work could be conducted to validate this conclusion. For example, it would be possible to date the movement of the fault using cosmogenic methods (e.g., Brown *et al.*, 2002; Tesson *et al.*, 2016) or by new coring on the fault to calculate sedimentation rates. In addition, bathymetric (**Figure 6-3**) and sediment sounder data were acquired in the fault area during the SLIDE-2020 expedition and by an AUV mission led by P. Lajeunesse in 2020. The resolutions of the bathymetric data are significantly better than those used by Normandeau *et al.* (2015) Pinet *et al.* (2021) to identify the fault. Processing and exploitation of these data could significantly improve knowledge of the seismic activity of the fault.

4.5. Slope stability calculations

The assessment of slope stability focused on areas chosen to be isolated from destabilizing

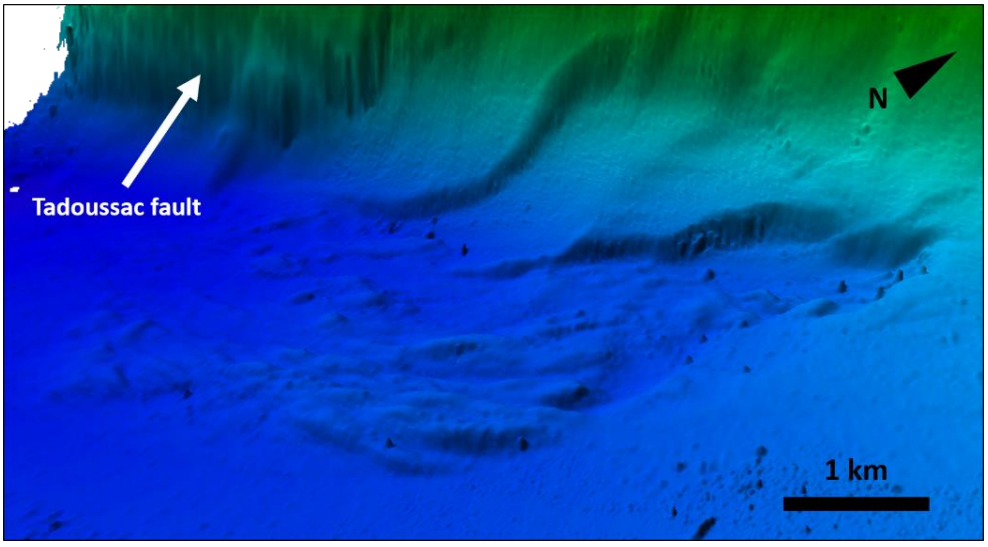

Figure 6-3. Bathymetric image of the submarine slides along the Tadoussac fault.

factors other than earthquakes. The investigated areas do not allow to study for example the role of fresh water, gas or sedimentary load on slope stability. Thus, in order to better characterize the regional gravity hazard, it would be relevant to extend the stability calculations to new areas not studied during the SLIDE-2020 expedition. Numerical simulations could also consider the role of gas from in situ measurements (e.g., piezometers, Cauchon-Voyer *et al.*, 2011).

In addition, slope stability modeling using GiD and OpenSees could only be done in one dimension. However, the software can accommodate two-dimensional slope stability calculations which would greatly improve the quality and reliability of the results. In 1D, only the thicknesses of the landslides could be determined whereas in 2D, or even 3D, the volumes can be determined. This parameter is crucial in tsunami modeling. The work in 2D was conducted over a one-month period during thesis (**Figure 6-4**), but this time was insufficient. Indeed, several problems were encountered and could not be solved. They were related to the quality of the mesh and the boundary conditions (**Figure 6-4**). Also, the input file was entirely written by hand which can generate syntax errors. However, several possibilities to solve them could be explored in the future (i.e., different mesh, codes to check the mesh, redefinition of the geometry etc.).

4.6. Tsunamogenic submarine landslide?

Seafloor instabilities and deformation processes do not necessarily pose a risk as they can occur without affecting society through damage or uncontrolled risk (Vanneste *et al.*, 2014). However, a submarine landslide implies a brutal variation in the height of the water column that can generate a tsunami, which can affect human activities in coastal areas, hence the need to map the coastal flood zones. The development of these maps is based on a Probabilistic Tsunami Hazard Analysis (PTHA) approach that considers the probability of tsunami occurrence over time periods ranging from

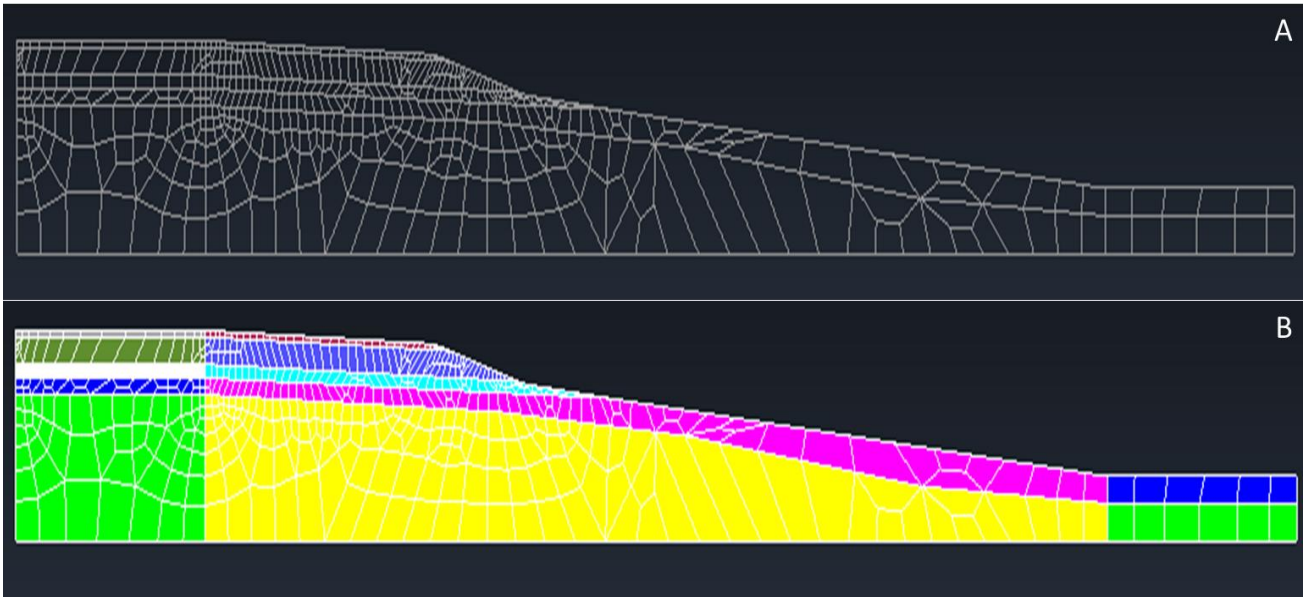

Figure 6-4. A) Modeling of the Baie-Comeau slope. B) Integration of the different sedimentary layers (seismic units 3 to 5 and the basement) with their geomechanical characteristics.

several hundreds to several thousands of years (Grezio *et al.*, 2017). While tsunamis generated by landslides propagate less efficiently than their earthquake-triggered counterparts, their maximum elevation and/or mobility may be greater (Harbitz *et al.*, 2006). The size of the tsunami depends on the acceleration and volume of the landslide (Harbitz *et al.*, 2006). In Québec, the majority of the population lives near the St. Lawrence estuary and the perception of tsunami risk by the inhabitants remains low compared to coastal erosion (Friesinger and Bernatchez, 2010). Like the studies of Poncet *et al.* (2010) at St. Siméon or Turmel *et al.* (2019) at Betsiamites, it becomes crucial to better characterize tsunami generation by submarine slides. This could be possible using data acquired during the SLIDE-2020 expedition (coring and geophysics), geotechnical analyses conducted on the sediment and slip volumes calculated by modeling (2D/3D). Indeed, tsunami propagation models that consider slip volumes, geometries, sediment nature, bathymetry, and initial slip velocities (e.g., GeoClaw; Turmel *et al.*, 2019) will be able to be used and applied to the areas investigated by the SLIDE-2020 expedition.

BIBLIOGRAPHIE

REFERENCES

Abrahamson, N.A., Silva, W.J., Kamai, R., 2014. Summary of the ASK14 ground motion relation for active crustal regions. Earthquake Spectra 30, 1025-1055.

Adams, J., Atkinson, G., 2003. Development of seismic hazard maps for the proposed 2005 edition of the National Building Code of Canada. Canadian Journal of Civil Engineering 30, 255-271.

Adams, J., Basham, P., 1989. The seismicity and seismotectonics of Canada east of the Cordillera. Geoscience Canada 16, 3-16.

Anglin, F., 1984. Seismicity and faulting in the Charlevoix zone of the St. Lawrence Valley. Bulletin of the Seismological Society of America 74, 595-603.

Appleby, P.G., Oldfield, F., 1978. The calculation of lead-210 dates assuming a constant rate of supply of unsupported 210Pb to the sediment. Catena 5, 1-8.

Assameur, D.M., Mareschal, J.-C., 1995. Stress induced by topography and crustal density heterogeneities: implication for the seismicity of southeastern Canada. Tectonophysics 241, 179-192.

ASTM, D., 2013. Standard test method for load controlled cyclic triaxial strength of soil. Annual book of ASTM 11.

Babonneau, N., Guérin, C., Ratzov, G., Lallemand, S., Condomines, M., Su, C.-C., Hsu, S.-K., Lin, A.T., Cattaneo, A., Mercier De Lepinay, B., 2019. Extreme events recorded in sediment cores of the Hateruma forearc basin, southern Ryukyus (MD214 EAGER Oceanographic Cruise), AGU Fall Meeting Abstracts, pp. OS51C-1501.

Banerjee, R., Chattaraj, R., Parulekar, Y., Sengupta, A., 2021. Numerical prediction of undrained cyclic triaxial experiments on saturated Kasai river sand using two constitutive models of liquefaction. Bulletin of Engineering Geology and the Environment 80, 8565-8582.

Barber, D.C., Dyke, A., Hillaire-Marcel, C., Jennings, A.E., Andrews, J.T., Kerwin, M.W., Bilodeau, G., McNeely, R., Southon, J., Morehead, M.D., 1999. Forcing of the cold event of 8,200 years ago by catastrophic drainage of Laurentide lakes. Nature 400, 344-348.

Basham, P., Weichert, D., Berry, M., 1979. Regional assessment of seismic risk in eastern Canada. Bulletin of the Seismological Society of America 69, 1567-1602.

Bernatchez, P., 2003. Évolution littorale holocène et actuelle des complexes deltaïques de Betsiamites et de Manicouagan-Outardes: synthèse, processus, causes et perspectives.

Bernatchez, P., Boucher-Brossard, G., Sigouin-Cantin, M., 2012. Contribution des archives à l'étude des événements météorologiques et géomorphologiques causant des dommages aux côtes du Québec maritime et analyse des tendances, des fréquences et des temps de retour des conditions météo-marines extrêmes. Rapport remis au ministère de la Sécurité publique du Québec. Chaire de recherche en géoscience côtière, Laboratoire de dynamique et de gestion intégrée des zones côtières, Université du Québec à Rimouski, Rimouski.

Bieber, A., St-Onge, G., Feuillet, N., Carlut, J., Moreno, E., Michel, E., 2021. Regional chronostratigraphy in the eastern Lesser Antilles quaternary fore-arc and accretionary wedge sediments: Relative paleointensity, oxygen isotopes and reversals. Quaternary Geochronology 65, 101179.

Blaauw, M., Christen, J.A., 2011. Flexible paleoclimate age-depth models using an autoregressive gamma process. Bayesian analysis 6, 457-474.

Boore, D.M., Atkinson, G.M., 1992. Source spectra for the 1988 Saguenay, Quebec, earthquakes. Bulletin of the Seismological Society of America 82, 683-719.

Bouma, A.H., 1962. Sedimentology of some flysch deposits. Agraphic approach to facies interpretation 168.

Brinkgreve, R., Kumarswamy, S., Swolfs, W., Waterman, D., Chesaru, A., Bonnier, P., 2016. PLAXIS 2016. PLAXIS bv, the Netherlands.

Broecker, W.S., 1997. Thermohaline circulation, the Achilles heel of our climate system: will man-made CO2 upset the current balance? Science 278, 1582-1588.

Bromhead, E., Dixon, N., 1986. The field residual strength of London Clay and its correlation with loboratory measurements, especially ring shear tests. Géotechnique 36, 449-452.

Brown, E., Bendick, R., Bourles, D., Gaur, V., Molnar, P., Raisbeck, G., Yiou, F., 2002. Slip rates of the Karakorum fault, Ladakh, India, determined using cosmic ray exposure dating of debris flows and moraines. Journal of Geophysical Research: Solid Earth 107, ESE 7-1-ESE 7-13.

Bruneau, M., Lamontagne, M., 1994. Damage from 20th century earthquakes in eastern Canada and seismic vulnerability of unreinforced masonry buildings. Canadian Journal of Civil Engineering 21, 643-662.

Bryn, P., Berg, K., Forsberg, C.F., Solheim, A., Kvalstad, T.J., 2005. Explaining the Storegga slide. Marine and Petroleum Geology 22, 11-19.

Bugge, T., Belderson, R., Kenyon, N., 1988. The storegga slide. Philosophical Transactions of the Royal Society of London. Series A, Mathematical and Physical Sciences 325, 357-388.

Campbell, K.W., 1997. Empirical near-source attenuation relationships for horizontal and vertical components of peak ground acceleration, peak ground velocity, and pseudo-absolute acceleration response spectra. Seismological research letters 68, 154-179.

Caris, H., 2013. SIPS 8.1 User Guide. Copyright (c).

Carlton, B., Løkke, A., Phillips, L., Macedo, J., Kaynia, A., comparison of multi-directional shaking of slopes using different numerical tools.

Casse, M., Montero-Serrano, J.C., St-Onge, G., 2017. Influence of the Laurentide Ice Sheet and relative sea-level changes on sediment dynamics in the Estuary and Gulf of St. Lawrence since the last deglaciation. Boreas 46, 541-561.

Cauchon-Voyer, G., Locat, J., St-Onge, G., 2008. Late-Quaternary morpho-sedimentology and submarine mass movements of the Betsiamites area, Lower St. Lawrence Estuary, Quebec, Canada. Marine Geology 251, 233-252.

Cauchon-Voyer, G., Locat, J., Leroueil, S., St-Onge, G., Demers, D., 2011. Large-scale subaerial and submarine Holocene and recent mass movements in the Betsiamites area, Quebec, Canada. Engineering Geology 121, 28-45.

Chagnon, J.Y., Locat, J., 1988. The effects of seismic activity on the soils of the Charlevoix area—Québec, Canada, Natural and Man-Made Hazards. Springer, pp. 125-136.

Clague, J.J., Munro, A., Murty, T., 2003. Tsunami hazard and risk in Canada. Natural Hazards 28, 435-463.

Clark, J.A., Farrell, W.E., Peltier, W.R., 1978. Global Changes in Postglacial Sea Level: A Numerical Calculation1. Quaternary research 9, 265-287.

CNRC, 2005. Code du bâtiment du Canada. Conseil national de recherches Canada, Ottawa, Ont.

Croudace, I.W., Rindby, A., Rothwell, R.G., 2006. ITRAX: description and evaluation of a new multi-function X-ray core scanner. Geological Society, London, Special Publications 267, 51-63.

D, A., 2015. Standard test method for measurement of hydraulic conductivity of porous material using a rigid-wall, compaction-mold permeameter. ASTM West Conshohocken PA, USA.

Dalrymple, R.W., Choi, K., 2007. Morphologic and facies trends through the fluvial–marine transition in tide-dominated depositional systems: a schematic framework for environmental and sequence-stratigraphic interpretation. Earth-Science Reviews 81, 135-174.

Dan, G., Sultan, N., Savoye, B., 2007. The 1979 Nice harbour catastrophe revisited: trigger mechanism inferred from geotechnical measurements and numerical modelling. Marine Geology 245, 40-64.

Dan, G., Sultan, N., Savoye, B., Deverchere, J., Yelles, K., 2009. Quantifying the role of sandy–silty sediments in generating slope failures during earthquakes: example from the Algerian margin. International Journal of Earth Sciences 98, 769-789.

Das, S.K., 2013. 10 Artificial neural networks in geotechnical engineering: modeling and application issues. Metaheuristics in Water Geotech Transp Eng 45, 231-267.

de Vernal, A., Guiot, J., Turon, J.-L., 1993. Late and postglacial paleoenvironments of the Gulf of St. Lawrence: marine and terrestrial palynological evidence. Géographie physique et Quaternaire 47, 167-180.

Dionne, J.-C., 1988. Évidence d'un bas niveau marin durant l'Holocène à Saint-Fabien-sur-Mer, estuaire maritime du Saint-Laurent. Norois 137, 19-34.

Dionne, J.-C., 2001. Relative-sea-level changes in the St. Lawrence Estuary from deglaciation to present day. Deglacial history and relative sea-level changes, northern New England and adjacent Canada 351, 271-284.

Doig, R., 1990. 2300 yr history of seismicity from silting events, in Lake Tadoussac, Charlevoix, Quebec. Geology 18, 820-823.

Douglas, J., 2002. Note on scaling of peak ground acceleration and peak ground velocity with magnitude. Geophysical Journal International 148, 336-339.

Douglas, J., 2003. Earthquake ground motion estimation using strong-motion records: a review of equations for the estimation of peak ground acceleration and response spectral ordinates. Earth-Science Reviews 61, 43-104.

Douglas, J., Boore, D.M., 2011. High-frequency filtering of strong-motion records. Bulletin of Earthquake Engineering 9, 395-409.

Doxsee, W., 1948. The grand banks earthquake of November 18, 1929. Publications of the Dominion Observatory Ottawa 7, 323-335.

Du Berger, R., Roy, D.W., Lamontagne, M., Woussen, G., North, R.G., Wetmiller, R.J., 1991. The Saguenay (Quebec) earthquake of November 25, 1988: seismologic data and geologic setting. Tectonophysics 186, 59-74.

Dubé, S., 1998. Analyse de l'écroulement rocheux du Mont Éboulé,(Québec).

Duchesne, M., Pinet, N., Bolduc, A., Bédard, K., Lavoie, D., 2007. Seismic stratigraphy of the lower St Lawrence River estuary (Quebec) Quaternary deposits and seismic signature of the underlying geological domains. Geological Survey of Canada.

Duchesne, M.J., Pinet, N., Bédard, K., St-Onge, G., Lajeunesse, P., Campbell, D.C., Bolduc, A., 2010. Role of the bedrock topography in the Quaternary filling of a giant estuarine basin: the Lower St. Lawrence Estuary, Eastern Canada. Basin Research 22, 933-951.

Ebel, J.E., 1996. The seventeenth century seismicity of northeastern North America. Seismological Research Letters 67, 51-68.

Ebel, J.E., 2011. A new analysis of the magnitude of the February 1663 earthquake at Charlevoix, Quebec. Bulletin of the Seismological Society of America 101, 1024-1038.

Elgamal, A., Yang, Z., Parra, E., 2002. Computational modeling of cyclic mobility and post-liquefaction site response. Soil Dynamics and Earthquake Engineering 22, 259-271.

Fear, C.E., Robertson, P.K., 1995. Estimating the undrained strength of sand: a theoretical framework. Canadian Geotechnical Journal 32, 859-870.

Filion, L., Quinty, F., Bégin, C., 1991. A chronology of landslide activity in the valley of Rivière du Gouffre, Charlevoix, Quebec. Canadian Journal of Earth Sciences 28, 250-256.

Fine, I.V., Rabinovich, A.B., Bornhold, B., Thomson, R., Kulikov, E.A., 2005. The Grand Banks landslide-generated tsunami of November 18, 1929: preliminary analysis and numerical modeling. Marine Geology 215, 45-57.

Finn, W., 1981. Liquefaction potential: developments since 1976, First International Conference on Recent Advances in Geotechnical earthquake Engineering and Soil Dynamics (1981: April 26-May 3; St. Louis, Missouri). Missouri S&T (formerly the University of Missouri--Rolla).

Friesinger, S., Bernatchez, P., 2010. Perceptions of Gulf of St. Lawrence coastal communities confronting environmental change: Hazards and adaptation, Québec, Canada. Ocean and Coastal Management 53, 669.

Gagné, H., Lajeunesse, P., St-Onge, G., Bolduc, A., 2009. Recent transfer of coastal sediments to the Laurentian Channel, Lower St. Lawrence Estuary (Eastern Canada), through submarine canyon and fan systems. Geo-Marine Letters 29, 191-200.

Gariel, J., Jacob, K., 1989. The Saguenay earthquake of November 25, 1988: the effect of the hypocentral depth on the peak acceleration: a modeling approach. The Saguenay earthquake of November 25, 1988, Quebec, Canada: strong motion data, ground failure observations, and preliminary interpretations.

Garziglia, S., Sultan, N., Thomas, Y., Ker, S., Marsset, B., Bompais, X., Woerther, P., Witt, C., Kopf, A., Apprioual, R., 2021. Assessing spatio-temporal variability of free gas in surficial cohesive sediments using tidal pressure fluctuations. Journal of Geophysical Research: Earth Surface 126, e2021JF006131.

Ge, Z., Nemec, W., Vellinga, A.J., Gawthorpe, R.L., 2022. How is a turbidite actually deposited? Science advances 8, eabl9124.

Goldfinger, C., Morey, A.E., Nelson, C.H., Gutiérrez-Pastor, J., Johnson, J.E., Karabanov, E., Chaytor, J., Eriksson, A., Party, S.S., 2007. Rupture lengths and temporal history of significant earthquakes on the offshore and north coast segments of the Northern San Andreas Fault based on turbidite stratigraphy. Earth and Planetary Science Letters 254, 9-27.

Goldfinger, C., Nelson, C.H., Morey, A.E., Johnson, J.E., Patton, J.R., Karabanov, E.B., Gutierrez-Pastor, J., Eriksson, A.T., Gracia, E., Dunhill, G., 2012. Turbidite event history—Methods and implications for Holocene paleoseismicity of the Cascadia subduction zone. US Geological Survey.

Goldfinger, C., Galer, S., Beeson, J., Hamilton, T., Black, B., Romsos, C., Patton, J., Nelson, C.H., Hausmann, R., Morey, A., 2017. The importance of site selection, sediment supply, and hydrodynamics: A case study of submarine paleoseismology on the northern Cascadia margin, Washington USA. Marine Geology 384, 4-46.

Goodacre, A., Hasegawa, H., 1980. Gravitationally induced stresses at structural boundaries. Canadian Journal of Earth Sciences 17, 1286-1291.

Gouin, P., 2001. Tremblements de terre historiques au Québec: de 1534 à mars 1925, identifiés et interprétés à partir des textes originaux contemporains. Guérin.

Gracia, E., Vizcaino, A., Escutia, C., Asioli, A., Rodes, A., Pallas, R., Garcia-Orellana, J., Lebreiro, S., Goldfinger, C., 2010. Holocene earthquake record offshore Portugal (SW Iberia): testing turbidite paleoseismology in a slow-convergence margin. Quaternary Science Reviews 29, 1156-1172.

Grezio, A., Babeyko, A., Baptista, M.A., Behrens, J., Costa, A., Davies, G., Geist, E.L., Glimsdal, S., González, F.I., Griffin, J., 2017. Probabilistic tsunami hazard analysis: multiple sources and global applications. Reviews of Geophysics 55, 1158-1198.

Hack, R., Alkema, D., Kruse, G.A., Leenders, N., Luzi, L., 2007. Influence of earthquakes on the stability of slopes. Engineering geology 91, 4-15.

Hampton, M.A., Lee, H.J., Locat, J., 1996. Submarine landslides. Reviews of geophysics 34, 33-59.

Harbitz, C.B., Løvholt, F., Pedersen, G., Masson, D.G., 2006. Mechanisms of tsunami generation by submarine landslides: a short review. Norwegian Journal of Geology/Norsk Geologisk Forening 86.

Harbitz, C.B., Løvholt, F., Bungum, H., 2014. Submarine landslide tsunamis: how extreme and how likely? Natural Hazards 72, 1341-1374.

Haworth, R.T., 1978. Interpretation of geophysical data in the northern Gulf of St. Lawrence and its relevance to lower Paleozoic geology. Geological Society of America Bulletin 89, 1091-1110.

Heaton, T.J., Köhler, P., Butzin, M., Bard, E., Reimer, R.W., Austin, W.E., Ramsey, C.B., Grootes, P.M., Hughen, K.A., Kromer, B., 2020. Marine20—the marine radiocarbon age calibration curve (0–55,000 cal BP). Radiocarbon 62, 779-820.

Higman, B., Shugar, D.H., Stark, C.P., Ekström, G., Koppes, M.N., Lynett, P., Dufresne, A., Haeussler, P.J., Geertsema, M., Gulick, S., 2018. The 2015 landslide and tsunami in Taan Fiord, Alaska. Scientific reports 8, 1-12.

Hodgson, E.A., 1925. The Saint Lawrence earthquake March 1, 1925. Publications of the Dominion Observatory Ottawa 7, 363-436.

Hodgson, E., 1928. The Probable Epicentre of the Saint Lawrence Earthquake of Feb. 5 1663. Journal of the Royal Astronomical Society of Canada 22, 325.

Howarth, J.D., Orpin, A.R., Kaneko, Y., Strachan, L.J., Nodder, S.D., Mountjoy, J.J., Barnes, P.M., Bostock, H.C., Holden, C., Jones, K., 2021. Calibrating the marine turbidite palaeoseismometer using the 2016 Kaikōura earthquake. Nature Geoscience 14, 161-167.

Hubert-Ferrari, A., Lamair, L., Hage, S., Schmidt, S., Çağatay, M.N., Avşar, U., 2020. A 3800 yr paleoseismic record (Lake Hazar sediments, eastern Turkey): Implications for the East Anatolian Fault seismic cycle. Earth and Planetary Science Letters 538, 116152.

Idriss, I., Dobry, R., Doyle, E., Singh, R., 1976. Behavior of soft clays under earthquake loading conditions, Offshore Technology Conference. OnePetro.

Ishihara, K., Yamazaki, A., Haga, K., 1985. Liquefaction of K0-consolidated sand under cyclic rotation of principal stress direction with lateral constraint. Soils and foundations 25, 63-74.

Ishihara, K., 1993. Liquefaction and flow failure during earthquakes. Geotechnique 43, 351-451.

Jaegle, M., 2015. Nature et origine des sédiments de surface de l'estuaire du Saint-Laurent. Université du Québec à Rimouski.

Jiaer, W., Kammerer, A., Riemer, M., Seed, R., Pestana, J., 2004. Laboratory study of liquefaction triggering criteria, 13th world conference on earthquake engineering, Vancouver, BC, Canada, Paper.

Josenhans, H., Lehman, S., 1999. Late glacial stratigraphy and history of the Gulf of St. Lawrence, Canada. Canadian Journal of Earth Sciences 36, 1327-1345.

King, L.H., MacLean, B., 1970. Origin of the outer part of the Laurentian Channel. Canadian Journal of Earth Sciences 7, 1470-1484.

Koppula, S., 1984. Pseudo-static analysis of clay slopes subjected to earthquakes. Geotechnique 34, 71-79.

Kvalstad, T.J., Andresen, L., Forsberg, C.F., Berg, K., Bryn, P., Wangen, M., 2005. The Storegga slide: evaluation of triggering sources and slide mechanics, Ormen Lange–an integrated study for Safe Field development in the Storegga submarine area. Elsevier, pp. 245-256.

Lajeunesse, P., Sinkunas, B., Morissette, A., Normandeau, A., Joyal, G., St-Onge, G., Locat, J., 2017. Large-scale seismically-induced mass-movements in a former glacial lake basin: Lake Témiscouata, northeastern Appalachians (eastern Canada). Marine Geology 384, 120-130.

Lamontagne, M., 2000. Rheological and geological constraints on the earthquake distribution in the Charlevoix Seismic Zone, Quebec, Canada.

Lamontagne, M., Beauchemin, M., Toutin, T., 2003. Earthquakes in the Charlevoix seismic zone, Quebec. International Journal on Hydropower & Dams 10, 98-99.

Lamontagne, M., Halchuk, S., Cassidy, J., Rogers, G., 2008. Significant Canadian earthquakes of the period 1600–2006. Seismological Research Letters 79, 211-223.

Lamontagne, M., Halchuk, S., Cassidy, J.F., Rogers, G.C., 2018. Significant Canadian Earthquakes 1600-2017. Geological Survey of Canada.

Lasalle, P., Chagnon, J.-Y., 1968. An ancient landslide along the Saguenay River, Quebec. Canadian Journal of Earth Sciences 5, 548-549.

Lastras, G., De Blasio, F.V., Canals, M., Elverhøi, A., 2005. Conceptual and numerical modeling of the BIG'95 debris flow, western Mediterranean Sea. Journal of Sedimentary Research 75, 784-797.

Lebreiro, S.M., McCave, I.N., Weaver, P.P., 1997. Late Quaternary turbidite emplacement on the Horseshoe abyssal plain (Iberian margin). Journal of Sedimentary Research 67, 856-870.

Lee, K.L., 1979. Cyclic strength of a sensitive clay of eastern Canada. Canadian Geotechnical Journal 16, 163-176.

Lee, H.J., Schwab, W.C., Edwards, B.D., Kayen, R.E., 1991. Quantitative controls on submarine slope failure morphology. Marine Georesources & Geotechnology 10, 143-157.

Leroueil, S., 2001. Natural slopes and cuts: movement and failure mechanisms. Géotechnique 51, 197-243.

Leroueil, S., 2004. Geotechnics of slopes before failure. Landslides: Evaluation and Stabilization, Lacerda, Ehrlich, Fontoura & Sayao (eds) 1, 863-884.

Levesque, C.L., Locat, J., Leroueil, S., 2006. Dating submarine mass movements triggered by earthquakes in the Upper Saguenay Fjord, Quebec, Canada. Norwegian Journal of Geology/Norsk Geologisk Forening 86.

Liao, S.S., Veneziano, D., Whitman, R.V., 1988. Regression models for evaluating liquefaction probability. Journal of Geotechnical Engineering 114, 389-411.

Liu, A.H., Stewart, J.P., Abrahamson, N.A., Moriwaki, Y., 2001. Equivalent number of uniform stress cycles for soil liquefaction analysis. Journal of Geotechnical and Geoenvironmental Engineering 127, 1017-1026.

Locat, J., Lee, H.J., 2002. Submarine landslides: advances and challenges. Canadian Geotechnical Journal 39, 193-212.

Locat, J., Martin, F., Levesque, C., Locat, P., Leroueil, S., Konrad, J.-M., Urgeles, R., Canals, M., Duchesne, M., 2003. Submarine mass movements in the upper Saguenay Fjord,(Québec, Canada), triggered by the 1663 earthquake, Submarine mass movements and their consequences. Springer, pp. 509-519.

Locat, J., 2011. La localisation et la magnitude du séisme du 5 février 1663 (Charlevoix) revues à l'aide des mouvements de terrain. Canadian Geotechnical Journal 48, 1266-1286.

Locat, J., Turmel, D., Habersetzer, M., Trottier, A.-P., Lajeunesse, P., St-Onge, G., 2016. Earthquake induced landslides in Lake Eternité, Québec, Canada, Submarine Mass Movements and their Consequences. Springer, pp. 361-370.

Loizeau, J.L., Arbouille, D., Santiago, S., Vernet, J.P., 1994. Evaluation of a wide range laser diffraction grain size analyser for use with sediments. Sedimentology 41, 353-361.

Løvholt, F., Harbitz, C.B., Haugen, K.B., 2005. A parametric study of tsunamis generated by submarine slides in the Ormen Lange/Storegga area off western Norway, Ormen lange–an integrated study for safe field development in the storegga submarine area. Elsevier, pp. 219-231.

Lysmer, J., Kuhlemeyer, R.L., 1969. Finite dynamic model for infinite media. Journal of the engineering mechanics division 95, 859-877.

Martin, F., Konrad, J.-M., Locat, J., Locat, P., Urgeles, R., Lee, H., 2001. Caracteristiques geotechniques et analyse du potentiel de liquefaction des sediments recents et post-glaciaires du fjord du saguenay, quebec (canada).

Masoudi, R., Sharifzadeh, M., Ghorbani, M., 2019. Partially decoupling and collar bonding of the encapsulated rebar rockbolts to improve their performance in seismic prone deep underground excavations. International Journal of Mining Science and Technology 29, 409-418.

Mazzotti, S., James, T.S., Henton, J., Adams, J., 2005. GPS crustal strain, postglacial rebound, and seismic hazard in eastern North America: The Saint Lawrence valley example. Journal of Geophysical Research: Solid Earth 110.

McCall, G.J., 2012. Geohazards: natural and man-made. Springer Science & Business Media.
McKenna, F., Fenves, G., Filippou, F., Mazzoni, S., 2009. Open System for Earthquake Engineering Simulation (OpenSees) 2000. URL: http://opensees. berkeley. edu/wiki/index. php/Main_Page.
McNeely, R., Dyke, A.S., Southon, J.R., 2006. Canadian marine reservoir ages preliminary data assessment. Geological Survey of Canada.
Mérindol, M., St-Onge, G., Sultan, N., Lajeunesse, P., Garziglia, S., 2022a. Earthquake-triggered submarine landslides in the St. Lawrence Estuary (Québec, Canada) during the last two millennia and the record of the major 1663 CE M≥ 7 event. Quaternary Science Reviews 291, 107640.
Mérindol, M., Sultan, N., St-Onge, G., Garziglia, S., Lajeunesse, P., 2022b. Location of the 1663 AD earthquake (M ~ 7) in the St. Lawrence Estuary (Canada) using sediment liquefaction analysis. Engineering Geology. En revision.
Miles, S.B., Keefer, D.K., 2000. Evaluation of seismic slope-performance models using a regional case study. Environmental & Engineering Geoscience 6, 25-39.
Miramontes, E., Eggenhuisen, J.T., Jacinto, R.S., Poneti, G., Pohl, F., Normandeau, A., Campbell, D.C., Hernández-Molina, F.J., 2020. Channel-levee evolution in combined contour current–turbidity current flows from flume-tank experiments. Geology 48, 353-357.
Miramontes, E., Garziglia, S., Sultan, N., Jouet, G., Cattaneo, A., 2018. Morphological control of slope instability in contourites: a geotechnical approach. Landslides 15, 1085-1095.
Moernaut, J., Van Daele, M., Strasser, M., Clare, M.A., Heirman, K., Viel, M., Cardenas, J., Kilian, R., de Guevara, B.L., Pino, M., 2017. Lacustrine turbidites produced by surficial slope sediment remobilization: a mechanism for continuous and sensitive turbidite paleoseismic records. Marine Geology 384, 159-176.
Mörner, N.-A., 2004. Estimating future sea level changes from past records. Global and Planetary Change 40, 49-54.
Mulder, T., Cochonat, P., 1996. Classification of offshore mass movements. Journal of Sedimentary research 66, 43-57.
Mulder, T., Syvitski, J.P., Skene, K.I., 1998. Modeling of erosion and deposition by turbidity currents generated at river mouths. Journal of Sedimentary Research 68, 124-137.
Mulder, T., Syvitski, J.P., Migeon, S., Faugères, J.-C., Savoye, B., 2003. Marine hyperpycnal flows: initiation, behavior and related deposits. A review. Marine and Petroleum Geology 20, 861-882.
Norem, H., Locat, J., Schieldrop, B., 1990. An approach to the physics and the modeling of submarine flowslides. Marine Georesources & Geotechnology 9, 93-111.
Normandeau, A., Lajeunesse, P., Philibert, G., 2013. Late-Quaternary morphostratigraphy of Lake St-Joseph (southeastern Canadian Shield): Evolution from a semi-enclosed glacimarine basin to a postglacial lake. Sedimentary Geology 295, 38-52.
Normandeau, A., Lajeunesse, P., St-Onge, G., 2015. Submarine canyons and channels in the Lower St. Lawrence Estuary (Eastern Canada): Morphology, classification and recent sediment dynamics. Geomorphology 241, 1-18.
Normandeau, A., Dietrich, P., Lajeunesse, P., St-Onge, G., Ghienne, J.-F., Duchesne, M.J., Francus, P., 2017. Timing and controls on the delivery of coarse sediment to deltas and submarine fans on a formerly glaciated coast and shelf. GSA Bulletin 129, 1424-1441.
Normandeau, A., Campbell, D.C., Cartigny, M.J., 2019. The influence of turbidity currents and contour currents on the distribution of deep-water sediment waves offshore eastern Canada. Sedimentology 66, 1746-1767.
North, R.G., Wetmiller, R.J., Adams, J., Anglin, F.M., Hasegawa, H.S., Lamontagne, M., Berger, R.D., Seeber, L., Armbruster, J., 1989. Preliminary results from the November 25, 1988 Saguenay (Quebec) earthquake. Seismological Research Letters 60, 89-93.

Obermeier, S., 1998. Liquefaction evidence for strong earthquakes of Holocene and latest Pleistocene ages in the states of Indiana and Illinois, USA. Engineering Geology 50, 227-254.

Obermeier, S., Bleuer, N., Munson, C., Munson, P., Martin, W., McWilliams, K., Tabaczynski, D., Odum, J., Rubin, M., Eggert, D.L., 1991. Evidence of strong earthquake shaking in the lower Wabash Valley from prehistoric liquefaction features. Science 251, 1061-1063.

Obermeier, S.F., Martin, J., Frankel, A., Youd, T., Munson, P., Munson, C., Pond, E., 1992. Liquefaction evidence for strong Holocene earthquake (s) in the Wabash Valley of southern Indiana-Illinois, with a preliminary estimate of magnitude. US Department of the Interior, US Geological Survey.

Obermeier, S.F., 1996. Use of liquefaction-induced features for paleoseismic analysis—an overview of how seismic liquefaction features can be distinguished from other features and how their regional distribution and properties of source sediment can be used to infer the location and strength of Holocene paleo-earthquakes. Engineering Geology 44, 1-76.

Onitsuka, K., Hong, Z., Hara, Y., Yoshitake, S., 1995. Interpretation of oedometer test data for natural clays. Soils and Foundations 35, 61-70.

Onwuemeka, J., Liu, Y., Harrington, R.M., 2018. Earthquake stress drop in the Charlevoix Seismic Zone, eastern Canada. Geophysical Research Letters 45, 12,226-212,235.

Ouellet, M., 1997. Lake sediments and Holocene seismic hazard assessment within the St. Lawrence Valley, Québec. Geological Society of America Bulletin 109, 631-642.

Papadopoulos, G.A., Plessa, A., 2000. Magnitude–distance relations for earthquake-induced landslides in Greece. Engineering Geology 58, 377-386.

Patton, J.R., Goldfinger, C., Morey, A.E., Ikehara, K., Romsos, C., Stoner, J., Djadjadihardja, Y., Ardhyastuti, S., Gaffar, E.Z., Vizcaino, A., 2015. A 6600 year earthquake history in the region of the 2004 Sumatra-Andaman subduction zone earthquake. Geosphere 11, 2067-2129.

Pennington, D.S., Nash, D.F., Lings, M.L., 2001. Horizontally mounted bender elements for measuring anisotropic shear moduli in triaxial clay specimens. Geotechnical testing journal 24, 133-144.

Pestana, J., Biscontin, G., Nadim, F., Andersen, K., 2000. Modeling cyclic behavior of lightly overconsolidated clays in simple shear. Soil Dynamics and Earthquake Engineering 19, 501-519.

Pezeshk, S., Zandieh, A., Campbell, K.W., Tavakoli, B., 2018. Ground-motion prediction equations for central and eastern North America using the hybrid empirical method and NGA-West2 empirical ground-motion models. Bulletin of the Seismological Society of America 108, 2278-2304.

Philibert, G., 2012. Évolution tardi-quaternaire du lac Jacques-Cartier, Réserve faunique des Laurentides, Québec.

Pickering, K., Stow, D., Watson, M., Hiscott, R., 1986. Deep-water facies, processes and models: a review and classification scheme for modern and ancient sediments. Earth-Science Reviews 23, 75-174.

Pinet, N., Duchesne, M., Lavoie, D., Bolduc, A., Long, B., 2008. Surface and subsurface signatures of gas seepage in the St. Lawrence Estuary (Canada): significance to hydrocarbon exploration. Marine and Petroleum Geology 25, 271-288.

Pinet, N., Brake, V., Campbell, C., Duchesne, M., 2011. Seafloor and shallow subsurface of the St. Lawrence River Estuary. Geoscience Canada 38, 31-40.

Pinet, N., Lavoie, D., Keating, P., Duchesne, M., 2014. The St Lawrence Platform and Appalachian deformation front in the St Lawrence Estuary and adjacent areas (Quebec, Canada): structural complexity revealed by magnetic and seismic imaging. Geological Magazine 151, 996-1012.

Pinet, N., Brake, V., Campbell, C., Duchesne, M.J., 2015. Geomorphological characteristics and variability of Holocene mass-transport complexes, St. Lawrence River Estuary, Canada. Geomorphology 228, 286-302.

Pinet, N., Lamontagne, M., Duchesne, M.J., Brake, V.I., 2021. Hunting for Quaternary faults in eastern Canada: A critical appraisal of two potential candidates. Seismological Society of America 92, 1102-1111.

Piper, D.J., Aksu, A.E., 1987. The source and origin of the 1929 Grand Banks turbidity current inferred from sediment budgets. Geo-Marine Letters 7, 177-182.

Piper, D.J., Cochonat, P., Morrison, M.L., 1999. The sequence of events around the epicentre of the 1929 Grand Banks earthquake: initiation of debris flows and turbidity current inferred from sidescan sonar. Sedimentology 46, 79-97.

Piper, D.J., Tripsanas, E., Mosher, D.C., MacKillop, K., 2019. Paleoseismicity of the continental margin of eastern Canada: rare regional failures and associated turbidites in Orphan Basin. Geosphere 15, 85-107.

Plourde, A.P., Nedimović, M.R., 2021. Earthquake depths, focal mechanisms, and stress in the Lower St. Lawrence Seismic Zone. Seismological Society of America 92, 2562-2572.

Poncet, R., Campbell, C., Dias, F., Locat, J., Mosher, D., 2010. A study of the tsunami effects of two landslides in the St. Lawrence estuary, Submarine Mass Movements and Their Consequences. Springer, pp. 755-764.

Pouderoux, H., Proust, J.-N., Lamarche, G., 2014. Submarine paleoseismology of the northern Hikurangi subduction margin of New Zealand as deduced from Turbidite record since 16áka. Quaternary Science Reviews 84, 116-131.

Praeg, D., d'Anglejan, B., Syvitski, J., 1992. Seismostratigraphy of the Middle St. Lawrence Esturary: A Late Quaternary Glacial Marine to Estuarine Depositional/Erosional Record. Géographie physique et Quaternaire 46, 133-150.

Prior, D.B., Suhayda, J.N., 1979. Application of infinite slope analysis to subaqueous sediment instability, Mississippi Delta. Engineering Geology 14, 1-10.

Ratzov, G., Cattaneo, A., Babonneau, N., Déverchère, J., Yelles, K., Bracene, R., Courboulex, F., 2015. Holocene turbidites record earthquake supercycles at a slow-rate plate boundary. Geology 43, 331-334.

Ravenne, C., Beghin, P., 1983. Apport des expériences en canal à l'interprétation sédimentologique des dépôts de cônes détritiques sous-marins. Revue de l'Institut français du pétrole 38, 279-297.

Rémillard, A.M., St-Onge, G., Bernatchez, P., Hétu, B., Buylaert, J.-P., Murray, A.S., Lajeunesse, P., 2017. Relative sea-level changes and glacio-isostatic adjustment on the Magdalen Islands archipelago (Atlantic Canada) from MIS 5 to the late Holocene. Quaternary Science Reviews 171, 216-233.

Riboulot, V., Cattaneo, A., Sultan, N., Garziglia, S., Ker, S., Imbert, P., Voisset, M., 2013. Sea-level change and free gas occurrence influencing a submarine landslide and pockmark formation and distribution in deepwater Nigeria. Earth and Planetary Science Letters 375, 78-91.

Ribó, R., Pasenau, M., Escolano, E., Ronda, J., González, L., 1998. GiD reference manual. CIMNE, Barcelona 27, 25.

Richardson, R.M., Reding, L.M., 1991. North American plate dynamics. Journal of Geophysical Research: Solid Earth 96, 12201-12223.

Robertson, P.K., Wride, C., 1998. Evaluating cyclic liquefaction potential using the cone penetration test. Canadian geotechnical journal 35, 442-459.

Roy, D.W., DuBerger, R., 1983. Relations possibles entre la microseismicité récente et l'astroblème de Charlevoix. Canadian Journal of Earth Sciences 20, 1613-1618.

Salamon, A., Di Manna, P., 2019. Empirical constraints on magnitude-distance relationships for seismically-induced submarine tsunamigenic landslides. Earth-Science Reviews 191, 66-92.

Saucier, F.J., Chassé, J., 2000. Tidal circulation and buoyancy effects in the St. Lawrence Estuary. Atmosphere-Ocean 38, 505-556.

Sbar, M.L., Sykes, L.R., 1973. Contemporary compressive stress and seismicity in eastern North America: An example of intra-plate tectonics. Geological Society of America Bulletin 84, 1861-1882.

Seed, H.B., 1979. Soil liquefaction and cyclic mobility evaluation for level ground during earthquakes. Journal of the Geotechnical Engineering Division 105, 201-255.

Seed, H.B., Idriss, I.M., 1967. Analysis of soil liquefaction: Niigata earthquake. Journal of the Soil Mechanics and Foundations Division 93, 83-108.

Seed, H.B., Idriss, I.M., 1971. Simplified procedure for evaluating soil liquefaction potential. Journal of the Soil Mechanics and Foundations division 97, 1249-1273.

Seed, R., Cetin, K., Moss, R., Kammerer, A., Wu, J., Pestana, J., Riemer, M., 2001. Recent advances in soil liquefaction engineering and seismic site response evaluation, 4th Int. Conf. Recent Advanced in Geotechnical Earthquake Engineering and soil dinamics, San Diego, California.

Seibert, C., Feuillet, N., Beck, C., Ducassou, E., Morena, P., Johannes, L., Ratzov, G., Goldfinger, C., Cattaneo, A., Moreno, E., 2019. Long Term Recurrence of Deeply Ponded Turbidites and Thick Homogenites in the Lesser Antilles Forearc: Imprint of Great Earthquakes, AGU Fall Meeting Abstracts, pp. OS51C-1503.

Shaw, J., Gareau, P., Courtney, R., 2002. Palaeogeography of Atlantic Canada 13–0 kyr. Quaternary Science Reviews 21, 1861-1878.

Smith, W.T., 1962. Earthquakes of eastern Canada and adjacent areas, 1534-1927. Department of Energy, Mines and Resources, Observatories Branch.

Somerville, P.G., Mclaren, J.P., Saikia, C.K., Helmberger, D.V., 1990. The 25 November 1988 Saguenay, Quebec, earthquake: Source parameters and the attenuation of strong ground motion. Bulletin of the Seismological Society of America 80, 1118-1143.

St-Onge, G., Hillaire-Marcel, C., 2001. Isotopic constraints of sedimentary inputs and organic carbon burial rates in the Saguenay Fjord, Quebec. Marine Geology 176, 1-22.

St-Onge, G., Stoner, J.S., Hillaire-Marcel, C., 2003. Holocene paleomagnetic records from the St. Lawrence Estuary, eastern Canada: centennial-to millennial-scale geomagnetic modulation of cosmogenic isotopes. Earth and Planetary Science Letters 209, 113-130.

St-Onge, G., Mulder, T., Piper, D.J., Hillaire-Marcel, C., Stoner, J.S., 2004. Earthquake and flood-induced turbidites in the Saguenay Fjord (Québec): a Holocene paleoseismicity record. Quaternary Science Reviews 23, 283-294.

St-Onge, G., Mulder, T., Francus, P., Long, B., 2007. Chapter two continuous physical properties of cored marine sediments. Developments in marine geology 1, 63-98.

St-Onge, G., Lajeunesse, P., Duchesne, M.J., Gagne, H., 2008. Identification and dating of a key Late Pleistocene stratigraphic unit in the St. Lawrence Estuary and Gulf (Eastern Canada). Quaternary Science Reviews 27, 2390-2400.

St-Onge, G., Chapron, E., Mulsow, S., Salas, M., Viel, M., Debret, M., Foucher, A., Mulder, T., Winiarski, T., Desmet, M., 2012. Comparison of earthquake-triggered turbidites from the Saguenay (Eastern Canada) and Reloncavi (Chilean margin) Fjords: Implications for paleoseismicity and sedimentology. Sedimentary Geology 243, 89-107.

Stow, D., Piper, D., 1984. Deep-water fine-grained sediments: facies models. Geological Society, London, Special Publications 15, 611-646.

Stow, D.A., Mayall, M., 2000. Deep-water sedimentary systems: New models for the 21st century. Marine and Petroleum Geology 17, 125-135.

Strachan, L.J., 2008. Flow transformations in slumps: a case study from the Waitemata Basin, New Zealand. Sedimentology 55, 1311-1332.

Stuiver, M., Reimer, P.J., 1993. Extended 14C data base and revised CALIB 3.0 14C age calibration program. Radiocarbon 35, 215-230.

Syvitski, J., Praeg, D., 1989. Quaternary sedimentation in the St. Lawrence Estuary and adjoining areas, Eastern Canada: An overview based on high-resolution seismo-stratigraphy. Géographie physique et Quaternaire 43, 291-310.

Syvitski, J.P., Schafer, C.T., 1996. Evidence for an earthquake-triggered basin collapse in Saguenay Fjord, Canada. Sedimentary Geology 104, 127-153.

Talling, P.J., CLARE, M.L., Urlaub, M., Pope, E., Hunt, J.E., Watt, S.F., 2014. Large submarine landslides on continental slopes: geohazards, methane release, and climate change. Oceanography 27, 32-45.

Talling, P.J., 2021. Fidelity of turbidites as earthquake records. Nature Geoscience 14, 113-116.

Terzaghi, K., Peck, R.B., Mesri, G., 1996. Soil mechanics in engineering practice. John Wiley & Sons.

Tesson, J., Pace, B., Benedetti, L., Visini, F., Delli Rocioli, M., Arnold, M., Aumaître, G., Bourlès, D., Keddadouche, K., 2016. Seismic slip history of the Pizzalto fault (central Apennines, Italy) using in situ-produced 36Cl cosmic ray exposure dating and rare earth element concentrations. Journal of Geophysical Research: Solid Earth 121, 1983-2003.

Tremblay, A., Long, B., Massé, M., 2003. Supracrustal faults of the St. Lawrence rift system, Québec: kinematics and geometry as revealed by field mapping and marine seismic reflection data. Tectonophysics 369, 231-252.

Trottier, A.-P., Lajeunesse, P., Normandeau, A., Gagnon-Poiré, A., 2019. Deglacial and postglacial paleoseismological archives in mass movement deposits of lakes of south-central Québec. Canadian Journal of Earth Sciences 56, 60-76.

Turmel, D., Locat, J., Leblanc, J., Cauchon-Voyer, G., 2019. Tsunami modelling of the 7250 cal years BP Betsiamites submarine landslide. Geological Society, London, Special Publications 477, 293-301.

Tuttle, M.P., Atkinson, G.M., 2010. Localization of large earthquakes in the Charlevoix seismic zone, Quebec, Canada, during the past 10,000 years. Seismological Research Letters 81, 140-147.

Uri, S., Lee, H.J., Geist, E.L., Twichell, D., 2009. Assessment of tsunami hazard to the US East Coast using relationships between submarine landslides and earthquakes. Marine geology 264, 65-73.

Vanneste, M., Mienert, J., Bünz, S., 2006. The Hinlopen Slide: a giant, submarine slope failure on the northern Svalbard margin, Arctic Ocean. Earth and Planetary Science Letters 245, 373-388.

Vanneste, M., Sultan, N., Garziglia, S., Forsberg, C.F., L'Heureux, J.-S., 2014. Seafloor instabilities and sediment deformation processes: The need for integrated, multi-disciplinary investigations. Marine Geology 352, 183-214.

Vaunat, J., Leroueil, S., 2002. Analysis of post-failure slope movements within the framework of hazard and risk analysis. Natural Hazards 26, 81-107.

Veillette, J., 1994. Evolution and paleohydrology of glacial lakes Barlow and Ojibway. Quaternary Science Reviews 13, 945-971.

Ward, S.N., 2001. Landslide tsunami. Journal of Geophysical Research: Solid Earth 106, 11201-11215.

Wu, J., Seed, R.B., 2004. Estimation of liquefaction-induced ground settlement (case studies).

Wu, P., Hasegawa, H.S., 1996. Induced stresses and fault potential in eastern Canada due to a realistic load: a preliminary analysis. Geophysical Journal International 127, 215-229.

Wu, P., 1998. Intraplate earthquakes and post-glacial rebound in eastern Canada and Northern Europe. Dynamics of the Ice Age Earth: A Modern Perspective, 603-628.

Yang, Z., 2000. Numerical modeling of earthquake site response including dilation and liquefaction. Columbia University.

Yang, Z., Elgamal, A., Parra, E., 2003. Computational model for cyclic mobility and associated shear deformation. Journal of Geotechnical and Geoenvironmental Engineering 129, 1119-1127.

Yoshimi, Y., Tokimatsu, K., 1977. Settlement of buildings on saturated sand during earthquakes. Soils and Foundations 17, 23-38.

Youd, T.L., Hoose, S.N., 1978. Historic ground failures in northern California triggered by earthquakes. US Government Printing Office.

Zakeri, A., Høeg, K., Nadim, F., 2009. Submarine debris flow impact on pipelines—Part II: Numerical analysis. Coastal engineering 56, 1-10.
Zhang, D., 2000. Flux de radio-isotopes à courte période dans les bassins marins marginaux de l'est canadien. Ph. D. thesis, Université du Québec à Montréal, Montréal, Québec.

ANNEXES

APPENDICES

Annexe 1 : Article Quaternary Science Reviews.

Annexe 2 : Analyses sédimentaires.

Annexe 3 : Analyses géotechniques.

Quaternary Science Reviews 291 (2022) 107640

Contents lists available at ScienceDirect

Quaternary Science Reviews

journal homepage: www.elsevier.com/locate/quascirev

Earthquake-triggered submarine landslides in the St. Lawrence Estuary (Québec, Canada) during the last two millennia and the record of the major 1663 CE M ≥7 event

Méril Mérindol [a, b, *], Guillaume St-Onge [a], Nabil Sultan [b], Patrick Lajeunesse [c], Sébastien Garziglia [b]

[a] Institut des sciences de la mer de Rimouski (ISMER), Canada Research Chair in Marine Geology, Université du Québec à Rimouski and GEOTOP, Canada
[b] Geo-Ocean UMR6538, Ifremer, CNRS, UBO, UBS, F-29280, Plouzané, France
[c] Département de géographie, Université Laval, Québec, Canada

ARTICLE INFO

Article history:
Received 17 February 2022
Received in revised form
28 June 2022
Accepted 1 July 2022
Available online xxx

Handling editor: A. Voelker

Keywords:
1663 CE earthquake
Canada
Geohazards
Geophysics
Holocene
Quebec
Paleoseismicity
Sedimentology
Submarine landslides
Turbidites

ABSTRACT

In eastern Canada, the Charlevoix-Kamouraska/Bas-Saint-Laurent (CKBSL) seismic zone presents a seismic hazard almost as high as that of the active Pacific zone. The major event of February 5, 1663 CE, with an estimated magnitude of ≥7, highlights the importance of this seismic hazard. The numerous submarine landslides mapped in the St. Lawrence Estuary in the CKBSL seismic zone suggest that earthquakes triggered series of submarine slope failures. In this context, the SLIDE-2020 expedition on board the RV Coriolis II in the St. Lawrence Estuary aimed to map, image and sample more than 12 zones of submarine instabilities and their associated deposits. The analysis of sediment cores sampled in the distal sedimentary deposits from these landslides reveals the presence of rapidly deposited layers (turbidites, hyperpycnites and debrites) directly linked to the submarine landslides. Dating these landslides with ^{210}Pb and ^{14}C techniques led to the identification of four periods of synchronous submarine landslides corresponding to the strongest historical earthquakes: 1663 CE, 1860/1870 CE, 1925 CE and 1988 CE (M ≥ 7, M = 6.1/6.6, M = 6.2, M = 5.9). This synchronicity over a distance reaching 220 km of several landslides supports a relationship between their triggering in the St. Lawrence Estuary and regional seismicity. The fact that as many as nine submarine landslides appear to have been triggered by the 1663 CE earthquake suggests that this event is the strongest recorded in the last two millennia in the region.

© 2022 Elsevier Ltd. All rights reserved.

1. Introduction

One of the strongest historical earthquakes felt in eastern North America occurred on February 5, 1663, along the St. Lawrence River, in southern Québec, Canada, when the region was sparsely inhabited and the European settling was at its beginning. Therefore, the precise epicenter and magnitude of this event are estimated only from written and personal accounts of the event (Gouin, 2001). Previous studies converge to indicate that its epicenter was located in the Charlevoix-Kamouraska seismic zone (CKSZ), in the western part of the St. Lawrence Estuary (Fig. 1), although its exact localisation is still debated (Hodgson, 1928; Locat, 2011; Locat *et al.*, 2003; Locat et al., 2016; Pinet et al., 2021). Gouin (2001) has compiled testimonies of damage to barns, chimneys and houses in eastern America in an area reaching 600 km around the suspected epicenter. From this historical data, Ebel (2011) estimated the magnitude (M) of the 1663 earthquake at 7.5 while the Canadian catalog of historical earthquakes, used to map the seismic hazard in Canada, considers a magnitude slightly lower, of M = 7 (Smith, 1962; Lamontagne et al., 2018).

Jesuits writings contemporary to the 1663 CE earthquake (e.g., Ebel, 1996) report "the formation of new lakes", "the disappearance of mountains" and "the displacement of forest down to the St. Lawrence River" as consequences of subaerial landslides most likely triggered by the 1663 earthquake. The historical observations are consistent with studies carried out on regional landslides which established a link between the 1663 CE earthquake and the

* Corresponding author. Geo-Ocean UMR6538, Ifremer, CNRS, UBO, UBS, F-29280, Plouzané, France.
E-mail address: meril.merindol@ifremer.fr (M. Mérindol).

https://doi.org/10.1016/j.quascirev.2022.107640
0277-3791/© 2022 Elsevier Ltd. All rights reserved.

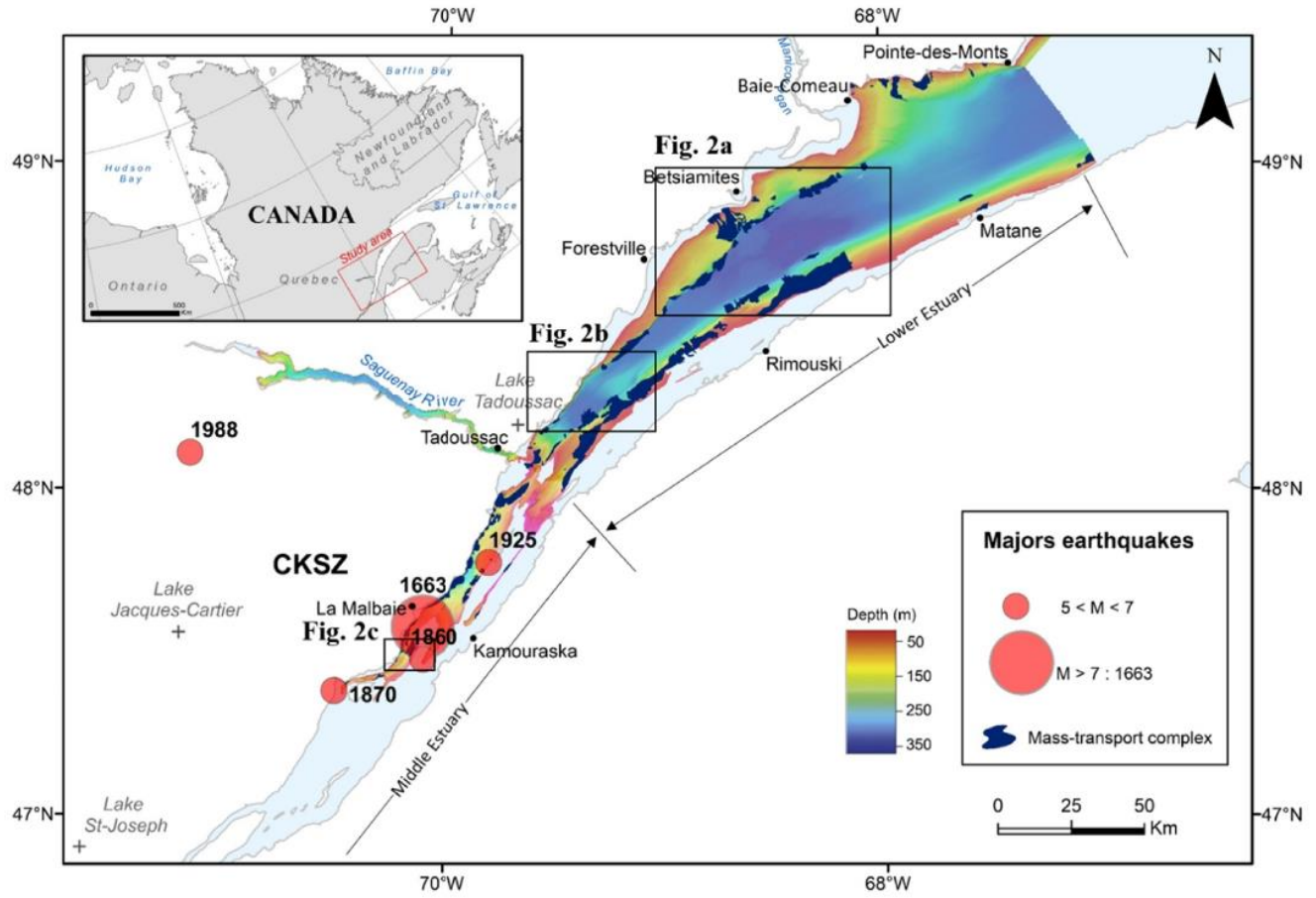

Fig. 1. Bathymetric map of the St-Lawrence Estuary and location of significant East Canadian Earthquakes of the period 1663-2005 (red circles) from Lamontagne et al. (2018). Dark blue areas indicate the mass-transport complexes mapped by Pinet et al. (2015). CKSZ corresponds of the Charlevoix-Kamouraska Seismic Zone. (For interpretation of the references to color in this figure legend, the reader is referred to the Web version of this article.)

landslides observed at Saint-Jean-Vianney (Lasalle and Chagnon, 1968), the Gouffre River (Filion et al., 1991), the Mont-Eboulé (Dubé, 1998) and Colombier (Cauchon-Voyer et al., 2008). The recent study conducted in the CKSZ (Fig. 1) by Pinet et al. (2015), indicates that more than one hundred submarine mass-movements occurred in the St. Lawrence Estuary. The high density of submarine landslides in the CKSZ suggests a possible link between submarine slope destabilization and seismicity (e.g., Cauchon-Voyer et al., 2008). Some submarine landslides have been related to regional seismicity such as in the Betsiamites River area, where Cauchon-Voyer et al. (2008), (2011) combined terrestrial and marine data to relate submarine landslides to major earthquakes occurring before 9280 cal yr BP, in 7250 cal yr BP and in 1663 CE. Other authors have observed this relationship in Québec using geomorphological, sedimentological and dating methods but outside the St. Lawrence Estuary such as in the Saguenay Fjord (Syvitski and Schafer, 1996a; 1996b; Locat et al., 2003; St-Onge et al., 2004) and in lacustrine environments (Doig, 1990; Ouellet, 1997; Locat et al., 2016; Trottier et al., 2019).

Submarine landslides, through erosion of the seafloor and incorporation of sediments and water, can evolve into a debris flow and a turbidity current (Bryn et al., 2005; Strachan, 2008). Over the last two decades, the marine turbidite record has been increasingly used as a proxy for earthquake recurrence (Lebreiro et al., 1997; Gracia et al., 2010; Goldfinger et al., 2012; St-Onge et al., 2012; Ratzov et al., 2015; Piper et al., 2019; Howarth et al., 2021). The recurrence of strong regional earthquakes and the risks they pose when associated with submarine slope failures can have major impacts on coastal environments (e.g., damage to coastal infrastructures and threats to coastal communities, risk of tsunamis, cable rupture, coastal erosion), particularly with increasing human populations along the coast. It is therefore essential to improve our knowledge of natural hazards by establishing a chronology of submarine landslides triggered by earthquakes.

Mapping and dating of submarine landslides at a regional scale provide the opportunity to assess their synchronicity and thus their possible triggering by an earthquake (Goldfinger et al., 2012, 2017; Patton et al., 2015). This paper involves 19 sediment cores recovered near 12 submarine landslides located over a distance of ~220 km in the St. Lawrence Estuary with the aim of: (1) identifying and characterizing rapidly deposited layers (RDLs) resulting from landslides (e.g., debrite, turbidite) dated by radiocarbon and ^{210}Pb; and (2) relate them to historical earthquakes (Fig. 1).

2. Regional setting

2.1. The St. Lawrence Estuary (Eastern Canada)

The St. Lawrence Estuary, located in Québec (eastern Canada), is one of the world's largest estuarine basins (~8000 km^2). It is

generally considered to be divided into two parts: the Lower Estuary, from the mouth of the Saguenay River to Pointe-des-Monts, and the Middle Estuary, upstream and southwest of the Saguenay River (Fig. 1) (e.g., Pinet et al., 2011). The maximum water depth of 355 m is reached in the central part of the estuary, in the Laurentian Channel, where the seafloor presents a sub-horizontal depression ~900 km long. This major feature is a U-shaped incised-valley bounded by steep escarpments inherited from Quaternary glacial successive erosions (Josenhans and Lehman, 1999; Shaw et al., 2002) and phases of preglacial subaerial erosion (King and MacLean, 1970). In the Lower Estuary, its topography is mostly shaped by mass-transport deposits and pockmarks (Locat et al., 2003; Pinet et al., 2008). In this study, six regions with submarine landslides were considered representing the estuary over its entire length (Fig. 1 and Table 1). The Rimouski, Baie-Comeau and Betsiamites sectors are located in the eastern part of the Lower Estuary and the Forestville and Saguenay sectors are located in its western part. Only the La Malbaie area is located in the Middle Estuary.

The basement of the St. Lawrence Estuary is mostly composed of carbonate and siliciclastic rocks from the St. Lawrence Platform (Duchesne et al., 2007). It is predominantly covered by Quaternary sediments, except in narrow strips at Anticosti and Mingan (Haworth, 1978). The St. Lawrence Platform is bordered to the north by the Grenville Formation, composed of metamorphic rocks, and to the south by the Appalachian Mountains, composed of Paleozoic sedimentary rocks (e.g., Duchesne et al., 2007). Less resistant to erosion, the Laurentian Channel is parallel to these two formations (Pinet et al., 2008). The estuary is divided into three physiographic regions: the shelf, the slope and the Laurentian Channel. In the Middle Estuary, the shelf is reduced and even absent (Figs. 1 and 2).

Inputs of sediments to the estuary originate from five main rivers in addition to the St. Lawrence River: the Saguenay, Rimouski, Betsiamites, Aux-Outardes and Manicouagan Rivers. The associated discharge areas correspond to gently sloping submarine fans (Pinet et al., 2015) with active turbiditic channels (Normandeau et al., 2017). One of the largest mass-transport complexes is located near a former mouth of the Betsiamites River (Cauchon-Voyer et al., 2008). Holocene mass-transport deposits are not consistently present near the mouth of major rivers, suggesting that the actual sedimentary inputs are not the predominant preconditioning factor for seafloor instability (Normandeau et al., 2015). However, most of them are located on steep slopes (>5°) bordering the Laurentian Channel, indicating that the seafloor gradient is an important preconditioning factor for slope instability (Normandeau et al., 2015; Pinet et al., 2015). If gas charging is considered a preconditioning factor for submarine slope instability (e.g., Riboulot et al., 2013), no link was clearly established between the presence of free gas and the mass-transport complexes in the St. Lawrence Estuary (Pinet et al., 2015).

Table 1
Location and length of the studied cores.

Area and core name	Zone	Lat. (°N)	Long. (°W)	Length (m)
Rimouski				
COR20-02-03 GC	Slope	48°34.71	68°29.66	3.87
Baie-Comeau				
COR20-02-13 GC	Slope - Deposit	48°58.71	68°10.74	4.20
COR20-02-14 GC	Deposit	48°57.94	68°12.25	3.87
Betsiamites				
COR20-02-17 GC	Deposit	48°53.27	68°29.93	3.45
COR20-02-18GC/BC	Deposit	48°50.97	68°32.10	3.97
COR20-02-04 GC	Lobe	48°34.77	68°29.76	3.86
COR07-03-11 PC	Deposit	48°48.58	68°38.34	2.45
COR07-03-13 PC	Scar	48°51.10	−68°37.24	4.09
COR20-02-19 GC	Deposit	48°48.37	68°37.30	2.32
Forestville				
COR20-02-20GC/BC	Deposit	48°27.96	69°10.04	5.05
COR20-02-21 GC	Deposit	48°21.14	69°08.47	2.49
Saguenay				
COR20-02-26GC/BC	Deposit	48°12.25	69°31.87	2.83
COR20-02-28GC/BC	Deposit	48°12.88	69°25.87	1.01
COR20-02-29 GC	Deposit	48°11.82	69°27.40	1.60
La Malbaie				
COR20-02-50 GC	Deposit	47°30.72	70°10.84	2.28

2.2. Quaternary sedimentation

The carbonate platform of the St. Lawrence Estuary is covered by Quaternary sediments with a maximum thickness of ~400 m controlled by the underlying topography of the bedrock (Duchesne et al., 2010). The seismo-stratigraphic sequence of Quaternary sedimentation in the St. Lawrence Estuary, first established by Syvitski and Praeg (1989), and completed with samples and dating (St-Onge et al., 2008; Duchesne et al., 2010), is composed of five units. Seismic Unit 1 overlies the bedrock. It is interpreted as ice-contact sediments (Syvitski and Praeg, 1989) when the ice extension was maximum during the Last Glacial Maximum (LGM: 21,000 cal yr BP). Unit 2 corresponds to ice-proximal, coarse-grained sediments in a glaciomarine environment. Fine-grained, ice-distal sediments characterize Unit 3. Units 2-3 were deposited when the Goldthwait Sea was present in the St. Lawrence Estuary and Gulf from 13,000 to 9000 cal yr BP (Dionne, 2001). Unit 4 marks the transition between glaciomarine and postglacial sedimentation. It comprises hemipelagic sediments (Duchesne et al., 2010) following the rerouting of meltwaters of the Laurentide Ice Sheet (LIS) from the St. Lawrence to Hudson Bay after the collapse of the proglacial Lake Agassiz-Ojibway around 8500 cal yr BP (St-Onge et al., 2003). Cauchon-Voyer et al. (2011) described stratified silty clays with thin layers of sand in Unit 4. Finally, Unit 5 differs from Unit 4 by the presence of coarser sediments that were deposited under modern oceanographic conditions. Modern sedimentation rates range between 0.74 $cm.yr^{-1}$ at the mouth of the Lower Estuary to 0.04 $cm.yr^{-1}$ in the Gulf, with an exponential decrease (Zhang, 2000).

2.3. Regional seismicity and sediment liquefaction

In addition to the 1663 CE earthquake, four earthquakes with M 5.9 to 6.6 occurred in the CKSZ in 1860, 1870, 1925 and 1988 CE (Smith, 1962; Lamontagne et al., 2003; Lamontagne et al., 2018) (Fig. 1). An average of 200 earthquakes are recorded annually in CKSZ and 50 to 100 in the Lower St. Lawrence zone (Lamontagne et al., 2003). They are localized at depths between 5 and 25 km in the Precambrian bedrocks (Anglin, 1984). Only a small proportion exceeds M 3.

The origin of intraplate earthquakes in Eastern Canada is not clearly identified, but two principal causes are conceivable: tectonic and glacio-isostatic (Wu, 1998). Most earthquakes are concentrated in the St. Lawrence Valley and related to a fault inherited from Paleozoic rifting (Adams and Basham, 1989). The depth of the hypocenters corresponds to the Appalachian thrust fault over the St. Lawrence Platform, named Logan fault (Anglin, 1984). These evidences support a tectonic origin but only a portion of the recorded earthquakes can be related to tectonics.

Thus, regional studies highlighted a higher frequency of mass movements in the early Holocene (St-Onge et al., 2004; Cauchon-Voyer et al., 2011) and liquefaction events interpreted as markers of enhanced seismic activity between 8000 and 1000 cal yr BP (Obermeier et al., 1992). These observations are consistent with deglaciation in the St. Lawrence region, which resulted in significant glacio-isotactic adjustment during the early Holocene (Wu, 1998).

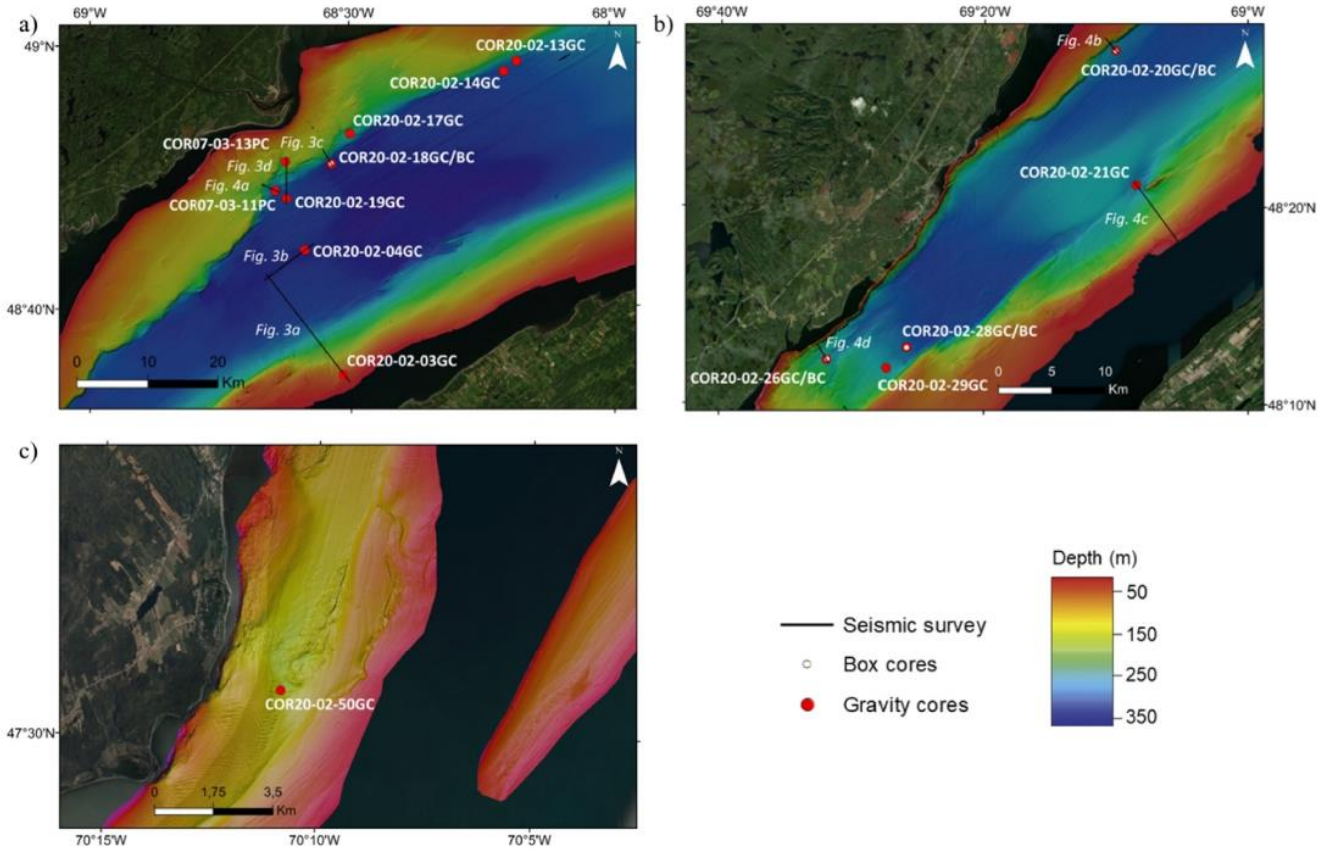

Fig. 2. Bathymetric maps of the Betsiamites – Baie Comeau – Rimouski a), of the Forestville – Saguenay b) and of the Charlevoix sectors c). The gravity and box cores are respectively represented by red and white circles. The black lines correspond to track lines of the acoustic sub-bottom profiler survey. (For interpretation of the references to color in this figure legend, the reader is referred to the Web version of this article.)

In addition to tectonic and glacio-isostatic processes, earthquakes can be influenced by fracturing caused by an asteroid impact in the Charlevoix region about 350 Ma ago (Roy and DuBerger, 1983). The weakness of the fractured crust coupled with glacio-isostatic rebound could partially explain regional seismicity and the high earthquake concentration observed by Roy and DuBerger (1983) in the CKSZ.

Seismicity is the main cause of sediment liquefaction (Seed and Idriss, 1967) which can destabilize submarine slopes and generate submarine landslides (Tuttle and Atkinson, 2010). Indeed, Cauchon-Voyer et al. (2008, 2011) suggest that the alternation of silty clays and sand layers in Unit 4 of the St. Lawrence Quaternary sedimentation could influence the permeability of materials and favor an increase in pore pressure in the case of an earthquake. Consequently, a weak layer in Unit 4 could be generated during an earthquake, thus promoting the development of slip surface. Based on geotechnical analyses and numerical simulations, Martin et al. (2001) showed that this alternation of silty clays and sand in Saguenay Fjord sediments implies high liquefaction susceptibility during an earthquake.

3. Data and methods

3.1. Geophysics

High-resolution swath bathymetry data was collected from 1997 to 2005 between Île-aux-Coudres and Pointe-des-Monts by the Canadian Hydrographic Service using multibeam echosounder systems mounted on the Coast Guard Ship *Frederick G. Creed* (before 2005: Kongsberg EM-1000; in 2005: EM-1002) and launch *Guillemot* (before 2005: EM-3000; in 2005: EM-3002). These surveys provided a full-bottom coverage below 30 m depths at a resolution of 5 m.

In summer 2020, the bathymetric coverage was completed during the SLIDE-2020 cruise on board the RV *Coriolis II* using a Kongsberg EM-2040 multibeam echosounder system coupled with the Applanix POS/MV inertial platform. Surveys were conducted in areas where Pinet et al. (2015) had previously mapped mass-transport complexes with the aim to significantly increase the resolution. A new bathymetric grid with a cell size of 1 m was generated using the Caris Hips & Sips software. Data acquired during the SLIDE-2020 cruise with the celerimeter *Minos* from *AML oceanographic* were used to account for the variability of sound velocity in the water column.

In addition, high-resolution seismic data were collected (Figs. 3 and 4) using the hull-mounted Edgetech X-Star 2.1 subsurface profiler. Hence, about 1500 km of seismic profiles were acquired during the SLIDE-2020 expedition. The source frequency was between 2 and 12 kHz with chirp pulses between 3 and 20 ms. Time-to-depth conversion of the seismic profiles was done using an average sound wave velocity value of 1500 $m.s^{-1}$ corresponding to the velocity in water and the mean value measured on sediment cores using the Multi Sensor Core Logger. Interpretation of the seismostratigraphic sequence was based on seismic attributes such

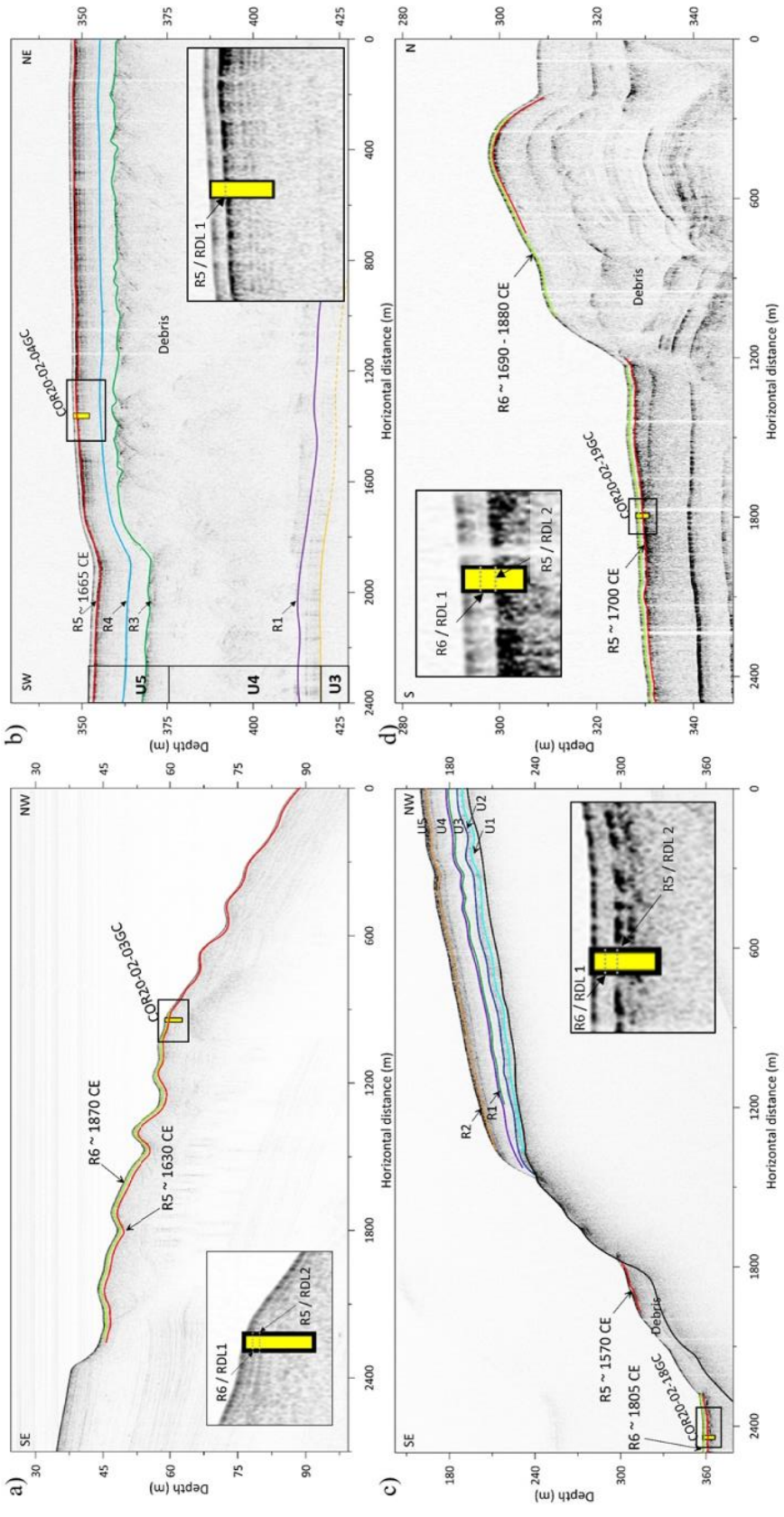

Fig. 3. a) Seismic profile RIM_1T (see Fig. 2 for the locations) on which reflectors R5 and R6 corresponds respectively to turbidites T2 and T1 in core COR20-02-03 GC. b) Seismic profile RIM_1A, transversal to the Betsiamites lobe in the Laurentian Channel. Labels U3 to U5 refer to seismic units and R1 to R5 to seismic horizons described by Cauchon-Voyer et al. (2008). The black square is a close-up view of R5. Reflector R5 correlates with turbidite T1 in the core 20-02-04 GC. c) Seismic profile BET_B_2T with R5 and R6 reflectors (cf. detailed view in the black square) which correspond to turbidites T3 and T2 in COR20-02-18 GC. d) Southern part of seismic profile BET_D_2T. Core COR20-02-19 GC reaches reflectors R6 and R5 at ~0.5 mbsf and ~1.2 mbsf, which are respectively interpreted as turbidites T1 and T2. See supplementary data for uninterpreted seismic profiles.

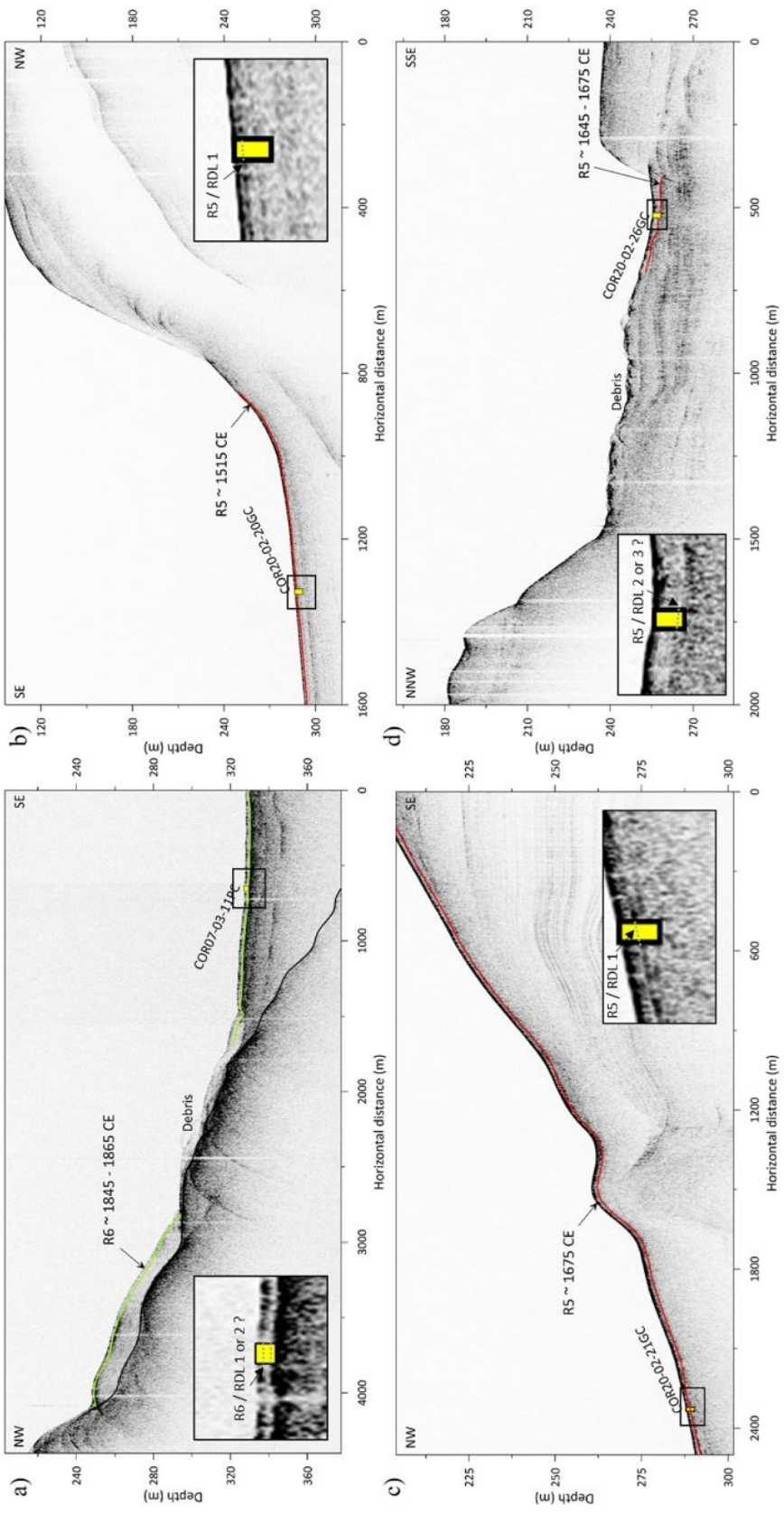

Fig. 4. a) Seismic profile BET_D_3T in the Betsiamites area (see Fig. 2 for the locations). The reflector R6 reached by core COR07-03-11 PC, corresponds to turbidite T1 or T2 dated around 1845–1865 CE. b) Seismic profile FOR_A_1T. Turbidite T1 in COR20-02-20 GC corresponds to R5. c) Seismic profile ESC_BCD_1T. Reflector R5 (cf. detailed view in the black square) correlates with turbidite T1 sampled in core COR20-02-21 GC. See supplementary data for the uninterpreted seismic profiles. d) The seismic profile SAG_H_1T with reflector R5 at the toe of a mass transport deposit. It corresponds to turbidites T2 or T3 observed in core COR20-02-26 GC. See supplementary data for the uninterpreted seismic profiles.

as reflections, geometry and amplitude of reflecting horizons detailed by Cauchon-Voyer et al. (2008).

3.2. Core sampling

During the SLIDE-2020 expedition, cores were recovered over a distance of more than 200 km along the St. Lawrence Estuary, at water depths between 34 and 354 m (Fig. 2). The cores were collected in the CKBSL seismic zone. All thirteen gravity cores and four box cores recovered during SLIDE-2020 are used in this study (Table 1 and Fig. 2). Box cores were subsampled with push cores connected to a pump to avoid compaction of sediment. Unlike gravity cores, they do not disturb the sediment/water interface, which allows for correlation of the gravity and box cores, as well as the use of ^{210}Pb dating on the box cores. The gravity corer used had a maximum length of 6 m. This study also used two piston cores of 2.5 m and 4.1 m long that were recovered during the COR07-03 expedition (RV *Coriolis II*, Cauchon-Voyer et al., 2007).

The core sites are located in the distal part of the mass-transport deposit in order to sample the finest part of the submarine landslide allowing to date the hemipelagic sediment above and below the RDLs. The targeted RDLs are theoretically not affected by local sedimentary processes because they were selected neither at the mouth of active rivers, nor at the end of active turbidity current channels (e.g., Normandeau et al., 2017), or in pockmark-rich areas described by Pinet et al. (2015). However, due to the estuarine context, regional sedimentary processes such as hyperpycnal flows could occur in the St. Lawrence Estuary.

3.3. Sedimentological analyses

Wet bulk density, low-field volumetric magnetic susceptibility (k) and P-Wave velocity were measured using the GEOTECK MSCL (Multi Sensor Core Logger) at ISMER (St-Onge et al., 2007, Figs. 5 and 6). Measurements were performed at intervals of 1 cm on whole sections of gravity cores and 0.5 cm on whole sections subsampled from the box cores.

After splitting the cores, archived halves were photographed and described (texture, color, lithology, structures and bioturbation). Subsequent digital X-ray images were then acquired with the GEOTECK XCT scanner. This non-destructive measurement allows to visualize the sedimentary structures. The denser materials that compose the RDLs appear as light gray on the X-ray images. On split cores, bulk magnetic susceptibility (k) was measured with a point source sensor, while L^*, a^* and b^* color parameters were determined using the Minolta CM-2600d spectrophotometer at 1 cm intervals (Figs. 5 and 6). Because k increases slightly with increasing grain size, this parameter is used to identify RDLs following the method presented by St-Onge et al. (2007). Grain-size analysis (1–2000 μm) was performed using the Master Sizer 3000 (Malvern) laser grain size analyzer with sampling intervals of 1–2 cm in each RDL and 5–20 cm for the background sedimentation. Prior to their analysis, the samples were diluted in a solution composed of distilled water and hexametaphosphate and stirred for 24 h to deflocculate clay particles.

The geochemical composition was measured on archive halves using the non-destructive Olympus Innov-X Delta X-Ray Fluorescence (XRF) scanner in line with the MSCL. The spacing of XRF measurements was similar to that of the other measurements previously mentioned. In this study, the Ca/Fe ratio (biogenic/detrital proxy) and the Rb/Zr ratio (grain size proxy) were used as criteria to identify RDL (Croudace et al., 2006) and to help distinguish the top of RDLs from hemipelagic sedimentation (Figs. 5 and 6). RDLs are numbered between 1 for the youngest and 7 for the oldest and are site-specific. As such, the RDL numbers do not refer to the synchronicity of the deposits.

3.4. Dating

Radiocarbon dating was performed on 45 samples of shells or organic matter that were sampled close to the bases of RDL in the hemipelagic sediments (Table 2). After pre-treatment and graphitization at the *Centre d'études nordiques* at Université Laval (Québec City), they were measured at the Keck-Carbon Cycle AMS facility at the University of California Irvine (USA). To obtain accurate RDL chronology, the ^{14}C ages of hemipelagic samples were calibrated using the Calib 8.2 software (Stuiver and Reimer, 1993) and the Marine20 curve (Heaton et al., 2020). To consider the local offset from the global ocean reservoir (ΔR), two reservoir ages from McNeely et al. (2006) were used. These reservoir ages are closest to the study area with one at Matane of $\Delta R = 77 \pm 60$ ^{14}C yr and one at Pointe John of $\Delta R = -13 \pm 70$ ^{14}C yr. They were averaged to have a final reservoir age of $\Delta R = 39 \pm 63$ ^{14}C yr for shell samples. Finally, the radiocarbon ages were converted to calendar ages (CE) for comparison with historical earthquakes (Table 2).

To construct the best-fit age models, the R software package Bacon 2.3 (Blaauw and Christen, 2011) was used. It considers Bayesian statistics with a normal distribution. Both standard deviations of 1 σ (probability of 0.95) and 2 σ (probability of 0.68) were used in calculations (Fig. 7). In these calculations, turbidite erosion was assumed negligible because it was not possible to quantify basal erosion.

Sedimentation rates were derived from ^{210}Pb measurements on sediments from 4 box cores (Table 3 and Fig. 8). The cores were sampled at intervals ranging from 1 to 5 cm and freeze-dried, then ground to a fine, homogenous powder. The ^{210}Pb activity was measured using a GMX50-S gamma counter from Ortec and GX7020 counter from Canberra. Considering the constant flux and constant rate model (Appleby and Oldfield, 1978), the sedimentation rates (cm.yr^{-1}) were derived from the slope of Ln (^{210}Pb$_{excess}$) in the region of radioactive decay (Fig. 8). The ages of turbidites were then calculated by extrapolating a constant sedimentation rate down to the hemipelagic depth of turbidites. Sediment compaction is neglected because the density curve of hemipelagic sedimentation appears constant with depth (Fig. 8).

4. Results

4.1. Facies identification

The four cores presented in Figs. 5 and 6 show the sedimentary facies observed on analyzed cores. They were selected to best illustrate the characteristics of the different types of RDLs. An exhaustive list of all the sediment cores is presented in the supplementary data. The results of core analysis identified two mains facies: hemipelagites and RDLs (Figs. 5 and 6). Hemipelagites are consistent with normal "background", hemipelagic sedimentation while RDLs are a result of almost instantaneous deposition. Hemipelagites consist of homogenous gray-colored silts (Munsell value 5 YR 5/1). The gray tone varies with the intensity of bioturbation from dark gray (5 YR 4/1) to very dark gray (5 YR 3/1). The hemipelagites are composed of 10–20% clay (<2 μm), 65–75% silt (2–63 μm) and 10–20% sand (63 μm - 2 mm). Their gamma density values are constant with depth and oscillate between 1.4 and 1.6 g cm^{-3}. On X-ray images, hemipelagites appear in homogenous black gray and their values of magnetic susceptibility are relatively low (~125.10^{-5} SI) compared to RDLs (~500.10^{-5} to 750.10^{-5} SI). Overall, hemipelagites have the same properties across the St.

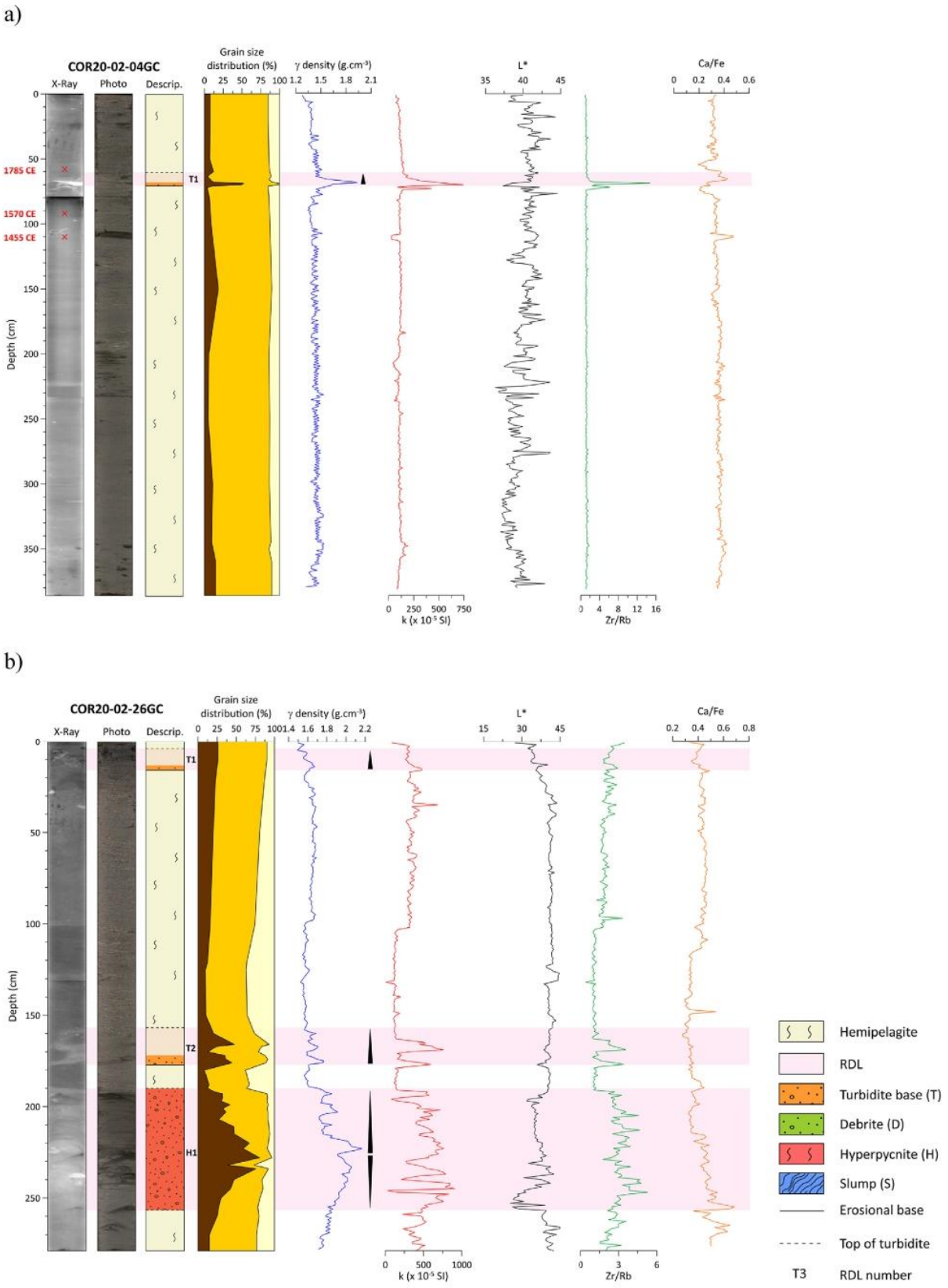

Fig. 5. Results of the sedimentological analyses carried out on cores a) COR20-02-04 GC and b) COR20-02-26 GC. From left to right: X-ray image, digital photography, sedimentological description, γ-density, magnetic susceptibility *k*, lightness *L**, Zr/Rb and Ca/Fe.

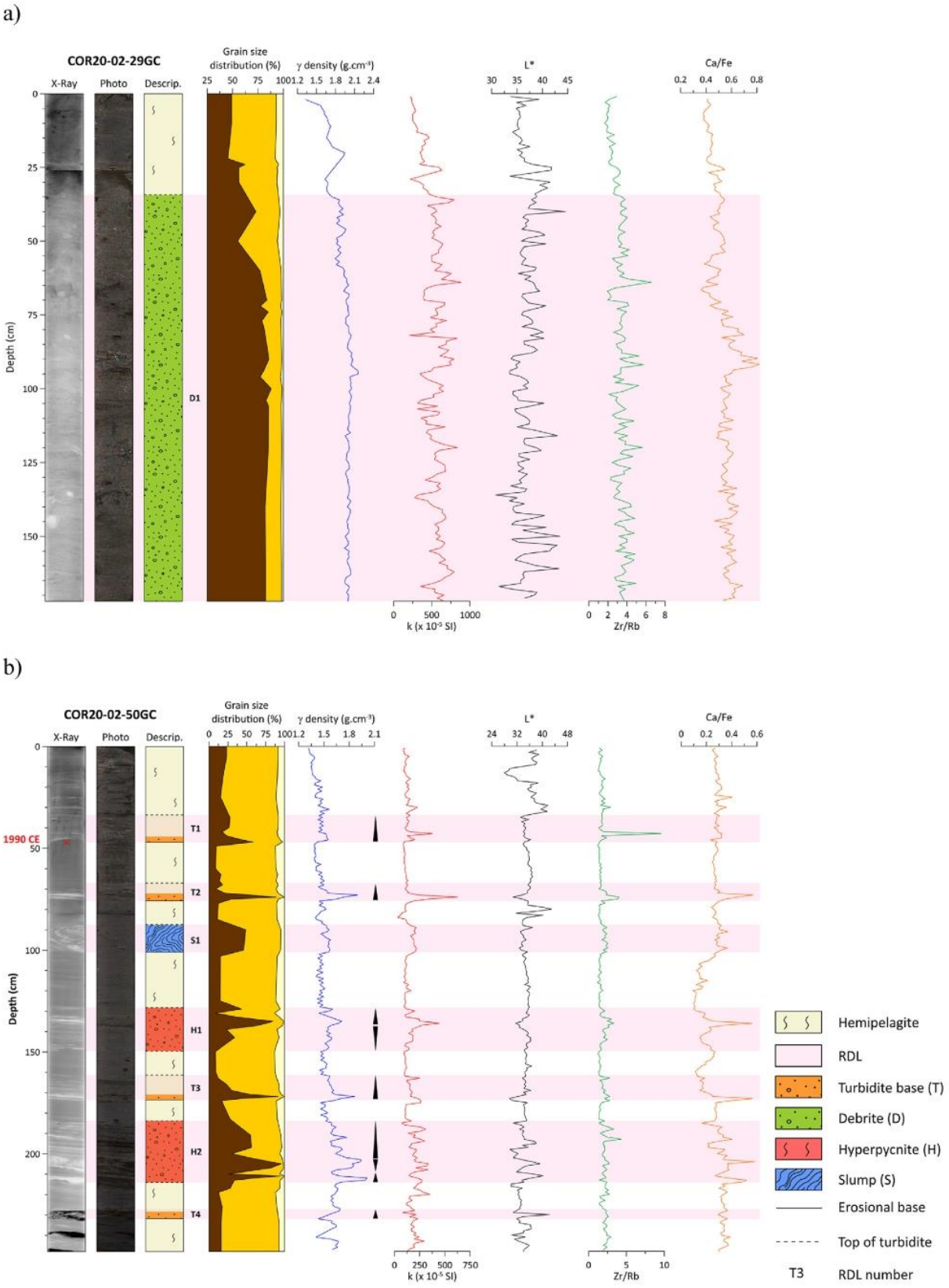

Fig. 6. Results of the sedimentological analyses carried out on cores a) COR20-02-29 GC and b) COR20-02-50 GC. From left to right: X-ray image, digital photography, sedimentological description, γ-density, magnetic susceptibility *k*, lightness *L**, Zr/Rb and Ca/Fe.

Table 2
Radiocarbon analyses from cores recovered in the St. Lawrence Estuary (Québec).

Core	Lab. num.	Depth (cm)	Sample type	^{14}C age (BP)	ΔR	Calibrated age (yr BP) ± 1σ	Calibrated age (CE) ± 1σ
COR07-03-13 PC	ULA-9628	10.00	Organic matter	255 ± 15	–	300 ± 5	1650 ± 5
COR20-02-03 GC	ULA-9787	8.00	Shell	Modern	39 ± 63	−55 ± 5	2005 ± 5
	ULA-9788	89.50	Shell	765 ± 15	39 ± 63	180 ± 95	1770 ± 95
	ULA-9789	99.50	Shell	780 ± 20	39 ± 63	195 ± 100	1755 ± 100
	ULA-9790	135.50	Shell	920 ± 15	39 ± 63	345 ± 85	1605 ± 85
	ULA-9791	356.75	Shell	2020 ± 20	39 ± 63	1380 ± 90	570 ± 90
COR20-02-04 GC	ULA-9645	47.00	Shell	745 ± 15	39 ± 63	165 ± 95	1785 ± 95
	ULA-9642	92.50	Shell	965 ± 15	39 ± 63	380 ± 80	1570 ± 80
	ULA-9644	109.50	Shell	1095 ± 15	39 ± 63	495 ± 80	1455 ± 80
COR20-02-13 GC	ULA-9652	17.50	Shell	1190 ± 15	39 ± 63	570 ± 50	1380 ± 50
	ULA-9653	19.50	Shell	1210 ± 15	39 ± 63	585 ± 70	1365 ± 70
	ULA-9647	84.75	Shell	2915 ± 15	39 ± 63	2465 ± 115	−515 ± 115
	ULA-9648	161.50	Shell	4875 ± 15	39 ± 63	4920 ± 110	−2970 ± 110
COR20-02-14 GC	ULA-9792	9.25	Shell	675 ± 20	39 ± 63	110 ± 80	1840 ± 80
	ULA-9793	46.0.	Shell	1640 ± 15	39 ± 63	995 ± 95	955 ± 95
	ULA-9794	65.00	Shell	2020 ± 15	39 ± 63	1380 ± 175	570 ± 175
	ULA-9816	71.50	Shell	2125 ± 15	39 ± 63	1490 ± 195	465 ± 195
	ULA-9817	97.50	Shell	2780 ± 15	39 ± 63	2280 ± 220	−330 ± 220
COR20-02-17 GC	ULA-9818	73.50	Shell	1655 ± 20	39 ± 63	1010 ± 95	940 ± 95
	ULA-9819	198.75	Shell	3285 ± 20	39 ± 63	2895 ± 105	−945 ± 105
	ULA-9820	259.50	Shell	4590 ± 15	39 ± 63	4565 ± 120	−2615 ± 120
COR20-02-18 GC	ULA-9654	80.25	Shell	1180 ± 15	39 ± 63	565 ± 70	1385 ± 70
	ULA-9682	204.50	Shell	3690 ± 20	39 ± 63	3395 ± 105	−1445 ± 105
	ULA-9620	213.25	Wood	3395 ± 15	–	3030 ± 80	−1135 ± 80
	ULA-9655	331.50	Shell	8485 ± 20	39 ± 63	8835 ± 125	−6885 ± 125
COR20-02-19 GC	ULA-925	14.00	Alga	Modern	–	−45 ± 5	1995 ± 5
	ULA-9646	201.50	Shell	2460 ± 15	39 ± 63	1885 ± 210	65 ± 210
COR20-02-20 GC	ULA-9650	40.00	Shell	790 ± 20	39 ± 63	205 ± 100	1745 ± 100
	ULA-9669	204.50	Shell	2255 ± 20	39 ± 63	1635 ± 100	315 ± 100
	ULA-9670	423.50	Shell	3915 ± 15	39 ± 63	3670 ± 110	−1720 ± 110
COR20-02-21 GC	ULA-9671	96.00	Shell	920 ± 15	39 ± 63	345 ± 85	1605 ± 85
	ULA-9672	178.50	Shell	2175 ± 15	39 ± 63	1545 ± 105	405 ± 105
COR20-02-50 GC	ULA-9784	46.50	Wood	Modern	–	−40 ± 5	1990 ± 5

Lawrence Estuary, though they are generally coarser in the Middle Estuary with 10% clay, 80% silt and 10% sand (e.g., COR20-02-50 GC). Likewise, the thickness of hemipelagites is between 10 and 20 cm in the Lower Estuary (e.g., COR20-02-50 GC) and higher than 50 cm in the Middle Estuary (e.g., COR20-02-04 GC).

On X-Ray images, light gray layers intersect the hemipelagic sedimentation. These layers correspond to RDL facies. Their physical properties, detailed below, contrast clearly with background sedimentation and their bases are mainly sharp, while their upper contacts are gradational. The internal structure and grain size distribution vary between RDLs, such that four groups can be distinguished: turbidites (T), debrites (D), hyperpycnites (H) and slump (S).

In the 15 cores, 43 turbidites (T) were identified (see supplementary data). Their thickness varies between ~3 and 73.5 cm with a mean value of 18.5 cm (Table 4). The bases are sharp and the grain size analyses reveal a normal grading typical of the Bouma-type turbidite (Bouma, 1962). Indeed, turbidites are characterized by a sandy base (fine to coarse sand) with sometimes gravels or rock fragments (<2 mm) as in turbidite T1 in core COR20-02-21 GC. The coarser material at the base of the turbidite layers is associated with high values of density and magnetic susceptibility, contrasting sharply with the overlying and underlying hemipelagic sediments. In core COR20-02-04 GC (Fig. 5), turbidite T1 presents a maximum density of 1.93 g cm^3 and a magnetic susceptibility of 744.10^{-5} SI, which both contrast with values of 1.45 g cm^3, and 144.10^{-5} SI in hemipelagic sediments. The coarse base of this turbidite layer likely comprises heavy minerals such as magnetite (e.g., Goldfinger et al., 2007; Jaegle, 2015) and is darker (L* = 37.5) compared to the under- and overlying background sediments (L* = 40.5), suggesting that this parameter could be used to discriminate the base of turbidites. Furthermore, the two chosen geochemical ratios in core COR20-02-04 GC are relatively constant in the hemipelagites (Zr/Rb = 1.22 and Ca/Fe = 0.34), but follow the grain size evolution of the turbidites with the highest values at the base (Zr/Rb = 14.75 and Ca/Fe = 0.43) gradually decreasing toward the top. These geochemical signatures, sensitive to grain size, can be used in addition to the previous parameters to accurately identify the base and top of turbidites.

Debrites (D) produced by debris flows constitute the second type of RDL identified in sediment cores. Only four debrites are identified in four cores. These deposits are more proximal to the source of submarine landslides than turbidites. The debrites include rock fragments up to ~10 cm in length, observable on XCT images (Fig. 6). As shown in D1 of core COR20-02-29 GC, these rock fragments vary in nature, size, angularity and orientation in a sandy-silty matrix composed of 75% sand, 20% silt and 5% clay (D_{50} ~150 μm). Thus, cores containing debrite layers are relatively short because the corer could not fully penetrate these deposits, unlike turbidites. Density and magnetic susceptibility are high with average values of respectively 1.95 g/cm^3 and 560.10^{-5} SI in core COR20-02-29 GC. In addition, contrary to turbidites, the debrites are massive and chaotic with no observable grading. The debrite in core COR07-03-11 PC (D1) (see supplementary data) is composed of a block of terrestrial organic material. Larger rock fragments are observed at the base of the debrite layer.

The RDLs characterized by reverse grading at the base followed by normal grading are interpreted as hyperpycnites (H) resulting from a hyperpycnal flow (Mulder et al., 2003; St-Onge et al., 2004). Hyperpycnites were observed in core COR20-02-26 GC (Fig. 5) recovered near the mouth of the Saguenay Fjord (~5 km). The

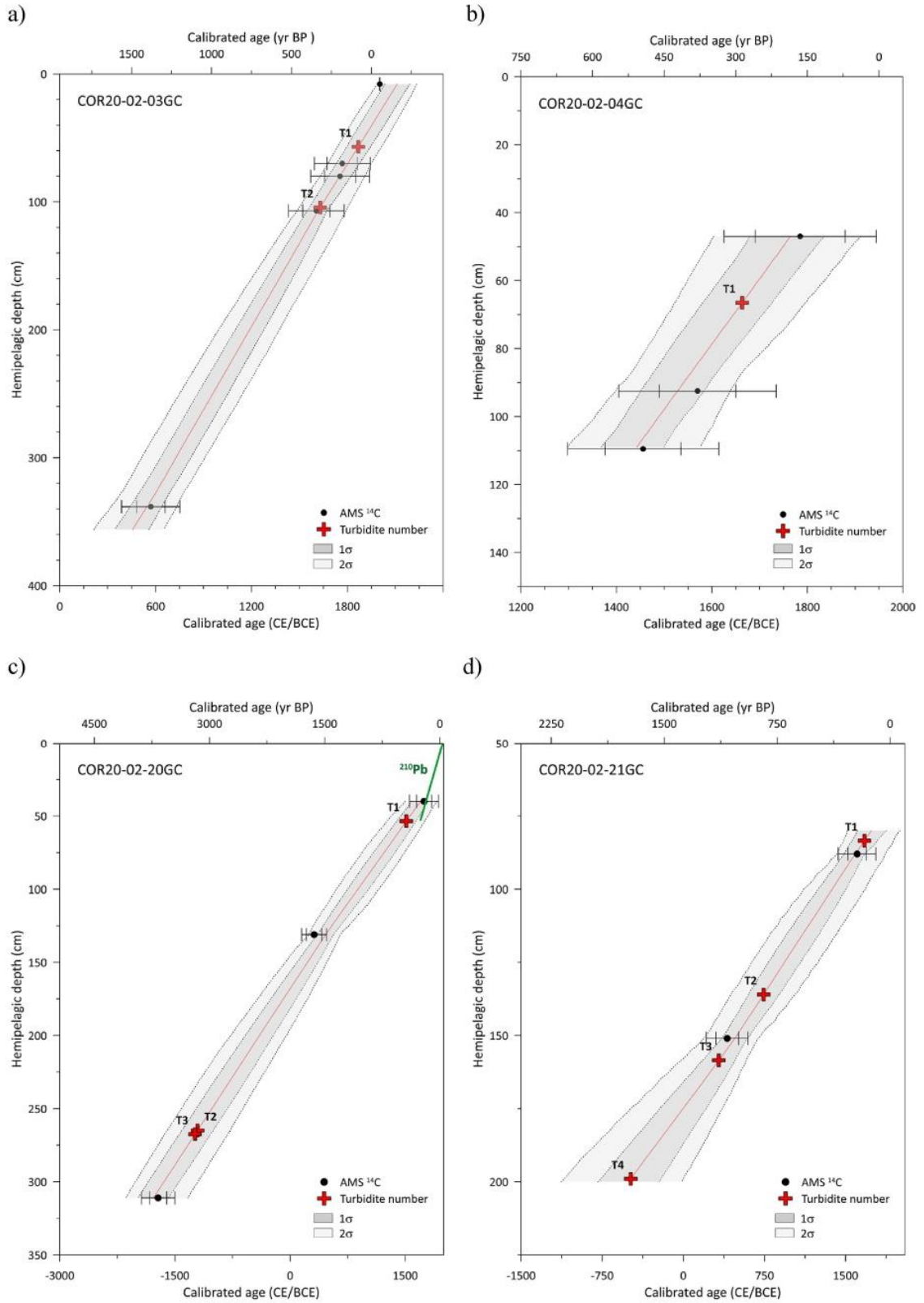

Fig. 7. Age models for cores COR20-02-03 GC a), COR20-02-04 GC b), COR20-02-20 GC c) and COR20-02-21 GC d). The hemipelagic depth, i.e., depth excluding RDLs, is plotted as a function of calibrated ages (BP and CE/BCE). The black circles correspond to the dated samples and the red crosses to the turbidites. The age probability of 2 σ and that of 1 σ, are respectively shown in light and medium gray tone. (For interpretation of the references to color in this figure legend, the reader is referred to the Web version of this article.)

Table 3
Sedimentation rates calculated and used in this study.

Box cores #	Date of sample (mm-dd-yyyy)	Sedimentation rate (cm.yr $^{-1}$)	Error ± 1 σ (cm.yr^{-1})
COR20-02-18BC-A	07-22-2020	0.32	0.045
COR20-02-20BC-B	07-23-2020	0.15	0.020
COR20-02-26BC-A	07-24-2020	0.42	0.040
COR20-02-28BC-B	07-24-2020	0.37	0.020

reverse grading at its base (256.5–226 cm) corresponds to the rising limb of the flood. Above 226 cm, the normal grading (226–190 cm) reflects the falling limb. Two hyperpycnites are also found in core COR20-02-50 GC (Fig. 6) sampled in the La Malbaie area.

A fourth type of RDL is characterized by the presence of a slump deposit (S) (Fig. 6). This deposit was found only at 100 cm in core COR20-02-50 GC. This is a 13.5-cm thick layer of silty-sand inducing peaks in density, magnetic susceptibility and Zr/Rb. The grains are not sorted and strong internal deformation is recognizable on the X-ray images. In summary, 43 of the RDLs are turbidites, four are debrites, three are hyperpycnites and one is a slump, highlighting the higher proportion of turbidites.

4.2. Age of the RDLs

The radiocarbon and ^{210}Pb results provided dating of 51 RDLs from 15 different cores (Table 4). The ages are between around 5035 cal yr BP and ~1991 CE. Only four age models are presented here (Fig. 7), the others are available in the supplementary data. In the next sections, the age of the RDLs are described for each area.

4.2.1. Baie-comeau

In the Baie-Comeau sector, turbidites T1, T2, T3, T4 and T5 in core COR20-02-13 GC were deposited respectively ~1145 CE, 520 CE, 4525 cal yr BP, 4905 cal yr BP and 4940 cal yr BP. In COR20-02-14 GC, four turbidites were deposited more recently around 1580 CE for the uppermost turbidite T1 and 1085 CE, 635 CE and 3270 cal yr BP for turbidites T2, T3 and T4.

4.2.2. Betsiamites-rimouski

Further west, in the Betsiamites area, the most recent turbidites (T1) in cores COR20-02-17 GC and COR20-02-18 GC are both dated ~ 1640–1680 CE while turbidite T2 in core COR20-02-17 GC is dated around 1560 CE. The age of the oldest turbidites is estimated at 5035 cal yr BP (T7) and 4830 cal yr BP (T6). Sedimentation rates calculated from the box core COR20-02-18BC-A provide respective ages of 1905 CE and 1805 CE for turbidites T1 and T2. In core COR07-03-13 PC recovered in the submarine landslide scar of the Betsiamites area, debrite D1 is estimated to be ~1650 CE based on dating of an intact block of terrestrial material. Turbidites T1 in cores COR20-02-04 GC and COR20-02-19 GC are dated to 1665 CE and 1690 CE respectively. Turbidite T2 in core COR20-02-19 GC is older with an age of 1115 CE. The ^{210}Pb-derived sedimentation rate of 0.32 cm.yr^{-1} in box core COR20-02-18BC-A yields more recent ages of 1880 CE and 1700 CE for T1 and T2 respectively. When considered for the nearby core COR07-03-11 PC, this sedimentation rate gives an age of 1865 CE for turbidite T1 and 1845 CE for T2. On the other side of the St. Lawrence Estuary, near of the city of Rimouski, turbidite T1 is dated at 1870 CE and T2 at 1630 CE.

4.2.3. Forestville

In core COR20-02-20 GC, collected in the Forestville area, turbidite T1 at a depth of 53.5 cm is dated at 1515 CE. Based on a ^{210}Pb-derived sedimentation rate of 0.15 cm.yr^{-1} calculated from the associated box core COR20-02-20BC-B, turbidite T1 dates back to 1665 CE. The older turbidites T2 and T3 are dated respectively to 3155 cal yr BP and 3190 cal yr BP. In core COR20-02-21 GC, recovered near a submarine landslide, turbidite T1 is observed at 83.5 cm depth and dated at 1675 CE. Turbidites T2, T3 and T4 in core COR20-02-21 GC have older ages of 745 CE, 325 CE and 2435 cal yr BP.

4.2.4. Saguenay

In the Saguenay area, the RDLs could not be dated by ^{14}C due to the absence of datable material. However, two sedimentation rates of 0.42 cm. yr^{-1} and 0.37 cm. yr^{-1} were calculated from the ^{210}Pb measurements in box cores COR20-02-26BC-A and COR20-02-28BC-B, respectively. The turbidite T1 found at 4 cm depth in core COR20-02-26 GC can thus be dated to 2010 CE, whereas turbidite T2 at 145 cm is dated at 1675 CE and the hyperpycnite H1 (158 cm) at 1645 CE. The debrite D1 identified in COR20-02-28GC-3 was dated at 1885 CE using the ^{210}Pb derived sedimentation rate of 0.37 cm. yr^{-1} in box core COR20-02–28BCE. Close to this coring site (~2.5 km), at the same water depth, core COR20-02-29 GC sampled the deposit linked to another submarine landslide. By using the sedimentation rate of box core COR20-02-28GC-3, the debrite D1 at 34 cm depth was dated at 1930 CE.

4.2.5. La Malbaie

In core COR20-02-50G from the Malbaie area, only one wood fragment could be sampled and dated at 1990 CE. As the hemipelagic sediments are close to the base of turbidite T1 from that core (~0.5 cm), we can consider an age of 1990 CE for T1. With seven RDLs preserved in a relatively short core (~2.28 m), core COR20-02-50 GC presents the highest frequency of RDLs of all the studied cores.

4.3. Correlation with seismic data

A sub-horizontal reflector with strong amplitude was identified at shallow depths (<2.0 m) on seismic profiles acquired across the different submarine landslide areas (Fig. 2). This reflector drapes the underlying sediments and is covered by a transparent acoustic facies (Figs. 2 and 3). According to the description and interpretation made by Cauchon-Voyer et al. (2008), the sedimentary deposits of the submarine landslide triggered by the 1663 CE earthquake were also characterized by the presence of a high amplitude reflector called R5 by these authors, underlying a transparent facies.

Near Rimouski, at the southern side of the Laurentian Channel, a reflector similar to R5 was identified in seismic profile RIM_1T (Fig. 3) at ~1.3 m depth below the deformed seafloor and shows an angular discordance with deeper, undisturbed reflectors. In the Betsiamites area, R5 type reflector was identified in seismic profile RIM_1A that crosses the lobe deposit of Betsiamites (Bernatchez, 2003) at a depth of ~0.75 m below the seafloor (Fig. 3). The deeper reflectors R1 to R4 and the seismic units U3 to U5 described by Cauchon-Voyer et al. (2008) are also visible and delimited. In seismic profiles BET_B_2T, R5 type reflector is found at a depth of ~1.8 mbsf (Fig. 3) while further to the south, it is identified at a depth of ~1.2 mbsf in the BET_D_2T profile (Fig. 3). In the Forestville area, the R5 type reflector is visible on both sides of the Laurentian

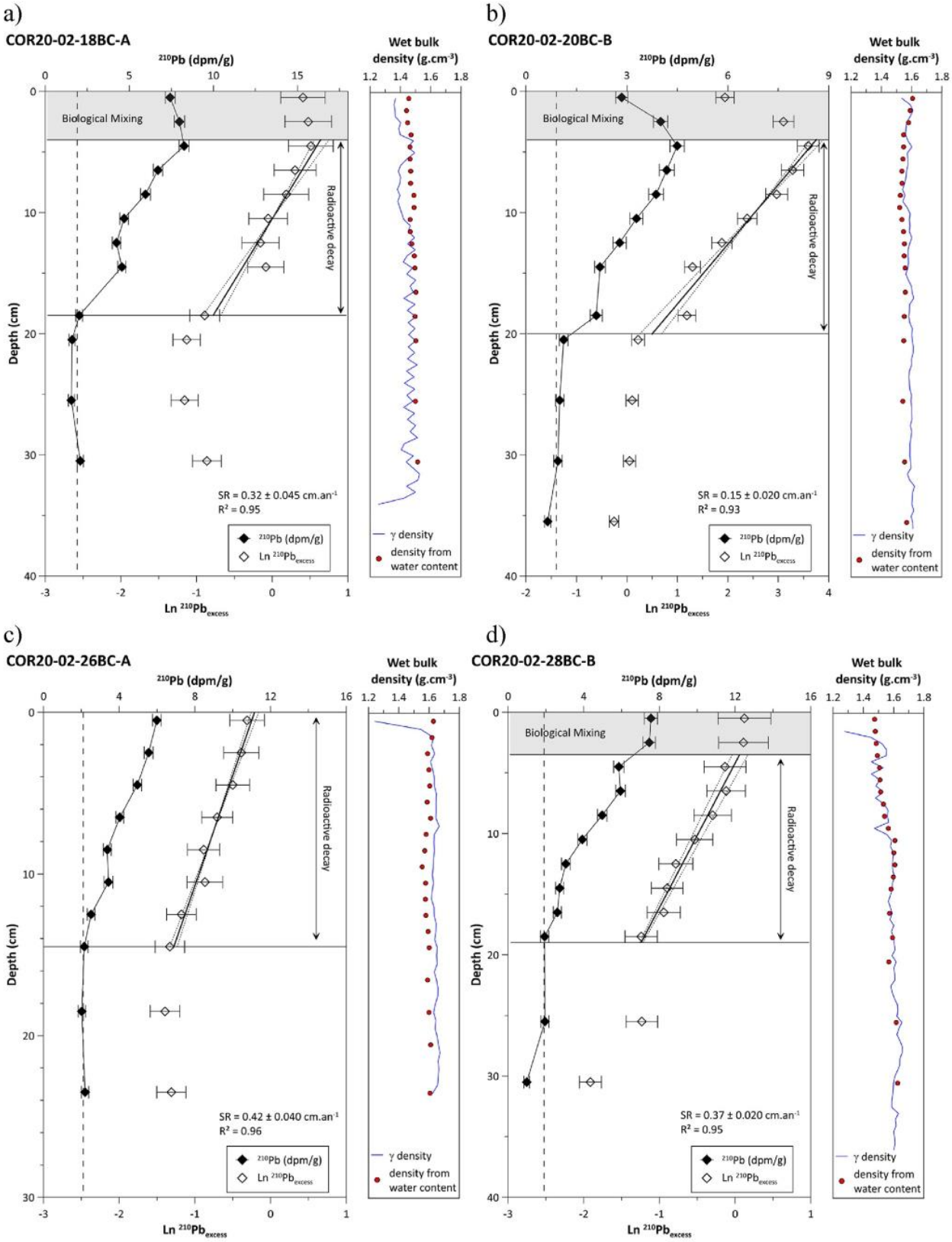

Fig. 8. Sedimentation rates (SR) calculated with the ^{210}Pb activity in cores COR20-02-18BC-A (SR = 0.32 cm.yr^{-1}, a), COR20-02-20BC-B (SR = 0.15 cm.yr^{-1}, b), COR20-02-26BC-A (SR = 0.42 cm.yr^{-1}, c) and COR20-02-28BC-B (SR = 0.37 cm. yr^{-1}, d). SR are calculated from the slope of Ln (^{210}Pb$_{excess}$) in the radioactive zone by excluding the biological mixing.

Table 4
Age[14]C (CE/BCE) of turbidites, hyperpycnites and debrites identified in the 15 cores used in this study (see supplementary data for all age models and sedimentological analyses of all cores).

Layer	Total depth (cm)	Hemipelagic depth (cm)	Thickness (cm)	Type of deposit	Estimated[14]C age (yr BP), or (CE) when reported	Error ± 1 σ	Estimated age[210]Pb (CE)	Error ± 1 σ
Baie-Comeau								
COR20-02-13 GC								
RDL1	23	23	13	Turbidite	1145 CE	110		
RDL2	50.5	37.5	18.5	Turbidite	520 CE	260		
RDL3	181	149.5	11	Turbidite	4525	645		
RDL4	210.5	168	55.5	Turbidite	4905	640		
RDL5	268	170	33	Turbidite	4940	660		
COR20-02-14 GC								
RDL1	15	15	15	Turbidite	1580 CE	135		
RDL2	43	28	3	Turbidite	1085 CE	95		
RDL3	64	46	3	Turbidite	635 CE	315		
RDL4	153.5	132.5	8.5	Turbidite	3270	320		
Betsiamites								
COR20-02-17 GC								
RDL1	14	14	4.5	Turbidite	1680 CE	180		
RDL2	25.5	21	12.5	Turbidite	1560 CE	180		
RDL3	104	87	7	Turbidite	195 CE	220		
RDL4	124	100	11	Turbidite	2075	235		
RDL5	173	138	21.5	Turbidite	3020	175		
RDL6	241.5	185	15	Turbidite	4540	395		
RDL7	279	207.5	18	Turbidite	5035	430		
COR20-02-18 GC								
RDL1	37.5	37.5	13.5	Turbidite	1640 CE	100	1905	15
RDL2	82	68.5	10	Turbidite	1245 CE	135	1805	30
RDL3	167	143.5	22	Turbidite	3200	240		
RDL4	193	147.5	8	Turbidite	3335	225		
RDL5	236.5	183	38	Turbidite	4630	540		
RDL6	279	187.5	8.5	Turbidite	4830	590		
COR07-03-11 PC								
RDL1	50	50	62.5	Turbidite			1865	25
RDL2	118.5	56	126.5	Debrite			1845	25
COR07-03-13 PC								
RDL1	3	3	101.5	Debrite	1650 CE	5		
RDL2	357	354	25	Turbidite				
RDL3	386	358	11.5	Turbidite				
COR20-02-04 GC								
RDL1	66.5	66.5	11.5	Turbidite	1665 CE	70		
COR20-02-19 GC								
RDL1	44.5	44.5	4	Turbidite	1690 CE	90	1880	20
RDL2	107	103	10.5	Turbidite	1115 CE	140	1700	50
Rimouski								
COR20-02-03 GC								
RDL1	57	57	19.5	Turbidite	1870 CE	75		
RDL2	124	104.5	9	Turbidite	1630 CE	60		
Forestville								
COR20-02-20 GC								
RDL1	53.5	53.5	73.5	Turbidite	1515 CE	125	1665	35
RDL2	338.5	265	10.5	Turbidite	3155	140		
RDL3	351.5	267.5	28.5	Turbidite	3190	150		
COR20-02-21 GC								
RDL1	83.5	83.5	18	Turbidite	1675 CE	115		
RDL2	154	136	19.5	Turbidite	745 CE	140		
RDL3	196	158.5	10.5	Turbidite	325 CE	150		
RDL4	247	199	11	Turbidite	2435	275		
Saguenay								
COR20-02-26 GC								
RDL1	4	4	12	Turbidite			2010	5
RDL2	157	145	20	Turbidite			1675	30
RDL3	190	158	66.5	Hyperpycnite			1645	35
COR20-02-28GC-3								
RDL1	50	50	not fully cored	Debrite			1885	10
COR20-02-29 GC								
RDL1	34	34	not fully cored	Debrite			1930	5
La Malbaie								
COR20-02-50 GC								
RDL1	33.5	33.5	13	Turbidite	1990 CE	5		
RDL2	67	54	9	Turbidite				
RDL3	87.5	65.5	13.5	Slump				
RDL4	128.5	93	21.5	Hyperpycnite Turbidite				
RDL5	161	104	12.5	Hyperpycnite Turbidite				
RDL6	184	114.5	30					
RDL7	227	127.5	5					

Channel at a depth between ~1.0 mbsf and ~1.3 mbsf, in the seismic profiles FOR_A_1T and ESC_BCD_1T (Fig. 4). The R5 type reflector is again identified in the Saguenay area in seismic profile SAG_H_1T at about 2.0 mbsf depth (Fig. 4).

A correlation between sedimentological data and seismic profiles reveals that the R5 type reflector systematically corresponds to the base of RDLs. Thus, the RDLs correspond to strong sub-horizontal and parallel reflectors above and at the end of mass-transport deposits characterized by a chaotic and transparent seismic facies (Figs. 3 and 4). In the Betsiamites area, reflector R5 corresponds to the presence of turbidite T1 dated to 1665 CE in core COR20-02-04 GC. In COR20-02-19 GC, R5 corresponds to turbidite T2 estimated at 1700 CE based on the ^{210}Pb derived sedimentation rate. Turbidite T3 in core COR20-02-18 GC is also related to reflector R5 and is dated to 1570 CE based on the ^{210}Pb derived sedimentation rate. In the Rimouski area, turbidite T2 dated to 1630 CE is at the same depth as the R5 reflector. In Forestville, the turbidites T1 in core COR20-02-20 GC and T2 in core COR20-02-21 GC, are respectively dated around 1515-1665 CE and 1675 CE and located at a depth corresponding to that of reflector R5. Finally, this reflector is at the same depth as turbidites T2 or T3 in core COR20-02-26 GC collected at the mouth of the Saguenay River and dated between 1645 and 1675 CE. The similarity of these ages with the age interpreted by Cauchon-Voyer et al. (2008) confirms that the sub-horizontal reflectors described in the present study correspond to the seismic reflector R5.

A second reflector R6, shallower than R5 (<1 m) and characterized by a weaker amplitude is observed in the Betsiamites and Rimouski areas (Fig. 3). R6 correlates with the depth of turbidite T2 (~0.80 m) in COR20-02-18 GC, turbidite T1 (~0.50 m) in core COR20-02-19 GC, turbidite T1 or T2 (~0.50–1.20 m) in core COR07-03-11 PC and turbidite T1 (~0.60 m) in core COR20-02-03 GC. These three turbidites dated 1805 CE, 1690–1880 CE and 1870 CE, respectively.

5. Discussion

5.1. Relationship between submarine landslides and rapidly deposited layers (RDL)

The irregularity of deposits and the presence of coarse material and debris in submarine landslides makes coring difficult. During the SLIDE-2020 expedition, the coring sites were determined in order to overcome this limitation by targeting sub-horizontal reflectors in the distal part of submarine landslides where they are thin enough for their underlying and overlying sediments to be dated (e.g., Piper et al., 2019). The relationship between these reflectors and the mass-transport deposits is observed in the Betsiamites area (seismic profile BET_D_2T) and the Saguenay area (seismic profile SAG_H_1T) where the R5 reflector corresponding to RDLs is in the continuity with the sliding mass and above (Strachan, 2008). However, the fact that this geometry is not systematically identified, does not imply that this genetic link does not exist. Indeed, the coring revealed that the R5 reflector extending over the Lower Estuary corresponds to RDLs that may have been triggered by a submarine landslide or debris flow. The large number of turbidites observed in the cores recovered during the SLIDE2020 expedition validates their correspondence with sub-horizontal seismic reflectors distal to submarine landslides. Furthermore, it implies that the submarine landslides have progressively transformed into turbidity currents. The proximal turbidites have a higher proportion of coarse sediment (e.g., T2 in COR20-02-19 GC, d_{50} ~ 103 μm) than distal turbidites (e.g., T1 in COR20-02-04 GC, d_{50} ~ 28 μm) and the cores recovered from a site very close to mass transport deposits revealed debrites (e.g., COR20-02-29 GC) confirming that the RDLs are deposited by submarine landslides. The fragment of terrestrial soil in debrite D1 of core COR07-03-13 PC which may have been transported by the 1663 CE Colombier event along coast of the Betsiamites area (see Bernatchez, 2003) tends to support this relationship.

5.2. Chronology of the RDLs and triggering factors

The dated RDLs are assembled in Fig. 9. This figure reveals four distinct periods with at least twelve concomitant submarine landslides at the regional scale. The first period is between 1560 CE and 1710 CE with nine submarine landslides with a mean age of 1635 ± 75 CE spread over 140 km. RDLs deposited at this period correspond to reflector R5, observed regionally and dated to 1630 ± 65 CE (Fig. 9). The second period begins at 1800 CE and ends at 1900 CE. It includes six submarine landslides over a distance of 110 km and RDLs deposited in this period correlate with the seismic reflector R6 dated to 1830 ± 70 CE. The third period spans from 1910 CE to 1930 CE with two submarine landslide in the Betsiamites area and another 110 km away in the Saguenay. Finally, the fourth period extends from 1990 CE to 2010 CE with two submarine landslides 80 km apart.

The dating of RDLs presented in Table 4 includes ages beyond 2000 years, but they are not included in the synthesis in Fig. 9. Indeed, from ages older than 2000 years, the uncertainties become more important and it is difficult to establish with certainty that RDLs are synchronous. Moreover, it is not possible to establish a link between these deposits and historical seismicity.

During the four periods identified, four to five major historical earthquakes occurred in the St. Lawrence Estuary region (Lamontagne et al., 2018): 1663 ($M \leq 7$), 1860 ($M = 6.1$) or 1870 ($M = 6.6$), 1925 ($M = 6.2$) and 1988 ($M = 5.9$) (Table 5). The difference between the ^{14}C ages and ages calculated from sedimentation rates for the different RDLs may be related to the accuracy of the dating method and RDL thickness measurements. The most accurate cases correspond to turbidites T1 in cores COR20-02-04 GC and COR20-02-20 GC. Indeed, in core COR20-02-04 GC, turbidite T1 is already considered to be associated with the 1663 CE earthquake by Cauchon-Voyer et al. (2008) and has been dated at 1665 CE based on ^{14}C dating of the immediately underlying hemipelagic deposits. The ^{210}Pb dating of turbidite T1 in core COR20-02-20 GC yields an age of 1665 ± 35 CE, in agreement with the ^{14}C age considering the dating uncertainties (1515 CE ± 125 at 1σ and 1515 CE ± 245 at 2σ). The density profiles obtained with the MSCL and from water content measurements do not show a linear evolution with depth, but a rather stable density over the upper 2 m, suggesting that compaction can be neglected for the age calculations of the RDL with ^{210}Pb-derived sedimentation rates. The reliability of these dates supports the correlation between submarine landslides and historical seismicity but the close age of the 1860 and 1870 CE earthquakes does not lend to differentiate these events from our chronology owing to the age uncertainty of the dated RDLs.

Submarine landslides triggered by earthquakes have already been described in other regions of the world (e.g., Bryn *et al.*, 2005; Dan et al., 2009). Ground shaking during an earthquake constitutes a major factor for slope destabilization (Hampton et al., 1996) and its influence can exceed several hundreds of kilometers to trigger several independent failures (Goldfinger et al., 2012, 2017). The synchronicity between RDLs in a seismic region is increasingly used for the study of paleoseismicity during the Holocene (Goldfinger et al., 2007; Gracia et al., 2010; Ratzov et al., 2015; Howarth et al., 2021). Storms, river floods and rapid relative sea level rise can also trigger submarine landslides and turbidites at the regional scale (~100 km) (Talling, 2014). However, the RDLs in this study were not connected to river mouths. At the scale of the last 500

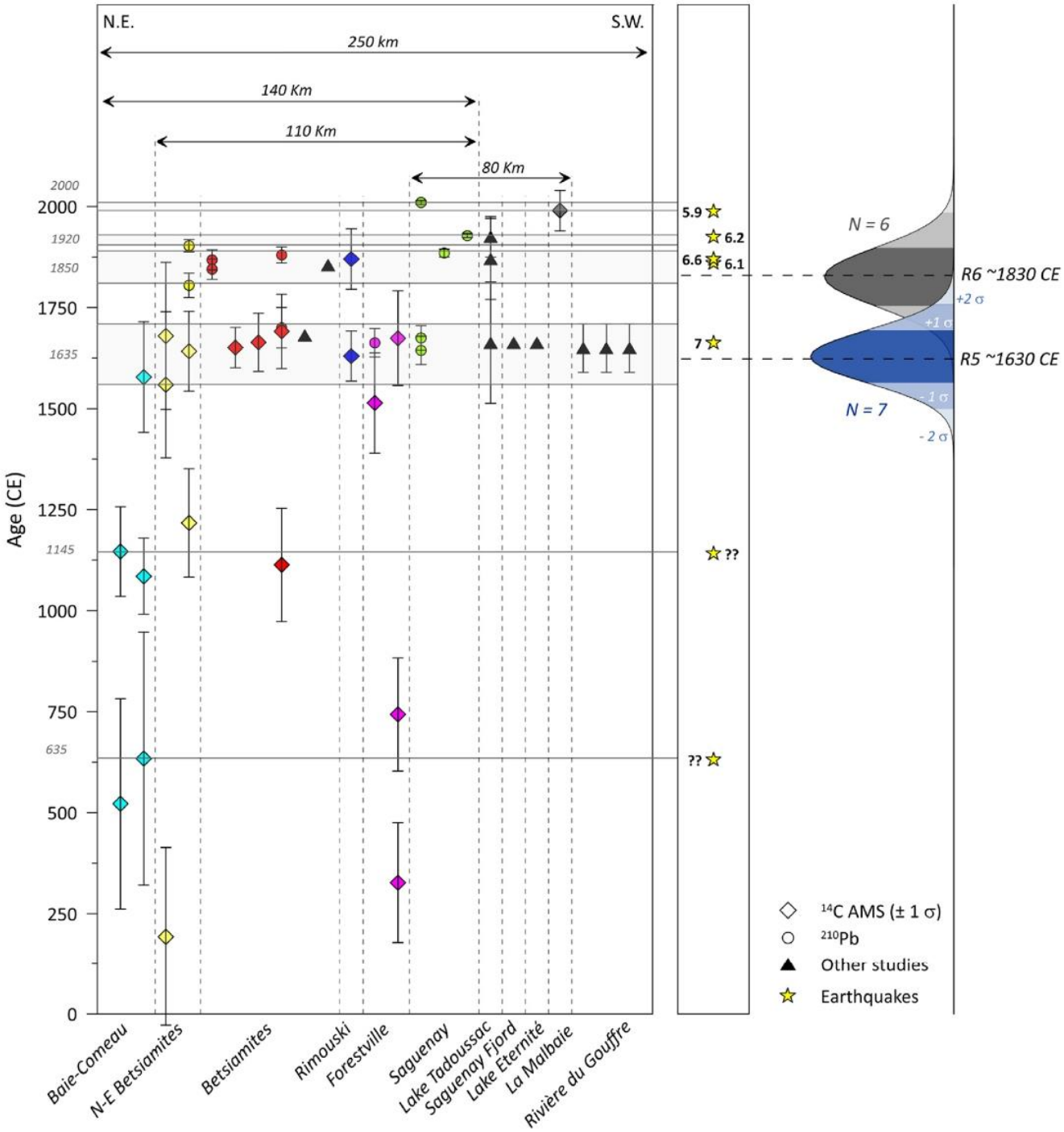

Fig. 9. Chronology of the RDLs (turbidites and debrites) dated by ^{14}C (colored diamonds) and ^{210}Pb (colored circles). The black triangles correspond to evidences provided by previous studies of aerial or submarine landslides in Québec (Doig, 1990; Filion *et al.*, 1991; St-Onge et al., 2004; Cauchon-Voyer et al., 2008; Locat et al., 2016). The gray intervals highlight periods of synchronous RDLs. The black arrows show the distance of synchronous submarine landslides for each period. The yellow stars indicate the timing of major historical earthquakes with their magnitude. To the right, the range of reflectors R5 (blue) and R6 (gray) considering a statistical error of ±1 σ and ±2 σ. (For interpretation of the references to color in this figure legend, the reader is referred to the Web version of this article.)

years, relative sea level variations are insignificant (Dionne, 2001; Shaw et al., 2002; Rémillard et al., 2017). Storms in eastern Canada are much weaker than tropical storms (e.g., Taiwan, New-Zealand) and the physiography of the estuary allows it to be relatively sheltered from oceanic swells (Bernatchez et al., 2012). Therefore, the synchronicity of submarine landslides that are reported here over a large area of a known seismic zone is a strong argument for relating their triggering to the regional seismicity of the CKBSL seismic zone.

The RDL 3 observed in core COR20-02-26 GC and dated around

Table 5
List of major historical earthquakes in the St. Lawrence Estuary (from Lamontagne et al., 2018).

Year	Lat (°N)	Long (°W)	Area	Magnitude	MMI	Magnitude information	Source
1663	47.60	−70.10	Charlevoix-Kamouraska	7.0	IX	Estimated	Gouin (2001)
1860	47.50	−70.10	Charlevoix-Kamouraska	6.1	VIII	Estimated	Gouin (2001)
1870	47.40	−70.50	Charlevoix-Kamouraska	6.6	IX-X	Estimated	(Gouin 2001)
1925	47.80	−69.80	Charlevoix-Kamouraska	6.2	VIII	Instrumented	Hodgson (1950); Bruneau and Lamontagne, 1994
1988	48.12	−71.18	Saguenay Region	5.9	VIII	Instrumented	North et al. (1989)

1645 CE in the Saguenay area is interpreted as a hyperpycnite. In the Saguenay Fjord, St-Onge et al. (2004) and Syvitski and Schafer (1996b) describe a similar deposit related to the 1663 CE earthquake. It was interpreted as a flood-induced hyperpycnal flow after the breach of a natural dam generated by an earthquake-triggered turbidite. Historical observations reported by the Jesuit mission and synthesized by Gouin (2001) support the generation of a hyperpycnal flow by the 1663 CE earthquake in the Saguenay area (e.g., Tadoussac) and throughout the estuary: *"Rivers were thoroughly polluted, the waters of some becoming yellow and of others red; and our great river St. Lawrence appeared all whitish as far as the region of Tadoussacq"*; *"displaced lands […] caused their gradual detrition by the water of the Rivers, which are still so thick and turbid as to change the color of the whole great St. Lawrence river."*

In the Middle Estuary, the tidal range and currents are stronger (Saucier and Chassé, 2000) as evidenced by the coarser sediments composing the hemipelagites observed in core COR20-02-50 GC. These forcings, particularly effective at low water depths could play a major role in preconditioning submarine landslides in the CKSZ, as currents can erode submarine slopes causing oversteepening (Hampton et al., 1996). These preconditioning factors combined with the high seismicity of the CKSZ (Lamontagne et al., 2018) could increase the submarine landslide hazard in the Middle Estuary, which in turn could explain the high frequency of RDL observed in core COR20-02-50 GC (four turbidites, two hyperpycnites and one slump). Moreover, the 1663 CE earthquake may have occurred in this region (Lamontagne et al., 2018).

5.3. Relative importance of the 1663 CE event

The 1663 CE earthquake was the strongest historical earthquake in Eastern Canada (Locat et al., 2003; Ebel, 2011; Lamontagne et al., 2018). This statement is confirmed by our study that allowed identifying at least 12 RDLs dated at ~1663 CE in 10 sediment cores distributed over a distance of 140 km, whereas only five RDLs dated at ~1860/1870 CE and two at ~1925 CE and ~1988 CE were observed over a less extensive area. The seismic survey revealed a strong shallow reflector present in almost all the studied area in the slopes and in the submarine landslide deposits. Intersecting cores analyzed and dated this reflector R5 (Figs. 3 and 4). Its approximate age is near to that of the 1663 CE earthquake. A second reflector has been identified (R6) and dated at about 1830–1860 CE, which is very close to the two other major historical earthquakes of 1860 and 1870 CE (Fig. 3). Shallower than R5, this seismic reflector is identified at fewer locations, confirming the relative importance of the 1663 CE earthquake compared to more recent events such as the 1860 and 1870 CE earthquakes.

In this study, it thus appears that the 1663 CE earthquake has triggered more submarine landslides over a larger area than more recent earthquakes (Fig. 9), attesting to the importance of this event at the scale of the last two millennia and corroborating historical observations reported by the first European settlers (Gouin, 2001; Ebel, 2011). Other studies in Québec (Doig, 1990; Filion et al., 1991; St-Onge et al., 2004; Cauchon-Voyer et al., 2008; Poncet et al., 2010a; 2010b; Locat et al., 2016) highlight the highest intensity of this major event. In comparison, more recent earthquakes (Table 5) appear to have had less impact than the 1663 CE earthquake. However, the relation between earthquake magnitude and the number of submarine landslides is not linear (e.g., Papadopoulos and Plessa, 2000). Some factors can interfere such as the sedimentary budget and predisposing factors (Hampton et al., 1996).

The compilation of submarine landslide ages leads to identify two older periods with synchronous ages of RDLs. The first at 1145 ± 145 CE with four synchronous deposits distributed over a distance of 40 km and the second at 645 ± 400 CE with three synchronous RDLs over a distance of 100 km. The first period has already been identified by Philibert , (2012) by the dating of RDL at ~ 1200 CE in Lake Jacques-Cartier (Fig. 1) and correlated with the seismicity of CKSZ. Moreover, Normandeau et al. (2013) found an earthquake-triggered submarine landslide deposit in Lake St-Joseph (Fig. 1) dated at ~1250 CE. Trottier et al. (2019) in Lake Maskinongé (CKSZ) also identified mass transport deposits about the same period at ~1180 CE through geomorphic and core analyses. Additionally, the major event identified and dated around 650 CE by Lajeunesse et al. (2017) in Lake Témiscouata near the Charlevoix area is likely synchronous with the RDLs dated at 645 ± 400 CE period in this study. The link between regional seismicity and the submarine landslides established in addition to these studies tends to suggest that two earthquakes could have triggered these older RDLs in the St. Lawrence Estuary.

6. Conclusions

The dating of 12 submarine landslides distributed over a distance of 220 km along the axis of the St. Lawrence Estuary allowed correlating them to the major historical earthquakes of 1663 CE, 1860 and/or 1870 CE and 1925 CE. The observation of older submarine landslide deposits suggests that two large earthquakes may have occurred around 645 CE and 1145 CE, in a period when historical data are not available. The criteria used to infer these relationships are:

(1) The careful location of the coring sites outside areas influenced by storms, sediment input (e.g., rivers) and active turbiditic channels;
(2) The ^{14}C and ^{210}Pb dating of turbidites and debrites revealing concomitant ages with the historical earthquakes;
(3) The synchronicity of submarine landslides and their associated turbidites described over a distance of ~220 km in a seismically active zone;

The results reported in this paper provide evidence that allow estimating the paleoseismicity of the last 2000 years in the St. Lawrence Estuary, which in turn improves the seismic hazard assessment in Eastern Canada. These results also allow demonstrating that the 1663 CE earthquake was the most important event of the last two millennia, although several submarine landslides observed in this study still remain to be dated. Investigating in detail these landslides would allow going even further back into the paleoseismological archives, refining the location of the epicenter

of the 1663 CE earthquake and assess landslide-related hazards. Additionally, characterizing of the mechanical behavior of sediments recovered in the St. Lawrence Estuary could help in evaluating the stability of slopes during an earthquake with specific attention on the stratified seismic unit 4, which seems susceptible to failure. Additional investigations are needed to characterize and understand the behavior and role of this unit during an earthquake, in particular its liquefaction potential.

Declaration of competing interest

The authors declare that they have no known competing financial interests or personal relationships that could have appeared to influence the work reported in this paper.

Acknowledgements

The authors wish to thank the captain and crew of the SLIDE2020 expedition on board the RV Coriolis II. They also thank Quentin Beauvais, Pascal Rioux and Sandrine Ouellet (ISMER) for their help in the laboratory, as well as Ray Burke for his contribution in the acquisition of geophysical data. The SLIDE2020 expedition was supported by ship time of the *Odyssée Saint-Laurent* program of the *Réseau Québec maritime* (RQM). G. St-Onge and P. Lajeunesse gratefully acknowledge the financial support of the Natural Sciences and Engineering Research Council of Canada (NSERC). Finally, the authors thank the two anonymous reviewers for their comments, which improved the quality of this paper.

Appendix A. Supplementary data

Supplementary data to this article can be found online at https://doi.org/10.1016/j.quascirev.2022.107640.

References

Adams, J., Basham, P., 1989. The seismicity and seismotectonics of Canada east of the Cordillera. Geosci. Can. 16, 3–16.
Anglin, F., 1984. Seismicity and faulting in the Charlevoix zone of the St. Lawrence valley. Bull. Seismol. Soc. Am. 74, 595–603.
Appleby, P.G., Oldfield, F., 1978. The calculation of lead-210 dates assuming a constant rate of supply of unsupported 210Pb to the sediment. Catena 5, 1–8.
Bernatchez, P., 2003. Évolution littorale holocène et actuelle des complexes deltaïques de Betsiamites et de Manicouagan-Outardes: synthèse, processus, causes et perspectives.
Bernatchez, P., Boucher-Brossard, G., Sigouin-Cantin, M., 2012. Contribution des archives à l'étude des événements météorologiques et géomorphologiques causant des dommages aux côtes du Québec maritime et analyse des tendances, des fréquences et des temps de retour des conditions météo-marines extrêmes. Rapport remis au ministère de la Sécurité publique du Québec. Chaire de recherche en géoscience côtière, Laboratoire de dynamique et de gestion intégrée des zones côtières, Université du Québec à Rimouski. Rimouski.
Blaauw, M., Christen, J.A., 2011. Flexible paleoclimate age-depth models using an autoregressive gamma process. Bayesian analysis 6, 457–474.
Bouma, A.H., 1962. Sedimentology of Some Flysch Deposits. Agraphic Approach to Facies Interpretation 168.
Bruneau, M., Lamontagne, M., 1994. Damage from 20th century earthquakes in eastern Canada and seismic vulnerability of unreinforced masonry buildings. Can. J. Civ. Eng. 21, 643–662.
Bryn, P., Berg, K., Forsberg, C.F., Solheim, A., Kvalstad, T.J., 2005. Explaining the storegga slide. Mar. Petrol. Geol. 22, 11–19.
Cauchon-Voyer, G., Locat, J., Leroueil, S., St-Onge, G., Demers, D., 2011. Large-scale subaerial and submarine Holocene and recent mass movements in the Betsiamites area, Quebec, Canada. Eng. Geol. 121, 28–45.
Cauchon-Voyer, G., Locat, J., St-Onge, G., 2008. Late-quaternary morphosedimentology and submarine mass movements of the Betsiamites area, lower St. Lawrence estuary, quebec, Canada. Mar. Geol. 251, 233–252.
Cauchon-Voyer, G., Turmel, D., Gagné, H., 2007. Rapport de mission COR0703, Estuaire du Saint-Laurent.
Croudace, I.W., Rindby, A., Rothwell, R.G., 2006. ITRAX: description and evaluation of a new multi-function X-ray core scanner. Geological Society, London, Special Publications 267, 51–63.
Dan, G., Sultan, N., Savoye, B., Deverchere, J., Yelles, K., 2009. Quantifying the role of sandy–silty sediments in generating slope failures during earthquakes: example from the Algerian margin. Int. J. Earth Sci. 98, 769–789.
Dionne, J.-C., 2001. Relative-sea-level changes in the St. Lawrence Estuary from deglaciation to present day. Deglacial history and relative sea-level changes, northern New England and adjacent Canada 351, 271–284.
Doig, R., 1990. 2300 yr history of seismicity from silting events, in Lake Tadoussac, Charlevoix, Quebec. Geology 18, 820–823.
Dubé, S., 1998. Analyse de l'écroulement rocheux du Mont Éboulé, (Québec).
Duchesne, M., Pinet, N., Bolduc, A., Bédard, K., Lavoie, D., 2007. Seismic Stratigraphy of the Lower St Lawrence River Estuary (Quebec) Quaternary Deposits and Seismic Signature of the Underlying Geological Domains. Geological Survey of Canada.
Duchesne, M.J., Pinet, N., Bédard, K., St-Onge, G., Lajeunesse, P., Campbell, D.C., Bolduc, A., 2010. Role of the bedrock topography in the Quaternary filling of a giant estuarine basin: the Lower St. Lawrence Estuary, Eastern Canada. Basin Res. 22, 933–951.
Ebel, J.E., 1996. The seventeenth century seismicity of northeastern North America. Seismol Res. Lett. 67, 51–68.
Ebel, J.E., 2011. A new analysis of the magnitude of the February 1663 earthquake at Charlevoix, Quebec. Bull. Seismol. Soc. Am. 101, 1024–1038.
Filion, L., Quinty, F., Bégin, C., 1991. A chronology of landslide activity in the valley of Rivière du Gouffre, Charlevoix, Quebec. Can. J. Earth Sci. 28, 250–256.
Goldfinger, C., Galer, S., Beeson, J., Hamilton, T., Black, B., Romsos, C., Patton, J., Nelson, C.H., Hausmann, R., Morey, A., 2017. The importance of site selection, sediment supply, and hydrodynamics: a case study of submarine paleoseismology on the northern Cascadia margin, Washington USA. Mar. Geol. 384, 4–46.
Goldfinger, C., Morey, A.E., Nelson, C.H., Gutiérrez-Pastor, J., Johnson, J.E., Karabanov, E., Chaytor, J., Eriksson, A., Party, S.S., 2007. Rupture lengths and temporal history of significant earthquakes on the offshore and north coast segments of the Northern San Andreas Fault based on turbidite stratigraphy. Earth Planet Sci. Lett. 254, 9–27.
Goldfinger, C., Nelson, C.H., Morey, A.E., Johnson, J.E., Patton, J.R., Karabanov, E.B., Gutierrez-Pastor, J., Eriksson, A.T., Gracia, E., Dunhill, G., 2012. Turbidite Event History—Methods and Implications for Holocene Paleoseismicity of the Cascadia Subduction Zone. US Geological Survey.
Gouin, P., 2001. Tremblements de terre historiques au Québec: de 1534 à mars 1925, identifiés et interprétés à partir des textes originaux contemporains. Guérin.
Gracia, E., Vizcaino, A., Escutia, C., Asioli, A., Rodes, A., Pallas, R., Garcia-Orellana, J., Lebreiro, S., Goldfinger, C., 2010. Holocene earthquake record offshore Portugal (SW Iberia): testing turbidite paleoseismology in a slow-convergence margin. Quat. Sci. Rev. 29, 1156–1172.
Hampton, M.A., Lee, H.J., Locat, J., 1996. Submarine landslides. Rev. Geophys. 34, 33–59.
Haworth, R.T., 1978. Interpretation of geophysical data in the northern Gulf of St. Lawrence and its relevance to lower Paleozoic geology. Geol. Soc. Am. Bull. 89, 1091–1110.
Heaton, T.J., Köhler, P., Butzin, M., Bard, E., Reimer, R.W., Austin, W.E., Ramsey, C.B., Grootes, P.M., Hughen, K.A., Kromer, B., 2020. Marine20—the marine radiocarbon age calibration curve (0–55,000 cal BP). Radiocarbon 62, 779–820.
Hodgson, E., 1928. The probable epicentre of the Saint lawrence earthquake of Feb. 5 1663. J. Roy. Astron. Soc. Can. 22, 325.
Hodgson, E.A., 1950. The St. Lawrence earthquake. Bull. Seismol. Soc. Am. 15 (2), 84–105.
Howarth, J.D., Orpin, A.R., Kaneko, Y., Strachan, L.J., Nodder, S.D., Mountjoy, J.J., Barnes, P.M., Bostock, H.C., Holden, C., Jones, K., 2021. Calibrating the marine turbidite palaeoseismometer using the 2016 Kaikōura earthquake. Nat. Geosci. 14, 161–167.
Jaegle, M., 2015. Nature et origine des sédiments de surface de l'estuaire du Saint-Laurent. Université du Québec à Rimouski.
Josenhans, H., Lehman, S., 1999. Late glacial stratigraphy and history of the Gulf of St. Lawrence, Canada. Can. J. Earth Sci. 36, 1327–1345.
King, L.H., MacLean, B., 1970. Origin of the outer part of the Laurentian Channel. Can. J. Earth Sci. 7, 1470–1484.
Lajeunesse, P., Sinkunas, B., Morissette, A., Normandeau, A., Joyal, G., St-Onge, G., Locat, J., 2017. Large-scale seismically-induced mass-movements in a former glacial lake basin: lake Témiscouata, northeastern Appalachians (eastern Canada). Mar. Geol. 384, 120–130.
Lamontagne, M., Beauchemin, M., Toutin, T., 2003. Earthquakes in the Charlevoix seismic zone, quebec. Int. J. Hydropower Dams 10, 98–99.
Lamontagne, M., Halchuk, S., Cassidy, J.F., Rogers, G.C., 2018. Significant Canadian Earthquakes 1600-2017. Geological Survey of Canada.
Lasalle, P., Chagnon, J.-Y., 1968. An ancient landslide along the Saguenay River, quebec. Can. J. Earth Sci. 5, 548–549.
Lebreiro, S.M., McCave, I.N., Weaver, P.P., 1997. Late Quaternary turbidite emplacement on the Horseshoe abyssal plain (Iberian margin). J. Sediment. Res. 67, 856–870.
Locat, J., 2011. La localisation et la magnitude du séisme du 5 février 1663 (Charlevoix) revues à l'aide des mouvements de terrain. Can. Geotech. J. 48, 1266–1286.
Locat, J., Martin, F., Levesque, C., Locat, P., Leroueil, S., Konrad, J.-M., Urgeles, R., Canals, M., Duchesne, M., 2003. Submarine Mass Movements in the Upper Saguenay Fjord,(Québec, Canada), Triggered by the 1663 Earthquake, Submarine Mass Movements and Their Consequences. Springer, pp. 509–519.
Locat, J., Turmel, D., Habersetzer, M., Trottier, A.-P., Lajeunesse, P., St-Onge, G., 2016. Earthquake Induced Landslides in Lake Eternité, Québec, Canada, Submarine

Mass Movements and Their Consequences. Springer, pp. 361–370.
Martin, F., Konrad, J.-M., Locat, J., Locat, P., Urgeles, R., Lee, H., 2001. Caracteristiques geotechniques et analyse du potentiel de liquefaction des sediments recents et post-glaciaires du fjord du saguenay. Quebec (Canada).
McNeely, R., Dyke, A.S., Southon, J.R., 2006. Canadian Marine Reservoir Ages Preliminary Data Assessment. Geological Survey of Canada.
Mulder, T., Syvitski, J.P., Migeon, S., Faugères, J.-C., Savoye, B., 2003. Hyperpycnal flows: initiation, behavior and related deposits. A review. Mar. Petrol. Geol. 20, 861–882. Marine.
Normandeau, A., Dietrich, P., Lajeunesse, P., St-Onge, G., Ghienne, J.-F., Duchesne, M.J., Francus, P., 2017. Timing and controls on the delivery of coarse sediment to deltas and submarine fans on a formerly glaciated coast and shelf. GSA Bulletin 129, 1424–1441.
Normandeau, A., Lajeunesse, P., Philibert, G., 2013. Late-Quaternary morphostratigraphy of Lake St-Joseph (southeastern Canadian Shield): evolution from a semi-enclosed glacimarine basin to a postglacial lake. Sediment. Geol. 295, 38–52.
Normandeau, A., Lajeunesse, P., St-Onge, G., 2015. Submarine canyons and channels in the Lower St. Lawrence Estuary (Eastern Canada): morphology, classification and recent sediment dynamics. Geomorphology 241, 1–18.
North, R.G., Wetmiller, R.J., Adams, J., Anglin, F.M., Hasegawa, H.S., Lamontagne, M., Berger, R.D., Seeber, L., Armbruster, J., 1989. Preliminary results from the November 25, 1988 Saguenay (quebec) earthquake. Seismol Res. Lett. 60, 89–93.
Obermeier, S.F., Martin, J., Frankel, A., Youd, T., Munson, P., Munson, C., Pond, E., 1992. Liquefaction Evidence for Strong Holocene Earthquake (S) in the Wabash Valley of Southern Indiana-Illinois, with a Preliminary Estimate of Magnitude. US Department of the Interior, US Geological Survey.
Ouellet, M., 1997. Lake Sediments and Holocene Seismic Hazard Assessment within the St. Lawrence Valley, Québec, vol. 109. Geological Society of America Bulletin, pp. 631–642.
Papadopoulos, G.A., Plessa, A., 2000. Magnitude–distance relations for earthquake-induced landslides in Greece. Eng. Geol. 58, 377–386.
Patton, J.R., Goldfinger, C., Morey, A.E., Ikehara, K., Romsos, C., Stoner, J., Djadjadihardja, Y., Ardhyastuti, S., Gaffar, E.Z., Vizcaino, A., 2015. A 6600 year earthquake history in the region of the 2004 Sumatra-Andaman subduction zone earthquake. Geosphere 11, 2067–2129.
Philibert, G., 2012. Évolution tardi-quaternaire du lac Jacques-Cartier, Réserve faunique des Laurentides. Québec.
Pinet, N., Brake, V., Campbell, C., Duchesne, M., 2011. Seafloor and shallow subsurface of the St. Lawrence river estuary. Geosci. Can. 38, 31–40.
Pinet, N., Brake, V., Campbell, C., Duchesne, M.J., 2015. Geomorphological characteristics and variability of Holocene mass-transport complexes, St. Lawrence river estuary, Canada. Geomorphology 228, 286–302.
Pinet, N., Duchesne, M., Lavoie, D., Bolduc, A., Long, B., 2008. Surface and subsurface signatures of gas seepage in the St. Lawrence Estuary (Canada): significance to hydrocarbon exploration. Mar. Petrol. Geol. 25, 271–288.
Pinet, N., Lamontagne, M., Duchesne, M.J., Brake, V.I., 2021. Hunting for Quaternary faults in eastern Canada: a critical appraisal of two potential candidates. Seismological Society of America 92, 1102–1111.
Piper, D.J., Tripsanas, E., Mosher, D.C., MacKillop, K., 2019. Paleoseismicity of the continental margin of eastern Canada: rare regional failures and associated turbidites in Orphan Basin. Geosphere 15, 85–107.
Poncet, R., Campbell, C., Dias, F., Locat, J., Mosher, D., 2010a. A Study of the Tsunami Effects of Two Landslides in the St. Lawrence Estuary, Submarine Mass Movements and Their Consequences. Springer, pp. 755–764.
Poncet, R., Campbell, C., Dias, F., Locat, J., Mosher, D., 2010b. A Study of the Tsunami Effects of Two Landslides in the St. Lawrence Estuary, Submarine Mass Movements and Their Consequences. Springer, pp. 755–764.
Riboulot, V., Cattaneo, A., Sultan, N., Garziglia, S., Ker, S., Imbert, P., Voisset, M., 2013. Sea-level change and free gas occurrence influencing a submarine landslide and pockmark formation and distribution in deepwater Nigeria. Earth Planet Sci. Lett. 375, 78–91.
Roy, D.W., DuBerger, R., 1983. Relations possibles entre la microseismicité récente et l'astroblème de Charlevoix. Can. J. Earth Sci. 20, 1613–1618.
Ratzov, G., et al., 2015. Holocene turbidites record earthquake supercycles at a slow-rate plate boundary. Geology 43 (4), 331–334.
Rémillard, A.M., St-Onge, G., Bernatchez, P., Hétu, B., Buylaert, J.-P., Murray, A.S., Lajeunesse, P., 2017. Relative sea-level changes and glacio-isostatic adjustment on the Magdalen Islands archipelago (Atlantic Canada) from MIS 5 to the late Holocene. Quat. Sci. Rev. 171, 216–233.
Saucier, F.J., Chassé, J., 2000. Tidal circulation and buoyancy effects in the St. Lawrence Estuary. Atmos.-Ocean 38, 505–556.
Seed, H.B., Idriss, I.M., 1967. Analysis of soil liquefaction: Niigata earthquake. J. Soil Mech. Found Div. 93, 83–108.
Shaw, J., Gareau, P., Courtney, R., 2002. Palaeogeography of Atlantic Canada 13–0 kyr. Quat. Sci. Rev. 21, 1861–1878.
Smith, W.T., 1962. Earthquakes of Eastern Canada and Adjacent Areas, 1534-1927. Department of Energy, Mines and Resources, Observatories Branch.
St-Onge, G., et al., 2012. Comparison of earthquake-triggered turbidites from the Saguenay (Eastern Canada) and Reloncavi (Chilean margin) Fjords: Implications for paleoseismicity and sedimentology. Sediment. Geol. 243, 89–107.
St-Onge, G., Lajeunesse, P., Duchesne, M.J., Gagne, H., 2008. Identification and dating of a key late Pleistocene stratigraphic unit in the St. Lawrence estuary and Gulf (eastern Canada). Quat. Sci. Rev. 27, 2390–2400.
St-Onge, G., Mulder, T., Francus, P., Long, B., 2007. Chapter two continuous physical properties of cored marine sediments. Developments in marine geology 1, 63–98.
St-Onge, G., Mulder, T., Piper, D.J., Hillaire-Marcel, C., Stoner, J.S., 2004. Earthquake and flood-induced turbidites in the Saguenay Fjord (Québec): a Holocene paleoseismicity record. Quat. Sci. Rev. 23, 283–294.
St-Onge, G., Stoner, J.S., Hillaire-Marcel, C., 2003. Holocene paleomagnetic records from the St. Lawrence Estuary, eastern Canada: centennial-to millennial-scale geomagnetic modulation of cosmogenic isotopes. Earth Planet Sci. Lett. 209, 113–130.
Strachan, L.J., 2008. Flow transformations in slumps: a case study from the Waitemata Basin, New Zealand. Sedimentology 55, 1311–1332.
Stuiver, M., Reimer, P.J., 1993. Extended 14C data base and revised CALIB 3.0 14C age calibration program. Radiocarbon 35, 215–230.
Syvitski, J., Praeg, D., 1989. Quaternary sedimentation in the St. Lawrence Estuary and adjoining areas, Eastern Canada: an overview based on high-resolution seismo-stratigraphy. Géogr. Phys. Quaternaire 43, 291–310.
Syvitski, J.P., Schafer, C.T., 1996a. Evidence for an earthquake-triggered basin collapse in Saguenay Fjord, Canada. Sediment. Geol. 104, 127–153.
Syvitski, J.P., Schafer, C.T., 1996b. Evidence for an earthquake-triggered basin collapse in Saguenay Fjord, Canada. Sediment. Geol. 104, 127–153.
Talling, P.J., 2014. On the triggers, resulting flow types and frequencies of subaqueous sediment density flows in different settings. Mar. Geol. 352, 155–182.
Trottier, A.-P., Lajeunesse, P., Normandeau, A., Gagnon-Poiré, A., 2019. Deglacial and postglacial paleoseismological archives in mass movement deposits of lakes of south-central Québec. Can. J. Earth Sci. 56, 60–76.
Tuttle, M.P., Atkinson, G.M., 2010. Localization of large earthquakes in the Charlevoix seismic zone, Quebec, Canada, during the past 10,000 years. Seismol Res. Lett. 81, 140–147.
Wu, P., 1998. Intraplate earthquakes and post-glacial rebound in eastern Canada and Northern Europe. Dynamics of the Ice Age Earth: A Modern Perspective 603–628.
Zhang, D., 2000. Flux de radio-isotopes à courte période dans les bassins marins marginaux de l'est canadien. Ph. D. thesis. Université du Québec à Montréal, Montréal, Québec.

Figures annexe 2. Synthèse des analyses sédimentologiques menées sur les carottes à gravité prélevées lors de la mission SLIDE-2020. De gauche à droite : image rayon-X, photographie (ronds rouges : échantillon granulométrique ; ronds bleus : échantillon matière organique/coquille), densité, vélocité des ondes P, susceptibilité magnétique sur carotte entière, susceptibilité magnétique sur demie section, D50, L*, rapports Ca/Ti et Zr/Rb.

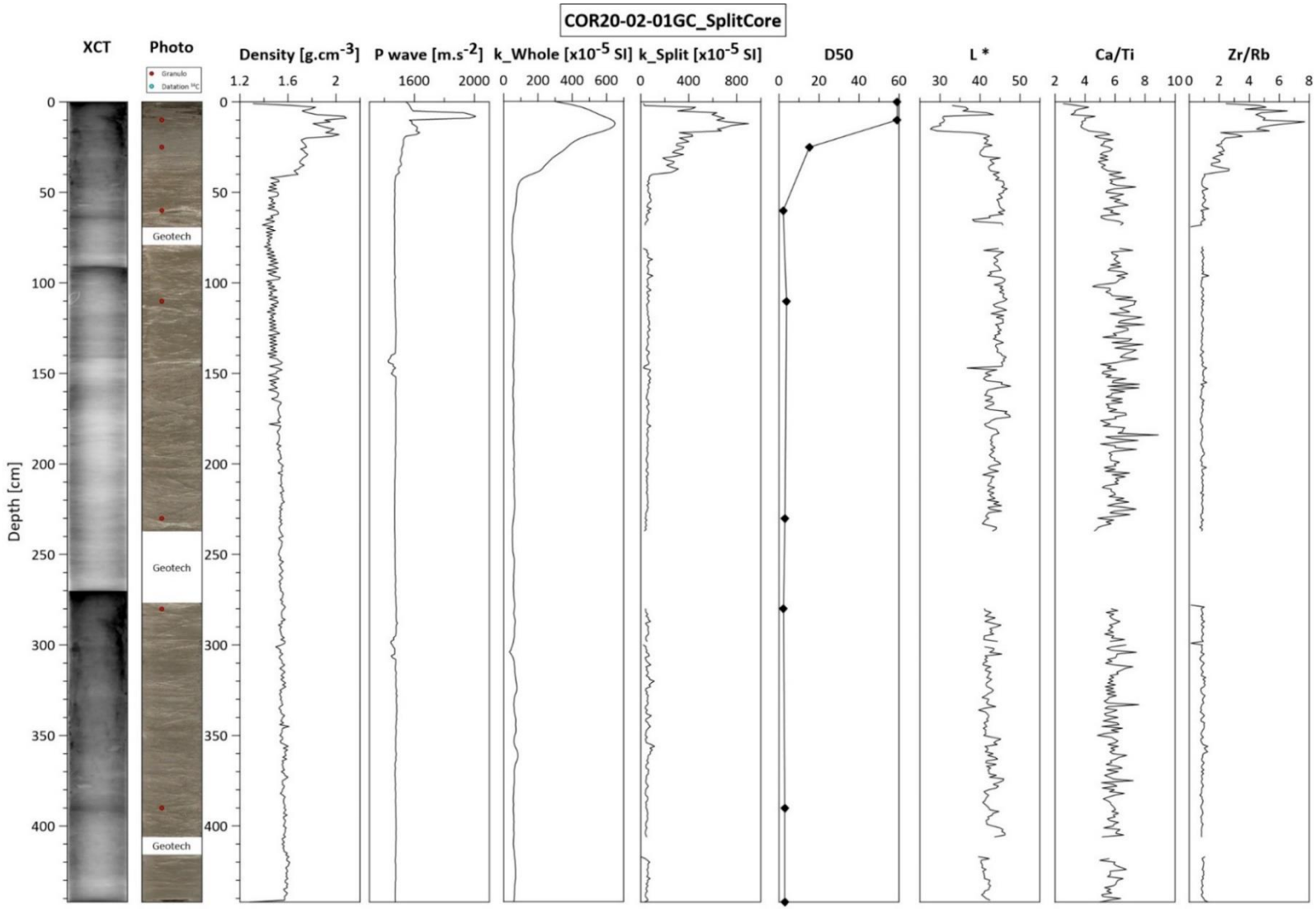

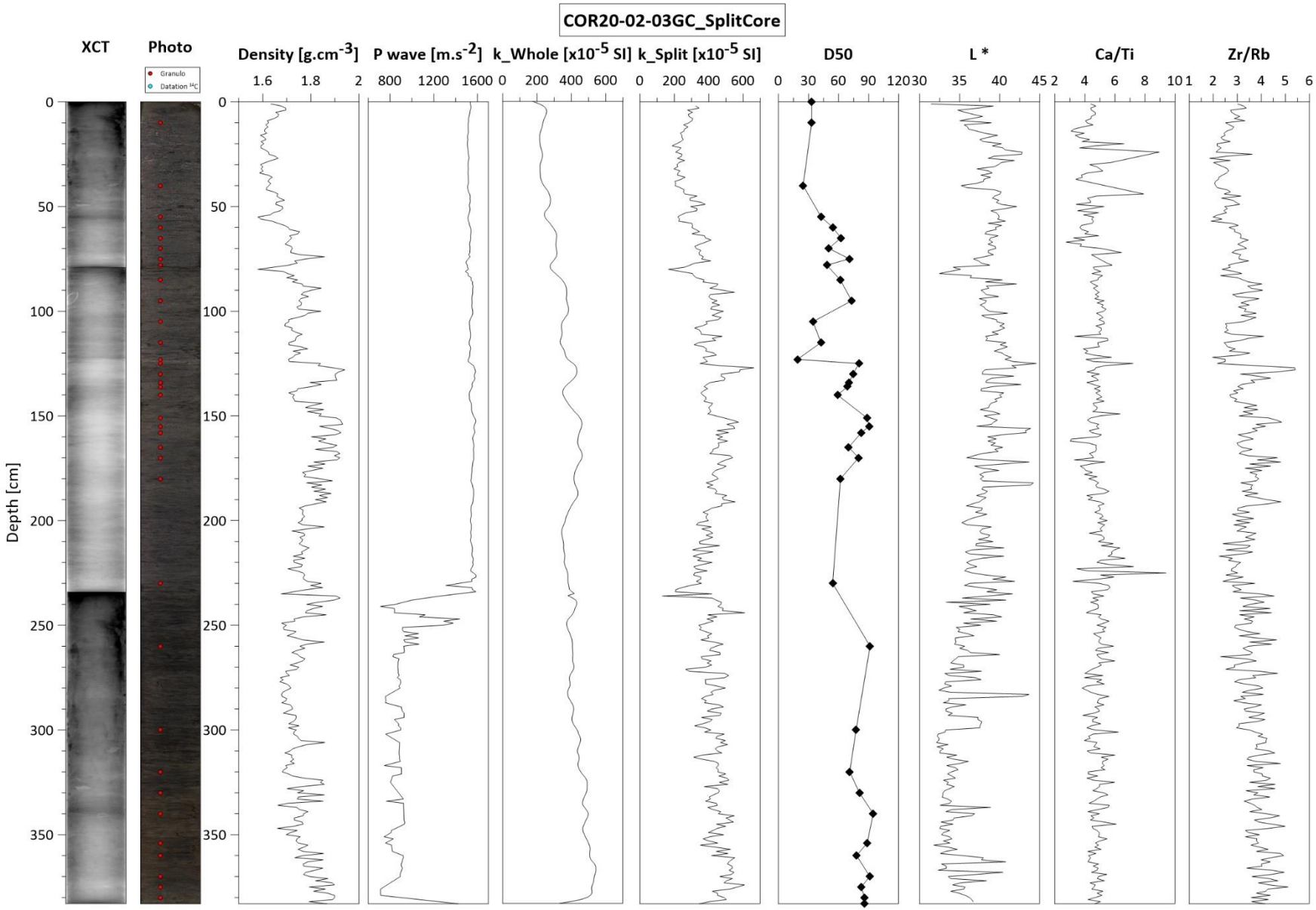
COR20-02-03GC_SplitCore
XCT
Photo
Granulo
Datation 14C
Density [g.cm-3]
P wave [m.s-2]
k_Whole [x10-5 SI]
k_Split [x10-5 SI]
D50
L *
Ca/Ti
Zr/Rb
Depth [cm]
0
50
100
150
200
250
300
350
1.6
1.8
2
800
1200
1600
0
200
400
600
0
30
60
90
120
30
35
40
45
2
4
6
8
10
1
2
3
4
5
6

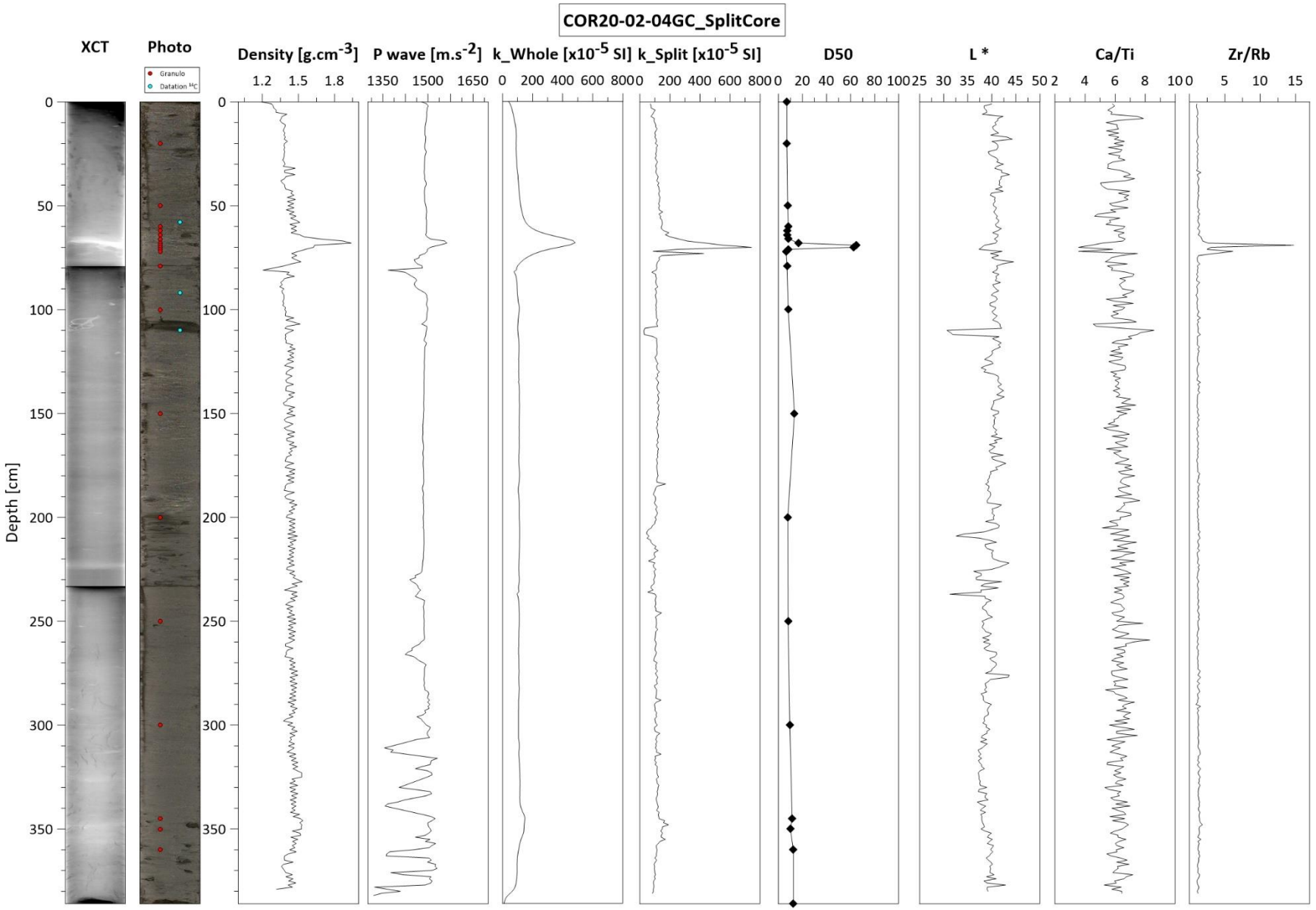
COR20-02-04GC_SplitCore
XCT
Photo
Granulo
Datation ¹⁴C
Density [g.cm-3]
P wave [m.s-2]
k_Whole [x10-5 SI]
k_Split [x10-5 SI]
D50
L *
Ca/Ti
Zr/Rb
Depth [cm]
0
50
100
150
200
250
300
350
1.2 1.5 1.8
1350 1500 1650
0 200 400 600 800
0 200 400 600 800
0 20 40 60 80 100
25 30 35 40 45 50
2 4 6 8 10
0 5 10 15

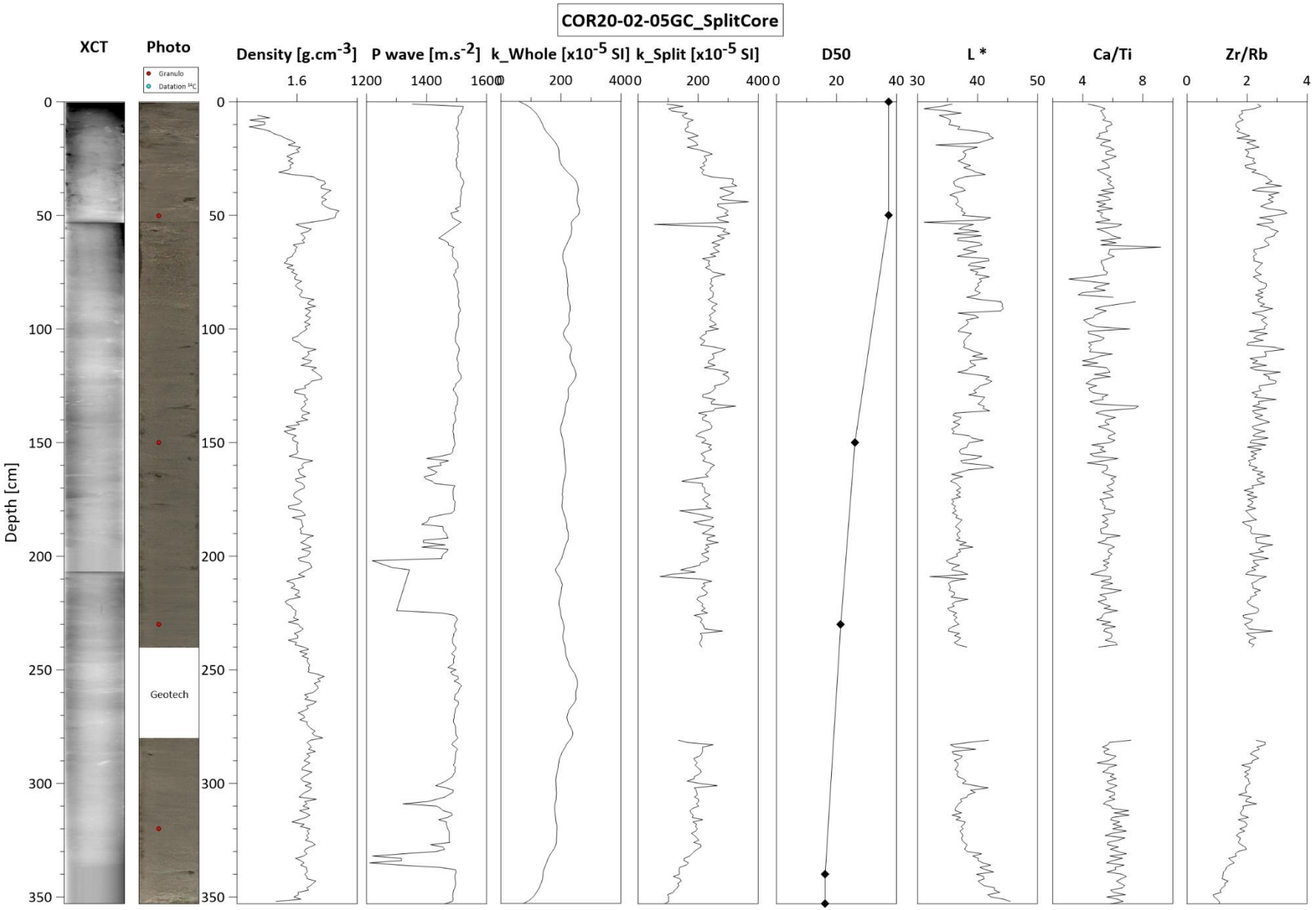
COR20-02-05GC_SplitCore
XCT
Photo
Granulo
Datation 14C
Geotech
Density [g.cm-3]
P wave [m.s-2]
k_Whole [x10-5 SI]
k_Split [x10-5 SI]
D50
L *
Ca/Ti
Zr/Rb
Depth [cm]
0
50
100
150
200
250
300
350
1.6
1200
1400
1600
0
200
400
0
200
400
0
20
40
30
40
50
4
8
0
2
4

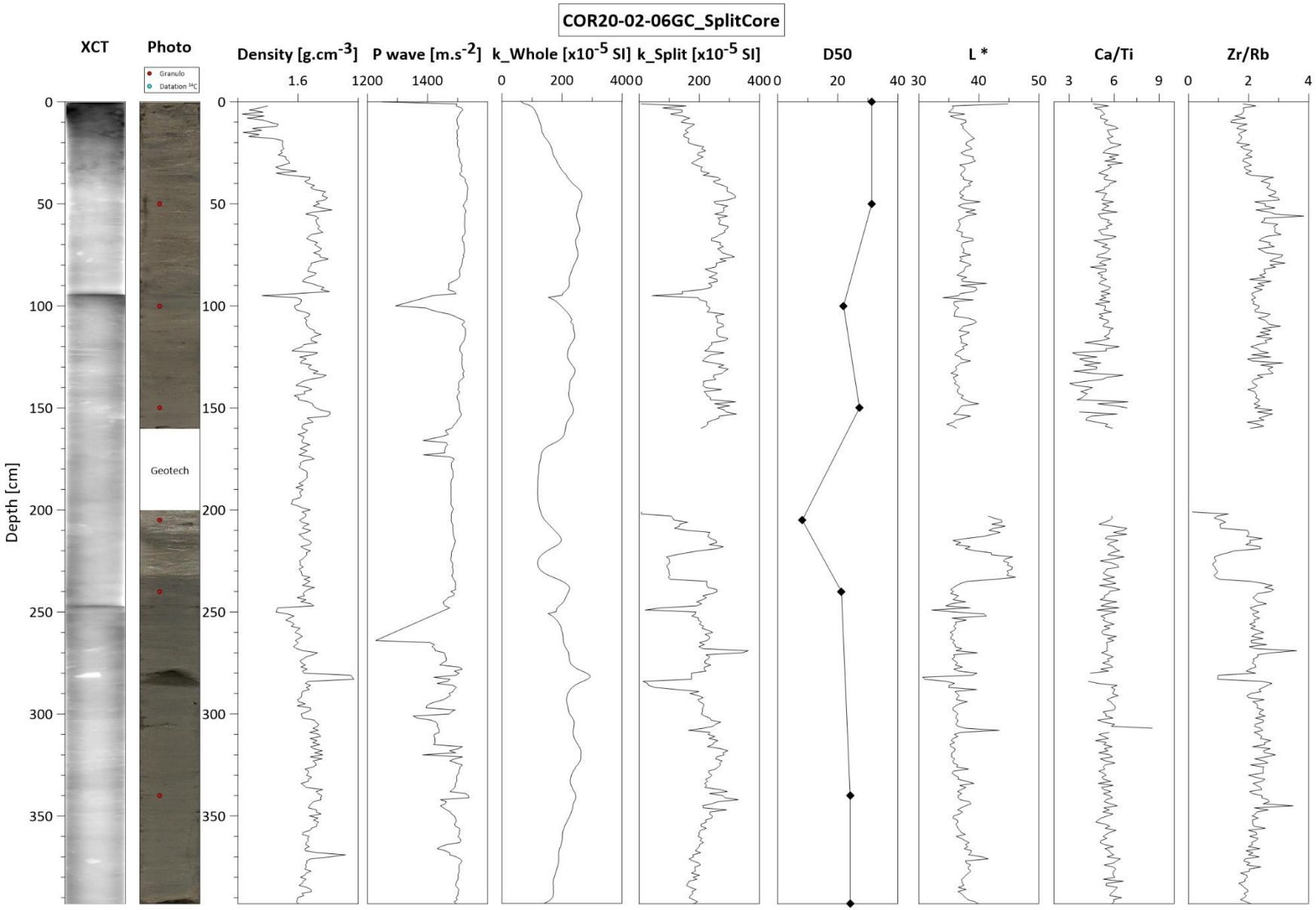
COR20-02-06GC_SplitCore
XCT
Photo
Granulo
Datation ¹⁴C
Geotech
Depth [cm]
Density [g.cm-3]
P wave [m.s-2]
k_Whole [x10-5 SI]
k_Split [x10-5 SI]
D50
L *
Ca/Ti
Zr/Rb
0
50
100
150
200
250
300
350
1.6
1200
1400
0
200
400
0
200
400
0
20
40
30
40
50
3
6
9
0
2
4

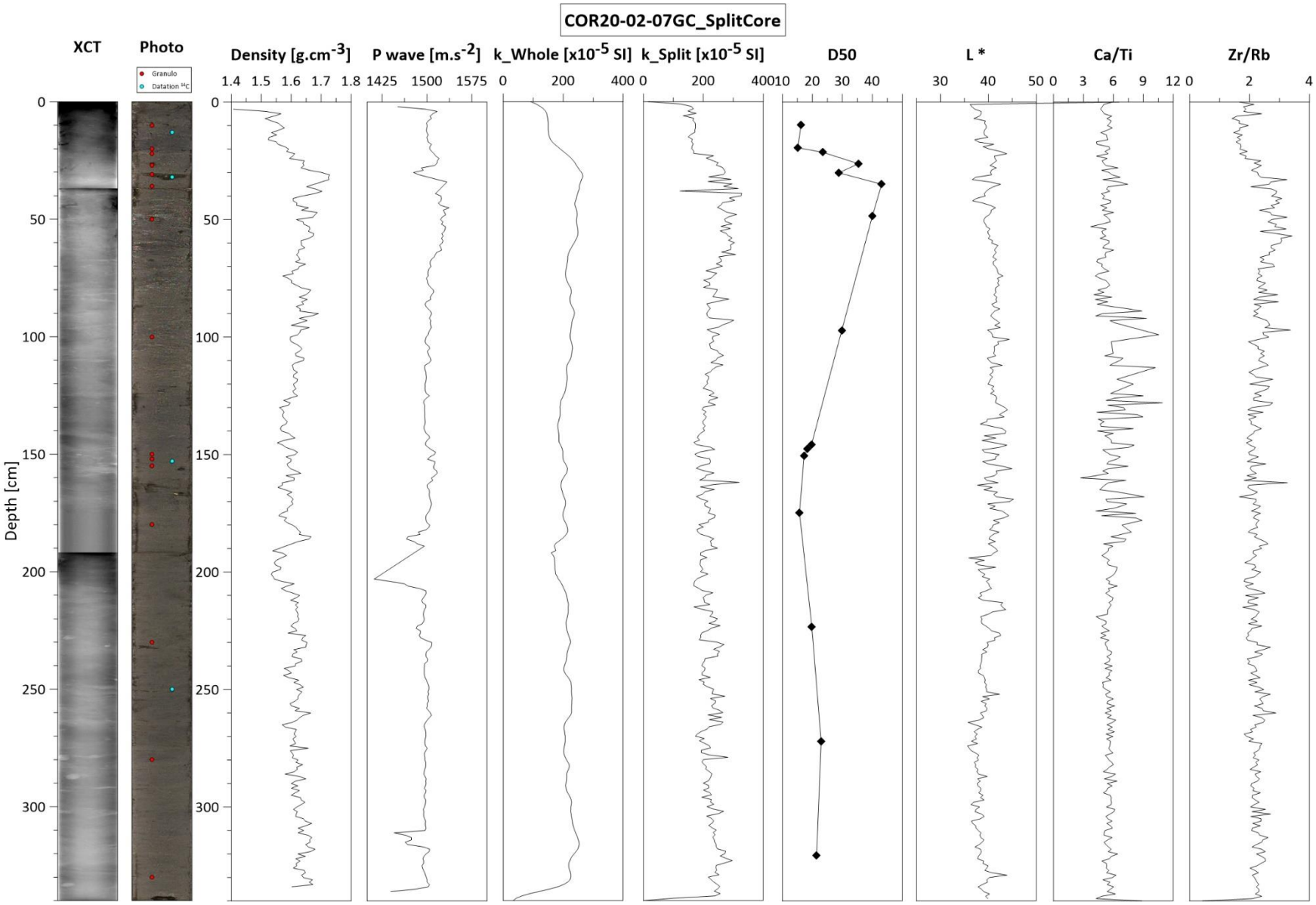
COR20-02-07GC_SplitCore
XCT
Photo
Granulo
Datation ¹⁴C
Density [g.cm-3]
P wave [m.s-2]
k_Whole [x10-5 SI]
k_Split [x10-5 SI]
D50
L *
Ca/Ti
Zr/Rb
Depth [cm]
1.4 1.5 1.6 1.7 1.8
1425 1500 1575
0 200 400
0 200 400
10 20 30 40
30 40 50
0 3 6 9 12
0 2 4
0 50 100 150 200 250 300

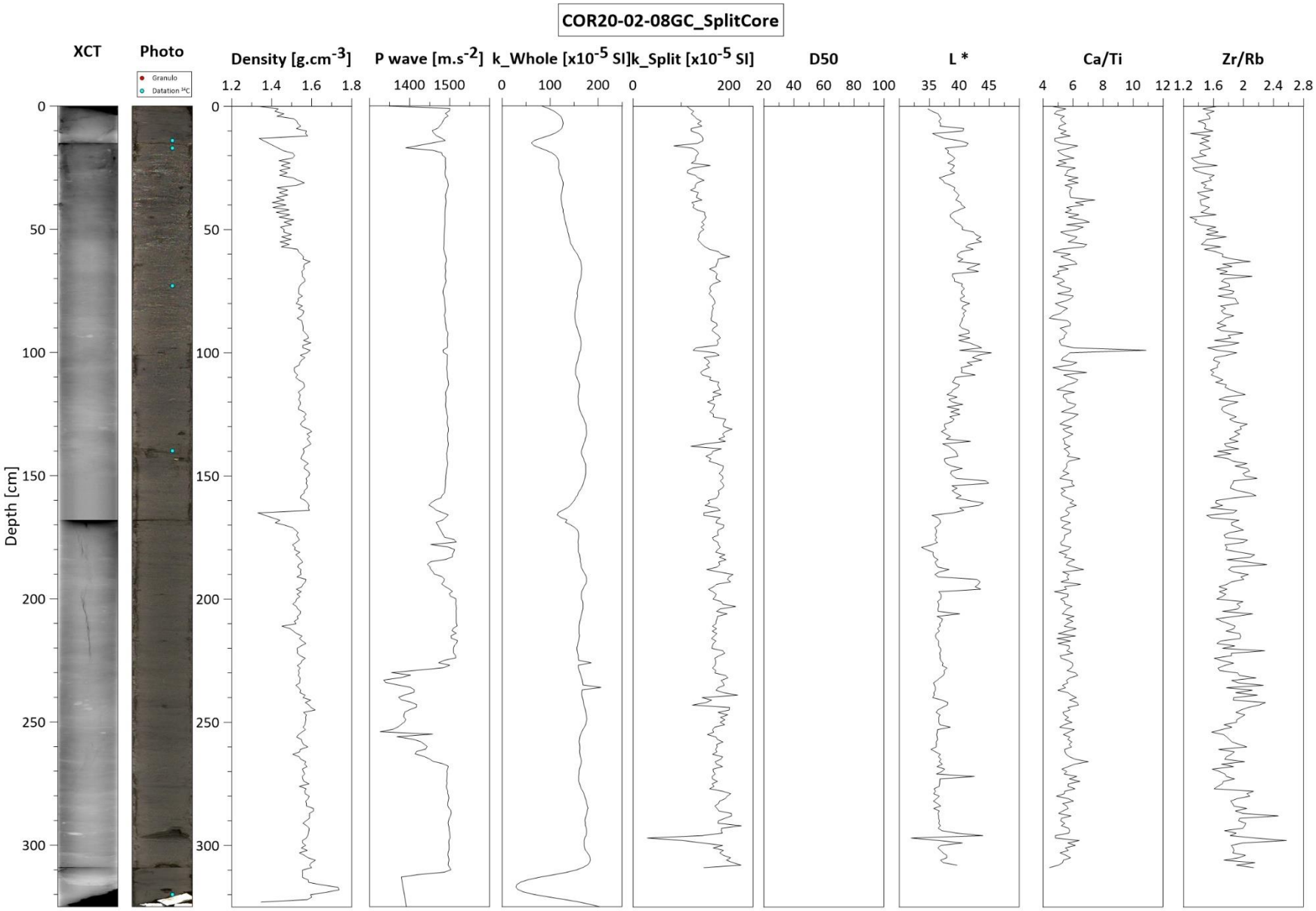
COR20-02-08GC_SplitCore
XCT
Photo
Granulo
Datation ¹⁴C
Density [g.cm-3]
P wave [m.s-2]
k_Whole [x10-5 SI]
k_Split [x10-5 SI]
D50
L *
Ca/Ti
Zr/Rb
Depth [cm]
0
50
100
150
200
250
300
1.2 1.4 1.6 1.8
1400 1500
0 100 200
0 200
20 40 60 80 100
35 40 45
4 6 8 10 12
1.2 1.6 2 2.4 2.8

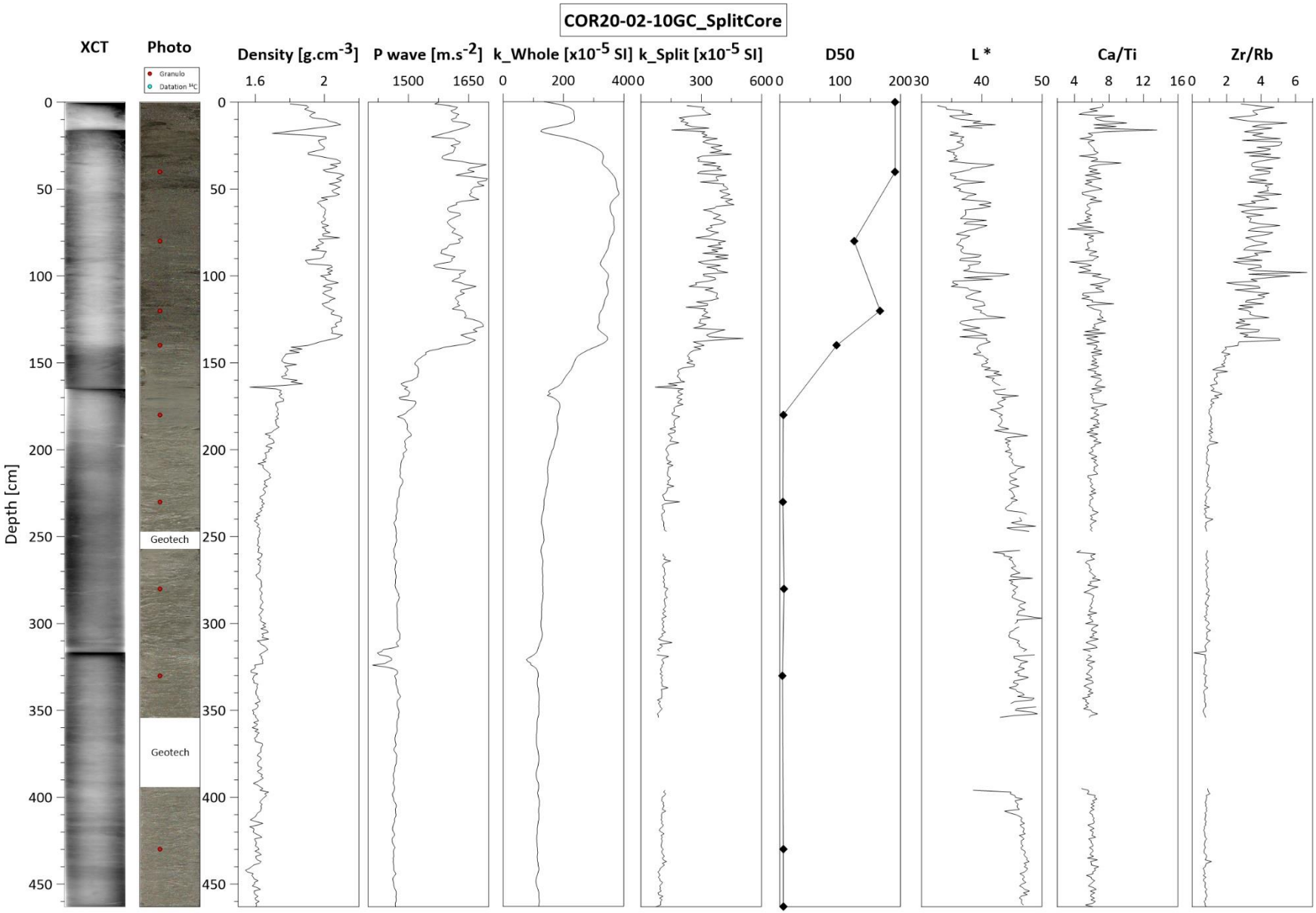
COR20-02-10GC_SplitCore
XCT
Photo
Granulo
Datation ¹⁴C
Density [g.cm-3]
P wave [m.s-2]
k_Whole [x10-5 SI]
k_Split [x10-5 SI]
D50
L *
Ca/Ti
Zr/Rb
Depth [cm]
Geotech
Geotech

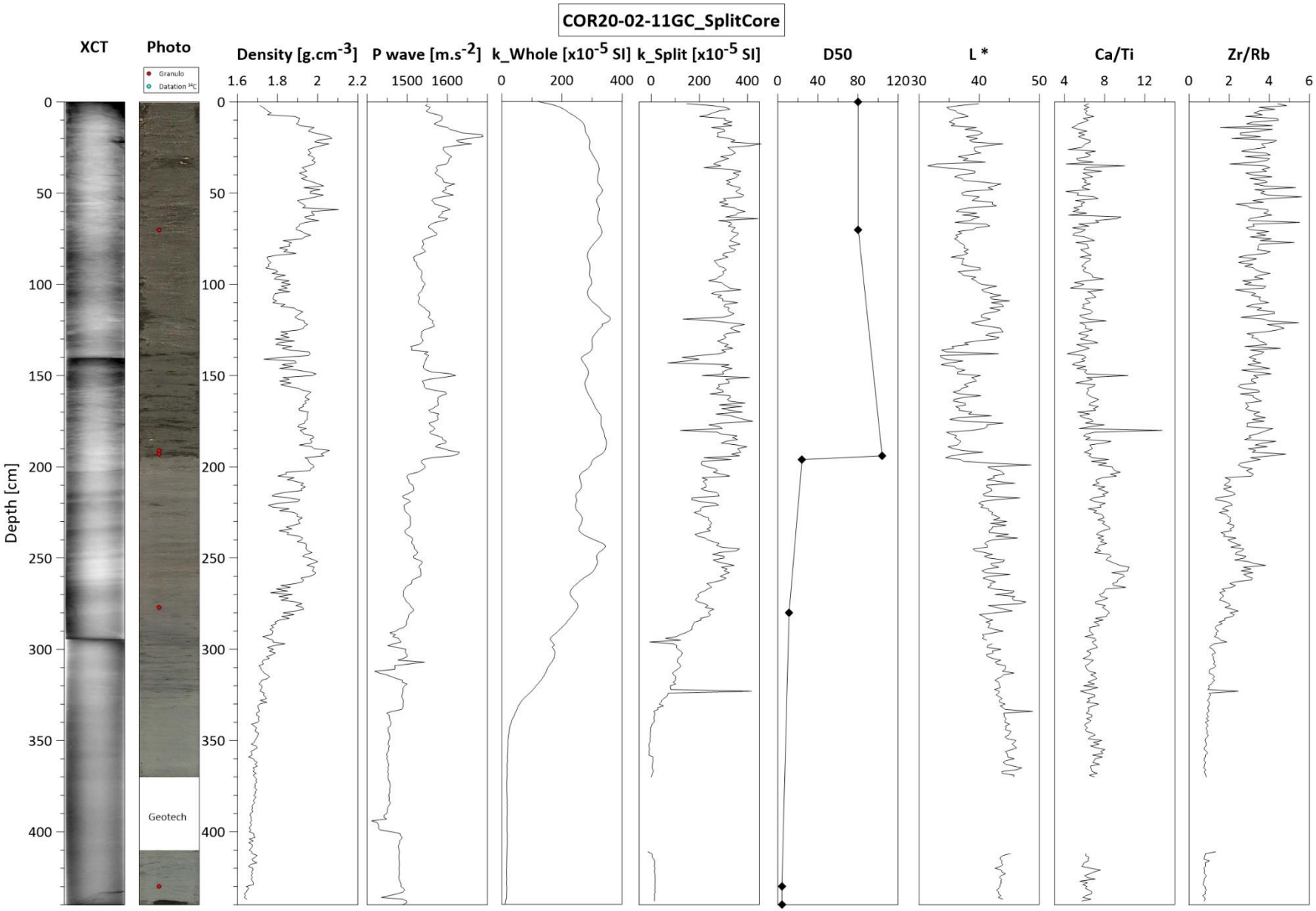
COR20-02-11GC_SplitCore
XCT
Photo
Granulo
Datation ¹⁴C
Geotech
Depth [cm]
Density [g.cm-3]
P wave [m.s-2]
k_Whole [x10-5 SI]
k_Split [x10-5 SI]
D50
L *
Ca/Ti
Zr/Rb

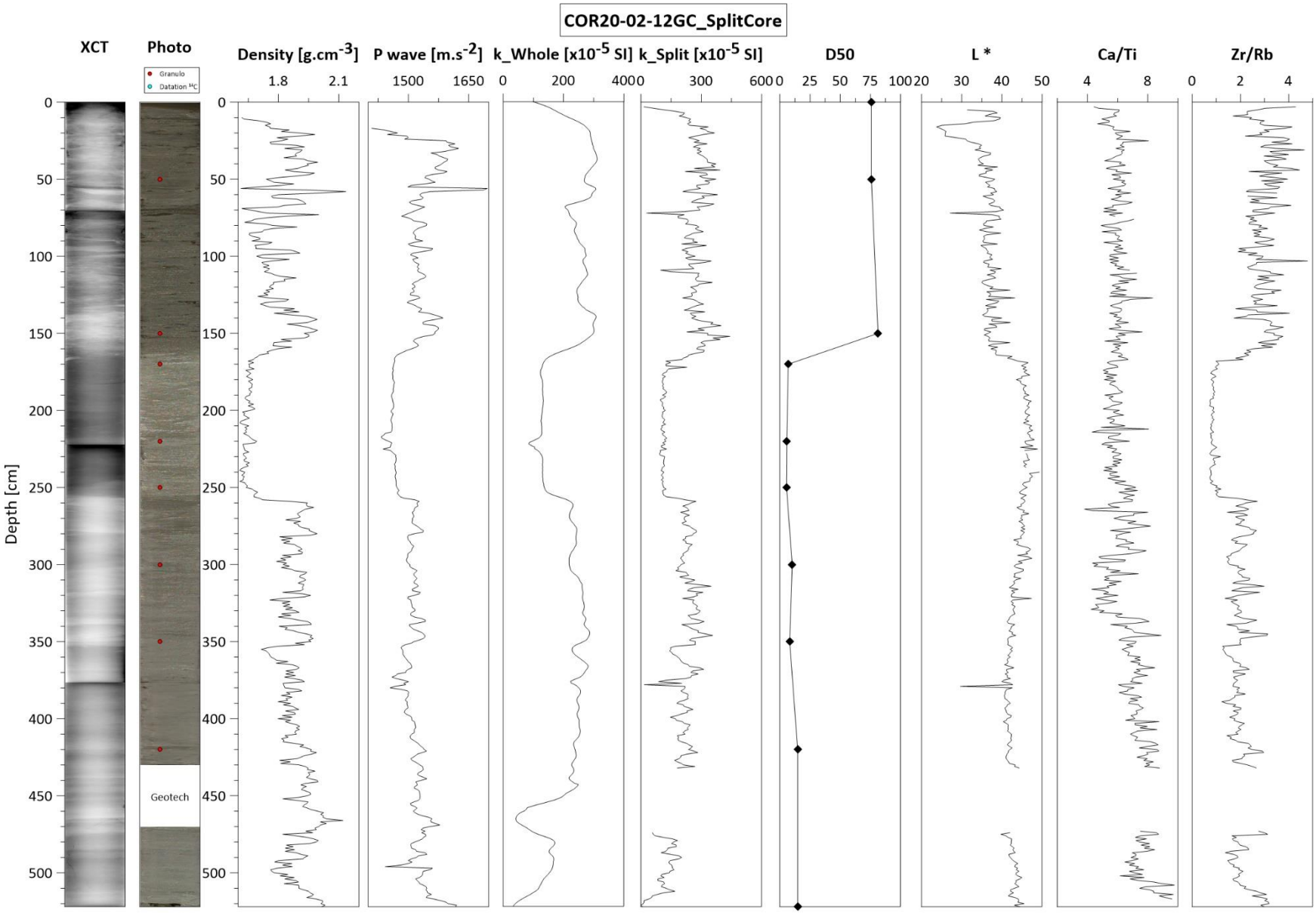
COR20-02-12GC_SplitCore
XCT
Photo
Granulo
Datation ¹⁴C
Geotech
Depth [cm]
Density [g.cm-3]
P wave [m.s-2]
k_Whole [x10-5 SI]
k_Split [x10-5 SI]
D50
L *
Ca/Ti
Zr/Rb

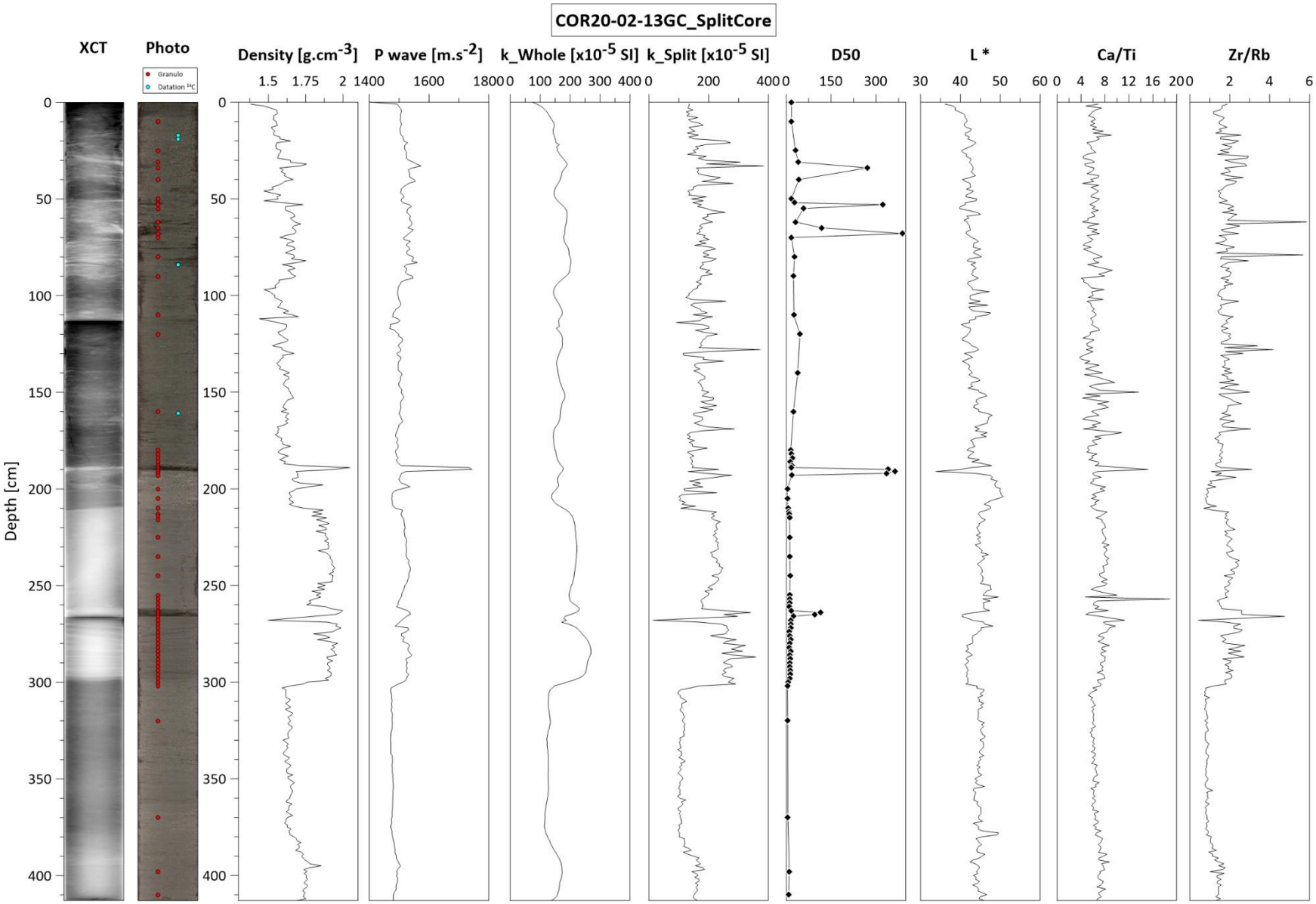
COR20-02-13GC_SplitCore
XCT
Photo
Granulo
Datation 14C
Density [g.cm-3]
P wave [m.s-2]
k_Whole [x10-5 SI]
k_Split [x10-5 SI]
D50
L *
Ca/Ti
Zr/Rb
Depth [cm]

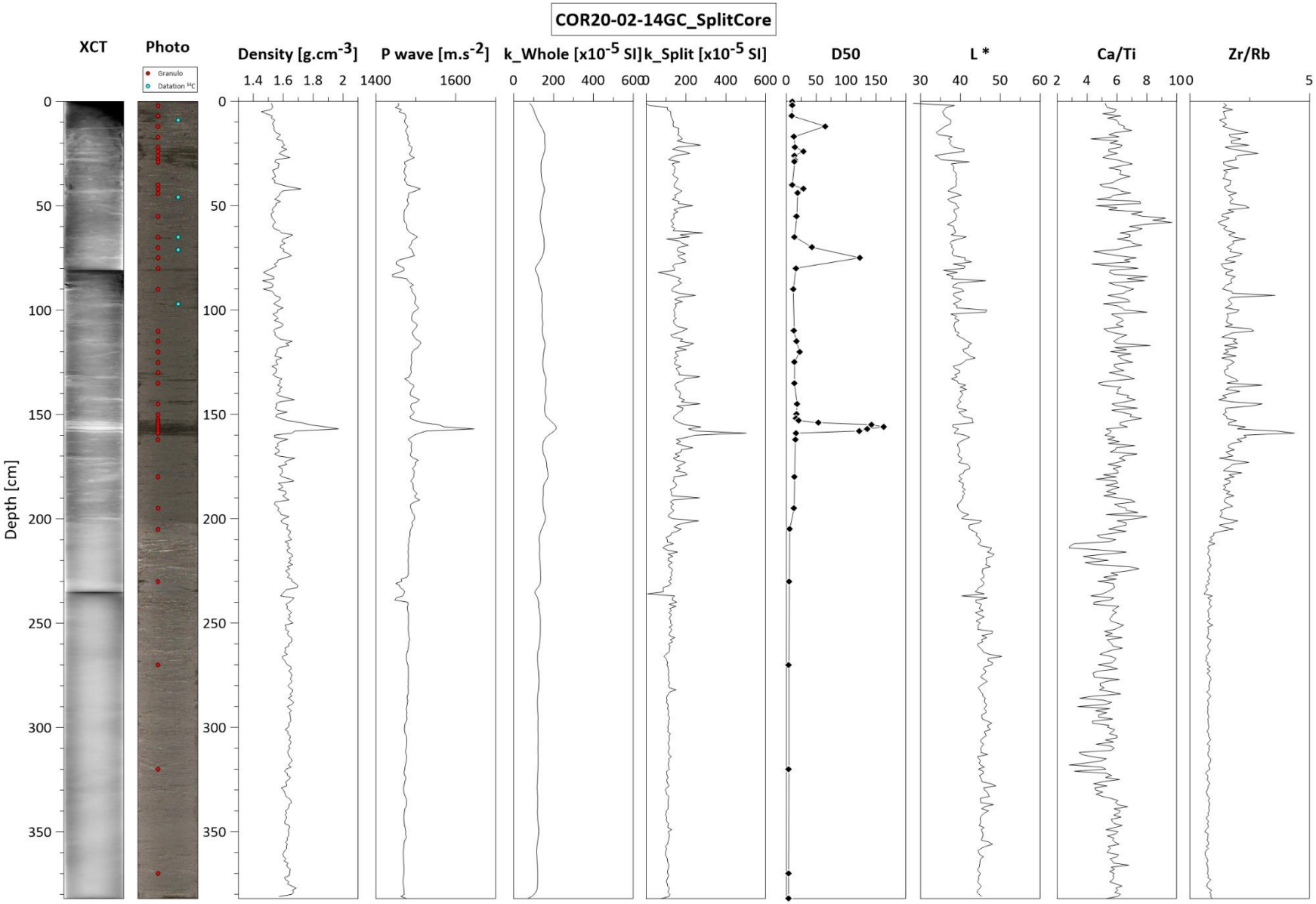
COR20-02-14GC_SplitCore
XCT
Photo
Granulo
Datation 14C
Density [g.cm-3]
P wave [m.s-2]
k_Whole [x10-5 SI]
k_Split [x10-5 SI]
D50
L *
Ca/Ti
Zr/Rb
Depth [cm]
0
50
100
150
200
250
300
350
1.4 1.6 1.8 2
1400 1600
0 200 400 600
0 200 400 600
0 50 100 150
30 40 50 60
2 4 6 8 10
0
5

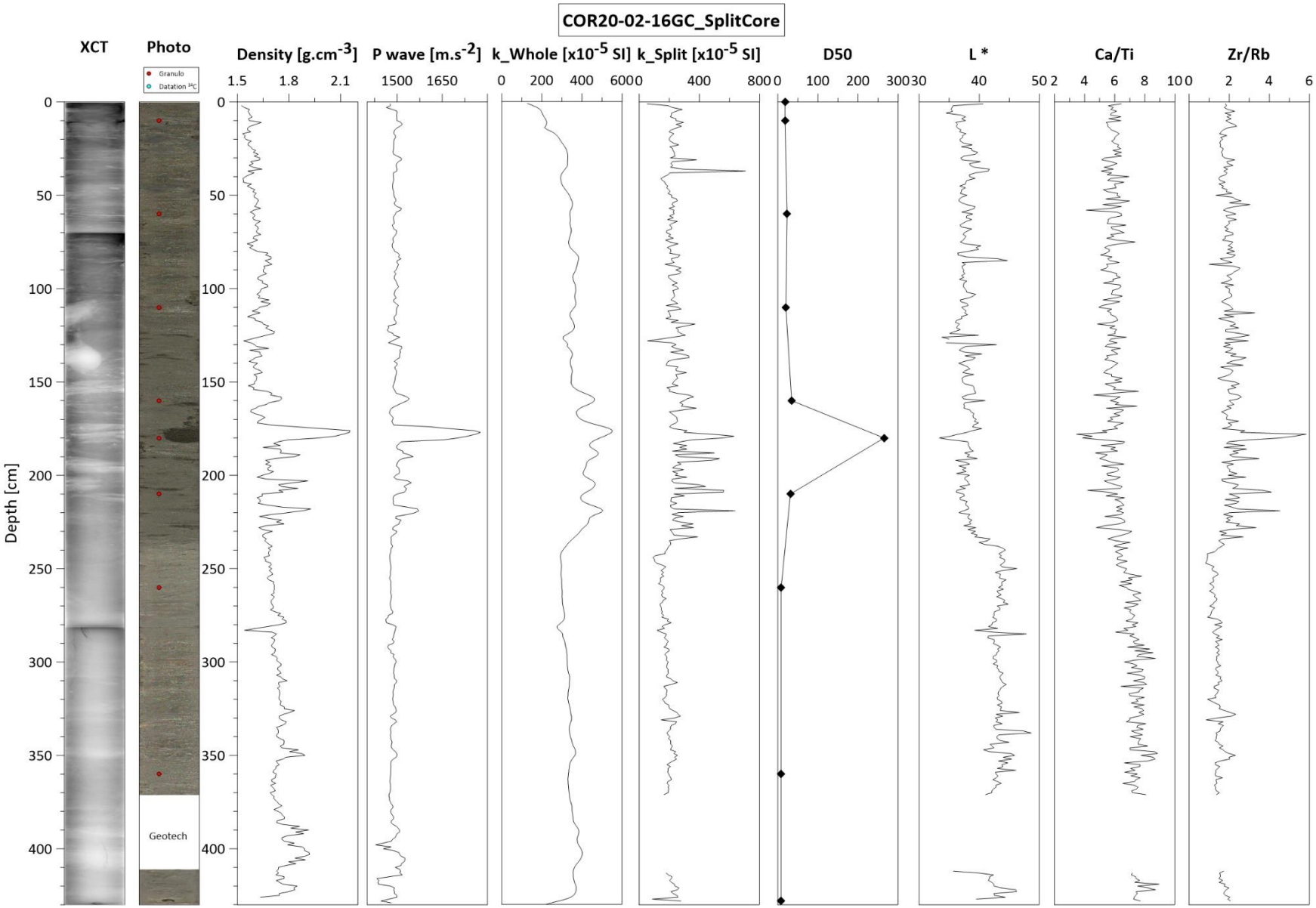
COR20-02-16GC_SplitCore
XCT
Photo
Granulo
Datation ¹⁴C
Density [g.cm-3]
P wave [m.s-2]
k_Whole [x10-5 SI]
k_Split [x10-5 SI]
D50
L *
Ca/Ti
Zr/Rb
Depth [cm]
Geotech

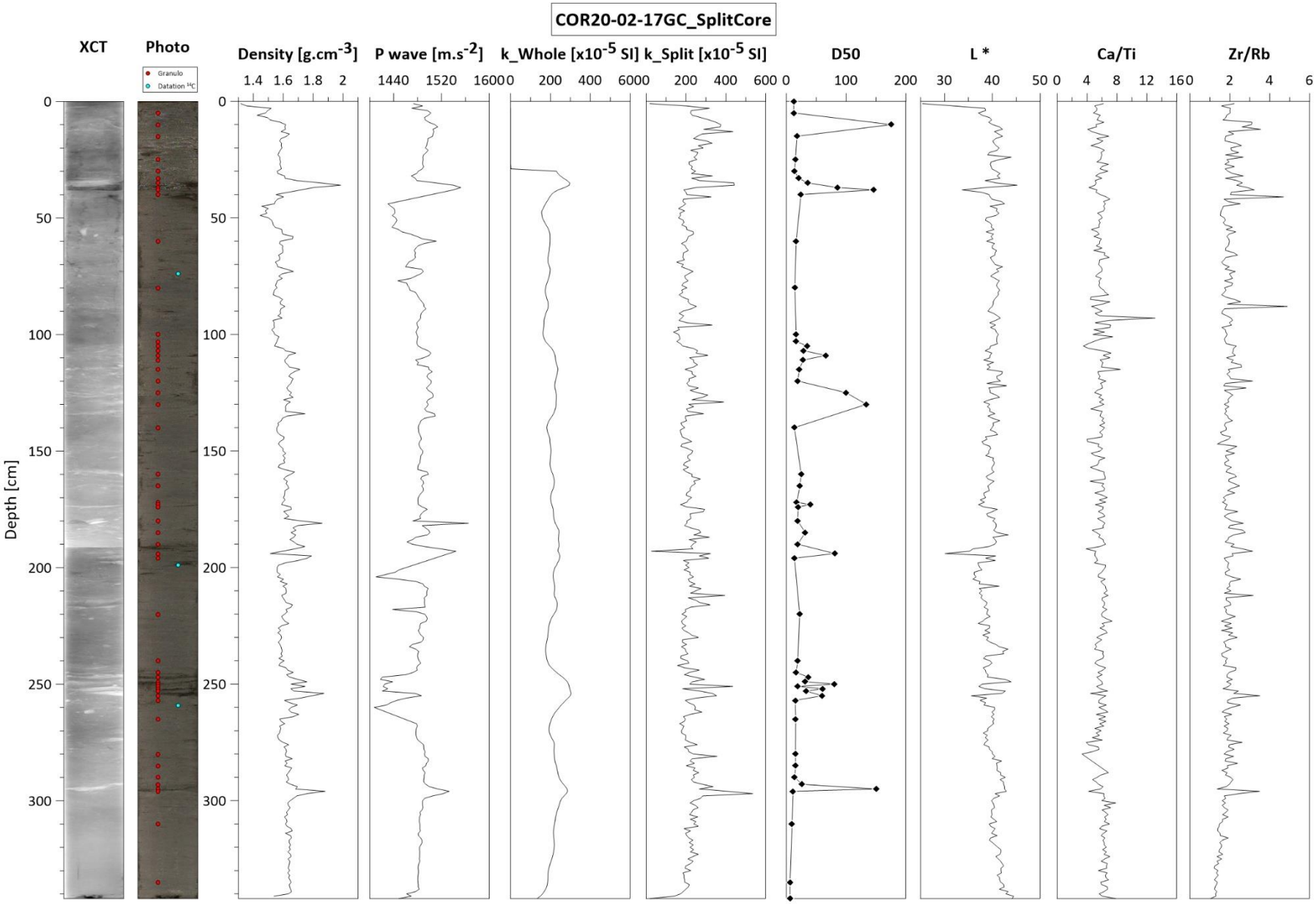
COR20-02-17GC_SplitCore
XCT
Photo
Granulo
Datation 14C
Density [g.cm-3]
P wave [m.s-2]
k_Whole [x10-5 SI]
k_Split [x10-5 SI]
D50
L *
Ca/Ti
Zr/Rb
Depth [cm]
0
50
100
150
200
250
300
1.4 1.6 1.8 2
1440 1520 1600
0 200 400 600
0 200 400 600
0 100 200
30 40 50
0 4 8 12 16
2 4 6

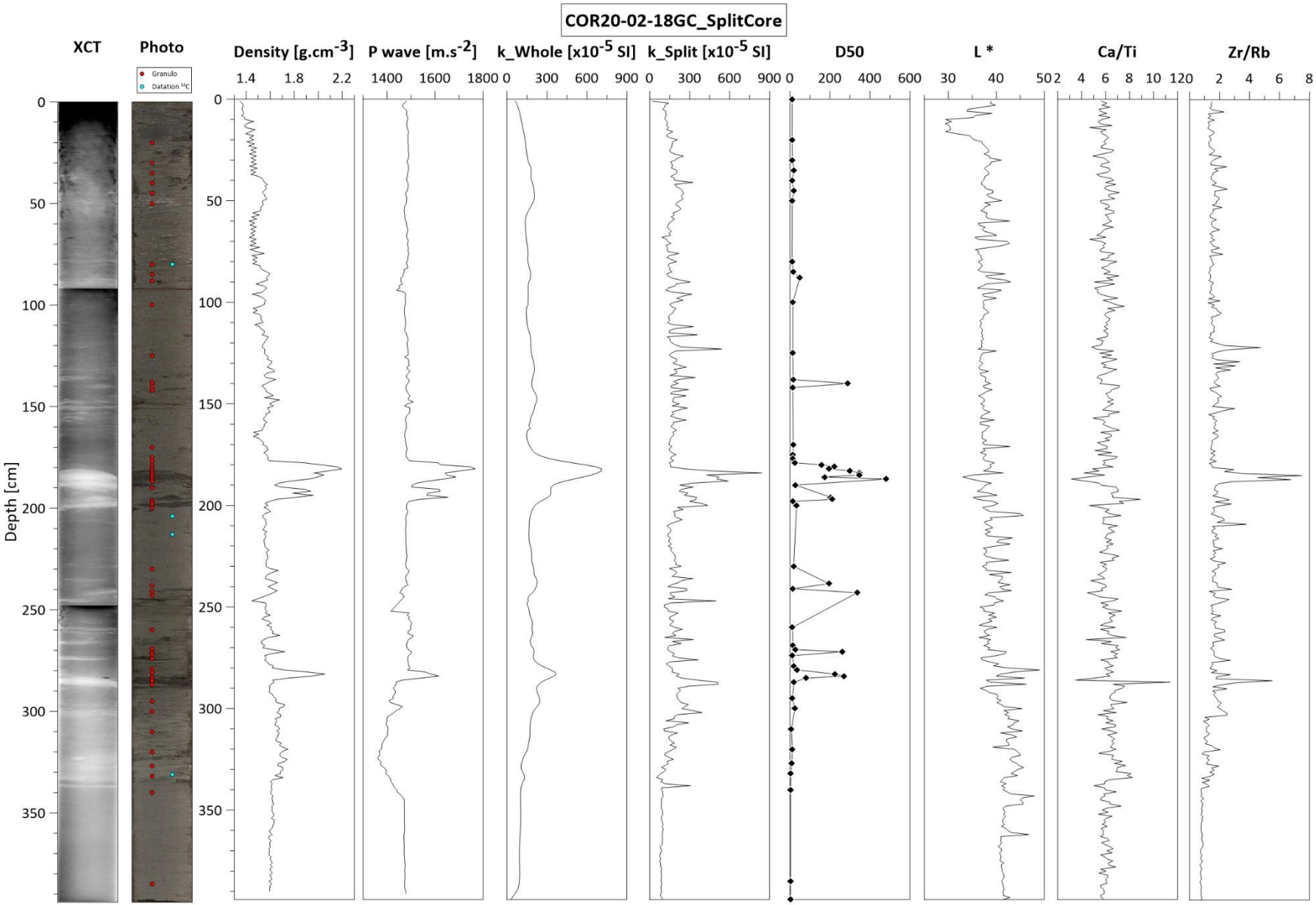
COR20-02-18GC_SplitCore
XCT
Photo
Granulo
Datation ¹⁴C
Density [g.cm-3]
P wave [m.s-2]
k_Whole [x10-5 SI]
k_Split [x10-5 SI]
D50
L *
Ca/Ti
Zr/Rb
Depth [cm]
0
50
100
150
200
250
300
350
1.4
1.8
2.2
1400
1600
1800
0
300
600
900
0
200
400
600
30
40
50
2
4
6
8
10
12
2
4
6
8

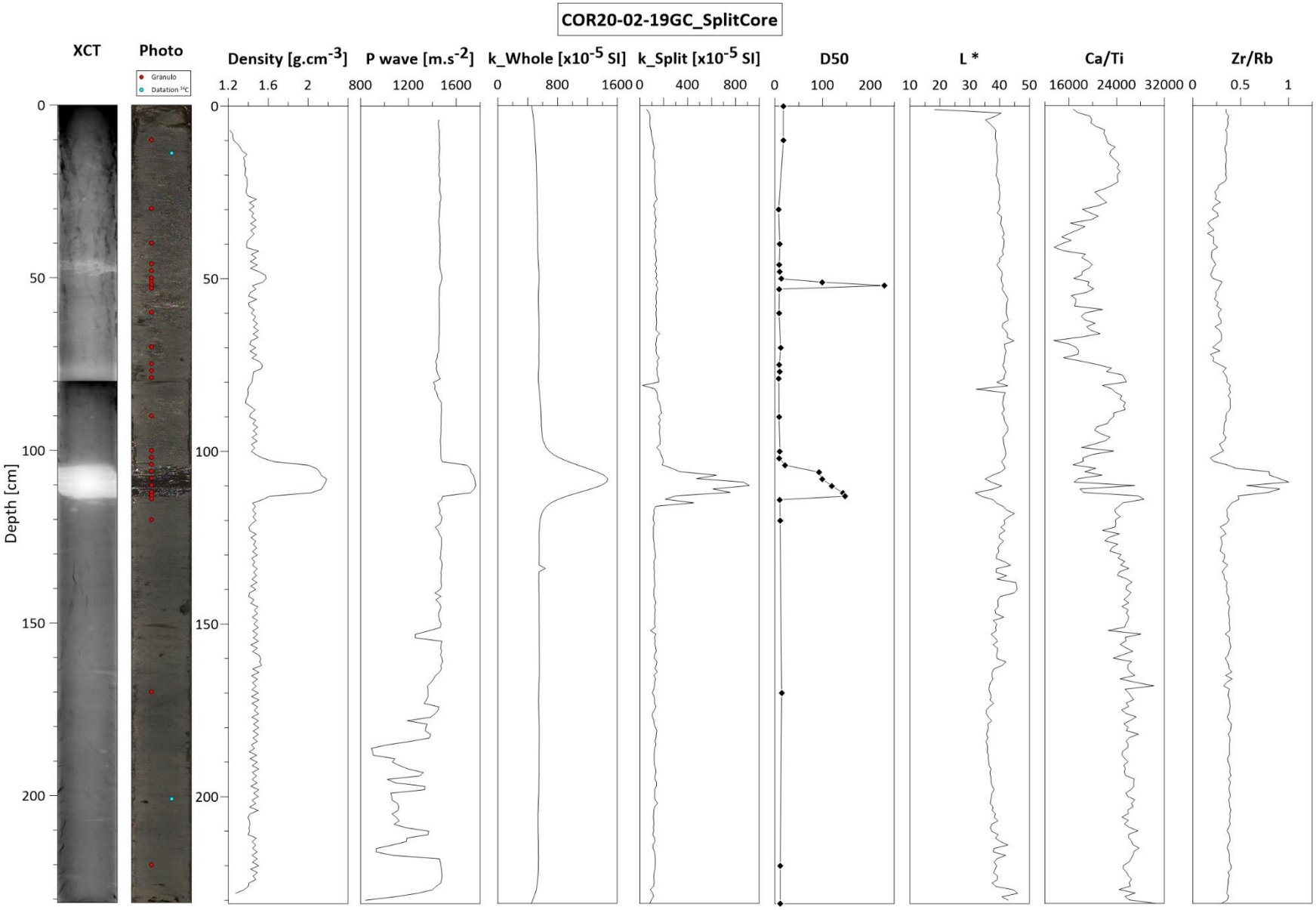
COR20-02-19GC_SplitCore
XCT
Photo
Granulo
Datation ¹⁴C
Density [g.cm-3]
P wave [m.s-2]
k_Whole [x10-5 SI]
k_Split [x10-5 SI]
D50
L *
Ca/Ti
Zr/Rb
Depth [cm]
0
50
100
150
200
1.2
1.6
2
800
1200
1600
0
800
1600
0
400
800
0
100
200
10
20
30
40
50
16000
24000
32000
0
0.5
1

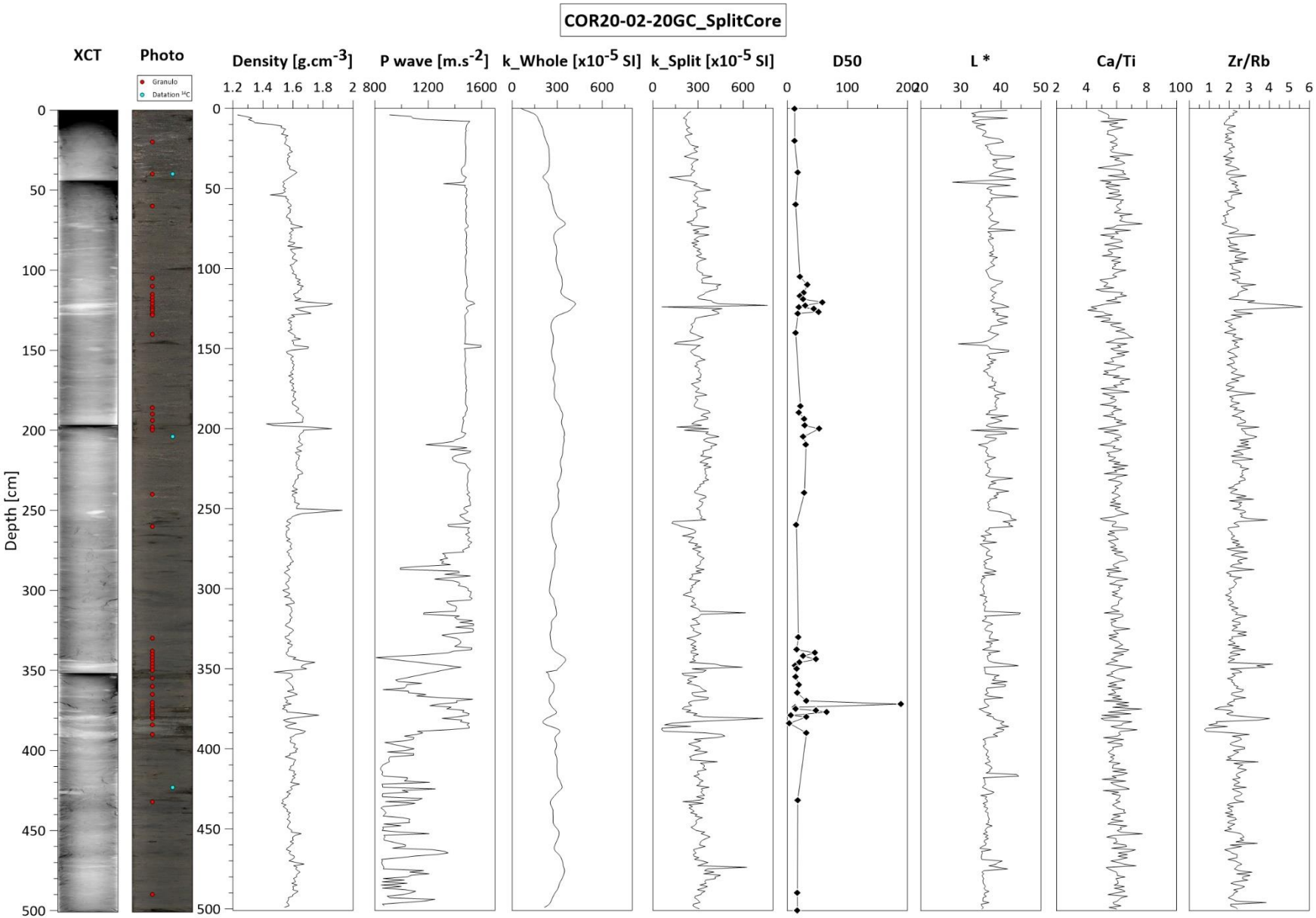
COR20-02-20GC_SplitCore
XCT
Photo
Granulo
Datation ¹⁴C
Density [g.cm-3]
P wave [m.s-2]
k_Whole [x10-5 SI]
k_Split [x10-5 SI]
D50
L *
Ca/Ti
Zr/Rb
Depth [cm]
0
50
100
150
200
250
300
350
400
450
500
1.2 1.4 1.6 1.8 2
800 1200 1600
0 300 600
0 300 600
0 100 200
20 30 40 50
2 4 6 8 100
1 2 3 4 5 6

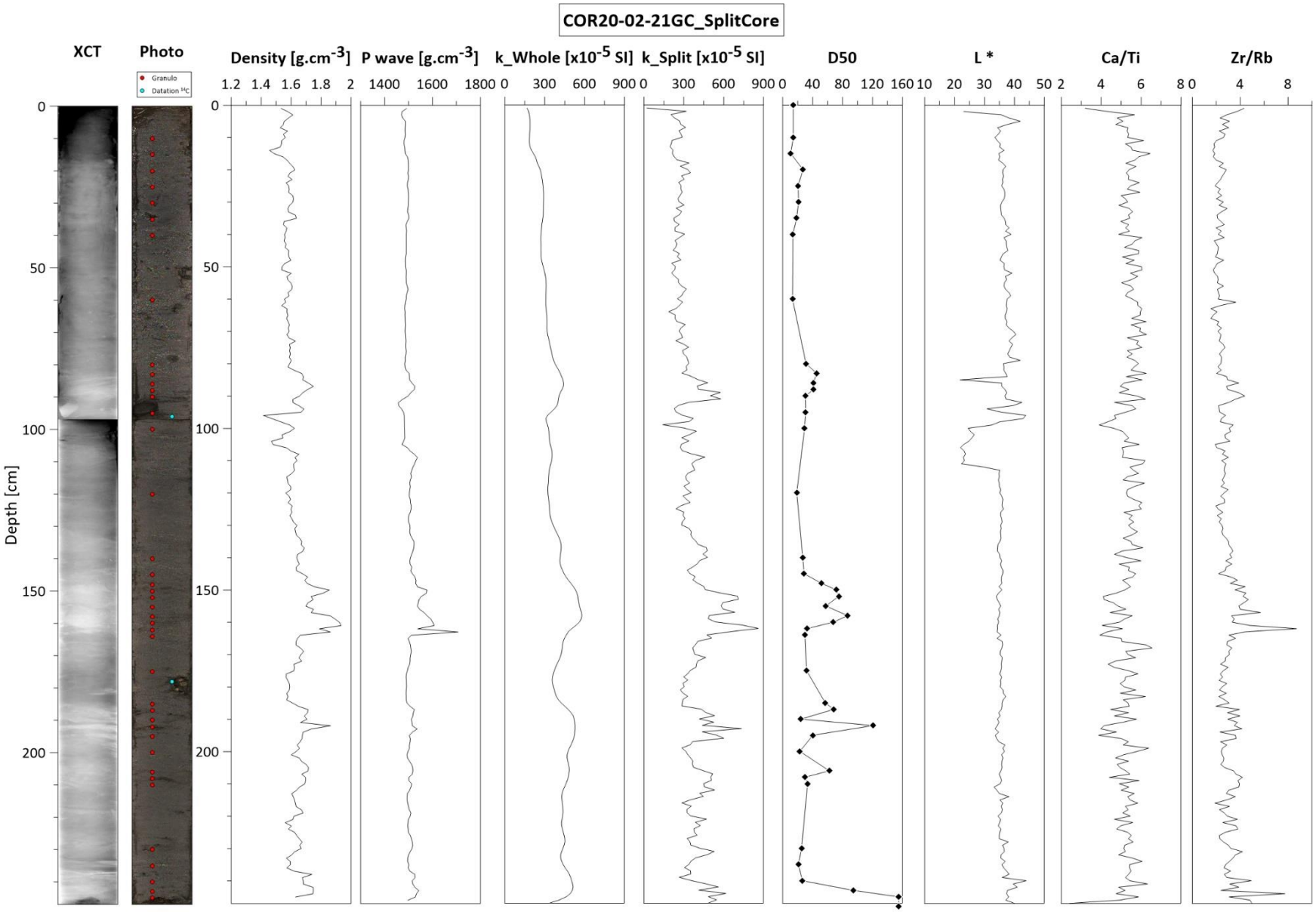
COR20-02-21GC_SplitCore
XCT
Photo
Granulo
Datation ¹⁴C
Density [g.cm-3]
P wave [g.cm-3]
k_Whole [x10-5 SI]
k_Split [x10-5 SI]
D50
L *
Ca/Ti
Zr/Rb
Depth [cm]
0
50
100
150
200
1.2 1.4 1.6 1.8 2
1400 1600 1800
0 300 600 900
0 300 600 900
0 40 80 120 160
10 20 30 40 50
2 4 6 8
0 4 8

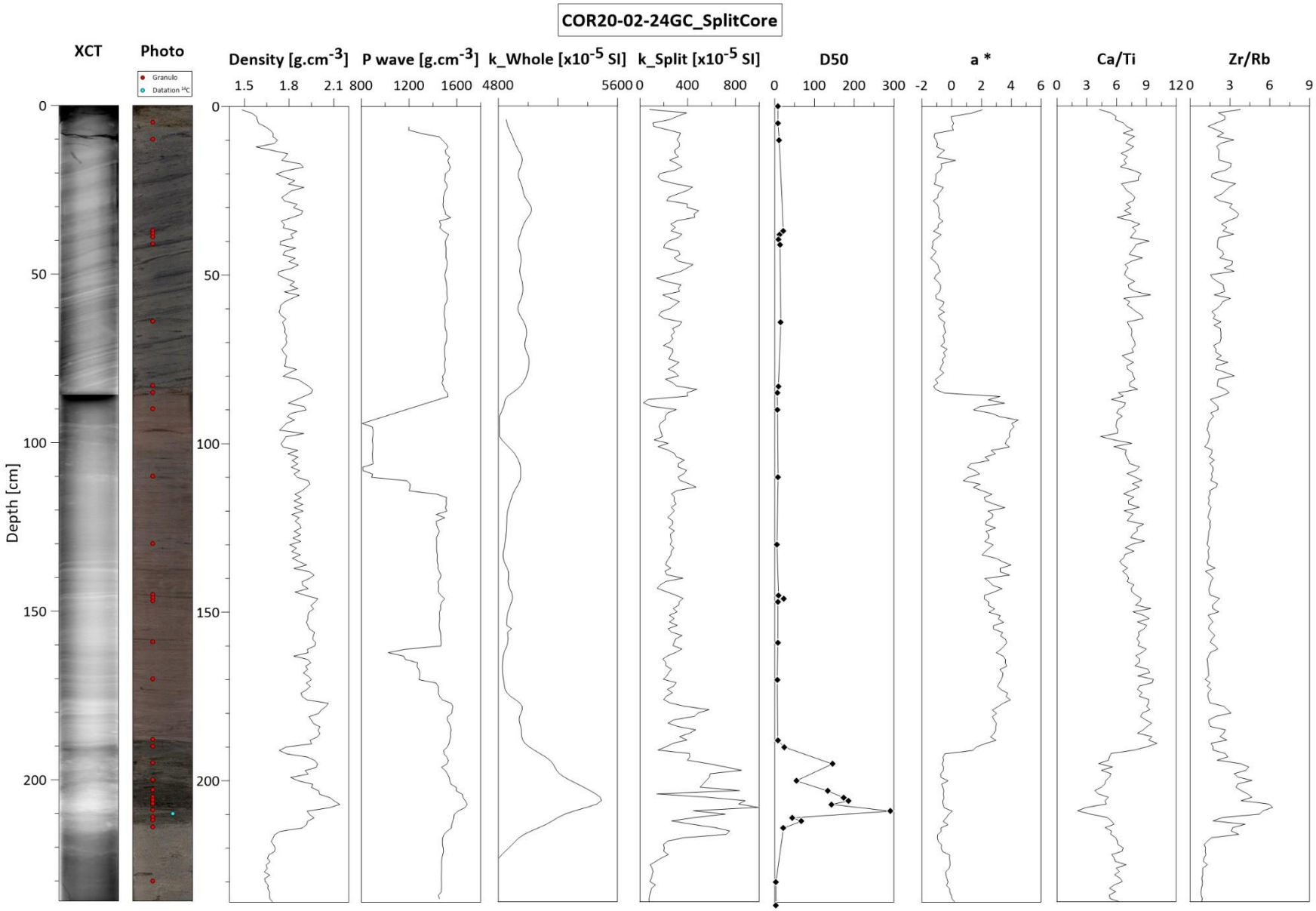
COR20-02-24GC_SplitCore
XCT
Photo
Granulo
Datation ¹⁴C
Density [g.cm-3]
P wave [g.cm-3]
k_Whole [x10-5 SI]
k_Split [x10-5 SI]
D50
a *
Ca/Ti
Zr/Rb
Depth [cm]
0
50
100
150
200
1.5
1.8
2.1
800
1200
1600
4800
5600
400
800
100
200
300
-2
2
4
6
3
9
12

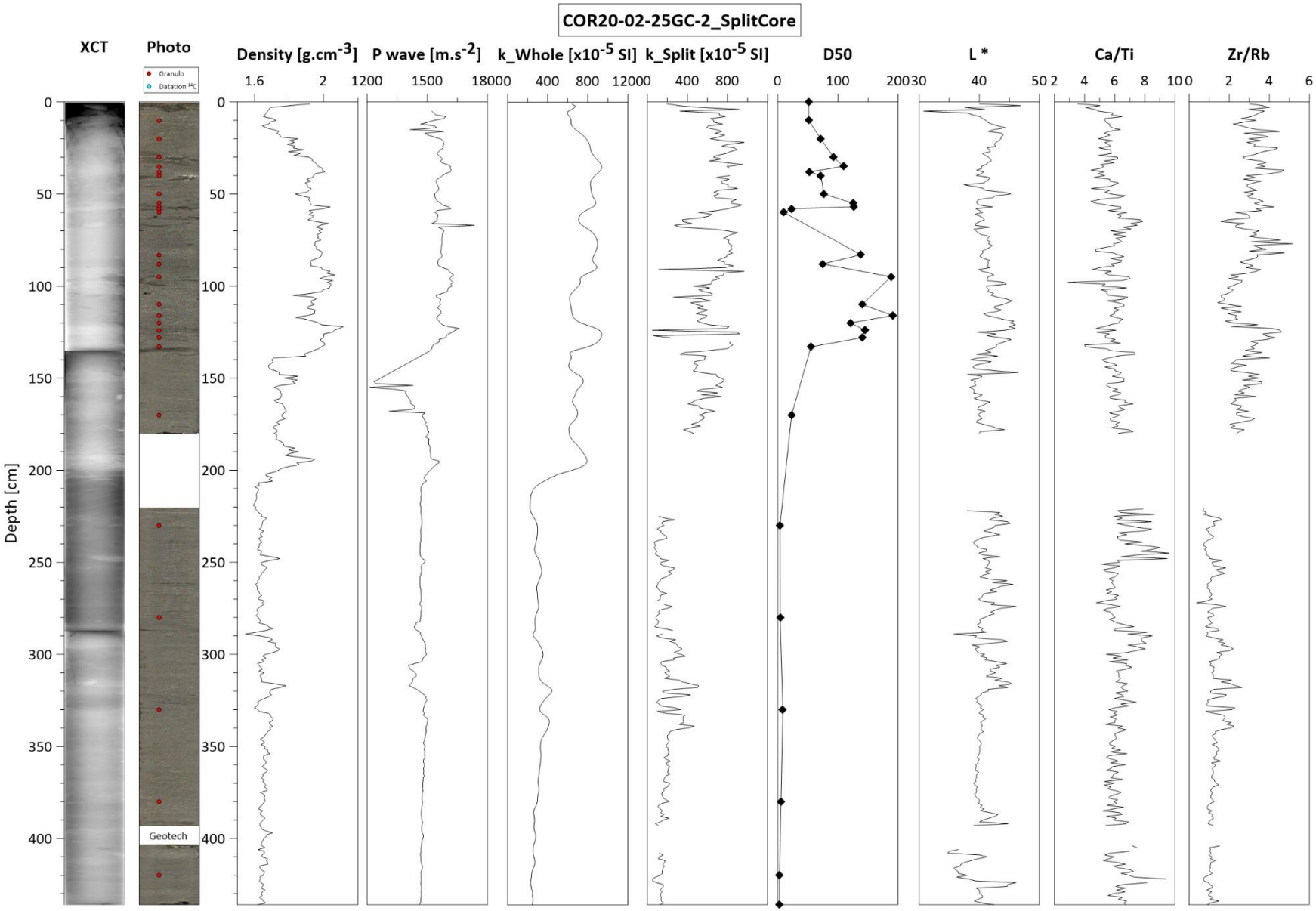
COR20-02-25GC-2_SplitCore
XCT
Photo
Granulo
Datation 14C
Density [g.cm-3]
P wave [m.s-2]
k_Whole [x10-5 SI]
k_Split [x10-5 SI]
D50
L *
Ca/Ti
Zr/Rb
Depth [cm]
Geotech

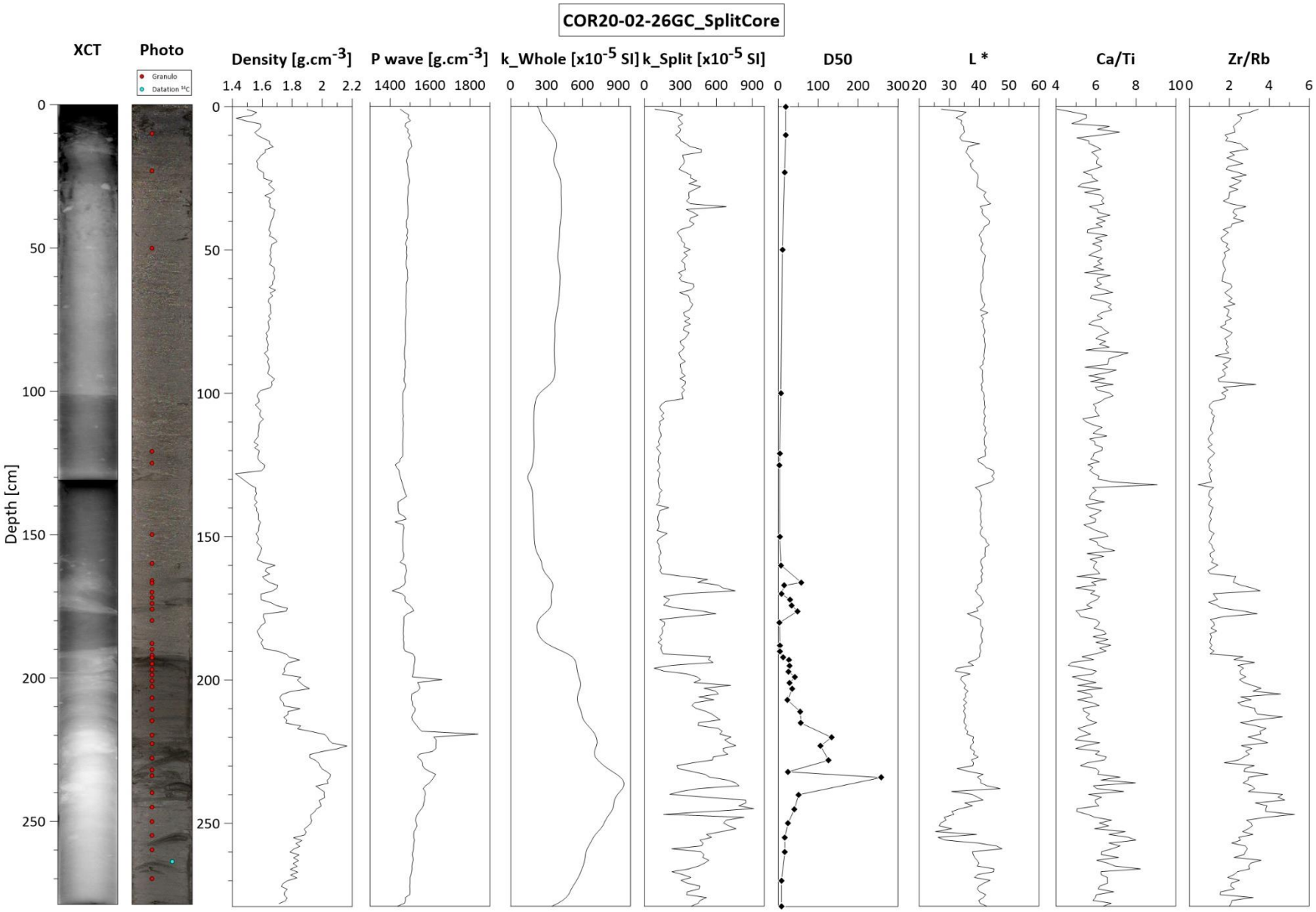
COR20-02-26GC_SplitCore
XCT
Photo
Granulo
Datation ¹⁴C
Density [g.cm-3]
P wave [g.cm-3]
k_Whole [x10-5 SI]
k_Split [x10-5 SI]
D50
L *
Ca/Ti
Zr/Rb
Depth [cm]
0
50
100
150
200
250
1.4 1.6 1.8 2 2.2
1400 1600 1800
0 300 600 900
0 300 600 900
0 100 200 300
20 30 40 50 60
4 6 8 10
0 2 4 6

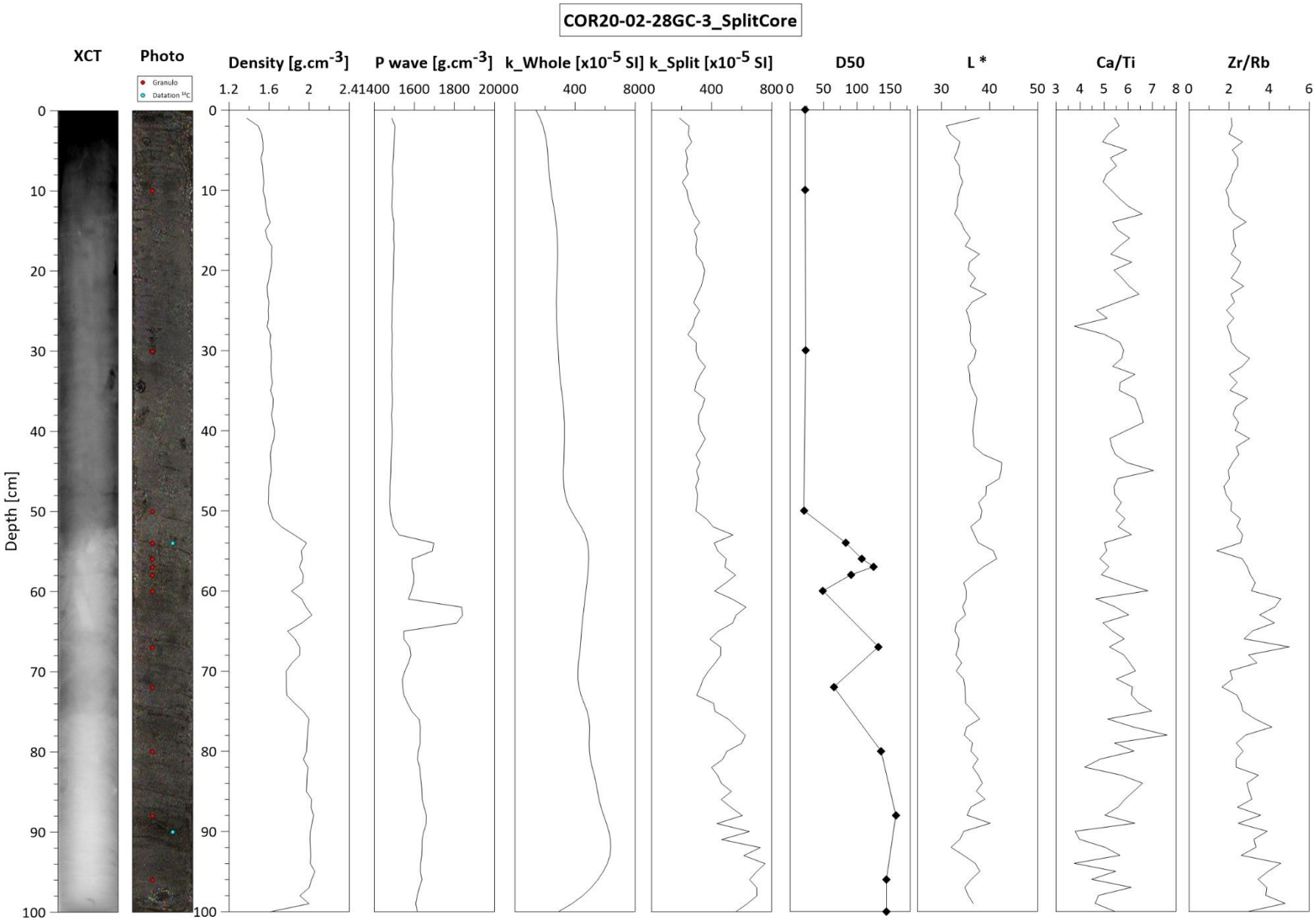
COR20-02-28GC-3_SplitCore
XCT
Photo
Granulo
Datation ¹⁴C
Density [g.cm-3]
P wave [g.cm-3]
k_Whole [x10-5 SI]
k_Split [x10-5 SI]
D50
L *
Ca/Ti
Zr/Rb
Depth [cm]
0
10
20
30
40
50
60
70
80
90
100
1.2
1.6
2
2.4
1400
1600
1800
2000
0
400
8000
400
800
0
50
100
150
30
40
50
3
4
5
6
7
8
0
2
4
6

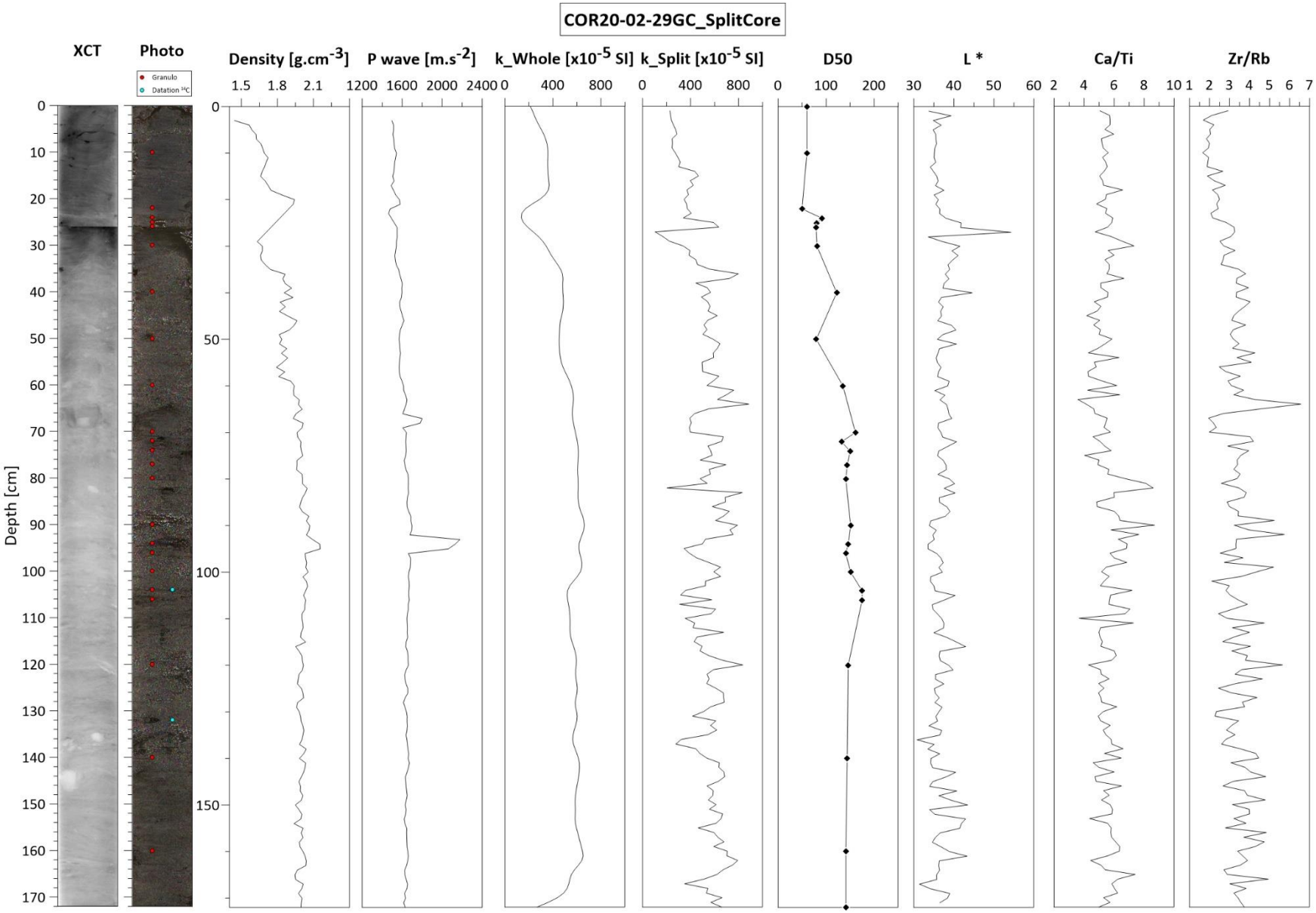
COR20-02-29GC_SplitCore
XCT
Photo
Granulo
Datation ¹⁴C
Density [g.cm-3]
P wave [m.s-2]
k_Whole [x10-5 SI]
k_Split [x10-5 SI]
D50
L *
Ca/Ti
Zr/Rb
Depth [cm]

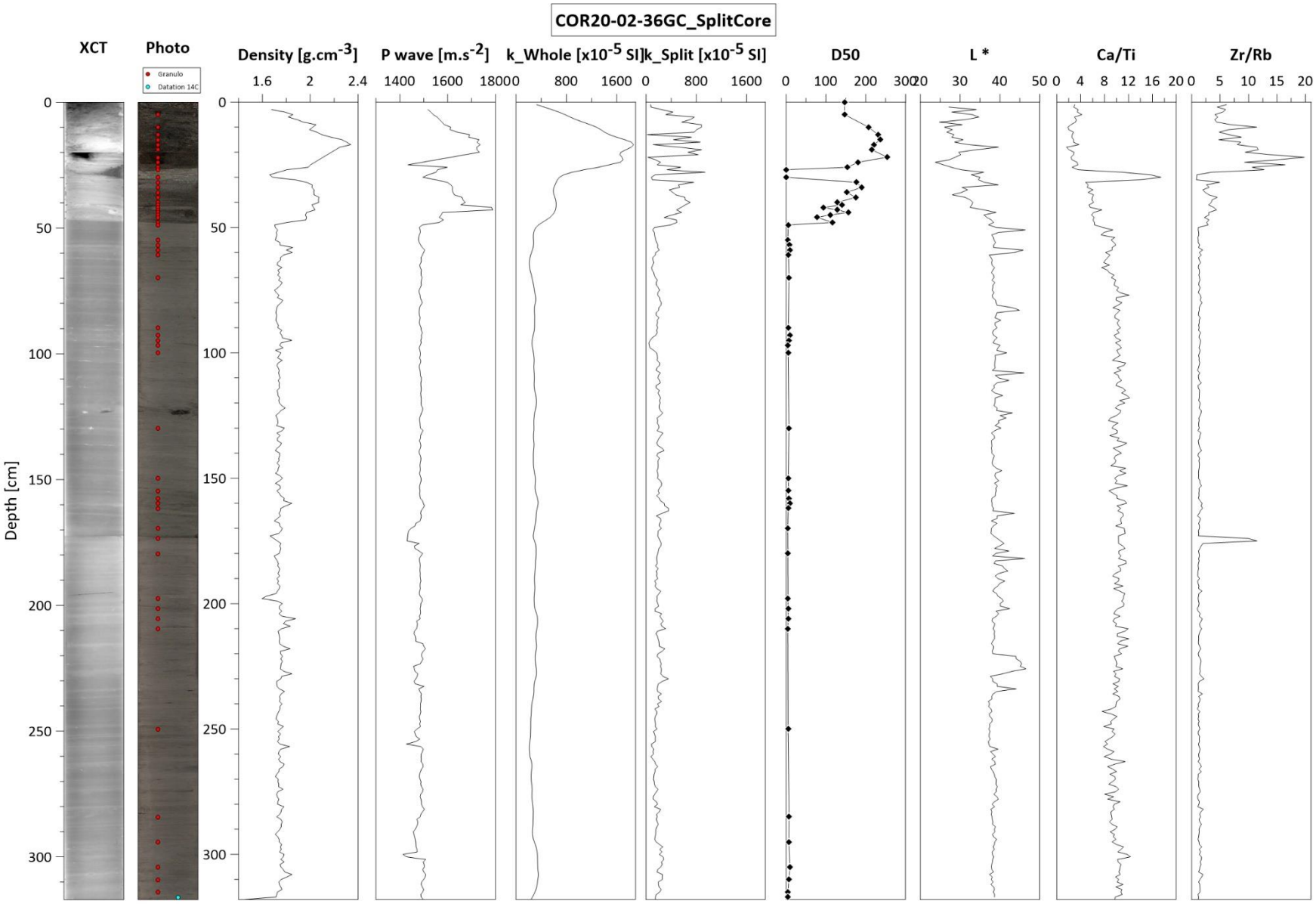
COR20-02-36GC_SplitCore
XCT
Photo
Granulo
Datation 14C
Density [g.cm-3]
P wave [m.s-2]
k_Whole [x10-5 SI]
k_Split [x10-5 SI]
D50
L *
Ca/Ti
Zr/Rb
Depth [cm]
0
50
100
150
200
250
300
1.6
2
2.4
1400
1600
1800
800
1600
800
1600
100
200
300
20
30
40
50
4
8
12
16
20
5
10
15
20

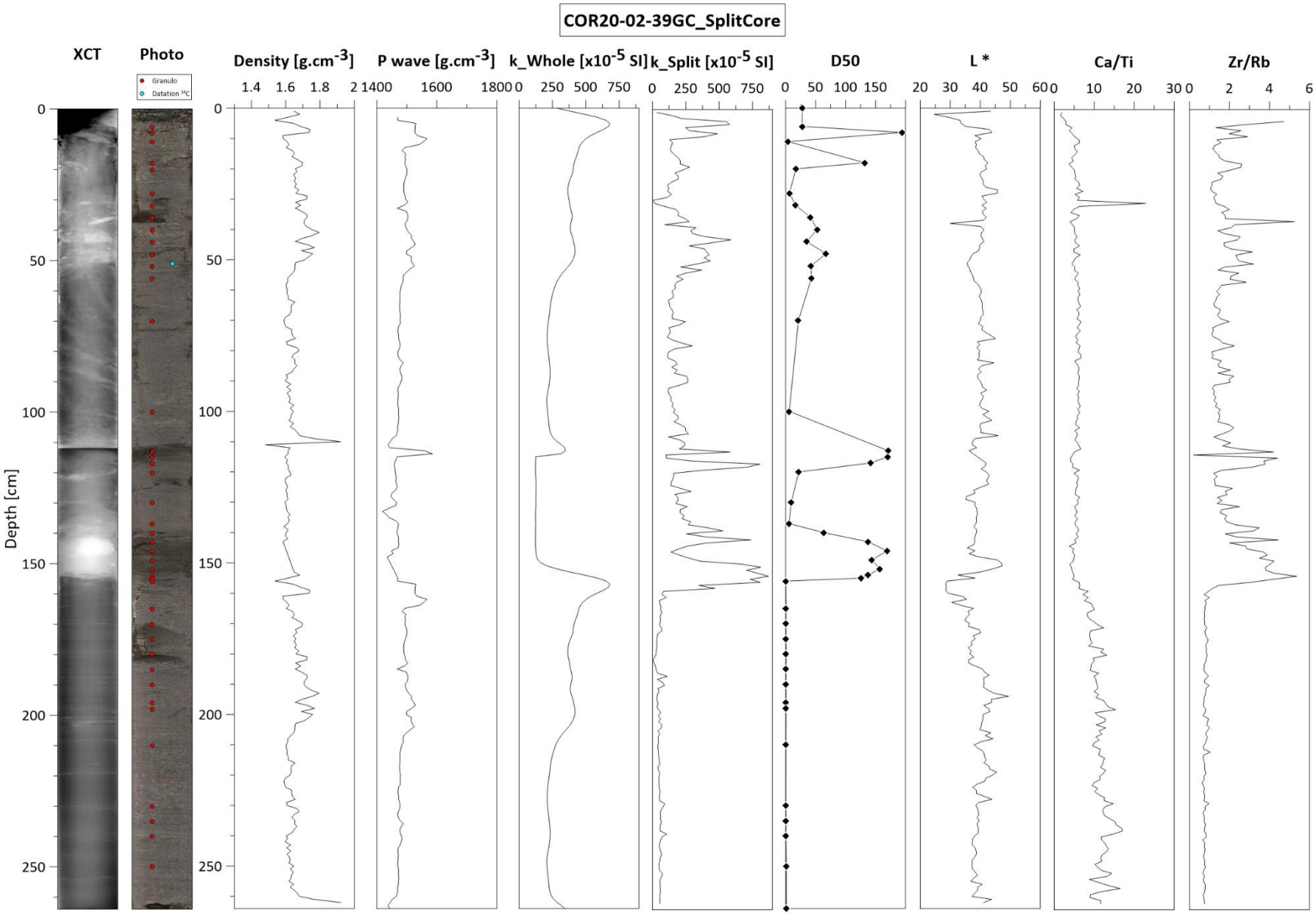
COR20-02-39GC_SplitCore
XCT
Photo
Granulo
Datation ¹⁴C
Density [g.cm-3]
P wave [g.cm-3]
k_Whole [x10-5 SI]
k_Split [x10-5 SI]
D50
L *
Ca/Ti
Zr/Rb
Depth [cm]
0
50
100
150
200
250
1.4 1.6 1.8 2
1400 1600 1800
0 250 500 750
0 250 500 750
0 50 100 150
20 30 40 50 60
0 10 20 30
0 2 4 6

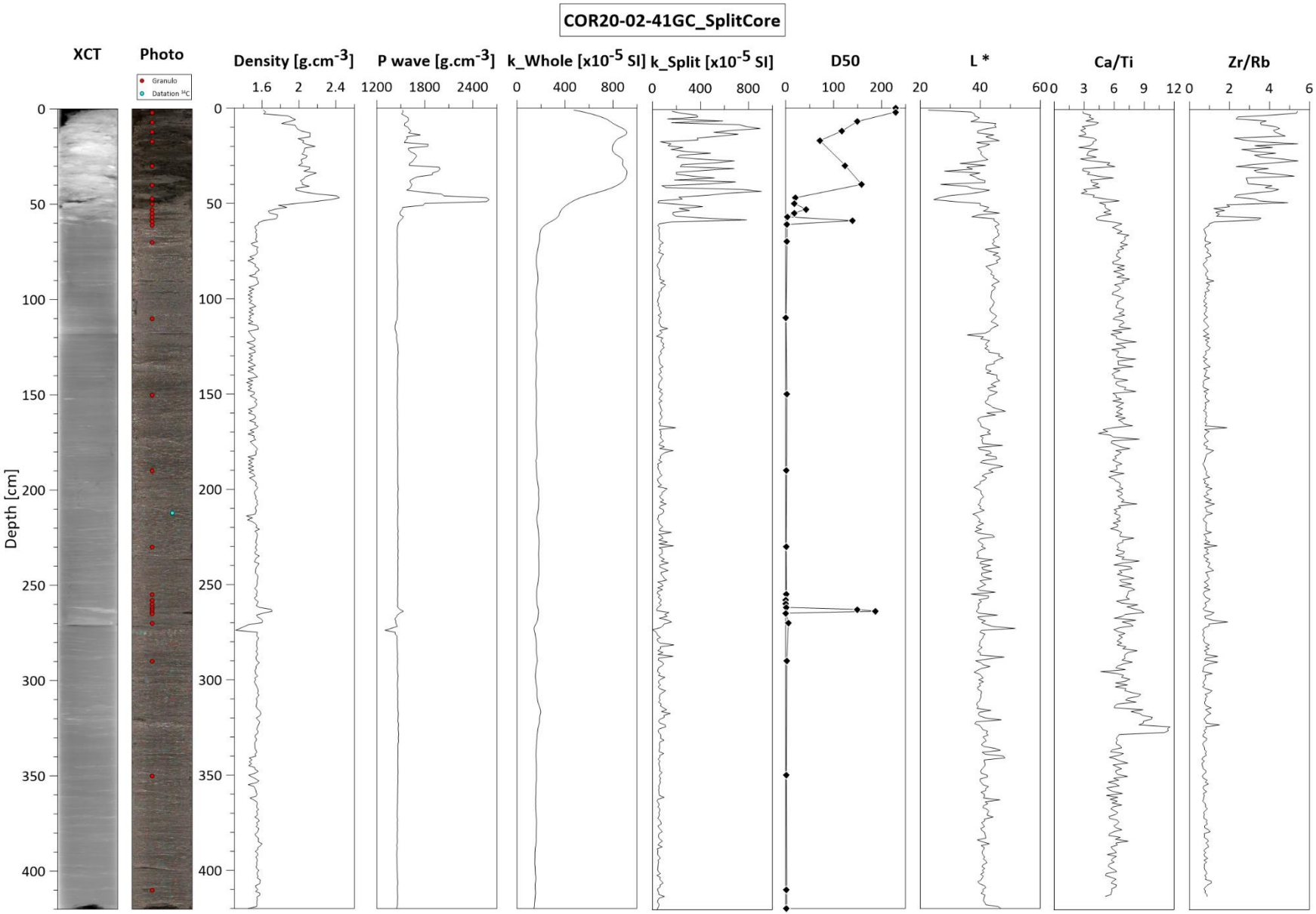
COR20-02-41GC_SplitCore
XCT
Photo
Granulo
Datation ¹⁴C
Density [g.cm-3]
P wave [g.cm-3]
k_Whole [x10-5 SI]
k_Split [x10-5 SI]
D50
L *
Ca/Ti
Zr/Rb
Depth [cm]
0
50
100
150
200
250
300
350
400
1.6
2
2.4
1200
1800
2400
0
400
800
0
100
200
20
40
60
3
6
9
12
2
4
6

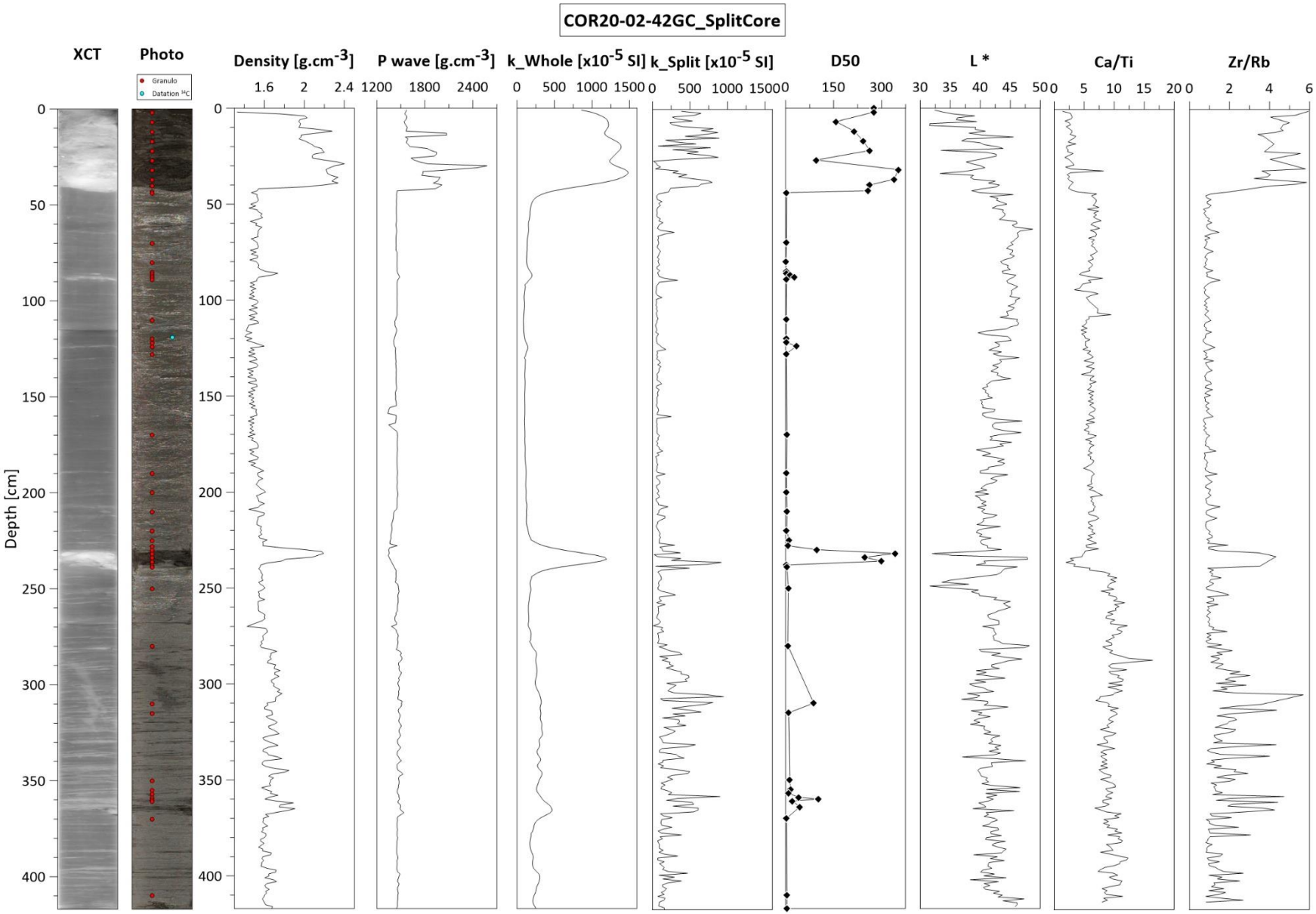
COR20-02-42GC_SplitCore
XCT
Photo
Granulo
Datation ¹⁴C
Density [g.cm-3]
P wave [g.cm-3]
k_Whole [x10-5 SI]
k_Split [x10-5 SI]
D50
L *
Ca/Ti
Zr/Rb
Depth [cm]

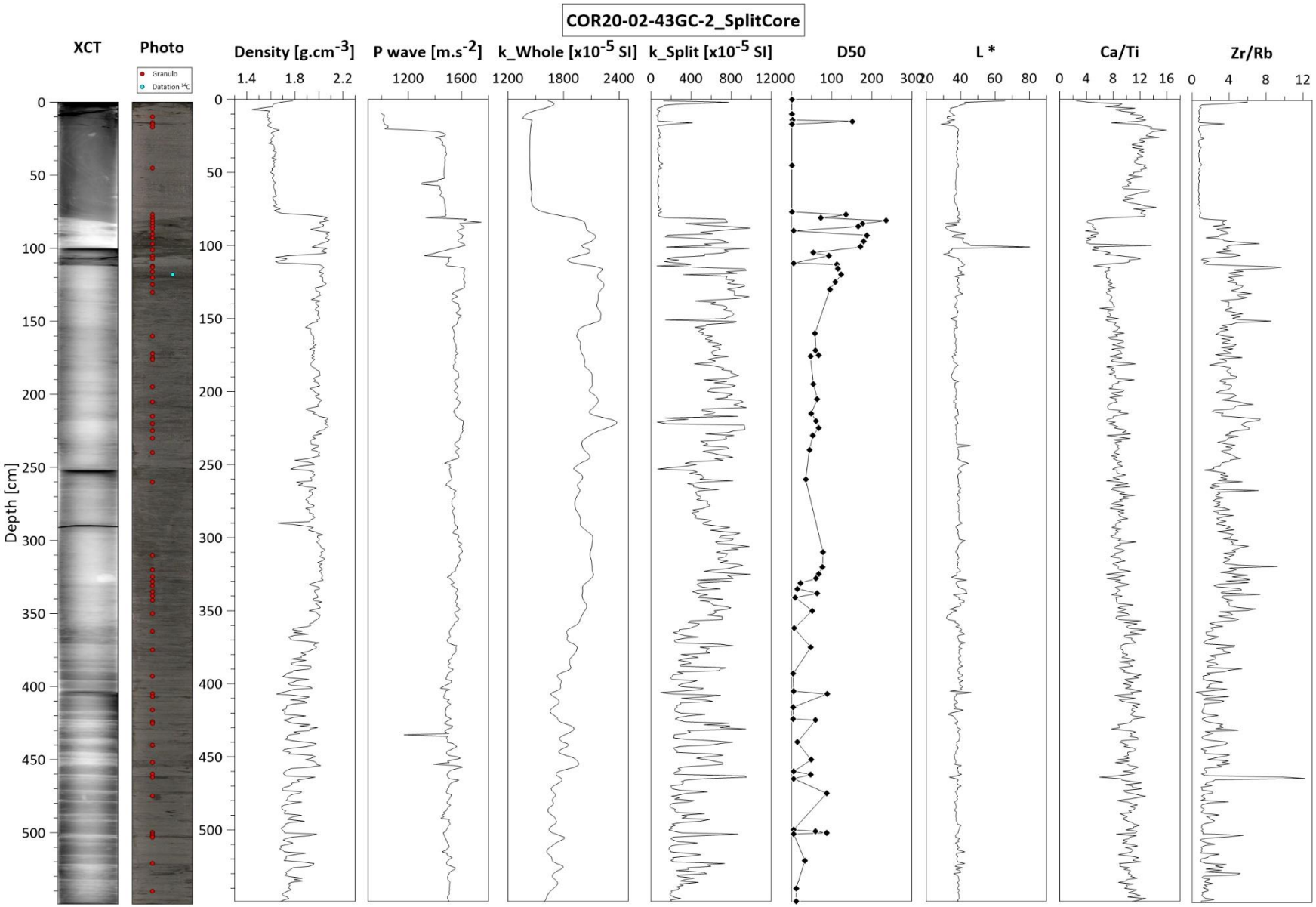
COR20-02-43GC-2_SplitCore
XCT
Photo
Granulo
Datation ¹⁴C
Density [g.cm-3]
P wave [m.s-2]
k_Whole [x10-5 SI]
k_Split [x10-5 SI]
D50
L *
Ca/Ti
Zr/Rb
Depth [cm]

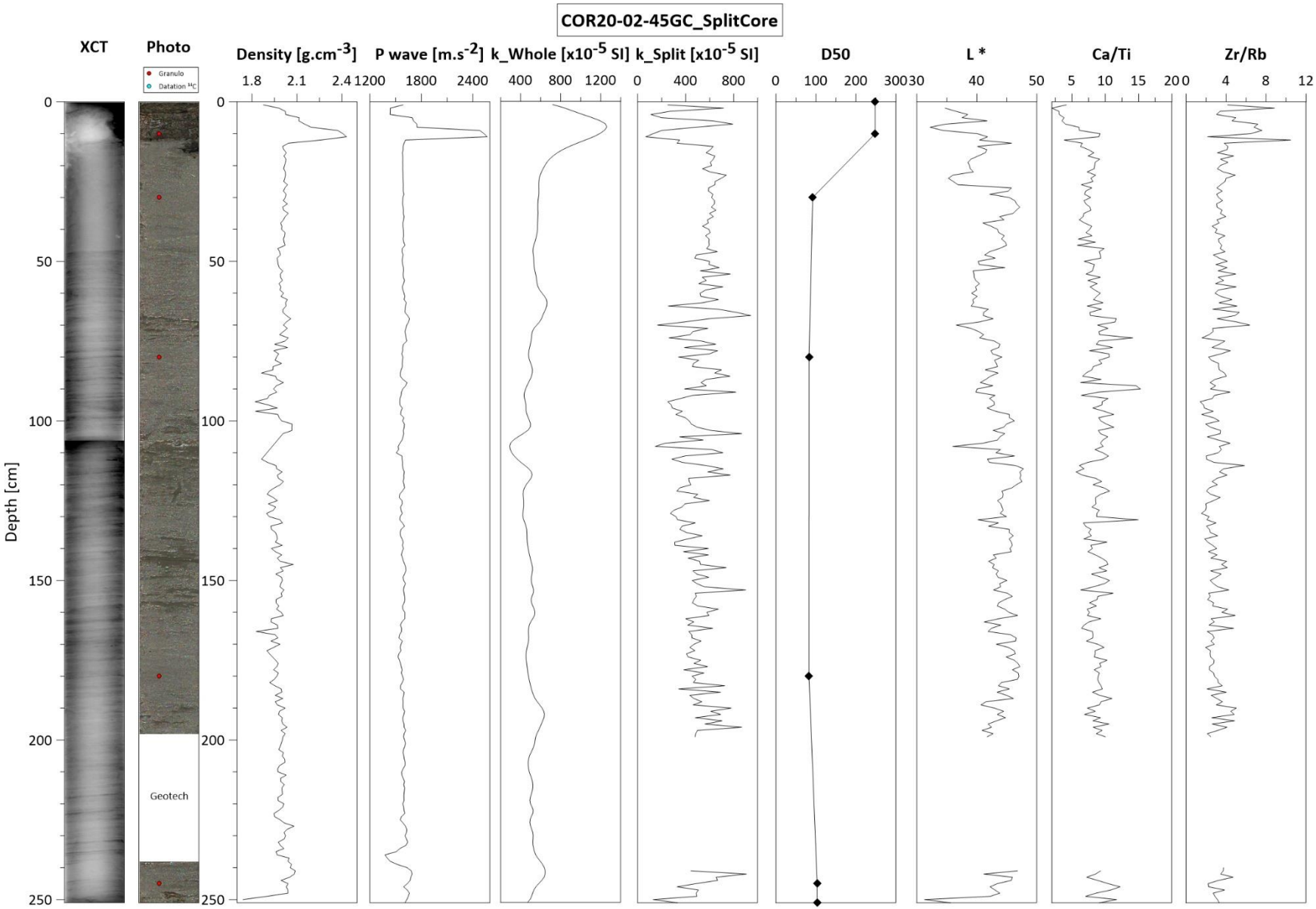
COR20-02-45GC_SplitCore
XCT
Photo
Granulo
Datation 14C
Density [g.cm-3]
P wave [m.s-2]
k_Whole [x10-5 SI]
k_Split [x10-5 SI]
D50
L *
Ca/Ti
Zr/Rb
Depth [cm]
Geotech

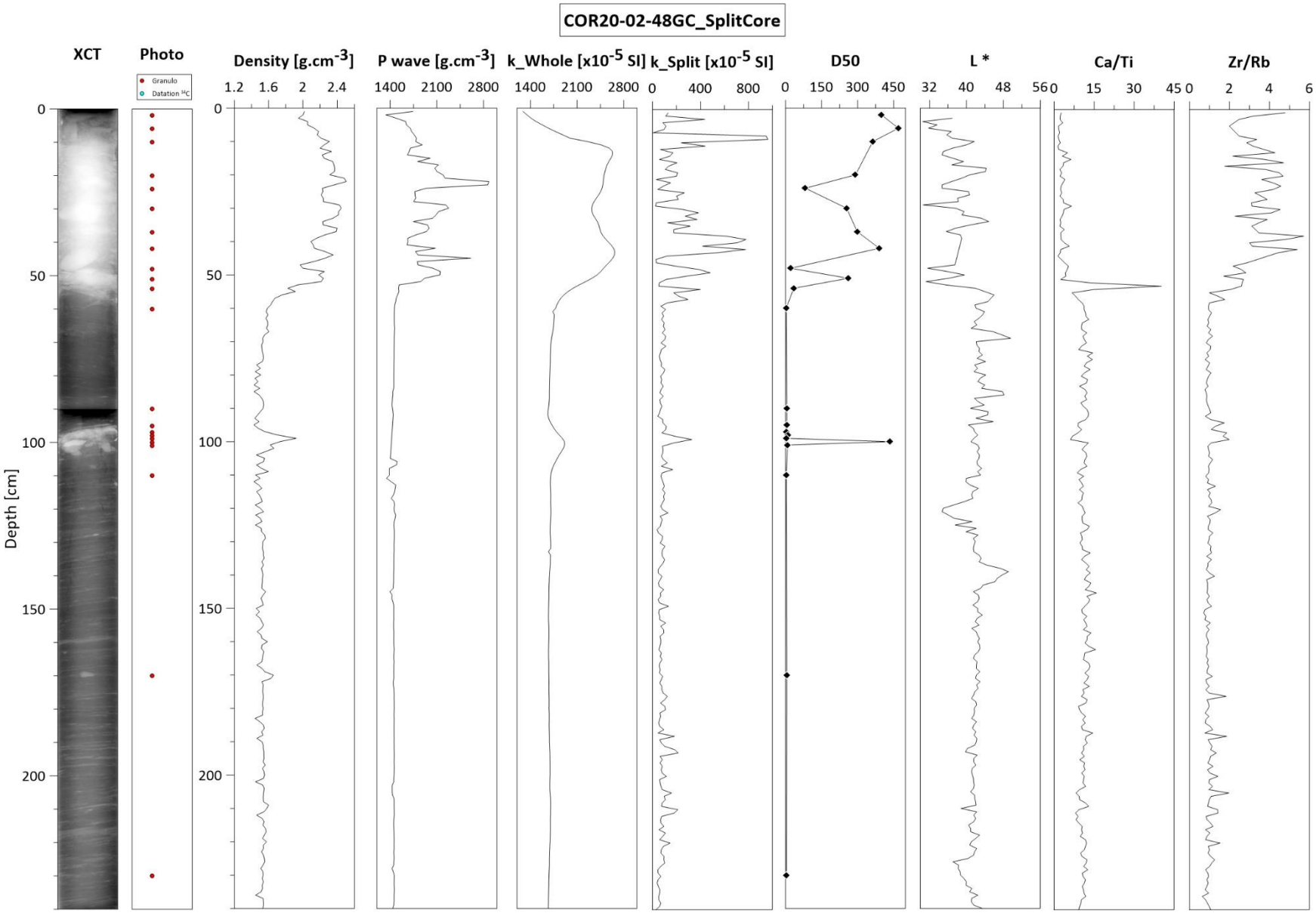
COR20-02-48GC_SplitCore
XCT
Photo
Granulo
Datation ¹⁴C
Density [g.cm-3]
P wave [g.cm-3]
k_Whole [x10-5 SI]
k_Split [x10-5 SI]
D50
L *
Ca/Ti
Zr/Rb
Depth [cm]
0
50
100
150
200
1.2 1.6 2 2.4
1400 2100 2800
1400 2100 2800
0 400 800
0 150 300 450
32 40 48 56
0 15 30 45
0 2 4 6

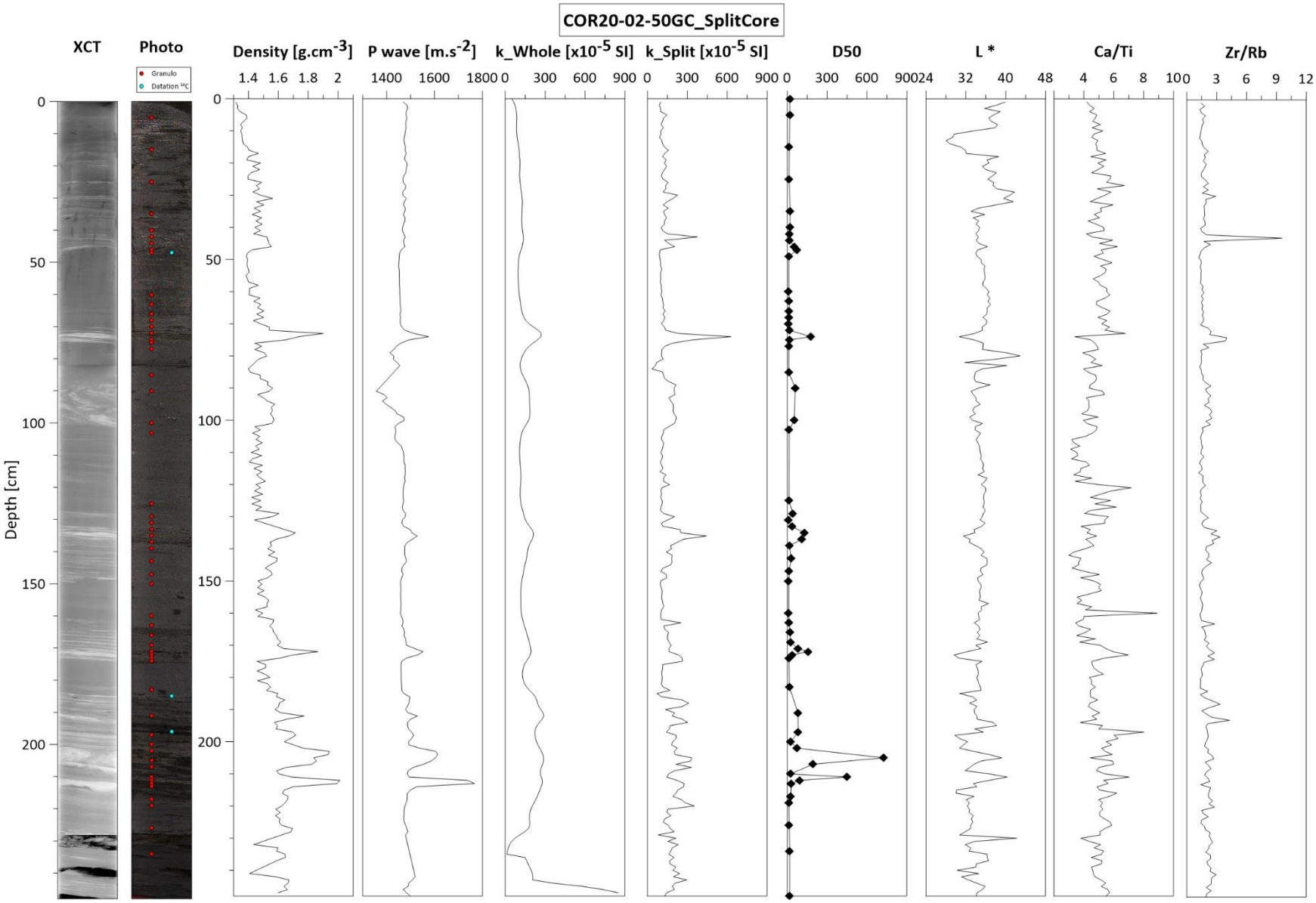
COR20-02-50GC_SplitCore
XCT
Photo
Granulo
Datation ¹⁴C
Density [g.cm-3]
P wave [m.s-2]
k_Whole [x10-5 SI]
k_Split [x10-5 SI]
D50
L *
Ca/Ti
Zr/Rb
Depth [cm]
0
50
100
150
200
1.4 1.6 1.8 2
1400 1600 1800
0 300 600 900
0 300 600 900
0 300 600 900
0 24 32 40 48
4 6 8 10
0 3 6 9 12

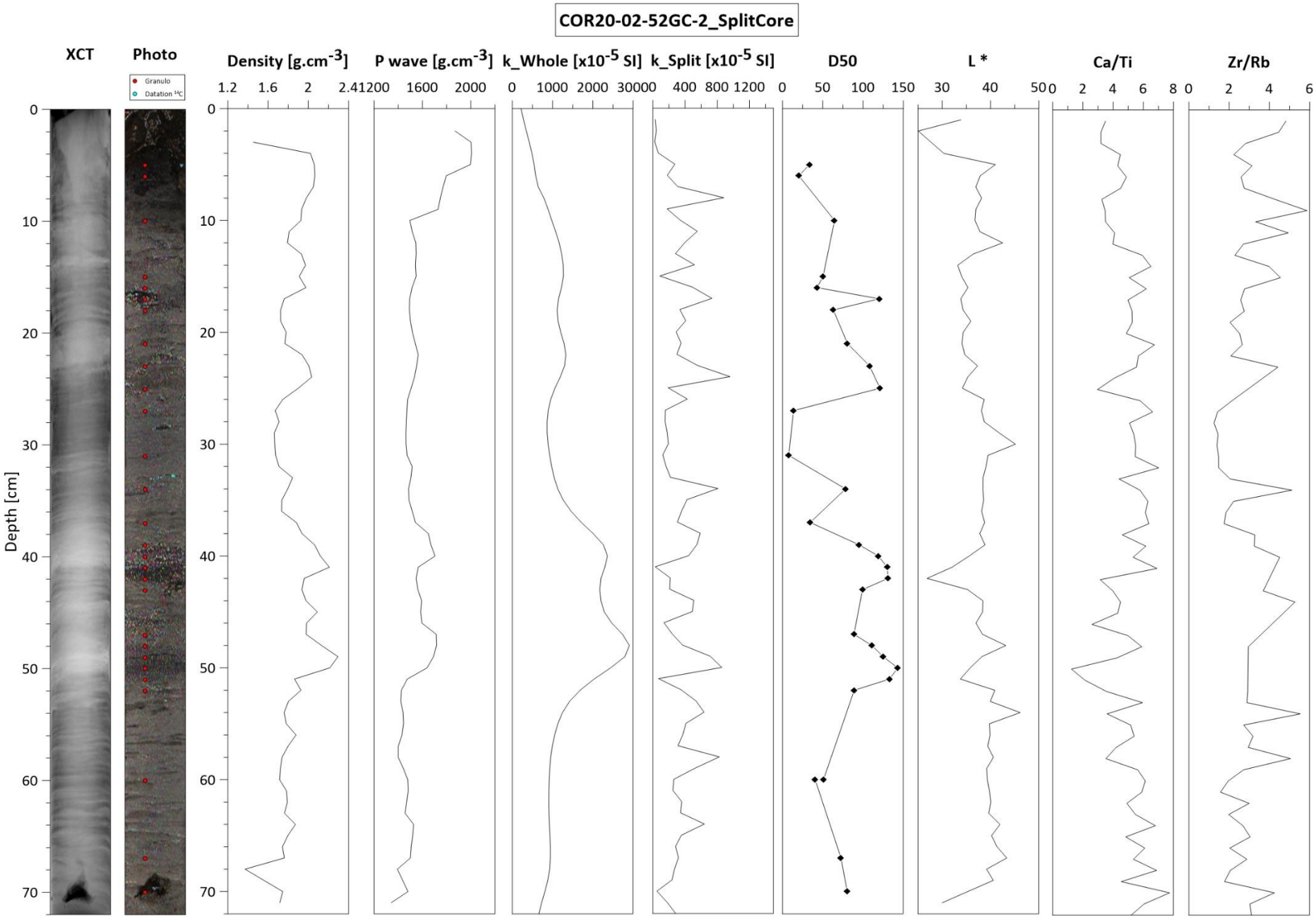
COR20-02-52GC-2_SplitCore
XCT
Photo
Granulo
Datation ¹⁴C
Density [g.cm-3]
P wave [g.cm-3]
k_Whole [x10-5 SI]
k_Split [x10-5 SI]
D50
L *
Ca/Ti
Zr/Rb
Depth [cm]
0
10
20
30
40
50
60
70
1.2
1.6
2
2.4
1200
1600
2000
0
1000
2000
30000
400
800
1200
0
50
100
150
30
40
50
0
2
4
6
8
0
2
4
6

Figures annexe 3. Résultats des essais triaxiaux cycliques menés au laboratoire de géotechnique à l'Ifremer à l'aide de la cellule triaxiale cyclique. Voir chapitre 2 pour l'explication des différents graphiques.

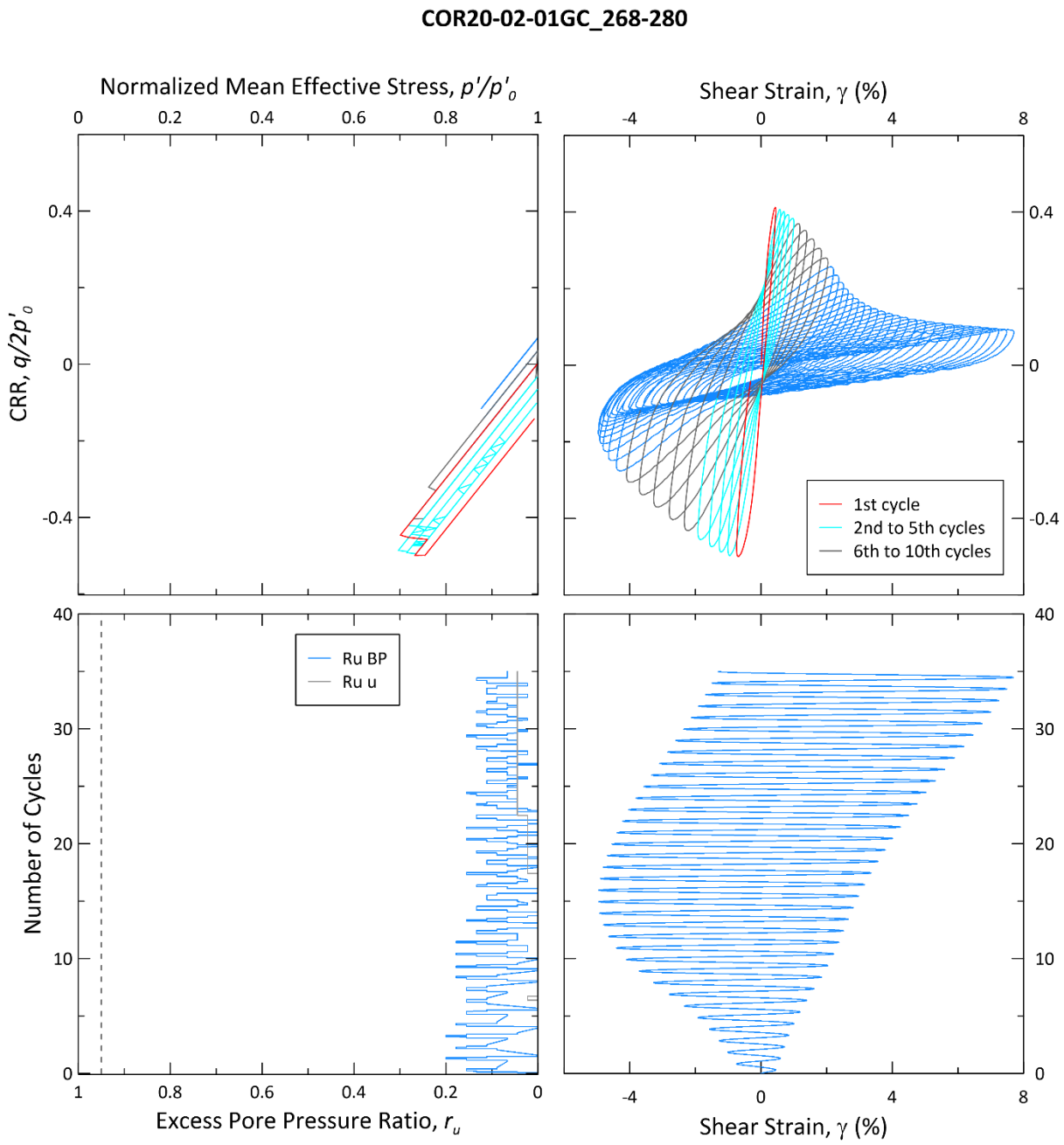

COR20-02-02GC_374-386

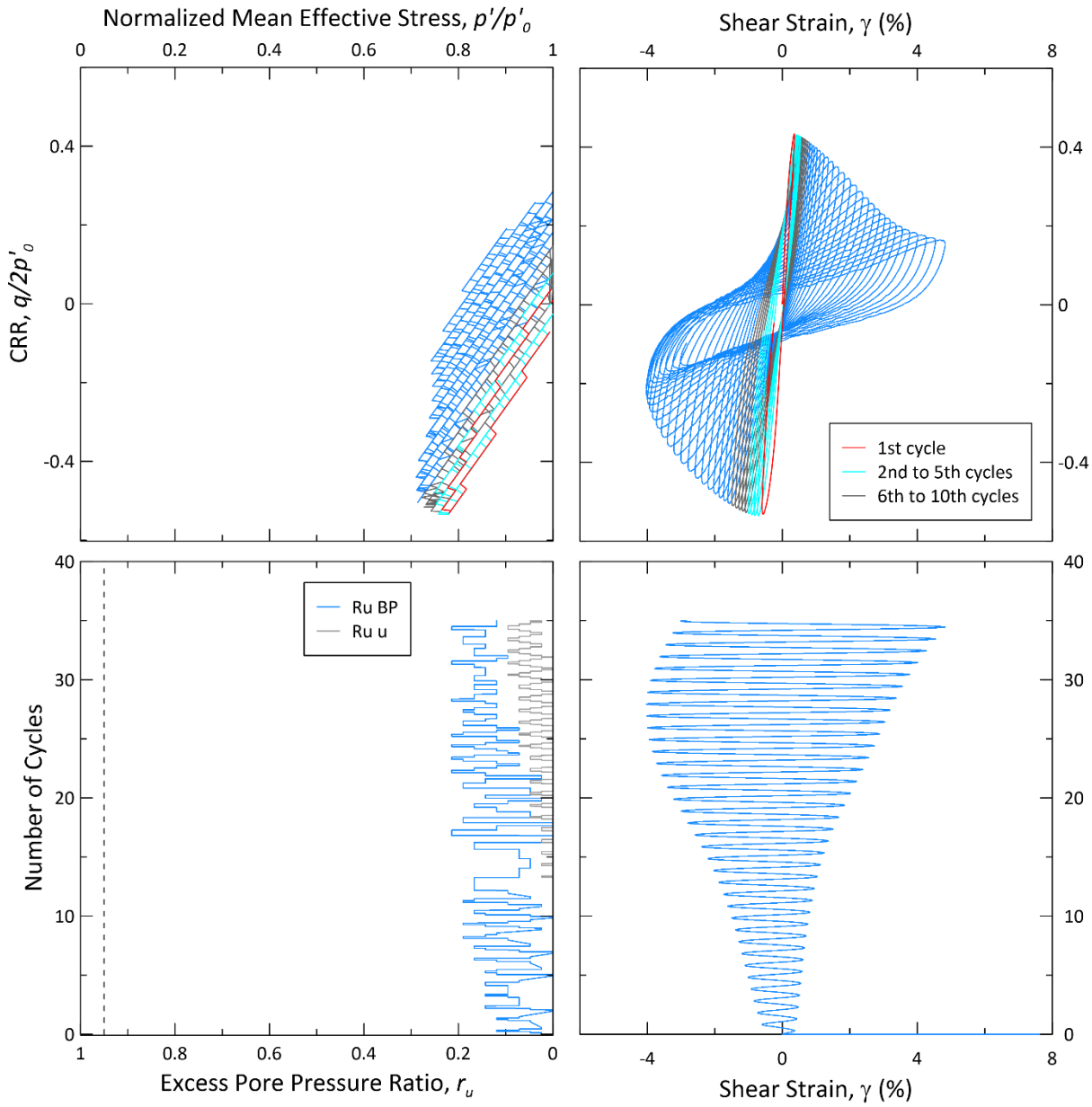

COR20-02-05GC_240-252

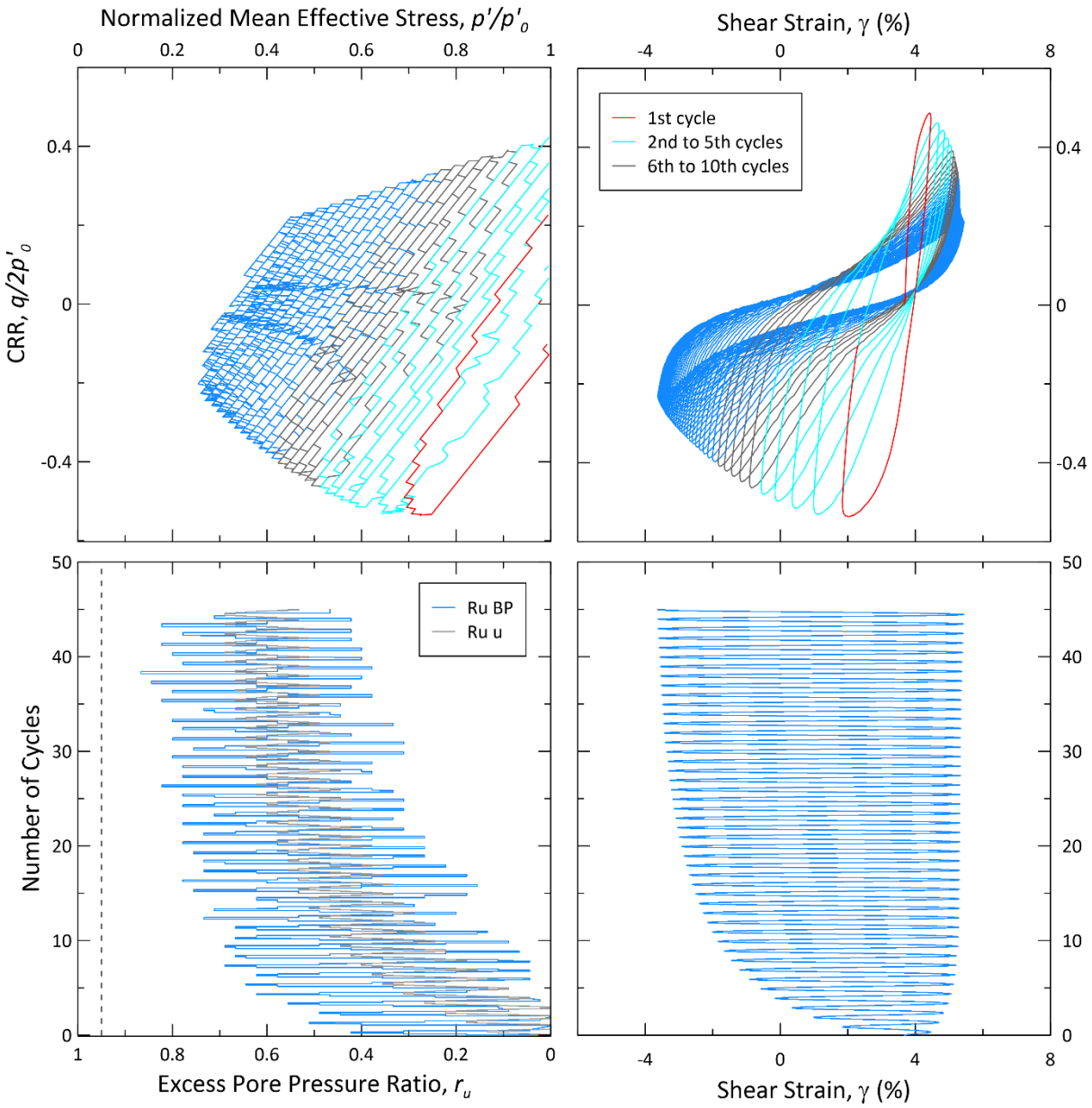

COR20-02-05GC_252-264

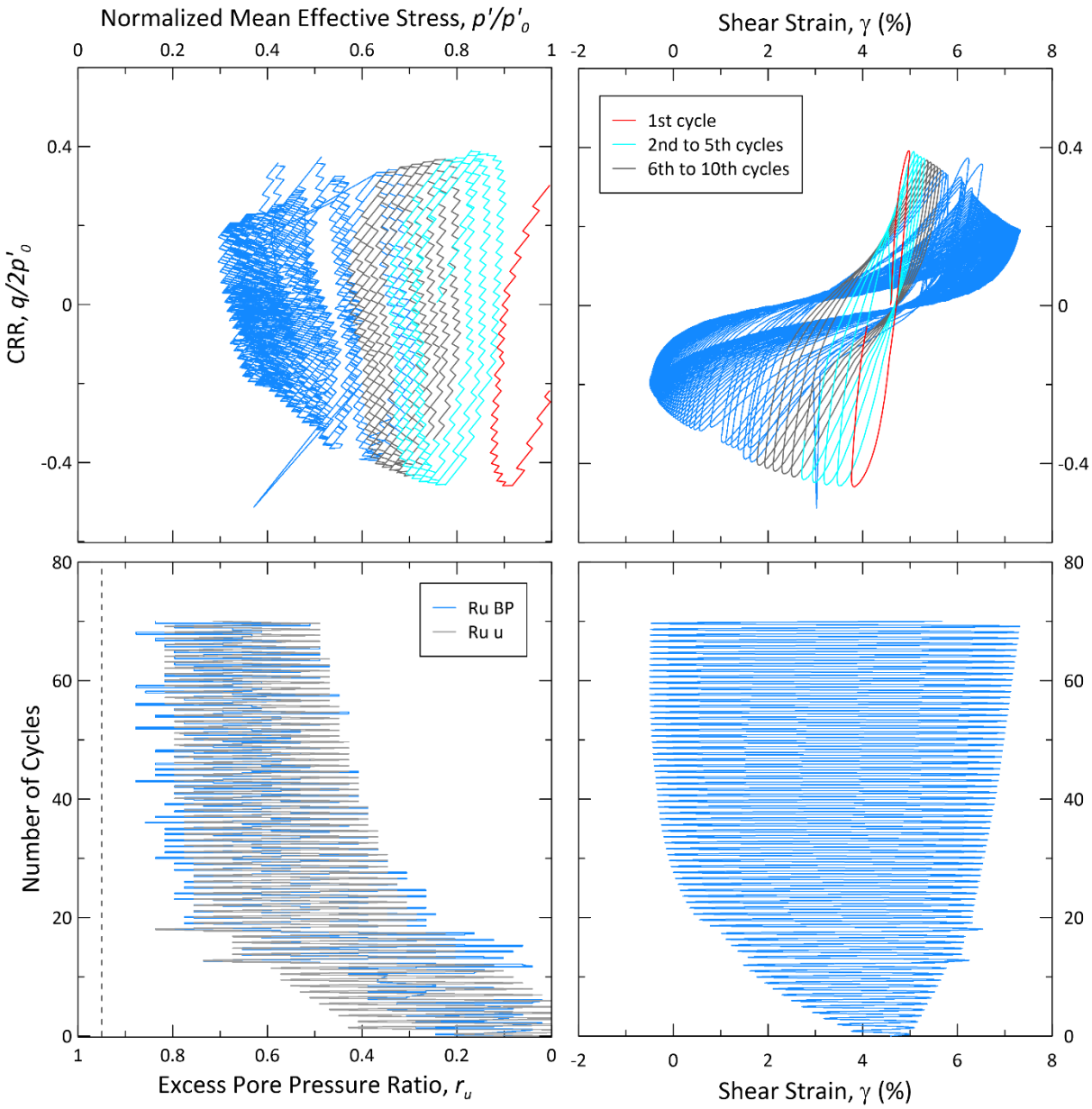

COR20-02-06GC_160-172

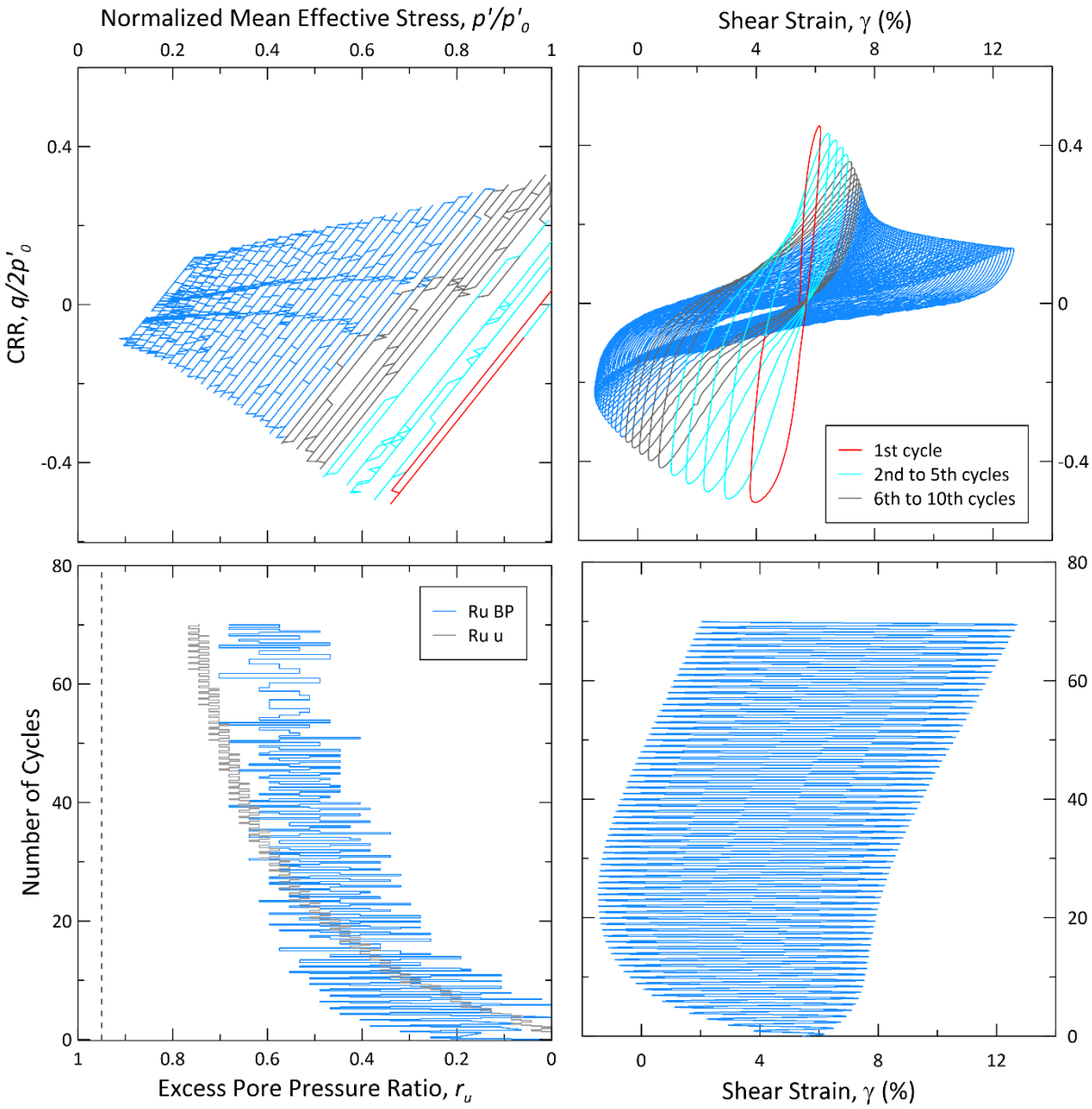

COR20-02-11GC_398-410

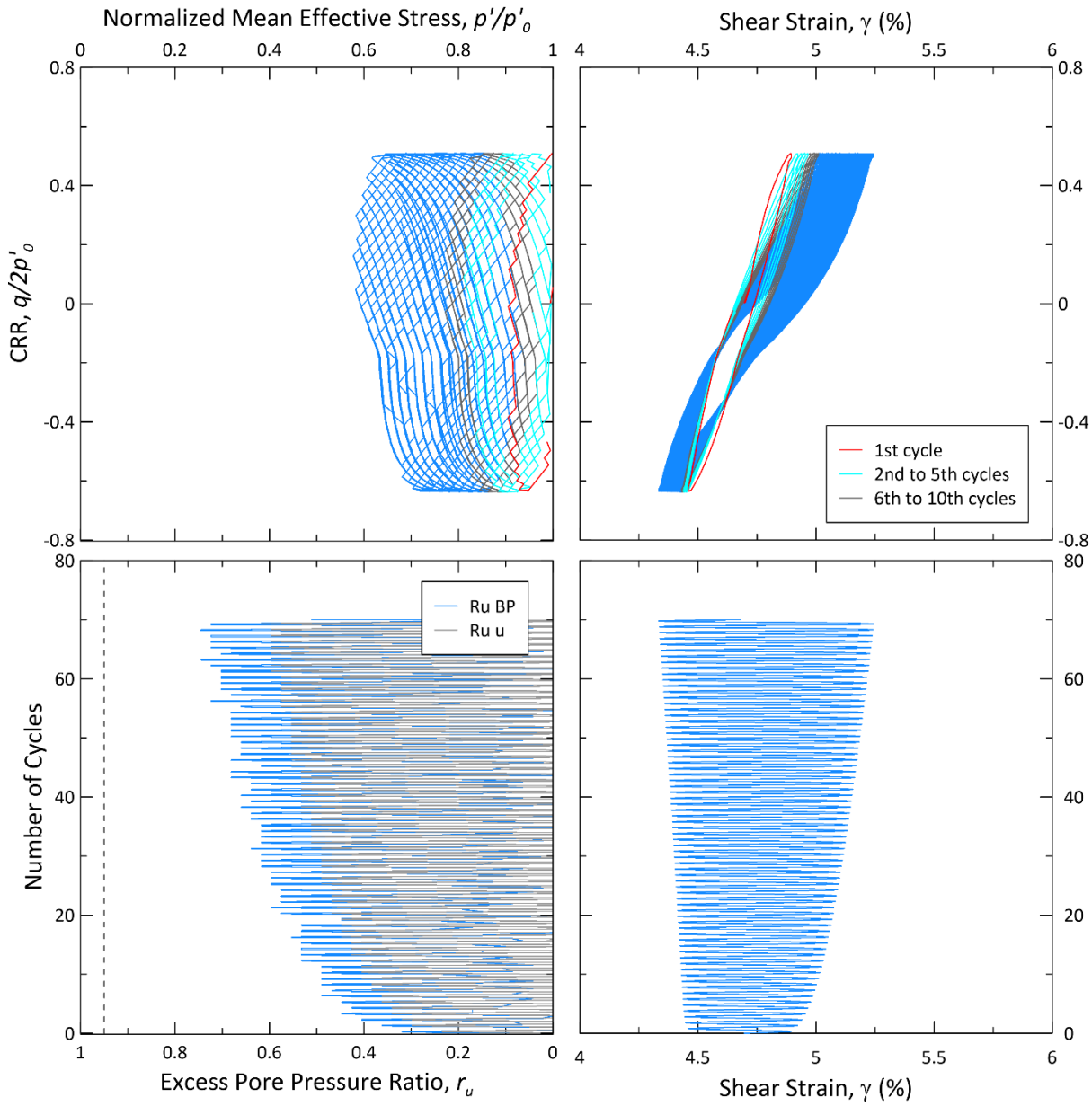

COR20-02-12GC_434-446

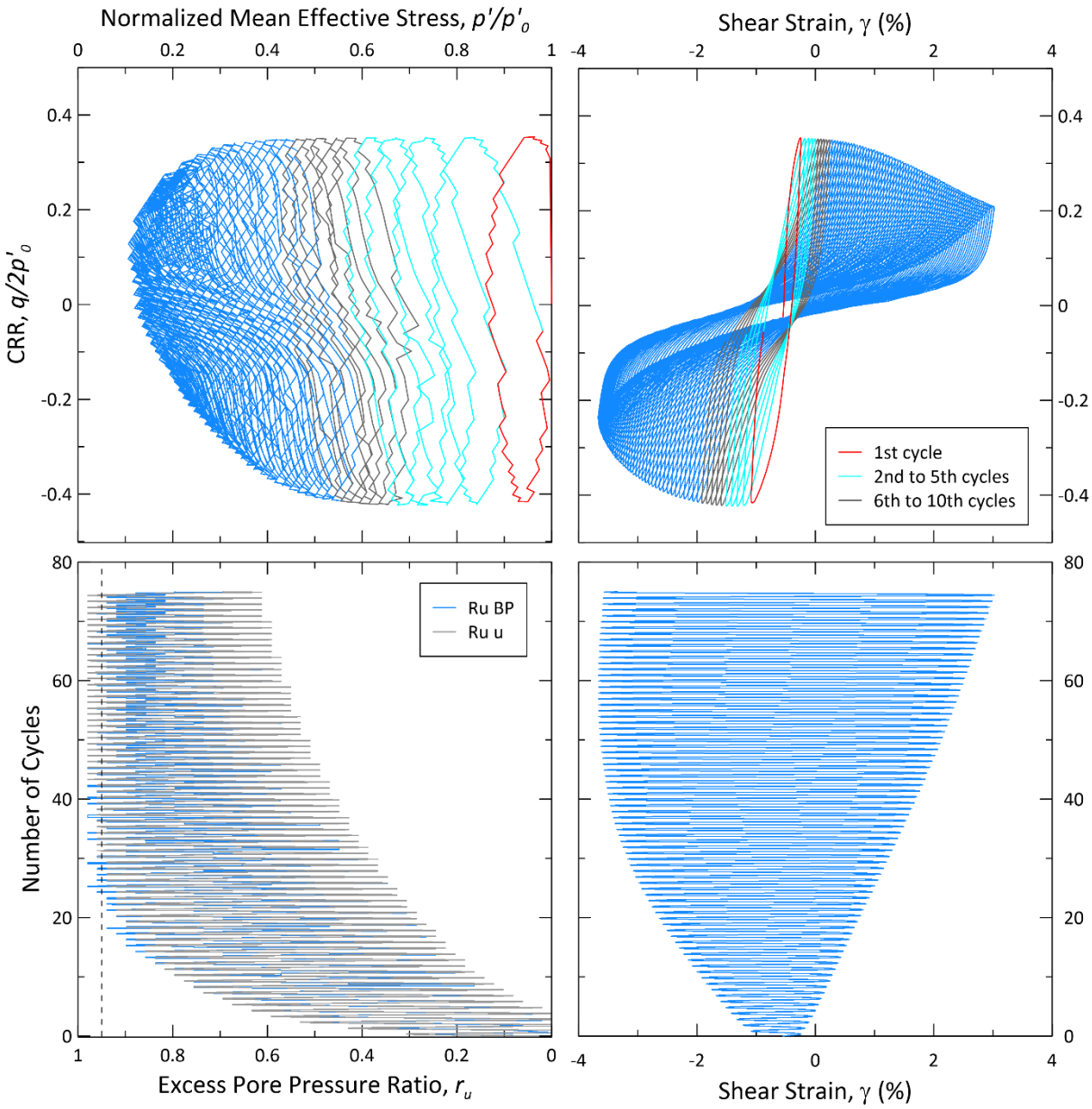

COR20-02-12GC_446-458

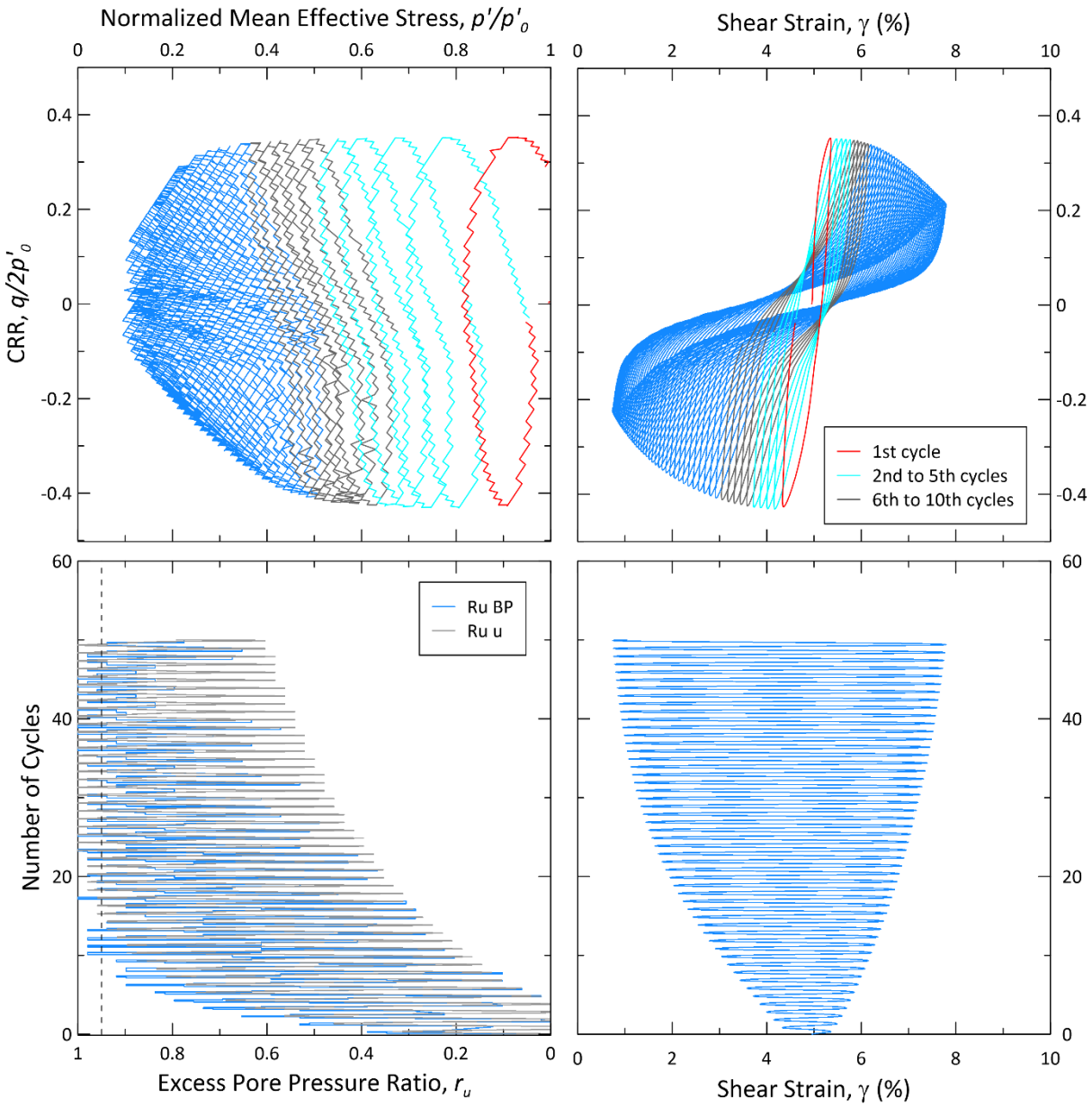

COR20-02-16GC_374-386

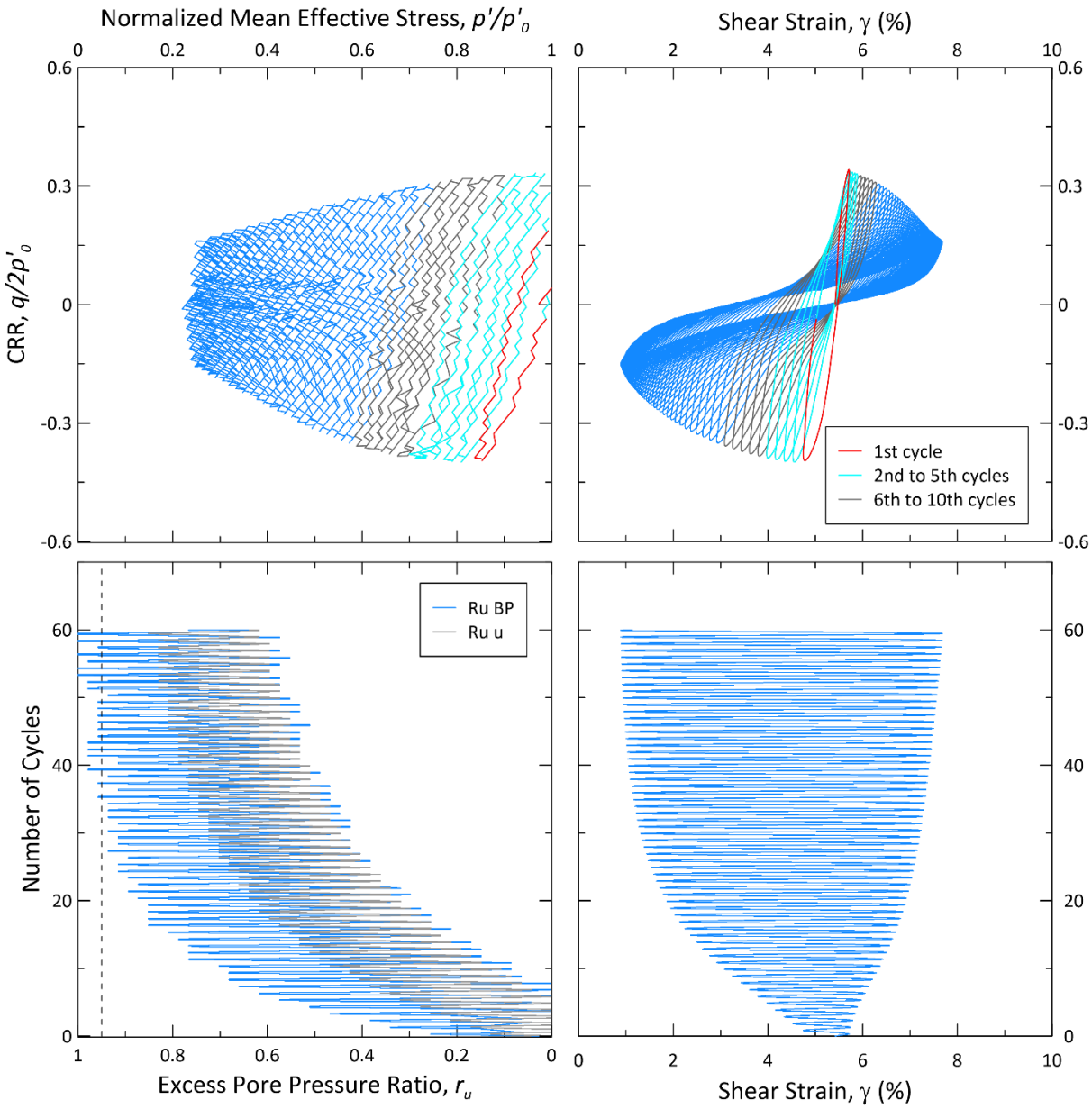

COR20-02-16GC_386-398

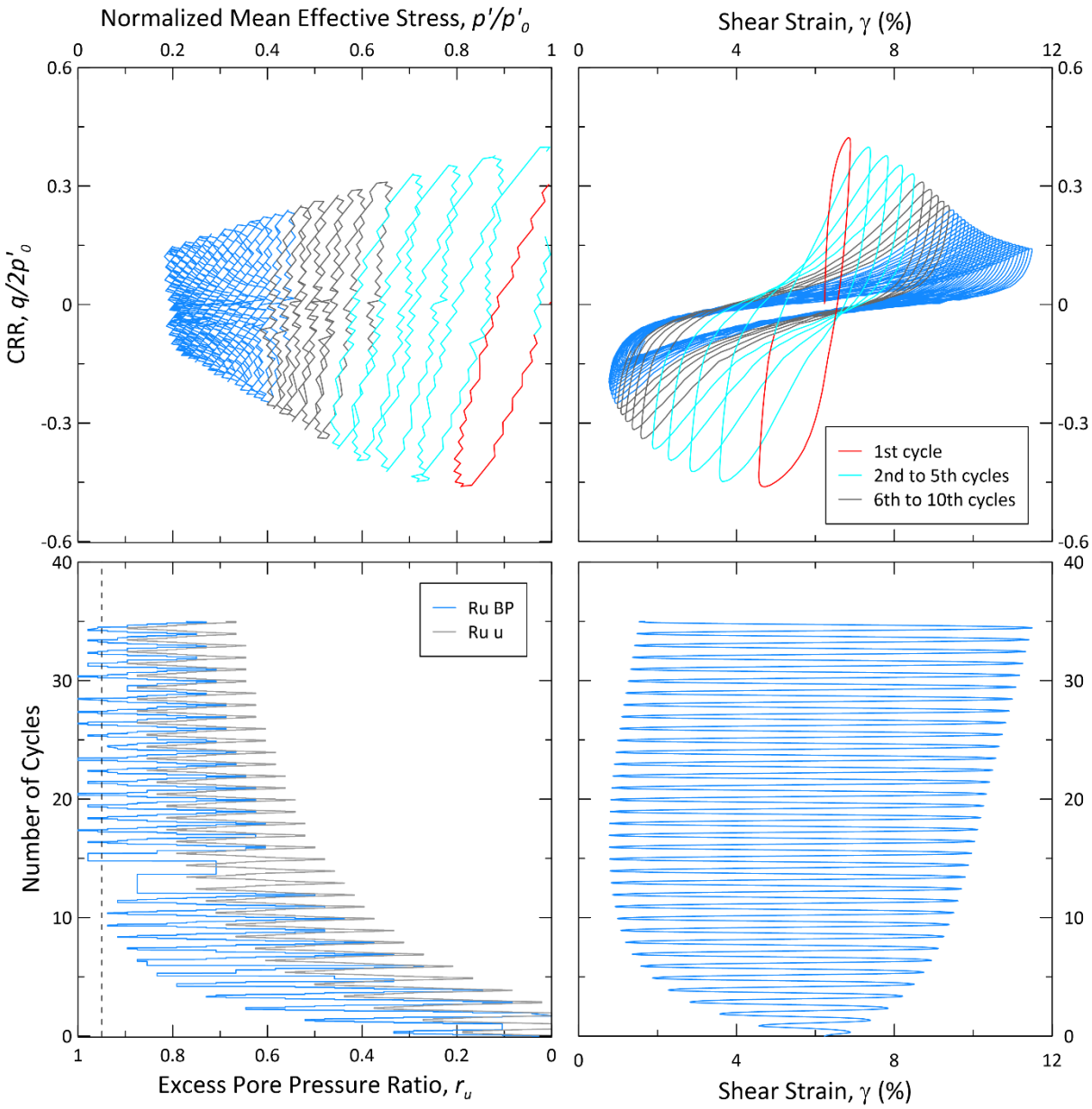

COR20-02-16GC_398-410

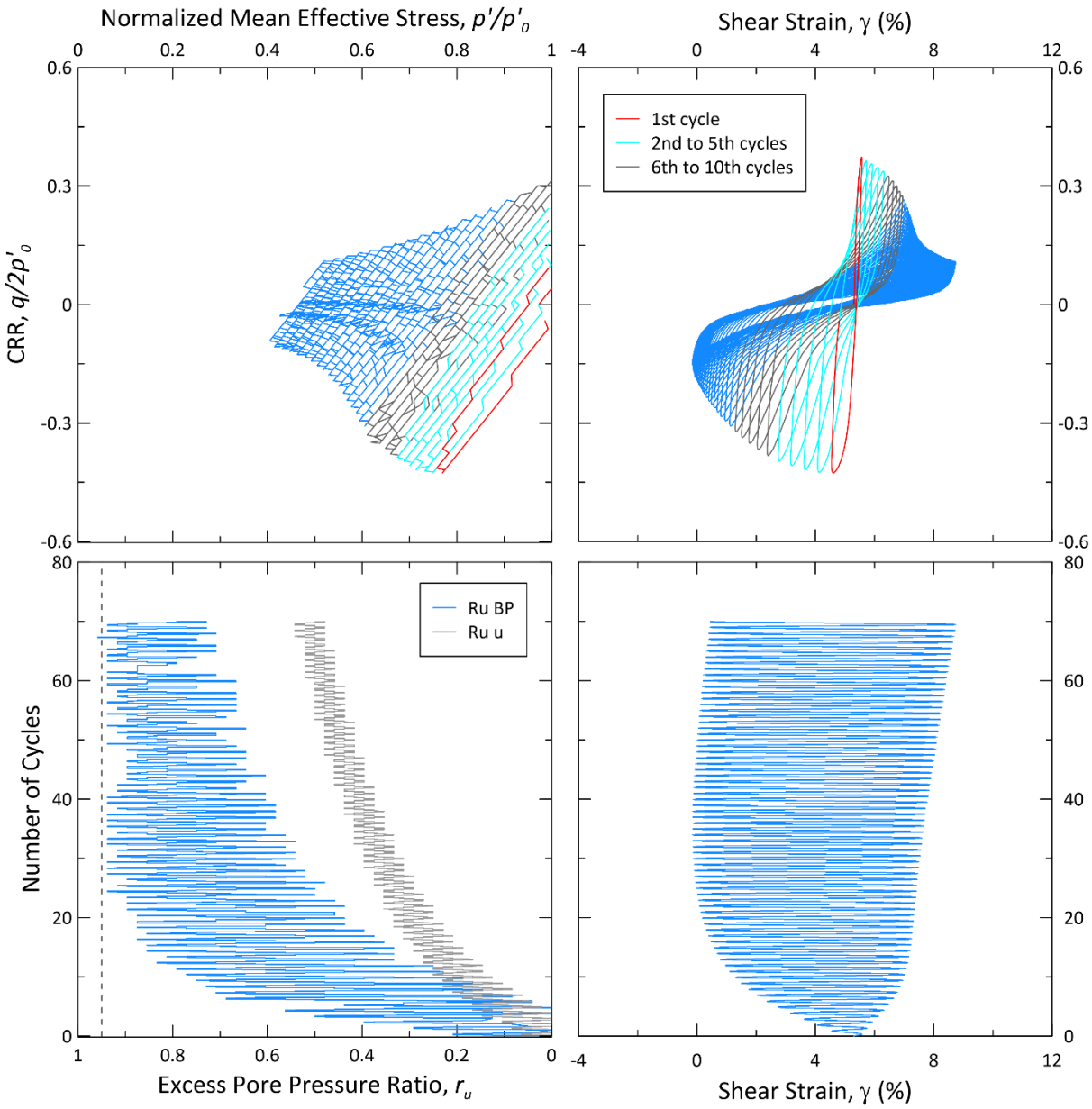

COR20-02-25GC_180-192

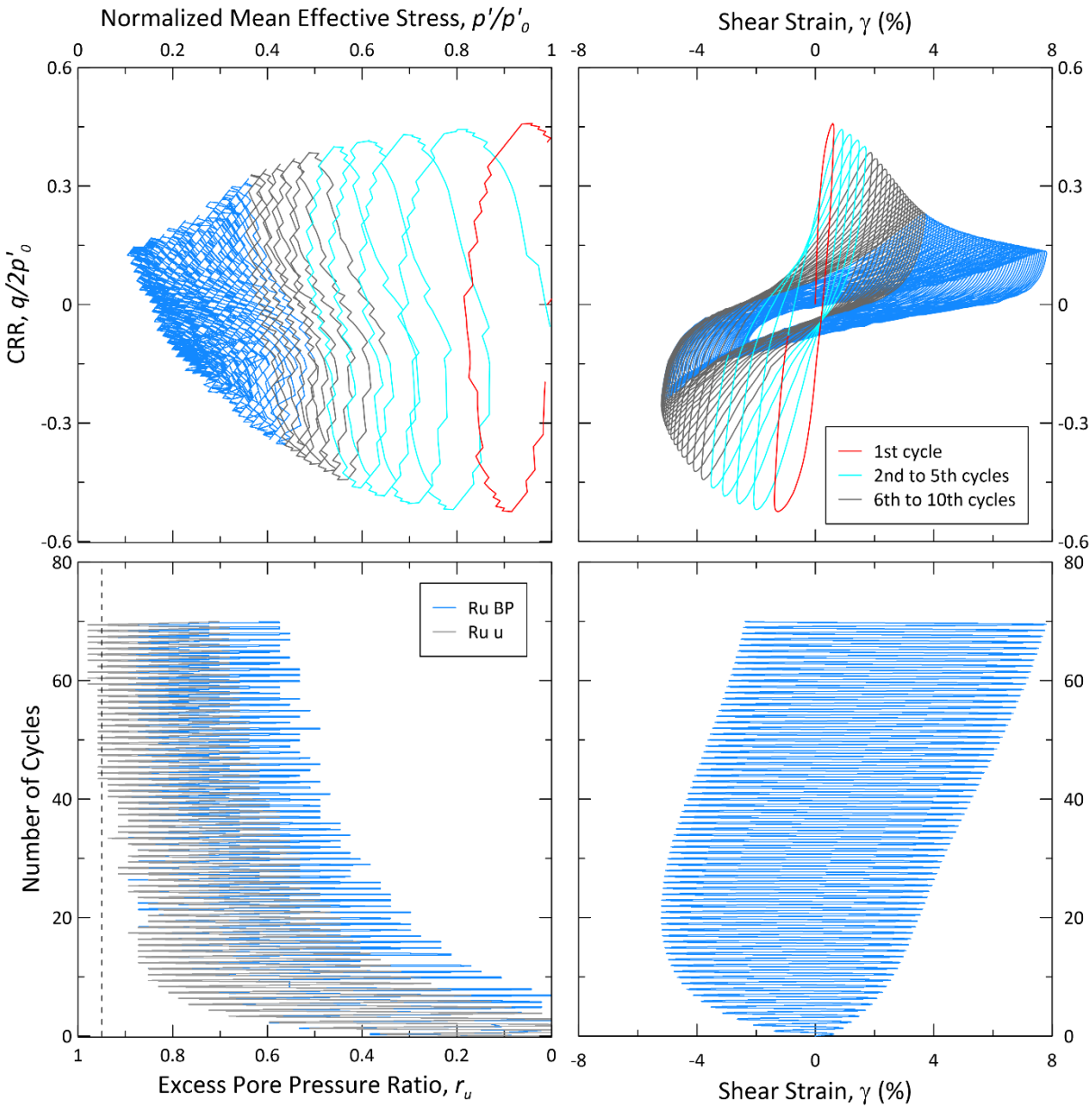

COR20-02-25GC_195-206

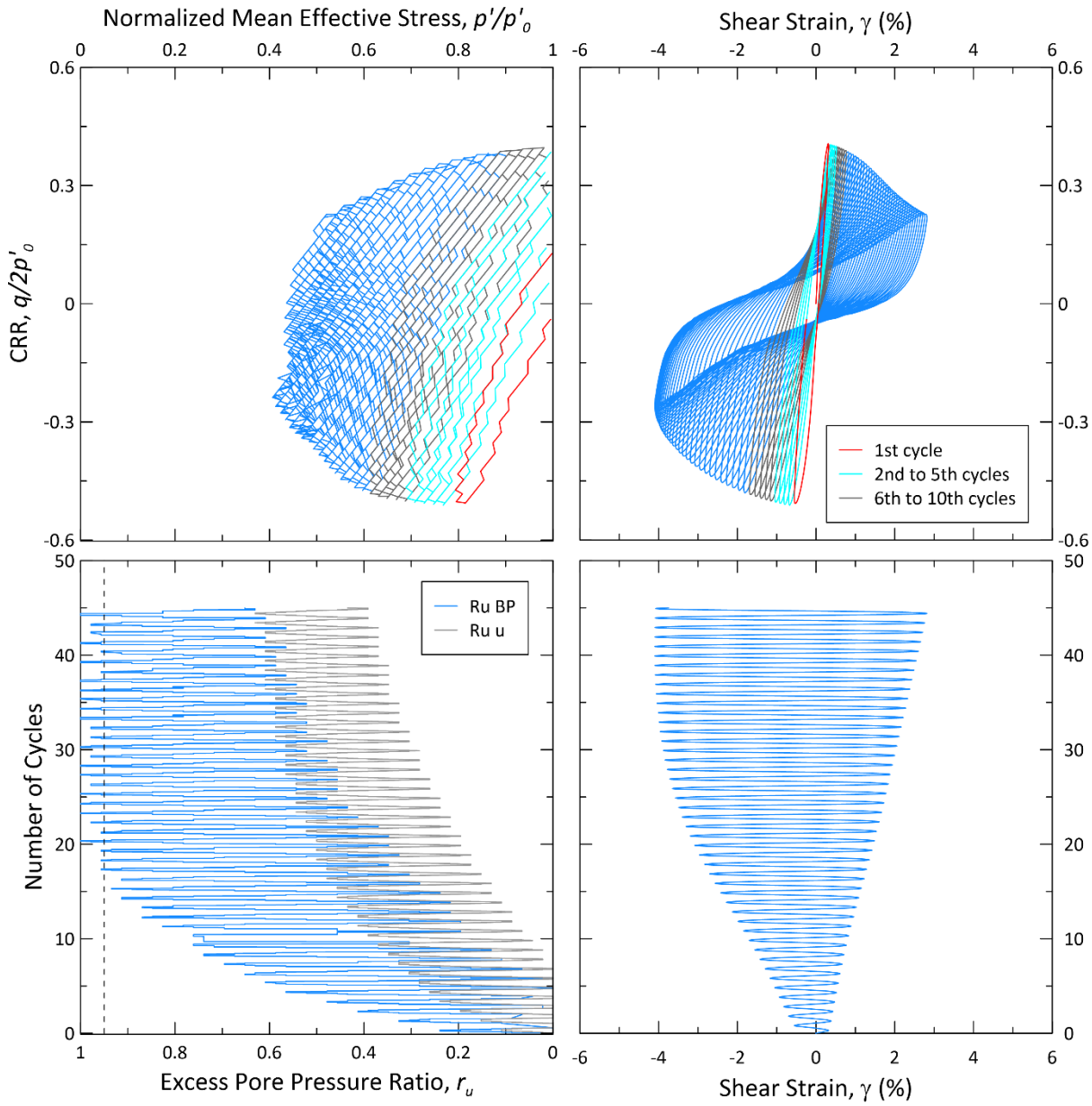

COR20-02-45GC_212-224

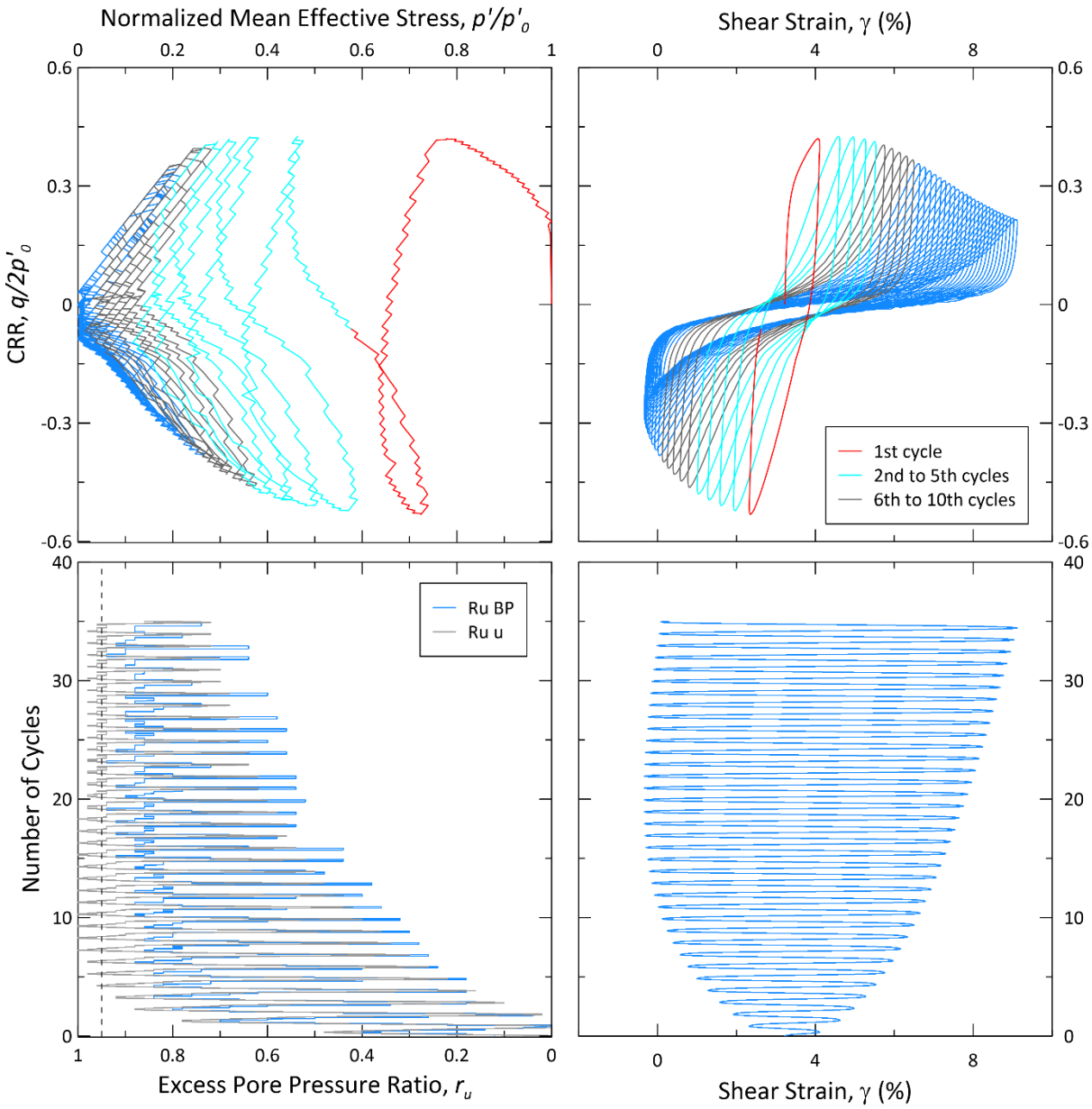

COR20-02-45GC_224-236

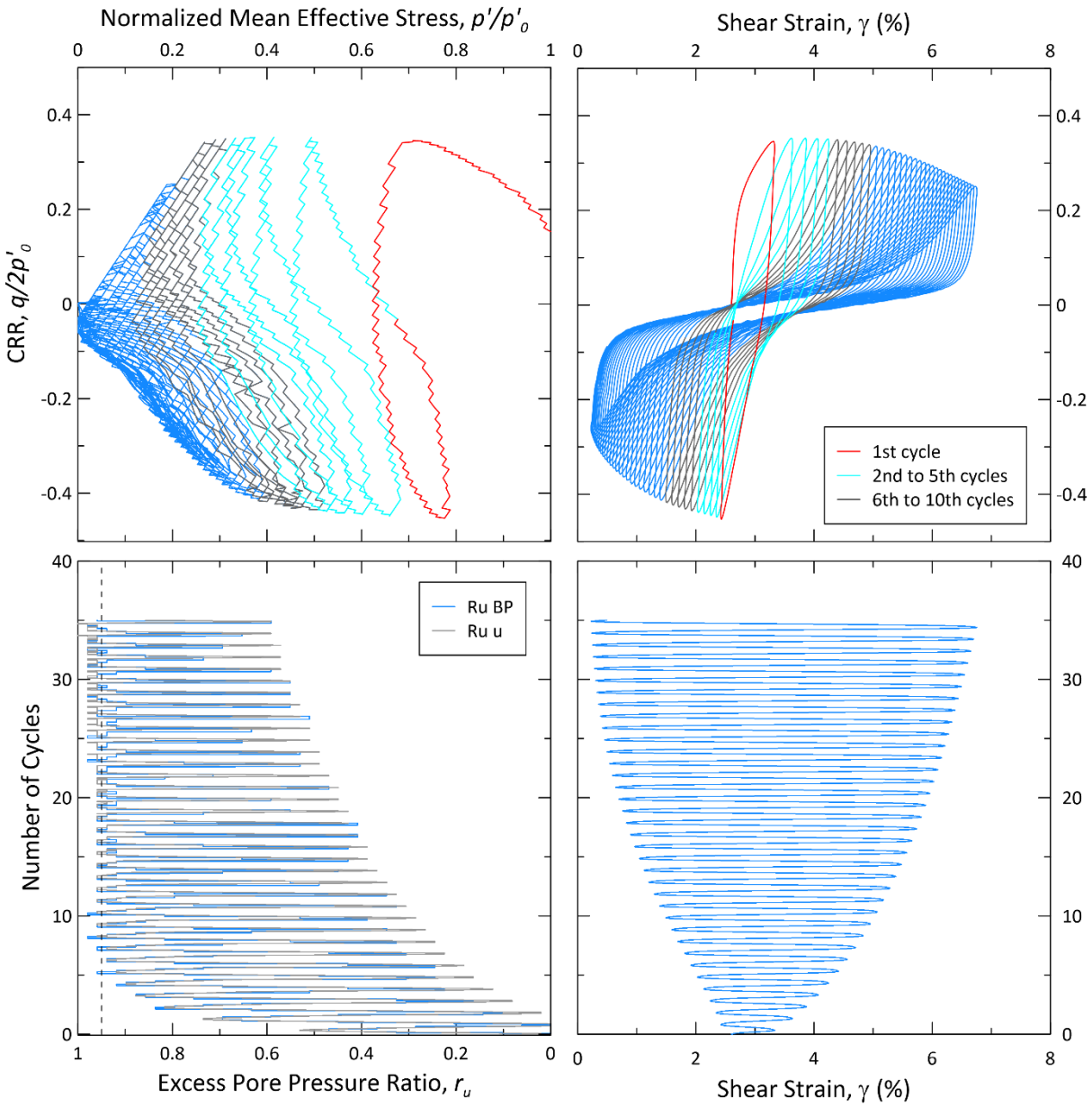

DOCTORAT SCIENCES BRETAGNE DE LA MER LOIRE ET DU LITTORAL

UBO Université de Bretagne Occidentale

Titre : Les glissements sous-marins dans l'estuaire du Saint-Laurent, Québec, Canada

Mots clés : Aléas-géologiques ; Géotechnique ; Liquéfaction ; Paléo-sismologie ; Sédimentologie ; Stabilité de pente.

Résumé : L'estuaire du Saint-Laurent, situé dans la province du Québec au sud-est du Canada, abrite près d'une centaine de glissements sous-marins. Leur présence dans cette région avec un haut niveau d'aléa sismique a conduit à supposer qu'ils ont été déclenchés par la sismicité régionale. Le présent projet de doctorat a donc pour objectif de comprendre l'origine de ces glissements sous-marins. Le projet utilise une grande quantité de données géophysiques, sédimentologiques, datations et géotechniques qui sont intégrées dans des modèles numériques.

Les glissements sous-marins de l'estuaire du Saint-Laurent ont des âges synchrones sur près de 220 km et sont corrélés aux séismes historiques majeurs. Ainsi, seule la sismicité peut les avoir déclenchés. L'établissement de cette relation permet d'identifier deux évènements sismiques antérieurs à la colonisation européenne en ~645 CE et ~1145 CE. De plus, le séisme de 1663 CE ressort comme l'évènement majeur des derniers 2000 ans car il a déclenché le plus de glissements sous-marins. Son épicentre positionné dans la région de Charlevoix n'avait pas été révisé depuis près d'un siècle. A partir des glissements sous-marins déclenchés par la liquéfaction du sédiment, l'épicentre du séisme de 1663 CE a pu être repositionné à plus de 120 km au nord-est de sa position initiale. Ainsi, il serait associé à une faille active au large de la ville de Tadoussac, proche de l'embouchure du fjord du Saguenay. Enfin, les plans de rupture des glissements sous-marins se développent aux interfaces d'unités sédimentaires qui correspondent à des transitions d'environnement de dépôt. L'intégration de ces niveaux de décollement dans des modèles numériques permettent de prédire les zones qui en cas de séisme majeur glisseront.

En conclusion, la sismicité est le facteur de déclenchement de glissements sous-marins dans l'estuaire du Saint-Laurent et cela s'explique par la liquéfaction de niveaux grossiers (silt à sable) générée par les secousses sismiques. De futurs glissements sous-marins sont susceptibles de se produire à l'avenir soulignant la nécessité d'étudier cet aléa naturel au Québec.

Title: Submarine landslide in the St. Lawrence Estuary

Keywords: Geological hazards; Geotechnics; Liquefaction; Paleoseismology; Sedimentology; Slope stability

Abstract: The St. Lawrence Estuary, located in the province of Québec in southeastern Canada, is home to almost one hundred submarine landslides. Their presence in this region of high seismic hazard has led to the assumption that they were triggered by regional seismicity. The aim of this PhD project is to understand the origin of these submarine landslides. The project comprises a huge amount of geophysical, sedimentological, age and geotechnical datas which are integrated into numerical simulations.

Submarine landslides in the St. Lawrence Estuary have synchronous ages over 220 km and are correlated with major historical earthquakes. Thus, only seismicity can have triggered them. Establishing this relationship allows us to identify two seismic events prior to European colonization around 645 CE and 1145 CE. Moreover, the 1663 CE earthquake appears to be the major event of the least 2000 years because it triggered the greatest number of submarine landslides. Its epicenter located in the Charlevoix region had not been revised for almost century. Using submarine landslides triggered by sediment liquefaction, the epicenter of the 1663 CE earthquake could be repositioned more than 120 km northeast of its originally presumed position. Thus, it could be associated with an active fault off the city of Tadoussac, near the mouth of the Saguenay Fjord. Finally, submarine landslide failure planes develop at interfaces of sedimentary units that correspond to depositional environment transitions. The integration of these levels of detachment in numerical models allows the prediction of areas that will slip in the future, in the case of a major earthquake.

In summary, seismicity is the triggering factor for submarine landslides in the St. Lawrence Estuary and this is due to the liquefaction of coarse levels (silt to sand) generated by seismic shaking. Submarine landslides are likely to occur in the future, hence the need to study this natural hazard in Québec.